

Lecture Notes in Electrical Engineering 201

Society of Automotive Engineers
of China (SAE-China)
International Federation
of Automotive Engineering Societies (FISITA)
Editors

Proceedings of the FISITA 2012 World Automotive Congress

Volume 13: Noise, Vibration
and Harshness (NVH)



 Springer

The Springer logo, featuring a white chess knight piece on a red background, followed by the word "Springer" in a white serif font.

Lecture Notes in Electrical Engineering

Volume 201

For further volumes:
<http://www.springer.com/series/7818>

Society of Automotive Engineers of China
(SAE-China) · International Federation of
Automotive Engineering Societies (FISITA)
Editors

Proceedings of the FISITA 2012 World Automotive Congress

Volume 13: Noise, Vibration
and Harshness (NVH)



 Springer

The Springer logo, consisting of a stylized chess knight (horse) facing left, positioned to the left of the word 'Springer' in a serif font.

Editors
SAE-China
Beijing
People's Republic of China

FISITA
London
UK

ISSN 1876-1100 ISSN 1876-1119 (electronic)
ISBN 978-3-642-33831-1 ISBN 978-3-642-33832-8 (eBook)
DOI 10.1007/978-3-642-33832-8
Springer Heidelberg New York Dordrecht London

Library of Congress Control Number: 2012948289

© Springer-Verlag Berlin Heidelberg 2013

This work is subject to copyright. All rights are reserved by the Publisher, whether the whole or part of the material is concerned, specifically the rights of translation, reprinting, reuse of illustrations, recitation, broadcasting, reproduction on microfilms or in any other physical way, and transmission or information storage and retrieval, electronic adaptation, computer software, or by similar or dissimilar methodology now known or hereafter developed. Exempted from this legal reservation are brief excerpts in connection with reviews or scholarly analysis or material supplied specifically for the purpose of being entered and executed on a computer system, for exclusive use by the purchaser of the work. Duplication of this publication or parts thereof is permitted only under the provisions of the Copyright Law of the Publisher's location, in its current version, and permission for use must always be obtained from Springer. Permissions for use may be obtained through RightsLink at the Copyright Clearance Center. Violations are liable to prosecution under the respective Copyright Law.

The use of general descriptive names, registered names, trademarks, service marks, etc. in this publication does not imply, even in the absence of a specific statement, that such names are exempt from the relevant protective laws and regulations and therefore free for general use.

While the advice and information in this book are believed to be true and accurate at the date of publication, neither the authors nor the editors nor the publisher can accept any legal responsibility for any errors or omissions that may be made. The publisher makes no warranty, express or implied, with respect to the material contained herein.

Printed on acid-free paper

Springer is part of Springer Science+Business Media (www.springer.com)

Contents

Part I Chassis Vibration and Noise Control

Parameters Sensitivity Analysis of Self-Excited Vibration of Tires . . .	3
F2012-J01-001	
Xianwu Yang and Shuguang Zuo	
Shimmy Identification Caused by Self-Excitation Components at Vehicle High Speed	15
F2012-J01-002	
Fujian Min, Wei Wen, Lifeng Zhao, Xiongying Yu and Jiang Xu	
Nonlinear Transient Dynamic Analysis of Disc Brake Squeal Using Improved Hilbert-Huang Transform	25
F2012-J01-003	
Xiandong Liu, Haixia Wang, Yingchun Shan and Tian He	
Application of an Experimental Tire Model for Comfort Analysis: Requirement for Accurate Low Frequency Tire-Patch Inputs	39
F2012-J01-009	
Alessandro Lepore, Theo Geluk, Massimiliano Gobbi and Ben Meek	

Part II Transmission Vibration and Noise Control

Torsional Finite Element Analysis of Driveline Torsional Vibration for a Front Wheel Driveline Vehicle Development	55
F2012-J02-001	
Yuanfeng Xia, Hongcheng Li, Xiong Tian, Hongying Wang and Yu Tang	

Transfer Paths Identification and Optimization of Transmission Gear Rattle Noise	73
F2012-J02-002 Tian Xiong, Hongcheng Li, Hongying Wang, Yang Xianwu, Yu Tang and Yuanfeng Xia	
Study on Driveline Component Torsional Stiffness Effect on RWD Driveline Torsional Vibration Modes	87
F2012-J02-003 Qian Zhao	
Reduction of Structure-Borne Noise by Simulation	103
F2012-J02-004 Sabine Sanzenbacher and Bernd Bertsche	
Dynamic Characteristics of Vehicular Planetary Gears Influenced by Engine Excitation and Backlash Based on Nonlinear Torsional Vibration Model	115
F2012-J02-005 Hui Liu, Zhongchang Cai and Changle Xiang	
Dynamic Optimization of Vehicle Planetary Transmission Based on GA and FEA	127
F2012-J02-007 Changle Xiang, Cheng Wang, Hui Liu and Zhongchang Cai	
NVH Optimization of Vehicle Powertrain	141
F2012-J02-008 Shouwei Lu, Huihua Feng, Zhengxing Zuo, Liyun Kang and Bo Yu	
Input Torque Shaping for Driveline NVH Improvement and Torque Profile Approximation Problem with Combustion Pressure	151
F2012-J02-009 Kazuhide Togai and Michael Platten	
Wheel Load Oriented Control of Semi-Active and Active Suspension Systems Using Pre-Located Road Sampling	167
F2012-J02-011 Sebastian Spirk and Kay-Uwe Henning	

Part III Engine Vibration and Noise Control

Optimization of the Range Extender Mounting System for Electric Vehicle 185
 F2012-J03-001
 Yutao Luo and En-ming Lai

Middle and High Frequency Sound Attenuation Optimization of Air Cleaner 197
 F2012-J03-002
 Liang Yang, Xiaohong Kuang, Shuo Zhang and Haiyan Zhang

NVH Performance Optimization of Cylinder Head in Concept Stage 209
 F2012-J03-004
 Zhanhui Li, Lei Zhang, Xiaoyu Ai, Fengqin Li and Yongjiang Xu

Rattle Simulation Analysis of a Manual Gearbox 219
 F2012-J03-005
 Xiaoying Ma, Zhan Zhangsong, Guoming Peng, Jun Lan, Bo Yu, Lei Zhang and Xiaofeng Li

Study about the Relationship Between Power-Train Modal and Connecting-Plane 235
 F2012-J03-007
 Yongjiang Xu, Zhangsong Zhan, Wenjun Chen, Yanlin Shi, Hangkui Lu, Junping Xue and Xin Zhao

Investigation on the Vibration of the Engine Fead Accessory Driving Belt 249
 F2012-J03-009
 Yanping Ding, Yifeng Dong, Hanjie Liu, Jincai Yang, Qingwei Gu and Liang Zhang

The Effect of EMS Calibration on Noise Control of Turbocharger for Gasoline Engine 261
 F2012-J03-010
 Pengyuan Liu, Shuxia Miao, Hui Zheng, Xianli Hu, Biao Du and Jugang He

The Method of Accurate Sound Source Localization for the Engine Abnormal Noise	269
F2012-J03-011 Jincai Yang, Zhangsong Zhan, Hanjie Liu, Liang Zhang, Lingfeng Qian and Yanping Ding	
Sound Source Identification Based on Acoustic Source Quantification by Measuring the Particle Velocity Directly	279
F2012-J03-012 Byung Hyun Kim, Tae Jin Shin and Sang Kwon Lee	
Noise Reduction Potential of an Engine Oil Pan	291
F2012-J03-018 Tommy Luft, Stefan Ringwelski, Ulrich Gabbert, Wilfried Henze and Helmut Tschöke	
Experimental Investigation of the Pulsation Noise Induced by Automotive Turbocharger Compressors	305
F2012-J03-019 Ho-il Park, Sungyou Hong, Jubong Seo and Hyeongill Lee	
Rotordynamics for Turbocharger Application Using Matlab Software	317
F2012-J03-021 Cosmin Boricean, Gheorghe Alexandru Radu and Anghel Chiru	
 Part IV Body Vibration and Noise Control	
A Systematic Approach for Rattle Problem Detection and Prevention of Seat Belt Retractors	333
F2012-J04-002 Youmin Guo, Xiaoping Gong, Zhiqiang Tu, Zhonghua Wu, Yangjia She, Peng Xu and Zhigong Li	
A Study on Optimization Design of Engine-Room NVH for a Modified Vehicle	341
F2012-J04-003 Honghua Li, Fengwei Sun, Hao Xu, Jielong Chen, Aijun Jin and Fuquan Zhao	
Mechanism of Vibration Noise Transfer of Trimmed Body	355
F2012-J04-006 Huimin Zhuang, Shuo Zhang, Xiaofeng Qu and Ye Zhang	

Automotive Concept Modelling: Optimization of the Vehicle NVH Performance. 365
 F2012-J04-008
 Naser Nasrolahzadeh, Mohammad Fard, Milad Tatari and Mohammad Mahjoob

Part V Vehicle Vibration and Noise Control

Improvements of Steering Wheel’s Idle Shaking. 379
 F2012-J05-002
 Wenku Shi, Guangming Wu, Shichao Wang and Zhiyong Chen

Squeak and Rattle Performance Degradation and Prevention in a Vehicle Design and Development Process 393
 F2012-J05-003
 Youming Guo, Zhonghua Wu, Yangjia She, Peng Xu, Xiaoli Duan, Yun Zhang and Li Tang

Test and Simulation Integrated Transfer Path Analysis and Optimization of the Steering Wheel Vibration in Idle 405
 F2012-J05-009
 Ran Xie, Zhifeng Liu, Shucheng Long and Zilong Tian

Study on Mount Matching Optimization for Removing Powertrain Abnormal Low Frequency Vibration 417
 F2012-J05-012
 Feili Dai, Wei Wu, Hailin Wang, Qiang Liu, Fangwu Ma and Fuquan Zhao

Study on Influence of High-Performance Acoustic Materials on a Vehicle’s NVH Performance 431
 F2012-J05-013
 Yang Yue, Qiang Liu, Yu Xie, Meng Zhang and Fuquan Zhao

The Identification and Countermeasure Analysis of Vehicle Idle Vibration 443
 F2012-J05-014
 Ye Zhang, Hui Wang, Qingjun Zhu, Yanghui Xu and Lie Wu

Study on Automotive Interior Structure-Borne Sound Based on TPA. 457
 F2012-J05-015
 Lingyun Yao and Guangrong Zhang

The Vibration Analysis of Eco-Friendly Vehicle Based on the Electric Motor Excitation	471
F2012-J05-016	
Peicheng Shi and Yuan Shang	
Apply Near-Field Acoustic Holography to Identify the Noise Source of Pass-by Vehicles	481
F2012-J05-021	
Lingzhi Li, Jun Li, Bingwu Lu and Yinjie Liu	
Part VI Analysis and Evaluation of In-Car Vibration & Noise	
Application Research of Statistical Energy Analysis on Vehicle Sound Package	507
F2012-J06-003	
Xiaoxuan Zhang, Xingrang Wu, Yuhu Cheng, Hongying Jin and Jun Zhang	
Optimization of Subframe Mounting System to Reduce the Interior Booming	521
F2012-J06-004	
Jianghua Fu, Xiaomin Xu, Jingbo Li, Dongzheng Ma and Debin Yu	
Disturbing Noise Identification and Sound Quality Research on Car Generator	535
F2012-J06-010	
Yanfang Hou, Guohua Han, Yaozhen Zhao and Xueying Xu	
Characterization of the Automotive Seat Structural Dynamics	541
F2012-J06-013	
Milad Tatari, Mohammad Fard, Naser Nasrolahzadeh and Mohammad Mahjoob	
Part VII Wind Noise Control Technology	
The CFD and Noise Simulating Research of Fan Based on the Dipole Noise Theory	555
F2012-J07-001	
Qing Zhu, Zhaocheng Yuan, Chong Liu and Jiayi Ma	

Wind Noise Testing at Shanghai Automotive Wind Tunnel Center . . . 571
 F2012-J07-002
 Yinzhi He, Zhigang Yang and Yigang Wang

Part VIII Vibration and Noise Testing Technology

**An Analysis of Vehicle Engine Vibration Signals with Digital
 Order Tracking Approaches** 581
 F2012-J08-001
 Wei Shao, Xiaofeng Wang, Dapeng Liu and Zong-an Shao

**A New Approach to the Presentation of Vibration Phenomena
 in Vehicles** 591
 F2012-J08-002
 Thomas Berberich, Peter Gebhard, Stephan Bohlen,
 Oliver Danninger and Markus Lienkamp

**Research on Noise Testing and Analysis of an
 Automatic Transmission** 599
 F2012-J08-003
 Wenfeng Zhan, Jian Wu, Fake Shao and Chuhua Huang

**The Application of Doppler Laser Vibrometer in the Engine
 NVH Dynocell Test** 607
 F2012-J08-004
 Jin Yang, Jun Lan, Xu YongJiang, Jin Cai, XiaoNan Zhang,
 HanJie Liu and YanLin Shi

Judder Test and Analysis for Electric Vehicle 619
 F2012-J08-005
 Xiumin Shen, Yong Wang, Bin Li and Lei Cai

**Tracking Algorithm and Its Implementation
 of the Vehicle BSR Noise Location** 629
 F2012-J08-008
 Choi Sung Uk, Kang Jun-Goo, Lee Tae-Woong and Mog Mu Gyun

**Contribution of Pass-by Noise Sources with Acoustic
 Holograph and Dynamic Transfer Path Model** 637
 F2012-J08-009
 Sifa Zheng, Jiabi Dan, Peng Hao and Xiaomin Lian

Research of Acoustic Parts in Vehicle Sound Transmission
Loss Test Method 645
F2012-J08-012
Xiufeng Wang and Jie Shi

Research of the Powertrain in Vehicle Sound Power Test Method . . . 653
F2012-J08-013
Xiufeng Wang and Jie Shi

Part IX Other

Research on Whine Noise of Automotive Radiator
Fan During Decelerating 663
F2012-J09-002
Wei Li, Xiaoping Gong and Haifeng Xu

Electromagnetic Noise Study of Permanent Magnet Synchronous
Motor for Electric Vehicle 677
F2012-J09-004
Xiumin Shen, Yong Wang, Bin Li and Yuanjian Yue

Evaluation and Improvement of Door Slamming Sound Quality 689
F2012-J09-005
Fangwu Ma and Dongmei Guo

Part I
Chassis Vibration and Noise Control

Parameters Sensitivity Analysis of Self-Excited Vibration of Tires

Xianwu Yang and Shuguang Zuo

Abstract To resolve the issues of multi-polygonal wear of tire with high-speed, a multi-dynamic model, considering the four inter-coupling degrees of toe angle, camber angle, vertical vibration and self-excited vibration of tread along with the lateral direction, is built. The model is motivated by the component velocity of vehicle driving speed along with the lateral direction of tire and the sensitivity analysis of parameters, affecting the bifurcation speeds of vehicle, is gained by a numerical simulation method. At the end of this paper, several control strategies with crucial engineering significance are concluded to suppress the self-excited vibration of tire, and then decrease the multi-polygonal ware of tread.

Keywords Multi-polygonal · Self-excited vibration · Friction coefficient · Bifurcation

F2012-J01-001

X. Yang (✉)

Changan Auto Global R&D Center, Beijing 401120, People's Republic of China
e-mail: sunqiemail@163.com

X. Yang

State Key Laboratory of Vehicle NVH and Safety Technology, Chongqing 401120,
People's Republic of China

S. Zuo

Automotive College of Tongji University, Shanghai 201804, People's Republic of China

1 Introduction

With the development and popularization of expressway, vehicles running time on freeway increase significantly, as a result of that, a polygonal wear caused by self-excited vibrations often occurs on the tires. This wear can lead to tires' early retirement and cause some seriously traffic accident, which severely damage the vehicle manufacturers' image. There are some potential reasons responsible for this kind of uneven wear, such as vehicle's dynamic characteristics and suspension parameters. Other reasons could be tire structure parameters and tread pattern of tire.

Many researchers [1–4] have been spent much time focusing on micro and macro mechanism of interaction between tread and road to study tire's uneven wear, however, a reasonable theoretical method has not been found out yet. In Japan, Atsuo Sueoka [5] research team successfully finished an experiment that two rotating machinery can generate a polygon to the tire wear, however, the model took no account of dynamic toe angel and multiple degrees of vibration.

Based on the previous study of automotive college of Tongji University [6, 7], more researches are forced on studying the interaction mechanism between tread and pavement. A four degree-of-freedom dynamic vibration model of suspension-tire-tread, taking time-delay into account, is established to study the range of vehicle speed to motivate self-excited vibration and the relationship of vibration character and speed.

2 Choice of Friction Co-efficient

It is much difficult to clearly describe the friction characteristic in building a tire model that reflects the force changing between tread and pavement. The friction coefficient is consist of dynamic friction coefficient and static friction coefficient, and the switch between the two kinds of coefficients, which is very common in tire driving, is the most complicated problem to understand the mechanism. An over-simplified friction model can't describe the changing laws correctly while an over-complicated model is hard to get its numerical simulation results, therefore, it is a critical task to establish the right friction model to analyze the self-excited vibration motivated by friction force.

Friction coefficient is often considered as a constant or just an experiential expression increasing or decreasing with the variation of relative slip velocity in a tire-road contact model [8]. However, by means of a friction experiment of rubble block, it is confirmed that the friction coefficient is increasing linearly at first and then decreasing with the variation of relative slip velocity. The decreasing trend of friction coefficient is changing rapidly at first and then getting slow [9].

In 1995, C. Canudas de wit proposed a Luge model [10], which was an improvement of bristle model. Compared with the numerous random elastic characteristic of bristle model, Luge model provides a mean deformation of those

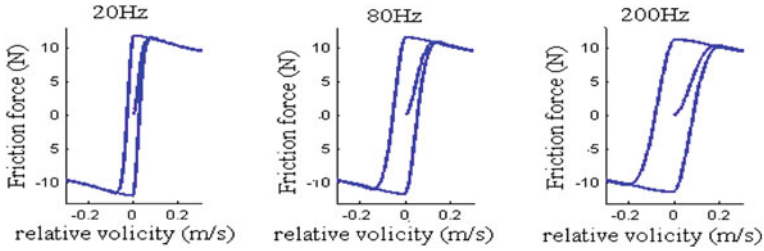


Fig. 1 Friction characteristic curves with different excitation frequencies

elastic characteristic, meanwhile, hysteresis characteristic and adherence friction between the two contact surfaces are also considered in Luge model. The Luge model equation can be written as expression (1).

$$\begin{cases} F = \sigma_0 z + \sigma_1 \frac{dz}{dt} + \sigma_2 v_r \\ \frac{dz}{dt} = v_r - \frac{\sigma_0 |v_r|}{G(v_r)} \cdot z \\ G(v_r) = F_c + (F_s - F_c) e^{-|v_r/v_s|^\delta} \end{cases} \quad (1)$$

where σ_0 is the stiffness of bristle, σ_1 is the damping coefficient of bristle, σ_2 is the relative viscous damping coefficient, z is the mean elastic deformation of bristle, v_r is the relative velocity of the two objects contacting with each other, v_s is the Stribeck velocity, δ is the Stribeck exponent, F_s is the maximum static friction force, F_c is the sliding friction and F is the total friction force.

As shown in Fig. 1, the Luge model has almost the same friction characteristics with static friction model while the variation frequency of relative velocity is low. With the increase of variation frequency of relative velocity, the dynamic hysteresis characteristics of Luge model is becoming more and more obviously, which is accordant with the friction characteristics between tread and pavement.

3 Self-Excited Vibration and Analysis of Influencing Factors for Tire Wear

3.1 Classification of Self-Excited Vibration

Self-excited vibration is caused by negative slope of friction coefficient. In a classical vibration system, the vibration energy becomes lower and lower because of the inter consumption with a phenomenon that phase trajectory is converge to a stable point in the phase diagram. At this moment, friction force is determined by the positive slope section of friction coefficient. On the other hand, if the friction

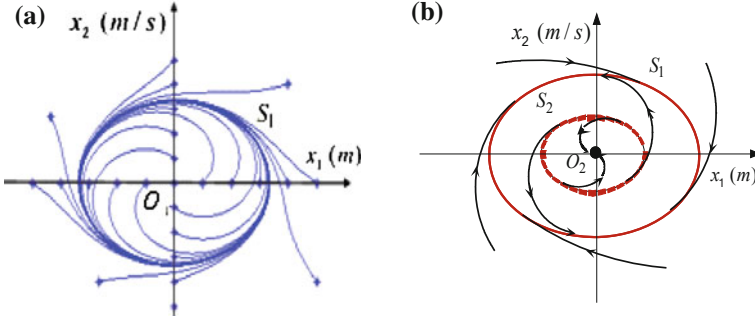


Fig. 2 Phase photogram of self-excited vibration. **a** Soft self-excited vibration. **b** Hard self-excited vibration

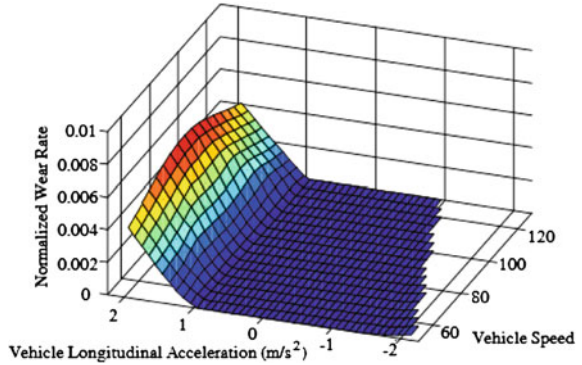
coefficient is at negative slope section, the vibration energy becomes higher and higher, which means that phase trajectory diverges more and more. Due to the existence of structure constrains, the friction coefficient swings alternately between positive slope section and negative slope section, that is to say, the vibration system balances between consuming energy and obtaining energy. Naturally, the self-excited vibration is generated.

Self-excited vibration usually consists of hard self-excited vibration and soft self-excited vibration. As shown in Fig. 2a, soft self-excited vibration is unstable. With any kind of exciting force, the vibration system will diverge to a stable state. It is obviously to understand the mechanism from the phase photogram that the phase trajectory diverges to the stable limit cycle S_1 at any initial situation. For a hard self-excited vibration, only if the initial exciting force is large enough to push the phase trajectory to pass the unstable limit cycle S_2 and to achieve the stable limit cycle S_1 , otherwise, it will converge to the stable point O_2 , which is shown in Fig. 2b. By analyzing the polygonal wear of tire, it is concluded that the tread's vibration is a typical hard self-excited vibration.

3.2 Factor Analysis of Influencing Tire Wear

Lupker [11] pointed out that the average wear rate of rubber would increase nonlinearly with the augment of vibration acceleration. As shown in Fig. 3, with the increase of vehicle speed, the normalized wear rate gets higher gradually, and then become smaller after the vehicle speed of 100 km/h. In another word, for a tire's self-excited vibration at the same frequency, different vibration accelerations can generate different vibration amplitudes, which cause different normalized wear rates. Therefore, it should be focused to control the tread's vibration amplitude or to move the vehicle speed that can cause hard self-excited vibration of tire out of the normal speed range.

Fig. 3 Wear rate with different accelerations and speeds



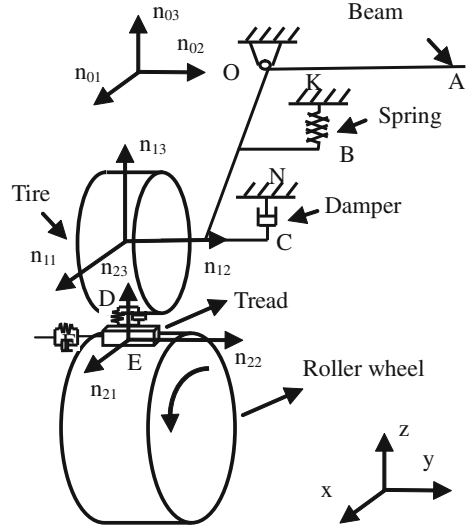
4 Multi-Body Model and Dynamic Equation

All the driving force is supplied by the friction force between tires and pavement except the wind drag while driving in an expressway. Hence, it is important to recognize the relationship between tire driving force and dynamic characteristic of vehicle. In order to represent the dynamic characteristics of tire driving force, a multi-body dynamic model, with a combination of tire and twist beam, driven by a rotary drum, is built. The schematic diagram is shown in Fig. 4 and the multi-body dynamic equation is given as expression (2).

$$\left\{ \begin{array}{l}
 (J_1 \sin^2 \gamma + J_2 \sin^2 \beta \cos^2 \gamma + J_3 \cos^2 \beta \cos^2 \gamma) \ddot{\alpha} + J_1 \sin \gamma \cdot \ddot{\beta} \\
 + (J_3 - J_2) \sin \beta \cos \beta \cos \gamma \cdot \dot{\gamma} = F_x + (J_3 - J_2) \sin \beta \cos \beta \sin \gamma \cdot \dot{\gamma}^2 \\
 - (J_1 + (J_3 - J_2) \cos 2\beta) \cos \gamma \cdot \dot{\beta} \cdot \dot{\gamma} + (J_3 - J_2) \sin 2\beta \cos^2 \gamma \cdot \dot{\alpha} \cdot \dot{\beta} \\
 - (J_1 - J_2 \sin^2 \beta - J_3 \cos^2 \beta) \sin 2\gamma \cdot \dot{\alpha} \cdot \dot{\gamma} \\
 J_1 \sin \gamma \cdot \ddot{\alpha} + J_1 \cdot \ddot{\beta} = F_\beta + (J_3 - J_2) \sin \beta \cos \beta (\dot{\gamma}^2 - \cos^2 \gamma \cdot \dot{\alpha}^2) \\
 - (J_1 - (J_3 - J_2) \cos 2\beta) \cos \gamma \cdot \dot{\alpha} \cdot \dot{\gamma} \\
 (J_3 - J_2) \sin \beta \cos \beta \cos \gamma \cdot \ddot{\alpha} + (J_2 \cos^2 \beta + J_3 \sin^2 \beta) \ddot{\gamma} = F_\gamma \\
 - (J_3 - J_2) \sin 2\beta \cos^2 \gamma \cdot \dot{\beta} \cdot \dot{\gamma} - (J_2 \sin^2 \beta + J_3 \cos^2 \beta - J_1) \cdot \\
 \sin \gamma \cos \gamma \cdot \dot{\alpha} - ((J_3 - J_2) \cos 2\beta - J_1) \cos \gamma \cdot \dot{\alpha} \cdot \dot{\beta} \\
 m_2 \ddot{x} = F_x
 \end{array} \right. \quad (2)$$

where J_1 , J_2 and J_3 are the rotational inertias of rear axle body around x , y , z axes, respectively, m_2 is the mass of tread, α , β and γ are the rotational angles of rear axle body around x , y , z axes, respectively, which reflect the toe angle, camber angle and vertical vibration, x is displacement of tread along with the lateral direction.

Fig. 4 Multi-body dynamic modal of suspension-tire-pavement



5 Numerical Simulation and Sensitivity Analysis

5.1 Bifurcation Simulation of Self-Excited Vibration of Tread Along with the Lateral Direction

Figure 5 shows the phase diagram of tread's self-excited at 110 km/h, simulated in MATLAB/SIMULINK. No matter what situation the initial condition is, the phase trajectory diverges or converges to a stable limit cycle at the end. The vibration amplitude can also be read from the phase diagram.

In order to describe the self-excited vibration of tread at different vehicle speeds, a bifurcation diagram of Eq. (2) is plotted in Fig. 6, in which the x axle is the vehicle speed and the y axle is the vibration amplitude of tread. The smaller bifurcation speed is called the first bifurcation speed and the bigger bifurcation speed is called the second bifurcation speed.

Thus it can be seen that the vibration energy, playing an important role in tire wear, becomes large while the self-excited vibration of tread occurring. To reduce the damage to a running vehicle, some control strategies should be done to decrease the tread's vibration energy or to move the vehicle speed that can cause hard self-excited vibration of tire out of the normal speed range. In order to accomplish the object, there is necessary to study how the parameters influence the characteristics of self-excited vibration.

Fig. 5 Phase diagram of self-excited vibration at 110 km/h

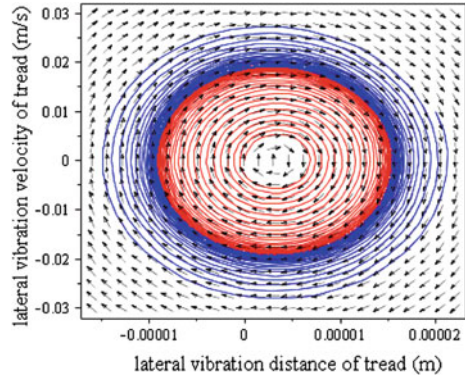
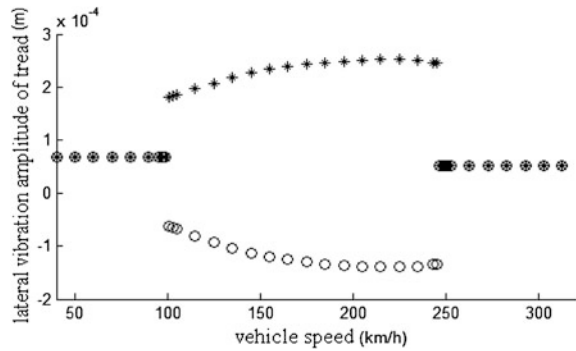


Fig. 6 Bifurcation of vibration amplitude of tread with vehicle speed



5.2 Analysis of the Impact of Parameters' Changing on Self-Excited Vibration Characteristic of Model

Take the toe angle and camber angel as an example to analyze the impact of parameters' changing on self- excited vibration characteristic of multi-body dynamic model. Figures 7 and 8 show the changing trend of lateral vibration of tread, toe angle, camber angle and vertical vibration by numerical simulation in MATLAB/SIMULINK with different initial toe angles and cambers angles alternately. In the phase diagrams, x axes are vibration displacement and y axes are vibration velocity.

As seen in above figures, vibration amplitudes of the four parameters magnify with the increase of initial toe angle. It means that a larger vibration energy causes a worse wear of tire. On the other hand, the vibration energy of toe angle is magnified by a big initial camber angle, and the feedback from the toe angle will aggravate the wear of tire.

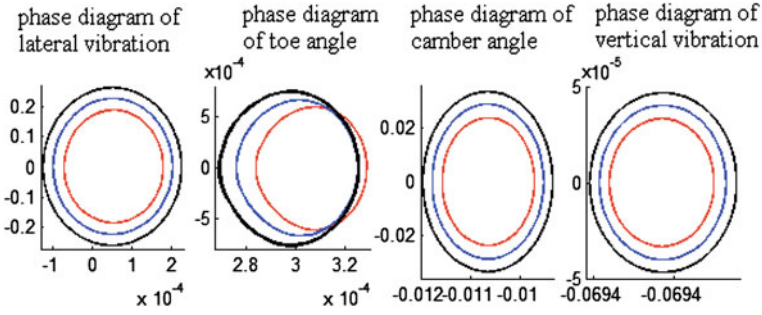


Fig. 7 Phase diagram with different toe angles

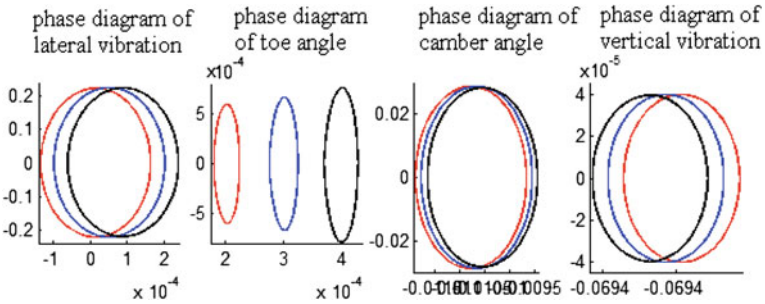


Fig. 8 Phase diagram with different camber angles

5.3 Calculation of Parameters' Sensitivity

A vibration model is often working with several affecting parameters. To optimize the vibration model, there is no need to analyze all the parameters, only a few of them are picked up to be optimized, and that is the core essence of accurate sensitivity analysis [12].

In engineering project, finite difference method is often used to calculate the system sensitivity [13]. It means that derivative method is approximately replaced by finite difference method while the design variable is changing just a little. The calculation expression of sensitivity analysis is given as

$$M = \frac{\partial f}{\partial \rho} = \frac{f(\rho^j) - f(\rho)}{\Delta \rho} \tag{3}$$

As shown in Figs. 9a and b, the sensitivity analysis of several parameters on the first bifurcation speed and the second bifurcation speed is calculated, where, parameters 1–7 are lateral stiffness and damping of tread, toe angel, camber angle, adhesion coefficient, tread mass and vertical load of tire.

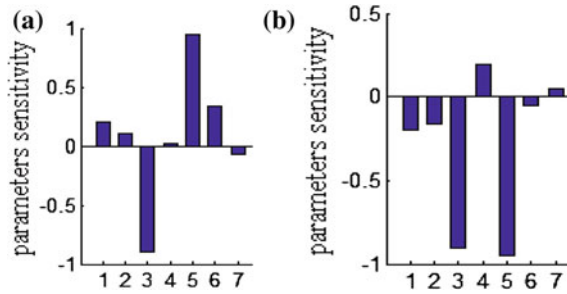


Fig. 9 Sensitivity analysis of different parameters. **a** Sensitivity analysis of the first bifurcation speed. **b** Sensitivity analysis of the second bifurcation speed

6 Control Strategies of Suppressing the Lateral Self-Excited Vibration of Tread

From the above analysis of parameter sensitivity, it is concluded that toe angle and adhesion coefficient are the most remarkable ones of all the parameters, including lateral stiffness and damping of tread, toe angle, camber angle, adhesion coefficient, tread mass and vertical load of tire.

Therefore, several control strategies are listed to reduce the polygonal wear of tire:

1. Wide radial tire, with the advantages of small slip rate, good adhesion performance and large contact area with road, should be chosen.

The friction coefficient depends on the material property contacting with each other. Big friction coefficient means good adhesion performance, and good adhesion performance results in small amplitude of self-excited vibration. It is well known that radial tire has the characteristics of small slip rate and good adhesion performance; wide tire can increase the contact area of road and suppress the lateral self-excited vibration of tire, which is in accordance with the Spinner [14]; moreover, tread patterns also has some influences on adhesion coefficient. The depth of pattern will change with the wear of tire, which leads to a bad adhesion performance. It explains why the self-excited vibration of tread often appears after running 250,000–40,000 km. The bifurcation comparison chart between original adhesion coefficient and optimized adhesion coefficient is given in Fig. 10.

2. Chose the proper toe angle and camber angel or it will aggravate the wear of tire. From the above analysis, it is known that toe angle should be adjusted firstly and then the camber angle.

Different OEM vehicle manufacturers have different positional parameters of tire. The positional parameters will change because of the looseness of wheel hub bearing, big clearance of rubber bushing and the deformation of rear axle. Hence, under the premise of meeting the request of auto control stability performance, it is necessary to adjust the toe angle and camber angle in order to reduce the vibration

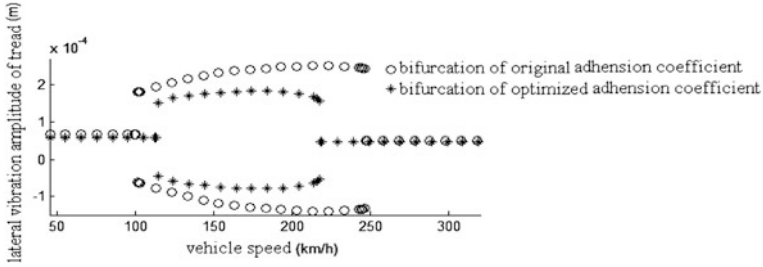


Fig. 10 Bifurcation comparison chart between original adhesion coefficient and optimized adhesion coefficient

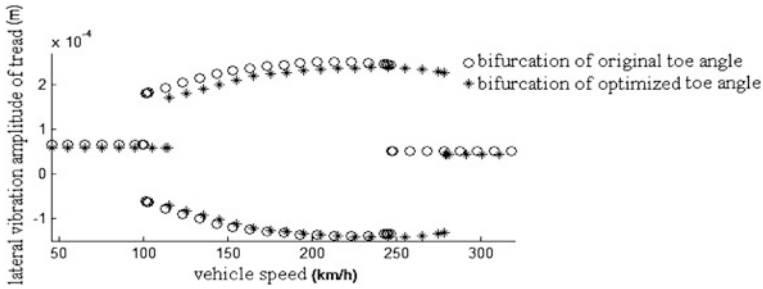


Fig. 11 Bifurcation comparison chart between original toe angle and optimized toe angle

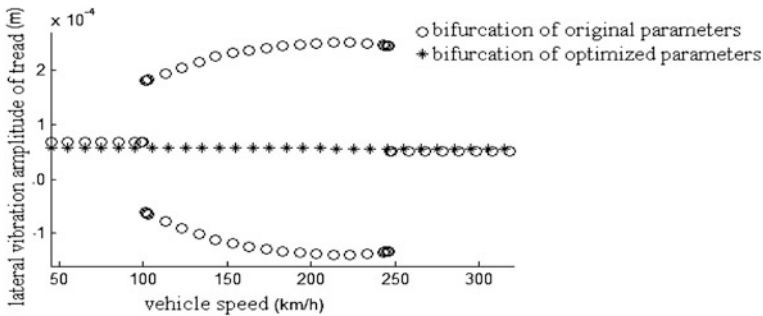


Fig. 12 Bifurcation comparison chart between original parameters and optimized parameters

amplitude of tread. The bifurcation comparison chart between original position parameters and optimized position parameters is given in Fig. 11.

3. Try not to drive an overloaded vehicle at low tire pressure for a long time.

Under the condition of overload, it is easily to increase the lateral friction force and to motivate the self-excited vibration of tire, and also it is easily to deform the rear axle while driving on a poor road and to destroy the normal positional

parameters. A low pressure tire can also motivate the self-excited vibration of tire because of the small lateral stiffness, which can be found out from the above parameters sensitivity analysis.

The range of vehicle bifurcation speed is narrowed or moved out of the normal one after optimizing the tire property parameters and position parameters, meanwhile, the vibration energy is lowered greatly, which reduces the tire average wear rate. As shown in Fig. 12, the polygonal wear of tire can be avoided completely if chosen the proper tire property parameters and position parameters theoretically.

7 Conclusions

1. The Lugre friction coefficient, taking time-delay into account, is used to research the form mechanism of polygonal wear of tire, and a multi-body dynamic mode that can reflect the hard self-excited vibration of tread is established in MATLAB/SIMULINK.
2. The influences of several parameters, including lateral stiffness and damping of tread, toe angel, camber angle, adhesion coefficient between tire and road, tread mass and vertical load of tire, on self-excited vibration of tread are analyzed by changing them alternatively, and the range of bifurcation vehicle speed is numerical simulated in MATLAB/SIMULINK.
3. It is concluded that toe angel and adhesion coefficient are the most remarkable ones of all the parameters, including lateral stiffness and damping of tread, toe angel, camber angle, adhesion coefficient, tread mass and vertical load of tire.
4. The range of vehicle bifurcation speed is lowered greatly or moved out of the normal one by adjusting the tire property parameters and position parameters, which can reduce the polygonal wear of tire remarkably. The control strategies of reducing the self-excited vibration of tread have an important engineering significance.

Acknowledgments The authors gratefully acknowledge the support and encouragement of Dr. Pang Jian and Dr. Li Chuanbing during the writing of this paper.

References

1. Peng X, Xie Y, Guo K (1999) Investigation and development trends of tire tribology. *China Mech Eng* 2(2):215–219
2. Huang H, Jin X, Ding Y (2006) Mechanism of uneven wear and its numerical methods evaluation. *J Tongji Univ* 34(2):234–238
3. Heinrich G, Klüppel M (2008) Rubber friction, tread deformation and tire traction. *Wear* 265:1052–1060
4. Walters MH (1993) Uneven wear of vehicle tires. *Tire Sci Technol* 21(4):202–219

5. Atsuo S, Takahiro R (1997) Polygonal wear of automobile tire. *JSME* 40(2):209–217
6. Li Y, Zuo S, Lei L et al (2010) Analysis on polygonal wear of automotive tire based on LuGre friction model. *J Vib Shock* 29(9):108–112
7. Yang X, Zuo S, Lei L et al (2010) Modeling and simulation for nonlinear vibration of a tire based on friction self-excited. *J Vib Shock* 29(5):211–214
8. Guo KH, Ren L, Hou YP (1998) A non-steady tire model for vehicle dynamic simulation and control. In: *AVEC'98, Nagoya Japan*
9. Konghui G, Ye Z, Shih-Ken C et al (2004) Experimental research on vehicle tire rubber. *Chin J Mech Eng* 40(10):179–184
10. Mcmillan AJ (1995) A non-linear friction model for C.CANUDAS de Wit. A new model for control of systems with friction. *IEEE Trans Autom Control* 40(3):419–425
11. Lupker H (2003) Numerical prediction of car tyre wear phenomena and comparison of the obtained results with full-scale experimental tests. Chassis and transport systems depart, TNO automotive, Helmond, Holland
12. Han L, Li X, Yan D (2008) Several mathematical methods of sensitivity analysis. *Chin Water Transp* 8(4):177–178
13. Qin Z, Wang X et al (2005) An interval method for sensitivity analysis of the structures. *Acta Armamentarii* 26(6):798–802
14. Spinner RJ, Spinner M (1996) Superficial radial nerve compression due to a scaphoid exostosis. *J Hand Surg J Br Soc Surg Hand* 21(6):781–782

Shimmy Identification Caused by Self-Excitation Components at Vehicle High Speed

Fujiang Min, Wei Wen, Lifeng Zhao, Xiongying Yu and Jiang Xu

Abstract The chapter introduces the shimmy mechanism caused by self-excitation components for a vehicle while shimmy is identified at 120 km/h. The Operating Deflection Shape (ODS) analysis used for the chassis from 90 to 140 km/h. The front-right lower arm is identified as the shimmy cause by analysis of movement characteristic change of the chassis components.

Keywords Shimmy · ODS · Modal · Self-excited vibration

1 Introduction

Car shimmy is a common problem as cars driven. For a long time, a lot of people thought that shimmy is a kind of malfunctions. In fact any car has shimmy phenomenon, but the shimmy level in difference Slight shimmy is not perceptible, often neglected, but this accumulation over a certain time period will cause the system worn and fatigue failure, and the life is greatly damaged. Serious shimmy will result in the system on the brink of collapse, eventually lead to the safety accidents. So it is very important to research the shimmy problem.

F2012-J01-002

F. Min (✉) · W. Wen · L. Zhao · X. Yu · J. Xu
Changan Auto Global R&D Center, Chongqing, China
e-mail: sunqiemail@163.com

F. Min · W. Wen · L. Zhao · X. Yu · J. Xu
State Key Laboratory of Vehicle NVH and Safety Technology, Chongqing, China

Shimmy is the phenomenon of vibration of wheel steer when the car is driven on smooth road. Research shows that: shimmy can be classified as the forced vibration and the self-excited vibration [1, 2], the forced vibration is mainly the resonance phenomenon excited by the tire unbalanced mass; The Self-excited type shimmy is Hopf bifurcation phenomena in nonlinear dynamics. Based on the coupling of steering system and the front suspension system [3], the steering system parameters had been studied on the effect of overloading of vehicles shimmy; In the literature [4], the bifurcation theory and numerical simulation were applied for the research of the turning wheel shimmy, and found that the turning wheel shimmy might produce transient chaos movement; In the literature [5], the numerical methods were used to study the parameters on the influence of the front wheel shimmy, and pointed out that the steering gear stiffness, horizontal bars stiffness, kingpin caster, tire cornering stiffness could cause a change of self-excited shimmy. From the results of the study for the last decades, the analysis of the problems of shimmy has been made a lot of breakthrough in theories. But it also shows that shimmy is a very complicated system problem with many influencing factors, and there are still a lot of problems not are completely resolved.

A robust shimmy performance is a system interaction between the tire, wheel, suspension and steering system. As a system issue it is usual process for the solution to optimize every component of the system individually until the results can be acceptable. This kind of practice can solve the problems, but the disadvantages are more time and higher cost. In this chapter, i.e. a car shimmy, in order to solve the shimmy problem, the method to quickly find the key components which affects the shimmy is provided here according to the study of the self-excited vibration characteristics, with the aid of the ODS analysis of the chassis systems movement characteristics, modal analysis.

2 Shimmy Mechanism

To solve the problem of shimmy, the characteristics of the steering wheel shimmy are considered as the beginning of the study, in which the shimmy vibration formats and vibration transmission paths will be concerned.

2.1 The Steering Wheel Shimmy Characteristics Analysis

The steering wheel shimmy is a rotating vibration. It can't be directly figured out through the acceleration sensor test. In this chapter, two accelerometers mounted on the circumference of the steering wheel are used for extraction of shimmy and shake, as shown in Fig. 1. Actually, the shimmy is determined by the difference of acceleration between two accelerometers.

Fig. 1 Schematic diagram for measurement of steering shimmy

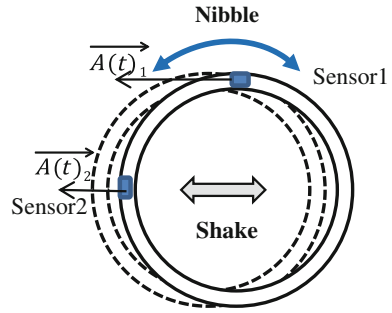
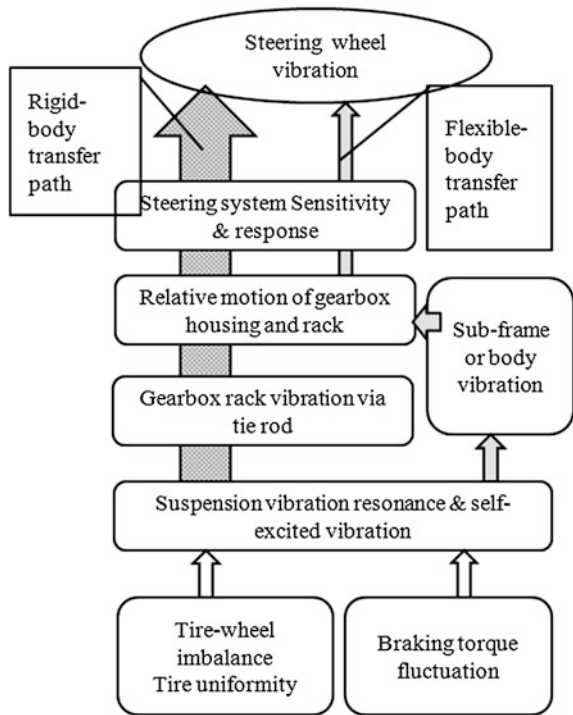


Fig. 2 Transfer path of steering shimmy and brake judder



2.2 Transfer Path Analysis

Figure 2 shows the typical transfer paths of steering shimmy and brake judder. The excitation forces firstly come into the suspension through the front wheel spindles and induce suspension system vibration. From suspension to steering system, there are two paths for the vibration transmission. In the primary path, the majority of the vibration energy is transmitted to the rack rod of the steering gearbox through rigid body motion. In the secondary path, energy is transferred to the gearbox

through vehicle body structural motion, i.e. flexible body motion. The vibration from the gearbox is then transferred to the steering system and eventually the steering wheel.

2.3 Potential Solutions

Shimmy can be divided into the forced vibration and the self-excited vibration. Forced vibration is mainly the resonance phenomenon excited by the tire unbalanced mass. Self-excited type shimmy is Hopf bifurcation phenomena in nonlinear dynamics. With the transmission path analysis in [Sect. 2.2](#), the proposals of shimmy solution measures are listed as the followings:

- Strength of Excitation (Uniformity/Brake DTV)
- Coupling Mechanisms between suspension motions/components (suspension dynamics)
- Dynamics of Steering Wheel/Column.

3 Shimmy Control

3.1 Descriptions of the Problem

The individual vehicle among the products was driven on smooth roads. When its speed was reached about 110–130 km/h, the steering wheel had serious shimmy in vibration ([Fig. 3](#)). The peak frequency was shown in [Fig. 4](#).

3.2 The Strategies for Shimmy Control

According to the above potential measures, the following three aspects shall be carried out in analysis.

- Checking the balance wheels and Toe-in;
- Evaluating the steering system sensitivity;
- Applying Operating Deflection Shape (ODS) analysis into chassis system to find the abnormal vibration parts; determining the problem part either in the forced vibration or in the self-excited vibration through by the modal analysis.

Fig. 3 The steering wheel shimmy with speeds

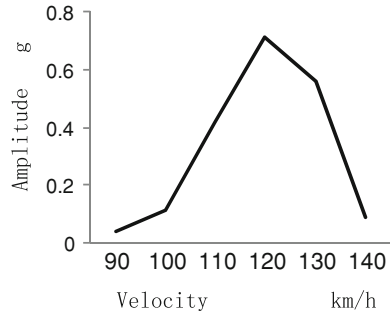
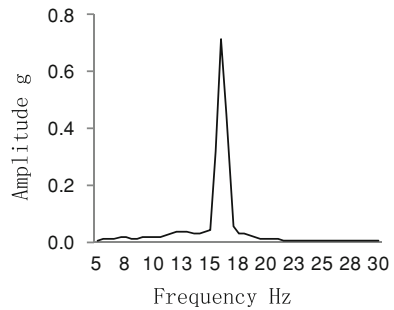


Fig. 4 120 km/h, steering wheel shimmy under different frequencies



3.3 Shimmy Analysis and Control

3.3.1 Tire-Wheel and Toe-In

Wheel imbalance mainly involves three aspects: Tire Uniformity, static unbalance and Couple Unbalance. For diagnosing the problem rapidly, the good wheels are selected and assembled into a car having the problems. If the problem of shimmy is still there, the cause due to the wheel imbalance will be ruled out (in Fig. 5).

As the vehicles in the course of driving, the beam angle results in the fore-half part of the tire on the road contact surface to slide laterally to the wheel inside, and the rear-half part of the tire forward to the wheel outside. That is the reason to lead the wheel steer swing. If the former bunch is improper, front wheel will produce a severe vibration around the dowel, thus produce a shimmy problem. Through the check list shown as in Table 1, the front bunch in problem vehicle meets the design requirement.

3.3.2 Sensitivity Analysis of the Steering System

Sensitivity analysis is a very simple and effective method to evaluate the dynamic characteristics of the material shape due to the deviation in dimensions in the procedure of massive production. So we need to have the vehicle steering shimmy

Fig. 5 The influence of the wheel

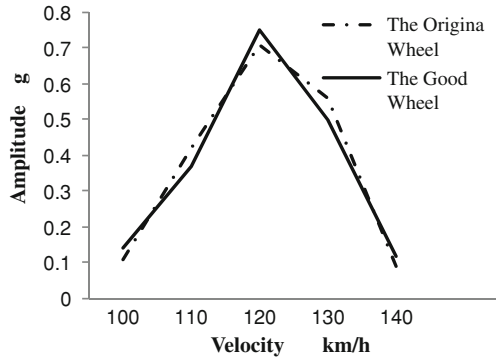


Table 1 Toe checklist

	Design requirements	Problem vehicles
Toe angle	$0^{\circ}5' \pm 5'$	$0^{\circ}3'$

comparison test, which is as shown in Fig. 6. Because two cars have the same levels, the steering system influence is ruled out.

3.3.3 Suspension Dynamics

If the vibration of the system is going to increase, one of the parts in the system is inevitable to have the resonance or self-excited vibration. The abnormal vibration in mode shape will be observed. So that ODS analysis is used for suspension system to confirm abnormal components with the shimmy problems, As comparing the chassis system vibration characteristics with and without shimmy, it is found that the front-right lower arm and the wheel vibration model are abnormalities if the car has shimmy problems. Figure 7 shows the sensor installation positions. Figure 8 shows the two parts in vibration mode.

There are two reasons can lead to abnormal vibration in resonance (or self-excited vibration), or forced vibration. So the natural frequencies of the two parts are needed in testing. The results show the vibration mode of wheel around the king pin is 15.5 Hz which is very close to the frequency of vehicle shimmy peak. (The vehicle in the operation process, because of the changes of friction damper, the frequency of the vehicles will be slightly changed). Since the frequency 101 Hz of the lower arm (in Fig. 5) is much higher than shimmy frequency, the problems of this car is mainly triggered by the self-excited vibration due to the wheel shimmy around the king pin. And the vibration of the arm is caused by the forced vibration.

Fig. 6 Sensitivity analysis of the steering system

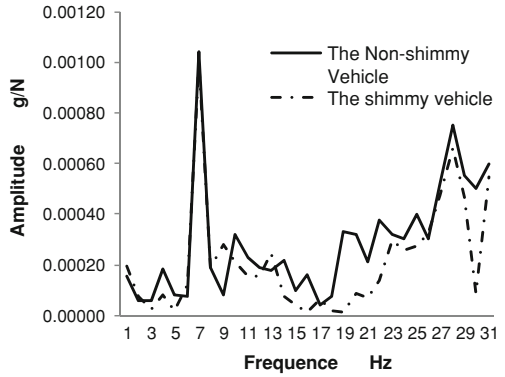


Fig. 7 Sensor installation positions

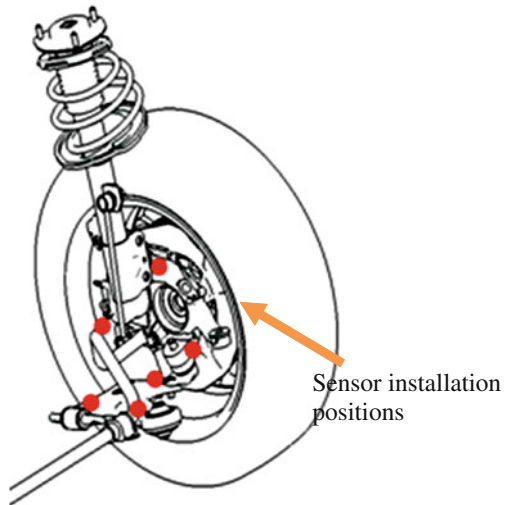


Fig. 8 Front-right lower arm and the wheel vibration model figure

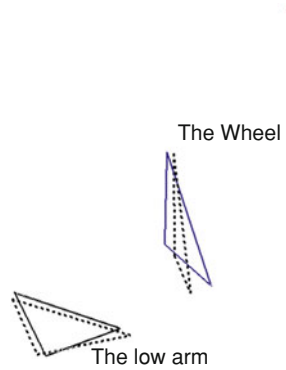


Table 2 the front-right lower arm bushing hardness checklist

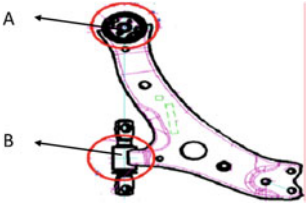
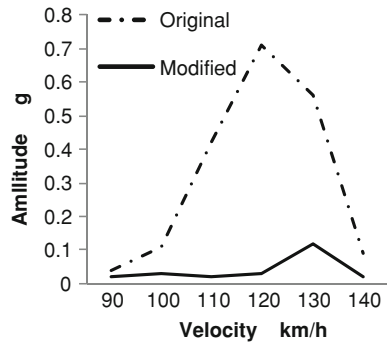
The lower arm		
		
	The design requirements	The shimmy vehicle
A	Hs65 ± 3	Hs55
B	Hs70 ± 3	Hs69

Fig. 9 The effect of the bushing modified



4 Problem Identification and Authentication

It is because of the self-excited vibration of the wheel to cause the steering wheel shimmy. Adding more lateral stiffness of the turning wheel reduces the wheel self-excited amplitude values. From Fig. 5 of the ODS test, it is found the lower arm and wheels are of great relevance. It is necessary to check whether or not the wishbone bushing stiffness meets the design requirements. In the vehicle status, the differences of bushing can only be examined in the hardness test. To check the result (in Table 2) shows that the bushing hardness of arm under point A doesn't meet the design requirements.

After the qualified parts replaced the modal frequency of wheel steer increases from 15.5 to 17.5 Hz. The steering wheel shimmy is basically eliminated, as shown in Fig. 9.

5 Conclusion

This chapter introduces the shimmy transmission path of steering wheel, and the diagnosis methods for the problem of shimmy. Combining with a typical cases respectively, the detailed analysis was carried on the balance wheels, steering system sensitivity analysis, suspension system ODS and modal analysis. Eventually the root causes of the shimmy in car are demonstrated that the unqualified parameters of the wishbone bushing result in the cancellation of the oscillation, thus create the serious steering wheel shimmy.

References

1. Kovacs AP (1998) Computational vibration analysis of vehicle shimmy by a power-work method. *Veh Syst Dyn* 29(6):341–364
2. Kimura T et al (1996) Analysis of steering shimmy accompanied by sprung mass vibration on light duty truck 3 fundamental mechanism. *JSAE Re0076* 17(3):301–306
3. Demic M (1996) Analysis of influence of design parameters on steered wheels shimmy of heavy vehicles. *Veh Syst Dyn* 26(5):343–379
4. Stepan G (1991) Chaotic motion of wheels. *Veh Syst Dyn* 20(6):341–351
5. Li Juan H, In-ye L et al (2008) A simulation study of the self-excited shimmy for automobiles with dependent suspension. *Comput Simulation* 25(2):269–273

Nonlinear Transient Dynamic Analysis of Disc Brake Squeal Using Improved Hilbert-Huang Transform

Xiandong Liu, Haixia Wang, Yingchun Shan and Tian He

Abstract Brake squeal is believed as a friction-induced, self-excited phenomenon. The nonlinear transient analysis is the only appropriate method for the brake system with strong nonlinearities. The braking simulation is conducted based on a finite element model of disc brake, and their time–frequency properties of transient and stationary nonlinear response obtained by the improved Hilbert-Huang Transform are presented to investigate the transient dynamic behavior of brake system. It is demonstrated that the dynamic response of the friction-induced vibration is composed of multiple IMF components. The low-frequency IMF components have relative constant instantaneous frequencies but fluctuated energy with time. On the contrary, the high-frequency components have significant fluctuated frequencies. It is considered that the variations of the high-frequency are attributed to the nonlinearity of the brake system that includes the friction damping and contact nonlinearity in the present work. Some higher frequencies appear in the stationary vibration stage after the transient response. The propensity of system instability and brake squeal rises with an increase in friction coefficient. The simulated processing results have also manifested that the improved HHT can clearly provide the time–frequency property of the brake system compared to the conventional HHT, hence, it is a promising tool for processing the complicated nonlinear and nonstationary signals.

Keywords Nonlinear · Transient dynamic analysis · Disc brake · Squeal

F2012-J01-003

X. Liu (✉)

State Key Laboratory of Vehicle NVH and Safety Technology, Chongqing 400039, China
e-mail: liuxiandong@buaa.edu.cn

X. Liu · H. Wang · Y. Shan · T. He

School of Transportation Science and Engineering, Beihang University,
Beijing 100191, China

1 Introduction

Undesirable brake vibration and noise in automobiles causes discomfort to passengers and degrades their perception of vehicle quality. A better understanding of brake noise generation and suppression mechanisms is required to design and manufacture safe and quiet brakes. Brake squeal has been the primary subject of past studies on brake noise. It is an annoying high-pitched sound, from about 1 to 20 kHz, whose occurrence is intermittent or perhaps even random. Despite almost 80 years of research and a good deal of progress having been made, the underlying mechanisms of brake squeal generation are not yet fully understood due to its complex nature, which involves multiple disciplines such as non-linear dynamics, contact mechanics, acoustics and tribology. From a nonlinear vibration viewpoint, several mechanisms such as stick-slip, sprag-slip, negative friction-velocity slope, hammering excitation, and modal coupling of structures have been proposed. As more experimental evidence and simulation results become available, it is clear that none of the above mechanisms alone can explain all the causes and symptoms of brake squeal noise.

Most of the research over the last two decades has utilized either experimental methods [1, 2], simplified analytical (linear or nonlinear) models [3, 4] or large scale numerical techniques [5] such as the finite element method (FEM) to investigate the acoustics of friction, various instability mechanisms, and parameter influence. The complex eigenvalue analysis (CEA) is widely applied to map the complex structural modes to examine modal coupling issues or the brake squeal propensity [6, 7]. The CEA approach linearizes the brake squeal solution at static steady states, and may be sufficient for providing information on the onset of squeal [8]. However, brake squeal is a nonlinear transient event due to the strong nonlinearities in a brake system associated with the contact problems, disc rotation, materials nonlinearity, etc. The nonlinearities cannot be neglected when investigating the generation and evolution of brake squeal. If the nonlinearity is present or an equilibrium point becomes unstable, the nonlinear transient analysis is the only appropriate method for such situations. But only a few studies have considered the transient nonlinear behavior of the brake systems. The dynamic behavior of the friction-induced vibration signal is often complicated and nonlinear, and their frequency components vary with time. The FFT method adopted in some articles [3, 6] to convert the transient response in time domain obtained through experiments or simulation into frequency domain provides very limited information for examining the characteristic of squeal history response. Therefore, the time–frequency analysis will be a superior tool to explore the transient nonlinear behavior of the brake systems, due to its ability of generating both time and frequency information of a signal simultaneously. Chen and Zhou [9] provided time–frequency analysis of experimental results applying short-time Fourier transform (STFT) and Zhao-Atlas-Marks distribution (ZAMD), and concluded that friction vibration system is generally a linear system in the phase of vibration initiation and then becomes a non-linear system in the phases of vibration

being bounded and disappearance. Sinou [10] investigated the contributions of fundamental frequencies and harmonic components in non-linear transient and stationary dynamics of disc brake system subjected to single and multi-instabilities, using a finite element model and the Continuous Wavelet Transform (CWT). He illustrated that new fundamental frequencies (linked to the appearance of the new unstable modes) can emerge in the signals due to the non-linear contact and loss of contact interactions at the frictional interface, which are not predicted by the complex eigenvalues analysis. However, these time–frequency analysis methods still have some inevitable deficiencies, such as non-adaptability for STFT and the interference terms, border distortion and energy leakage for CWT. In 1998, Huang [11] proposed a new time–frequency analysis method named Hilbert-Huang transform (HHT) that works through performing a time adaptive decomposition operation named empirical mode decomposition (EMD) on the signal to decompose it into a set of complete and almost orthogonal mono-components named intrinsic mode function (IMF), and utilizing Hilbert transform on those obtained IMFs to get a full energy-frequency-time distribution of the signal, designated as the Hilbert-Huang spectrum. The HHT method has good computation efficiency and does not involve the concept of the frequency resolution and the time resolution. Empirically, many tests indicate that HHT is a superior tool for time–frequency analysis of nonlinear and non-stationary data. Unfortunately, the HHT also has some unsolved problems caused by EMD. First, the EMD will generate some pseudo-components at low-frequency region due to the spread of endpoint oscillation. Second, the first IMF may cover a wide frequency range at the high-frequency region and therefore cannot satisfy the mono-component definition very well. Third, the EMD operation often cannot separate close components and low-energy components from the analysis signal. Fourth, the same IMF may contain multiple modes when the time scale features change significantly in a given period of time which is called mode mixing. To alleviate these deficiencies to some extent, an improved HHT with the help of singular value decomposition (SVD) [12], wavelet packet transform (WPT) and IMF selection is present in this paper.

This paper is aimed at analyzing the nonlinear transient dynamic behaviors of brake systems both in the time and frequency domain and investigating the vibration properties of brake components in the process of squeal evolution using the improved HHT. An outline of this paper is as follows: In the next section, the brief theory of the conventional HHT and its shortcoming are addressed, and the improved HHT is put forward. The brake finite model under study is presented in Sect. 3. In Sect. 4, the transient response results of braking simulation are analyzed adopting improved HHT to discuss the dynamic properties of brake components during transient vibrations. And the influences of friction coefficient between pad and disc on the transient nonlinear dynamic behavior of the brake system are investigated.

2 The Principal of Conventional HHT and Improved HHT

2.1 The Conventional Hilbert-Huang Transform and its Deficiencies

The Hilbert-Huang transform (HHT) consists of two parts: empirical mode decomposition (EMD) and Hilbert spectral analysis (HSA). The EMD provides a decomposition method to separate a complicated multi-component signal into some almost orthogonal, nearly mono-component IMFs. It is based on the simple assumption that any data consists of different simple intrinsic modes of oscillations. Each intrinsic mode, linear or nonlinear, represents a simple oscillation, which will have the same number of extrema and zero-crossings. Furthermore, the oscillation will also be symmetric with respect to the “local mean”. The detailed EMD sifting process can be found in [13]. Finally, the real valued signal $x(t)$ can be expressed as

$$x(t) = \sum_{i=1}^n c_i + r_n. \quad (1)$$

Thus, a decomposition of the data into n -intrinsic mode functions c_i is achieved, and a residue r_n obtained which can be either the mean trend or a constant.

Then, the Hilbert transform can be applied to each IMF to identify the instantaneous frequencies. The Hilbert transform $\hat{c}_i(t)$ of the real valued function $c_i(\tau)$ can be determined by

$$\hat{c}_i(t) = \frac{1}{\pi} PV \int_{-\infty}^{+\infty} \frac{c_i(\tau)}{t - \tau} d\tau, \quad (2)$$

where, PV indicates the principal value of the singular integral. With the Hilbert transform, the analytic signal is defined as

$$z_i(t) = c_i(t) + j\hat{c}_i(t) = a_i(t)e^{j\theta_i(t)}, \quad (3)$$

where

$$a_i(t) = \sqrt{c_i^2(t) + \hat{c}_i^2(t)}, \text{ and } \theta_i(t) = \arctan\left(\frac{\hat{c}_i(t)}{c_i(t)}\right). \quad (4)$$

In Eq. (4), $a_i(t)$ is the instantaneous amplitude which reflects how the energy of the signal varies with time, and $\theta_i(t)$ is the phase function. Then the time derivative of instantaneous phase $\theta_i(t)$ will be the physical meaning of instantaneous frequency $f_i(t)$ of the signal $c_i(t)$, as follows:

$$f_i(t) = \frac{1}{2\pi} \omega_i(t) = \frac{1}{2\pi} \times \frac{d\theta_i(t)}{dt}. \quad (5)$$

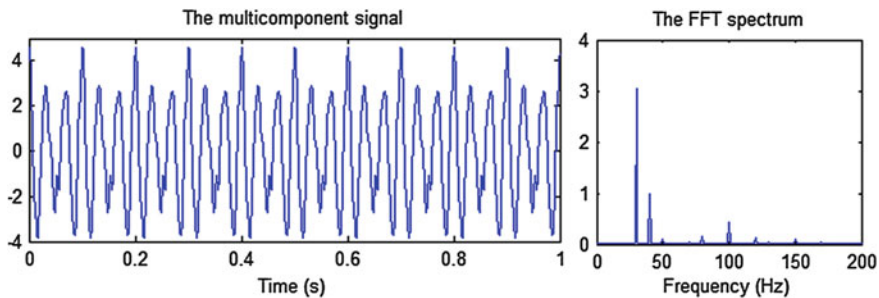


Fig. 1 The simulated multicomponent signal and its FFT spectrum

After performing the Hilbert transform on each IMF component, the original data can be expressed as the real part RP in the following form:

$$x(t) = RP \sum_{i=1}^n a_i(t) e^{j\theta_i(t)} = RP \sum_{i=1}^n a_i(t) e^{j \int \omega_i(t) dt}, \quad (6)$$

and, the residue r_n has been left out on purpose, for it is either a monotonic function or a constant. Equation (6) enables us to depict the instantaneous amplitude and frequency as functions of time in a three-dimensional plot or contour map. This frequency-time distribution of the amplitude is designated as the ‘‘Hilbert amplitude spectrum’’, or simply ‘‘Hilbert spectrum’’.

As mentioned in Sect. 1, the conventional HHT has some shortcomings. To illustrate these problems, the conventional HHT is performed on a simulated nonlinear and nonstationary multi-component signal that is formulated as follows:

$$x(t) = 3 \cos(60\pi t) + \cos(80\pi t) + 0.3(1.5 + \cos(40\pi t)) \times \sin(200\pi t + 0.5 \cos(100\pi t)). \quad (7)$$

This signal is composed of two cosine signals with close frequency and a nonstationary signal which is a low energy nonlinear signal with fundamental frequency of 100 Hz, modulation frequency of 50 Hz and amplitude modulation frequency of 20 Hz. The sampling rate of signal is set to 2,000 Hz, and the time duration is 1.0 s. Its time history and FFT spectrum are shown in Fig. 1. Figure 2 displays the IMFs obtained by applying the conventional HHT to this signal. Figure 3 illustrates its conventional Hilbert spectrum whose frequency-scale is in a normalized frequency. It can be clearly found that the conventional HHT fails to decompose the signal correctly. The signal has been decomposed into five IMFs and its residue. The low energy component is not separated from the original signal, and some pseudo-components (IMF4 and IMF5) generate at the low-frequency region. Therefore the instantaneous frequencies are also not reasonable.

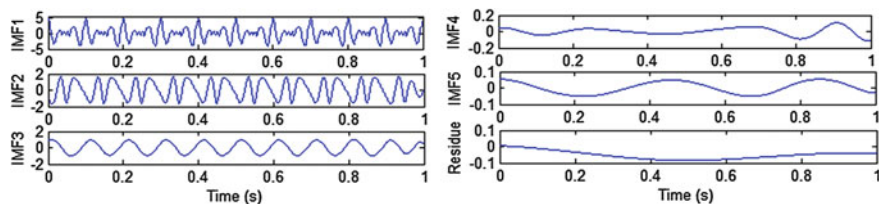


Fig. 2 The IMFs and the residue of simulated signal produced by conventional HHT

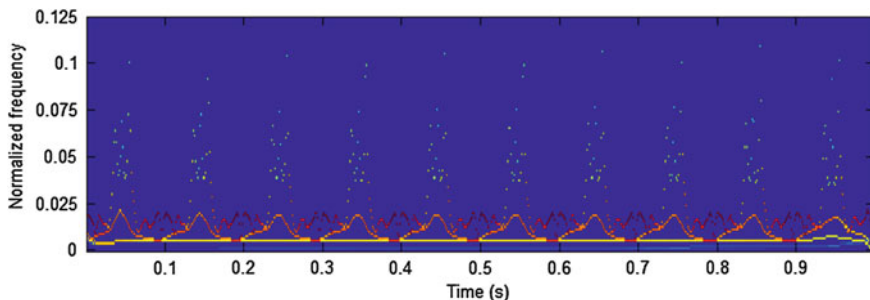


Fig. 3 The conventional Hilbert spectrum of simulated signal

2.2 The Improved Hilbert-Huang Transform

To solve the drawbacks of the conventional HHT, we present an improved HHT that perform SVD and WPT on the signal before the EMD process and involve the IMF selection method.

The SVD has been widely used in signal processing problem in recent years, such as feature extraction, data compression, noise reduction, and so on. A matrix can be created by phase space reconstruction or continuous interception of the one-dimensional signal. Then the singular values of the data matrix can be calculated and arranged in descending order, which reflect the energy distribution of the signal. The singular values are divided into several groups according to their size to reconstruct the components. Therefore, based on the singular value decomposition and its inverse process, the original signal is decomposed into a series of components located in narrow energy bands. The advantages of SVD are as follows: first, the weak signal with low energy can be separated from original signal in advance; second, the components with close frequency but different energy can be distinguished; third, due to the narrowband property of signals in the same energy region, the components obtained by SVD often locate in narrow frequency band. And then the well-known WPT is applied to the components (reconstructed through many similar singular values) that have wide frequency range to split them into narrow frequency bands. After the SVD and the WPT operation, the original signal is decomposed into a series of components expressed by SWC_i in narrow frequency and energy bands. Then the operation of EMD will

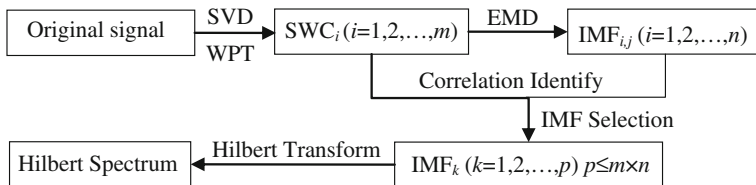


Fig. 4 The flowchart of the improved HHT

be applied to each SWC_i . It is worth noting that it is significant to choose appropriate reconstruction dimension and the number of reconstructed components for SVD and level for WPT, according to the complexity of the signal.

To eliminate those pseudo-components, Peng [13] put forward a simple but effective IMFs selection method using the correlation coefficients between the IMFs and the signal as a criterion to decide which IMF should be retained or eliminated. It is thought that the real IMF components have relative strong correlation with the original signal, while the pseudo-components have weak correlation with the signal. A threshold can be set for this sifting process. For all correlation coefficients μ_i where $i = 1, 2, \dots, n$ (n is the number of IMF), the threshold λ is set by the ratio of the maximal μ_i , which is

$$\lambda = \text{Max}(\mu_i) / \eta, \quad (8)$$

where, η is a ratio factor usually determined empirically. In this study, $\eta = 10$ is used. Any IMF that has a correlation coefficient equal to or higher than λ will be retained, whilst, other IMFs will be added to the residue.

Then the Hilbert transformation is applied to the rest IMFs respectively to obtain the instantaneous frequency and Hilbert spectrum of the original signal. Therefore the operation procedures of the improved HHT with SVD, WPT and IMF selection can be summarized in the flowchart as shown in Fig. 4.

The IMFs and the Hilbert spectrum obtained through applying the improved HHT to the simulated signal are displayed in Figs. 5 and 6 respectively. Figure 5 shows that the original signal is decomposed into three IMFs which are exactly corresponding to the three components of the original signal formulated in Eq. (7). Note that the new residue is not the mean trend or a constant because the irrelevant pseudo-IMFs have been added to the residue. Figure 6 also manifests that the characteristics of the simulated signal are demonstrated perfectly. The two components (IMF3 and IMF2, corresponding to the first two parts in Eq. (7) with close frequency are separated from each other. The low energy component (IMF1, corresponding to the third part in Eq. (7) is also distinguished and its frequency modulation property is clearly displayed.

Thus, the improved HHT is a superior tool to processing the nonlinear and nonstationary signal, compared with the conventional HHT. In Sect. 4, the improved HHT will be utilized to study the dynamic behaviors of a brake system.

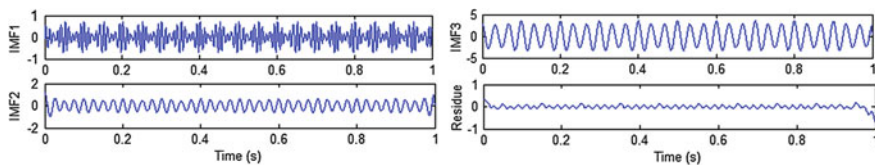


Fig. 5 The IMFs and the residue of simulated signal produced by improved HHT

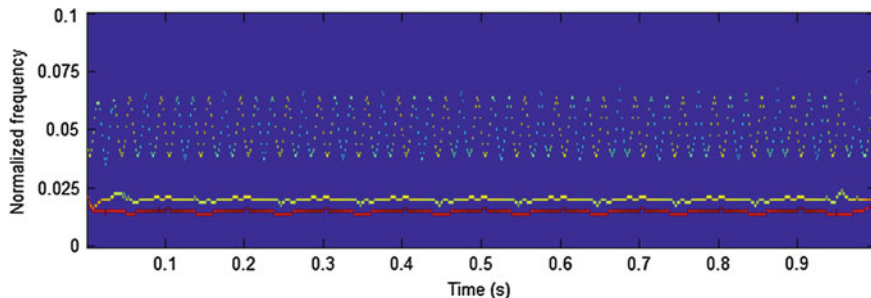


Fig. 6 The improved Hilbert spectrum of simulated signal

3 Finite Element Model of the Brake System

The brake system considered in this paper represents a simplified brake consisting of a disc, two pads and their back plates, as illustrated in Fig. 7. Table 1 lists the material properties of each disc brake component, and the nonlinear properties of materials are not taken into consideration. The natural frequencies of each component are extracted using the finite element model software ABAQUS. Preliminary modal experiments have also been conducted. The structural models are updated until the numerical frequencies are nearly consistent with experimentally observed frequencies to improve the accuracy of subsequent braking event simulations and dynamic analysis.

The software ABAQUS allows for a convenient, but general definition of contact interfaces by specifying the friction properties. For the transient dynamic analysis, explicit dynamic integration method is used to simulate the behavior of the brake system in the time domain. In this simulation, the isotropic Coulomb friction model with a penalty method is applied, enabling to evaluate the normal and tangential contact stresses along the contact region and to determine whether the contact surfaces stick, slide or separate from each other locally. The finite-sliding contact formulation is chosen, which allows for arbitrary separation, sliding, and rotation of the surfaces in contact. Therefore, the slave nodes may come in contact anywhere along the master surface and the load transfers are updated throughout the analysis. The effects of non-uniform frictional sliding contact are incorporated in the solving process.

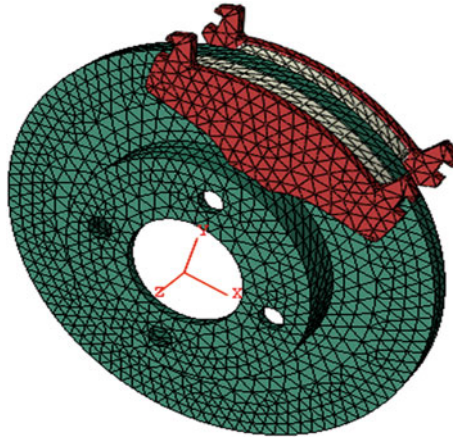


Fig. 7 The finite element model of a disc brake

Table 1 Material properties of each disc brake component

	Disc	Pad	Back plate
Young modulus (MPa)	1.2×10^5	5.0×10^4	2.06×10^5
Poisson's ratio	0.25	0.30	0.28
Density (ton/mm ³)	7.0×10^{-9}	2.4×10^{-9}	7.8×10^{-9}

The disc is constrained in the x-, y-, z-direction (the corresponding coordinates are shown in Fig. 7). The pads are firmly attached to their back plate whose trailing edges are constrained both at circumferential and at the radial directions but the x-direction. Hence, the pad is free to move toward the disc or away from it. At the initial time of simulation, an increasing brake pressure starting from zero is applied on the back plate along the z-direction until it reaches a pre-selected value of 0.5 MPa. The application of this force pushes the pad in contact with the disc, whose angular velocity is kept constant with a value of 5 rad/s throughout the simulation time. The braking simulation is conducted for three friction coefficients, 0.2, 0.3 and 0.5, respectively. For each case, the effects of slip rate and surface temperature on friction coefficient are ignored, and the friction coefficient is assumed to be constant.

4 Simulation Results and Analysis

When brake squeal occurs, the vibration response of the system can be identified as an initially divergent response or a new limit cycle. Figure 8 shows the transient dynamic simulation results for the friction coefficient equal to 0.2. Figure 8a

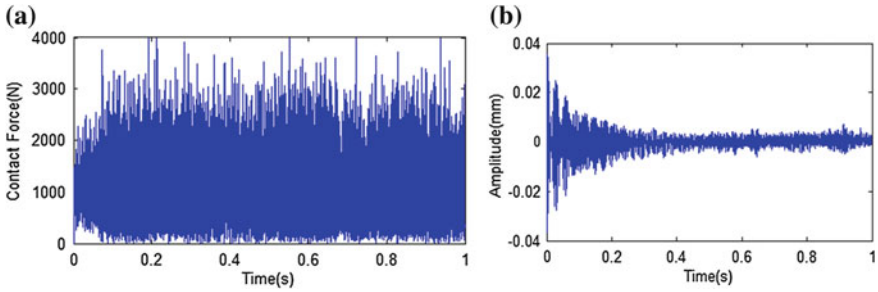


Fig. 8 Transient dynamic simulation for $\mu = 0.2$: **a** the normal contact force; **b** the transient non-linear displacement response of pad in the z -direction

clearly displays that the amplitudes of normal contact force vibrate versus time but no detachment occurs during the transient simulation for this case (zero normal contact force means that the pad separates from the disc). Figure 8b illustrates the displacement in the z -direction (normal to the contact surface) of a pad node near the trailing edge. The highest displacement oscillation amplitudes are observed when the contact between the pad and the disc occurs from Fig. 8b. The transient oscillation is harmonic and decreases with time until the stationary non-periodic vibrations. A similar phenomenon is observed for the tangential displacement response of the pad, but with lower order of magnitude. This observation illustrates that the transient behavior of the brake system due to the impacts generated by the contact between disc and pads can be a key issue in braking process for predicting brake squeal even if the brake system can perform properly during the final stationary vibrations (i.e. the stationary friction-induced self-excited vibrations are assumed to be too small to generate brake squeal).

In order to improve the processing speed and effect, the time history of pad's z -direction displacement is divided into two parts, i.e. the transient stage (0–0.3 s) and the stationary stage (0.3–1.0 s). The Hilbert spectrums generated by applying the conventional HHT and improved HHT are shown in Fig. 9a and b, respectively. As mentioned in Sect. 2.1, the conventional Hilbert spectrum fails to decompose the signal correctly and to reflect the true frequency pattern, which can be clearly found in Fig. 9a. The low energy component is masked and the low close frequency components are not separated from each other. However, the improved Hilbert spectrum as shown in Fig. 9b can clearly indicate the real properties of the signal. It reveals that the dynamic behavior of the friction-induced vibration is complicated and nonlinear, containing multiple components. It also clearly displays that the low-frequency IMF components around 0.03 have relative constant instantaneous frequency values but fluctuated energy (different grey scale) with time, but the higher frequency component 0.05 have relative constant energy. Furthermore, the frequency of the component around 0.05 bounds to a higher value and some higher frequencies (e.g. from 0.1 to 0.15 and around 0.25) appear from transient response stage to stationary vibration. It is considered that the variations of the frequency are attributed to the nonlinearity of the brake

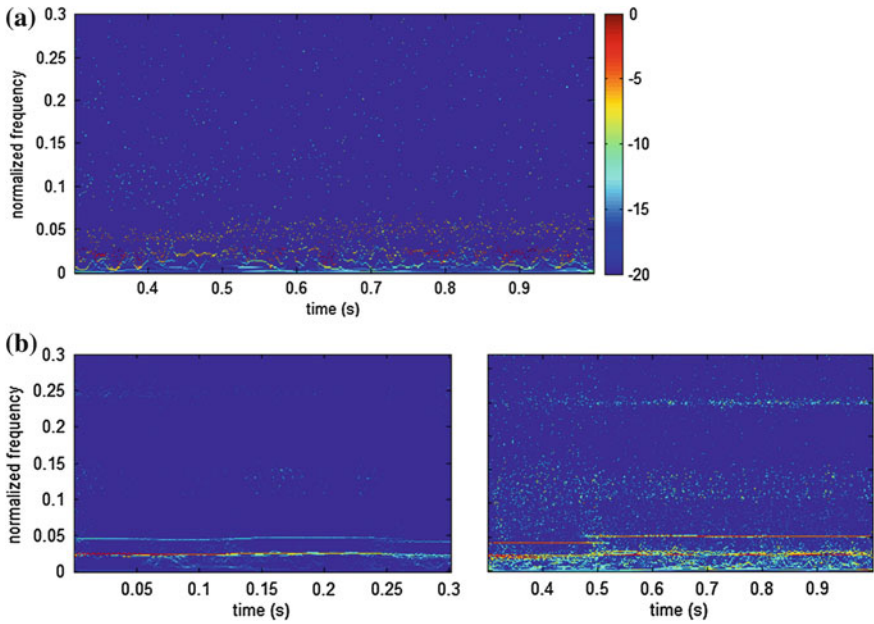


Fig. 9 The result of conventional HHT and improved HHT of pad transient displacement response for $\mu = 0.2$: **a** the conventional Hilbert spectrum; **b** the improved Hilbert spectrum

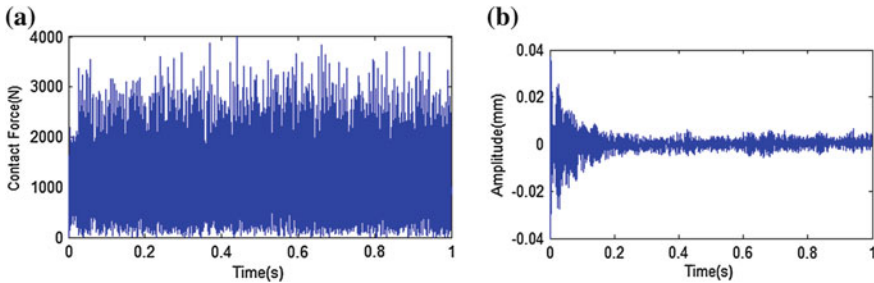


Fig. 10 Transient dynamic simulation for $\mu = 0.3$: **a** the normal contact force; **b** the transient non-linear displacement response of pad in the z-direction

system that include the friction damping and contact nonlinearity in the present work. Also the nonlinearities bound the vibration amplitudes in limited magnitude.

Figure 10 illustrates the transient dynamic simulation results for the friction coefficient equal to 0.3. It can be seen in Fig. 10a, the normal contact force peaks at earlier time of about 0.028 s compared with 0.07 s for the condition of friction coefficient equal to 0.2. And more number of detachments (about 5 times) emerge, but not remarkable. Figure 10b demonstrates that the transient displacement response of pad decreases more quickly and has larger stationary vibration magnitudes. The similar symptoms of instantaneous frequency distribution can be

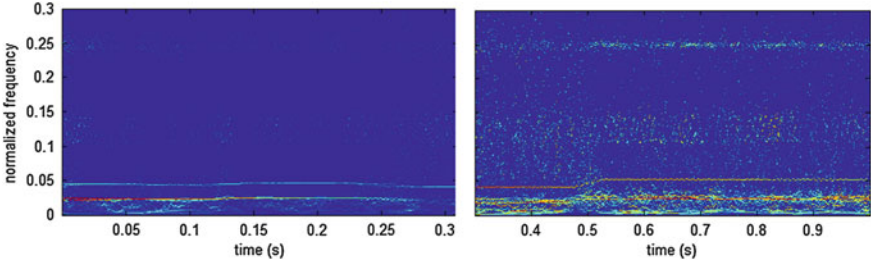


Fig. 11 The improved Hilbert spectrum of pad transient displacement response for $\mu = 0.3$

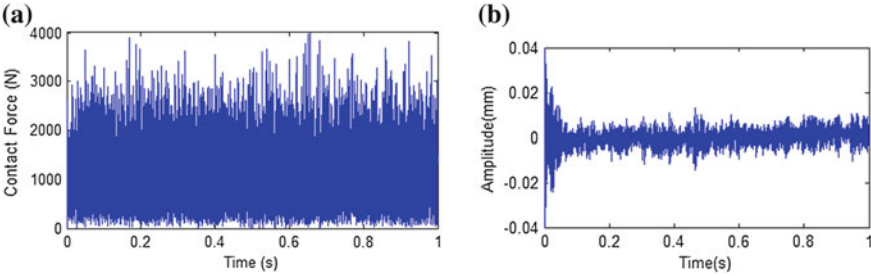


Fig. 12 Transient dynamic simulation for $\mu = 0.5$: **a** normal contact force; **b** the transient non-linear displacement response of pad in the z-direction

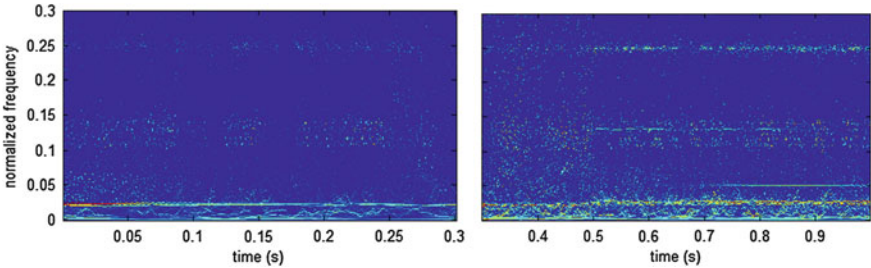


Fig. 13 The improved Hilbert spectrum of pad transient displacement response for $\mu = 0.5$

revealed from its improved Hilbert spectrum as shown in Fig. 5. However, the instantaneous frequency of the component (around 0.05) changes periodically with time. Moreover, the energy of the high frequency components (from 0.1 to 0.15 and around 0.25) increases compared with that of friction coefficient 0.2, which indicates higher brake squeal tendency (Fig. 11).

Compared to the analyzed results for conditions of friction coefficient equal to 0.2 and 0.3, the transient dynamic simulation results for the friction coefficient equal to 0.5, which is shown in Fig. 12, display more frequent detachments (about 120 times) between disc and pad and fast decrease of the transient oscillation followed by larger amplitude (means higher vibration energy) stationary vibration. As illustrated in its Hilbert spectrum Fig. 13, the component of 0.05 generates at

the time of 0.75 rather than the beginning of the simulation. A new component of 0.13 can be identified and more low frequency components are closely packed to each other. Therefore the brake system possesses more complicated vibrations and is more likely to become unstable and generate brake squeal.

5 Conclusions

The transient nonlinear dynamic simulation is conducted based on a finite element model of disc brake, and the time–frequency properties of transient and stationary nonlinear response obtained by the improved Hilbert-Huang Transform are presented to investigate the transient dynamic behavior of brake system. It is demonstrated that the dynamic behavior of the friction-induced vibration is complicated and nonlinear. The low-frequency IMF components have relative constant instantaneous frequencies but fluctuated energy with time. On the contrary, the high-frequency components have significant fluctuated frequencies. It is considered that the variations of the high-frequency are attributed to the nonlinearity of the brake system that includes the friction damping and contact nonlinearity in the present work. These nonlinearities also bound the vibration amplitudes in limited magnitude. Some higher frequencies appear in the stationary vibration stage after the transient response. The greater the friction coefficient is, the more detachments and frequency components appear, at the same time and the stationary vibrations deteriorate, which manifest that the propensity of system instability and brake squeal rises with an increase in friction coefficient.

Acknowledgments The authors would like to thank the financial support provided by the opening project of State Key Laboratory of Vehicle NVH and Safety Technology of China (No. NVHSL-201108).

References

1. Bergman F, Eriksson M, Jacobson S (1999) Influence of disc topography on generation of brake squeal. *Wear* 225–229:621–628
2. Akay A, Giannini O, Massi F, Sestieri A (2009) Disc brake squeal characterization through simplified test rigs. *Mech Syst Sign Process* 23:2590–2607
3. Massi F, Baillet L, Giannini O et al (2007) Brake squeal: linear and nonlinear numerical approaches. *Mech Syst Sign Process* 21:2374–2393
4. Kinkaid NM, O'Reilly OM, Papadopoulos P (2005) On the transient dynamics of a multi-degree-of-freedom friction oscillator: a new mechanism for disc brake noise. *J Sound Vib* 287:901–917
5. Júnior MT, Gerges SNY, Jordan R (2008) Analysis of brake squeal noise using the finite element method: a parametric study. *Appl Acoust* 69:147–162
6. AbuBakar AR, Ouyang Huajiang (2006) Complex eigenvalue analysis and dynamic transient analysis in predicting disc brake squeal. *Int J Veh Noise Vib* 2:143–155

7. Liu P, Zheng H, Cai C et al (2007) Analysis of disc brake squeal using the complex eigenvalue method. *Appl Acoust* 68:603–605
8. Ouyang HJ (2005) Numerical analysis of automotive disc brake squeal: a review. *Int J Veh Noise Vib* 1:207–231
9. Chen GX, Zhou ZR (2007) Time-frequency analysis of friction-induced vibration under reciprocating sliding conditions. *Wear* 262:1–10
10. Sinou JJ (2010) Transient non-linear dynamic analysis of automotive disc brake squeal on the need to consider both stability and non-linear analysis. *Mech Res Commun* 37:96–105
11. Huang NE, Shen SSP (2005) *The Hilbert-Huang transform and its applications*. World Scientific Publishing Co. Pvt. Ltd
12. Yang WX, Tse PW (2003) Development of an advanced noise reduction method for vibration analysis based on singular value decomposition. *NDT&E Int* 36:419–432
13. Peng ZK, Tse PW, Chu FL (2005) A comparison study of improved Hilbert–Huang transform and wavelet transform: application to fault diagnosis for rolling bearing. *Mech Syst Sign Process* 19:974–988

Application of an Experimental Tire Model for Comfort Analysis: Requirement for Accurate Low Frequency Tire-Patch Inputs

Alessandro Lepore, Theo Geluk, Massimiliano Gobbi and Ben Meek

Abstract Physically correct and invariant inputs are important in vehicle development to perform virtual optimization at the suspension or body-level. These inputs can be applied to vehicle models in order to predict interior vibration or noise-levels and evaluate NVH performances without having a physical prototype. The applied inputs can be wheel-center loads or, even more invariant, tire-patch displacements. These tire-patch inputs, applied to a tire model, allow accurate predictions up to 300 Hz. A limitation of this approach however, is that no accurate inputs can be obtained at lower frequencies, therefore application for comfort analysis is not possible. In this study it is investigated if the low-frequency quality loss in the input identification is related to the measurement approach, the data post-processing steps, or non-linearities in the tire or suspension. An alternative measurement setup including the use of strain-sensors is evaluated and compared with the original acceleration-based methodology. A comparison of predicted target vibrations at the seat rail as well as obtained inputs is presented for the different methods. The results indicate that the proposed alternative methodology increases the quality of the estimated inputs in the low-frequency region. With these improved low-frequency inputs, the methodology of using tire-patch displacements as inputs to hybrid models can now also be applied for lower frequency (ride, comfort) applications.

Keywords NVH tire model · Tire-patch input identification · Transfer path analysis

F2012-J01-009

A. Lepore · T. Geluk · B. Meek (✉)
LMS International, Leuven, Belgium
e-mail: ingegnerelepore@hotmail.it

M. Gobbi
Politecnico Di Milano, Milan, Italy

1 Introduction

When dealing with Road Noise and Vibration problems, invariant and accurate inputs are of primary importance to be able to correctly assess the structural–acoustic behavior of a vehicle and predict target responses. Moreover, operational inputs at the wheel or tire-level can be applied to a CAE vehicle model to perform virtual tuning of suspension/body parameters and optimize road noise performances in the early stage of the development process.

What is commonly done in the industry is using experimental spindle forces measured on the full vehicle with dynamometric hubs or smart wheels [1, 2]. Big limitation of this approach is that accurate predictions can only be made for the vehicle configuration that has been used for the measurements, meaning that the identified loads are not invariant. Moreover, if the test rig is not optimized, measured forces/moments can be contaminated by fixture dynamics [3].

A direct measurement of the actual tire-patch displacements is not possible. To describe the displacement input (spectrum) of a certain road, the actual road surface can be measured/scanned [4]. An issue is that the actual phasing of the road input with respect to the four wheels is unknown, therefore assumptions on the phase relations must be made when applying them on the vehicle model. For this reason, comparison and validation with test results is not always immediate. Moreover, with this procedure only inputs in vertical direction can be obtained.

For both wheel-center forces and tire-patch displacements inverse load-identification technique can be used. This is a test-based approach where spindle or tire inputs are estimated using operational data and FRF measurements on the suspension system [5–7]. This is also called the Matrix-Inversion method, since the FRF matrix describing the chassis dynamics is inverted and multiplied times the operational measurements.

With inverse load-identification methods accurate vehicle road simulation can be performed up to 300 Hz [8]. However, accuracy of predictions is limited at low frequency where computed responses tend to overestimate the measured targets (see Fig. 1).

In this scenario, both wheel-center-forces and tire-patch inputs are still not reliable in the low-frequency region. Therefore, when equivalent patch-displacements are combined with a tire model and applied to a vehicle model, simulations involving ride comfort analysis are not possible. Improvements in the methodology for the inverse input estimation need to be achieved to be able to use identified tire inputs also at low frequencies.

In this paper a study is performed to get some insight in the cause of the low-frequency inaccuracy in current target predictions and to improve the quality of the inputs estimation at low frequency.

In Sect. 1, investigations are performed to understand whether the main negative effect in the inverse load-identification procedure is coming from tire or suspension non-linearities. In Sect. 2, a new methodology for load-identification via matrix-inversion is presented. Strain sensors are used to increase the quality of

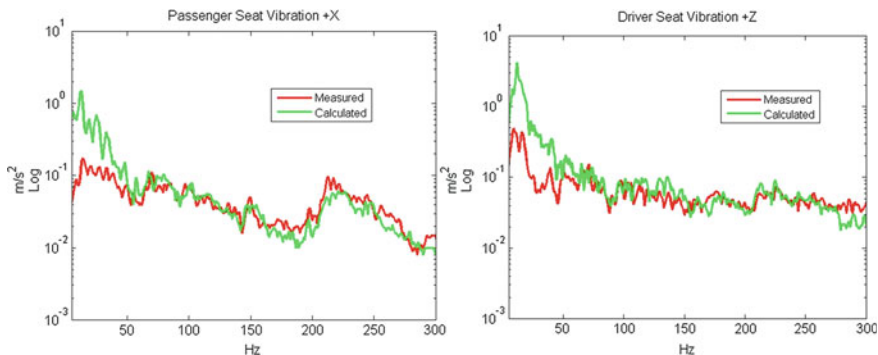


Fig. 1 Comparison between measured and predicted seat vibration

the estimated tire-patch inputs in the low-frequency region and to check the robustness of the method to different chassis characteristics.

Measurements performed with the new approach are described in Sect. 3. A validation is performed in Sect. 4. Estimated wheel-center loads and tire-patch displacements are presented in Sect. 5.

2 Problem Definition

A study is undertaken on the target prediction quality in the frequency range of interest to identify the most significant effect in worsening the input estimation procedure.

Contribution analyses performed with different tires are compared in terms of prediction accuracy. The estimation error has been quantified as the percentage difference between the RMS values of predicted and measured target response

$$Err(f) = \frac{RMS_{predict}(f) - RMS_{measur}(f)}{RMS_{measur}(f)} 100 \quad (1)$$

Different tires are coupled to the same vehicle body model used for the load identification procedure to investigate the effect of different tire characteristics.

Figure 2 shows the error plot as a function of frequency. A very large error (several orders of magnitude) is present at low frequencies close to 0 Hz, while the error tends to rapidly decrease for higher frequencies. After 50 Hz the error is stable on low values (between 1 and 3 dB); in this region well-correlating results can be obtained between measured and predicted target responses. In the low-frequency range (below 30 Hz) the influence of the tire appears limited since switching from a tire to another has no significant effect in the prediction error. Above that frequency, tire characteristics have a certain influence in the quality of the prediction.

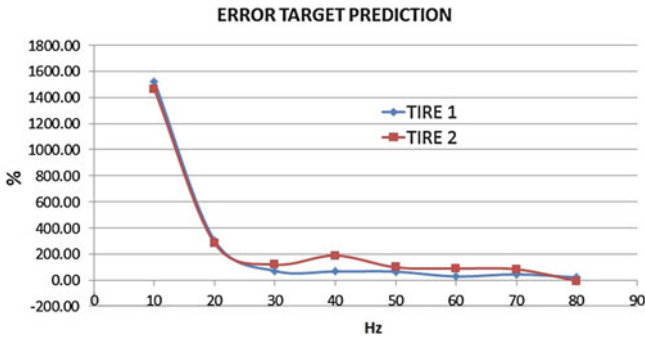


Fig. 2 Prediction error as a function of frequency for two different tires

However, the maximum errors can be found between 10 and 20 Hz, where the tire has almost no influence. Since suspension modes occur in that frequency range, non-linearities in the suspension system could be the source of inaccuracy.

One of the main non-linearities in the suspension is related to the damper friction, resulting in deteriorated isolation capability of the suspension system when a vehicle is driven on a smooth road [9]. While performing transfer-function measurements with the suspension in static conditions there is no input from the road and therefore the shock absorber is in the ‘stick’ phase, while during operational measurements it is in the desired gliding phase. The reduced damping and the vertical suspension stiffening due to the damper stick phase can shift low-frequency suspension modes that appear in the transfer-functions used for the inverse load-identification. This mismatching between static and operating conditions can bring a poor load-identification in the frequency range where these modes occur (below 50 Hz).

Next to the stiffening of the suspension that occurs when the shock-absorber is in the ‘stick’ phase, there is also the non-linear damping characteristic of the shock-absorber. The changes in the suspension stiffness between ‘stick’ and ‘slip’ condition will be significantly larger as the variation of the damping values due to its non-linear characteristic. Therefore, the assumption is made that the effect of the damping non-linear characteristic on the load-identification is less relevant as the effect of the stiffening of the suspension due to stick in the shock-absorber.

3 New Strain-Sensors Instrumentation

For FRF measurements in laboratory condition, the vehicle with no tires has to be free to move at the wheel spindles. A typical setup consists of four rubber blocks supporting the vehicle spindles. The setup can still influence the measurements at low frequency, the spindles rotation are constrained, so the rigid body modes are shifted above 10 Hz. In this study, a softer setup is used to have a completely

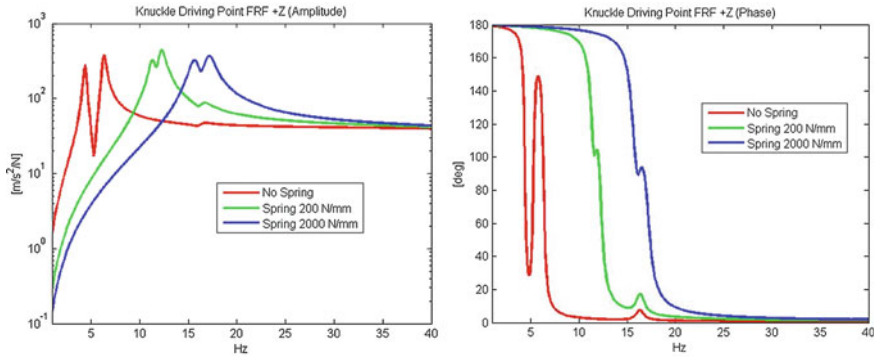


Fig. 3 Synthesized driving point FRFs on the knuckle with different values for suspension vertical stiffness

free–free condition on the spindles and to shift rigid body modes of the car at very low frequency (below 2 Hz) in order not to occur in the frequency range of interest.

A promising approach in the inverse force identification problem is the use of strain sensors. It is known that strain responses at body-level are more localized than acceleration responses, hence they are less affected by the global dynamic behavior of the structure. This leads to a better de-coupled FRF matrix and the capability of separating highly coupled input loads, for instance when forces on close-by connection points have to be identified [10, 11]. Moreover, this means a better conditioning of the inversion matrix and therefore more numerically stable force identification, especially at low frequency.

The same behavior is shown when we want to identify interface forces at suspension or wheel-level. Since our main goal is to have more accurate inputs in the low-frequency region, strain measurement can be an attractive approach.

An investigation has been carried out to check whether significant changes have to be expected in the structural acceleration measurements on the suspension when the damper is in stick condition.

A suspension FE model is used to synthesize the acceleration over force FRFs on the knuckle. The model is a full front axle Nastran model, and to simulate the effect of the stick condition an extra spring element is added in parallel to the shock absorber to increase the suspension stiffness in the vertical direction.

In Fig. 3 the amplitude and phase of a driving point transfer function on the knuckle with different vertical suspension stiffness is reported. The dominant response in these transfer functions is related to suspension rigid body modes—especially the vertical wheel-hop mode (7–15 Hz). By increasing the suspension vertical stiffness—simulating the effect of the shock absorber in stick condition—the peaks shift to higher frequencies generating significant changes in the FRFs, both in amplitude and phase.

This shows that knuckle indicator FRFs change in a significant way when the friction of the shock absorber increases the vertical stiffness of the suspension.

Fig. 4 Knuckle instrumentation for indicator points FRF measurements



Through that, the measured indicator FRFs for inverse load-identification are not a proper representation of the actual suspension behavior in operational condition which leads to the risk of reduced load input estimation quality.

4 Measurements

A vehicle has been instrumented with both accelerometers and strain sensors to perform load-identification and target vibration prediction. Piezo-electric strain sensors are used in this study since they are more sensitive than normal strain gauges and they can measure signals from 2 Hz up to very high frequencies.

15 strain sensors are placed on each wheel providing over-determination to the problem to have a numerically stable matrix inversion. Indicator points are chosen on the passive side, on the knuckles. The classic acceleration-based instrumentation is added for comparison, with 4 tri-axial accelerometers placed on each knuckle.

Target accelerometers are placed on the driver seat rail for the vibration comfort study (Fig. 4).

Operational measurements are performed on a chassis-dynamometer with cleat impacts for an impulsive excitation. All signals are acquired during this test, both on indicator and target locations. These measurements are then processed into indicator and target spectra, which are needed for the frequency-domain load-estimation and analysis.

Hammer based FRF measurements are completed at each of the four spindle-centers. These measurements are performed on the vehicle with tires removed, while suspended in free-free condition. Structural FRFs are measured on indicator points for accelerometers and strain sensors. Vibro-acoustic FRFs needed for path contributions are measured from input locations to target seat. Local acceleration

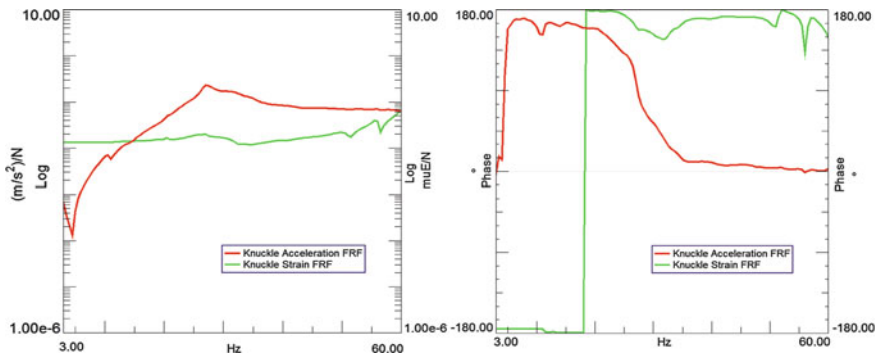


Fig. 5 Indicator FRFs on the knuckle. Comparison between strain and acceleration responses

over force FRFs on the wheels are also measured for the coupling of the vehicle body + suspension model (vehicle model) to a tire model with Frequency Based Substructuring (FBS). This is needed to have a full vehicle model where tire-patch displacement inputs can be estimated.

Figure 5 shows an example of strain and acceleration FRFs measured on suspension passive side.

As expected from the pre-study, strain signals provide a more flat response in the frequency range of interest while acceleration FRFs are much more influenced by suspension dynamics.

An experimental tire model is created with a direct measurement of the patch-rim FRFs as reported in [8]. It describes the non-rotating dynamics of a pre-loaded tire in free-free condition with a displacement input at the tire patch. Also local FRFs on the rim are measured to have the local stiffness matrix at the connection point to the vehicle.

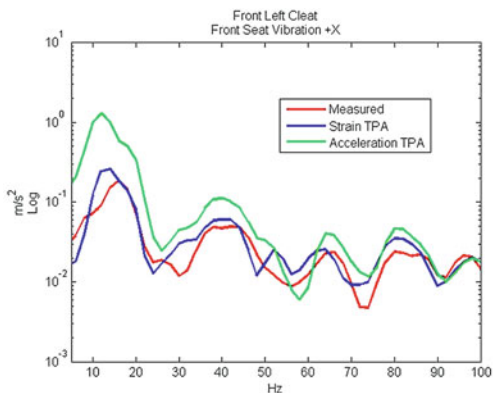
Finally, the tire FRF model and the vehicle FRF model are assembled by means of their transfer functions with FBS to create a complete car model. Free interface FRFs at the coupling points are required for both the subsystems together with the stiffness properties of the connection (which is rigid in this case). With FBS a new set of FRFs is obtained that describes the transfer between an input at the tire patch and an output at the targets or indicator locations on the knuckles.

5 Results and Validation

With all the gathered information, inverse load-identification can be performed on the vehicle model to obtain spindle forces and on the full car model with patch displacements as results.

Identified road inputs are then used to perform a contribution analysis or Transfer Path Analysis (TPA) with front seat vibrations as targets. With the superposition of all the contributions of the considered paths (i.e. input loads),

Fig. 6 Front seat vibration in X direction for front left cleat impact



the total target spectrum can be synthesized and compared to the measured response during operational test (see Eq. 2).

$$P_k(\omega) = \sum_i p_{ik}(\omega) = \sum_i H_{ik}(\omega)F_i(\omega) = \sum_i \left(\frac{P_k}{F_i}(\omega) \right) F_i(\omega) \quad (2)$$

Where:

$p_{ik}(\omega)$ Partial contribution of path i to target response k [Pa] or [m/s^2]

$H_{ik}(\omega)$ Vibro-acoustic FRF between target response k and input force at path i [$\frac{Pa}{N}$] or [$\frac{m/s^2}{N}$]

$F_i(\omega)$ Operational load acting at path i [N]

First only the vehicle model is used for validation, namely wheel-center loads are used as inputs for the calculations with no tire coupled to the system.

Figure 6 shows the predicted seat acceleration in longitudinal direction due to a cleat impact at the front left wheel. The contributions of all the paths (namely the wheel forces) are summed to obtain the total prediction.

As presented in the previous graphs, strain-based target prediction shows a significant improved correlation in the frequency region of interest. Acceleration-based approach shows an overestimation of target response at low frequency.

Remaining errors are still present in strain predictions: in general, low quality correlation can be explained with the stick-slip phenomenon influencing also the strain signals (but less than acceleration responses) and target FRFs.

A validation on the full vehicle model (body + suspension coupled to the tires) is then performed.

Figure 7 shows the resulting seat predictions in longitudinal direction for a front left cleat input.

Predicted seat response provides a good correlation with measured target also when the tires are coupled to the vehicle. Strain-based prediction is still better than

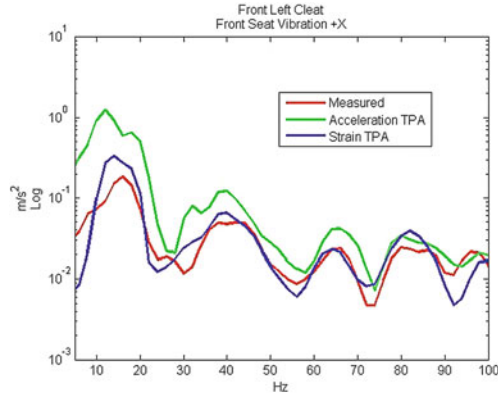


Fig. 7 Front seat vibration in X direction for front left cleat impact (full vehicle FBS model)

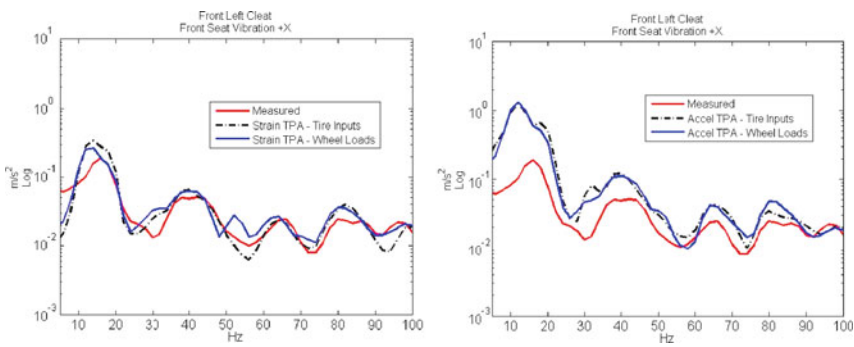


Fig. 8 Comparison between vehicle model and FBS model prediction for strain-based (*left*) and acceleration-based (*right*) approach

acceleration-based, especially at low frequency (below 30 Hz) where acceleration TPA overestimates the response.

A comparison has been made on the seat vibration predicted with the body model and the full vehicle model, to evaluate the target prediction quality when using wheel-center-forces or tire-patch displacements. Figure 8 shows the results of the comparison for the strain-based and acceleration-based front seat prediction.

As presented above, nearly identical target-predictions are obtained when using wheel-center-forces as inputs or when using tire-patch displacements as inputs. The strain-based results clearly show a better correlation with the measured response as the acceleration-based results. This means that the NVH full vehicle model with tire-patch inputs based on strain indicator data can now also be applied for comfort studies below 50 Hz.

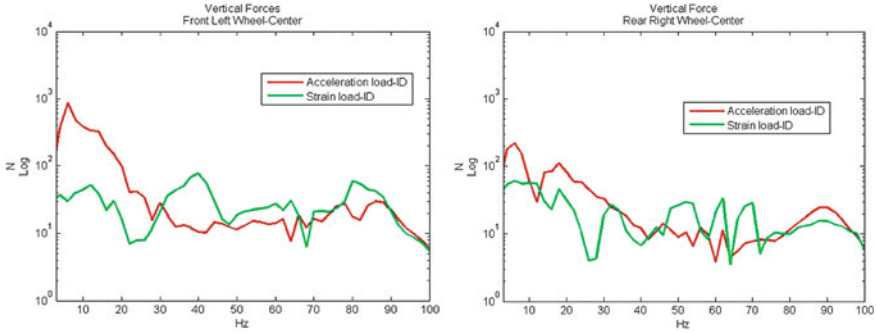


Fig. 9 Vertical wheel loads for front left cleat (*left*) and rear right cleat (*right*)

The input estimation is improved through the use of strain indicators that are more robust for suspension non-linearities. However, the target FRFs can also be influenced by the stick phase of the shock-absorbers. Since that effect has not yet been corrected, this can be a possible source for the remaining small errors in the target prediction.

6 Identified Inputs

With the vehicle body FRFs Inverse Load-Identification has been performed to estimate interface forces at the wheel-level. 3 forces and 2 moments are identified at each wheel center. The torque along Y axis is not considered since the spindle is free to rotate with respect to that axis.

Figure 9 provides some samples of estimated loads in Z direction for front and rear axles due to the cleat excitation.

At lower frequencies the acceleration-based forces show significantly higher levels as the ones resulting from strain-based approach. This difference tends to reduce at higher frequencies where the estimated loads have comparable amplitudes.

The target predictions have shown that the acceleration-based approach gives a significant overestimation of the target responses. Based on the above it can be concluded that the strain-based approach provides more reliable inputs in this low-frequency range as the acceleration-based approach.

Evaluation of the strain FRF matrix shows that a stable inverse load-identification at low frequencies is achieved. Figure 10 compares the condition number of the acceleration FRF matrix and strain FRF matrix. The strain FRF matrix is well conditioned since the condition number is always below the threshold of 100 in the whole frequency range of interest except for few peaks.

With the full vehicle FBS model matrix-inversion is performed on the FRF matrix from tire patch inputs to indicator points. Tire-patch inputs are estimated by

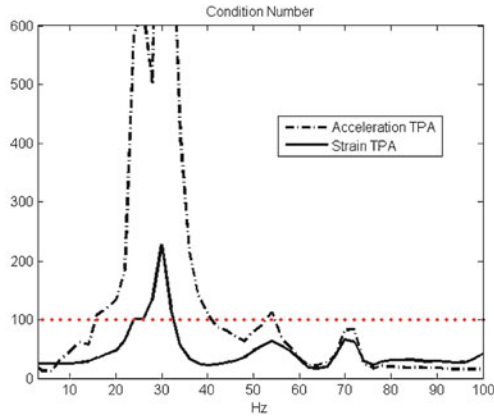


Fig. 10 Condition number for acceleration-based and strain-based load identification

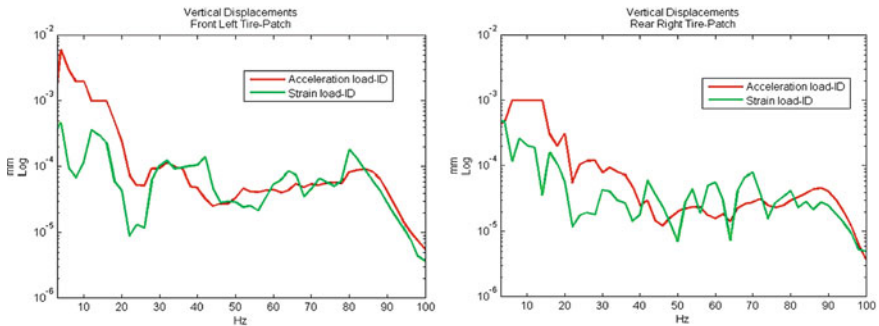


Fig. 11 Vertical patch displacements for front left cleat (left) and rear right cleat (right)

using spectra of operational acceleration and strain data. These are the operational equivalent displacements at the contact patch (Fig. 11).

Vertical tire-patch displacements show a similar trend to the wheel-center forces, meaning that a gap is present at low frequency between acceleration-based and strain-based inputs. At higher frequency the two methods provide similar results.

7 Conclusions

Tire models for NVH applications can be combined with equivalent patch-inputs to perform road noise analysis when coupled to a vehicle model. Ride comfort studies with the same approach are difficult, because of the inverse input identification process that does not provide reliable results at low frequencies.

In this paper a study has been carried out to understand the main cause of the low-frequency inaccuracy in the input estimation, and an alternative methodology is developed to improve current results.

Investigations performed on an FE suspension model showed that significant changes in the FRFs measured on suspension components are present due to damper non-linearities mainly related to dry friction. Tire non-linearity does not seem to play a dominant role in the frequency range of interest (below 50 Hz) compared to the non-linear effects in the suspension.

The assumption is made that the suspension stiffening effect due to stick in the shock-absorber is more relevant as changes in damping values due to the non-linear damping characteristic.

The equivalent tire-patch inputs need to be estimated such that the identification process is less influenced by suspension non-linearity, in order to extend its applicability below 50 Hz. It is shown that strain signals provide a more localized response on indicator points on the knuckles used for the FRF matrix-inversion, leading to a more de-coupled FRF matrix and a better input estimation at low frequency.

An experimental methodology is proposed to obtain more accurate low-frequency patch inputs using the inverse load-identification approach in combination with strain measurements on the vehicle suspension. Equivalent tire-patch displacements—from the ‘old’ acceleration-based approach and from the ‘new’ strain-based approach—are estimated by using a full vehicle FBS model specially created.

Validation on road induced vibration prediction is performed in the frequency domain with a Transfer Path Analysis. The strain-based results do show good correlation between predicted and measured seat responses—also below 50 Hz. A comparison with the typical acceleration-based approach shows a significant increase on the obtained results. Hence, the strain-based approach provides more reliable inputs in the low-frequency region compared to typical acceleration-based methodology.

With the new method, the quality of the estimated equivalent tire-patch is highly improved. This means that the process where these tire-patch inputs are used for application to e.g. hybrid vehicle models (for suspension or body optimization) can now also be used for lower frequency applications such as comfort.

Acknowledgments We gratefully acknowledge IWT Vlaanderen for their support of the project IWT-090408 “CHASING”.

References

1. Gobbi M, Mastinu G, Giorgetta F (2005) Sensor for measuring forces and moments with application to ground vehicle design and engineering. Proceedings of IMECE2005, ASME conference, Orlando, 2005

2. Gobbi M, Guarneri P, Mastinu G, Rocca G (2008) Test rig for characterization of automotive suspension systems. SAE-paper 2008-01-0692
3. Lee JU, Suh JK, Jeong SK, Kandarpa S, Ahsan A, Wolf WL (2003) Development of input loads for road noise analysis. Proceedings of the 2003 SAE noise and vibration conference, paper 2003-01-1608
4. Gagliano C, Gobbi M, Mastinu G, Pennati M (2012) Indoor/outdoor testing of a passenger car suspension for vibration and harshness analysis. SAE Int J Passeng Cars Mech Syst 5(2):937–948. doi:[10.4271/2012-01-0765](https://doi.org/10.4271/2012-01-0765)
5. Gagliano C, Martin A, Cox J, Clavin K, Gerhard F, Michelis K (2005) A hybrid full vehicle model for structure borne road noise prediction. Proceedings of the 2005 SAE noise and vibration conference, paper 2005-01-2467
6. Park J, Gu P, Juan J, Archie N, Van Loon J (2001) Operational spindle load estimation methodology for road NVH applications. SAE noise and vibration conference and exposition
7. Park J, Gu P (2003) A new experimental methodology to estimate chassis force transmissibility and applications to road NVH improvement. SAE noise and vibration conference and exposition
8. Gagliano C, Tondra M, Fouts B, Geluk T (2008) Development of an experimental tire and road surface model for vehicle interior noise prediction. SAE-paper, 09AC-0081
9. Geluk T, Van der Linden PJG, Van de Wouw N, Nijmeijer H (2006) Test-based modeling of friction-induced deterioration of suspension vibration isolation on smooth roads. The 8th international symposium on advanced vehicle control, Aug 20–24, 2006, Taipei, Taiwan
10. Geluk T, Van der Linden PJG, Vige D, Caudano M, Gottardi S, Ciruolo F, Mir H (2011) Noise contribution analysis at suspension interfaces using different force identification techniques. SAE-paper, 2011-01-1600
11. Shiozaki H, Geluk T, Daenen F, Iwanaga Y et al (2012) Time-domain transfer path analysis for transient phenomena applied to tip-in/tip-out (shock & jerk). SAE technical paper 2012-01-1545, doi:[10.4271/2012-01-1545](https://doi.org/10.4271/2012-01-1545)

Part II
Transmission Vibration
and Noise Control

Torsional Finite Element Analysis of Driveline Torsional Vibration for a Front Wheel Driveline Vehicle Development

Yuanfeng Xia, Hongcheng Li, Xiong Tian, Hongying Wang and Yu Tang

Abstract The purpose of this paper is to study the torsional vibration of Front Wheel Driveline (FWD), to avoid the torsional resonance with vehicle, to reduce the torsional vibration and gear rattle noise, and to find out the sensitive factors for controlling the torsional vibration. A torsional finite method is used to establish a 4D-freedom torsional vibration analysis model for FWD system. The natural frequency and modal shapes are calculated, and the torsional vibration characteristics are acquired by system excitation. A 4D-freedom torsional vibration model is established, and numerical simulation for the characteristics of the driveline is analyzed. An optimal method is established to reduce driveline torsional vibration and gear rattle noise. Many factors, such as rotational shaft unbalance, shaft offset its rotation center due to the clearance of universal joints, splines and other components, and non-straight of driveshaft, influence torsional vibration. In order to simplify the analysis model, these factors are not considered. A torsional vibration analysis model with torsional finite method is established, A matching method between system stiffness and damping is presented to reduce driveline torsional vibration and gear rattle noise. In the third order mode of the driveline system, the input shaft of the transmission has the biggest amplitude and its modal frequencies vary with different gears. In order to avoid torsional resonance with other components, the torsional modal frequency could be changed by modulating the stiffness of clutch, driveshaft and tire. The NVH tests show that it's effective to reduce the torsional vibration by modulating the clutch stiffness and torsional angle.

F2012-J02-001

Y. Xia (✉) · H. Li · X. Tian · H. Wang · Y. Tang
Changan Auto Global R&D Center, Chongqing 401120, China
e-mail: sunqiemail@163.com

Y. Xia · H. Li · X. Tian · H. Wang · Y. Tang
State Key Laboratory of Vehicle NVH and Safety Technology, Chongqing 401120, China

Keywords Torsional finite element methods · FWD · Torsional mode · Forced vibration · Gear rattle noise

1 Introduction

Currently, the Front Wheel Driveline (FWD) system is widely used in passenger cars due to the compact room and fuel economy. As people's living standards improved, vehicle's NVH (Noise, vibration and Harshness) performance also attracts more and more attention of consumers and enterprises. The rattle noise caused by low frequency torsional vibration in transmission system becomes a NVH research hot spot at home and abroad.

Many authors have studied the transmission gear rattle behavior which is produced by torsional vibrations of the complete driveline [1–3], while other authors focused on transmission gear parameters research. Mehmet Bozca developed a dynamic model with four degrees of freedom model for an automatic transmission. The optimization of gearbox geometric design parameters, such as the module, numbers of teeth, axial clearance, and backlash to reduce rattle noise based on a torsional vibration model approach is studied [4]. Younes Kadmiri developed a test method and numerical simulation model to analyze the transient response of gear under drag torque [5]. In Ref. [6], firstly, an instrumented test rig consisting of a simplified gearbox was designed in order to recreate the rattle noise for a multi harmonic excitation imposed to the input shaft. Secondly, different gearbox configurations were used to characterize the rattle threshold and the rattle noise evolution, in relation to excitation parameters and mechanical gearbox parameters. Finally, a simplified model of the rattle phenomenon was drawn, using a Kelvin–Voigt model in order to determine the most significant parameters influencing the rattle noise.

The torsional vibration is the excitation source of gear rattle noise. There are many research methods to solve torsional vibration, such as Holzer method, transfer matrix method, etc. The traditional finite element method is used by torsional finite element method to analyze the torsional vibration. For straight-gear system, two rotating disks coupled by an elastic shaft segment are considered as a finite element. But for gear transmission system, gear-branched system is a common structure. In general, the FEM formulation for gear-branched system is much more difficult than that of a straight-gear system. Wu and Chen [7] used finite element method to establish natural modal frequency and shape. Crowther established five basic torsional finite elements for direct, branched, grounded connections, and geared connections with rigid or elastic tooth mesh. All the torsional vibration system can be simplified by the five basic elements. Crowther [8] established the model of manual transmission system and automatic transmission system with five basic elements, and analyzed the natural vibration and transient vibration.

In this paper, the finite element method is used to establish four degrees of freedom torsional vibration analysis model for manual transmission system, and to calculate the natural frequencies and modal shapes. The torsional modal sensitivity to critical parameters is analyzed, which supplies the theoretical support for avoiding resonance between torsional and bending modes. Besides, the forced vibration is also analyzed, and the crankshaft is forced by fluctuation torque excitation, the results show that reducing the clutch stiffness, increasing the inertia of flywheel, and increasing the damping of clutch can significantly decrease the torsional vibration of transmission input shaft, which has been proved by experiments.

2 Modeling the Fwd System with Torsional Element Method

FWD system mainly consists of crank shaft, flywheel, clutch, transmission, half shaft, and wheel, as shown in Fig. 1.

The stiffness, inertia and damping model is given in Fig. 1, which can be simplified with the basic torsional finite elements. They are direct, geared, branched, grounded, geared and gear meshed elements [8], as shown in Fig. 2, where k is torsional stiffness or gear meshed stiffness, J is inertia, and c is damping.

The FWD dynamic model given in Fig. 1 can be simplified with five basic torsional finite elements, as shown in Fig. 3. It is assumed that the gear mesh stiffness is large enough, and the vehicle is replaced by equivalent rotational inertia instead of translation inertia, where T_{eng} is engine torque, T_{drag} is drag torque, J_1 is flywheel inertia, J_2 is clutch hub inertia and transmission gear inertia, J_2' is differential inertia, J_3 is wheel inertia, J_4 is equivalent inertia of the whole vehicle, k_1 is clutch stiffness, k_2 is half shaft stiffness, and k_3 is tire stiffness.

Figure 3 presents a dynamic model for FWD system, the system inertia, stiffness and damping matrices and local coordinate vectors for this system are:

$$J = \begin{bmatrix} J_1 & 0 & 0 & 0 \\ 0 & J_2+n^2J_2' & 0 & 0 \\ 0 & 0 & nJ_3 & 0 \\ 0 & 0 & 0 & nJ_4 \end{bmatrix} \quad (1a)$$

$$K = \begin{bmatrix} k_1 & -k_1 & 0 & 0 \\ -k_1 & k_1+n^2k_2 & -nk_2 & 0 \\ 0 & -nk_2 & nk_2 + nk_3 & -nk_3 \\ 0 & 0 & -nk_3 & nk_3 \end{bmatrix} \quad (1b)$$

$$C = \begin{bmatrix} c_1 & -c & 0 & 0 \\ -c_1 & c_1+n^2c_2 & -nc_2 & 0 \\ 0 & -nc_2 & nc_2 + nc_3 & -nc_3 \\ 0 & 0 & -nc_3 & nc_3 \end{bmatrix} \quad (1c)$$

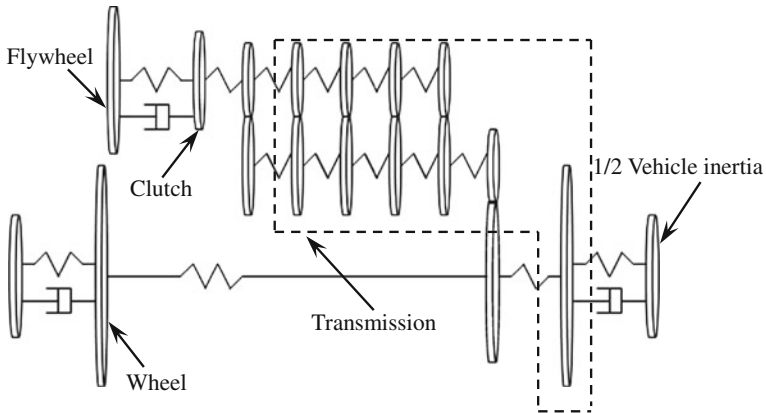


Fig. 1 Torsional model of FWD

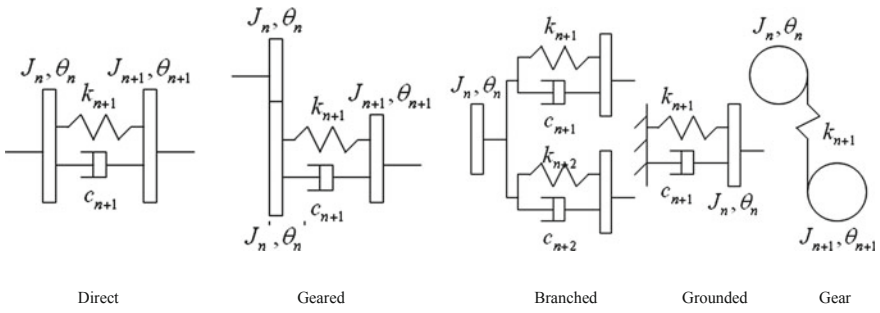
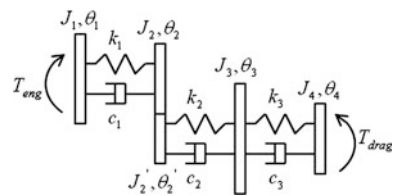


Fig. 2 The five basic torsional elements

Fig. 3 The dynamic model for FWD with manual transmission



$$\theta = \begin{bmatrix} \theta_1 \\ \theta_2 \\ \theta_3 \\ \theta_4 \end{bmatrix} \tag{1d}$$

Where n is gear ratio.

Table 1 Natural mode of gear two

Frequency (Hz)	First order	Second order		Third order
	3.09	9.52	12.16	61.29
Engine	1.00	1.00	1.00	-0.05
Input shaft	0.95	0.48	0.15	1.00
Differential	0.29	0.15	0.05	0.31
Wheel	0.27	-0.80	-0.27	-0.01
Vehicle	-0.01	0.01	0.01	0.01
Damped frequency	3.10	9.41	12.13	61.28
Damping ratio (%)	15.3	7.48	3.04	0.02

3 The Torsional Mode and Modal Sensitivity Analysis

3.1 Modal Analysis

Combination of the inertia, stiffness, damping matrices, the final control equation is as follows:

$$J\ddot{\theta} + C\dot{\theta} + K\theta = T \quad (2)$$

The undamped torsional mode is solved, and the Eq. 2 is changed as:

$$J\ddot{\theta} + K\theta = 0 \quad (3)$$

For natural frequency vibration:

$$\theta(t) = \theta^* e^{i\omega t} \quad (4)$$

Equation 4 is inserted into Eq. 3, obtain:

$$(K - \omega^2 J)\theta^* = 0 \quad (5)$$

Taking gear two for example, the dynamic model of Fig. 3 is solved, and the modal frequency, relative modal amplitude and damping ratio are obtained, as shown in Table 1.

The second order mode shows different shapes and frequencies between left wheel and right wheel because of different length and torsional stiffness between left and right half shafts.

The first, second, and third order modal shapes are listed in Table 1 according to the relative modal amplitude are shown in Fig. 4.

The first order mode closely corresponds to the so called shuffle vibration mode occurring on the vehicle, and the second order mode corresponds to judder vibration. It is easy for the third order mode also known as transmission gear rattle mode to produce gear rattle noise, and its modal frequency corresponds to the engine speed that in the commonly used speed range.

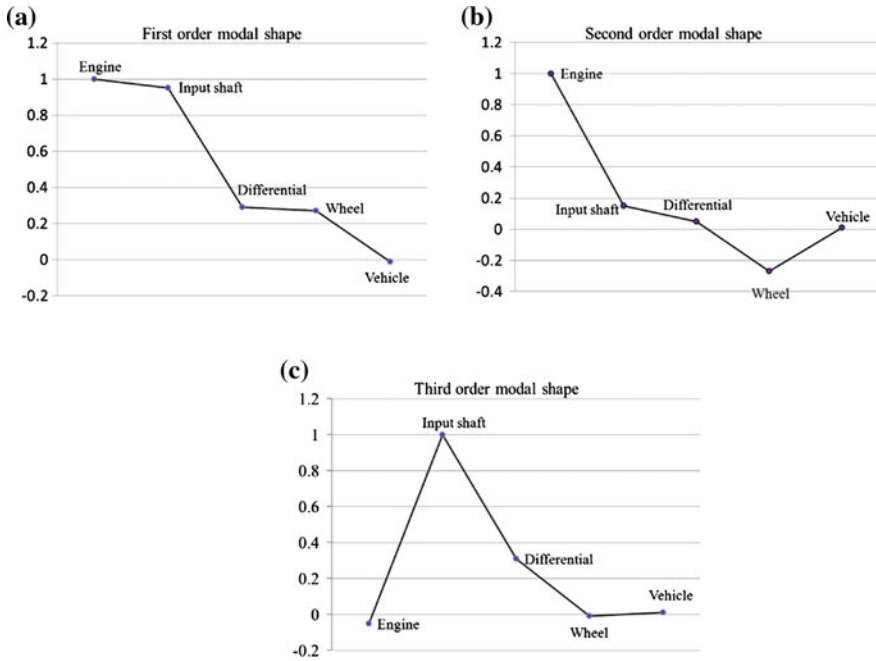


Fig. 4 a The first order modal shape, b the second order modal shape, c the third order modal shape

Table 2 Natural mode with different gear

Modal frequency(Hz)	First order	Second order	Third order
Gear 2	3.09	9.52	61.29
Gear 3	3.27	9.59	63.05
Gear 4	3.48	9.68	65.88
Gear 5	3.58	9.72	67.57

Different gear has the different modal frequencies, as shown in Table 2.

The modal frequency varies with different gears. The third order modal frequency changes significantly, while the first and second order modal frequencies change lightly. This is due to the equivalent inertia and stiffness changing with gear variation.

3.2 Modal Sensitivity Analysis

Clutch stiffness, half shaft stiffness, flywheel inertia, and transmission inertia which influence the system torsional mode distribution, are critical parameters for the optimization and system matching. Modal sensibility analysis can be used to

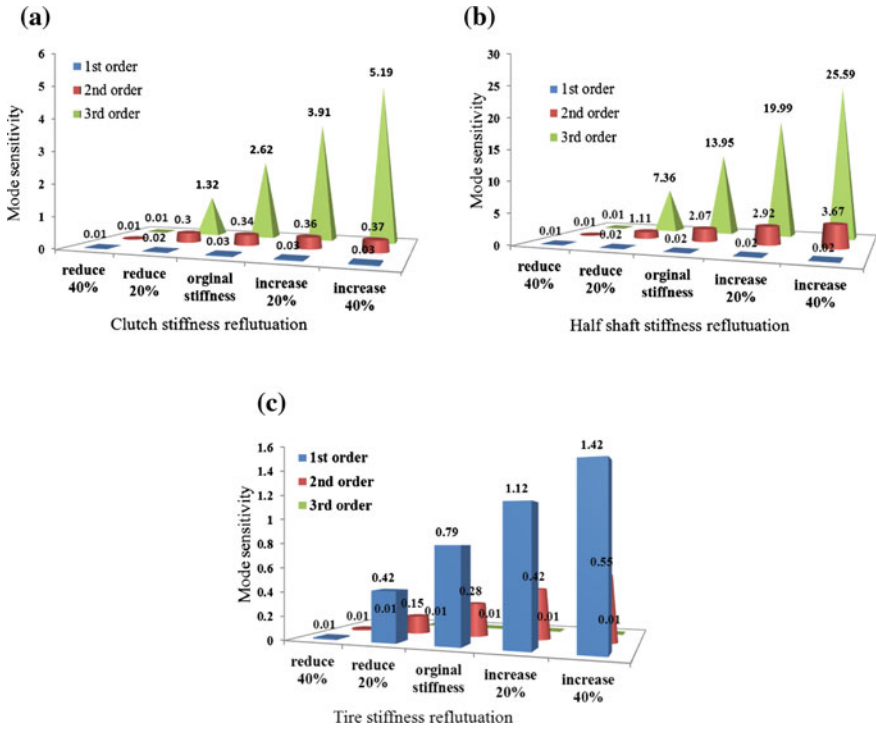


Fig. 5 **a** Modal sensitivity to clutch stiffness, **b** modal sensitivity to half shaft stiffness, **c** modal sensitivity to tire stiffness

find the critical parameters that influence the modes greatly. At the same time, it provides an important guide in engineering application.

3.2.1 Stiffness Sensitivity Analysis

Taking gear five for example, the result for modal sensitivity analysis is shown in Fig. 5.

Torsional mode sensitivity to the torsional stiffness of the critical components is analyzed by increasing and decreasing the torsional stiffness by 20 and 40 percent. The conclusion shows that in the same gear, the torsional stiffness has a different disturbance to the torsional mode, as shown in Fig. 5. The analytical conclusions are as follow:

- A. Assuming that other parameters unchanged, and the clutch stiffness is fluctuating, the results show that the first and second order modal frequencies are less affected by clutch stiffness, and third order modal frequency is the same as previous one. The clutch stiffness is increased by 20 percent, and the third order modal frequency is increased only by 1.3 Hz.

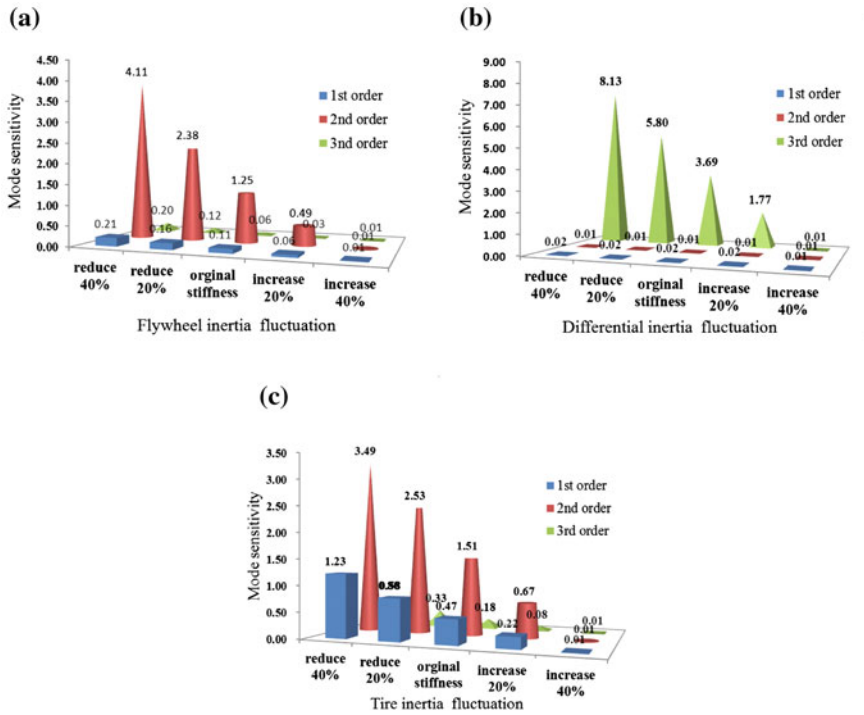


Fig. 6 **a** Modal sensitivity to flywheel inertia, **b** modal sensitivity to differential inertia, **c** modal sensitivity to tire inertia

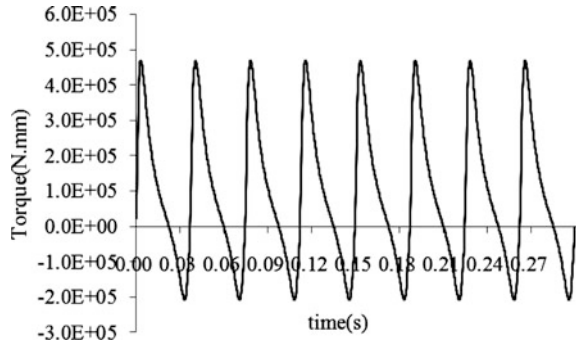
- B. Assuming that other parameters unchanged, and the half shaft stiffness is fluctuating, the results show that the first order and second order modal frequencies are less affected by half shaft stiffness, but the third modal frequency is much more affected by half shaft. The half shaft stiffness is increased by 20 percent, and the third order modal frequency is increased by 6 Hz, so, the transmission gear rattle mode can be changed by adjusting half shaft stiffness.
- C. The same analysis is applied to tire stiffness. The results show that first order modal frequency has relatively more change.

3.2.2 Stiffness Sensitivity Analysis

Modal sensitivity to the inertia of critical components is analyzed by increasing and decreasing the inertia by 20 and 40 percent, the results are shown in Fig. 6.

The conclusion shows that in the same gear, the inertia has a different disturbance in torsional mode, as shown in Fig. 6. The analytical conclusions are as follow:

Fig. 7 Torque fluctuation at 800 rpm



- A. Assuming that other parameters unchanged and only the inertia is increased, the second order modal frequency is decreased much more compared with increasing the inertia of flywheel, while with first and third order modal frequencies have less change.
- B. Assuming that other parameters unchanged, the third order modal frequency is significantly affected by inertia of differential. So, the transmission rattle modal frequency can be changed by adjusting the inertia of differential.
- C. The same analysis is applied to tire inertia. The results show that the torsional mode is less affected by inertia of tire. For example, the inertia of tire is increased by 20 percent; the second order modal frequency is decreased by only 1 Hz.

4 Forced Vibration Analysis

Forced vibration analyzes time response of the system. The equation of force vibration based on the Eq. 2 is obtained as follows.

$$J\ddot{\theta}(t) + C\dot{\theta}(t) + K\theta(t) = T(t) \tag{6}$$

The torque fluctuation of engine is the primary excitation sources of torsional vibration. The torque fluctuation of four cylinders engine is shown in Fig. 7.

The FWD dynamic model of system is excited with time-varying torque, and the vibration response of flywheel and transmission is obtained, as shown from Figs. 8 to 9. The angular acceleration response of flywheel shows that second order torsional vibration is the primary response under engine torque excitation.

Figure 9 presents the torsional response of transmission input shaft. The figures show that the torsional vibration of transmission shaft is amplified hugely at 2.5 s, which is due to third order torsional resonance. In frequency domain, there is peak amplitude at 61 Hz which is corresponding to the third order modal frequency.

The torsional vibration amplitude of transmission is decreased from input shaft to differential, as shown in Fig. 10, which is corresponding with Fig. 3c.

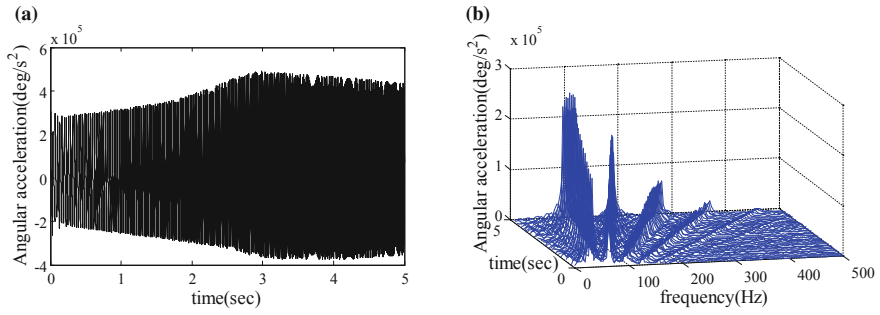


Fig. 8 **a** Angular acceleration response of flywheel in time domain, **b** Angular acceleration response of flywheel in frequency domain

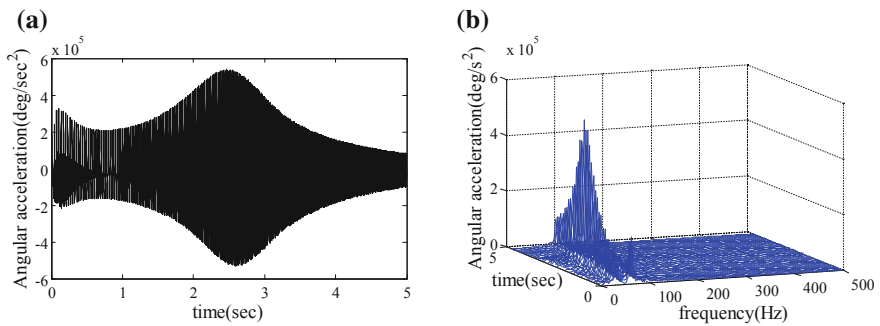


Fig. 9 **a** Angular acceleration response of input shaft in time domain, **b** Angular acceleration response of input shaft in frequency domain

Fig. 10 The different angular acceleration response of input shaft, middle shaft and differential

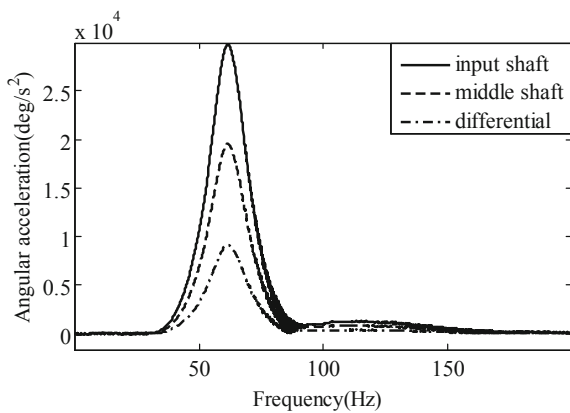
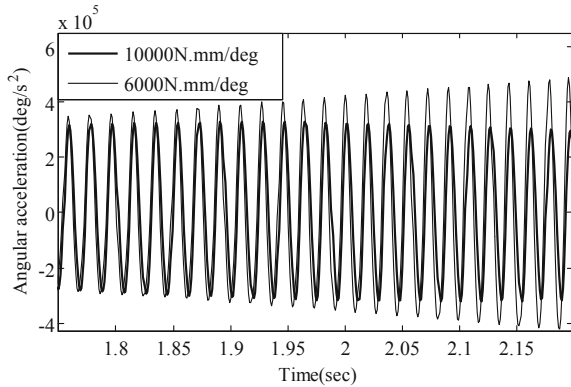


Fig. 11 The response of input shaft with different clutch stiffness



The second order torsional resonance of transmission shaft is much high, which can easily produce gear rattle noise.

5 The Critical Parameters to Torsional Vibration Response

The modal analysis and modal sensitivity analysis show that stiffness and inertia are not only the critical parameters influencing modal frequency, but also have an effect on torsional vibration response. The following studies show the affection of inertia, stiffness and damping to torsional vibration.

5.1 The Affection of Stiffness to Torsional Vibration

Assume other parameters are unchanged. The response at transmission input shaft is calculated by reducing clutch stiffness and applying the same torque to the engine crankshaft, as shown in Fig. 11. The Fig. 12 shows that the amplitude of torsional vibration is decreased greatly, and the resonance frequency is also reduced by decreasing clutch stiffness.

Assume other parameters unchanged. The results show that system torsional vibration changes little, but the torsional resonant frequency decreases significantly by reducing half shaft torsional stiffness and applying the same torque to the engine crankshaft, as shown in Figs. 13 and 14.

Fig. 12 The response of input shaft and differential with different clutch stiffness

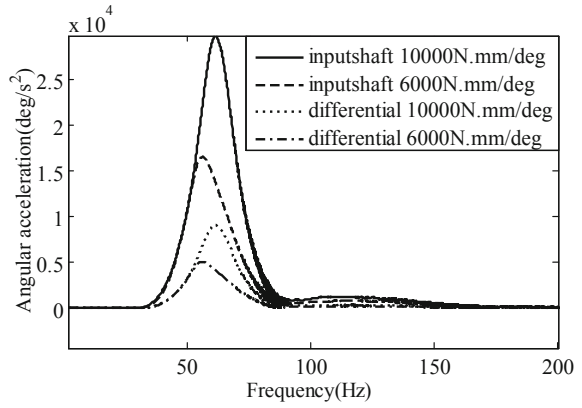


Fig. 13 The response of input shaft with different half shaft stiffness

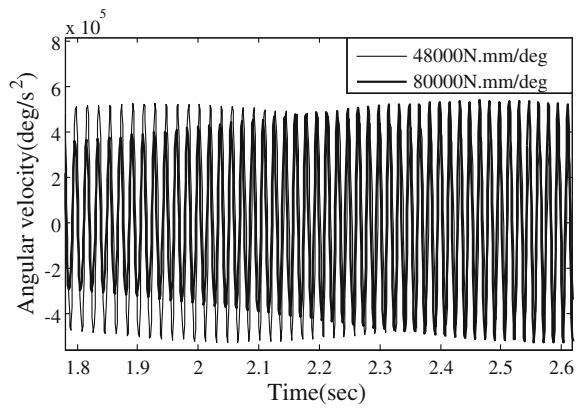


Fig. 14 The response of input shaft and differential with different half shaft stiffness

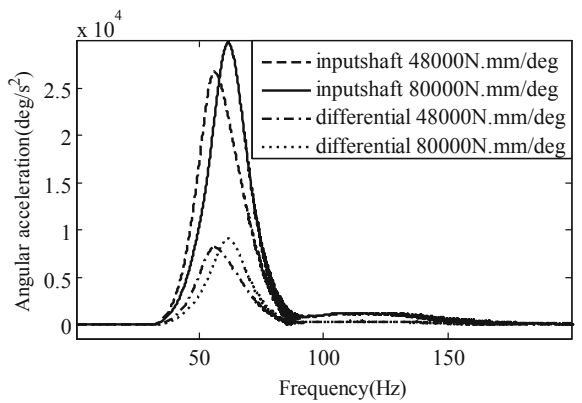


Fig. 15 The response of input shaft with different flywheel inertia

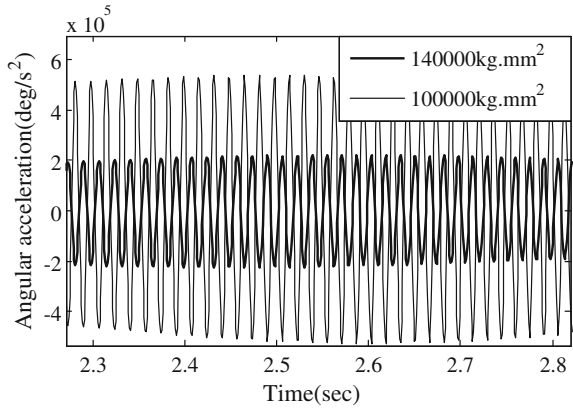
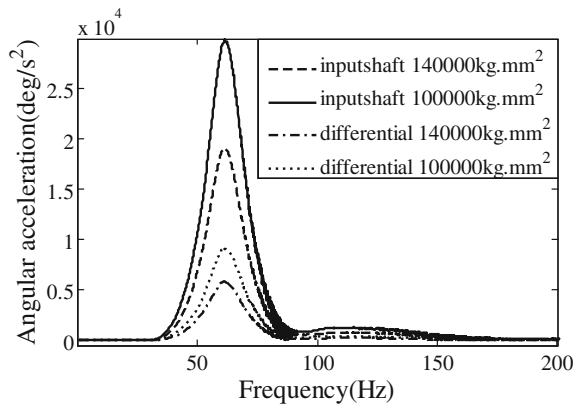


Fig. 16 The response of input shaft and differential with different flywheel inertia



5.2 The Affection of Inertia to Torsional Vibration

The inertia of flywheel is increased by 40 percent and other parameters unchanged. The results show that the torsional vibration is decreased by 55 percent, as shown in Figs. 15 and 16. The torsional resonance frequency is not changed, because the flywheel inertia has no effect on the third order torsional modal frequency.

5.3 The Affection of Damping to Torsional Vibration

The clutch damping is increased and other parameters are fixed. The results show that the angular acceleration fluctuation of input shaft is decreased much more, and the torsional vibration of system is reduced considerably, as shown in Figs. 17 and 18.

Fig. 17 The response of input shaft with different clutch damping

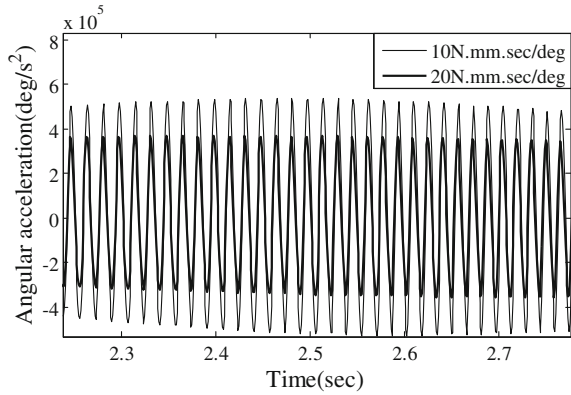
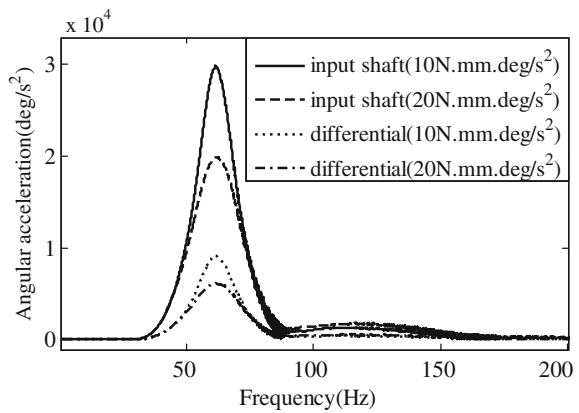


Fig. 18 The response of input shaft and differential with different clutch damping



6 The Torsional Vibration Test Analysis

The torsional vibration test method is shown in Fig. 19. The square signal of flywheel and transmission input shaft in gear three are measured, and the measured curves are presented in Fig. 20. The angular acceleration as a function of engine speed is obtained by calculating flywheel teeth and gear teeth. The second order angular acceleration amplitudes of flywheel and the input shaft under WOT (Wide Open Throttle) condition are displayed as a function of the mean engine speed of rotation in rpm, the curve of gear four is shown in Fig. 21.

The angular acceleration of transmission input shaft is amplified at torsional resonance rpm, the rattle noise is considerably reduced in around 2,000 Hz, and articulation index is increased 5 percent by covering the transfer case with absorption cotton, as shown in Figs. 22 and 23. The articulation index of is reduced considerably at resonance engine rpm.

Fig. 19 The test of torsional vibration

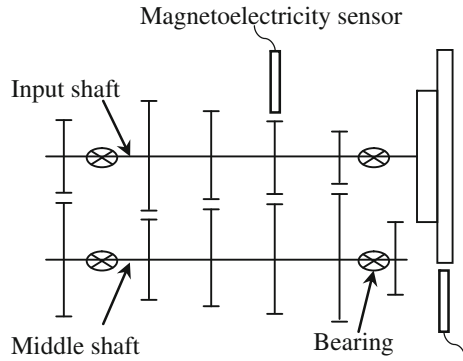


Fig. 20 Time signal of flywheel

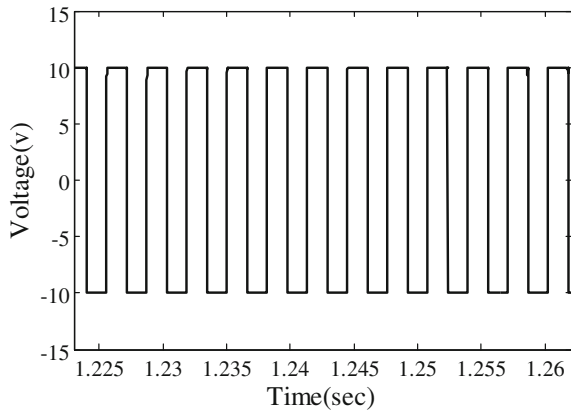


Fig. 21 The angular acceleration of input shaft and flywheel

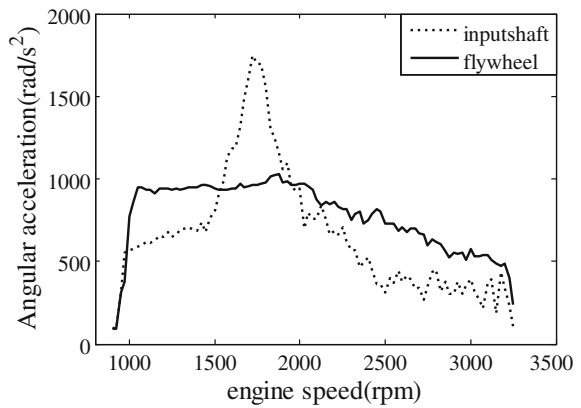


Fig. 22 The articulation index vs. rpm

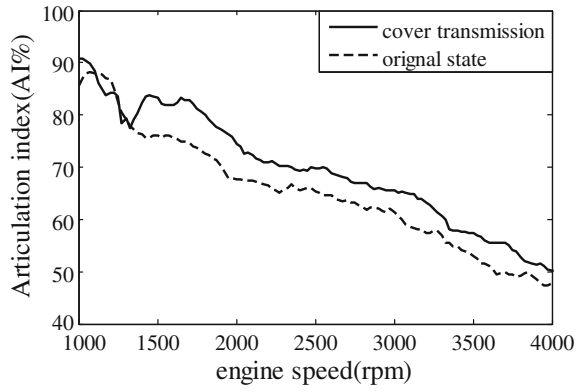


Fig. 23 The sound pressure of driver inboard ear in frequency domain

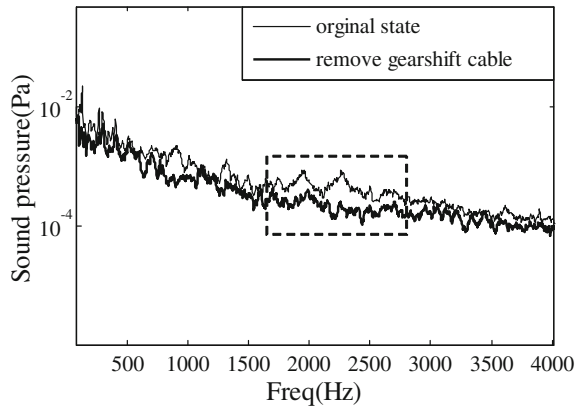
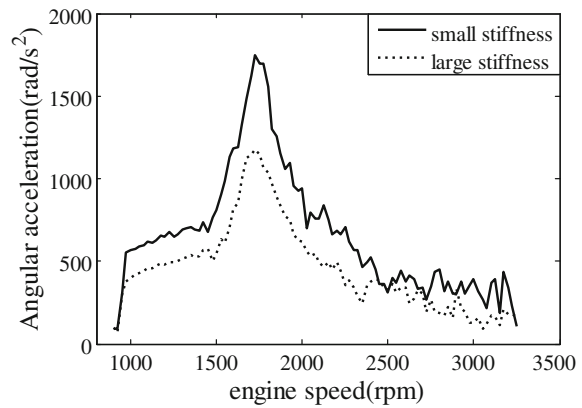


Fig. 24 The different angular acceleration between high clutch stiffness and low clutch stiffness



The torsional vibration produces rattle noise in transmission gear pair, so decreasing the angular acceleration amplitude of input shaft is the key point. The torsional vibration amplitude is reduced by using a clutch with big torsional angle and small stiffness, which corresponds to simulation results, as shown in Fig. 24.

7 Conclusions

1. The torsional finite element method is used to establish the FWD model, and to calculate the modal shapes and frequencies. The modal frequency is changed with gear, and the first and second order modal frequencies is changed smaller than the third modal frequency, and the third order modal frequency is increased from gear two to gear five due to the equivalent inertia and stiffness variation with gear ratio.
2. The modal sensitivity of clutch and half shaft stiffness is much higher in the third order mode, so the clutch and half shaft stiffness can be changed to tune gear rattle mode.
3. The modal sensitivity of flywheel inertia is much higher in the second order mode, and the modal sensitivity of differential is much higher to the third mode.
4. The forced vibration analysis shows that flywheel responses present order phenomenon, and the second, four and six order vibrations are primary. The second order vibration of transmission input shaft is much higher than others, and the resonant frequency is corresponding to the third modal frequency of system.
5. There is a great effect on reducing transmission shaft torsional vibration by reducing clutch stiffness, increasing flywheel inertia and clutch damping.
6. The torsional vibration test analysis shows that the clutch with large torsional angle and small stiffness achieves a good function to reduce torsional vibration and to control gear rattle noise.

Acknowledgments The authors wish to thank Dr Pang Jian and Li Chuanbing, for their valuable comments.

References

1. Szakowski A (1991) International congress and exposition detroit Michigan, SAE Technical Paper Series 910641, 81–97. Mathematical model and computer simulation of idle gear rattle
2. Fudala GJ, Engle TC, Karvelis AV (1987) SAE Technical Paper Series870396. A system approach to reducing gear rattle

3. Laschet A (1994) SAE Technical Paper Series 941011. Computer simulation of vibrations in vehicle power trains considering nonlinear effects in clutches and manual transmissions
4. Bozca M (2010) Torsional vibration model based optimization of gearbox geometric design parameters to reduce rattle noise in an automotive transmission. *J Sound Vibr* 45: 1583–1598
5. Kadmiri Y, Rigaud E (2012) Experimental and numerical analysis of automotive gearbox rattle noise. *J Sound Vib* 331:3144–3157
6. Barthod M, Hayne B (2007) Experimental study of gear rattle excited by a multi-harmonic excitation. *Appl Acoust* 68:1003–1025
7. Wu J-S, Chen C-H (2001) Torsional vibration analysis of gear-branched systems by finite element method. *J Sound Vib* 240(1):159–182
8. Crowther AR, Zhang N (2005) Torsional finite elements and nonlinear numerical modeling in vehicle power train dynamics. *J Sound Vib* 284:825–849

Transfer Paths Identification and Optimization of Transmission Gear Rattle Noise

Tian Xiong, Hongcheng Li, Hongying Wang, Yang Xianwu, Yu Tang
and Yuanfeng Xia

Abstract The purpose of this study is to solve the transmission gear rattle phenomenon. The whole vehicle transmission loss (TL) method is used to calculate air-borne rattle noise and to identify if the interior sound is dominated by structure-borne noise and air-borne noise. The major noise transfer paths are found. The experiment analysis indicates that structural transfer paths are identified as the major noise transfer paths for gear rattle noise. The paper provides two ways to improve the transmission gear rattle phenomenon. The test results show the good performance. Some structural transfer paths such as clutch cable, gear shift cables are considered and other factors such as drive half-shafts, suspension systems and subframe system are not considered. All structural transfer path parameters will be considered in the future research.

Keywords Gear rattle noise · Transfer paths · Air-borne · Structure-borne noise · Cables

F2012-J02-002

T. Xiong (✉) · H. Li · H. Wang · Y. Xianwu · Y. Tang · Y. Xia
Changan Auto Global R&D Center, 401120 Chongqing, China
e-mail: sunqiemail@163.com

T. Xiong · H. Li · H. Wang · Y. Xianwu · Y. Tang · Y. Xia
State Key Laboratory of Vehicle NVH and Safety Technology, 401120 Chongqing, China

1 Introduction

The traditional NVH performance research mainly focuses on noise and vibration magnitude, but with the increasing needs of comfort requirement from customers, the vehicle sound quality is becoming more and more important.

Transmission gear rattle noise has an obvious impact on the vehicle sound quality among all the possible noise and vibration phenomenon, so it is very important to control gear rattle noise effectively to improve the vehicle sound quality.

Gear rattle noise could be solved by the following means, such as reducing engine torsional vibration [1], adjusting clutch torsional stiffness rate and hysteresis [2–4], optimizing transfer paths, increasing drag torque, reducing backlash and increasing shell model frequency [5, 6]. Chang-Kook from Hyundai-Kia and Ingo Schulz from GIF analyzed some reasons of gear rattle noise, such as fluctuation of input-shaft torsional acceleration and gear rattle sensitivity, which achieved good result [7–10]. Magalhaes from Ford studied the gear rattle noise of 4WD by transfer paths analysis, and then optimized suspension and body connecting point stiffness, which improved gear rattle noise [11]. Ruhlander explored gear rattle with gear shift cables isolation cushion made of rubber material with good absorption effectiveness, and provided a better solution [12].

This paper introduces a method which optimizes the structural transfer paths to solve the transmission gear rattle phenomenon of an economy passenger car. Because of limitation to modify the engine, it is neither economical nor short-period to improve the rattle noise by reducing engine torsional vibration or optimizing the transmission response sensitivity of gear rattle noise. Eventually, transfer paths are selected to solve the phenomenon by optimizing the clutch and gear shift cables systems, and the good performance is achieved.

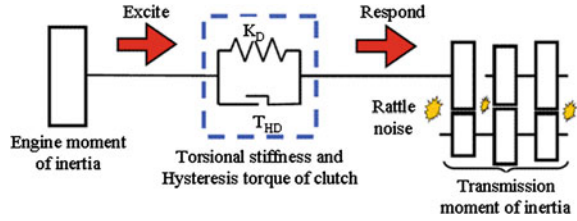
2 Gear Rattle Noise Mechanism Analysis

The major excitation source of gear rattle noise is engine torsional vibration which is passed from clutch system to the transmission. The torsional vibration causes the unload gears inside the transmission to impact each other that induces gear noise and transfers into the vehicle cabin through the transmission shell, and called gear rattle noise.

Most drivelines have their torsional natural frequency in the 1,500–2,400 rpm ranges. Gear rattle noise can be easily heard when the vehicle is driven normally through their natural frequency ranges.

The explanatory drawing of gear rattle mechanism is provided in Fig. 1. The engine and transmission are simplified as a mass system with certain inertial; the clutch system is simplified as a spring system with certain damping. The excitation

Fig. 1 Transmission gear rattle mechanism scheme



generated by engine mass system is transferred to the transmission mass system through the spring damping, which causes gear rattle noise.

3 Transfer Paths Identification Analysis of Gear Rattle Noise

3.1 Transfer Paths Analysis

For a linear constant system, assume the input incentive is $x_i(t)$ and the output response is $x_o(t)$, The ratio between output and input is called transfer function $H(f)$, which can be expressed in the frequency domain as:

$$X_o(f) = H(f)X_i(f) \tag{1}$$

where $X_i(f)$ and $X_o(f)$ are obtained from $x_i(t)$ and $x_o(t)$ by Fourier transformation.

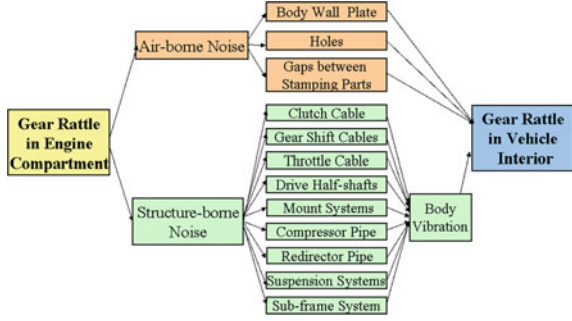
The vehicle is a complex system composed of various components, and it is excited by various vibration and noise sources. Each excitation can be transferred from different routes to the multi-response points. Gear rattle noise has two sources: one is transferred from body plates, holes and gaps between stamping parts, which is called air-borne noise; the other is transferred through structures, such as clutch cable, gear shift cables, throttle cable, engine mount systems, suspension system, sub-frame, the battery line and pedal bracket to the body, which is called structure-borne noise.

The air-borne and structure-borne noise sources should be considered simultaneously in order to find the major sources, so that the optimized results can be achieved. Figure 2 demonstrates the transfer paths of gear rattle noise from engine compartment to the vehicle cabin.

3.2 Air-Borne and Structure-Borne Noise Contribution Analysis

It is necessary to separate air-borne and structure-borne noise from transmission gear rattle noise, which means to estimate the contribution of air-borne and structure-borne noise. The air-borne noise is calculated by Transmission Loss (TL) method in this study.

Fig. 2 Gear rattle noise transfer paths scheme



3.2.1 Introduction of Transmission Loss Method

Firstly, a diffuse field is formed in the engine compartment, the vehicle TL is measured from the engine compartment to the vehicle interior by placing four microphones in the engine compartment and two microphones inside the car. The engine compartment microphones are placed: between the engine and the firewall, between the transmission and the firewall, between the transmission and the accumulator, and above the transmission. The vehicle interior microphones are placed at the FLR and FRR positions. A white noise source is used to produce noise at four different locations in the engine compartment. For each source location, the average SPL in the engine compartment is calculated using the formula (2):

$$L_{Out-Avg} = 10Lg_n^1 \sum_n 10^{L_n/10} \tag{2}$$

where $L_{Out-Avg}$ is the average SPL in the engine compartment, n is the number of microphones being averaged. If one microphone is significantly louder than the others because of its proximity to the sound source, it is not included in the average, The average SPL in the vehicle interior is calculated using the same formula.

The vehicle transmission loss could be calculated by formula (3):

$$TL = L_{Out-Avg1} - L_{In-Avg1} \tag{3}$$

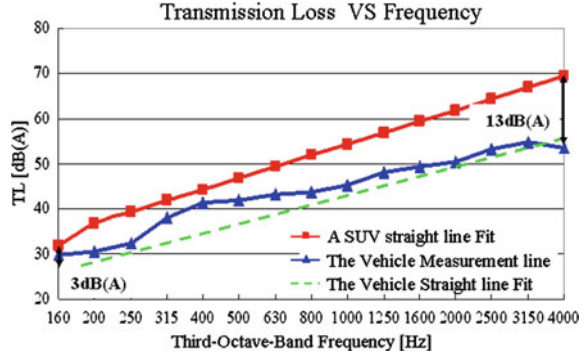
where $L_{Out-Avg1}$ $L_{In-Avg1}$ represent the average SPLs at stationary condition in the engine compartment and inside car, respectively.

3.2.2 Comparison of Air-Borne and Structure-Borne Noise

The air-borne contribution noise could be calculated using the following formula (4):

$$L_{Air} = L_{Out-Avg2} - TL \tag{4}$$

Fig. 3 Measured TL between the engine compartment and the vehicle cabin



where $L_{Air}L_{Out-Avg2}$ separately represent the average SPLs at the operating condition in the engine compartment and inside car, respectively.

The structure-borne contribution is calculated (assuming that all the noises are structure-borne) using the formula (5):

$$L_{Str} = 10Log\left(10^{L_{In-Avg2}/10} - 10^{L_{Air}/10}\right) \tag{5}$$

where $L_{Str}L_{In-Avg2}$ represent the SPL levels of structure-borne and air-borne noise transferred to the vehicle cabin, respectively.

Figure 3 is the measured TL curves of the vehicle and a other referred SUV. The vehicle’s TL curve is lower 3–13 dB (A) compared with the referred SUV.

Figure 4 demonstrates the colormap of FLR position at 4th gear WOT condition. The gear rattle noise mainly occurred from 1,600 to 2,400 rpm, and major frequency contribution is from 1,000 through 4,000 Hz.

The air-borne and structure-borne noise contributions versus engine speed are shown in Fig. 5. The 1,000 through 4,000 Hz frequency bands have been combined. Figure 5 shows that in this frequency range the structure-borne is dominant contribution at engine speeds up to 3,000 rpm. So the rattle noise could be optimized by improving the structural transfer paths.

4 Transfer Paths Optimization Analysis of Gear Rattle Noise

4.1 Experiment Analysis of the Effectiveness with Cables Disconnected

Figure 6 shows the SPL level of the interior microphones (FLR and Under-dash position) versus engine speed with and without clutch and gear shift cables disconnected at gear 4 WOT condition. FLR position is improved by 2 dB(A), under-dash position is improved by 5 dB(A).

Fig. 4 Colormap of FLR position gear rattle noise at 4th gear WOT condition

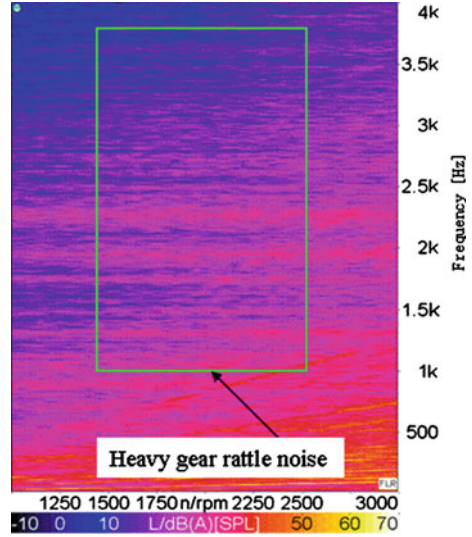


Fig. 5 The air-borne and structure-borne contribution comparison at gear 4 WOT condition of gear rattle noise from 1,000 through 4,000 Hz third octave bands

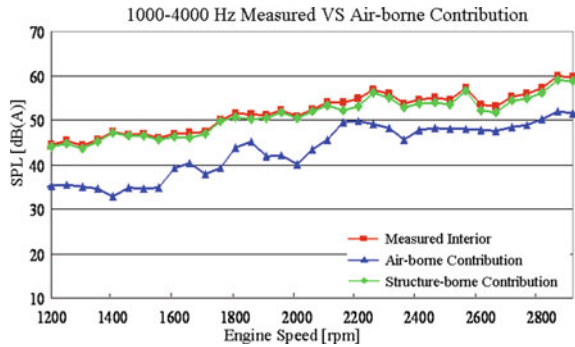


Fig. 6 SPL of FLR and Under-dash position versus engine speed with and without cables disconnected

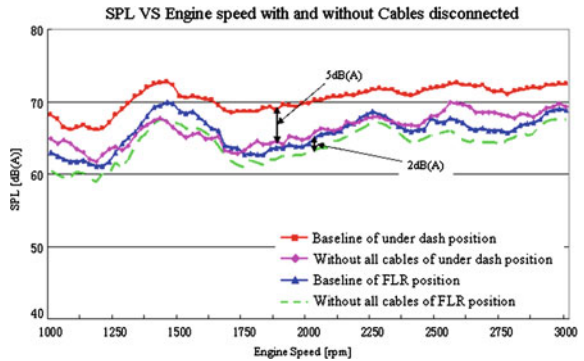


Fig. 7 Colormap of FLR position versus engine speed with and without cables disconnected

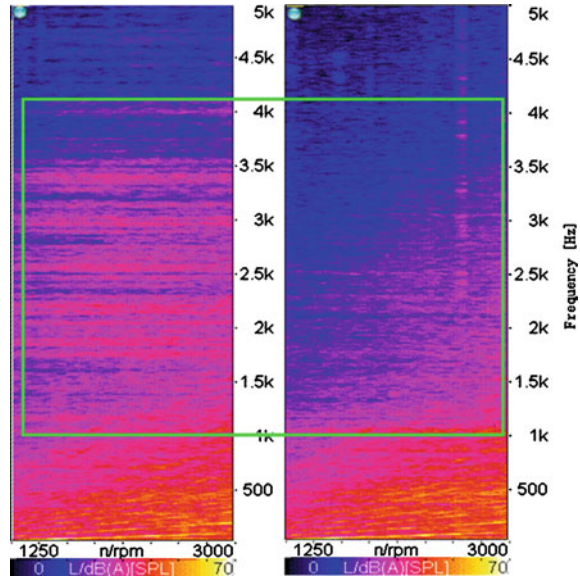


Figure 7 shows the colormap of FLR position versus engine speed with and without clutch and gear shift cables disconnected at gear 4 WOT condition. The high frequency noise from 1,000 through 4,000 Hz is improved obviously after the cables are disconnected.

Gear rattle noise is improved obviously after the clutch cable and the gear shift cables are disconnected, which means the cables are the major structural transfer paths of the gear rattle. Subjective evaluation of the vehicle that the rattle noise is significantly improved.

4.2 Experiment Optimization and Analysis of Clutch Cables

Figure 8 shows the SPL level of FLR position versus engine speed with optimized clutch cable (the thickness of rubber increased from 3 to 8 mm, the rigidity from $65 \pm 5^\circ$ to $50 \pm 5^\circ$) at 4th gear WOT condition, FLR position is improved by 1 dB(A).

Figure 9 shows the colormap of FLR position versus engine speed with optimized clutch cables structure at 4th gear WOT condition. The high frequency noise from 1,500 through 3,000 Hz is reduced obviously after clutch cables are optimized.

Fig. 8 SPL of FLR versus engine speed with optimized clutch cable

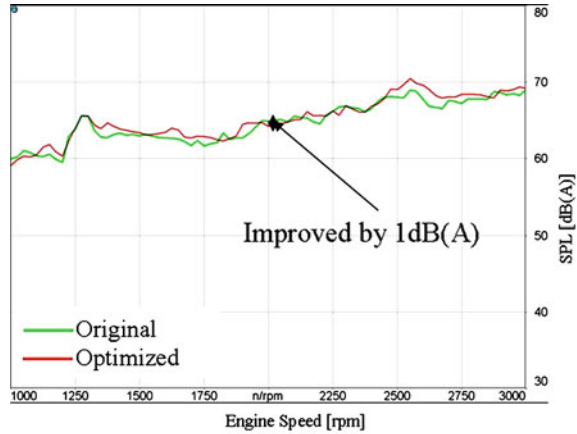
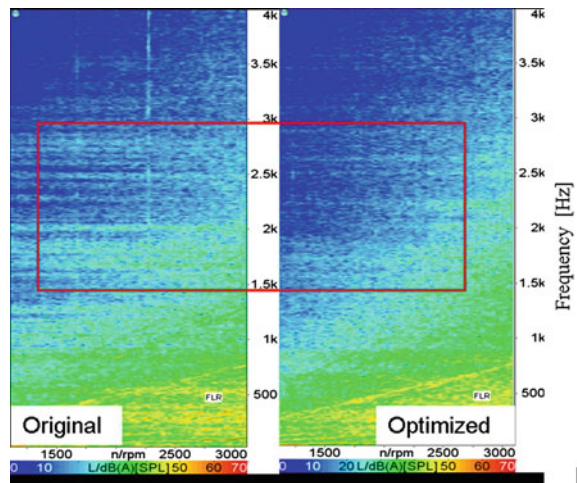


Fig. 9 Colormap of FLR versus engine speed with optimized clutch cable



4.3 Experiment Optimization and Analysis of Gear Cable Bracket

The clutch cable and gear shift cables are optimized simultaneously. The gear shift bracket is optimized by adding rubber, which is demonstrated in Fig. 10.

Figure 11 shows the SPL level of the interior microphones (FLR and Under-dash position) versus engine speed with and without optimized gear shift bracket at 4th gear WOT condition. FLR position is improved by 1 dB(A), under-dash position is improved by 4 dB(A) (Fig. 12).

Fig. 10 Gear shift bracket with added rubber scheme



Fig. 11 SPL of FLR and Under-dash position versus engine speed with and without optimized bracket

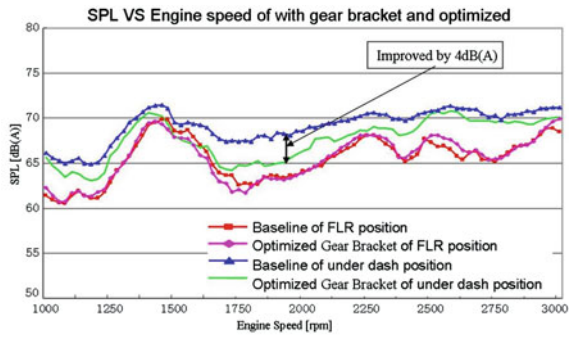
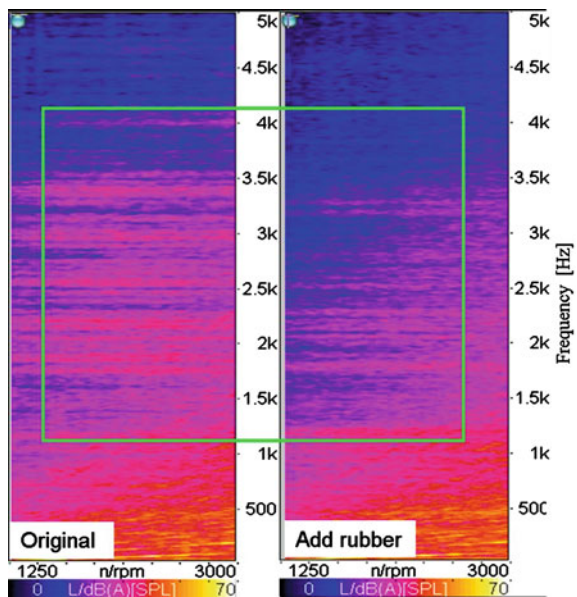


Fig. 12 Colormap of FLR position versus engine speed with and without optimized bracket



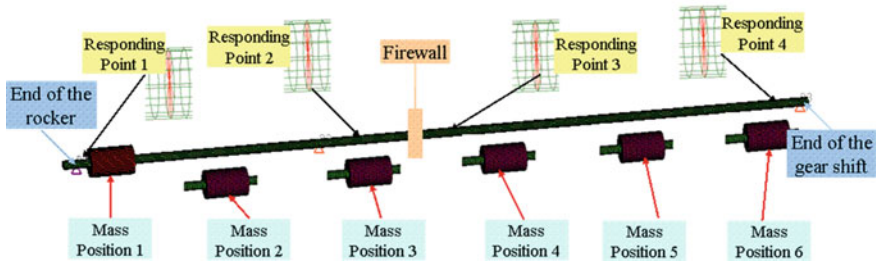


Fig. 13 Different fixing position of 6 masses and 4 different responding points scheme

4.4 Optimization Analysis of Gear Shift Cables

Masses are attached to the housings of the gear shift cables. The optimized weight and the fixing position of the mass will be ascertained by CAE analysis.

4.4.1 CAE Optimization and Analysis of Gear Shift Cables

The 3D model of a simplified gear shift cable is preprocessed by HYPERMESH. The model is divided into hexahedral grids. The frequency response curves of different responding points with different weight of the mass and different fixing position analyzed using CAE.

The different fixing position of the mass and different responding points are illustrated in Fig. 13.

Figure 14 shows the frequency response curves of 4 responding points with different weight of the mass. The vibration response is reduced obviously in high frequency range band (above 1,000 Hz), and the effectiveness is directly proportional to the weight of the mass.

Figure 15 shows the frequency response curves of 4 responding points with different fixing position of the mass. For fixing position 1, because it is installed in the rear of the gear shift bracket, the effectiveness is the best. Finally, fixing position 1, 3, 4 and 6 are the better positions.

Figure 16 shows the third octave curves of 4 responding points with different fixing positions of the mass, which illustrates that the dB level of position 3, 4, and 6 are best.

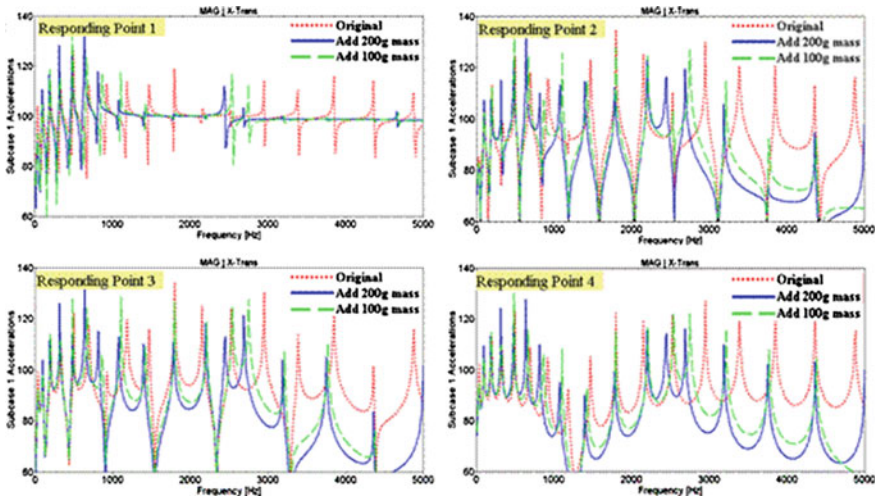


Fig. 14 Frequency response curves of 4 responding points with different weight of the mass

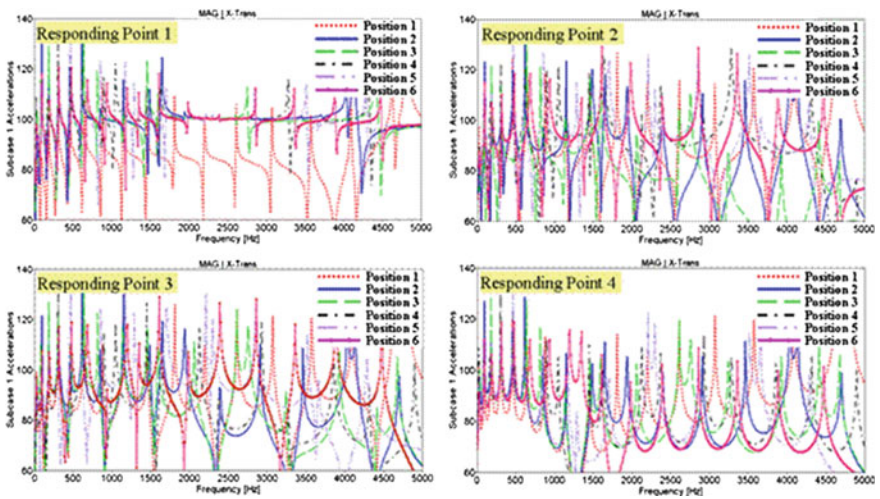


Fig. 15 Frequency response curves of 4 responding points with different fixing position of the mass

4.4.2 Experiment Optimization and Analysis of Gear Shift Cables

Two 200 g masses are attached to the metal sleeve of the gear shift bracket and the end of the gear shift cables through the CAE analysis result. Figure 17 shows the SPL level of the interior microphones (FLR and Under-dash position) versus engine speed with and without masses are attached to the housings of the gear shift

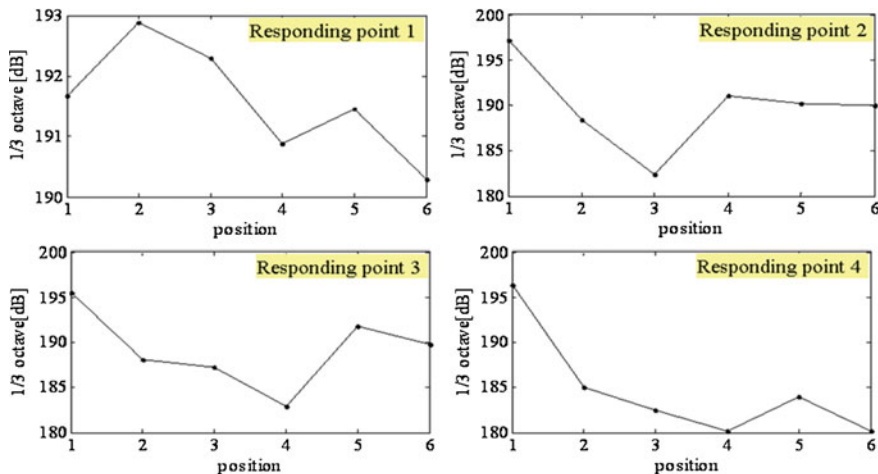
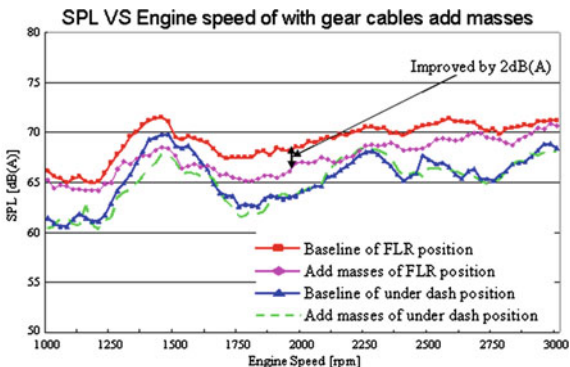


Fig. 16 Third octave curves of 4 responding points with different fixing position of the mass

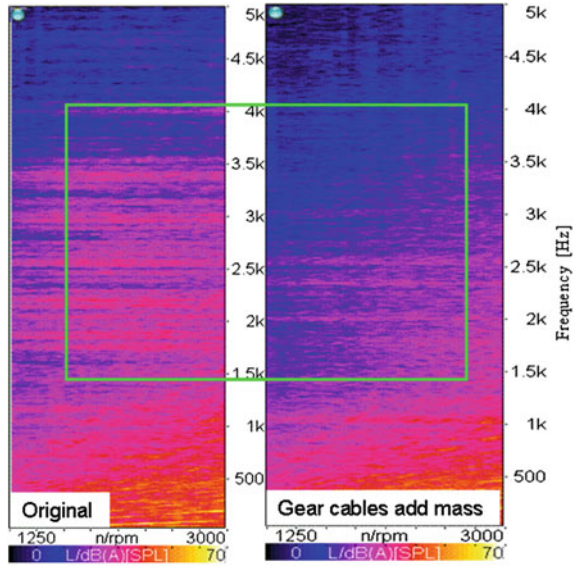
Fig. 17 SPL of FLR and Under-dash position versus engine speed with and without gear optimized cables



cables at 4th gear WOT condition. FLR position is improved by 0.5 dB(A), under-dash position is improved by 2 dB(A) (Fig. 18).

Above all the optimization, such as increasing the thickness of the clutch cable rubber from 3 to 8 mm, reducing the rigidity from $65 \pm 5^\circ$ to $50 \pm 5^\circ$, adding rubber of gear shift bracket and adding mass to gear shift cables, the gear rattle noise phenomenon is highly improved, which optimizes the NVH performance and improves the vehicle sound quality. Subjective evaluation of the vehicle indicates that the gear rattle noise is significantly improved.

Fig. 18 Colormap of FLR position versus engine speed with and without gear optimized cables



5 Conclusions

The air-borne contribution of the gear rattle noise is calculated through the vehicle TL method, then the structural transfer paths are identified as the major transfer paths for gear rattle noise,. The following statements are concluded

- (1) The transfer paths test analysis method can effectively separate air-borne and structure-borne contribution of transmission gear rattle noise.
- (2) Structure-borne noise is the major contribution of the rattle noise for the analyzed case, and the cables are the major paths. The gear rattle noise could be improved by the following methods: optimized the clutch cable, optimized gear shift bracket and gear shift cables.
- (3) The key transfer paths could be found rapidly through the structural transfer paths analysis method, by CAE analysis in early phase of a vehicle development, which could save the cost and shorten the R&D period.

Acknowledgments Thank Dr. Pang Jian, Li Chuanbing and Yang Xianwu for their guidance and help in the completion process of this study, thank them very much! At the same time, thank all the colleagues of Changan transmission NVH group for their non-selfish help.

References

1. Forcelli A, Grasso C, Pappalardo T (2004) The transmission gear rattle noise: parametric sensitivity study. SAE:2004-01-1225
2. Steinel K (2000) Clutch tuning to optimize noise and vibration behavior in trucks and buses. SAE:2000-01-3292E
3. Steinel K, Tebbe G (2004) New torsional damper concept to reduce idle rattle in truck transmissions. SAE:2004-01-2722
4. Wang MY, Manoj R, Zhao W (2002) Gear rattle modeling and analysis for automotive manual transmissions. Drive Syst Tech 16(04):27–41
5. Barthod M, Hayne B, Tebec JL et al (2007) Experimental study of gear rattle excited by a multi-harmonic excitation. J Appl Acoust 68:1003–1025
6. Robinette D, Beikmann RS, Piorkowski P et al (2009) Characterizing the onset of manual transmission gear rattle part 1: experimental results. SAE.:2009-01-2063
7. Chae CK (2003) Correlation of analytical model with experimental results in ranking the gear meshes in order of contribution to rattle. Inter-Noise
8. Bertsche B (2001) Investigation of rattling and clattering noise behavior of automotive transmissions. ATA
9. Kamo M, Yamamoto H, Koga H et al (1996) Analysis Method for the Contribution Rate of Each Pair of Gears on the Driveline gear Rattle. SAE:960726
10. Chang-K, Won K, Kang K et al (2005) Measurement of transmission rattle sensitivity and calculation of driveline torsional vibration for gear rattle analysis. SAE:2005-01-1785
11. Magalhaes M, Arruda F, Filho J (2003) Driveline structure-borne vibration and noise path analysis of an awd vehicle using finite elements. SAE:2003-01-3641
12. Ruhlander GP (2006) Deformation of NVH materials used in transmission shift cable systems through their life cycle. SAE:2006-01-0704

Study on Driveline Component Torsional Stiffness Effect on RWD Driveline Torsional Vibration Modes

Qian Zhao

Abstract *Research and/or Engineering Questions/Objective* As driveline torsional vibration modes are very critical for RWD vehicle NVH issues, like vehicle shuffle, gear rattle, gear/axle whine, and interior noise booming, it is very helpful to find out how driveline component torsional stiffness affect driveline torsional vibration modes, that make set the torsional vibration mode target much easier from the very start of driveline development and more effectively tune the driveline torsional vibration modes during refine stage, that way, the major goal of this paper is to find out the RWD driveline torsional vibration mode sensibility to driveline component torsional stiffness, in terms of clutch damper, propshaft, axle shaft and rules how to tune the RWD driveline torsional vibration modes to alleviate torsional vibration induced NVH issues. *Methodology* A RWD SUV driveline lumped mass model is firstly established to predict the 3 most critical torsional modes, then, in-vehicle torsional vibration measurement in this SUV is implemented, and the correlation between the prediction and measurement is judged to decide whether the model can be employed to make driveline torsional vibration mode sensibility study to driveline component torsional stiffness or not. If the model is accurate, the clutch torsion damper stiffness, propshaft stiffness, axle shaft stiffness are chosen as the parameter, with stiffness increased/decreased 20–80 % compared to original value, to calculate relevant torsional mode for respective component torsional stiffness, hence, the sensibility study can be implemented. *Results* The model prediction correlates very well to the in-vehicle torsional vibration measurement, thus, the model is employed to make driveline torsional vibration mode sensibility study to driveline component torsional stiffness, as aforementioned way of analysis, to conclude how the driveline

F2012-J02-003

Q. Zhao (✉)
CATARC, Shanghai, China
e-mail: yyzhq20@163.com

component torsional stiffness affect the driveline torsional vibration modes. *Limitations of this study*: This study is only limited to RWD driveline, while, FWD driveline is not covered, hence, the FWD driveline torsional vibration mode sensitivity to driveline component torsional stiffness will be the following study. *What does the paper offer that is new in the field in comparison to other works of the author* This paper involves the systematic study on the driveline component torsional stiffness effect on torsional vibration modes, and give some suggestion addressing the driveline torsional modes from the very start of driveline NVH development, while, the author previous work mainly focused on specific problem solving. In this sense, the work in this paper provides study from new angle. *Conclusion* (1) axle shaft stiffness is the dominant factor for 1st torsional mode, say vehicle shuffle (2) clutch torsion damper stiffness is the dominant factor for 2nd torsional mode, say gear rattle (3) propshaft stiffness is the dominant factor for 3rd torsional mode, say axle whine (4) the study outcome is beneficial for driveline NVH target setting and tuning direction for vehicle shuffle, gear rattle, axle whine.

Keywords Driveline · Torsional vibration · Torsional stiffness · Sensibility study

1 Introduction

Typical RWD driveline consists of engine, transmission, propshaft, rear axle, axle shaft and wheel, that has some inertia and stiffness, hence, specific torsional vibration modes. Under engine torque pulse, these modes will be excited and transmitted to body through rear suspension, leading to interior noise booming [1, 2]. It is very helpful to well distribute the driveline torsional vibration modes, getting round from the sensitive engine excitation rpm, to reduce the torsional vibration induced interior noise. Typically, RWD vehicle is more susceptible to driveline torsional excitation, compared to FWD vehicle, that way, it is very important to well manage the RWD driveline torsional vibration modes [3].

It is known that torsional stiffness of driveline component do influence the driveline torsional vibration modes [4, 5], while, systematic investigation on how torsional stiffness of clutch damper, propshaft and axle shaft affect driveline torsional vibration modes is rare. In this paper, a RWD SUV is employed, establishing the RWD driveline model, to predict the driveline torsional vibration modes by in-house software. The prediction is validated by in-vehicle testing, therefore, the model is adopted to investigate the RWD driveline torsional vibration mode sensitivity to torsional stiffness of clutch damper, propshaft and axle shaft, as well as the relevant rules, which is meaningful to distribute the torsional vibration modes and expedite the driveline NVH process, from the very start of the vehicle driveline development.

2 Driveline Torsional Vibration Model and Modes

A typical driveline for a front installed engine and rear wheel driven vehicle is shown as Fig. 1 [6], where engine and transmission is longitudinally installed at front end, transmission is connected to rear axle through propshaft, and rear axle is connected to wheel through axle shaft.

When implementing torsional vibration calculation, the engine, transmission, propshaft, rear axle and rear wheel + body is simplified as 5 inertias, connected by spring has torsional stiffness, to formulate a lumped mass model, shown as Fig. 2.

Based on the driveline torsional vibration theory, the model vibration equation can be written as,

$$J\ddot{\theta} + K\theta = 0$$

$$J = \begin{bmatrix} J_1 & & & & \\ & J_2 & & & \\ & & \ddots & & \\ & & & \ddots & \\ & & & & J_5 \end{bmatrix} \quad k = \begin{bmatrix} K_{12} & -K_{12} & & & \\ -K_{12} & K_{12} + K_{23} & & & \\ & -K_{23} & K_{23} + K_{34} + K_{35} & & \\ & & -K_{34} & K_{34} & \\ & & -K_{35} & & K_{35} \end{bmatrix}$$

In this equation, J1, J2, J3, J4, J5 stand for moment of inertia of engine, transmission, rear axle and wheel + body, while, K12, K23, K34, K35 stand for torsional stiffness of clutch damper, propshaft, left and right axle shaft. The equivalent calculation of moment of inertia and torsional stiffness can be referred to [7].

A RWD SUV, equipped with 2.5 L turbocharged diesel and 6-speed MT, whose driveline lumped mass parameters are shown as Table 1.

The in-house software is employed to predict the driveline torsional vibration modes, as in,

1. The 1st mode is a whole vehicle fore-aft vibration, in which engine, transmission and rear axle vibrate torsionally, out of phase to wheel + vehicle, and maximal amplitude occurs at engine side. The mode frequency is increased as gear position is higher, and corresponding frequency and shape is shown as Table 2 and Fig. 3. This mode normally is easy to be excited by engine torque pulsation, during tip-in/out maneuver, leading to vehicle fore-aft vibration.
2. The 2nd mode is transmission and rear axle mode, manifesting the modal shape as in phase transmission and rear axle torsional vibration the modal frequency increases, as gear position is lower. The modal frequency and shape is shown as Table 3 and Fig. 4. This mode is prone to be excited by engine torque pulsation, either leading to gear rattle, or transmitting to body through suspension, resulting in interior noise peak.
3. The 3rd mode is rear axle mode, manifesting the modal shape as big amplitude torsional vibration at rear axle. The modal frequency increases, as gear position is higher. The modal frequency and shape is shown as Table 4 and Fig. 5. This mode might be excited by engine torque pulsation, propshaft bending, torsional excitation, resulting in axle whine.

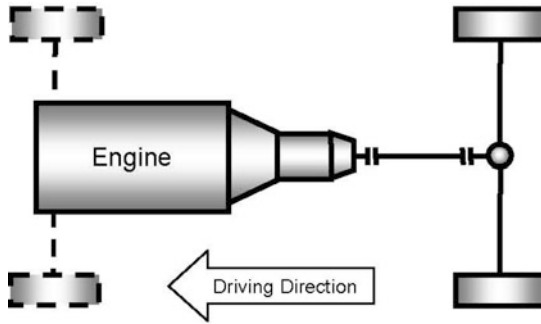


Fig. 1 Typical RWD vehicle driveline

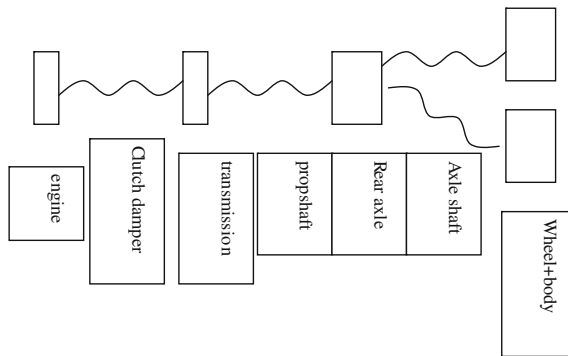


Fig. 2 Driveline model of 5 DOF

Table 1 Driveline lumped mass parameter of a RWD SUV

Item		Engine	Transmission	Rear axle	Wheel + vehicle
Torsional vibration parameter					
	Gear				
Moment of inertia (Kgm ²)	1	0.29	0.013	0.00055	0.41
	2	0.29	0.013	0.0013	0.93
	3	0.29	0.0152	0.00334	2.46
	4	0.29	0.018	0.0069	5.07
	5	0.29	0.021	0.0098	7.22
	6	0.29	0.025	0.014	10.47
	Reverse	0.29	0.017	0.0046	3.41
Torsional stiffness (Nm/deg)			Clutch damper	Propshaft	Axle shaft
	1		2177.2	830.3	21.6
	2		2177.2	1912.4	49.7
	3		2177.2	5034.7	130.8
	4		2177.2	10382	269.6
	5		2177.2	14784	384
	6		2177.2	21432	556.6
Reverse		2177.2	6975.2	181.2	

Table 2 A SUV 1st driveline torsional vibration mode

	1st gear	2nd gear	3rd gear	4th gear	5th gear	6th gear	Reverse
Modal frequency (Hz)	2.1	3	4.4	5.9	6.8	7.7	5.1

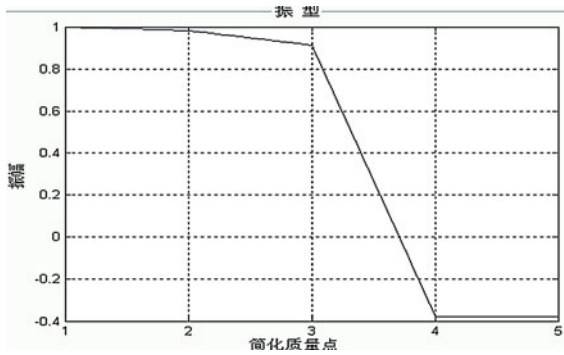


Fig. 3 1st driveline torsional vibration mode

Table 3 A SUV 2nd driveline torsional vibration mode

	1st gear	2nd gear	3rd gear	4th gear	5th gear	6th gear	Reverse
Modal frequency (Hz)	92	89	70	65	60	57	70

3 Validation to Prediction Model

To validate the prediction model and to employ this model to investigate the torsional vibration sensitivity to driveline component torsional stiffness, the in-vehicle driveline torsional vibration measurement is implemented, by installing magnetic pickup close to flywheel ring gear, input shaft gear of transmission, machined gear of rear axle companion flange, to collect the angular acceleration during WOT acceleration in 2nd, 3rd, 4th, 5th, 6th gear, then, the 2nd order angular acceleration frequency of each measurement point could be correlated to prediction results. The magnetic pickup position is shown as Figs. 6, 7, and 8 and the 2nd order angular acceleration of each measurement point is shown as Figs. 9, 10, 11, and 12.

It can be found by investigating the above figures that all 2nd order angular acceleration in each gear has a resonance peak, corresponding the driveline 2nd torsional vibration mode, whose frequency is 87 Hz at 2,600 rpm in 2nd gear,

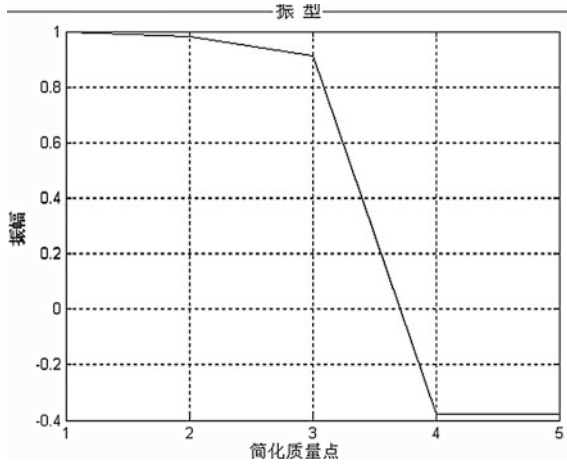


Fig. 4 2nd driveline torsional vibration mode

Table 4 A SUV 3rd driveline torsional vibration mode

	1st gear	2nd gear	3rd gear	4th gear	5th gear	6th gear	Reverse
Modal frequency (Hz)	205	210	221	234	241	249	226

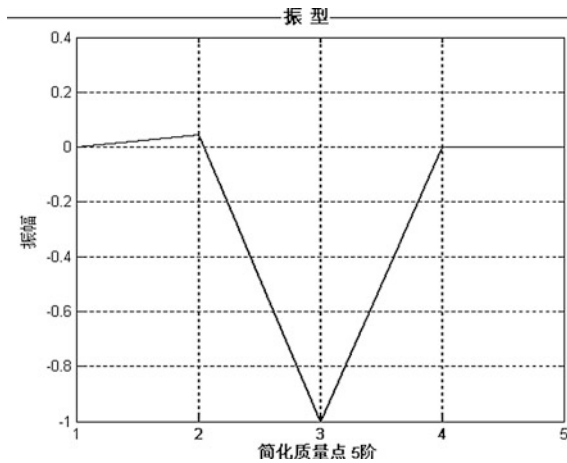


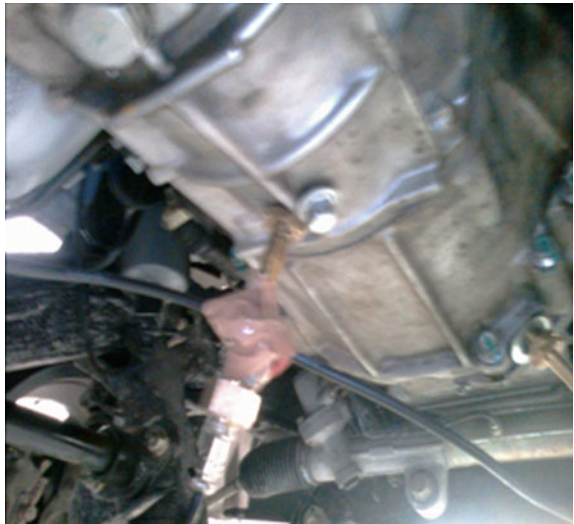
Fig. 5 3rd driveline torsional vibration mode

67 Hz at 2,000 rpm in 3rd gear, 62 Hz at 1,850 rpm in 4th gear, and 58 Hz at 1,750 rpm in 5th gear. The measurement results correlate very well to the prediction results, see Table 5 for comparison, that proves the model, adopted in this paper, can be employed for further driveline related investigation.

Fig. 6 Pickup at flywheel ring gear



Fig. 7 Pickup at transmission input shaft gear



4 Driveline Torsional Vibration Mode Sensitivity to Driveline Component Torsional Stiffness

Driveline component torsional stiffness affects the driveline torsional vibration modes and engine torque pulsation transmission, hence, it is meaningful to investigate the driveline torsional vibration sensitivity to driveline component torsional stiffness, plus summarizing most dominant parameter to driveline modes and relevant rules, then, the driveline parameters can be chosen, from the very start of vehicle development, to reach satisfactory driveline torsional vibration target.

Fig. 8 Pickup at machined gear of rear axle companion flange



Fig. 9 2nd order torsional vibration acceleration during WOT acceleration in 2nd gear. Red line stands for flywheel, green line stands for transmission input shaft, blue line stands for rear axle input

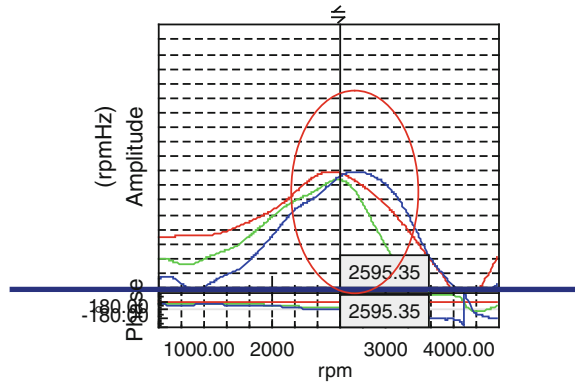
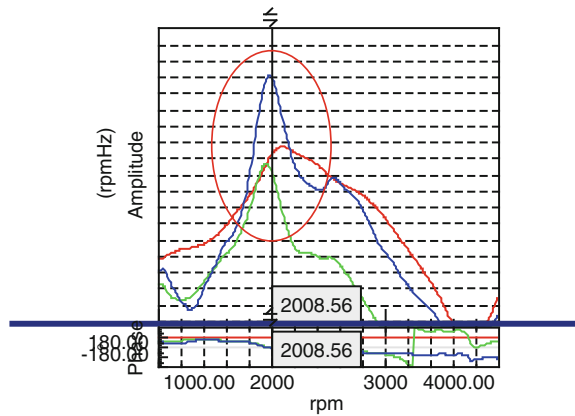


Fig. 10 2nd order torsional vibration acceleration during WOT acceleration in 3rd gear. Red line stands for flywheel, green line stands for transmission input shaft, blue line stands for rear axle input



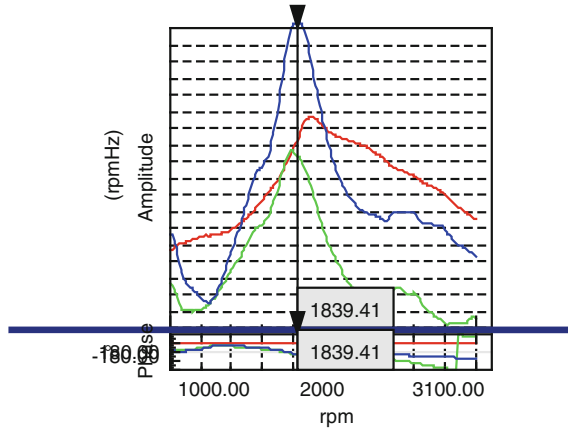


Fig. 11 2nd order torsional vibration acceleration during WOT acceleration in 4th gear, *red* line stands for flywheel, *green* line stands for transmission input shaft, *blue* line stands for rear axle input

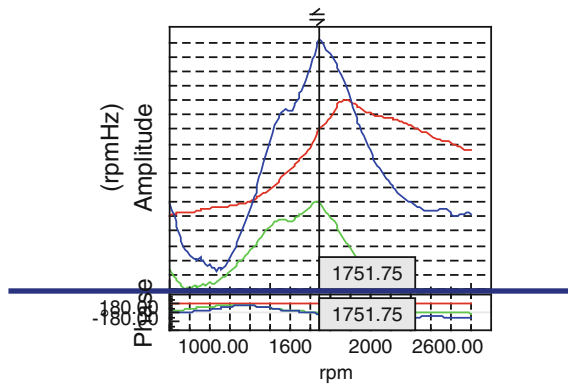


Fig. 12 2nd order torsional vibration acceleration during WOT acceleration in 5th gear, *red* line stands for flywheel, *green* line stands for transmission input shaft, *blue* line stands for rear axle input

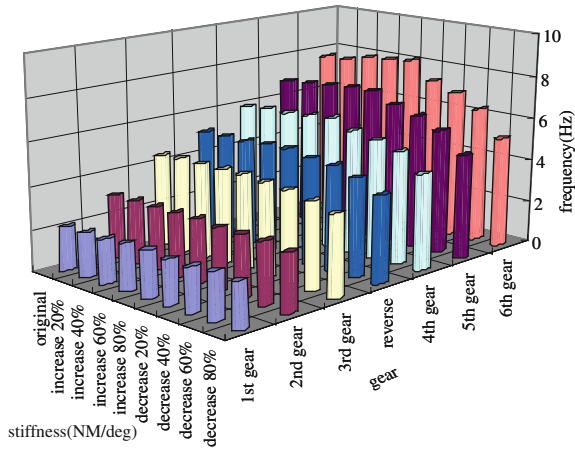
Table 5 Correlation between measurement and prediction

	2nd gear	3rd gear	4th gear	5th gear
Prediction (Hz)	89	70	65	60
Measurement (Hz)	87	67	62	58
Error	2 %	4 %	5 %	3 %

Table 6 Clutch damper torsional stiffness variation

Stiffness increase compared to original value (%)	Stiffness decrease compared to original value (%)
20	20
40	40
60	60
80	80

Fig. 13 Driveline 1st mode sensitivity to clutch damper torsional stiffness



4.1 Driveline Torsional Vibration Sensitivity to Clutch Damper Torsional Stiffness

The clutch damper torsional stiffness will be varied as Table 6, in regards to driveline torsional vibration sensitivity to clutch damper torsional stiffness.

Taking the stiffness into in-house software for calculation, the driveline mode sensitivity to clutch damper torsional stiffness could be collected, shown as Figs. 13, 14, and 15. Corresponding modal shape is unvaried.

From above 3 figures, it can be found, as in,

1. When clutch damper torsional stiffness is varied, the effect on 1st driveline mode is very small, thus, clutch damper torsional stiffness is not the parameter tuning the 1st driveline mode.
2. When clutch damper torsional stiffness is varied, the effect on 3rd driveline mode is very small, thus, clutch damper torsional stiffness is not the parameter tuning the 3rd driveline mode.
3. When clutch damper torsional stiffness is varied, the effect on 2nd driveline mode is obvious. As the stiffness increase/decrease, the 2nd mode frequency correspondingly varies, that way, the clutch damper stiffness can be the dominant parameter tuning 2nd driveline mode. As 2nd driveline mode is very sensitive to interior noise booming. Clutch damper torsional stiffness could be optimized, to get the 2nd driveline mode out of critical engine torque pulsation rpm.

Fig. 14 Driveline 2nd mode sensitivity to clutch damper torsional stiffness

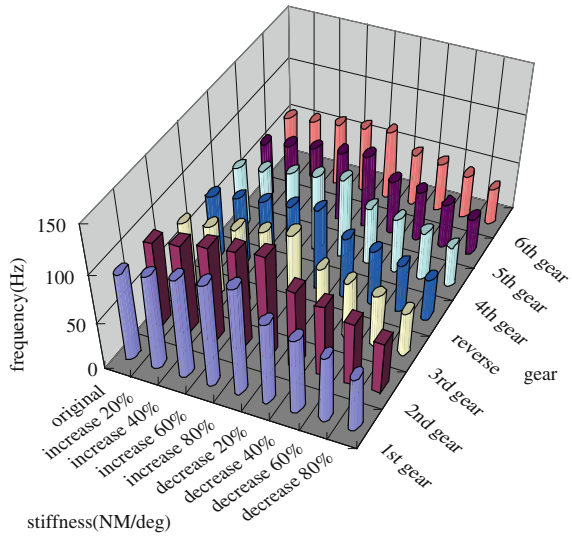
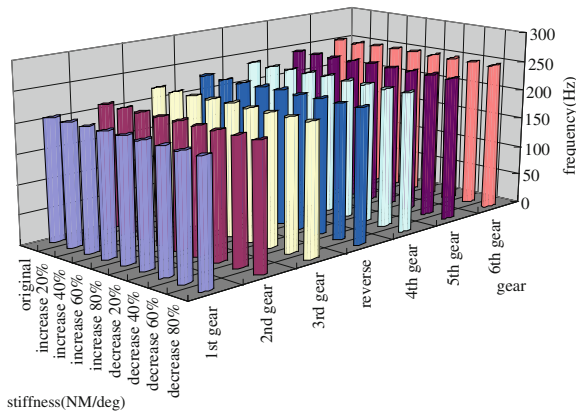


Fig. 15 Driveline 3rd mode sensitivity to clutch damper torsional stiffness



4.2 Driveline Torsional Vibration Sensitivity to Propshaft Torsional Stiffness

The propshaft torsional stiffness will be varied as Table 7, in regards to driveline torsional vibration sensitivity to propshaft torsional stiffness.

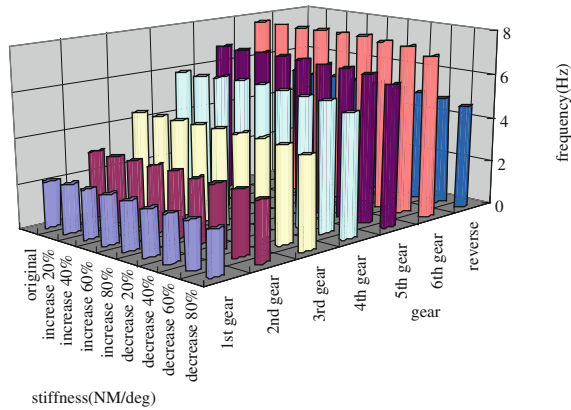
Taking the stiffness into in-house software for calculation, the driveline mode sensitivity to propshaft torsional stiffness could be collected, shown as Figs. 16, 17, and 18. Corresponding modal shape is unvaried.

From above 3 figures, it can be found, as in,

Table 7 Propshaft torsional stiffness variation

Stiffness increase compared to original value (%)	Stiffness decrease compared to original value (%)
20	20
40	40
60	60
80	80

Fig. 16 Driveline 1st mode sensitivity to propshaft torsional stiffness



1. When propshaft torsional stiffness is varied, the effect on 1st driveline mode is very small, thus, propshaft torsional stiffness is not the parameter tuning the 1st driveline mode.
2. When propshaft torsional stiffness is varied, the effect on 2nd driveline mode is very small, thus, propshaft torsional stiffness is not the parameter tuning the 2nd driveline mode.
3. When propshaft torsional stiffness is varied, the effect on 3rd driveline mode is obvious. As the stiffness increase/decrease, the 3rd mode frequency correspondingly varies, that way, the propshaft stiffness can be the dominant parameter tuning 3rd driveline mode. As 3rd driveline mode is susceptible to be excited by propshaft bending and torsional excitation, propshaft torsional stiffness could be optimized, to get the 3rd driveline mode out of critical propshaft excitation frequency.

4.3 Driveline Torsional Vibration Sensitivity to Axle Shaft Torsional Stiffness

The axle shaft torsional stiffness will be varied as Table 8, in regards to driveline torsional vibration sensitivity to axle shaft torsional stiffness.

Fig. 17 Driveline 2nd mode sensitivity to propshaft torsional stiffness

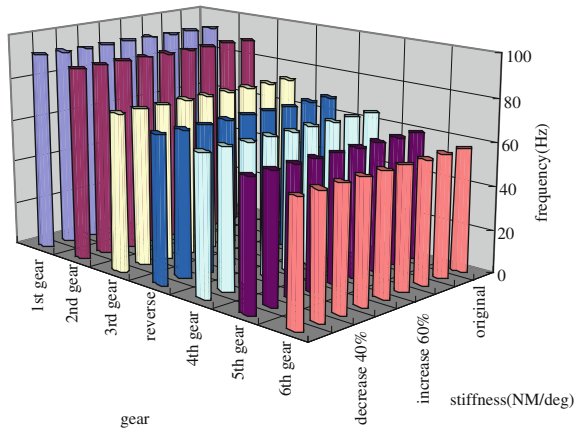
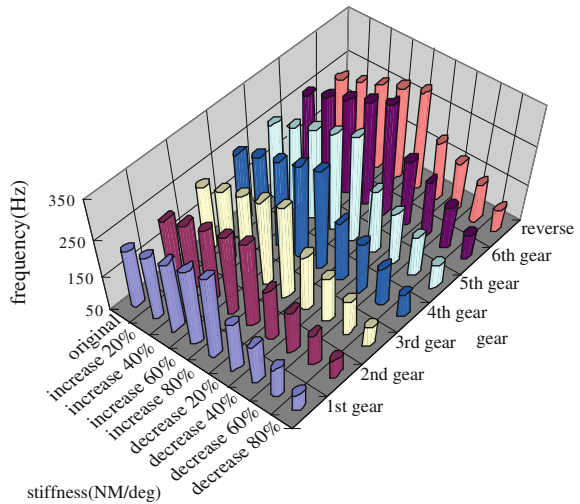


Fig. 18 Driveline 3rd mode sensitivity to propshaft torsional stiffness



Taking the stiffness into in-house software for calculation, the driveline mode sensitivity to axle shaft torsional stiffness could be collected, shown as Figs. 19, 20, and 21. Corresponding modal shape is unvaried.

From above 3 figures, it can be found, as in,

1. When axle shaft torsional stiffness is varied, the effect on 2nd driveline mode is very small, thus, axle shaft torsional stiffness is not the parameter tuning the 2nd driveline mode.
2. When axle shaft torsional stiffness is varied, the effect on 3rd driveline mode is very small, thus, axle shaft torsional stiffness is not the parameter tuning the 3rd driveline mode.

Table 8 Axle shaft torsional stiffness variation

Stiffness increase compared to original value (%)	Stiffness decrease compared to original value (%)
20	20
40	40
60	60
80	80

Fig. 19 Driveline 1st mode sensitivity to axle shaft torsional stiffness

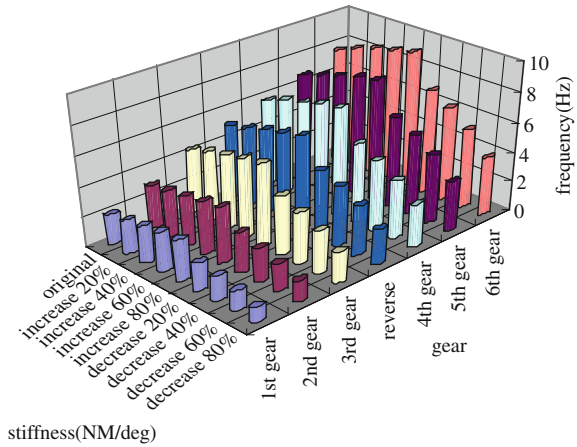
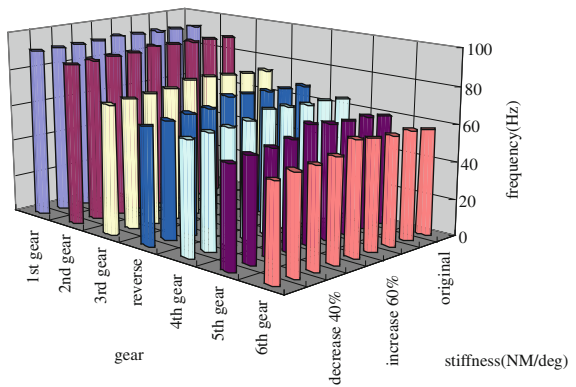
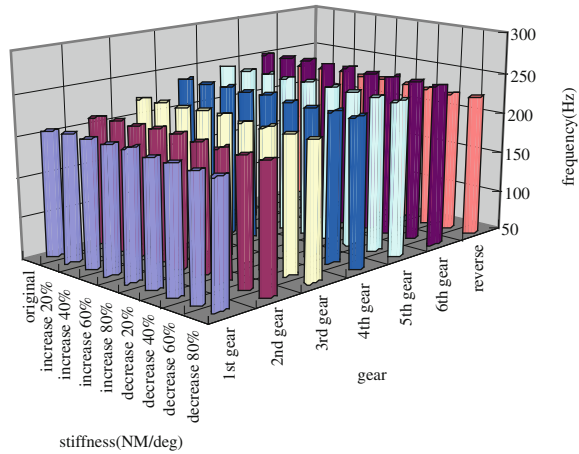


Fig. 20 Driveline 2nd mode sensitivity to axle shaft torsional stiffness



- When axle shaft torsional stiffness is varied, the effect on 1st driveline mode is obvious. As the stiffness increase/decrease, the 1st mode frequency correspondingly varies, though not so huge, the axle shaft stiffness still can be a parameter tuning 1st driveline mode.

Fig. 21 Driveline 3rd mode sensitivity to axle shaft torsional stiffness



5 Summary/Conclusion

In this paper, A RWD SUV driveline lumped mass model is built, to predict the torsional vibration modes. The prediction is turned out to correlate very well to in-vehicle torsional vibration measurement, hence, the model, adopted in this paper, is employed to investigate the driveline torsional vibration mode sensitivity to driveline component torsional stiffness, then, the conclusion can be drawn out of sensitivity study, as in,

1. For 1st driveline mode, axle shaft torsional stiffness play comparatively stronger role. Within broad range variation of axle shaft torsional stiffness, the 1st driveline in high gear (6th gear) has bigger variation (5 Hz), while, minor variation in low gear (1.7 Hz in 1st gear). As matter of fact, it is unrealistic to vary the axle shaft torsional stiffness that much, like decribed in this paper, therefore, axle shaft torsional stiffness only has minor tuning effect on 1st driveline mode, and other count measures should be emphasized, like hysteresis, engine torque rising rate, etc., to control the 1st driveline mode, especially during tipin/out maneuver to say the least, the axle shaft torsional stiffness could be tuned to check how it affect the 1st driveline during the driveline concept phase. Clutch damper and propshaft torsional stiffness have little effect on 1st driveline mode.
2. For 2nd driveline mode, clutch damper torsional stiffness has dominant effect, while, little effect by propshaft and axle shaft torsional stiffness. The clutch damper torsional stiffness can be tuned, in conjunction with hysteresis, to control the 2nd driveline mode, hence, the gear rattle or interior noise booming.
3. For 3rd driveline mode, the propshaft torsional stiffness has major effect, while, little effect by axle shaft and clutch damper torsional stiffness. The propshaft torsional stiffness could be optimized to tune 3rd driveline mode.

4. From the very start of driveline development, the torsional stiffness of axle shaft, propshaft, clutch damper can be employed to respectively check the influence on 3 major driveline modes, together with other parameter, to control the driveline mode frequency and amplitude, that can expedite driveline NVH development process.

References

1. Thomas Wellmann, Kiran Govindswamy (2007) Aspects of driveline integration for optimized vehicle NVH characteristics. SAE 2007-01-2246
2. Kalsule DJ, Vikram MR, Ambardekar MN, David Hudson (2011) Reduction of in-cab boom and transmission rattling using cost effective driveline refinement. SAE 2011-26-0060
3. Darrell Robinette, Michael Grimmer, Jeremy Horgan, Jevon Kennell, Richard Vykydal (2011) Torque converter clutch optimization: improving fuel economy and reducing noise and vibration. SAE 2011-01-00146
4. Fudala GJ, Engle TC A systems approach to reducing gear rattle. SAE 870396
5. Aldo Sorniotti (2008) Driveline modeling, experimental validation and evaluation of the influence of the different parameters on the overall system dynamics. SAE 2008-01-0632
6. Gerhard Wagner (2001) Application of transmission systems for different driveline configurations in passenger cars. SAE 2001-01-0882
7. Jian Pang et al (2006) Automobile noise and vibration. Beijing Institute of Technology Press, Beijing

Reduction of Structure-Borne Noise by Simulation

Sabine Sanzenbacher and Bernd Bertsche

Abstract The main targets in the development of transmissions are increasing driving performance, efficiency and driving comfort. An important aspect in this context is decreasing transmission noise. The most significant transmission noise is whining. It is caused by mesh contact noise of gear pairs under load. The excitations caused by the tooth contact are transferred to the gearbox housing by gearwheel bodies, shafts and bearings. Here from they are either transmitted to the attached parts (by structure-borne noise) or emitted to the environment as air-borne noise. In this paper an approach for the simulation of the noise behaviour of a transmission will be presented. To compute the level of structure-borne noise on the surface of the gearbox housing, a simulation model was built in a multi-body simulation environment. The excitation phenomenon of whining as well as the propagation of the resulting structure-borne noise up to the surface of the housing is considered in this model. Therefore, shafts and housing are integrated in the multi-body simulation as flexible bodies. Additionally, an element to abate propagation of structure-borne noise is introduced. An effective way is to encapsulate the bearings. In this case a ring between the bearing outer ring and the housing is used. Different designs of the rings will be presented as well as their potential to reduce the transmission of structure-borne noise which is estimated in a finite element simulation. To validate the model, measurements of an experimental transmission are made. On a testing bench, a single-stage transmission is driven under specified load and speed. Accelerometers are installed at different positions on the housing and measured results are compared to the simulation results at these positions.

F2012-J02-004

S. Sanzenbacher (✉) · B. Bertsche
Institute of Machine Components, University of Stuttgart, Stuttgart, Germany
e-mail: sabine.sanzenbacher@ima.uni-stuttgart.de

Keywords Transmission noise · Whining · Structure-borne noise · Gear mesh frequency · Tooth contact

1 Introduction

Due to increasing customer requirements, an important goal in passenger car development is to decrease transmission noises. To be able to influence the acoustic behaviour of a transmission, it is necessary to estimate its affection to propagate structure-borne noise in an early development stage. Therefore, simulation models are needed that predict the excitation phenomena as well as the propagation of structure-borne noise. The aim is to develop models that are able to estimate the potential of different designs to abate structure-borne noise without the necessity of an experiment to validate the results.

The most significant transmission noise is whining [1], not only because of its absolute loudness but also because of its tonal characteristic, has it been described as annoying by customers. Whining noises are caused by gear pairs driven under load. From the toothing, the excited structure-borne noise waves are transferred to the housing by means of gear wheel bodies, shafts and bearings. Here from they are either transmitted to the attached parts (by structure-borne noise) or radiated as air-borne noise. In this paper, a computational model to simulate the excitation phenomena and the propagation within the gearbox is presented. In a further step, a newly developed component is introduced. It is part of the acoustic transmission path and its purpose is to reduce the propagation of structure-borne noise. The element that is used is a ring between the bearing outer ring and the housing. It has been chosen because it is one of the last parts in the structure-borne noise transmission path inside the gearbox. Additionally, the load in this part is primarily static and no other functions have to be fulfilled. Different physical principles were considered for the design of the ring and transferred into real design proposals.

2 Excitation and Propagation of Transmission Noises

As described in the introduction, whining is the most significant transmission noise that occurs when a gear pair is driven under load. By definition, the main function of a transmission is the conversion of torque and speed. The main component in this case is the gear stage whose purpose it is to transmit rotation and torque from the input to the positively locking output shaft. During this transfer process, three types of excitations occur that may be divided into parametrical excitation, displacement excitation and shock excitation.

Mainly, involute profiles are used for gears in passenger car transmissions. With this profile type in load-free cases the rotation is transmitted uniformly from the

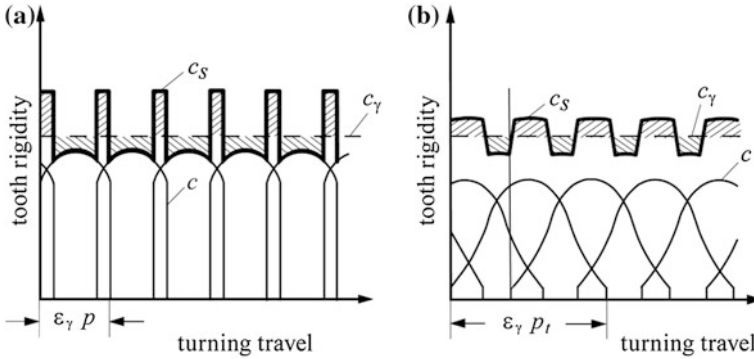


Fig. 1 Overall tooth rigidity pattern c_s , meshing rigidity c_γ (average value of c_s over time). **a** Straight spur gearing; **b** helical gearing [2]

input to the output shaft. Additionally, these profiles can be produced easily and cost-effectively, and are insensitive to centre distance fluctuation [2]. Under load, the driving and the driven gear wheel, as well as the shafts and the housing, undergo deformation. This consists of driving wheel deformation, driven wheel deformation and Hertzian flattening of the tooth flanks [2]. Depending on the meshing position, the rigidity of a straight spur gear pair varies as shown in Fig. 1a.

As one or two tooth pairs are in contact alternately, the overall rigidity c_s results from a superposition of the individual tooth pair rigidity c of all tooth pairs in contact. If two pairs of teeth are in contact, the rigidity reaches its maximum. During the phase of only one tooth pair in contact, the highest rigidity is reached if the levers of both teeth are nearly similar. In case of tip or root contact, the rigidity decreases. Figure 1b shows the tooth rigidity of a helical gear pair. There is less variation in rigidity compared to straight spur gears. One reason is the more sinusoidal characteristic of the rigidity of one pair of teeth; the other reason is the contact ratio. Normally, in helical cut gear pairs more than two tooth pairs are always in contact. Therefore, the absolute value of rigidity varies less than that of straight spur gearings. In a first approximation, the characteristic of gear pair rigidity can be described by a sine function. Equation (1) illustrates the relation between the gear mesh frequency f_{mesh} in Hz, the operating speed n in rpm and the number of teeth z .

$$f_{mesh} = \frac{n}{60} z \tag{1}$$

Even in unloaded condition, deviations from an ideal flank lead to variations in the law of gears. They can occur as tooth trace deviation or as deviations from an ideal involute profile. They result either from manufacturing imperfections or are part of the tooth design.

In most cases, tooth design is a complicated optimization problem. Even a gear pair which has been optimised for its load-carrying capacity may produce

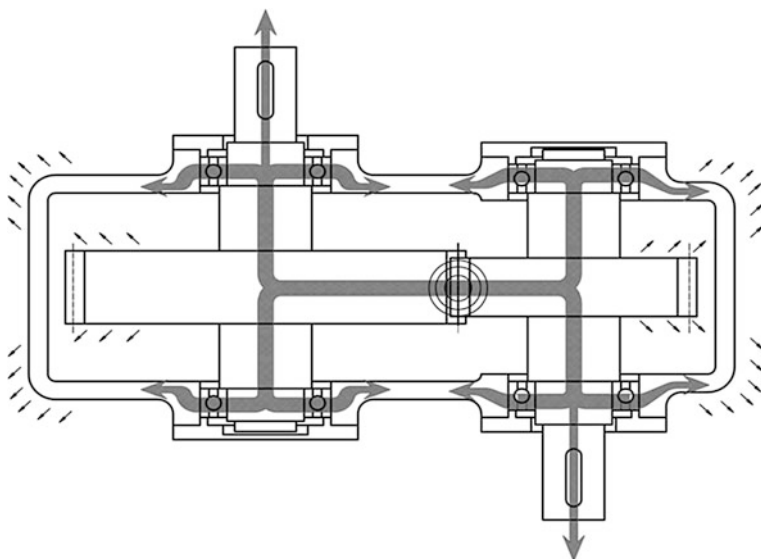


Fig. 2 Acoustic transmission path of a gearbox

unfavourable noise. The load case significantly influences the behaviour of gear pairs. Under different load and speed conditions deformations of teeth, shafts, and housing vary. As a consequence tooth contact conditions change as well. For an automotive transmission a high torque range is required. Different types of drivers as well as different driving situations (e.g. up-hill driving) generate varying speed and torque demands.

A third phenomenon of excitation is shock excitation. Under load, the driving and driven teeth are deformed. Consequently, the unloaded tooth of the driving wheel comes in contact with an unloaded tooth of the driven wheel. Due to these modified engagement conditions, the teeth knock against each other. These meshing impacts can also be caused by pitch errors.

The excitation arising from this phenomenon is periodic and pulse-like. Profile corrections, such as tip or root relief, or accurate manufacturing, can reduce or even eliminate this type of excitation.

Only a small share of vibrational energy caused by tooth contact is radiated inside the gearbox housing as air-borne noise. A large part of the excitations are propagated by gear bodies, shafts and bearings as structure-borne noise. One part is transmitted to the gearbox housing and radiated as air-borne noise. Another part is transmitted to other parts attached to the gearbox as structure-borne noise. The propagation path of the excitation is shown in Fig. 2, the small, thin arrows symbolizing air-borne noise, the bold ones structure-borne noise.

Vibrations and waves in solid bodies are commonly known as structure-borne noise. The propagation results from stress and strain deformation of the solid body and can be described by a vector of velocity and a stress tensor [3]. Due to material

damping and absorption processes, the amplitudes of the waves decrease. Based on these facts, concepts to reduce the propagation of structure-borne noise are developed and presented in this paper.

3 Testing Transmission in Simulation and Testing Environment

To analyze the potential of different design approaches to minimise the propagation of structure-borne noise, a testing transmission, shown in Fig. 3, was developed. In this single-stage transmission that is driven via an input shaft (1), torque and speed are changed by a gear stage (2) which is spur-toothed and passed to the output via an output shaft (3). The design modifications to abate structure-borne noise will be integrated in the adapter ring (4) between the bearing outer ring and the housing. This component was chosen because it is one of the last parts in the structure-borne noise transmission path inside the gearbox. Additionally, the load case in this ring is predominantly static and no other functions, such as converting torque or sealing, have to be fulfilled. Under these conditions the design approach can be developed with few limitations. To be able to validate the different designs of the ring, an accelerometer is fixed on the surface of the gearbox housing (5).

Being able to forecast the dynamic behaviour of the testing transmission, a simulation model was developed in the multi-body simulation environment SIMPACK. Within the simulation model the excitations in the tooth contact as well as the acceleration of the gear-box housing due to the transmitted structure-borne noise is computed. In this case, the excitations are caused by the tooth contact. As whining noises are generated in the meshing contact, a main focus is on the modelling of the teeth and on the link between the driving and driven wheel. Important impacts on the whining noise like the macro and micro geometry were taken into account by measuring the tooth flanks on a 3-dimensional coordinate measuring machine. In modelling the gearwheels in SIMPACK these measurements were used to define the geometry of the tooth flanks.

In addition to the geometry, the connection between the driving and the driven gearwheel has to be considered. SIMPACK provides a force element called “Gear Pair” which is useful in this case. Gear wheel body deformation stiffness, tooth bending and share stiffness as well as Hertzian contact stiffness are taken into account in computing the stiffness of the tooth contact [4] which is a function of the meshing position. Another important impact that is considered is the tilt of the gear wheels. Due to geometrical dislocations in the transmission under load, the meshing conditions vary from the unloaded case and thereby the gear pair stiffness changes as well.

Figure 4 shows the frequency analyses of the gear load at an input speed of 1,000 rpm. The time signal of the gear loads was analysed by means of a fast Fourier transformation. The gear mesh frequency f_{mesh} , dependant on the number

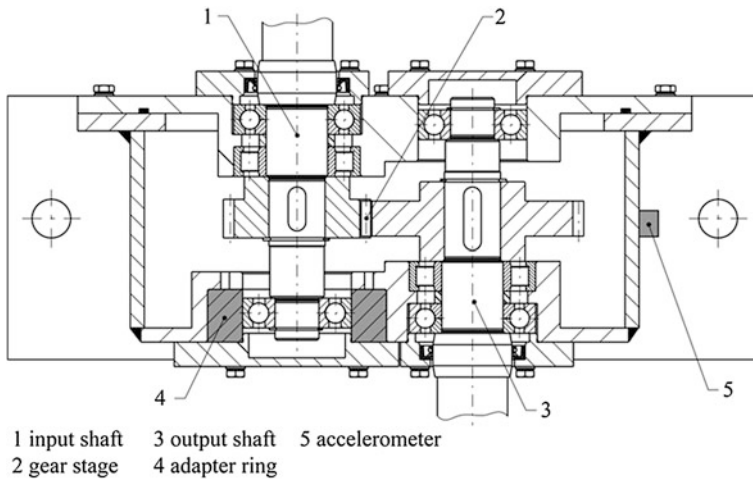
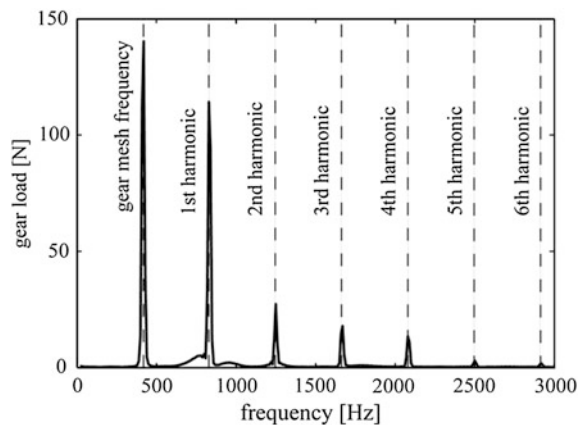


Fig. 3 Testing transmission

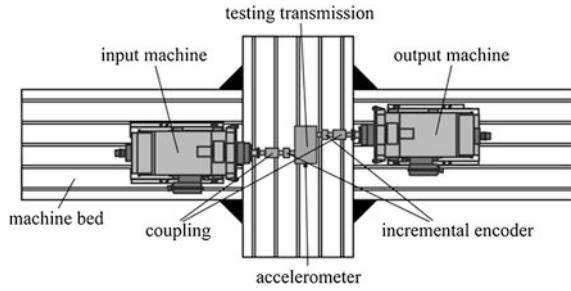
Fig. 4 Frequency response characteristics of the gear load at an input speed of 1,000 rpm



of teeth is clearly visible. With a number of teeth of $z = 25$, the gear mesh frequency $f_{mesh} = 417$ Hz calculated as given in Eq. (1). The harmonic frequencies appear with decreasing amplitudes over the number of the order.

The shafts that the gearwheels are fixed to are included in the model as flexible bodies. As the transmission is driven under load, the shafts as well as all other parts that belong to the power flow undergo deformation. As the gearwheels are fixed on the shafts by a key connection, the meshing contact conditions vary and a flexible formulation of the shafts is necessary. With the use of flexible bodies in a multi-body simulation, the behaviour of each body under load is considered and can be described nearly as well as in a complete finite element computation, but in a fraction of simulation time. All parts that are integrated as flexible bodies were modelled in the finite element software ANSYS. The meshing was done there and

Fig. 5 Transmission testing bench



nodes that should be available in the multi-body simulation to impinge loads or evaluate deformations were defined as interface nodes. For the modal reduction in ANSYS, all nodes of the finite element structure are divided into interface nodes which are available afterwards in the multi-body simulation environment and internal nodes. During the modal reduction, the static constraint modes and the eigenmodes of the part are calculated [5]. Hence, in the multi-body simulation deformations caused by an exciting force are calculated efficiently.

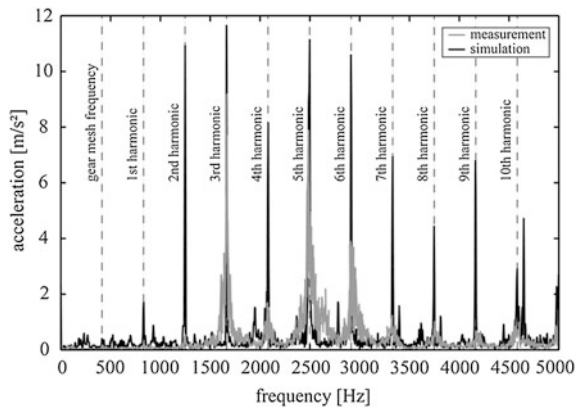
The bearings of the shafts are important parts in the acoustic transmission path. Their stiffness varies with the dislocation and tilt of the bearing inner ring relative to the bearing outer ring. In the model, the bearings are represented by a force element which uses a nonlinear map containing the bearing stiffness [6]. As the structure-borne noise is transmitted by the adapter ring and the gearbox housing, these components are integrated as flexible bodies as well. On a node that is located on the surface of the gearbox housing at the same position as the accelerometer on the testing transmission, the acceleration is calculated to be able to validate the simulation model.

For the measurements, the transmission was mounted on a testing bench at the Institute of Machine Components. It was fixed between an input machine ($P_{max} = 300$ kW; $T_{nom} = 704$ Nm at 4,475 rpm; $n_{max} = 8,000$ rpm) and an output machine ($P_{max} = 460$ kW; $T_{nom} = 1,494$ Nm at 2,960 rpm; $n_{max} = 8,000$ rpm) as shown in Fig. 5. Incremental encoders with 10,000 counts per revolution are mounted on the input and output shaft. This allows high-precision measuring of the state of speed. The transmission is connected to the input and output machine by two elastic and torsional rigid couplings.

The simulated and the measured values of the acceleration of the gearbox housing are shown in Fig. 6. The maximum amplitude of acceleration in the measurement, as well as the simulation, appears at the third harmonic of the gear mesh frequency at 1,667 Hz. The fifth and the sixth harmonic are also dominant in the measurement as well as in the simulation. In general the simulated values are higher than those that are measured. The reason is that the housing is modelled as one part where the housing joint is neglected where structure-borne noise energy can be dissipated.

The measurement as well as the simulation illustrates the influence of all the parts belonging to the acoustic transmission path. In Fig. 4, the maximum excitation force of the structure-borne noise is located at 417 Hz. In the acceleration signal measured

Fig. 6 Measured and simulated acceleration on the surface of the gearbox housing at 1,000 rpm



on the surface of the housing, this frequency is inconspicuous. Contrarily higher orders of the gear mesh frequency with a smaller level of gear load excite a major vibration of the housing. Hence the need to consider the entire acoustic transmission path is apparent. To reduce the propagation of structure-borne noise, propagation an adapter ring, shown in Fig. 3, is used. This element is designed to absorb vibrations caused by the toothings.

4 Design Approaches for the Adapter Ring

In a first step, the designs of the adapter ring are developed analytically by considering different possibilities to abate structure-borne noise. To be able to compare the different designs, finite element models were built in ANSYS. In the models, the exciting forces caused by the toothings are approximately described by a sine function with a varying excitation frequency from 16 Hz to 10 kHz. Representative values to characterize the acoustic behaviour are calculated by mounting the rings in a plate that represents the housing.

In this paper, one design approach to attenuate the propagation of structure-borne noise waves by integrating geometrical discontinuities into the component is presented. The discontinuities can be by produced by removing material. The crucial parameters of the discontinuities are: geometry, frequency and distance to the excitation point. The propagation of structure-borne noise may be described as wave fronts moving through solid bodies. Impinging a discontinuity the waves are reflected, diffracted or spread. Based on the reflection progresses, the design of the adapter ring is acoustically optimised. An aspect to be considered is that mass and stiffness parameters should not be reduced too much. Otherwise the input impedance of the component is too small to improve the acoustic behaviour. A design approach that is shown in Fig. 7a includes slot-shaped discontinuities. The advantage of these kinds of discontinuities is that the transmission path for

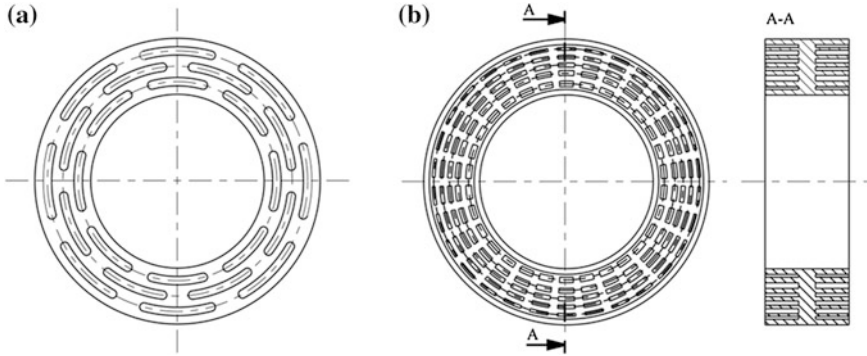


Fig. 7 **a** Design approach using geometrical discontinuities (M1); **b** resonator design approach (M2)

structure-borne noise can be significantly extended and material damping can reduce the vibration energy.

Another possibility to abate structure-borne noise is to use resonators. Therefore, additional spring-mass systems are integrated in the ring design. If appropriate, mechanical properties are chosen whereby, a significant amount of vibration energy can be eliminated. In the design approach shown in Fig. 7b, resonators are fixed as exposed beams at the vibrating body. Those free-standing structures are easily excited, especially by bending vibration waves, the most important waves in the propagation of structure-borne noise. If damping materials are mounted on the surface of these structures, vibration energy is converted into another, acoustically uninteresting, kind of energy. In case of efficient use, they have to be actuated near their eigenfrequencies. For a known frequency, they can be aligned to this by their geometrical properties such as length and thickness. With the vibration of the beams, a lot of vibration energy can be withdrawn. Without any further damping, nearly all the converted energy is radiated as air-borne noise.

Finite element calculations were made to compare these design approaches. In the simulation environment each ring is mounted in a plate and excited concentrically by an alternating sinusoidal force. The behaviour of each design caused by the excitation is measured as acceleration at nodes on the inner and outer surface of the ring. To evaluate the acoustic characteristics, two specific values are used, the transfer function and the insertion loss. The transfer function $T(f)$ is calculated as quotient of output $a_{out}(f)$ and input $a_{in}(f)$ acceleration [7].

$$T(f) = \frac{a_{out}(f)}{a_{in}(f)} \quad (2)$$

The insertion loss ΔL_a directly describes the efficiency of a design approach compared to a non-optimised ring by relating the effective value of acceleration of the optimised ring \hat{a}_{opt} and the non-optimised ring \hat{a}_0 as given in Eq. (3).

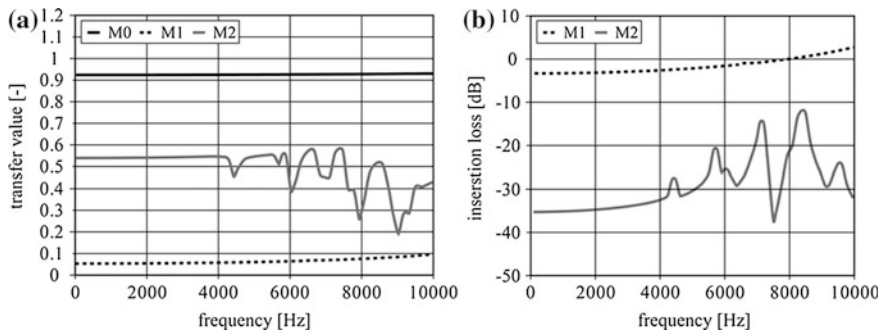


Fig. 8 Transfer value (a) and insertion loss (b) for a ring with holes (M1.1) a ring with slots (M1.2)

$$\Delta L_a = 20 \log \frac{\hat{a}_{opt}}{\hat{a}_0} \quad (3)$$

Results given by this finite element calculation can only be used to compare the different designs. In reality, the values can vary tremendously.

In Fig. 8, the transfer values and insertion losses for a non-optimised ring (M0), the ring with slots (M1), and the resonator ring (M2) are shown. The frequency range of interest is based on the number of teeth, which, in this case, is 25. With a maximum input speed of 6,000 rpm, the gear mesh frequency is mainly about 2,500 Hz, with the first harmonic frequency at roughly 5,000 Hz.

The transfer values for model M1 and M2 are less than those of the original model M0. The insertion loss shows that Model M1 achieves a reduction of noise level in the lower frequency range of about 3 dB and Model M2 achieves values up to a reduction of 37 dB. The calculated values can only be used for a comparison between the different ring designs. To prove the real potential, experimental results or simulation models of the whole transmission are required.

5 Conclusion

A testing transmission to analyze different possibilities to abate the propagation of structure-borne noise was developed. For this transmission, a simulation model to calculate the excitation phenomena in the tooth contact as well as the transmission of structure-borne noise by shafts, bearings and housing was developed. A comparison of simulated and measured values shows that it is possible to forecast acoustic behaviour by a multi-body simulation model that includes all parts of the acoustic transmission path as flexible bodies. Comparing the values of the exciting forces in the tooth contact and the acceleration values on the gearbox housing, the need to consider the acoustic transmission path is apparent. Some excitation frequencies, but

not necessarily the one with the highest energy, affect the acceleration of the gearbox housing. Others do not appear on the surface of gearbox housing as structure-borne noise.

Different rings to encapsulate the bearings are used to reduce the propagation of structure-borne noise. Two design approaches taking into account different physical principals are introduced in this paper. The potential of the rings is estimated using a simple finite element model. In a further step, the real potential of those rings has to be tested by integrating them into the multi-body simulation model of the transmission, or by mounting them in the testing transmission and perform measurements on the testing bench.

References

1. Naunheimer H, Bertsche B, Ryborz J, Novak W (2011) Automotive transmissions. Springer, Berlin
2. Niemann G, Winter H (1983) Maschinenelemente band II. Springer, Berlin
3. Cremer L, Heckel M (2005) Structure-borne sound. Springer, Berlin
4. Simpack AG (2012) SIMPACK documentation, version 9.1, Gilching
5. Craig RR, Bampton MDD (1968) Coupling of substructures for dynamic analysis. AIAA J 6(7):1313–1319
6. Vesselinov V, Weber J, Hahn T (2007) Wälzlagerkennfelder für MKS-Programme. In: Gold PW(ed) Proceedings of the ATK 2007. Aachen, p 213–223
7. Schmidt A (1997) Impedanzelement, Forschungsvereinigung Antriebstechnik e.V., Forschungsvorhaben Nr. 522, Abschlussbericht, TU Clausthal, Institut für Maschinenwesen

Dynamic Characteristics of Vehicular Planetary Gears Influenced by Engine Excitation and Backlash Based on Nonlinear Torsional Vibration Model

Hui Liu, Zhongchang Cai and Changle Xiang

Abstract Multiple gear ratios in automatic transmission are achievable with multi-stage planetary gears, where there are both the loaded planetary gear and the idle planetary gear under some gear ratios operation. Due to the change of road conditions, engine runs with different rotational speed and torque, which brings an external fluctuation excitation to the automatic transmission planetary gear set. In addition, the gear backlash becomes larger with the wear increasing during the running. Both engine excitation and gear backlash are important factors that not only influence the vibration characteristic and meshing state of the loaded planetary gear but also those of the idle planetary gear. The objective of this paper was to investigate the change of meshing force state of loaded planetary gear and idle planetary gear influenced by the different backlash and the engine excitation based on a nonlinear torsional vibration model.

Keywords Planetary gears · Torsional vibration · Nonlinear vibration · Backlash · Meshing force

F2012-J02-005

H. Liu (✉) · Z. Cai · C. Xiang
School of Mechanical and Engineering, Beijing Institute of Technology,
100081 Beijing, China
e-mail: lh@bit.edu.cn

H. Liu · C. Xiang
National Key Laboratory of Science and Technology on Vehicle Transmission Laboratory,
Beijing Institute of Technology, 100081 Beijing, China

1 Introduction

Planetary gears are widely used in automotive and aerospace applications due to their compactness, high torque/weight ratio, diminished bearing loads. Despite their distinguishing advantages, planetary gears noise and vibration remain key concerns. Kahraman [1] developed a generic dynamic model of a planetary gears with helical gears, and perform a parametric study on the effect of mesh phasing on dynamic behavior. Kahraman [2] developed a family of torsional dynamic model capable of predicting the free vibration characteristics of compound gear sets under different kinematic configurations resulting in different speed ratios. Ambarisha and Parker [3] analyzed the response from the dynamic analysis using analytical and finite element models, and successfully compared their response qualitatively and quantitatively. Abousleiman [4] developed a hybrid 3D finite element/lumped parameter model for quasi-static and dynamic analyses. Kahraman [5] developed a kinematics and power flow analysis methodology for automatic transmission planetary gear trains. Inalpolat and Kahraman [6, 7] developed a dynamic model to predict modulation sidebands of planetary gears due to gear manufacturing errors. Kiracofe and Parker [8] extended previous analytical models of single, simple-stage planetary gears to compound, multi-stage planetary gears. Alshyyab and Kahraman [9] a nonlinear dynamic model for planetary gear sets using multi-body dynamics. Bahk and Parker [10] developed a analytical solution for the nonlinear dynamics of planetary gears. Park and Lin [11] analyzed the mesh phasing relationships in planetary.

The most of literature cites focus on loaded planetary gear, the effect of the backlash on the nonlinear mesh force is obtained under the constant torque. The effect of idle planetary gear is ignored in linear dynamics research, but it does not agree with the practical operation. The objectives of this study are to build the lumped parameter model of multi-stage planetary gears, which contains loaded planetary gear and idle planetary gear, planetary gears are excited by fluctuant torque of engine, and to obtain the dynamic characteristics of forced vibration response of mesh force in steady-state in time domain and frequency domain using numerical simulation.

2 Modeling and Equations of Motion

2.1 Lumped Parameter Model of Multi-Stage Planetary Gears

For single-stage planetary, most of researchers chose a basis that rotates with carrier. This allows the planet positions to be described by fixed angles even with gear rotation. The choice of a coordinate basis for the multi-stage is different from single-stage planetary. In the multi-stage planetary gear case, there are potentially several different carriers, each rotating at different speeds. It is necessary to construct multiple rotating bases and then describe the coupling between the

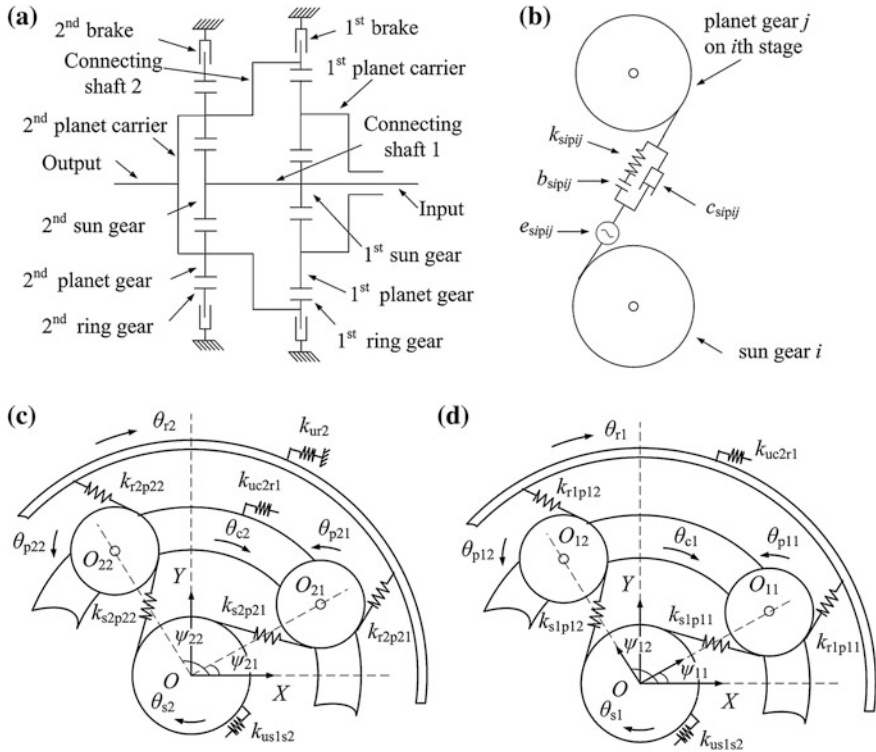


Fig. 1 Lumped parameter model of multi-stage planetary gears. **a** multi-stage planetary gears. **b** model of meshing gears. **c** 2nd stage planetary. **d** 1st stage planetary

rotating components by means of time-varying coordinate transformations. This method is difficult to understand. Another way is describe all components in a single fixed basis and then describe the angle of planet position to change with time. In this paper, the latter was adopted. A automatic transmission that consists of two single-planet planetary gear stages is used here as an example for modeling and analysis, these process and method is the same with three and more stages.

The lumped parameter model of multi-stage planetary gears in automotive transmission was shown in Fig. 1. In this work, the dynamic modeling assumptions of the system are as follows: (1) Mesh stiffness of each gear pair is simplified by considering a rectangular nonlinear time-varying spring acting along the line of action of the gear mesh, the backlash is consider as a stepwise linear function, and torsional stiffness of connecting shafts are equivalent to linear torsional spring. (2) In each stage planetary gears, each parts rotates in a plane that is normal to axis of rotation, planets are equally spaced, each planet gear has the same physical parameters, e.g. mass, inertia, mesh stiffness, et al. (3) Friction forces due to gear teeth contact and other dissipative effects are equivalent to damping. (4) Manufacturing errors, assembling errors and tooth errors are considered along the meshing line.

In general, the subscript i is used for denoting the number of stage, the subscript j is used for denoting the number of planet gear in one stage. In Fig. 1, J_{si} , J_{pij} , J_{ci} , J_{ri} , m_{pij} ($i = 1, 2; j = 1, 2, 3, 4$) respectively represents the inertia of sun gear, planet gear, planet carrier and ring gear, and mass of j th planet in i th stage planetary gears. θ_a ($a = si, ci, ri, pij$) is the angular displacement for part a . k_{sipij} , k_{ripij} respectively represent sun-planet and planet-ring mesh stiffness in i th stage planetary gears. k_{mqnl} ($q, l = 1, 2; m, n = s, c, r$) is torsional stiffness of shaft that connects part m in q th stage to part n in l th stage. c_{sipij} , c_{ripij} , e_{sipij} , e_{ripij} , b_{sipij} , b_{ripij} respectively represents meshing damping coefficient, cumulative meshing errors, backlash in sun-planet and planet-ring meshing gear pairs. ψ_{ij} is the angle of j th planet position angle in i th stage planetary gears, and it can be written as $\psi_{ij} = \omega_{ci}t + (j-1)\pi/2$, ω_{ci} are angular velocities of i th sun gear.

The cumulative meshing errors which are analyzed along the meshing line, its calculating equations are

$$\begin{aligned} e_{sipij} &= E_{si} \sin(\omega_{si}t + \beta_{si} - \psi_{ij} + \alpha) + A_{si} \sin(\gamma_{si} - \psi_{ij} + \alpha) \\ &\quad + E_{ci} \sin(\omega_{ci}t + \beta_{ci} - \psi_{ij} + \alpha) + A_{ci} \sin(\gamma_{ci} - \psi_{ij} + \alpha) \\ &\quad + E_{pij} \sin(\omega_{pi}t + \beta_{pij} + \alpha) + A_{pij} \sin(\gamma_{pij} + \alpha) + E_{sipij} \sin[\omega_{mi}(t + \gamma_{sipij}T_{mi})] \\ e_{ripij} &= -E_{ri} \sin(\omega_{ri}t + \beta_{ri} - \psi_{ij} - \alpha) - A_{ri} \sin(\gamma_{ri} - \psi_{ij} - \alpha) \\ &\quad - E_{ci} \sin(\omega_{ci}t + \beta_{ci} - \psi_{ij} - \alpha) - A_{ci} \sin(\gamma_{ci} - \psi_{ij} - \alpha) \\ &\quad + E_{pij} \sin(\omega_{pij}t + \beta_{pij} - \alpha) + A_{pij} \sin(\gamma_{pij} - \alpha) + E_{ripij} \sin[\omega_{mi}(t + (\gamma_{ripij} + \gamma_{sri})T_{mi})] \end{aligned}$$

In the above equations, E_a , A_a ($a = si, ci, ri, pij$) are amplitude of manufacturing error and assembling error of part a respectively. E_{sipij} , E_{ripij} are tooth error of corresponding meshing gear pairs. ω_a are angular velocities, ω_{mi} , T_{mi} are meshing frequency and meshing time period in i th stage planetary. β_a , γ_a are the phase angle of corresponding errors, γ_{sipij} , γ_{ripij} are the mesh phase angle of j th sun-planet and j th ring-planet relative to 1st sun-planet and 1st ring-planet in i th stage planetary. γ_{sri} is the mesh phase angle between the sun-planet and ring-planet in i th stage planetary. α is pressure angle at sun-planet and ring-planet meshes. t is defined as time.

Time-varying mesh stiffness of each gear pair is simplified by considering a periodic rectangular time function, it can be written in Fourier series as

$$\begin{aligned} k_{sipij} &= \bar{k}_{sipij} + \sum_{\lambda=1}^H k_{sipij}^{\lambda} \sin \left[\lambda (\omega_{mi}t + \gamma_{sipij}) + \phi_{sipij}^{\lambda} \right] \\ k_{ripij} &= \bar{k}_{ripij} + \sum_{\lambda=1}^H k_{ripij}^{\lambda} \sin \left[\lambda (\omega_{mi}t + \gamma_{ripij} + \gamma_{sri}) + \phi_{ripij}^{\lambda} \right] \end{aligned}$$

where \bar{k}_{sipij} , \bar{k}_{ripij} , is mean components, k_{sipij}^{λ} , k_{ripij}^{λ} , ϕ_{sipij}^{λ} , ϕ_{ripij}^{λ} is the amplitude and phase angle of λ th alternating components. λ , H are integer.

Table 1 Parameters of planetary gears transmission

Parameter	Value	Parameter	Value	Parameter	Value
Module m/mm	4	$E_{s1}, E_{s1}/\mu\text{m}$	28, 40	$A_{s1}, A_{s1}/\mu\text{m}$	30, 30
Number of teeth $Z_{s1}, Z_{r1} Z_{p1}$	36, 76, 20	$E_{r1}, E_{r1}/\mu\text{m}$	40, 40	$A_{r1}, A_{r1}/\mu\text{m}$	60, 60
Number of teeth $Z_{s2}, Z_{r2} Z_{p2}$	27, 77, 25	$E_{c1}, E_{c2}/\mu\text{m}$	60, 60	$A_{c1}, A_{c2}/\mu\text{m}$	50, 30
Backlash b/mm	0.4	$E_{p1j}, E_{p2j}/\mu\text{m}$	28, 28	$A_{p1j}, A_{p2j}/\mu\text{m}$	28, 28
Pressure angle $\alpha/^\circ$	20	$E_{sp1j}, E_{sp2j}/\mu\text{m}$	27, 27	$E_{rp1j}, E_{rp2j}/\mu\text{m}$	27, 27

Meshing damping is complex, because it is affected by many factors and can not be calculated accurately. In this paper, meshing damping coefficient was calculated by experiential formula, it can be written as

$$c_{sipij} = 2\zeta \sqrt{\bar{k}_{sipij}/(m_{si} + m_{pij})}, \quad c_{ripij} = 2\zeta \sqrt{\bar{k}_{ripij}/(m_{ri} + m_{pij})}$$

where ζ is damping ratio, $\zeta = 0.07$.

The backlash of a gear pair is a nonlinear function for relative displacement of meshing action line, and can be considered as a stepwise linear function. When backlash of a gear pair is $2b$, this function f can be written as

$$f(L, b) = \begin{cases} L - b & L > b \\ 0 & |L| \leq b \\ L + b & L < -b \end{cases}$$

where L is relative displacement of meshing action line, b is a half of backlash of a gear pair.

Relative displacement of meshing action line L_{sipij}, L_{ripij} consist of cumulative meshing errors and torsional displacement of correlative parts. They can be written as

$$\begin{cases} L_{s1p1j} = \theta_{s1}R_{bs1} - \theta_{c1}R_{bs1} - \theta_{p1j}R_{bp1j} + e_{s1p1j} \\ L_{r1p1j} = \theta_{p1j}R_{bp1j} - \theta_{c1}R_{br1} - \theta_{r1}R_{br1} + e_{r1p1j} \\ L_{s2p2j} = \theta_{s2}R_{bs2} - \theta_{c2}R_{bs2} - \theta_{p2j}R_{bp2j} + e_{s2p2j} \\ L_{r2p2j} = \theta_{p2j}R_{bp2j} - \theta_{c2}R_{br2} - \theta_{r2}R_{br2} - e_{r2p2j} \end{cases}$$

where R_{ba} represents the equivalent radius of part a .

The dynamic gear mesh force F_{sipij}, F_{ripij} were defined as

$$\begin{aligned} F_{sipij} &= k_{sipij}(t)f(L_{sipij}, b_{sipij}) + c_{sipij}\dot{L}_{sipij}, \\ F_{ripij} &= k_{ripij}(t)f(L_{ripij}, b_{ripij}) + c_{ripij}\dot{L}_{ripij} \end{aligned}$$

Parameters of planetary gears transmission are shown in Table 1.

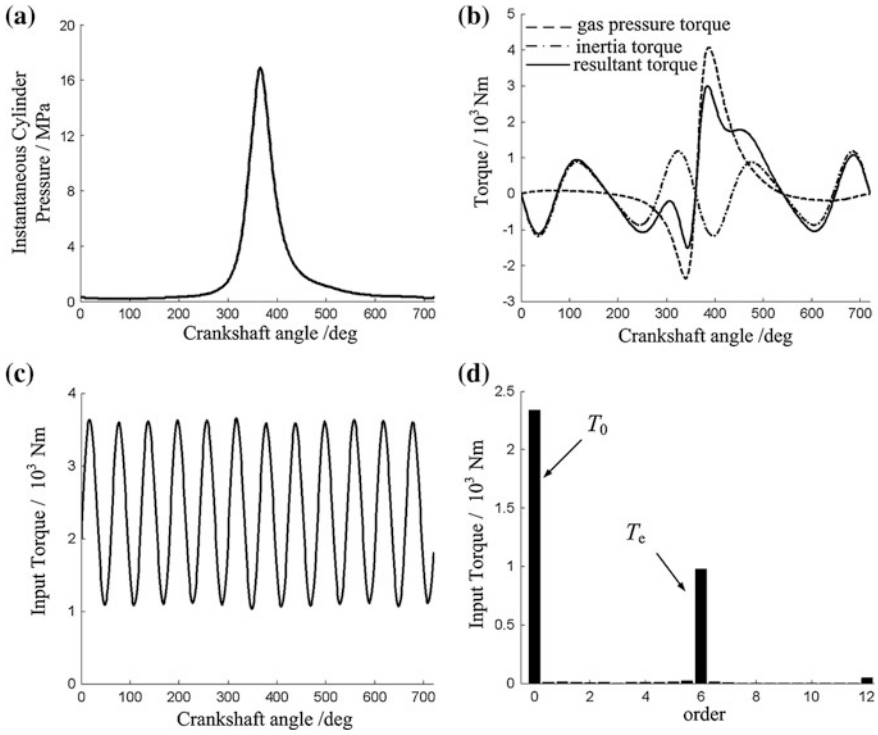


Fig. 2 Torque analysis of engine in rated condition. **a** instantaneous cylinder pressure. **b** torque on single cylinder. **c** input torque. **d** order analysis

2.2 Model of Fluctuant Input Torque and Output Torque

The torque acted on crankshaft is primary excitation source that cause forced torsional vibration of powertrain. In this paper, the four-stroke engine with V-12, and 60° crankshaft configuration fires six times within a crankshaft revolution. When hydraulic torque converter is under lock-up condition, engine torque acts on input shaft of planetary gears via mechanical connection. In this case, input torque T_{in} is equivalent to engine torque. The output torque T_{out} is in proportion to input torque T_{in} , and this proportion coefficient is gear ratio. Engine torque mainly contains combustion gas pressure torque and inertia torque of reciprocating components. Torque analysis of engine in rated speed (4200 r/min) was shown in Fig. 2. Input torque T_{in} includes of the static torque T_0 and 6th order dynamic torque T_e mainly. It can be equivalent to the sum of T_0 and T_e , and can be expressed as

$$T_{in} = T_0 + T_e = T_0 + \mu T_0 \sin(2\pi f_e t + \varphi)$$

Here, f_c is the frequency of fluctuant torque T_e , it is six times of crankshaft rotation frequency, φ is phase angle of T_e , μ is the ratio the amplitude of T_e to T_0 , it is 0.3.

2.3 Equations of Motion

For multi-stage planetary gears, the dynamic model can be developed based on the single planetary gears lumped parameter model and considering the connecting relationships. According to the Lagrange's equation, for two-stage planetary gears with fixed 2nd ring gear, equation of motion are given as

$$\left\{ \begin{array}{l} J_{s1}\ddot{\theta}_{s1} + k_{s1s2}(\theta_{s1} - \theta_{s2}) + c_{s1s2}(\dot{\theta}_{s1} - \dot{\theta}_{s2}) + \sum_{j=1}^4 F_{s1p1j}R_{s1} = T_{in} \\ J_{r1}\ddot{\theta}_{r1} - k_{c2r1}(\theta_{c2} - \theta_{r1}) - c_{c2r1}(\dot{\theta}_{c2} - \dot{\theta}_{r1}) + \sum_{j=1}^4 F_{r1p1j}R_{r1} = 0 \\ J_{c1}\ddot{\theta}_{c1} + \sum_{j=1}^4 J_{p1j}(-\ddot{\theta}_{c1} + \ddot{\theta}_{p1j}) + \sum_{j=1}^4 m_{p1j}R_{bc1}^2\ddot{\theta}_{c1} - \sum_{j=1}^4 (F_{s1p1j}R_{bs1} + F_{r1p1j}R_{br1}) = 0 \\ -J_{p1j}\ddot{\theta}_{c1} + J_{p1j}\ddot{\theta}_{p1j} - (F_{s1p1j} - F_{r1p1j})R_{p1j} = 0 \end{array} \right.$$

$$\left\{ \begin{array}{l} J_{s2}\ddot{\theta}_{s2} - k_{s1s2}(\theta_{s1} - \theta_{s2}) - c_{s1s2}(\dot{\theta}_{s1} - \dot{\theta}_{s2}) + \sum_{j=1}^4 F_{s2p2j}R_{s2} = 0 \\ J_{r2}\ddot{\theta}_{r2} - \sum_{j=1}^4 F_{r2p2j}R_{r2} = -k_{ur2}\theta_{r2} - c_{ur2}\dot{\theta}_{r2} \\ J_{c2}\ddot{\theta}_{c2} + \sum_{j=1}^4 J_{p2j}(-\ddot{\theta}_{c2} + \ddot{\theta}_{p2j}) + \sum_{j=1}^4 m_{p2j}R_{bc2}^2\ddot{\theta}_{c2} - \sum_{j=1}^4 (F_{s2p2j}R_{bs2} + F_{r2p2j}R_{br2}) \\ + k_{c2r1}(\theta_{c2} - \theta_{r1}) + c_{c2r1}(\dot{\theta}_{c2} - \dot{\theta}_{r1}) = -T_{out} \\ -J_{p2j}\ddot{\theta}_{c2} + J_{p2j}\ddot{\theta}_{p2j} - (F_{s2p2j} - F_{r2p2j})R_{p2j} = 0 \end{array} \right.$$

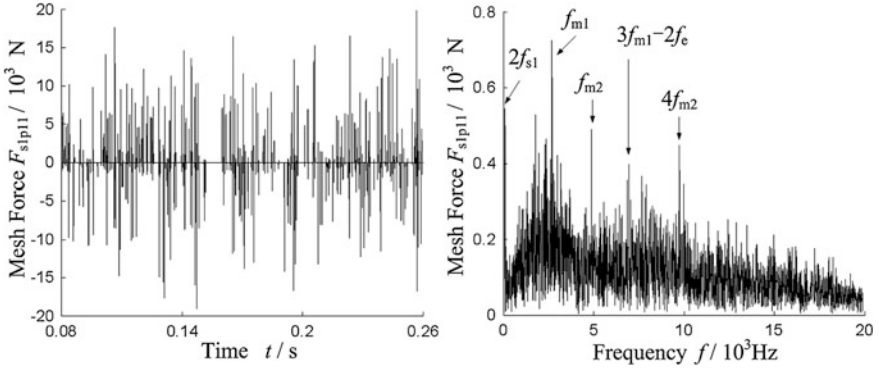


Fig. 3 Time domain and frequency domain analysis of mesh force F_{s1p11}

3 Results and Discussion

3.1 Analysis of Dynamic Force in Light-Load High-Speed Condition

The light-load high-speed condition is that the average of engine torque T_0 was 1,000 Nm, input speed of 1st sun gear n_{s1} is 6,000 r/min. The analysis of mesh force F_{s1p11} was shown in Fig. 3. Because the 1st stage planetary was under idle condition, mesh force F_{s1p11} was zero in static theory. In fact, F_{s1p11} was on double-sides impact state, because of the fluctuant speed, the mass moment of inertia of idle parts, fluctuant engine torque and backlashes. The maximum and minimum of F_{s1p11} was 19465 and -18750 N respectively, F_{s1p11} was zero at most of time. In frequency domain, frequency band was continuous. The main frequency included double rotational frequency of 1st sun $2f_{s1}$, meshing frequency of 1st stage planetary gear f_{m1} and its 4 times harmonic, and modulation sidebands of $2f_c$ and $3f_{m1}$.

The analysis of mesh force F_{s2p21} was shown in Fig. 4. The 2nd stage planetary was under load, mesh force F_{s2p21} was 3472 N in static theory. But F_{s1p11} was on double-sides impact state, because of time-varying mesh stiffness, backlashes and engine fluctuant torque. The maximum and minimum of F_{s1p11} was 31550 and -2665 N respectively, and it was larger than zero at most of time. The dynamic load coefficient was 9.09, and the load sharing coefficient was 1.18. In frequency domain, frequency spectrum was complicated. The main frequency included double rotational frequency of 2nd carrier $2f_{c2}$, rotational frequency of 2nd planet f_{p21} , double rotational frequency of fluctuant engine torque $2f_c$, meshing frequency of 2nd stage planetary gear f_{m2} and its higher harmonics ($2f_{m2}$, $3f_{m2}$, $4f_{m2}$ and so on). Besides that, the modulation sidebands of $2f_{c2}$ and $2f_c$, $1f_{m2}$, $2f_{m2}$, $4f_{m2}$ appeared that were caused by manufacturing error of carrier. The modulation sidebands of $2f_c$ and $2f_{m2}$, $4f_{m2}$ appeared that were caused by fluctuant engine torque.

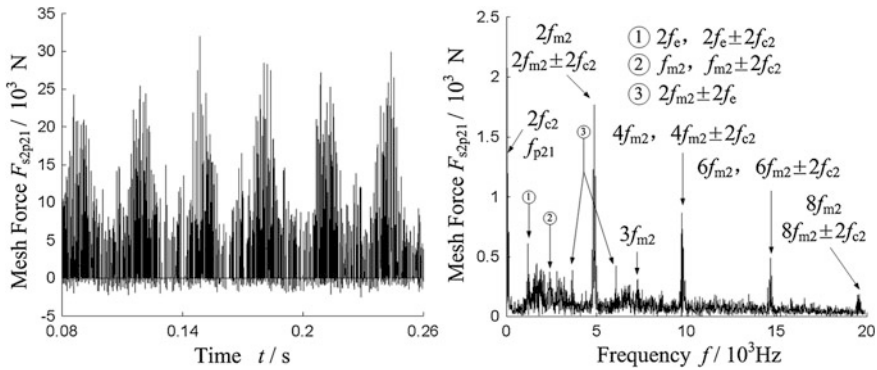


Fig. 4 Time domain and frequency domain analysis of mesh force F_{s2p21}

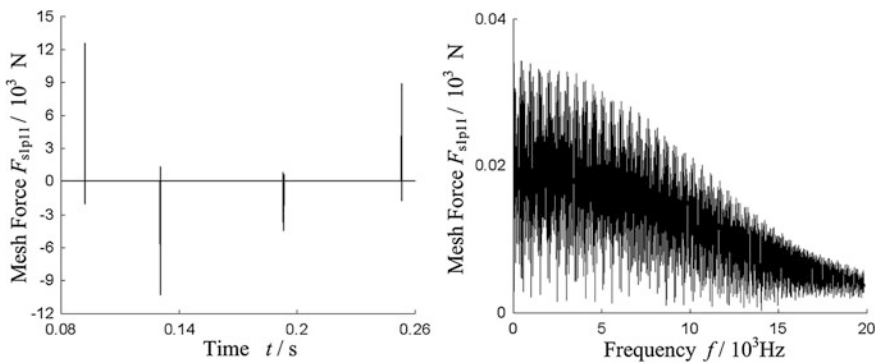


Fig. 5 Time domain and frequency domain analysis of mesh force F_{s1p11}

3.2 Analysis of Dynamic Force in Heavy-Load Low-Speed Condition

The heavy-load low-speed condition is that the average of engine torque T_0 was 4,000 Nm, input speed of 1st sun gear n_{s1} is 2,000 r/min. The analysis of mesh force F_{s1p11} was shown in Fig. 5. The mesh force F_{s1p11} was also on double-sides impact state, the maximum and minimum of F_{s1p11} was 13232 and -10437 N respectively. It was zero at most of time. Its frequency spectrum was different from the case that was under light-load high-speed condition. In frequency domain, frequency band was continuous, but its amplitude at every frequency was very small.

The analysis of mesh force F_{s2p21} was shown in Fig. 6. The mesh force F_{s2p21} was on non-impact state at most of time, and was on double-sides impact state at little of time. The mesh force F_{s2p21} was 13889 N in static theory. The maximum and minimum of F_{s2p21} was 56016 and -3221 N respectively. The dynamic load

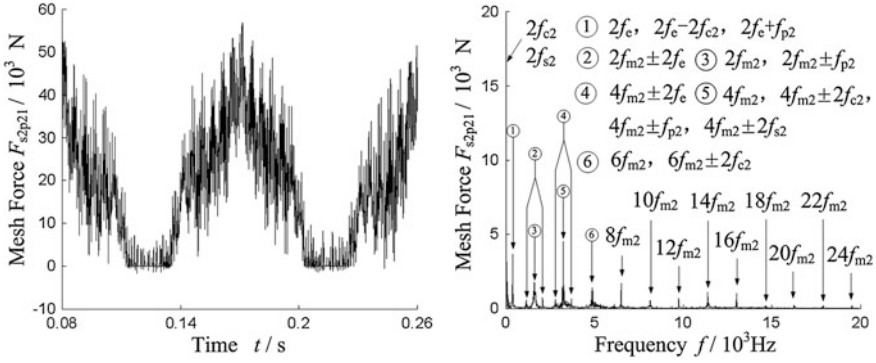


Fig. 6 Time domain and frequency domain analysis of mesh force F_{s2p21}

coefficient was 4.03, and the load sharing coefficient was 1.09. In frequency domain, double rotational frequency of 2nd sun $2f_{s2}$ appeared. The number of higher even harmonics meshing frequency of 2nd stage planetary gear ($2f_{m2}$, $4f_{m2}$, $6f_{m2}$ and so on) was more than the case that was under light-load high-speed condition.

3.3 Contact State and Amplitude of Mesh Force in Different Backlash

In order to describe the change of different states of nonlinear mesh force in planetary gears under the effect of different backlashes and engine excitation, three kinds of percentage of mesh state were defined. η_d is the ratio of contact number in driving gear interface to total number, η_b is the ratio of cut-off contact number to total number, η_u is the ratio of contact number in non-driving gear interface to total number, they are given as

$$\eta_d = \frac{N_d}{N_d + N_b + N_u} \quad \eta_b = \frac{N_b}{N_d + N_b + N_u} \quad \eta_u = \frac{N_u}{N_d + N_b + N_u}$$

where, N_d is the number of mesh that is larger than zero, N_b is the number of mesh that is equal to zero, N_u is the number of mesh that is less than zero.

Contact state percentage of sun-planet mesh force F_{s1p11} and F_{s2p21} were shown in Table 2, the subscript 1, 2 is used for denoting the number of stage. For idle stage planetary gear, its mesh force was zero at most of time. The percentage of this state η_b was increased along with the backlash became larger, regardless of input torque. For loaded stage planetary gear, when system was under light-load high-speed condition, η_d was little smaller than η_b . When system was under heavy-load low-speed condition, η_d greatly increased. At the same time, η_b was a sharp decline, and η_d was larger than η_b . With the backlash became larger, η_b was increased.

Table 2 Contact state percentage of sun-planet mesh force in planetary gears

<i>b</i>	$T_0 = 1,000 \text{ Nm}, n_{s1} = 6,000 \text{ r/min}$						$T_0 = 4,000 \text{ Nm}, n_{s1} = 2,000 \text{ r/min}$					
	η_{d1}	η_{b1}	η_{u1}	η_{d2}	η_{b2}	η_{u2}	η_{d1}	η_{b1}	η_{u1}	η_{d2}	η_{b2}	η_{u2}
0.1	6.87	87.70	5.43	47.67	51.26	1.07	0.09	99.77	0.14	85.81	13.85	0.34
0.2	7.65	88.41	3.94	47.48	51.57	0.94	0.06	99.85	0.09	85.74	14.03	0.23
0.4	8.13	89.15	2.72	46.39	52.60	0.19	0.01	99.97	0.02	85.59	14.24	0.17

Table 3 Amplitude of sun-planet mesh force in planetary gears

<i>b</i>	$T_0 = 1,000 \text{ Nm}, n_{s1} = 6,000 \text{ r/min}$				$T_0 = 4,000 \text{ Nm}, n_{s1} = 2,000 \text{ r/min}$			
	\bar{F}_{s1p11}		F_{s2p21}		\bar{F}_{s1p11}		F_{s2p21}	
0.1	22940	-21829	29465	-2349	14164	-12611	55713	-3151
0.2	19465	-18750	31550	-2665	13232	-10437	56016	-3221
0.4	9054	-11351	34576	-3362	9606	-8764	57111	-3368

Amplitude of sun-planet mesh force F_{s1p11} and F_{s2p21} were shown in Table 3. While backlash increasing, the amplitude of F_{s1p11} fell. On the contrary, the amplitude of F_{s2p21} rose. The amplitude of F_{s1p11} was more impressionable than F_{s2p21} by the change of backlash. The mesh force of idle planetary gear exists and cannot be ignored, despite its probability of appearance is vary small and load intensity of gear is not primary problem at that time.

4 Conclusions

A torsional nonlinear dynamic model of a multi-stage planetary gear train that contained the loaded planetary and idle planetary at same time was developed in this study for evaluation of the planetary gears of automatic transmissions in early states of design for their dynamic analysis. The model contains many non-linear factors, for example, backlash, time-varying mesh stiffness and its mesh phase angle. For describing the mesh force accurately, manufacturing errors, assembling errors and tooth errors are considered. The time-varying angle of planet position and the torsional stiffness of connecting shaft between different stages are main primary difference from single-stage planetary gears.

The change of engine torque plays an important effect for contact state and frequency of meshing force. When the system is on the light-load high-speed condition, the frequency of engine fluctuant torque and meshing frequency of different stage of planetary gears modulated respectively. When the system is on the heavy-load low-speed condition, the frequency of engine fluctuant torque and meshing frequency of loaded planetary gears only modulated.

The dynamic characteristics of idle planetary gears are affected by loaded planetary gears. The meshing frequency of loaded planetary gears appears in the frequency band of mesh force of idle planetary gear. The amplitude of mesh force

of idle planetary gear is large and it cannot be ignored. While backlash increasing, the amplitude of mesh force in idle planetary gear falls. On the contrary, the amplitude of mesh force in loaded planetary gear rises, the former more impressionable than the latter by the change of backlash.

Acknowledgements This work was partially supported by Natural Nature Science Foundation of China (50905018,51075033). The authors would like to express gratitude to its financial support.

References

1. Kahraman A (1994) Planetary gear train dynamics. *J Mech Des* 116:713–720
2. Kahraman A (2001) Free torsional vibration characteristics of compound planetary gear sets. *Mech Mach Theory* 36(6):953–971
3. Ambarisha VK, Parker RG (2007) Nonlinear dynamics of planetary gears using analytical and finite element models. *J Sound Vib* 302(3):577–595
4. Abousleiman V, Velex P (2006) A hybrid 3D finite element/lumped parameter model for quasi-static and dynamic analyses of planetary/epicyclic gear sets. *Mech Mach Theory* 41(6):725–748
5. Kahraman A (2004) A kinematics and power flow analysis methodology for automatic transmission planetary gear trains. *J Mech Des* 126(6):1071–1081
6. Inalpolat M, Kahraman A (2009) A theoretical and experimental investigation of modulation sidebands of planetary gear sets. *J Vibr Vibr* 323:677–699
7. Inalpolat M, Kahraman A (2010) A dynamic model to predict modulation sidebands of a planetary gear set having manufacturing errors. *J Vibr Vibr* 329:371–393
8. Kiracofe DR, Parker RG (2007) Structured vibration modes of general compound planetary gear systems. *J Vib Acoust* 129:1–16
9. Alshyyab A, Kahraman A (2007) A non-linear dynamic model for planetary gear sets. *J Multi-Body Dyn* 221(4):567–576
10. Bahk CJ, Parker RG (2011) Analytical solution for the nonlinear dynamics of planetary gears. *J Comput Nonlinear Dyn* 6:1–15
11. Park RG, Lin J (2004) Mesh phasing relationships in planetary and epicyclic gear. *J Mech Des* 126:365–370

Dynamic Optimization of Vehicle Planetary Transmission Based on GA and FEA

Changle Xiang, Cheng Wang, Hui Liu and Zhongchang Cai

Abstract Based on the nonlinear model of vehicle planetary transmission, the dynamic optimization model is established. This work use a combined objective function, internal and external load sharing coefficients and peak-to-peak mesh forces of second stage planetary are taken as objectives. The structure parameters of transmission shafts are considered as design variables. Finite Element Analysis (FEA) is carried out to obtain the bending and torsional stiffness, and the maximal Von-Mises stress constraint. Innovatively, we propose and introduce the nonlinear characteristic constraint aim at increasing the reliability of optimization. The Isight-Matlab-Ansys co-simulation method is applied to build the optimization platform. Finally, the optimization moel of vehicle planetary transmission is solved by Genetic Algorithm (GA).

Keywords Dynamic optimization · Nonlinear · Planetary transmission · Genetic algorithm · Chaos

F2012-J02-007

C. Xiang · C. Wang (✉) · H. Liu · Z. Cai
School of Mechanical Engineering, Beijing Institute of Technology, Beijing, China
e-mail: zhiaichengzi@yahoo.com.cn

C. Xiang · C. Wang · H. Liu · Z. Cai
Science and Technology on Vehicle Transmission Laboratory,
Beijing Institute of Technology, Beijing, China

1 Introduction

With the rapid development of high-speed and heavy-load vehicle transmission, the traditional static design method could not meet the design requirements of transmission, therefore, dynamic optimal design methodology is more and more prevalence.

1986, Houser [1] stated that the next step for the optimization design of gear should introduce the dynamic characteristics. In 1988, Japanese scholar Umezawa [2] provided a curve of helical gear vibration characteristics in order to design low vibration and low noise gears. In 1992, Cai [3] analyzed the static optimization of nonlinear dynamic model. The same year, Wang [4] took the dynamic performance of gear pair as objective, after optimization the dynamic load and the vibration was much smaller than the initial design in a wide range of speeds. Fonseca [5] used genetic algorithms to optimize the static transmission error, which is one of the earliest literatures that introduced genetic algorithm into the gear optimization. LUO [6] used the method of gray relation to change multi-objective optimization to a single objective optimization. Li [7] considered the bearing capacity, volume and stability of operation as objectives, then optimized the gear transmission with self adaptive genetic algorithm. Padmanabhan [8] considered the power, efficiency, volume, center distance as objectives, and then he used genetic algorithms to optimize the gear pair. Finally, the finite element analysis (FEA) was used to carry on further study of tooth bending stress. Recently, Faggioni [9] presented a global optimization method focused on gear vibration reduction by means of profile modifications. The optimization method considered different regimes and torque levels. He also pointed out that the static optimal design of the gear transmission system probability made the dynamic performance of gear transmission even worse. But the nonlinear dynamic characteristic and the bending-torsional coupled stress of shaft was not considered in previous studies.

This paper proposed a nonlinear model of vehicle planetary transmission. Based on the dynamic performance of transmission, the dynamic optimization model was built. This paper introduced the nonlinear characteristic constraint and the bending-torsional coupled Von-mises stress as constraint, innovatively. Then, the co-simulation method is used to build optimization platform. Finally, the dynamic optimization model is solved by genetic algorithm.

2 Nonlinear Model of Vehicle Planetary Transmission

Physical model of vehicle planetary transmission (Fig. 1).

There are two forward gears and one reverse gear in this vehicle transmission. The two forward gears correspond to the first and third clutch engagement, while the reverse gear corresponding to the second clutch engagement. In this paper,

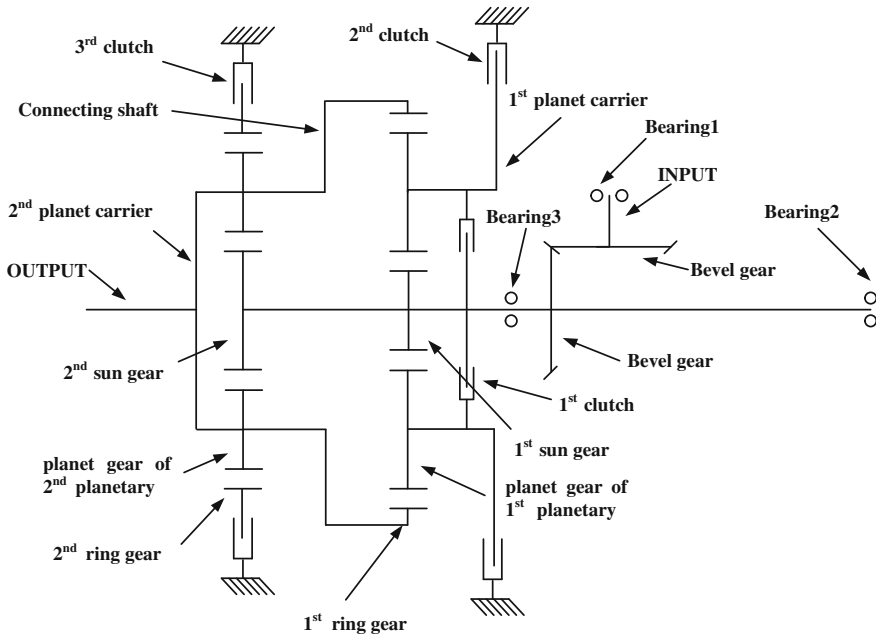


Fig. 1 Physical model of vehicle transmission

we only consider the dynamic performance of first gear. As the engagement of the third clutch, the second planetary is under load while the other with no-load.

Nonlinear dynamic behavior of planetary transmission takes the backlash, time-varying mesh stiffness, installation error and tooth error into consideration [10–12]. The time-varying mesh stiffness is periodic and is expanded in Fourier series form with the gear meshing frequency ω , in order to assure the accuracy, $M = 9$ (Eq. (1)).

$$k(t) = k(t + 2\pi/\omega) = k_0 + \sum_{r=1}^M k_r \cos(r\omega t + \phi_r) \tag{1}$$

Equations (2)–(5) are the nonlinear equations of planetary, where, $i = 1, 2$, $N = 4$, $j = 1, 2, 3, 4$. In the equations, J are moment of inertias, R are pitch diameters, e_M are eccentric distances, ω are rotational speeds, m are masses, x and y are bending displacements, θ are torsional displacements, γ and ψ are initial phase angles. α is pressure angle. The index s, r, c represent the sun, ring, carrier, planet. The index i and j represent the stage of planetary, the number of planet gear. The index x, y represent the direction of bending displacement.

The equations of motion for the sun gears are

$$\begin{aligned}
m_{si}\ddot{x}_{si} - m_{si}e_{Msi}\omega_{si}^2 \cos(\omega_{si}t + \gamma_{si}) + \sum_{j=1}^N \sin(\psi_{pij} + \alpha) F_{sipij} + F_{xsi}^c + F_{xsi}^k &= 0 \\
m_{si}\ddot{y}_{si} - m_{si}e_{Msi}\omega_{si}^2 \sin(\omega_{si}t + \gamma_{si}) - \sum_{j=1}^N \cos(\psi_{pij} + \alpha) F_{sipij} + F_{ysi}^c + F_{ysi}^k &= 0 \\
J_{si}\ddot{\theta}_{si} + \sum_{j=1}^N R_{si}F_{sipij} + T_{si}^c + T_{si}^k &= 0
\end{aligned} \tag{2}$$

where, F^c and F^k are damping force and bending forces of sun gear, T^c and T^k are relative torques and damping forces between nearby lumped masses. F_{sipij} is external mesh forces, F_{ripij} is internal mesh forces.

The equations of motion for the carrier are

$$\begin{aligned}
m_{ci}\ddot{x}_{ci} - m_{ci}e_{Mci}\omega_{ci}^2 \cos(\omega_{ci}t + \gamma_{ci}) - \sum_{j=1}^4 \sin(\psi_{pij} + \alpha) F_{xpij} + \sum_{j=1}^4 \sin(\psi_{pij} - \alpha) F_{ypij} \\
+ F_{xci} + F_{xcir1} &= 0 \\
m_{ci}\ddot{y}_{ci} - m_{ci}e_{Mci}\omega_{ci}^2 \sin(\omega_{ci}t + \gamma_{ci}) + \sum_{j=1}^N \cos(\psi_{pij} + \alpha) F_{xpij} - \sum_{j=1}^N \cos(\psi_{pij} - \alpha) F_{ypij} \\
+ F_{yci} + F_{yc2r1} &= 0 \\
J_{ci}\ddot{\theta}_{ci} - R_{ci} \sum_{j=1}^N F_{ypij} + T_{c2rj} + T_o &= 0
\end{aligned} \tag{3}$$

where, F_{xcirj} , F_{ycirj} and T_{cirj} are interaction forces of 2nd carrier and 1st ring. F_{xci} and F_{yci} are bearing forces, T_o is block torque. F_{xpij} and F_{ypij} are bearing forces of planet.

The equations of motion for the ring gears are

$$\begin{aligned}
m_{ri}\ddot{x}_{ri} - m_{ri}e_{Mri}\omega_{ri}^2 \cos(\omega_{ri}t + \gamma_{ri}) - \sum_{j=1}^N \sin(\psi_{pij} - \alpha) F_{ripij} + F_{xri} &= 0 \\
m_{ri}\ddot{y}_{ri} - m_{ri}e_{Mri}\omega_{ri}^2 \sin(\omega_{ri}t + \gamma_{ri}) + \sum_{j=1}^N \cos(\psi_{pij} - \alpha) F_{ripij} + F_{yri} &= 0 \\
J_{ri}\ddot{\theta}_{ri} - R_{ri} \sum_{j=1}^N F_{ripij} + T_b &= 0
\end{aligned} \tag{4}$$

where, F_{xri} and F_{yri} are bearing forces of x, y direction, T_b is brake torque.

The equations of motion for the planet gear j are

$$\begin{aligned}
& m_{p_{ij}}\ddot{x}_{ci} \cos \psi_{p_{ij}} + m_{p_{ij}}\ddot{y}_{ci} \sin \psi_{p_{ij}} + m_{p_{ij}}\dot{x}_{p_{ij}} + m_{p_{ij}}(-2\omega_{ci}\dot{y}_{p_{ij}} - \omega_{ci}^2 x_{p_{ij}}) \\
& - m_{p_{ij}}e_{M_{p_{ij}}}\omega_{p_{ij}}^2 \cos(\psi_{p_{ij}} - \omega_{p_{ij}}t - \gamma_{p_{ij}}) - \sin \alpha F_{s_{ip_{ij}}} - \sin \alpha F_{r_{ip_{ij}}} + F_{x_{p_{ij}}} = 0 \\
& - m_{p_{ij}}\ddot{x}_{ci} \sin \psi_{p_{ij}} + m_{p_{ij}}\ddot{y}_{ci} \cos \psi_{p_{ij}} + m_{p_{ij}}\dot{y}_{p_{ij}} + m_{p_{ij}}(2\omega_{ci}\dot{x}_{p_{ij}} - \omega_{ci}^2 y_{p_{ij}}) \\
& + m_{p_{ij}}e_{M_{p_{ij}}}\omega_{p_{ij}}^2 \sin(\psi_{p_{ij}} - \omega_{p_{ij}}t - \gamma_{p_{ij}}) + \cos \alpha F_{s_{ip_{ij}}} - \cos \alpha F_{r_{ip_{ij}}} + F_{y_{p_{ij}}} = 0 \\
& - J_{p_{ij}}\ddot{\theta}_{ci} + (J_{p_{ij}} + e_{M_{p_{ij}}}^2 m_{p_{ij}})\ddot{\theta}_{p_{ij}} - R_{p_{ij}}F_{s_{ip_{ij}}} + R_{p_{ij}}F_{r_{ip_{ij}}} = 0
\end{aligned} \tag{5}$$

For these planet gears, the inertia forces are much more complicated than the other parts due to the planet gears are attached to the carrier. The equations of other lumped mass model are not present here.

3 Optimization Model

This section describes about the objective functions, design variables and constraints of dynamic optimization model.

3.1 Objective Functions

The effect of dynamic performance caused by first stage planetary not play a crucial role for the second gear, so we take the internal and external load sharing coefficients and the peak-to-peak meshing forces of second stage planetary as objectives. The objectives are as follows.

$$\begin{aligned}
f_1 &= \frac{\max((F_{r_{2p21}}^m), (F_{r_{2p22}}^m), (F_{r_{2p23}}^m), (F_{r_{2p24}}^m))}{(\sum_{j=1}^4 (F_{r_{2p2j}}^m))/4} \\
f_2 &= \frac{\max((F_{s_{2p21}}^m), (F_{s_{2p22}}^m), (F_{s_{2p23}}^m), (F_{s_{2p24}}^m))}{(\sum_{j=1}^4 (F_{s_{2p2j}}^m))/4}
\end{aligned}$$

where, $F_{r_{2p2j}}^m$ are the mean internal mesh forces of second stage planetary, respectively. $F_{s_{2p2j}}^m$ are the mean external mesh forces of second stage planetary, respectively.

$$f_{j+2} = F_{r_{2p2j}}^{p-p}, f_{j+6} = F_{s_{2p2j}}^{p-p}$$

where, $j = 1, 2, 3, 4$, represent the external peak-to-peak mesh forces of second stage planetary.

$$\mathbf{f} = [f_1, f_2, f_3, f_4, f_5, f_6, f_7, f_8, f_9, f_{10}]^T$$

There are ten different objectives considered in this work. These objectives can be classified into two groups, f_1 and f_2 are load sharing coefficients, f_3 to f_{10} are peak-to-peak mesh forces. Since the parameters of each group are on different scales, these factors are to be normalized to the same scale [13]. The normalized objective function is obtained as follows:

$$\text{COF} = \sum_{k=1}^{10} W_k * N(f_k) * N(f_k) = \frac{f_k}{S_k}$$

where, COF is combined objective function. $N(f_k)$ represent normalized objective. W_k represent weight factor, all equal to 0.1. S_k represent normalization factor, for load sharing coefficient $S_k = 1$, for peak-to-peak mesh forces $S_k = 10,000$.

3.2 Design Variables

According to the engineering design requirements, the inner diameters of shaft, the gear parameters and layout of planetary are determined. So there are nine parameters can be taken as design variables, the five outer diameters of shaft, R_i , $i = 1, 2, 3, 4, 5$, and the layout of bearing 1, 3 and bevel gear L_j , $j = 1, 2, 3$. The optimization model contains eight independent design variables.

$$\mathbf{X} = [x_1, x_2, x_3, x_4, x_5, x_6, x_7, x_8]^T = [R_1, R_2, R_3, R_4, R_5, L_1, L_2, L_3]^T.$$

3.3 Design Constraints

Basically, there are three types of constraints: the boundary constraints, the static performance constraints and the dynamic performance constraints. In order to increase the reliability of optimization result, the nonlinear characteristic constraint is proposed in this work.

3.3.1 Boundary Constraints

Boundary constraints, mainly refer to the lower bound (LB) and the upper bound (UB) of the design variables.

According to the actual parameters variation ranges, the boundary constraints are show in Table 1.

Table 1 Boundary constraints (unit mm)

	R ₁	R ₂	R ₃	R ₄	R ₅	L ₁	L ₂	L ₃
LB	22	22	22	17	17	100	44.5	148
Initial	27.5	31.5	31.5	22.6	22.6	211.5	44.5	148
UB	35	35	35	22.6	22.6	211.5	156	259.5

3.3.2 Static Constraints

The tooth breakage and surface failures are the most likely failures of transmission gears. To safeguard the tooth against the breakage and surface failure, the gear should have adequate bending strength and contact strength. The bending fatigue stresses and crushing fatigue stresses of external meshing are considered.

$$\sigma_F \leq [\sigma_F] \quad \sigma_H \leq [\sigma_H]$$

The bending stress (σ_F) and contact stress (σ_H) are adopted from [14]

$$\sigma_F = \frac{F_t}{b m_n} Y_{Fa} Y_{Sa} Y_\epsilon Y_\beta K_A K_v K_{F\beta} K_{F\alpha}$$

$$\sigma_H = Z_E Z_H Z_\beta Z_\alpha \sqrt{K_A K_v K_{H\beta} K_{H\alpha} F_t \frac{1}{d_1 b} \frac{u + 1}{u}}$$

where, F_t is transmitted tangential load at operating pitch diameter, b is contacting face width, d_1 is pinion pitch diameter, u is gear teeth/pinion teeth, m_n is normal module. The other parameters are mostly correction factors.

The allowable value of bending stress [σ_F] and contact stress [σ_H] are 525 and 1650 MPa, respectively.

3.3.3 Dynamic Constraints

Bearing is one of the most important parts in vehicle transmission. In order to avoid the fatigue failure of the bearing, the bearing forces should be lesser then the allowable value.

$$F_{iMax} \leq [F_i]$$

where, F_i is maximal bearing force, $[F_i]$ is allowable value of bearing. The allowable value of three bearings are 59500, 82500 and 58500 N, respectively.

For bending-torsional coupled transmission shaft, the maximum Von-Mises stress should be considered. FEA method is used to model the shaft at different parameters and calculate the dynamic Von-Mises stress at different time steps. Because of the difficulty to determine all the forces acting on the shaft, the displacements of every lumped mass on shaft are extracted as boundary conditions of FEA.

$$\sigma_{\text{Max}} \leq [\sigma]$$

where, σ_{max} is maximal dynamic stress, $[\sigma]$ is allowable value equal to 350 MPa.

3.3.4 Nonlinear Characteristic Constraint

The nonlinear dynamic model take time-varying mesh stiffness, backlash and tooth errors into consideration, so it's inevitable to appear chaotic motion for some design variables. In order to avoid chaotic motion, we introduce the nonlinear characteristic constraints. Lyapunov exponent provides one of the most useful test for the presence of chaos [15]. As long as the largest lyapunov exponent (LE_{max}) is greater than 0, the system appears chaotic motion. It is reasonable that the largest lyapunov exponent is taken as nonlinear characteristic constraint. Here, the method of computing the LE_{max} proposed by Benettin is used [16].

$$\text{LE}_{\text{Max}} \leq 0.$$

4 Results and Discussion

The nonlinear dynamic equations of vehicle transmission was solved using the fourth order Runge–Kutta method with input torque and speed of vehicle transmission are 2,000 Nm and 7,000 r/min, respectively. The time series data corresponding to the first 5,000 revolutions of the two gears were deliberately excluded from the dynamic analysis to ensure that the analyzed data related to steady-state conditions [17]. Isight-Matlab-Ansys co-simulation is used to build optimization platform. The optimization flow shows in Fig. 2.

Due to non-analytic of objective functions, the traditional gradient-based optimization method is no longer applicable. So we use modern optimization methods—Binary Coded based Genetic Algorithm (GA) with one-point crossover to optimize the system [18]. The values of Genetic Algorithm operators are shown in Table 2. There are 200 individuals participate in iteration. The Isight automatic determines the parameters of design variables. In order to reduced the mapping error of binary encoding and decoding, the size of gene is set as 20.

The optimal result occurs at step 140. The optimum values of objective function and design variables corresponding to the minimum COF value are shown in Tables 3 and 4. From Table 3, we can conclude that the optimal parameter of L2, L3, R1, R2, R5 are remain the same, while the L1, R3, R4 are reduced. Figure 3 shows the finite element model of shaft with initial parameters and optimal parameters.

From Fig. 4, we can obtain that all the objectives of optimal design are lesser then the initial design more or less exceptt the external peak-to-peak meshing

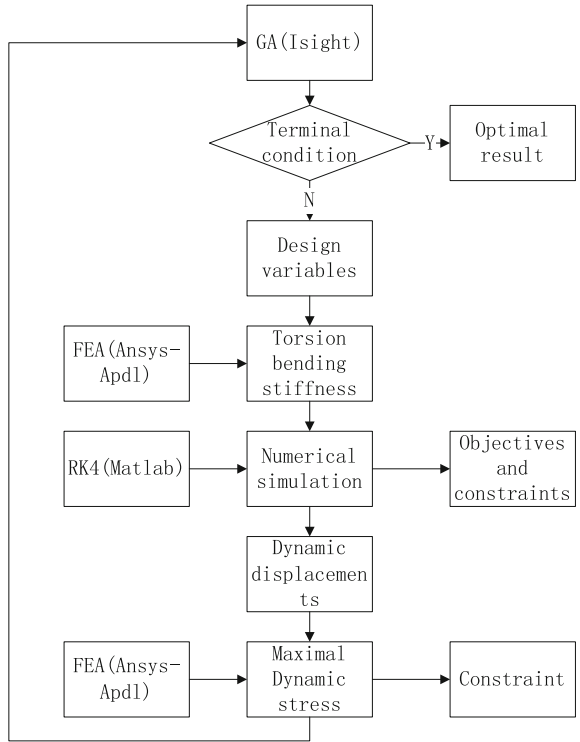


Fig. 2 Optimization flow of co-simulation method

Table 2 Values of genetic operators

Operators	Values
Gene size	20
Population size	10
Number of generations	20
Crossover rate	1.0
Mutation rate	0.01

Table 3 Parameters of initial and optimal design Unit(mm)

	Initial design	Optimal design
L ₁	211.5	210.74
L ₂	44.5	44.5
L ₃	148	148
R ₁	27.5	27.5
R ₂	31.5	31.5
R ₃	31.5	28.86
R ₄	22.6	22.51
R ₅	22.6	22.6

Table 4 Objectives of initial and optimal design

	Initial objectives	Optimal objectives	Reduce rates (%)
f_1	1.1398	1.1394	0.03
f_2	1.1399	1.1395	0.03
f_3	24424.695 N	25007.938 N	-2.3879
f_4	25544.321 N	24899.610 N	2.5239
f_5	25256.015 N	22579.027 N	10.5994
f_6	25841.594 N	25097.327 N	2.8801
f_7	23842.044 N	23319.950 N	2.1898
f_8	25034.291 N	24230.382 N	3.2112
f_9	22851.970 N	22145.995 N	3.0893
f_{10}	25850.720 N	24472.345 N	5.3321

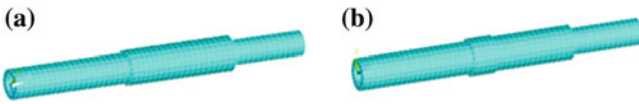


Fig. 3 Finite element model of transmission shaft, **a** Initial design. **b** Optimal design

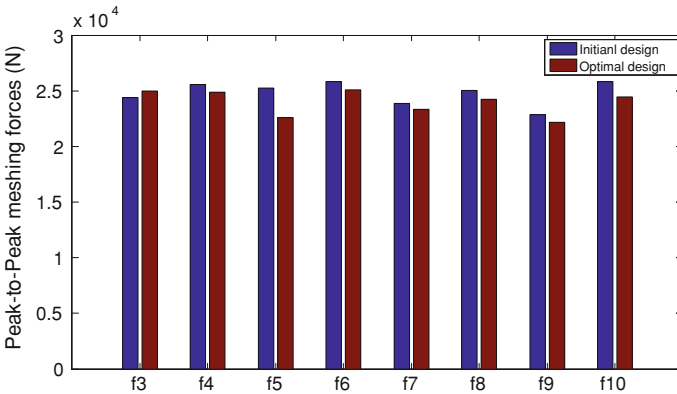


Fig. 4 Histogram of peak-to-peak mesh forces before and after optimization

forces f_3 , for the sake of naturally conflicting of multi-objective optimization problems (MOP). The reduction rates of peak-to-peak mesh forces shows in the fourth column of Table 4. It can be seen that the objective f_5 reduces about 10 %, while f_3 increases about 2 %. The two load sharing coefficients objectives are both less than the initial values about 0.0004, which means that the dynamic characteristic of sharing caused by dynamic load appears to be easing.

Figure 5 shows that as the iteration step goes the design parameters generate by GA seems more and more suitable to satisfy the Von-Mises stress constraint. Dynamic stress analysis was conducted for the transmission shaft before and after design through FEA. Through Fig. 6 we can reach that the Von-mises stress of shaft clearly reduced lower than 300 Mpa at some peaks after optimization. The

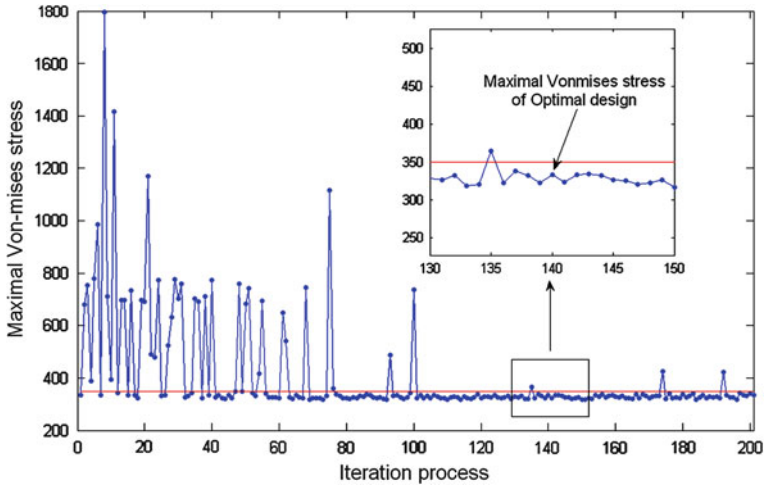


Fig. 5 Maxmal Von-mises stress of shaft

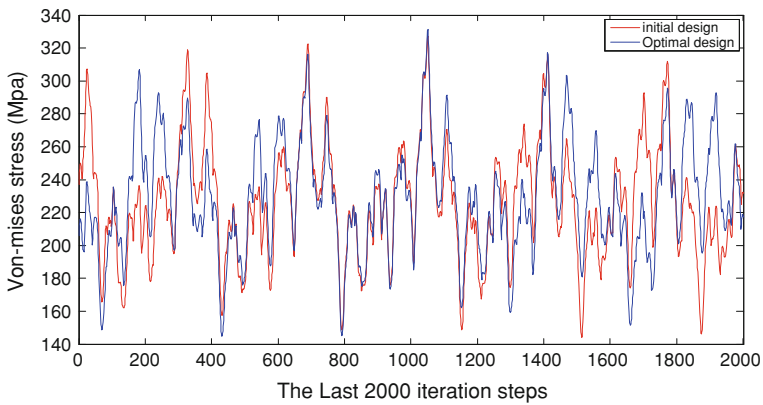


Fig. 6 Dynamic stress of initial and optimal design within the last 2,000 steps

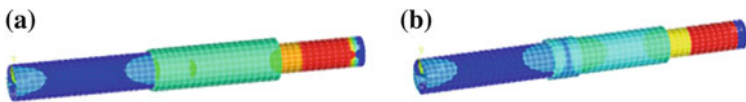


Fig. 7 Von-mises stress of shaft at last calculation step, a Initial design. b Optimal design

maximal Von-mises stress of shaft before and after optimizations are 335 and 333 MPa, which are both less than the allowable value 350 MPa. From Fig. 7, we can realize that the maximal Von-mises stress on the shaft appears between the two sun gears.

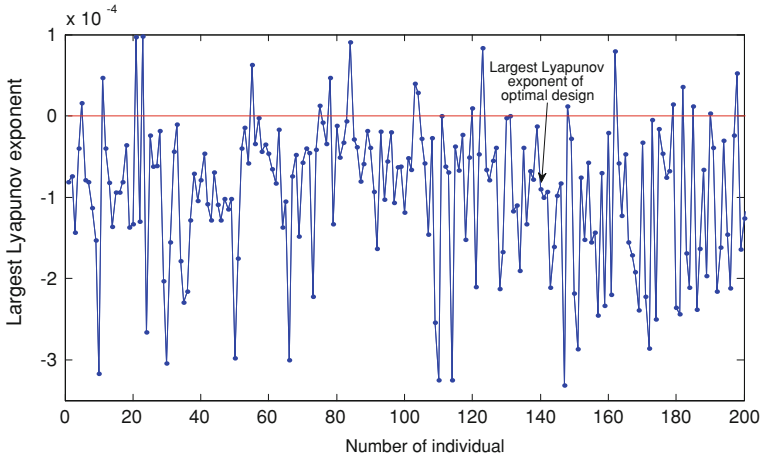


Fig. 8 Largest Lyapunov exponent during optimization

Figure 8 shows there are only 21 group of parameters lead to the chaotic motion of transmission, while the others including the optimal design appear non-chaotic motion. With the nonlinear characteristic constraint, the chaotic solutions have been effectively removed. The largest Lyapunov exponent of transmission under initial design and optimal design are $-8.1\text{E}-5$ and $-9.0\text{e}-5$ respectively, which means dynamic motion of initial and optimal design are both non-chaotic.

5 Conclusion

A dynamic optimization model, based on the nonlinear dynamic of vehicle planetary transmission, has been built in order to improve the dynamic performance. Parameters of shaft were considered as design variables. In order to improve the reliability of transmission shaft, the finite element method (FEA) is used calculated the maximal dynamic stress constraint. The bending and torsional displacements of lumped masses on shaft were extracted as boundary conditions of FEA. Innovatively, by introducing the nonlinear characteristic constraint, chaos solutions has been effectively removed.

Isight-Matlab-Ansys co-simulation method was used to build the optimization platform. Binary coding Genetic Algorithm was utilized in this work. The optimization model and method proposed in this work are both suitable for the other vehicle transmission.

After optimization, most of the objectives of optimal design were lesser then the initial design more or less. The largest Lyapunov exponent of optimal design transmission was less than zero, which means the dynamic performance of vehicle transmission can predict. The dynamic stress of shaft clearly reduced at some

peaks before and after optimization, but the maximal stress was not significantly reduces. Finally, the optimization results not only avoid the chaotic behaviour, but also improve the dynamic performance of vehicle transmission and extending the system life.

Acknowledgments This work was partially supported by Natural Science Foundation of China (50905018,51075033). The authors would like to express gratitude to its financial support.

References

1. Tavakoli MS, Houser DR (1986) Optimum profile modifications for the minimization of static transmission errors of spur gears. *J Mech Transmissions Autom Des* 108:86–95
2. Umezawa K (1988) Estimation of vibration of power transmission helical gears by means of performance diagrams on vibration. *JSME Int J* 31:598–605
3. Cai Y, Hayashi T (1992) The optimum modification of tooth profile for a pair of spur gears to make its rotational vibration equal to zero. *ASME proceedings of power transmission and gearing conference* (43–2):453–460
4. Wang T (1992) An optimal design for gears with dynamic performance as an objective function. *J Huazhou University* (20–5):13–18
5. Fonseca DJ (2005) A genetic algorithm approach to minimize transmission error of automotive spur gears sets. *Appl Artif Intell* 19–2:53–179
6. Luo Y, Liao D (2009) High dimensional multi-objective grey optimization of planetary gears type AA with hybrid discrete variables. *International conference on computational intelligence and natural computing*
7. Li R, Chang T, Wang J, Wei X (2008) Multi-objective optimization design of gear reducer based on adaptive genetic algorithm. *IEEE* 229–233
8. Padmanabhan S, Ganesan S, Chandrasekaran M (2010) Gear pair design optimization by genetic algorithm and FEA. *IEEE* 301–307
9. Faggioni M (2011) Dynamic optimization of spur gears. *Mech Mach Theo* 46:544–557
10. Guo Y, Parker RG (2010) Dynamic modeling and analysis of a spur planetary gear involving tooth wedging and bearing clearance nonlinearity. *Eur J Mech A/Solids* 29:1022e–1033
11. Kahraman A, Singh R (1991) Interactions between time-varying mesh stiffness and clearance non-linearities in a geared system. *J Sound Vib* 146:135–156
12. Kahraman A, Blankenship GW (1994) Planet mesh phasing in epicyclic gear sets. *International gearing conference Newcastle* 99–104
13. Saravanan R, Sachithanandam M (2001) Genetic algorithm for multivariable surface grinding process optimization using a multi-objective function model. *Int J Adv Manuf Technol* 17:330–338
14. Dudley DW (1983) *Handbook of practical gear design*, McGraw-Hill Book Co, New York
15. Wolf A, Swift JB, Swinney HL, Vastano JA (1985) Determining Lyapunov exponents from a time series. *Physica* 16D:285–331
16. Benettin G, Galgani L, Giorgilli A, Strelcyn J-M (1980) Lyapunov characteristic exponents for smooth dynamical systems and for Hamiltonian systems; a method for computing all of them. *Meccanica* 15:9
17. Cai-Wan Chang-Jian, Chang Shih-Ming (2011) Bifurcation and chaos analysis of spur gear pair with and without nonlinear suspension. *Nonlinear Anal: Real World App* 12:979–989
18. Deb K (2001) *Multi-objective optimization using evolutionary algorithms*. Wiley, Chichester

NVH Optimization of Vehicle Powertrain

Shouwei Lu, Huihua Feng, Zhengxing Zuo, Liyun Kang and Bo Yu

Abstract The noise and vibration performance of powertrain is main contributor for vehicle NVH (Noise, Vibration and Harshness) issue. To achieve better NVH performance, it is critical to conduct NVH optimization during the powertrain initial design stage. This paper presents an investigation of optimize vehicle powertrain NVH performance via modification of excitation–radiation system of powertrain. To minimize excitation force of the gearbox with special focus on gear pair dynamic characteristics via the gear profile modification, and to reduce transmission housing noise radiation via enhance its stiffness, are the main objective of optimization. The excitation forces are analyzed by Multi Body Dynamics (MBD) method, considering different excitation mechanisms of the powertrain. The vibro-acoustic behavior of powertrain is obtained by FEM/BEM coupled analysis. The acoustic transfer vector (ATV) calculation is used to predict the powertrain sound power level (SPL) and panel contributions. Based on the acquired NVH data of the powertrain, the optimization which couples the transmission gear profile modification for attenuating gear system excitation and the structure stiffness modification for reducing transmission housing noise radiation is proposed. Experiment validation is conducted in order to evaluate the modified results. The evaluation shows that the optimization can effectively reduce powertrain noise and vibration.

Keywords NVH · Powertrain · Transmission · Profile modification

F2012-J02-008

S. Lu (✉) · H. Feng · Z. Zuo
School of Mechanical Engineering, Beijing Institute of Technology, Beijing, China
e-mail: lswwt007@163.com

L. Kang · B. Yu
Chongqing Changan Automobile Co.Ltd, Chongqing, China

1 Introduction

The increasing safety, quality and comfort demands of customers have become important indicators for making market strategies of automotive manufacturers [1]. Excellent NVH performance of vehicles is essential for manufactures to gain the opportunities to win the competition and dominate the market in the global automotive industry. Particularly, the NVH performance of vehicle essentially depends on powertrain characteristics. Less noise and vibration, good sound quality powertrains, which can be applied to meet the customer demands, are needed in the vehicle design and development process.

In general, the powertrain noise and vibration optimization can be divided into three main solution process: reduce excitation, optimization of structural transfer behaviour and modified radiation surface [2, 3]. This paper presents a systematic analysis process to optimization powertrain NVH performance. Initially, the powertrain excitation forces are calculated through MBD method. The calculated excitation result is applied as input data for powertrain vibro-acoustic evaluation. The transmission gear profile modification for attenuating gear system excitation is performed. Transmission near-filed sound pressures distribution analysis is carried out to find out critical areas effecting the noise radiation. Based on the critical areas of weak stiffness identification, transmission housing stiffness is optimized by modify these critical areas. Finally the results of optimization have been verified with experimental result in this study.

2 Excitation Force Analysis of Powertrain

Since the key parts of the powertrain, transmission and engine, are different in excitation mechanism, it is absolutely essential for the selection of different analysis tools to achieve accurate calculation. The detailed investigations for excitation mechanisms of the powertrain by analysing the excitation forces are conducted, depending on different analysis process. For powertrain dynamic characteristic evaluation, four main excitation forces are required as input data:

- boost pressure
- engine main bearing reacting force
- piston slap force
- transmission bearing reacting forces.

2.1 Engine Excitation Force

There are two main noise sources of ICE (internal combustion engine): combustion noise and mechanical noise. Combustion noise is induced by the firing pulses

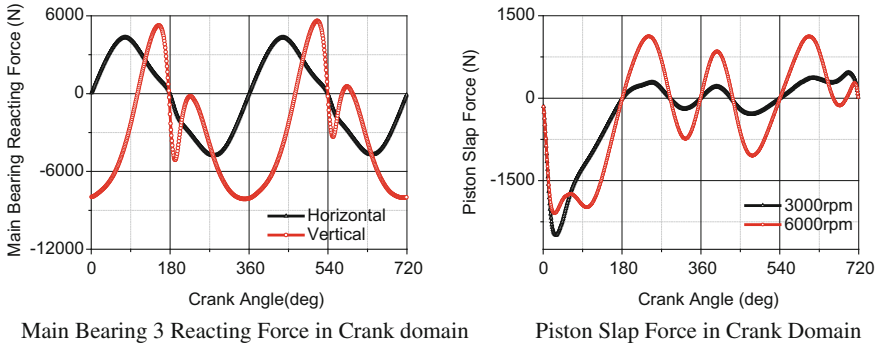


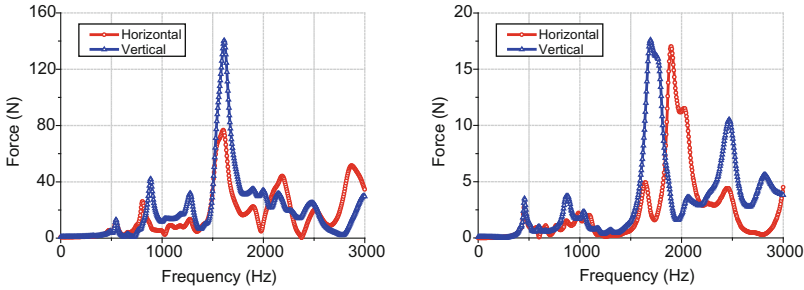
Fig. 1 Engine excitation force

due to the explosions of the fuel in the combustion chambers. The mechanical noise is induced by the various inertia forces and torque oscillations caused by the rotating and reciprocating parts. The major sources of engine mechanical noise are the main bearing reacting force, the piston slap force, timing gear rattle, fuel injection system, valve system and accessories operation. The main contributors among these sources are the piston slap force and the main bearing reacting force. The high excitation load caused by main bearing reacting force resulting from combustion gas pressure and inertia forces of reciprocating masses are transferred via the crank mechanism. The piston slap force is caused by the lateral motion of pistons across the cylinder clearances.

Figure 1 shows the bearing reaction force at main bearing #3 of a 4-cylinder inline engine, which is plotted as a curve of engine speed versus crank angle. The bearing reaction force depends on combustion force at certain operating condition with the engine firing order. Figure shows the piston slap force at different engine speed. To evaluate the engine excitation forces with respect to the relevant powertrain NVH issue, the data is transferred into frequency domain using Fast Fourier Transformation (FFT).

2.2 Excitation Force of Transmission

The excitation force of transmission is generated by transmission error (TE), rotary fluctuations of the gear shaft, and friction induced bearing forces, transmitting via transmission bearings and then radiating from transmission housing by means of vibration and noise [4]. The loads acting on bearings are not only influenced by the gear shift position changing, but also by the engine rotating speed variability. The calculation of the bearing reacting force is a difficult process, since it is the interaction for gear meshing, lubrication, transmission error and several mechanical effects. The detailed parameters of gears are required to establish a sophisticated analysis model. The transmission gear system model which is used to



Input shaft right bearing reacting force (1st gear) Input shaft right bearing reacting force (2nd gear)

Fig. 2 Transmission excitation force

calculate the bearing reacting force is built by software ROMAX and the calculation results are shown in Fig. 2.

3 Forced Response Calculations

The main objective of this process is evaluation of powertrain structural transfer behaviour and surface velocities. The excitation forces are transmitted as structure-borne noise to the surfaces of the powertrain components where it is subsequently radiated as airborne noise [5]. In concept stage of powertrain development process, the forced response analysis provides basic dynamic characteristics of the powertrain to support designer making NVH optimized decisions. During the analysis process, a full powertrain model gradually develops as the design progresses. At the end of the process, the powertrain surface velocity is summarized over the frequency range 0–2,000 Hz associated with a specific load and engine speed. Using the principle of modal superposition, the response is calculated. The result is done in vector solution, which contains the response of a large set of outputs for different operating condition. Figure 3 shows the predicted vibration velocity distribution for powertrain.

4 Near-Filed Sound Pressure Distribution

In order to investigate the transmission housing panel acoustic characteristics at different operating condition, the near field sound pressure analysis is carried out, providing the structure stiffness information. Particularly for this powertrain, the differential cover has a significant large area, hence, is responsible for most of the noise. The near field point mesh is divided into four panels which are shown in Fig. 4.

Fig. 3 Predicted surface velocity distribution

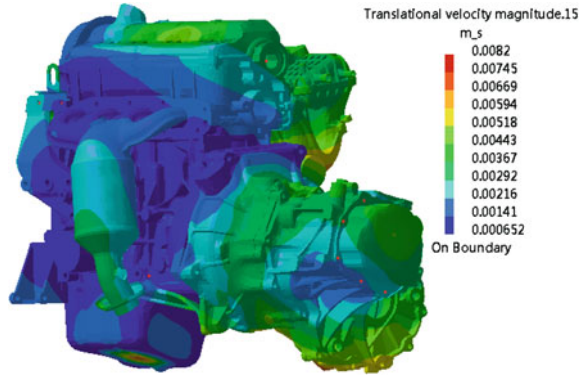
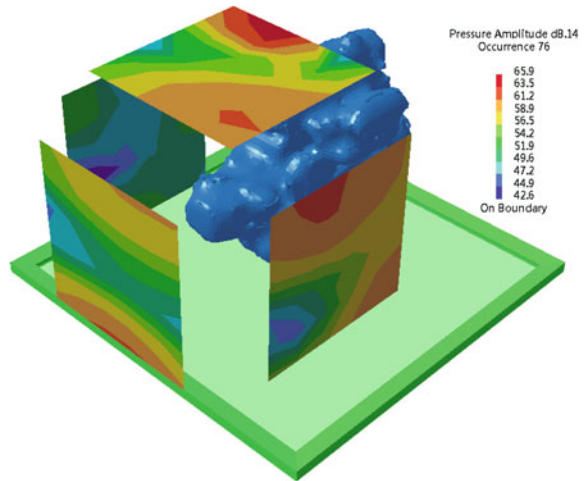


Fig. 4 Predicted sound pressure distribution



5 Transmission Housing Stifness Optimization

Based on the near field sound pressure distribution references, different modification strategies are carried out. In conventional optimizing process of the dynamic behaviour of structures, it is usually required to shift natural frequencies of system by making modifications to the mass, stiffness or damping characteristics of the structure. Rib stiffening is a frequently adopted method [6]. Therefore, in the transmission housing modification, reinforcement ribs are added on the transmission housing to enhance its stiffness. The layout of most effective position of stiffeners is designed by the previous analysis results of near field sound pressure distribution. Figure 5 shows the modified layout.

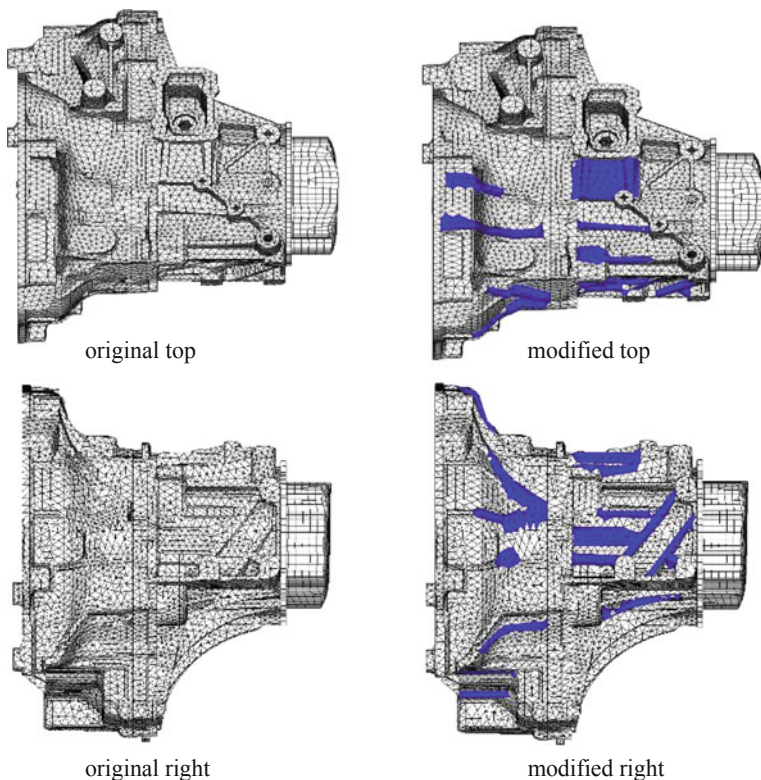


Fig. 5 Structure modified layout

6 Transmission Gear Profile Modification

Transmission gear systems have two types of noise sources: one known as the internal noise generating by gear mesh excitation, and the other known as the external noise generating by input torque fluctuation of engine. The most dominant noise source of gear system is from the gear mesh excitations of the gear teeth. More accurately, the gear mesh excitations are caused by transmission error fluctuation and fluctuation in the load transmitted by the gear mesh. Gear tooth profile modification is a widely used method to reduce dynamic excitation load for improving performance of transmission NVH performance. Different type of profile modifications has different effects on gear system performance [7]. The tooth profile modification technique, tooth crowning, was used to minimize bearing reacting force. The main aim of this methodology is to search for the optimum profiles of tooth crowning that eventually lead to optimum dynamic tooth load in the gear mesh. The 2nd gear pair modification is chosen for illustrating the gear profile modification process. The transmission error analysis of the 2nd gear

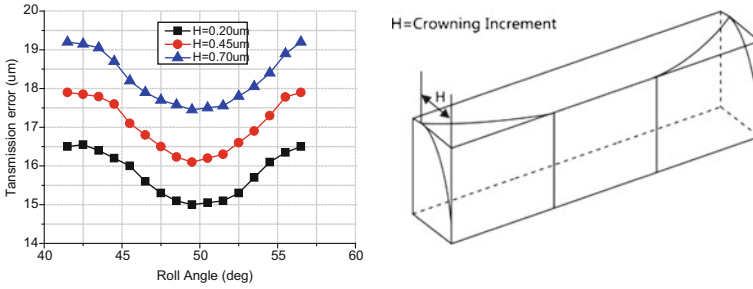


Fig. 6 The relationship between influence of tooth crowning increment and transmission error

was carried out first. The relationship between influence of tooth crowning increment and transmission error is given in Fig. 6.

The gear profile modifications that are often required to maintain a good contact for durability are not always conducive to low TE (good NVH performance) and some sort of balance must be considered. Thus, to achieve good NVH performance, the low TE was set as target of optimization of gear profile modification [8]. The changes of panel contribution and SPL comparison between original and modified are used to evaluating the validity of the transmission gear profile modification.

7 Experimental Validation

To evaluate the validity of the optimization performed in this study, an experimental validation is carried out. Figure 7 shows the test setup. The experiment is performed in semi-anechoic chamber under different torques and rotary speed. Three microphones are adapted to measure sound pressure of transmission. All of the microphones are perpendicular to longitudinal centerline of transmission, and the measurement distance is 1 m from the transmission housing to each of microphones respectively. The average sound pressure calculation is based on the equation given below:

$$\bar{L}_p = 10 \cdot \log \frac{1}{N} \cdot \sum_{i=1}^N 10^{0.1 \cdot L_{pi}} \tag{1}$$

Where \bar{L}_p is the A-weighting average sound pressure level of the measured points; L_{pi} is the A-weighting sound pressure level of i measured point; N is the total number of measured points.

Figure 8 show the experimental results under different running conditions. The results shows that the optimization, which couples the transmission gear profile modification and the transmission housing stiffness modification, can reduce the vibration and noise of transmission to achieving the improvement of NVH performance of the powertrain. However, comparison from the Fig. 8 shows that this

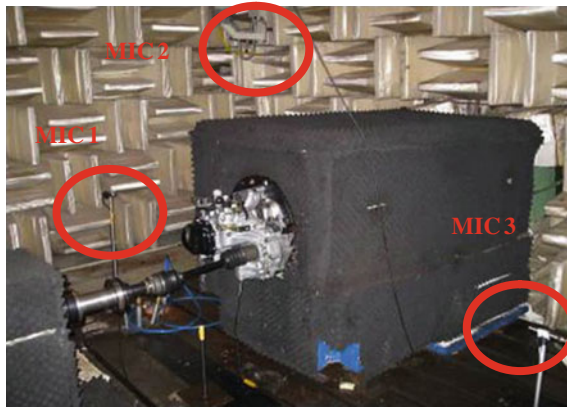


Fig. 7 Experiment setup

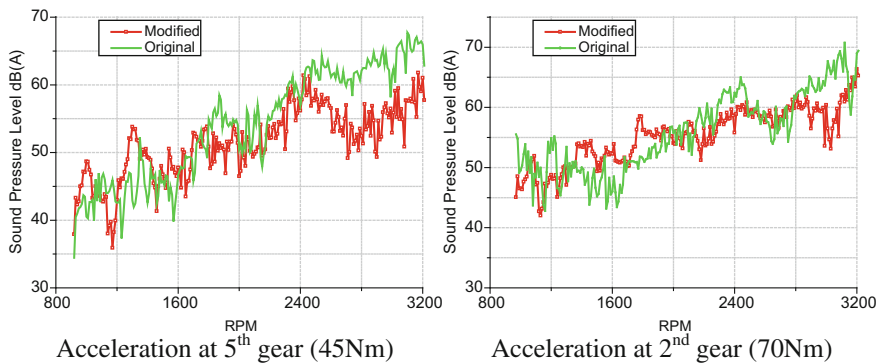


Fig. 8 Sound pressure level comparison between original and modified

hybrid approach is not validity enough during the rpm range (1400–1800 rpm). This is due to excitation force order coincide with the natural frequency of transmission housing, generating high level of vibration and noise. A precise investigation of dynamic behaviour for gear system is necessary in further research.

8 Conclusion

NVH optimization process of a powertrain is proposed. From the beginning of excitation analysis to the end of panel radiated noise contribution analysis, a detailed analysis process is present. Based on the difference of excitation mechanism, engine excitation analysis model and transmission gear system model, are

developed. The excitation models are the most critical models for whole research process. The calculated results of excitations show that all the excitations are related to the harmonic order which can easily draw from the excitation force results in frequency domain. Through extensive dynamic and acoustic analysis, it is found that not only the dynamic characteristic which is reflected by the powertrain surface vibration velocity, but also the acoustic characteristic which is reflected by the powertrain sound pressure are all involves with the excitation force. That means excitation force optimization can achieve dramatic noise and vibration reduction. Both the excitation force and radiated surface are modified, thus making the NVH improvement more achievable. For reasonable evaluation of validity of modification, validation experiment is conducted under various running condition in the semi-anechoic chamber. The average sound pressure level is calculated using measurement data by Eq. (1). Despite a little increase of sound pressure level during certain rpm range, the overall sound pressure level decreased dramatically. In this case, the NVH optimization of the powertrain, combining transmission gear profile modification and transmission housing modification, can significantly reduce powertrain noise and vibration to a sufficiently desired level. In further research work, investigations should focus on the transmission gear system dynamic behaviour.

References

1. Bousseau Y, Gagliardini L (2003) Powertrain acoustic characterization at high frequencies: acoustic source modeling based on sound intensity measurements. In: SAE paper 2003-01-1457
2. Jeong G, Jeong W, Young S, Wan S (2007) Optimization of crank angles to reduce excitation forces and moments in engines. *J Mech Sci Technol* 21(2):272–281
3. Charles LY, Karl DS (2003) Acoustic analysis of isolated engine valve covers. In: SAE paper 2003-01-1674
4. Dominic E, Andrew W (2005) Minimizing turbocharger whoosh noise for diesel powertrains. In: SAE paper 2005-01-2485
5. Feng H, Zuo Z, Liao R, Ma C (2004) Outer sound field simulation of a diesel engine based on coupled BEM/FEM method. *Trans Csice* 22(2):155–161
6. Platten M, Blockley C, James B, Prabahakaran S, Scott D (2009) Optimization of gear microgeometry for durability and NVH. *Sound vibr* 43(4):7–10
7. Hao Z, Jin Y, Yang C (2007) Study of engine noise based on independent component analysis. *J Zhejiang University Sci A* 8(5):772–777
8. Hwang JY, Kim DW, Jeong WJ, Shin DH, Kang KT (2009) Optimization of the high frequency noise for the passenger car diesel engine. In: SAE paper 2009-01-2082

Input Torque Shaping for Driveline NVH Improvement and Torque Profile Approximation Problem with Combustion Pressure

Kazuhide Togai and Michael Platten

Abstract The powertrain is the largest excitation source of automotive noise and vibration. Torque variations from the engine cause noise and vibration in two frequency regimes: Engine firing fluctuations at the engine rotation frequency and its harmonics and driver-demanded propulsion torque variations at lower frequencies. This paper examines the mechanisms of gear rattle noise caused by engine firing fluctuations and shock and jerk caused by propulsion torque variations. Gear rattle behaviour is simulated and various approaches for reducing gear rattle are investigated. It is found that isolation of engine firing fluctuations from the transmission is the most effective practical way to reduce rattle. Torque profile shaping by robust control is a method that can be used to reduce shock and jerk. A pre-compensator approach based on knowledge of the driveline resonant properties is proposed and the sensitivity of the controller to errors in the assumed resonant frequencies is investigated. It is shown that one of the constraints of this strategy is that the resolution of control system depends on the firing frequency.

Keywords Transmission • NVH • Gear rattle • Modelling • Active control

F2012-J02-009

K. Togai (✉)
Mitsubishi Motors Corporation, Minato, Japan
e-mail: kazuhide.togai@mitsubishi-motors.com

M. Platten
Romax Technology Ltd, Pune, UK

1 Introduction

A passenger car be thought of as flexible structure of masses and springs distributed over the vehicle to balance handling, fuel efficiency and comfort. Resonances in this structure can lead to noticeable vibration and audible noise. As part of this flexible system the transmission and driveline transfers the power from the engine to propel the vehicle. But the dynamic behaviour of the driveline can also generate or amplify unwanted noise and vibration.

There are some noise phenomena that are generated by the driveline itself such as unbalance excitation or gear whine. In others, the driveline is a passive system that is excited externally, often by forces from the engine. In the case of gear rattle and shock and jerk it is the interaction of the engine acting as a source and the driveline acting as a transfer path that cause the noise and vibration problems. Generally with noise problems it is more effective to reduce noise at source, but sometimes there are limits to what can be achieved and changes to the transfer path may also be required to achieve an economically satisfactory result. In this paper mathematical models are used to simulate both the excitation and transfer path. Results of these simulations for gear rattle and driveline shock response are used to investigate some proposed methods of reducing annoyance caused by these phenomena.

Gear rattle is common in manual transmissions and is caused by engine torque fluctuations associated with engine firing which lead to torsional vibrations inside the transmission. Idling gears can lose contact in these conditions and the resulting noise when they come back into contact causes an unpleasant rattling sound. Rattle occurs when the fluctuating dynamic torque at the gear mesh exceeds the static driving torque of the gear—this is the rattle. In this study, the gear meshing behaviour with backlash is investigated and the effects of the reduction in lubricant viscosity, backlash and engine firing torque fluctuations on gear mesh impact force are calculated.

Driveline vibrations can be excited by sudden changes in supplied torque caused by changes in acceleration demanded by the driver such as sudden acceleration for overtaking or tip-in/tip-out. The driveline torsional vibrations that are generated by this process can cause noticeable longitudinal vibrations (“shunt” or “shuffle”) of the chassis and sometimes also noise (e.g., “clunk”).

One way to mitigate this problem is by input torque shaping where a control system adjusts the throttle input supplied by the driver to change the combustion of the engine. When combined with knowledge of the resonant behaviour of the driveline, this can reduce the longitudinal vehicle vibrations. There is a fundamental upper limit to the frequencies that can be suppressed in this way due to the fact that engine torque can only be controlled during firing. This means that the method is less effective as engine rpm decreases. Simulations are used to illustrate this method.

2 The Engine as a Vibration Source

An ideal transmission and driveline transfers power efficiently from the engine to a vehicle. Along with the power needed for propulsion there is also a dynamic aspect to the transferred power which can lead to noise and vibration (Fig. 1). Sometimes this dynamic behaviour is caused by self-excitation within the driveline (unbalance and gear whine are examples of this). However, there is class of vibration problems where the source of the vibration is the engine and driveline plays an important role in the amplification and transfer path for this engine excitation.

This engine excitation is in the form for torque fluctuations and occurs in two frequency regimes: Driver torque demand and combustion pulses.

2.1 Driver Torque Demand

This is the changing mean engine output torque as demanded by the driver to achieve the necessary speed changes required to control the vehicle. When these changes occur fast enough, (e.g., sudden acceleration, sudden change from driving to coasting—tip-in/tip-out, clutch re-engagement after shifting) then they can excite the resonant behaviour of the vehicle and driveline system. These torque variations are non-periodic.

2.2 Combustion Pulses

Superimposed on the mean torque signal is a large fluctuating torque which comprises two components: the torque that results from the change in cylinder pressure during combustion and the torque that results from the changing inertia seen at the crankshaft due to motion of the piston and conrod. The torque variations are periodic for a steady speed and load.

Figure 2 shows the individual contributions from piston inertia and combustion pressure to the total crankshaft force on a 4-cylinder 4-stroke engine. Also shown is the corresponding frequency content of the combined signal. It can be seen that as well as the main contribution at 2nd order (firing frequency) there is also contributions at higher orders. Typically in powertrain management, frequencies up to 8th order are considered significant for a 4 cylinder engine.

Flywheel design is the usual method for reducing the transfer of both kinds of torque fluctuation to the rest of the driveline. A single mass flywheel clutch attenuates engine vibrations with a roll-off of 40 dB per decade. For a dual mass flywheel the roll-off is 80 dB per decade (Fig. 3). This means that the drive torque and very low frequency vibrations can pass through the flywheel to the trans-

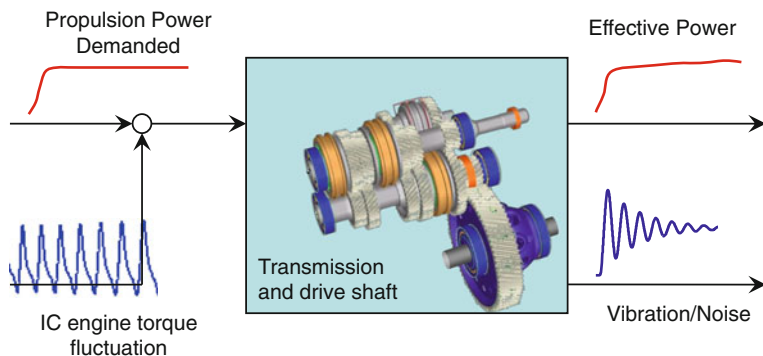


Fig. 1 Power transfer concept via a transmission

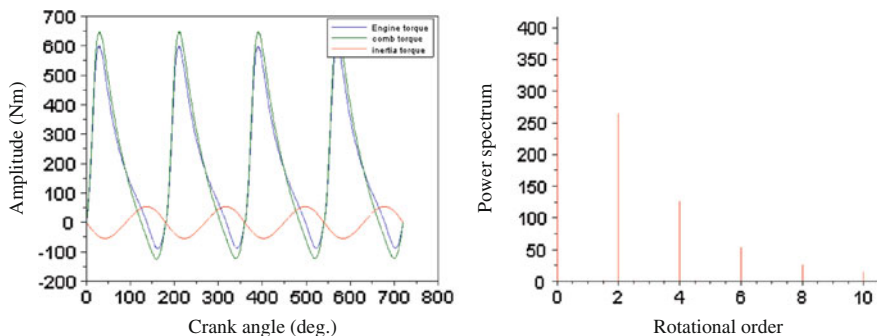


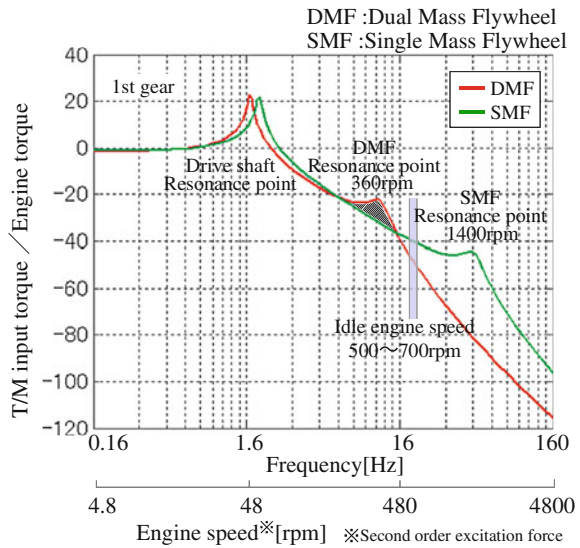
Fig. 2 Excitation torque with an IC engine model

mission, but higher frequencies vibrations are reduced. The flywheel subsystem has its own internal dynamic resonance behaviour which interacts with the resonant behaviour of the rest of the driveline (transmission, driveshafts etc.)

3 Gear Rattle with Internal Combustion Engine

Gear rattle occurs inherently in a powertrain consisting of an internal combustion engine and a manual type transmission. A meshing gear pair with backlash is excited by fluctuation torque in the powertrain which causes idling gears (usually) to lose contact. There is an impact when the gear teeth come back into contact again and when this happens repeatedly an unpleasant rattling sound is perceived.

Fig. 3 Input torque fluctuation attenuation with a single and dual mass flywheel clutch



3.1 Gear Rattle Mechanism and Simulation

If driven gears are sufficiently loaded, meshing gear pairs don't lose contact under torque fluctuations from the engine. When driven gear load is small, contact between two meshing gear pair can be lost temporarily as the drive gear decelerates due to the fluctuating combustion torque. Strong impulsive contact then occurs when the drive gear accelerates under the influence of the next combustion pulse. Even when an idling gear is not supplied by a driving torque from the engine there is still some torque applied by the drag of the gear through the lubricant sump and by the drag of the lubricant in the bearing under the gear. The most severe forms of gear rattle involve the gear mesh repeatedly bouncing across the backlash between the drive and coast flanks of the gear pair. The most basic form of a system which exhibits gear rattle is shown in Fig. 4. It comprises a single degree of freedom system with backlash and represents a single gear pair.

In a real driveline, the model is not as simple as this as there may be many degrees of freedom with many backlashes and there are many factors that influence the response such as temperature, lubricant viscosity, gear inertia and amount of backlash. The general resonant dynamic behaviour of the entire driveline also has an effect on the occurrence of rattle. However, in all cases, the fundamental noise-generating mechanism is the same with tooth impacts causing vibrations in the gears which travel through the shafts to the transmission housing where they are either radiated directly as noise or the vibrations are transferred to the chassis and are radiated elsewhere in the structure.

The resonant behaviour of the transfer path is usually less important as it is the impulsive nature of the force that causes annoyance rather than its tonal qualities.

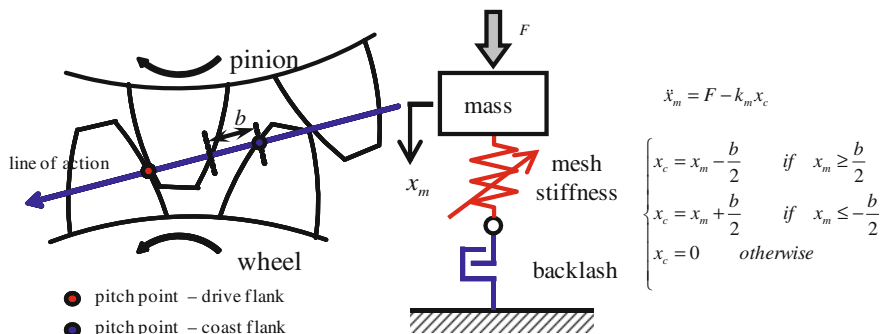


Fig. 4 Gear rattle concept

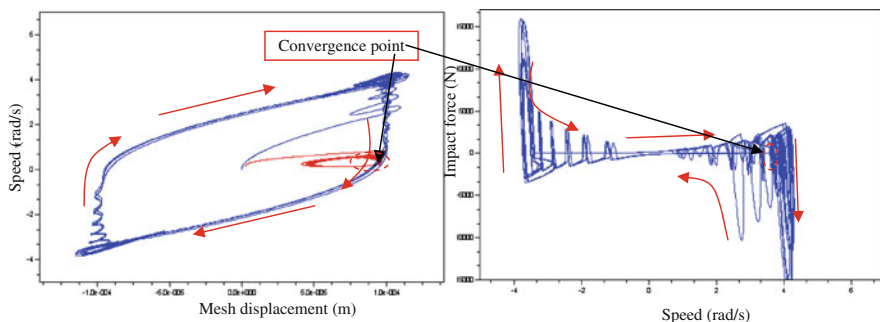


Fig. 5 Mesh displacement—relative speed—impact force

Many different metrics are used to quantify annoyance from gear rattle and most of them are related to the peak level of gear mesh force at the point of impact.

The gear rattle behaviour in a driveline can be simulated using low-level simulation tools, multi-body dynamic software or by dedicated software for gear rattle analysis [1].

3.2 Gear Rattle Vibration Response and Rattle On-Set Threshold

Gear rattle vibrations are often of the limit cycle type. Mesh displacement vs relative speed for a rattling gear pair is shown in Fig. 4. Both double and single sided impact events can be observed. As the speed fluctuations caused by the input torque fluctuations decreases the double-sided impacts become single-sided impacts and below a certain level, they converge on a point where no mesh displacement occurs. The magnitude of the impact force also decreases as the speed fluctuations decrease and eventually become zero (Fig. 5).

3.3 Gear Rattle On-Set Threshold

The magnitude of torque fluctuation below which no rattle occurs is called the rattle on-set threshold. This is a function of both the torque fluctuation at the gear mesh and the drag torque on the driven gear. Provided the instantaneous dynamic torque at the gear mesh does not exceed the static drag torque then no rattle will occur and the teeth will remain in contact [2].

Mathematically the rattle on-set threshold can be derived as follows: A driven gear is accelerated by the drive gear and will rotate freely. If deceleration of the wheel is larger than that of the pinion during deceleration, contact between two teeth is kept. The pinion and wheel behaviour is expressed mathematically as.

$$\begin{aligned}v_w(t) &= v_{p2} - \int_0^t \left(\frac{T_{dr}}{I_w}\right) d\tau \\v_p(t) &= v_{p2} + \int_0^t \left(\frac{T_{in}(t)}{I_p}\right) d\tau \\v_w(0) &= v_p(0)\end{aligned}$$

It is assumed that the drag torque is constant and the fluctuation torque is monotonously decreasing during a half cycle of combustion pulse. When deceleration of the wheel is smaller than that of the pinion, then, contact between teeth is lost. And the gear rattle on-set threshold is written as

$$\frac{T_{dr}}{I_w} < \frac{T_{fl1}}{I_p} \rightarrow T_{dr} < \frac{I_w}{I_p} T_{fl1}.$$

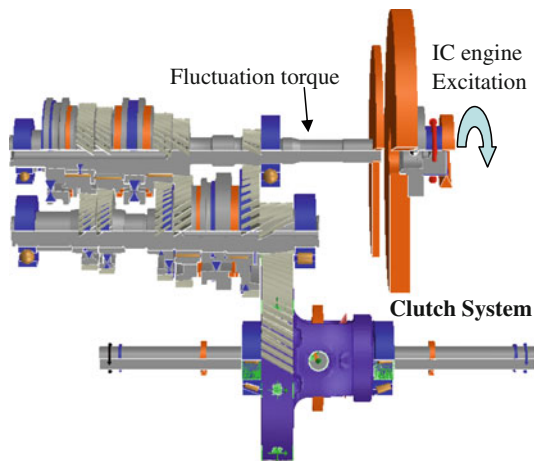
3.4 Drag Torque Evaluation

It is clear from the above discussion that for accurate simulation of gear rattle on-set, the drag torque must be known. Drag torque between an input shaft and an output shaft of a transmission can be measured in a carefully designed test rig. However, drag torque measurement for individual gears is more technically challenging. Using calculated drag torque with a transmission model is a practical and rather accurate method. Drag torque correlation between measurement and a transmission model calculation has been published previously [2].

3.5 Calculation of Torque Fluctuations at the Transmission Input

In the complete driveline, the amplitude of the excitation torque from an IC engine (Fig. 2) is attenuated mechanically with a clutch/flywheel arrangement. Typical attenuation properties of such a clutch system is shown in Fig. 3. In some driveline

Fig. 6 Transmission system resonance calculation model



arrangements, the resonant frequencies of the driveline may be close to firing frequencies of the engine and the input fluctuation torque must be calculated using dedicated software which can accurately model the dynamics of the entire driveline (Fig. 6).

3.6 Measures for Reducing Gear Rattle

There three main ways in which gear rattle can be reduced are backlash reduction, drag torque increase and engine fluctuation torque amplitude reduction. The effects of these can be simulated using the models described previously.

The effect of lubricant viscosity (which directly affects gear drag) on the peak impact force is shown in Fig. 7. Increasing the lubricant viscosity reduces the peak force by reducing the speed of the driven gear during a rattle event. In the extreme case, increasing the lubricant viscosity may cause the drag torque to be great enough to bring the system below the rattle on-set threshold and eliminate gear rattle entirely. Increasing the amount of lubricant in the gearbox may have the same effect. However, increasing the drag torque of course reduces the efficiency of the transmission and increases fuel consumption which is not generally acceptable. Also lubricant viscosity is chosen for particular operational and durability reasons and should not be changed without consideration for these effects.

It can be seen that reducing backlash has an effect on the reduction of the peak mesh force however gear rattle can never be eliminated by backlash reduction (unless the backlash is zero, which is undesirable for other reasons). Again, backlash reduction is not an acceptable solution in a production environment as the increased quality of manufacturing required to control backlash to this degree would be prohibitively expensive for a mass production transmission.

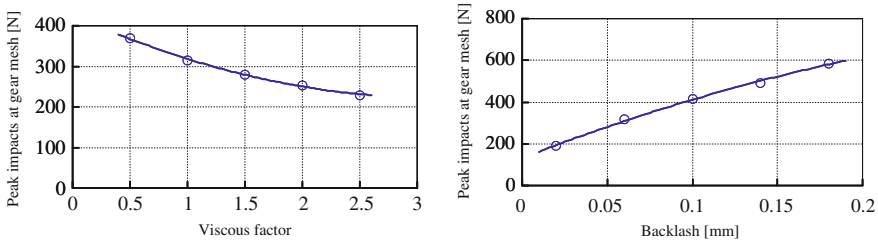


Fig. 7 Gear rattle sensitivity to lubricant viscosity and backlash

The conclusion is that the engine torque fluctuations must be reduced if rattle is to be avoided. Engine calibration is not an option in this case as changing the engine management system to reduce torque fluctuations has a negative impact on fuel economy. The only practical way to achieve gear rattle reductions is by careful design of flywheel and clutch assemblies to reduce the transfer of the engine torque fluctuations to the transmission input.

Fortunately, as has been demonstrated here, the kinds of specialist tool required to simulate the driveline dynamic behaviour are now available and much of this work can now be carried out by CAE methods with rattle noise can be reduced or eliminated before a design is finalised. Gear rattle is still a major challenge and this problem will only get worse with the current trends for downsizing engines and increasing combustion pressures and the increased engine torque fluctuations they generate.

4 Acceleration/Deceleration Vibration

The gear rattle phenomena described above were caused by the periodic engine torque fluctuation pulses associated with combustion. The phenomena such as shunt and tip-in/tip-out which cause longitudinal vibration of the whole vehicle are caused by longer, lower frequency, transient torque fluctuations caused by driver demand through the throttle pedal.

The entire driveline from engine to tires is involved in these acceleration/deceleration drivability events (Fig. 8). The torque variations are supplied by the engine and the driveline acts as a passive resonator with many natural frequencies. Vibration is transferred to the vehicle either through acceleration and deceleration of the entire vehicle by the tires or as structure-borne sound through the various drive train mounts and suspension.

The driveline can be represented as a system of equations of motion of the form

$$M\ddot{x} + C\dot{x} + Kx = f$$

Where *M*, *C* and *K* are respectively the mass, damping and stiffness matrices, *x* is the component displacement vector and *f* is the equivalent vector of external

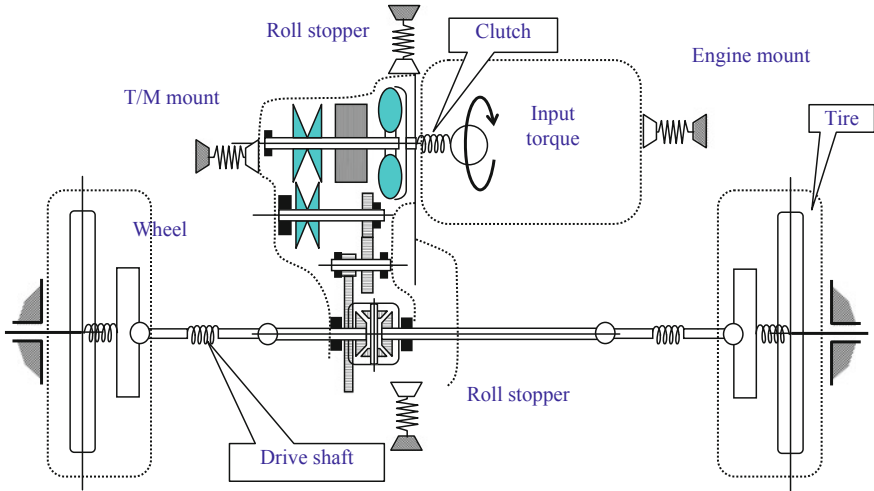


Fig. 8 Driving force transmission path

forces which may vary with time. For the types of problem studied here, it has been shown in other studies [3] that the number of degrees of freedom may be reduced to just the effective referred inertias upstream and downstream of the driveshaft with the driveshaft as a flexible component. The transfer function of the reduced order model is described as

$$G_p(s) = \frac{K\omega_p^2}{(s^2 + 2\zeta_p\omega_p s + \omega_p^2)}$$

Where ω_p is the resonance frequency of the driveline and ζ_p is the damping ratio of the driveline

4.1 Methods of Vibration Reduction

Measures to reduce the sensitivity of the transfer path are increased damping and amplitude attenuation (gain reduction). As the transfer path is a torsional rotating one, any attempt to remove energy by damping may also lead to reduced driveline efficiency and hence fuel economy. Mechanical amplitude reduction measures will not be effective without major vehicle structure modification, sometimes tuned mass dampers are employed as a method of last resort but the add additional weight and cost.

As with gear rattle, the best solutions come from reducing the source of the vibration, the engine torque fluctuation. One method which is described in detail here is “input torque profile shaping”. This is a combustion control technique and

as such is relatively low cost and does not add any heavy or unreliable mechanical components to the system.

With electronic throttle or injector control, the inputs from the accelerator pedal can be mitigated by a controller. In its most simple form a passive low pass filter can be used to prevent sudden acceleration demands from reaching the throttle/injector system. This type of control is not suitable because drivers complain of the accelerator response being too low.

Input torque shaping is a more sophisticated system that replaces the low pass filter with a notch filter tuned to the dominant resonant frequency of the driveline. This method requires that the driveline resonance frequencies are known a priori for all ratio conditions. The method must also be robust enough to cope with changes in vehicle mass which will also change the driveline resonance frequency.

4.2 Increasing Damping by Speed Feedback

One way to add damping is to measure speed changes and use this as feedback to create an additional input force proportional to the output speed. This form of motion feedback active vibration control is very robust and can provide high levels of damping. However, this only works well for very low frequency vibrations.

There is a delay from increasing throttle/fuel injection to increased output torque. This is due for the time taken for the increased fuel/air mixture to be delivered to the cylinders and also because the system must wait for the next firing before any torque control can take place.

Model prediction can be used to minimise such delay and increase the useful frequency range. This works by replacing the measured speed feedback with a simulated speed feedback calculated from a simplified dynamic model of the driveline and torque response delay of the engine is avoided. Two model prediction approaches are described below.

4.3 Pole Cancellation of Transfer Function with Pre-compensator

This model prediction control method is implemented by using a pre-compensator. The compensator has polynomials corresponding to denominator of the driveline transfer function as its numerator and transfer function with desirable damping in its denominator. The compensator shapes input torque and functions as a notch filter. The method was proposed by authors [3–5] and applied to production cars [6]. The concept is shown graphically in Fig. 9.

The compensator transfer function to counteract the dynamic behaviour of the driveline is

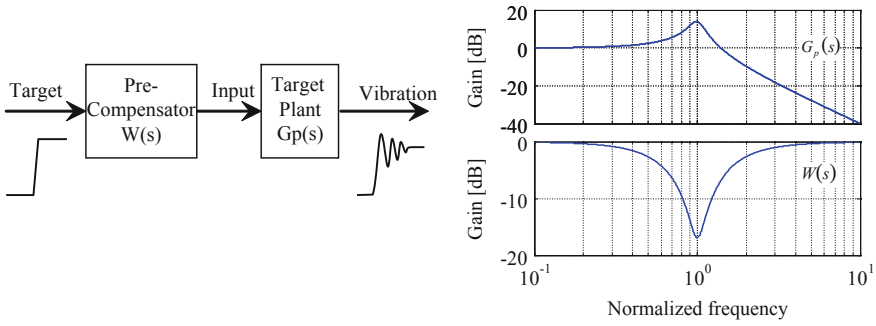


Fig. 9 Pre-compensator strategy and frequency property

$$W(s) = \frac{\omega_m^2 (s^2 + 2\zeta_p \omega_p s + \omega_p^2)}{\omega_p^2 (s^2 + 2\zeta_m \omega_m s + \omega_m^2)}$$

where ω_m is the resonance frequency of the model and ζ_m is the damping ratio of the model.

4.4 Nonlinear Input Torque Waveform Conversion

An alternative method is to replace the driver demanded torque with a torque that aims to avoid exciting resonance. When a sudden step change in torque demand is requested by the driver the torque should instead be delivered in a way which suppresses the resonance of the driveline and thus minimises vibration. Two such waveforms are shown below (Fig. 10). One is a ramp input which lasts for a full cycle of the resonance frequency. The other is a 2 stages step input where each step lasts a half cycle of the resonant frequency. The Fourier transform of these functions show the required notch filter behaviour at the model resonant frequency.

4.5 Robustness to Model Errors and Driver Operation

Both the pre-compensator and nonlinear input conversion methods rely on the model used to predict the driveline resonances being accurate to achieve maximum calculation. This cannot be achieved in practice. For example an increase in mass of the vehicle due to more passengers or more load will change the driveline resonant frequencies. It is important to evaluate performance deterioration of the proposed methods which results from such model errors.

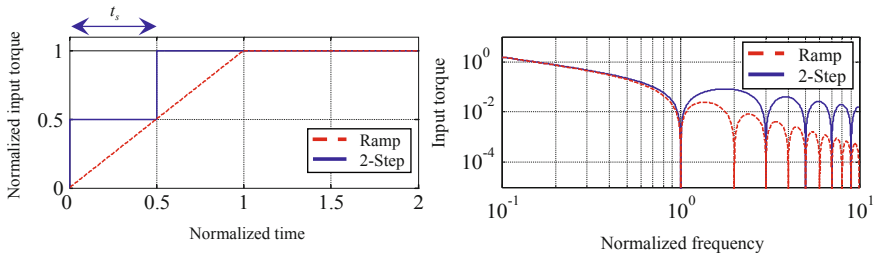


Fig. 10 Nonlinear input profile to avoid vibration

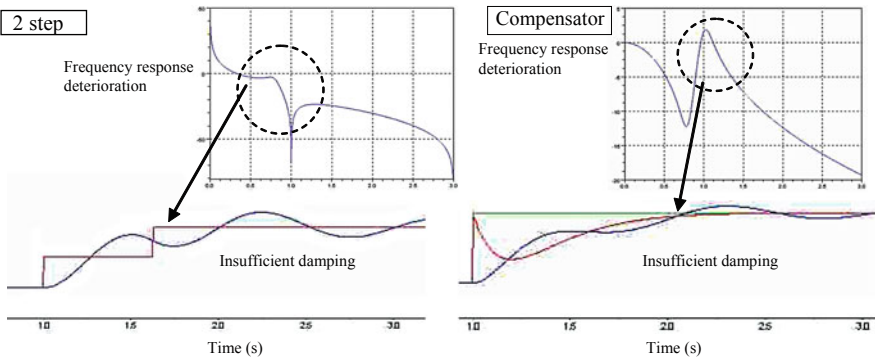


Fig. 11 Influence of model error in time domain and frequency domain

Resonance frequency is the most important property in pre-compensator or nonlinear input shaping applications. The frequency depends on total inertia of powertrain and stiffness of drive shafts. Relationship between the inertia and the stiffness changes as the gear ratio changes. This means that the target frequency to be compensated changes during gear shift. For the CVT example shown in Fig. 8 for example, the controller needs to take account of a continuous range of ratios and associated resonant frequencies.

The effect of an error in the expected resonant frequency is shown below (Fig. 11) for both methods. The effect is more severe for the 2-step non-linear input conversion method. This is because the notch is very narrow and a small frequency error can lead to a large deterioration in performance. In the case of the pre-compensator, the damping can be altered by changing the damping in the transfer function. There is still some fluctuation in the frequency response as the effects of damping quickly become reduced away from resonance.

An additional drawback of the nonlinear input conversion method is that there is an inherent delay in tracking the driver’s requested torque demand. This is because the step or ramp input can only be calculated once the accelerator pedal

action is completed whereas the pre-compensator method can start to act from the moment the pedal starts to move. As a result, drivers may complain of a response delay of acceleration or strange feel in engine response.

4.6 Realisation of Target Torque Profiles

So far it has been assumed that any target torque profile requested by the controller can actually be generated by the engine. Reasons why there may be errors in the generated torque profile include:

- Negative torque is uncontrolled.
- Maximum torque is limited. Any torque up to the maximum is feasible at each stroke with a common rail diesel engine.
- Torque generated from the IC engine is not continuous but in discrete pulses as shown in Fig. 2.
- Suppression of the resonance requires a high enough engine speed so that the “sampling frequency” of the engine pulses is high enough to generate the signal requested by the controller as per the Shannon-Nyquist sampling theorem.

A gasoline engine has inherent delay in air intake and fuel transportation process to the combustion cylinder. There also is nonlinearity in throttle-torque relationship. Despite these limitations, the control strategies described here were applied to a vehicle with a gasoline port fuel injection engine. The tip-in shock was found to be well suppressed for comfort, even though some measurable vibration remained [7].

5 Conclusion

- Two examples of NVH phenomena caused by engine torque fluctuations have been presented.
- Methods for simulating gear rattle have been presented for a complete transmission with backlash.
- Based on these simulation models the effects of backlash and lubrication on gear rattle performance have been investigated.
- It was concluded that neither backlash reduction nor lubrication viscosity increase were suitable approaches for rattle reduction.
- The best approach to reduce rattle is to reduce the engine torque fluctuations transferred to the transmission by careful design of the clutch/flywheel assembly.
- Methods for controlling drivability NVH issues caused by changes in driver demanded torque were investigated.

- Three active control methods were discussed—Speed feedback control, compensator model feedback control and model-based nonlinear torque waveform conversion.
- Measured speed feedback control is not suitable for this problem due to the delay between throttle command and engine response.
- The effect of errors in the model resonance frequency was investigated for the other methods and other limiting factors were discussed.
- The resolution of the torque control is shown to be proportional to engine speed and therefore there is an inherent lower speed limit for any torque shaping approach.

References

1. Togai T, Yamaguchi H, Dixon A, Halse C, Potter T (2007) Towards a verified tool for the investigation of transmission gear rattle. JSAE 2007 annual congress (Spring), JSAE20075339
2. Togai T, Yamaguchi H, Yamaura H, Pears J, Potter T (2009) Gear rattle modelling and meshing gear teeth behaviour estimation considering lubrication influence, FISITA2010C095
3. Togai K, Choi K, Takeuchi T (2002) Vibration suppression strategy with model based command shaping: application to passenger car powertrain, Proceedings of SICE annual congress 2002 in Osaka SICE02-0607
4. Takeuchi T, Choi K, Kan S, Togai K (2003) Sensibility analysis of vibration transfer path and control of input force for reduction of acceleration and deceleration shock. Mitsubishi Motors Tech Rev 15:32–41
5. Togai K, Takeuchi T (2005) CVT Drive train vibration analysis and active control system design. Mitsubishi Motors Tech Rev 17:11–22
6. Kuwahara S, Kuno K, Kaigawa M, Kubonoya H, Mizuno H (2007) Toyota's new integrated drive power control system, SAE world congress, SAE2007-01-1306
7. Togai T, Kido K, Yamaura H (2009) NVH Problem causes in passenger car drive line and alleviation measures with input force shaping based on excitation and transfer path modeling, MPT2009, Sendai

Wheel Load Oriented Control of Semi-Active and Active Suspension Systems Using Pre-Located Road Sampling

Sebastian Spirk and Kay-Uwe Henning

Abstract The conflict of objectives in vertical suspension control could be significantly eased by adjusting the settings of stiffness and damping according to the actual driving state. With an adaptive reference model based control emulating a passive suspension with time-varying stiffness and damping coefficient this can be realized using an active or hybrid suspension system. The concept offers huge benefits in comfort for smooth and uncritical excitations. However, in safety critical situations the possibilities for a safety-oriented setting are limited to the dynamic wheel load Pareto-optimal configuration reachable of passive suspensions. Using road profile information, gained by vertically sampling the road underneath the vehicle, a wheel load optimal disturbance compensation can be derived and is applied to a semi-active and hybrid suspension system. Applying this transparent feedforward control law in combination with a reference model based control, dynamic wheel load deviations can be significantly reduced while additionally reducing chassis accelerations.

Keywords Active vehicle suspensions · Semi-active dampers · Vehicle dynamics · Vehicle suspensions · Disturbance compensation

F2012-J02-011

S. Spirk (✉) · K.-U. Henning
Institute of Automatic Control, Technische Universität München, Munich, Germany
e-mail: s.spirk@gmx.de

1 Introduction

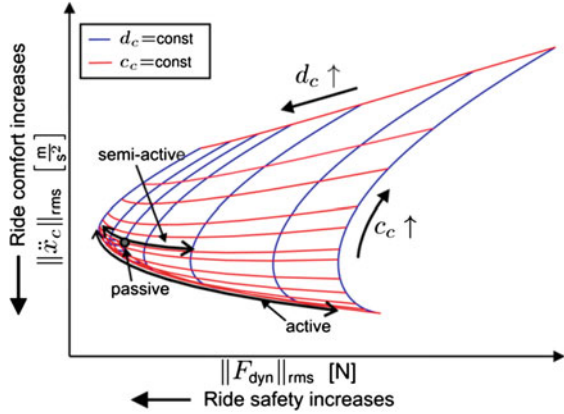
Vehicle suspension systems have been and still are one of the main focuses of automobile development, as they are essentially responsible for ride comfort and active safety. The major challenge is to ease the existing conflict between the aims of good ride comfort, high ride safety and keeping suspension deflection within constructional limits.

Vehicle suspensions should isolate passengers from road induced vibrations and keep the tires in consistent contact with the road. The objective of ride comfort can be quantified in chassis acceleration rms-values, while the safety issue can be expressed as minimal wheel load deviations from the static wheel load, [1–3]. As shown in Fig. 1 both aims cannot be reached in an optimal way at the same time by passive suspensions: The point of minimum wheel load deviations refers to a clearly different configuration of damping coefficient d_c and spring stiffness c_c than the point of minimum chassis acceleration. The variation of damping (Fig. 1, semi-active) offers some margin to adapt between more safety or more comfort depending on the driver's preference or the actual road excitation and vehicle states, but the potential range of variation in comfort is small due to the fact that an alteration of damping with fixed spring stiffness does not enable a movement along the Pareto optimal curve. Alternating damping and stiffness ratio (Fig. 1, active) instead offers a huge potential of adapting between safety and comfort-oriented vehicle dynamics along the Pareto optimum. The idea of emulating a time-varying spring stiffness and damping ratio adapted along the Pareto optimal curve has been used for the reference model based controller introduced in [4–6].

Fully active actuators have not yet made their way into series production or near-series research of cars as their high bandwidth demands—a cut-off frequency more than 20 Hz is needed (e.g. see [1])—in combination with high force demands are coupled with high production costs and power consumption. In this paper a hardware configuration, consisting of a low bandwidth actuator in series to the passive spring and a continuously variable damper, is discussed. The potential of the used actuator configuration, called hybrid suspension, has been proved generally in [7] and especially for the reference model based controller in [4–6].

The controller concept is based on a passive reference model with time-varying stiffness and damping. By adaption to the driving states regarding wheel load deviations and suspension deflection with fast and slow reacting algorithms the basic controller can already provide good ride comfort on rough and smooth roads, but for critical single event and stochastic road excitations the reduction of occurring dynamic wheel loads by adaptation to more safety oriented setting is limited to the wheel load optimal point (left end of the Pareto front in Fig. 1). Neglecting the constraint of the suspension deflection limits, chassis accelerations can be theoretically reduced towards zero by consequently lowering suspension stiffness and damping coefficient. In contrast, even with highly damped passive suspension configurations the reduction of dynamic wheel load deviations is limited. Therefore the need of an additional control component arises to achieve a

Fig. 1 Vehicle suspension conflict diagram (carpet plot)



further reduction of wheel load deviations. First simulative analysis in [8] showed that by using sensor information of the road excitation, wheel load deviations can be reduced, yet not at the expense of comfort, but with a further reduction of chassis accelerations. In this paper the concept is developed using real sensor information gained by vertically sampling the road underneath the vehicle and is validated at a quarter-car test rig using active and semi-active suspension systems.

2 Modeling

2.1 Quarter-Car

If only the vertical degree of freedom of a passenger car is considered a 2-DOF quarter-car model can be used. Regarding only the frequency range up to 25 Hz, which is the frequency range that can be influenced by spring, damper or (semi-) active suspension system, these models show a good approximation of the vertical car dynamics, [1, 9]. Road profile excitation is decreasing approximately proportional to the excitation frequency. Above 20 Hz, according to the noise-vibration-harshness classification the area of harshness starts, where vibrations are more and more heard instead of felt and dynamic behaviour is mainly affected by the top mount, joints and other connecting elements. Figure 2 shows quarter-car models of a fully active suspension (middle) in comparison to a semi-active configuration with the variable damping coefficient $d_c(t)$ and the discussed hybrid suspension system with the hydraulic actuator displacement x_{act} in series with the primary spring in combination with a continuously variable damper.

The model of the passive suspension results from the fully active suspension model if the control force vanishes ($F(t) = 0$). The state-vector x and the output vector y are introduced as $x = [x_c - x_w, \dot{x}_c, x_w - x_g, \dot{x}_w]^T$, $y = [\ddot{x}_c, F_{dyn}, x_c - x_w]^T$

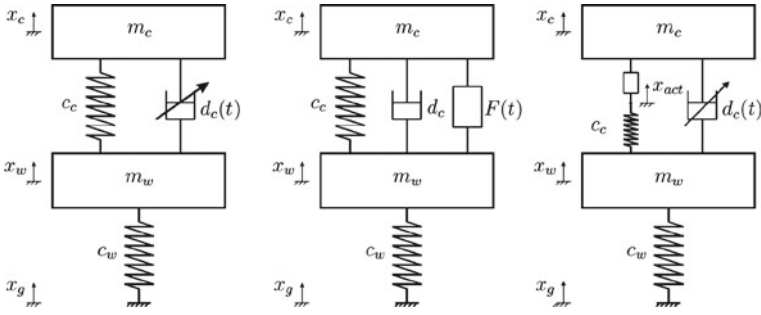


Fig. 2 Quarter-car model of semi-active, active and hybrid suspension system



Fig. 3 Qualitative plot of the damper characteristics and realization of the hybrid suspension strut

where $F_{dyn} = -c_w(x_w - x_g)$ denotes the dynamic wheel load. With the deflection of the actuator as control input $u_{hy}(t) = x_c(t) - x_{act}(t)$ and the semi-active damper $u_{cvd}(t) = F_d(t)$ as well as the disturbance input $u_d(t) = \dot{x}_g(t)$, the quarter-car model with the hybrid vehicle suspension system can be expressed as a fourth order state spacemodel in the form $\dot{x}(t) = \mathbf{f}(\mathbf{x}(t), u_{hy}(t), u_{cvd}(t), u_d(t))$, $\mathbf{y}(t) = \mathbf{g}(\mathbf{x}(t), u_{hy}(t), u_{cvd}(t), u_d(t))$.

For realistic simulation results, the model is extended by some non linearities. The so-called Gehmann Model is used for the frequency-dependant damping behaviour of the tire and the tire stiffness is modelled using a quadratic characteristic and considering wheel lift-off. Forces between wheel and chassis mass constitute from a Coulomb friction force, a nonlinear spring characteristic including compression and rebound stop and the semi-active damper characteristic with degressive curve and asymmetry in rebound and compression (see Fig. 3). For the simulation of a passive suspension configuration, the damper valve current is kept constant and the actuator force $F(t)$ is equal zero. The passive suspension of the used front suspension of an upper class sedan can be characterized by its natural eigenfrequency $f_{c,p} = \frac{1}{2\pi} \sqrt{\frac{c_c}{m_c}}$ of about 1.1 Hz and an approximate damping ratio $D_{c,p} = \frac{d_c}{2\sqrt{c_c m_c}}$ of 0.21. The eigenfrequency of the wheel is approximately 12 Hz.

The aims of the suspension control are to maximize ride comfort and ride safety by simultaneously keeping the suspension deflection limits. For the controller design, a control objective for each aim is needed. One of these objectives for ride comfort is the acceleration of the chassis mass, especially in the frequency range of 4–8 Hz where the human body is most sensitive for vertical mechanical vibrations. A shaping Filter according to [10] is used to derive a weighted signal of the chassis acceleration $\ddot{x}_{c,comf}$ considering the frequency-dependant sensitivity of the human body to vertical vibrations. Its root mean square value is used as ride comfort index in this paper. In order to describe the ride safety, the rms-value of the dynamical wheel load F_{dyn} , is a reasonable choice. Furthermore, suspension travel has to be kept within the limits, while the rms-value is not of interest here.

3 Wheel Load Optimal Disturbance Compensation

3.1 Derivation of the Wheel Load Optimal Feedforward Algorithm

The optimum for ride comfort would be a full decoupling of chassis and wheel, thus $c_c(t)/d_c(t) \rightarrow 0$ for passive suspension. This could be achieved with the presented controller concept, provided that suspension limits are kept and arising wheel load deviations are not of interest. The choice of the lower boundaries for f_c/D are therefore just a matter of the wheel load and suspension deflection constraints. A comparable extreme orientation towards minimal wheel load deviations would not be possible, even if arbitrary chassis accelerations are tolerated, dynamic wheel load deviations cannot be fully suppressed. The dynamic wheel loads can—by passive reference models—not be improved beyond the wheel load optimal point of the Pareto front (compare Fig. 1). From the equation of motion of the wheel for a fully active quarter-car (Fig. 2, left)

$$m_w \ddot{x}_w = c_c(x_c - x_w) + d_c(\dot{x}_c - \dot{x}_w) - c_w(x_w - x_g) - F(t), \quad (1)$$

emerges, with the unrestricted force

$$F_{cw}(t) = F(t) - c_c(x_c - x_w) - d_c(\dot{x}_c - \dot{x}_w) \quad (2)$$

between chassis and wheel, the simplified equation of motion

$$m_w \ddot{x}_w = -c_w(x_w - x_g) - F_{cw}(t). \quad (3)$$

Inserting the desired term for disappearing wheel load deviations

$$F_{dyn} = -c_w(x_w - x_g) = 0 \quad (4)$$

results in the wheel load freed equation of motion of the wheel

$$m_w \ddot{x}_w = -F_{cw}(t). \quad (5)$$

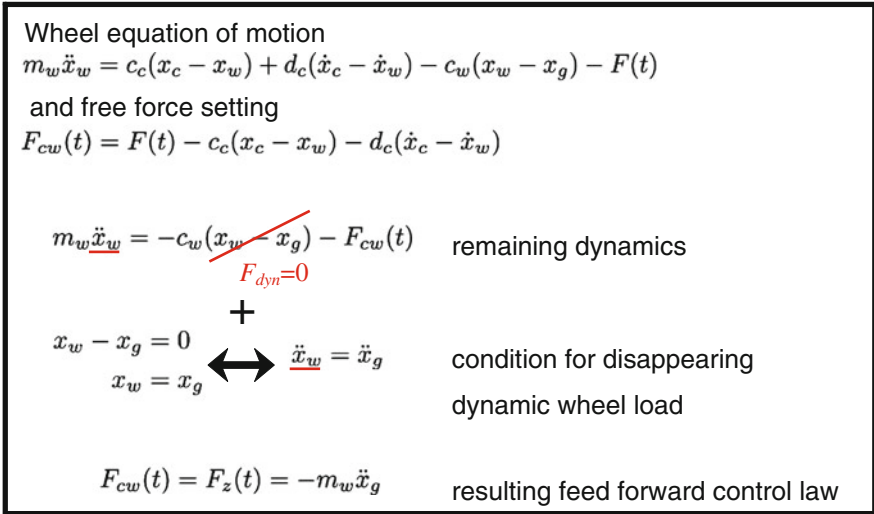


Fig. 4 Schematic derivation of wheel load optimal feedforward control law

For satisfying (4), furthermore, $x_w = x_g$ must be held. As only the wheel's acceleration can be influenced directly,

$$\ddot{x}_w = \ddot{x}_g \tag{6}$$

must be reached and therefore according to [3] the wheel load optimal force $F_z(t)$ results from (5) and (6) to (Fig. 4)

$$F_{cw}(t) = F_z(t) = -m_w \ddot{x}_g. \tag{7}$$

For the chassis acceleration this results in $\ddot{x}_c = -\frac{m_w}{m_c} \ddot{x}_g$ respectively the amplification function $\frac{\ddot{x}_c}{\ddot{x}_g} = \frac{m_w}{m_c} \omega$, which can be seen in Fig. 5. Due to this strong amplification of high frequencies, the algorithm can only be applied after lowpass-filtering of the road profile acceleration to avoid great loss of comfort for high frequency excitations.

The resulting control law (7) for zero wheel load deviations is feedforward only and must be amended by a global control law, e.g. a passive reference model. Regarding the amplification functions in Fig. 6 arising from a disturbance compensation according to (7) and 12.5 Hz lowpass filtering in parallel to a passive suspension (compare Fig. 2, middle), it can be seen that for comfort and safety the disturbance feedforward control (DFF) outperforms a passive suspension with a safety oriented Damping ratio of $D_{c,p} = 0.45$ regarding the dynamic wheel load and keeps up with it in comfort aspects. Hence, a cut-off frequency of 12.5 Hz represents a good trade-off between dynamic wheel load reduction up to the wheel hop frequency and a moderate deterioration of comfort for high frequency

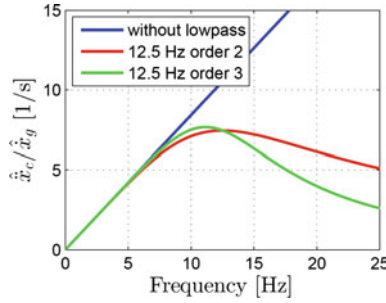


Fig. 5 Amplification function between vertical excitation velocity and chassis acceleration of the resulting feedforward control law for zero wheel load deviations (*blue*) and effects of an additional low pass filtering

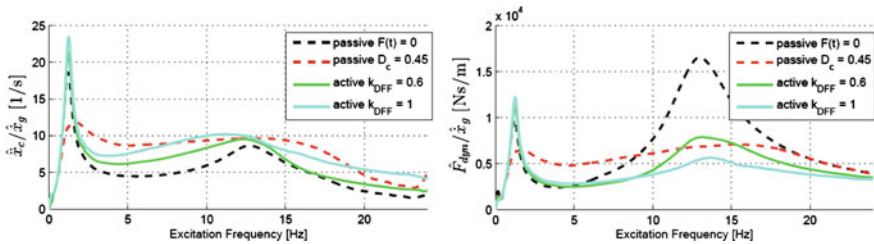


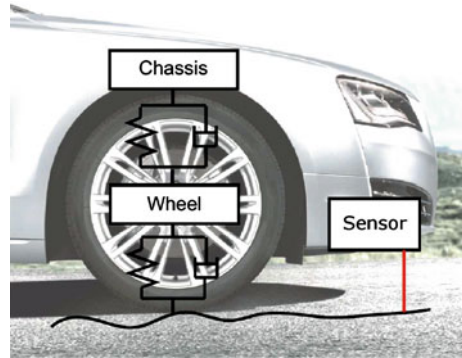
Fig. 6 Amplification from road disturbance \dot{x}_g to chassis acceleration \dot{x}_c (*left*) and dynamic wheel load F_{dyn} (*right*) for passive suspension and active suspension with DFF and a cut-off frequency of 12.5 Hz

excitations compared to the standard passive suspension. Using the passive reference model based control, comfort can be regained by emulating softer passive suspension settings and thus a combined increase of comfort and safety is attainable.

3.2 Road Sampling Concept

The developed algorithm needs the vertical road profile acceleration signal. Many research works deal with estimation of unmeasured quantities of car dynamics, where in all road profile estimation (without preview sensor information) shows the worst signal quality. Additionally this algorithm depends on the second derivative and requires a lowpass-filtering. Therefore this concept needs a good signal quality of the vertical road profile height and sufficient time for lowpass-filtering. Preview concepts like in [11] have limited signal quality due to their flat angle of vision, but they offer a large preview time for signal processing. Nevertheless, in this research project a different road sampling concept has been

Fig. 7 Concept of vertical road profile measurement under the car by a laser distance sensor offering sufficient time for signal processing due to pre-located sampling



applied. It is based on the idea of sampling the road profile underneath the vehicle in a vertical angle.

To be able to compensate the phase delay of the low pass filter, the sensor is located in front of the wheel as shown in Fig. 7. This concept also allows the compensation of further time delays caused from the actuators and the distance sensor. However, the maximum compensation time is limited, depending on the distance between the sensor and the wheel and the actual velocity of the vehicle. Modern upper class sedans provide a distance of about 1 m allowing sufficiently pre-located sampling.

3.3 Signal Processing

For the realization at the test rig a laser distance sensor has been chosen, which is especially designed for automotive testing usage as a measurement of the car body movements against the road. It meets automotive requirements regarding, e.g. vibration and shock resistance or interface requirements, and the measurement is based on triangulation. With a resolution of at least 0.3 mm, a sampling frequency up to 1.5 kHz and a measuring range of 0.25 m it is suitable for the pre-located road sampling concept. Additional to the measured distance $x_{meas} = x_c - x_g$ between the road and the sensor (fixed at the chassis mass), the chassis acceleration is needed to determine the road acceleration $\ddot{x}_g = \ddot{x}_c - \ddot{x}_{meas}$ according to the block diagram in Fig. 8.

The measured distance signal of the pre-located sensor x_{meas} is lowpass-filtered with a butterworth-filter of order n and the desired cutoff frequency f_{cut} . After two times discrete derivating the runtime is adjusted with the variable time delay T_{delta} in order to synchronize the signal to the actual road excitation at the wheel. The acceleration of the sensor mounting point \ddot{x}_c (needs to be amended by roll and pitch acceleration effects in the full-car case) passes the same filtering and an additional time delay of 1 ms to compensate derivation delay and is then added to the measured relative acceleration. By multiplication of this signal with the wheel

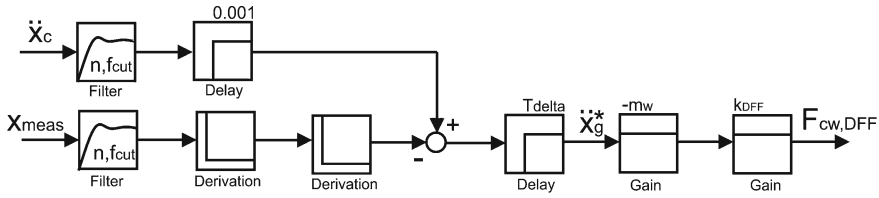


Fig. 8 Signal Processing from road profile measurement to wheel load optimal control force

mass m_w and the disturbance compensation gain k_{DFF} , the desired force $F_{cw, DFF}$ between chassis and wheel is calculated.

The maximal available time for signal processing depends on the pre-location distance $x_{pre-sense}$ of the sensor and the vehicle velocity v_{veh} via $T_{pre-sense} = x_{pre-sense} \cdot v_{veh}^{-1}$.

The phase delay of the butterworth-filter at the cutoff frequency can be approximated by

$$T_{phase, filter} = \frac{n}{f_{cut}} \cdot \frac{45}{360} = \frac{0.125 \cdot n}{f_{cut}}$$

Hence, considering the additional 1 ms delay of the discrete derivations, the maximum vehicle velocity calculates to

$$v_{veh, max} = 8 \cdot \frac{x_{pre-sense} \cdot f_{cut}}{(n + 8 \cdot f_{cut} \cdot 0.001ms)}$$

With a second order butterworth filter, a cutoff frequency of 12.5 Hz and a distance between measuring point and wheel of 1 m from an upperclass vehicle, the algorithm can be applied up to a maximum vehicle velocity of more than 170 km/h.

3.4 Potential Analysis

For initial potential analyses, nonlinear simulation models are used assuming an active or a semi- active suspension system with the presented damper characteristics. The primary spring stiffness c_c and the damping coefficient d_c are manipulated to vary the chassis eigenfrequency and the chassis damping ratio. In the case of the active suspension configuration, the nonlinear degressive passive damper characteristic was up- or downscaled in order to tune the chassis damping ratio and spring stiffness could be manipulated by a reference model based control. In the semi-active case, the emerging reference force is clipped to the damper characteristics. Variation of spring stiffness shows the possibility of changing to more soft characteristics of the real spring as dynamic wheel load is reduced by the

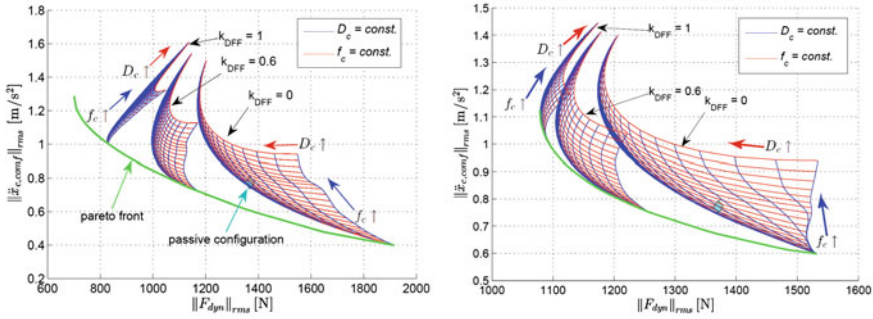


Fig. 9 Potential Analysis of DFF concept in parallel to a passive suspension varying damping ratio, spring stiffness and disturbance compensation gain k_{DFF}

disturbance compensation. The controlled quarter-car is excited by a white noise signal for the vertical road profile velocity with amplitudes corresponding to a medium quality highway road profile and vehicle velocity. Figure 9 shows the conflict diagrams of the control objectives comfort, in terms of frequency weighted chasis acceleration, and ride safety, in terms of dynamic wheel load deviations. Three different disturbance compensation gains $k_{DFF} = 0$ (passive suspension configuration), $k_{DFF} = 0.6$ and $k_{DFF} = 1$ are compared. The green line illustrates the new pareto front with the disturbance compensation algorithm and the passive configuration point marks the point of the passive configuration of the original upper class vehicle suspension with comfort-oriented damper setting.

Dynamic wheel load deviations can be reduced by increasing chasis eigenfrequency and damping ratio for the passive suspension case, but this is limited to the wheel load optimal point with an rms-value of 1175 N. Even in the semi-active case this ride safety value can be reached with a comfort value of 0.83 (−30 %) instead of 1.18 in the passive case. For the safety-optimal point a reduction to 1080 N is possible (−8 %). The wheel load optimal disturbance compensation in combination with an active suspension configuration is able to reduce the dynamical wheel load down to approx. 700 N, which is 40 % less than the optimal passive suspension configuration, without a loss in the ride comfort objective. A decrease in the chasis eigenfrequency and damping ratio results in better ride comfort and ride safety. So, the reduction of the dynamical wheel load due to the disturbance compensation allows the choice of a smaller chasis eigenfrequency and damping ratio. This fact causes the eigenfrequency and damping ratio to be optimal at very low values over the whole range of the pareto front. Based on the passive configuration point, with this concept, either improvements of 18 % in ride safety or 20 % in ride comfort are possible compared to the point of the original passive configuration.

Passive reference model	
→ Variation of chassis eigenfrequency	$F_{cw,fc} = (m_c(2\pi f_c)^2 - c_{c,pass}) \cdot x_{cw}$
→ Variation of chassis damping ratio	$F_{cw,Dc} = (\frac{4\pi f_c m_c D_c}{d_{c,pass}} - 1) \cdot F_{d,pass}(\dot{x}_{cw})$
Skyhook	
→ Damping of the chassis movement	$F_{cw,SH} = -d_{sky} \cdot \dot{x}_c$
Relative Groundhook	
→ Further reduction of dynamic wheel load deviations	$F_{cw,GH} = -d_{gro} \cdot (\dot{x}_w - \dot{x}_g)$

Fig. 10 Global feedback control laws

4 Wheel Load Oriented Control

4.1 Global Controller

The presented disturbance compensation for the minimization of wheel load deviations is just feedforward and does not consider other control objectives as ride comfort and suspension deflection. It therefore has to be complemented by a global feedback controller, which can be a reference model based controller, presented in [4–6], emulating an adjustable passive suspension configuration (realizing a desired stiffness and passive damping). In addition to the potential analysis in Sect. 3.3 global control is further amended with the well-known suspension control skyhook and groundhook algorithm (see Fig. 11), [12]. Where in this case of known road disturbance the groundhook concept can especially be properly realized by using the relative wheel deflection velocity between ground and wheel (not the absolute wheel velocity), still having a very good feedback signal as the road profile velocity can be easily estimated using the road profile measurement signal (Fig. 10).

As described in Sect. 2 the used hybrid suspension consists of two actuators, the desired force between chassis and wheel therefore has to be allocated between both actuators. For first analysis and due to the good performance in the semi-active case, according to Fig. 11 just the reference model based variation of the stiffness and a very slow suspension levelling is realized by the active spring mount adjustment (F_{HY}), while the other control laws are realized by the continuously variable damper system (F_{CVD}). So the active case from the potential analysis applying the DFF to a fully-active actuator is not considered further for the upcoming analysis at the test rig due to the lack of full realization possibilities.

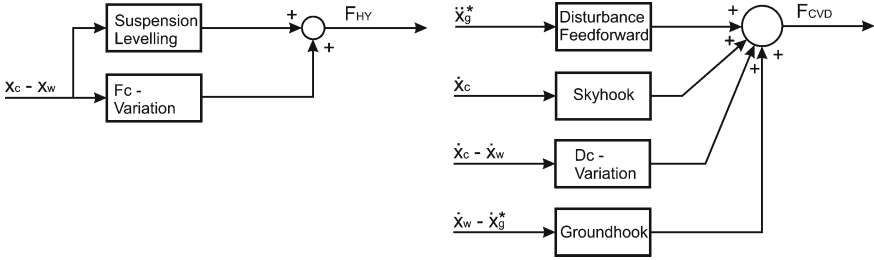
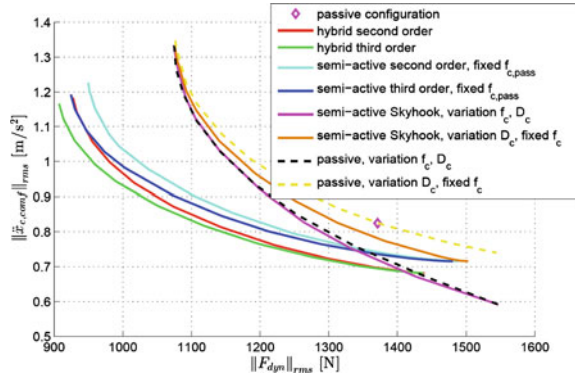


Fig. 11 Control allocation used at the test rig

Fig. 12 Pareto Fronts comparing the potential of passive suspension, semi-active skyhook-controlled with/without variation of main spring stiffness and DFF control concept for hybrid and semi-active suspension



4.2 Pareto-Optimal Parameterization

By numerical optimization the pareto-optimal parameterizations of the global controller and disturbance feedforward control are determined regarding the trade-off between ride comfort and ride safety. The generated pareto fronts can be compared regarding the potential of each suspension system in combination with the control concept. Figure 12 shows the curvatures for passive suspension, skyhook-based control with (active) and without (semi-active) additional varying of spring stiffness and for the presented concept with feedforward disturbance compensation. For fixed spring stiffness the semi-active implementation of the skyhook concept offers slight comfort benefit, which almost vanishes when stiffness is varied as the skyhook concepts gains comfort at the expense of ride safety. Compared to these curvatures the semi-active implementation of the DFF in combination with the mentioned global control algorithms offers a huge potential for reducing wheel load deviations and thus improving traction of the vehicle. A further variation of spring stiffness by the spring mount adjustment offers some additional benefits in ride comfort and safety. For both, the semi-active and the active case, five controller parameterizations varying between focus on comfort to

Fig. 13 Quarter-car test rig based on the front suspension of an upper class sedan extended with the hybrid suspension strut



full safety-focus are picked and their performance is validated under realistic conditions at the quarter-car test rig.

5 Experimental Results at the Test Rig

5.1 Quarter-Car Test Rig

The test rig is based on the front suspension of a current upper class sedan. The original continuously variable damper is used as well as wishbones, bump stops and wheel. So this test rig allows the validation of the designed control concepts in a realistic framework including all vertical nonlinearities and dynamic effects. The damper has two current-driven valves to independently adjust rebound and compression behavior within the characteristics shown in Fig. 13. Beyond the semi-active variable damper system the suspension has been equipped with a spring mount adjustment in series to the main spring allowing the realization of active forces. Due to energy consumption constraints the bandwidth of the active actuator can be limited to a certain value, which is chosen to be 12 Hz here.

5.2 Experimental Results

At the test rig the road cannot be sampled in advance. Thus a first run with the desired road profile excitation and disabled DFF is done and the distance between chassis and wheel is measured by the laser distance sensor and recorded together with the occurring chassis acceleration. Then the road profile acceleration can be calculated online at the second run pretending that the chassis-road-distance measurement signal is known 1 m ahead.

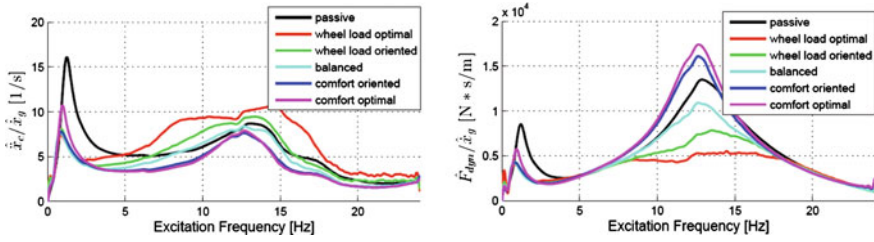


Fig. 14 Amplification functions at the test rig for excitation with a chirp signal

For the analysis of resulting amplification functions the quarter-car is excited with a chirp signal. For best results, frequency change rate and amplitude of the excitation is adopted to the four different areas of the two eigenfrequencies, in between and the high frequency part. As Fig. 14 shows, the five different parameterizations of the controller enable a smooth adaptation to the desired dynamic behavior focus or the excitation conditions. The wheel load optimal configuration completely flattens the wheel eigenfrequency peak for the dynamic wheel loads amplification function, but at the expense of significantly higher amplification beyond the chassis eigenfrequency. The balanced setting outperforms the passive suspension at both chassis and wheel eigenfrequency for dynamic wheel load, while being below the passive suspension from chassis eigenfrequency up to 8 Hz and then following the passive amplification function for chassis acceleration. The dynamic behavior of the comfort optimal setting resembles the comfort oriented parameterization, which has the lowest chassis acceleration amplification, while allowing more wheel load deviations at wheel eigenfrequency and realizing less at chassis eigenfrequency area. Suspension deflection are only slightly increased for some configuration.

Finally the concept is validated using the real road profile of a bad country road. The measurement results of the controlled suspension in comparison to the original passive configuration are given in Table 1. In the semi-active case (no variation of spring stiffness) dynamic wheel load reductions of 19.9 % are possible almost without decreasing comfort (-0.6 %) for a wheel load-oriented parameterization, while the comfort-oriented controller still improves safety by 8.6 % with an additional benefit of 12.8 % in comfort. For the hybrid configuration allowing the manipulation of stiffness between chassis and wheel the DFF concept the occurring wheel load deviations are further reduced up to 29.2 % with a small loss of comfort or by 27.5 % with an additional benefit in comfort of 14.8 %. The comfort-oriented configuration leads to an improvement over 30 % for chassis acceleration, while still keeping 12 % of dynamic wheel load reduction. Suspension deflections are significantly reduced for all configurations due to the positive effects of the skyhook algorithm effectively damping the chassis movements at its eigenfrequency.

Table 1 Experimental results for the excitation with the road profile of a bad country road

Semi-active	Passive	w.opt	w.ori.	bal.	c.ori	c.opt
$\ \ddot{x}_{c,conf}\ _{rms}$ in m/s^2	1.29	1.50	1.29	1.19	1.12	1.10
Benefit vs. passive	–	–16.5 %	–0.6 %	7.6 %	12.8 %	14.4 %
$\ F_{dyn}\ _{rms}$ in N	1,319	1,044	1,056	1,112	1,205	1,275
Benefit vs. passive	–	20.8 %	19.9 %	15.6 %	8.6 %	3.3 %
Min(x_{cw}) in cm	8.7	7.8	7.6	7.6	7.6	7.7
Benefit vs. passive	–	10.2 %	11.9 %	12.4 %	12.8 %	11. %1
<i>Hybrid</i>						
$\ \ddot{x}_{c,conf}\ _{rms}$	1.29	1.33	1.10	0.98	0.90	0.91
Benefit vs. passive	–	–3.4 %	14.8 %	24.1 %	30.5 %	29.1 %
$\ F_{dyn}\ _{rms}$	1,319	933	955	1,023	1,160	1,249
Benefit vs. passive	–	29.2 %	27.5 %	22.4 %	12.0 %	5.3 %
Min(x_{cw}) in cm	8.7	7.2	7.2	7.1	7.3	7.9
Benefit vs. passive	–	17.5 %	17.8 %	18.3 %	16.4 %	8.5 %

6 Conclusion

This paper proposes a wheel load oriented suspension control with a wheel load optimal disturbance compensation using road profile information gained by sampling the road underneath the vehicle in front of the wheel. From the equation of motions of the wheel a feedforward control algorithm for zero wheel load deviations is derived. The potential is analysed in combination with a global controller for the semi-active and active case showing possible traction improvements of up to 40 % reduction of dynamic wheel load deviations or offering comfort improvements of up to 30 % while keeping ride safety of a passive suspension. Experimental validation of the control concept at the test-rig with numerically optimized parameters showed significant improvements in the wheel load amplification function and a wheel load reduction of almost 20 % was possible without decreasing comfort in the semi-active case. Implementation for the hybrid suspension concept, combining an slow-active spring mount adjustment and the continuously variable damper eased the conflict between comfort and safety by simultaneously reducing dynamic wheel load rms-value by 28 % and chassis acceleration values by 14.8 % compared to the passive suspension system.

References

1. Heiing B, Ersoy M (2010) Chassis handbook: fundamentals, driving dynamics, components, mechatronics, perspectives. Vieweg + Teubner Verlag, 2010
2. Wong JY (2008) Theory of ground vehicles. Wiley, Hoboken
3. Mitschke M, Wallentowitz H (2004) ‘‘Dynamik der Kraftfahrzeuge‘‘. Springer, Wiesbaden

4. Koch G, Spirk S, Lohmann B (2010) Reference model based adaptive control of a hybrid suspension. In: Proceedings of the IFAC symposium advances in automotive control, Munich, Germany
5. Koch G, Spirk S, Pellegrini E, Pletschen N, Lohmann B (2011) Experimental validation of a new adaptive control approach for a hybrid suspension system. In: Proceedings of the 2011 American control conference, San Francisco, USA
6. Spirk S (2012) Adaptive Regelung aktiver Fahrwerke. Diplomarbeit. Bachelor + Master Publishing, Hamburg
7. Koch G, Fritsch O, Lohmann B (2008) Potential of low bandwidth active suspension control with continuously variable damper. In: Proceedings of the 17th IFAC world congress, Seoul, Korea
8. Spirk S, Koch G, Lohmann B (2011) Improving suspension control with an optimal control component and disturbance compensation. In: 18th IFAC world congress, Milano, Italy
9. Matschinsky W (1998) Road vehicle suspensions. Wiley, Hoboken
10. ISO 2631-1 (1997) Mechanical vibration and shock—evaluation of human exposure to whole-body vibration. International Standard Organization
11. Streiter R (2008) Active preview suspension system—ABC Prescan in the F700. ATZ worldwide eMagazines, Vieweg + Teubner, Wiesbaden
12. Guglielmino E, Sireteanu T, Stammers CW, Ghita G, Giuclea M (2008) Semi-active suspension control: improved vehicle ride and road friendliness. Springer, London

Part III
Engine Vibration and Noise Control

Optimization of the Range Extender Mounting System for Electric Vehicle

Yutao Luo and En-ming Lai

Abstract In this chapter, the mounting system of a range extended electric vehicle is studied. The energy decoupling method and the stiffness matrix method is applied. The optimization calculation of the range extender mounting system is carried out in MATLAB and ADAMS, and the results show that there is good consistency between them. Energy decoupling method is well known to decouple the engine mounting system. The energy distribution of dominant vibration is selected as the objective function under stiffness and natural frequency constraints. The traditional optimal algorithms such as sequential quadratic programming and genetic algorithms are adopted in the energy decoupling optimization for the range extender mounting system. Both optimal coordinates of installation location and best stiffness values are achieved through genetic algorithm method and sequential quadratic programming method. Consequently, the result calculated by genetic algorithm is considered as the final result of energy decoupling method, because genetic algorithm is a global optimum algorithm but sequential quadratic programming is not. The optimum results show that the energy decoupling of genetic algorithms and stiffness matrix method are reliable and accurate. However, the energy decoupling method based on genetic algorithm will be better. A reliable basis is provided for the further optimization design of engine mounting system.

Keywords Mounting system · Genetic algorithm · Decoupling · Optimization

F2012-J03-001

Y. Luo (✉) · E. Lai
School of Mechanical and Automotive Engineering, South China University of Technology,
Guangzhou, 510641, P. R. China
e-mail: laienming@gmail.com

1 Introduction

The consumption of petroleum energy has been accelerated by the rapid increase in the number of cars, which brings pressure to bear on general global energy crisis. In order to cope with the environment issues and global energy crisis, a series of energy saving technologies have been developed for vehicles [1]. As the new energy policies getting mature, the industrialization of new energy vehicle is speeding up in China. However, limited range and high expenses on batteries have always been the main barriers of the popularization of electric vehicles. On this background, range extended electric vehicle has great market potential with its advantages of extended range and lower expenses on batteries. Range extended electric vehicle means that when the battery is enervated to the floor threshold, the range extender will automatically start to provide electricity power further and extended the range up to an additional hundreds of kilometres. In this way, the range anxiety of the electric vehicle drivers can be effectively relieved and the costs are significantly lowered because the battery capacity of range extended electric vehicle can be reduced to around 40 % of that in pure electric vehicles. Obviously, range extended electric vehicle has advantages over other new energy vehicle in several aspects, such as energy efficiency, price and convenience.

A certain type of range extended electric vehicle which based on the improvement of the Trumpchi is the research object in this chapter. The range extender which includes a small engine and a generator has replace traditional gasoline engine and be attached to the frame by mounting system. The engine is not only the power plant but also the source of vehicle vibration. The vehicles often need engines work in the optimum consumption-zone which means high speed and causes large noises especially hybrid vehicle. The isolation of mounting system plays a significant role in the structure-born noise when the range extended vehicle is in range extended condition. So it is necessary for the mounts of the range extended vehicle to be taken an optimization. Therefore, how to minimize the vibration from the engine to the chassis is the key technical of isolation and optimization of mounting system. The ideal mount should have the property that small stiffness and damping in low-frequency or large stiffness and damping in high-frequency.

Professor Xu discusses the relationship among the theoretical basis, isolation and decoupling of engine vibration simplified model and optimal decoupling method which is more suitable for computer through the method based on function of transfer rate in mount optimization design [2]. The energy decoupling method was adopted to optimize the stiffness of mountings by Professor Yan and Professor Xu. Further-more, they achieve the decoupling rate according to the energy distribution of engine mounting system. In addition, the energy distribution of dominant vibration was selected as objective function under the natural frequency constraints [3]. An optimization model, in which the minimal force transferred to chassis is taken as objective function and stiffness of mounting system is taken as variable, is established and recursion secondary programming is used to solve the problem by Swanson [4]. An optimization model, in which the minimal force

transferred to floor is taken as objective function with the constraint that keep mount in an especial range of deformation by Tao [5].

In this chapter, the essential technique for optimization of the range extender mounting system through an example of range extended electric vehicle is studied. And by the principle of optimization technology, an optimization model with constraint of stiffness and the natural frequency was set up which aimed to improve the decoupling rate in all directions. In addition, the optimization model, in which the mount stiffness and the installation location are taken as variables, is figured out by energy decoupling method and stiffness matrix method. The result shows the optimization of range extended electric vehicle is effective through comparing the two methods.

2 Establishment of Range Extender Mounting System Vibration Model

It is necessary to establish the mechanical model and mathematical model in the optimization of mounting system design. From the isolation of engine perspective, the natural frequencies of aero elastic system which consists of engine and mounts system are mainly in the 5–30 Hz frequency range, and far below than the minimum order vibration of elastic bending modal frequency [6]. Therefore, when the isolation range extender mounting system is analysis, the engine and generator are regard as rigid bodies, and its vibration is ignored. Because the torsion flexibility is very small, it could be simplified to three spatial axial flexibility damper in the progressing [7].

The simplified range extender system has six degrees of freedom includes x translation, y translation, z translation, x rotation, y rotation and z rotation. Thus, the system has six natural frequencies and modes of vibration. Figure 1 shows CATIA model of range extender. Based on the above simplified model and relevant parameters, six degrees of freedom dynamic model for range extender is established, as shown in Fig. 2.

3 Optimization of Range Extender Mounting System

The movement and position of range extender which has six degrees of freedom can be described as the three directional translation and rotation of the centre of the mass. And system's six directional generalized displacement vectors can be represent as follow:

$$\{X\} = \{x \ y \ z \ \alpha \ \beta \ \gamma\} \quad (1)$$

The calculational methods for natural frequencies and decoupling rate of the mounting system in this chapter can be referred to the related literature. Beginning with the assumption of little change for the mass parameters of the engine, the

Fig. 1 Range extender model

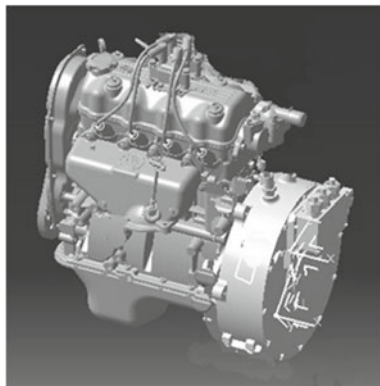
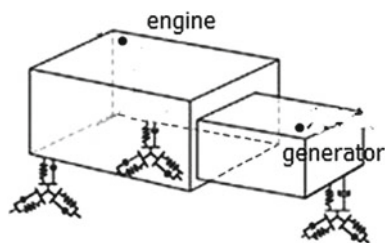


Fig. 2 Range extender simplified model



parameters of mounting system are selected as design variables in the progress of optimization. What's more, the main function of mount system damping which isn't usually selected as optimal variable and hard to control in production is to reduce the peak value of resonance area. However, installation angle as main parameter has not used as design variable because of the structure problem. Therefore, the stiffness of mounts and installation locations are considered as the design variables in optimal progress finally.

3.1 Optimization Based on Energy Decoupling Method

Energy decoupling method as the most commonly utilized method for decoupling is often used to decouple the range extender mounting system, and the calculational method for energy distribution can be referred to the related literature. If energy decoupling method is used in optimization, the modal parameters can be obtained just through the free vibration. Furthermore, this approach has universal application for range extender mounting system design. In any case these parameters can be adjusted in original position without limitation of engine types and space.

3.1.1 Establishment of Objective Function

Six degrees of freedom decoupling rate are selected as the objective function under stiffness and the natural frequency constraints, and vertical vibration and crankshaft rotation directions are the main directions of decoupling. Both optimal coordinates of the installation locations and best stiffness values are achieved through genetic algorithms and sequential quadratic programming.

For the range extender simplified model, the percent of kinetic energy of k-generalized coordinates can be represented as follow

$$r_k^j = \frac{E_k^j}{E_{total}^j} \times 100 \% \quad (2)$$

where E_{total}^j is total kinetic energy of range extender mounting system. E_k^j is the kinetic energy which acts on the k-generalized coordinates, r_k^j represents decoupling level in the k direction of mounting system [8]. If the value of E_k^j is relatively large, it means that the system movement under the jth vibration mode is dominated by the k though generalized coordinate vector's mode type, and it indicates that the system energy decoupling level is high.

When the decoupling in one direction reaches 100 %, this direction can be considered full decoupling. Thus, the objective function could be defined as follow:

$$\min F(x) = \sum_{i=1}^6 \omega_j (100 - \max(\gamma_k^j)) \quad (3)$$

where j is the order of vibration, r_k^j represents decoupling level in the k direction of mounting system. ω_j is the weighting factor. By changing the weight coefficients transforming the multi-objective problem into a single-objective one. Based on the practical situation of mounting system, the weighting factor of vertical vibration and crankshaft rotation directions should be larger than other directions in order to achieve the better decoupling effect.

3.1.2 Establishment of Constraints

Mounting optimization constraints are mounting installation position, installation angle, mounting stiffness and so on. In this chapter, the stiffness and position of mounting part along the principal elastic axle is selected as the optimization, and the angel is supposed to be a constant value. The minimum natural frequency should be higher than half order excitation frequency of engine idle, or else it will cause vibration in low frequency. According to vibration isolation theory, the maximum natural frequency should be lower than the 0.707 times lowest exciting frequency. On the other hand, the natural frequency of crankshaft rotation direction should be lower than the half lowest exciting frequency. In general each natural frequency of system should be in the range of 5 and 25 Hz, and the final frequency constraints are as follow:

$$\begin{aligned}
6 \text{ Hz} &\leq f_x \leq 18 \text{ Hz} \\
5 \text{ Hz} &\leq f_y \leq 15 \text{ Hz} \\
8 \text{ Hz} &\leq f_z \leq 16 \text{ Hz} \\
6 \text{ Hz} &\leq f_{rx} \leq 18 \text{ Hz} \\
6 \text{ Hz} &\leq f_{ry} \leq 18 \text{ Hz} \\
6 \text{ Hz} &\leq f_{rz} \leq 18 \text{ Hz}
\end{aligned} \tag{4}$$

In consideration of actual mounting production, it is necessary to suggest some constraints in mounting design, and the relationships are as follow:

$$\begin{aligned}
l_{uwi} &\leq \frac{ku_i}{kw_i} \leq u_{uwi} \\
l_{vwi} &\leq \frac{kv_i}{kw_i} \leq u_{vwi} \\
l_{uvi} &\leq \frac{ku_i}{kv_i} \leq u_{uvi}
\end{aligned} \tag{5}$$

where ku_i is the x directional stiffness of i th mount, kv_i is the y directional stiffness of i th mount and kw_i is the z directional stiffness of i th mount. In general, the maximum displacement of engine should not exceed 10 mm, the angle of crankshaft rotation cannot be greater than six degrees, the lateral displacement of mount should not exceed 2 mm and the vertical displacement should not exceed 5 mm.

3.1.3 Solution Methods

Sequential quadratic programming and genetic algorithm are considered to solve the problem in this chapter. Sequential quadratic programming is an iterative method for nonlinear optimization. Sequential quadratic programming methods are used on problems for which the objective function and the constraints are twice continuously differentiable. On one side sequential quadratic programming only can get local solution, and hardly get global solution. Genetic algorithm is an overall algorithm, it can escape local minima. In the computer science field of artificial intelligence, a genetic algorithm is a search heuristic that mimics the process of natural evolution. Genetic algorithms belong to the larger class of evolutionary algorithms, which generate solutions to optimization problems using techniques inspired by natural evolution.

3.2 Optimization Based on Stiffness Matrix Method

The vibration equation of range extended device can be expressed in moment axes coordinate system as follow:

$$[M_0]\{\ddot{x}\} + [K_0]\{x\} = \{P_0\} \tag{6}$$

where, $[M_0]$ is the quality matrix of system, $[K_0]$ is the stiffness matrix of system, $\{P_0\}$ is the exciting force which system suffering. The quality matrix $[M_0]$ can be obtained through the differential equation using Lagrange approach. Simultaneously, the stiffness matrix $[K_0]$ is also be obtained by the same method [9]. In order to remove the inertial coupling, it is necessary to switch the vibration equation in moment axes coordinate system to vibration equation in principle axes coordinate system. The vibration equation in principle axes coordinate system is as follow:

$$[M_1]\{\ddot{x}\} + [K_1]\{x\} = \{P_1\} \tag{7}$$

$$M_1 = [T]^T[M_0][T] \tag{8}$$

$$K_1 = [T]^T[K_0][T] \tag{9}$$

$$P_1 = [T]^T[P_0][T] \tag{10}$$

where $[T]$ is transformation matrix, $[M_1]$ is a diagonal matrix.

$$[M_1] = \begin{bmatrix} m & & & & & \\ & m & & & & \\ & & m & & & \\ & & & J_{X1} & & \\ & 0 & & & J_{Y1} & \\ & & & & & J_{Z1} \end{bmatrix} \tag{11}$$

The stiffness matrix is given after the coordinate transformation. When all off-diagonal elements of stiffness matrix are equal to zero, it can be regard as full decoupling. Therefore, the absolute off-diagonal elements should be designed as small as possible in order to decouple. This method which we called the stiffness matrix method provides the objective function as follow:

$$J_i = (\sum_{j=1}^6 k_{ij}^2 + \sum_{i=1}^6 k_{ji}^2) / k_{ii}^2 \quad i \neq j$$

$$J = \sum_{i=1}^6 w_i J_i \tag{12}$$

where w_i is the weighting factor. The constraints of stiffness matrix method would be similar to the energy decoupling method.

Table 1 Energy matrix calculated by MATLAB and ADAMS

Directions		X	Y	Z	RX	RY	RZ
Frequency (Hz)	MATLAB	9.6052	5.5619	6.9515	12.0840	14.5646	13.2238
	ADAMS	9.5996	5.6226	7.0265	12.0130	14.5451	13.2860
Decoupling rate %	MATLAB	62.4758	83.7842	56.4729	45.3870	71.3659	54.5292
	ADAMS	61.0500	82.5200	55.6300	43.7200	73.1500	53.7600

4 Optimization Results

4.1 Model Validation Based on ADAMS Simulation

At present, ADAMS is the most prestigious system dynamics simulation software, it can generate virtual prototype of complex mechanical system, and can analysis rapidly and compare the various parameters programme until getting the optimized performance. Thus greatly reducing the expensive physical prototype manufacturing and testing frequency, substantially shorten the product development cycle and cost [10]. In this chapter, range extender is viewed as rigid mass which has six degrees of freedom. Body is also simplified to a rigid mass, mounts are viewed as spring-damper with three axial directions [11]. In addition, the corresponding simulation model is established in software MATLAB and ADAMS, and the result of system energy matrix is calculated as shown in Table 1.

Comparing the results of Table 1, the system energy matrix which is calculated through theoretical analysis and mathematical model established in MATLAB is in consistent with the one calculated by ADAMS simulation model [12]. Both of the two calculated results are only different from each other on percentile about the value of non-damping natural frequencies of system. To evaluate the result, it is verify the operational and validity of model which established in MATLAB through theoretical analysis, which provides guarantee to the correctness of the follow optimization. Besides, all directional decoupling rates are extremely low but y direction according to the energy matrix, which show that it has a bad vibration isolation effect. So it is necessary to optimize the mounting system. Because of the difficult arrangement of mounts, the coordinates are required to change from -10 to 10 mm.

4.2 Analysis of Optimization Results

The traditional optimization such as sequential quadratic programming and genetic algorithms are selected in the energy decoupling optimization for the engine mounting system. The objective function value with sequential quadratic programming is 69.1249, and the objective function value with genetic algorithms

Table 2 Energy matrix calculated by two methods

Directions	X	Y	Z	RX	RY	RZ
Before optimization (%)	62.4758	83.7842	56.4729	45.3870	71.3659	54.5292
Stiffness matrix method (%)	85.6068	93.4132	75.3219	89.8156	77.1082	75.9117
Energy decoupling method (%)	77.2979	87.4758	90.2408	94.0014	77.3722	100

Table 3 The installation locations after optimization

Method	Directions (mm)	Bushing 1	Bushing 2	Bushing 3
Before optimization	X	-116.0940	-111.8850	734.0350
	Y	-292.1210	275.8098	11.4927
	Z	-133.4390	-133.8910	-298.6320
Stiffness matrix method	X	-126.0940	-121.8850	744.0350
	Y	-302.1210	285.8098	21.4928
	Z	-123.4390	-123.8910	-288.6320
Energy decoupling method	X	-126.0937	-121.8850	744.0169
	Y	-302.0468	285.8098	9.5309
	Z	-123.4765	-143.8306	-308.6267

method is 78.0117. Results of the simulation show that the genetic algorithm is more efficient compared with the sequential quadratic programming, because genetic algorithm is a global optimum algorithm but sequential quadratic programming is not. Consequently, the result calculated by genetic algorithm is considered as the final result of energy decoupling method. The stiffness matrix method also gets the desirable result. Comparing the two methods, the result of system energy matrix is calculated as shown in Table 2, the installation locations after optimization are in Table 3, the optimal stiffness of mounts are in Table 4.

It is obvious that each directional decoupling rate are markedly improved according to the energy decoupling method, especially for Z direction, almost non-existent the coupling of one degree of freedom with others, and the natural frequency of Z direction decreased significantly. All the natural frequencies of six modes are less than 30 Hz and decoupling rate are all higher than 75 % which meets decoupling requirement. The result after optimization according to the stiffness matrix method also gets the excellent result. Each directional decoupling rate is more than 75 % which meets design requirement. Comparing the result in Table 2, the decoupling rates of X and Y directions according to the stiffness matrix are larger than the decoupling rate according to the energy decoupling method and the rest directions are opposite. Based on energy decoupling by genetic algorithms method, decoupling rate of crankshaft rotation direction increased from 45.39 to 94 %, decoupling rate of vertical direction increased from 56.47 to 90.24 %. Based on the stiffness matrix method decoupling, decoupling rate of crankshaft rotation direction increased from 45.39 to 89.82 %, decoupling rate of vertical direction increased from 56.47 to 75.3 %. The result indicates that the energy decoupling method base on genetic algorithm will be better. Also each method has its own advantages and disadvantages. The energy decoupling based on genetic algorithm has a primary disadvantage that computational cost increases

Table 4 The stiffness of mounts after optimization

Method	Directions (N/mm)	Bushing 1	Bushing 2	Bushing 3
Before optimization	U	430.0	345.0	200.0
	V	160.0	170.0	120.0
	W	240.0	210.0	270.0
Stiffness matrix method	U	240.0	200.0	100.0
	V	191.0	133.3	80.0
	W	400.0	330.0	195.1
Energy decoupling method	U	240.0	200.1	176.1
	V	207.9	200.2	185.9
	W	342.3	330.0	180.0

greatly for over much evaluation of objective functions and their fitness, which usually results in an abnormal termination of the calculation. Therefore, the stiffness matrix method is also a good choice. The good isolation effect also shows that the optimal design for range extender is effective.

5 Conclusion

In this chapter, the mounting system of a range extended electric vehicle is studied. Both the energy decoupling method and the stiffness matrix method are used for decoupling. Thereby the traditional optimization such as sequential quadratic programming and genetic algorithms are adopted in the energy decoupling optimization for the engine mounting system. MATLAB and ADAMS are conjunct with each other to optimize the engine mounting system. The optimum results show that the energy decoupling of genetic algorithms and stiffness matrix method are reliable and accurate. However, the energy decoupling method will be better. In addition the degree of freedom decoupling problem is being solved after optimization design, and the purpose of isolation is reached.

Acknowledgments This research is sponsored by Chinese National High-tech Project (863) (Grant No: 2012AA110702) and Supported by Program for New Century Excellent Talents in University (Grant No: NCET-11-0157).

References

1. Chan CC (2002) The state of the art of electric and hybrid vehicles. Proc IEEE 90(2):249–275
2. Shian X (1995) The decoupling approach to engine mounting system. Automot Eng 17(4):198–204
3. Hongyu Y, Shian X (1993) The optimization and energy decoupling method of engine mounting system. Automot Eng 15(6):321–328

4. Swanson DA et al (1993) Optimization of aircraft engine suspension systems. *J Aircr* 30(6):979–984
5. Tao JS, Liu GR, Lam KY (2000) Design optimization of marine engine mount system. *J Sound Vib* 235(3):477–494
6. Wenku S et al (2006) Automobile multi-objective optimization design of powertrain mounting system and software development. *J Jilin Univ* 9(5):654–658
7. Zhang Q et al (2008) The study of fuel cell car powertrain mounting system design using MATLAB and ADAMS. In: International conference on computer science and software engineering, pp 1106–1109
8. Cho S (2000) Configuration and sizing design optimization of powertrain mounting system. *Int Veh Des* 24(1):34–37
9. Pang J et al (2006) Automotive noise and vibration: principle and application. Beijing Institute of Technology Press, China
10. Liping C et al (2005) Mechanical system dynamics analysis and the application tutorial of ADAMS. Tsinghua University Press, Beijing
11. Lee DH, Hwang WS (2002) Design sensitivity analysis and optimization of an engine mount system using an based substructuring method. *J Sound Vib* 255:383–397
12. Jianfeng H et al (2011) Multi-objective optimization of hybrid electric vehicle powertrain mounting system using hybrid genetic algorithm. *Appl Mech Mater* 87:30–37

Middle and High Frequency Sound Attenuation Optimization of Air Cleaner

Liang Yang, Xiaohong Kuang, Shuo Zhang and Haiyan Zhang

Abstract According to the spectral characteristics of vehicle intake orifice noise, the dominant noise contribution is identified in the range of frequency 800–1200 Hz. Based on the three-dimensional FEM method, the acoustic performance of the air cleaner is studied. The transmission loss of the air filter with additional chamber is improved in middle and high frequency. The acoustic attenuation of the additional chamber is related to the location and structure parameters. By increasing the cross-sectional area and the height of additional chamber, the acoustic attenuation bandwidth and amplitude are improved. Applied this procedure to the optimization of air cleaner structure, the results testified show that the procedure is reasonable and feasible. It can be applied in air cleaner design to increase the middle and high frequency of transmission loss of air intake systems.

Keywords Air cleaner · Sound transmission loss · Intake noise · Middle and high frequency noise

F2012-J03-002

L. Yang (✉) · X. Kuang · S. Zhang · H. Zhang
Changan Auto Global R&D Center, Chongqing, China
e-mail: sunqiemail@163.com

L. Yang · X. Kuang · S. Zhang · H. Zhang
State Key Laboratory of Vehicle NVH and Safety Technology, Chongqing, China

1 Introduction

Intake system noise of I.C. engine is the main noise source of an automobile. Intake orifice noise has significant impact on sound quality for passenger cars [1]. The primary function of an air cleaner is firstly to filtrate air into the engine, and secondly to minimize intake orifice noise emissions.

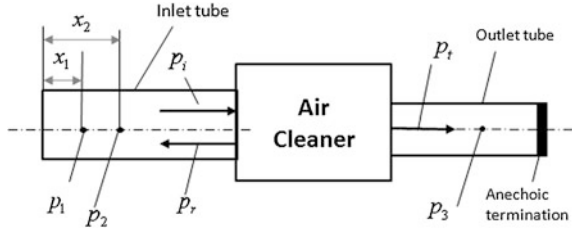
The general method to control intake orifice noise is through combination of air cleaners and intake mufflers which target specific problem frequencies. Appropriate side branch silencers, such as such as quarter-wave resonators, Helmholtz resonator, and so on [2], are usually used to reduce some specific frequency noise while the air cleaner is designed for wide band frequency noise attenuation. Many researchers have been investigating the air intake system noise mechanism and control methods. Eric P. Trochon [3] developed a silencer based on a combination of a Herschel-Quincke tube and two quarter-wave resonators to reduce the high frequency intake noise of turbocharger. I. J. Lee et al. [4] developed a multi-chamber parallel structure of Helmholtz resonator to suppress the turbocharger whoosh noise. PU Da-yu et al. [5] investigated acoustic attenuation by placing absorptive material in the air cleaner where transmission loss of the air cleaner is improved greatly in middle and high frequency ranges, however, it is difficult to guarantee reliability of the sound-absorptive material and its application. Mufflers with added side branch resonators increase sound attenuation effectiveness at middle and high frequency range, but the package of air intake system is difficult. The sound attenuation characteristics for quarter waver relates to a system structure. The higher the ratio between quarter waver section area and the main tube section area, the wider the sound attenuation. The attenuation magnitude is determined by its length. The quarter waver is usually used to attenuate noise above 300 Hz.

This chapter investigates a new intake system where a big section area and short length tube called additional chamber is added to the air cleaner box by Finite Element Analysis. The aim of the case study is to reduce high intake orifice noise of a passenger car. It is extremely difficult to package side branch resonators due to space limitation of the engine compartment. Sound attenuation of the air cleaner is optimized by adding an additional chamber on the air cleaner box. The tested results show that the orifice noise is significantly reduced at middle and high frequency range.

2 Analytical Approach

The air cleaner is composed of plastic box and filter element. The air cleaner is usually regarded as an expansion muffler, so its acoustics performance can be evaluated using traditional expansion muffler evaluation method. Transmission Loss (TL) is an important index to evaluate the acoustic attenuation of a muffler.

Fig. 1 Sound transmission loss analytical model



TL is only related to air cleaner structure, and independent from sound source and orifice sound radiation, which makes it easy to be analyzed theoretically.

Assume that only plane wave propagates in the tubes of air cleaner, the transmission loss can be expressed as follow,

$$TL = 10 \lg \frac{W_i}{W_t} = 20 \lg \left| \frac{P_i}{P_t} \right| + 10 \lg \frac{S_1}{S_2} \tag{1}$$

where W_i and W_t denote sound power levels of incident wave and transmitted wave, respectively; P_i and P_t denote sound pressure levels of incident wave and transmitted wave, respectively; S_1 and S_2 denote the sectional areas of inlet and outlet tubes, respectively.

An anechoic termination is used at the end of the air clear outlet, i.e., all incident wave are absorbed and no reflective wave exists, shown in Fig. 1. p_1 and p_2 are the sound pressures at two points (x_1 and x_2) in the inlet tube. p_3 is the sound pressure at outlet tube. p_i and p_r are the incident pressure and reflective pressure respectively, p_t is the transmitted pressure. x_1 and x_2 are the distances between locations at p_1 , p_2 and the inlet orifice location, respectively. p_1 , p_2 and p_3 can be expressed as follows

$$\begin{cases} p_3 = p_t \\ p_1 = p_i e^{-jkx_1} + p_r e^{jkx_1} \\ p_2 = p_i e^{-jkx_2} + p_r e^{jkx_2} \end{cases} \tag{2}$$

Solving Eq. 2, p_i , p_r and p_t can be written as

$$\begin{cases} p_t = p_3 \\ p_i = (p_1 e^{jkx_2} - p_2 e^{jkx_1}) / 2j \sin k(x_2 - x_1) \\ p_r = (p_1 e^{-jkx_2} - p_2 e^{-jkx_1}) / 2j \sin k(x_1 - x_2) \end{cases} \tag{3}$$

The TL of a given air cleaner can be evaluated by the Eqs. 1 and 3, when the sound pressures p_1 , p_2 and p_3 are obtained. In this chapter, the air cleaner's TL can be calculated by using 3D FE method and by calculating the sound pressures at nodes of the air cleaner.

3 Sound Transmission Loss Analysis of Air Cleaner with Additional Chamber

The influence of an additional chamber added to the air cleaner on sound attenuation of middle and high frequency range will be explained. Figure 2 is a scheme of the air cleaner with the additional chamber. Assume that the air cleaner and the additional chamber are cuboids. The inlet and outlet tubes which have the same diameters are installed at front and rear sides of the air cleaner. The additional chamber is installed on the center points of other sides, respectively. The influence of the air filter is neglected.

3.1 Influence of the Additional Chamber Locations

To study the sound attenuation characteristics of the additional chamber located in the different surfaces of the air cleaner, the geometrical parameters of the air cleaner and the additional chamber are fixed, shown in the Table 1. The additional chamber positions are located in the center of the six surfaces of the air cleaner, respectively. Figure 3 shows three FEM modes for different locations of the additional chamber on the air cleaner.

Figure 4 shows the TL results of the additional chamber located on the up and down surfaces, respectively. The sound attenuations for the both cases are magnified obviously in the range of frequency 700–900 Hz compared with the base line. Figure 5 shows the TL results of the additional chamber located on the front and rear surfaces, respectively. The sound attenuations for these two cases are magnified obviously in the range of frequency 800–1100 Hz compared with the base line. Figure 6 shows the TL results of the additional chamber located on the left and right surfaces respectively. The sound attenuation is decreased obviously in the range of frequency 800–1000 Hz compared with the base line, but the TL amplitudes of the additional chamber located on the left and right surfaces have some difference.

3.2 Influence of the Additional Chamber Structure Parameters

To study the sound attenuation characteristics of the additional chamber with different height (h) and cross-sectional area ($l \times d$), The geometrical parameters of the air cleaner are fixed as shown in the Table 1. During the analysis process, firstly, the structure parameter h is changed to 10, 30, 60 and 80 mm alternatively, while keeping the length l and the width d at 100 mm; secondly, the structure parameters l and d are changed to 45, 100, 130 and 175 mm alternatively, while keeping the height h at 30 mm.

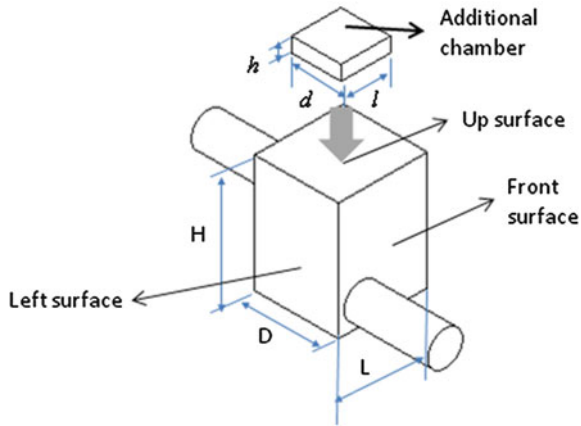


Fig. 2 Structure diagram of air cleaner with additional chamber

Table 1 Structure parameters of analytical model unit: mm

Air cleaner			Inlet and outlet tubes		Additional chamber	
Length (L)	Width (D)	Height (H)	Radius (r)	Length (l)	Width (d)	Height (h)
180	170	240	35	100	100	30

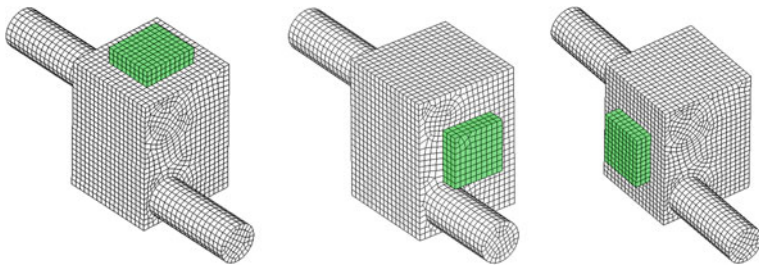


Fig. 3 FEM model of the air cleaner with the additional chamber

Fig. 4 TL comparison for up and down surfaces

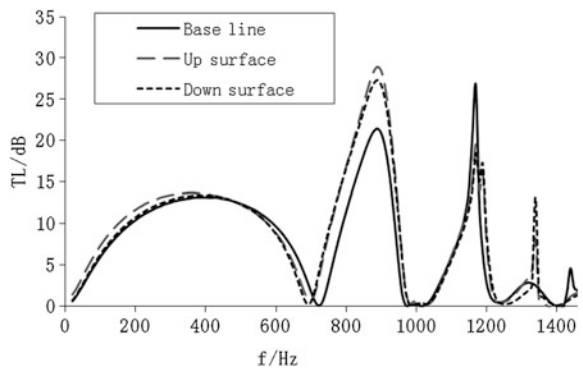


Fig. 5 TL comparison for front and rear surfaces

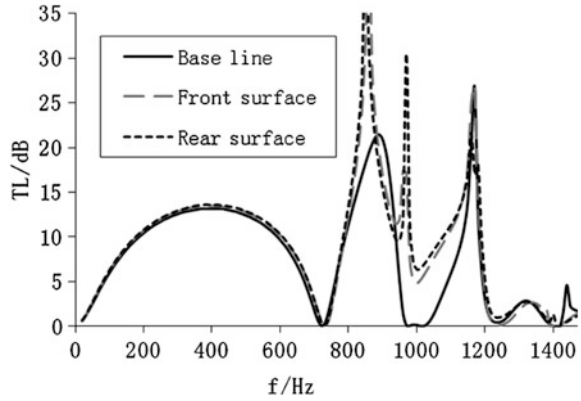


Fig. 6 TL comparison for left and right surfaces

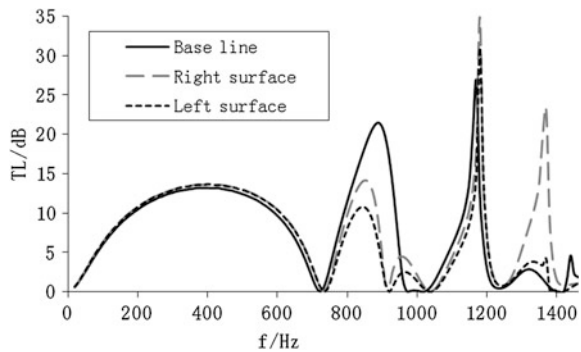


Fig. 7 TL comparison for different heights

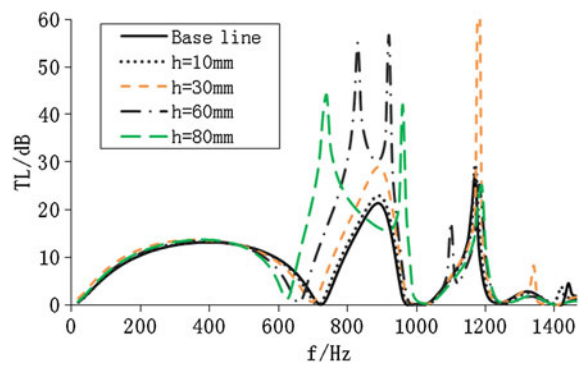


Figure 7 shows the TL results of the additional chamber with different heights. The acoustic attenuation bandwidth in middle and high frequency is magnified with increase of height compared with the base line. Figure 8 shows the TL results of the additional chamber with different cross-sectional areas. The acoustic

Fig. 8 TL comparison for different sectional areas

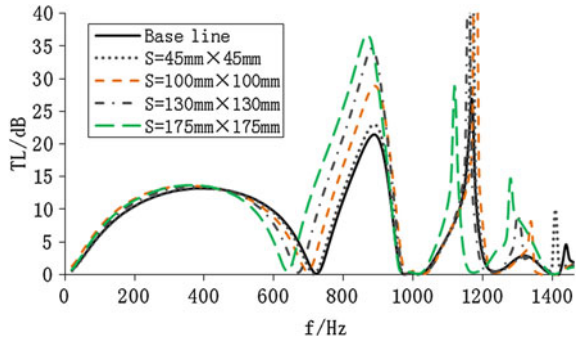
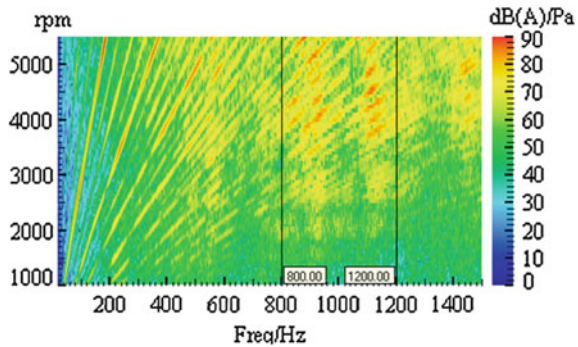


Fig. 9 Spectrum of intake orifice noise



attenuation bandwidth and amplitude in middle and high frequency is magnified with increase of cross-sectional area compared with the base line.

4 Optimization of the Air Cleaner Structure

Figure 9 shows the spectral characteristics of the intake orifice noise, which is tested at run up condition for a passenger car. The dominant noise contribution is identified in frequency range of 800–1200 Hz by filtering analysis. A band stop filter is applied to analyze the noise contribution of 800–1200 Hz. Figure 10 shows the differences of sound pressure levels of the intake orifice noise for original data and filtered data. The data shows noise in middle and high frequency is the major contribution at 2500 rpm. The TL calculated result shows that the sound attenuation of the intake system is low in frequency range of 800–1200 Hz. Based on the layout of the intake system, the air cleaner with the additional chamber ($l = 125$ mm, $d = 105$ mm, $h = 26$ mm) is applied. Figure 11 shows the comparison of original and optimized structures. The TL is improved obviously in the range of frequency 800–1200 Hz, shown as Fig. 12.

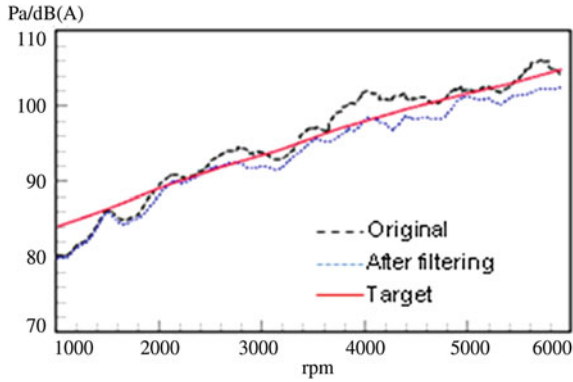


Fig. 10 SPL comparison for original and filtered cases

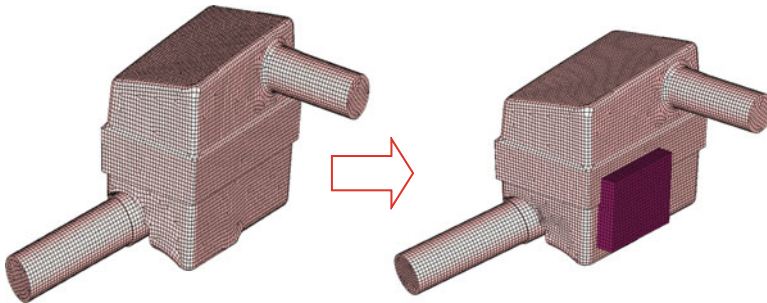


Fig. 11 FEM model of original and optimized air cleaners

Fig. 12 Comparison of TL analyzed results

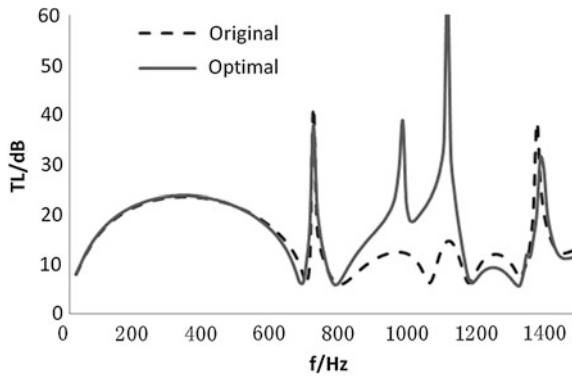


Figure 13 shows the air cleaner prototype. The TL of the air cleaner prototype is tested and verified by an acoustic impedance tube. The measurement setup is shown in Fig. 14. The tested results of original and optimized air cleaners are shown as Figs. 15 and 16.

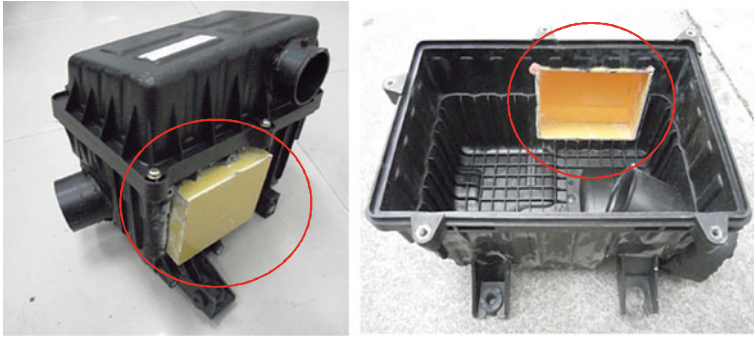
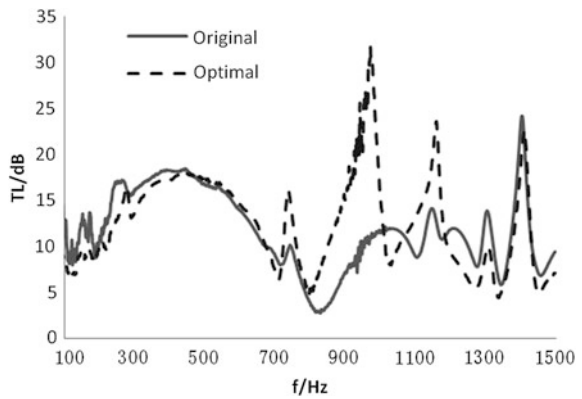


Fig. 13 Prototype of optimized air cleaner

Fig. 14 TL measurement setup

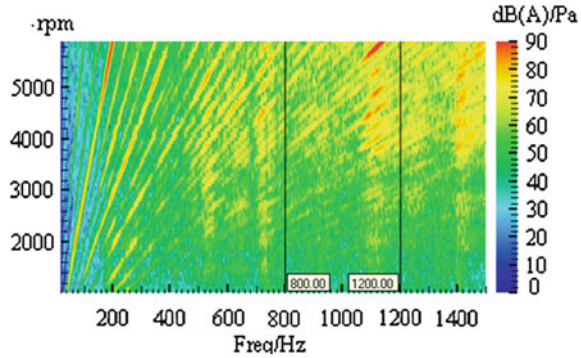


Fig. 15 Comparison of TL tested results



The TL in the frequency range between 800 and 1200 Hz of the air cleaner with the additional chamber is significantly increased, which is consistent with the analytical results. The method effectively increases noise reduction effectiveness in middle and high frequency ranges. The tested intake orifice noise spectrum shows that the orifice noise is significantly reduced from 800 to 1200 Hz, shown in Fig. 15.

Fig. 16 Spectrum of intake orifice noise for optimal air cleaner



5 Conclusions

To reduce intake orifice noise in middle and high frequency ranges, a new type of air cleaner structure with high noise attenuation performance is presented. The basic conclusions are summarized below:

- (1) The acoustic attenuation of the additional chamber is influenced by location and structure parameters. The case analyzed in this paper shows that the sound attenuation of the additional chamber located on symmetrical surfaces is the almost same. The positions located on the up, down, front and rear surfaces provide a good sound attenuation effectiveness while the positions located on the left and right surfaces have negative results for sound attenuation in middle and high frequency ranges.
- (2) The acoustic attenuation of the additional chamber is related to the parameters. By increasing cross-sectional area and the height of the additional chamber, the acoustic attenuation bandwidth and amplitude are improved.

The analyzed and tested results show that the new type of air cleaner structure is reasonable and feasible for engineering application, which can be used to increase the sound attenuation of air cleaner system at middle and high frequency range.

Acknowledgments The authors gratefully acknowledge Dr. Pang Jian for his encouragement and guidance of during the writing of this paper.

References

1. Pang J, Shen G, He H (2006) Automotive noise and vibration—principle and application. Beijing Institute of Technology Press, Beijing
2. Hao Z-Y, Jia W-X, Fang F (2005) Virtual design and performance prediction of a silencing air cleaner used in an I.C. engine intake system. *J Zhejiang Univ Sci* 6(10):1107–1114
3. Trochon EP (2001) A new type of silencers for turbocharger noise control. SAE: 2001-01-1436

4. Lee I.J, Selamet A, Kim H (2009) Design of multi-chamber silencer for turbocharger noise. SAE: 2009-01-2048
5. Pu D-Y, Zuo Z-X, Feng H-H et al (2009) Investigation on absorptive material placement in air cleaner. J Vibr Shock 28(2):178–180

NVH Performance Optimization of Cylinder Head in Concept Stage

Zhanhui Li, Lei Zhang, Xiaoyu Ai, Fengqin Li and Yongjiang Xu

Abstract Cylinder head with good concept design provides possibility for excellent NVH performance of engine. In order to achieve this, NVH function of cylinder head should be taken into account at concept stage to make sure a good foundation for late stage of engineering. In this chapter, at concept stage of engine development, designs of three different cylinder heads such as global architecture, water jacket, bolt number, bolt position and ribs in different sections are evaluated and compared. In this way, good designs and weaknesses are separated and sorted out in views of NVH. Along with these good designs, one head design of these three is rebuild and recalculated by means of simulation. Results show good NVH improvement of modes and responses and eventually proved the validity of designs. By the research in this chapter, firstly, the NVH performance of production has been improved. Secondly, reasonable structure characteristics of cylinder head are obtained which could be a part of cylinder head design database in view of NVH. And one creditable simulation working flow, by use of mode analysis method and structural attenuation method, for improving cylinder head NVH performance in engine concept development stage is established as well.

Keywords Cylinder head · Concept design · NVH · Structure characteristics

F2012-J03-004

Z. Li (✉) · L. Zhang · X. Ai · F. Li · Y. Xu
Powertrain Global R&D Center of Changan Automobile Co. Ltd, Chongqing, China
e-mail: sunqiemail@163.com

1 Introduction

Cylinder head suffers from gas forces and valve forces (see Fig. 1). From the point of view of radiation noise, heads contributes little to overall structure borne noise thanks to its small surface. However, head is the main path of excitation to main contributors such as cam cover, intake manifold, exhaust manifold, timing cover and so on. This means weak head design will causes significant NVH problems such as high level vibrations and noise radiation, even reliability problem. Therefore, it makes sense to design cylinder head with good NVH performance which not only influence itself, but also links to other components.

Normally, cylinder head design can be classified in global design and local design. Local design (or detailed design sometimes) decides the local stiffness behavior of structure. Normally, changes on local structure is more possible in engineering development phase (concept phase, layout phase and detailed phase) because it won't influence project too much. Compared to local design, global design decides the overall NVH behavior such as head global bending stiffness, global torsion stiffness. In some way of view, good cylinder head global design is precondition of good cylinder head NVH performance. In engineering, global design must be defined and frozen at early concept stage because it directly links to other components and aspects. Therefore, how to design the head structure in global with good NVH at concept phase is the key to finally achieve good engine NVH performance.

In order to achieve this purpose, in this chapter, one cylinder head of ongoing engine development project is involved and another two existing heads are used as reference to compare the structure characteristic and guide designs. Considering the lack of prototype at concept, this chapter proposed simulation method including mode analysis and structural attenuation for research work.

2 Objects

The objects are three cylinder heads as shown in Fig. 2, which are from four-stroke, in-line three-cylinder gasoline engines. Head A adopts GDI and TC technology, head B and C are from natural aspirated engines. These three head adopts the same valve train layout strategy. That means the structure of three heads is somehow comparable and the designs of head B and C could be the guidance for head A.

Main parameter is shown in Table 1.

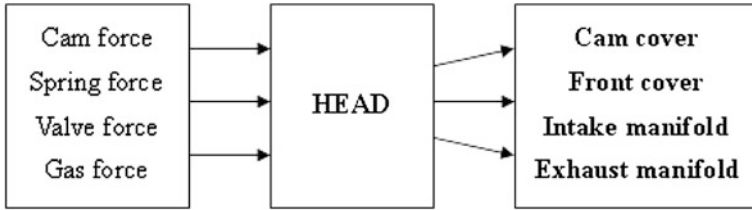


Fig. 1 Head as energy transfer path

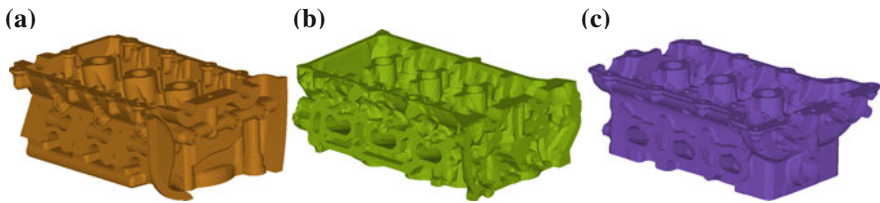


Fig. 2 Three cylinder heads. a Head A. b Head B. c Head C

3 Mode Results Comparison and Design Review

3.1 Head Mode Comparison

As we know, component with high stiffness could avoid significant response due to structure resonance and provides better NVH potential. In order to understand the stiffness of head A, mode analysis method is used and another two head are calculated as well to compare to head A.

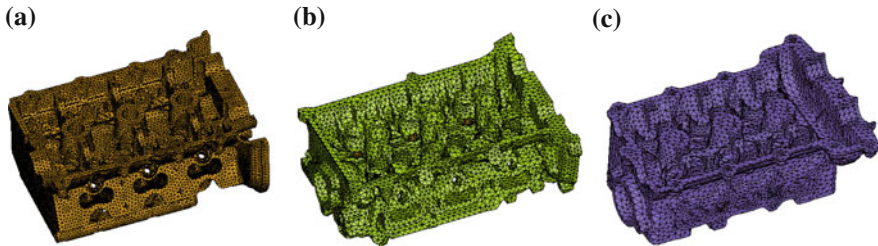
Figure 3 shows finite element of head A, B and C. The node numbers of these three models of head A, B and C is 187,694, 122,335 and 131,800 respectively.

Table 2 shows the global mode results of three heads. Results shows (1) head C achieves highest torsional frequency of 2,056 Hz and head A and B owns almost same torsional frequency of about 1,590 Hz. (2) head C achieves highest vertical bending frequency of 3,393 Hz and frequency of head A is lower and then head B. (3) Head A achieves highest horizontal bending frequency of 3,274 Hz and frequency of head B at third place and head C in between.

In conclusion, the stiffness of head C is better than head A and B. Head A shows good stiffness in horizontal direction but poor torsional and vertical bending stiffness.

Table 1 Parameter of heads

	Bore diameter in mm	Spacing in mm	Valve seat diameter at Int./Ex. in mm
Head A	72	80	28/26
Head B	73	81	28/24
Head C	66	72	25/22

**Fig. 3** Heads FE model. **a** Head A. **b** Head B. **c** Head C**Table 2** Heads modal result

Mode	Head A (Hz)	Head B (Hz)	Head C (Hz)
Torsion	1,594	1,592	2,056
Vertical bending	2,540	2,485	3,393
Horizontal bending	3,274	2,988	3,121

Table 3 Dimension and mass of heads

	Head A	Head B	Head C
Mass/kg	7.57	7.31	4.73
Length \times width \times height/mm	292 \times 183 \times 128	317 \times 167 \times 118	282 \times 158 \times 107

3.2 Design Review

3.2.1 Dimension and Mass Comparison

Dimensions and mass are shown in Table 3.

According to Table 3, it is clear the mass of head is just about 60 % of head A and B. And naturally, the dimension of head C is smallest in these three head. Therefore, the mass and dimension of head C ensure the highest natural global frequencies itself. Comparing head A and B, these two heads is the approximate equivalent in mass and size.

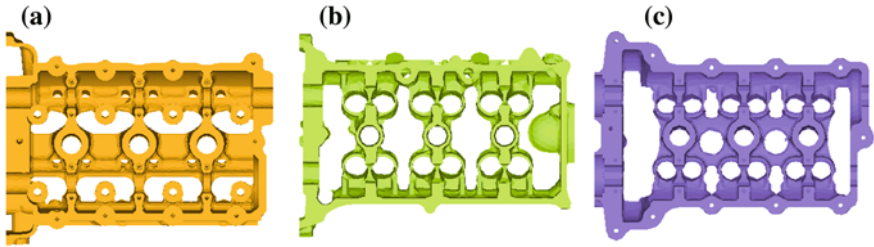


Fig. 4 Heads upside design. **a** Head A. **b** Head B. **c** Head C

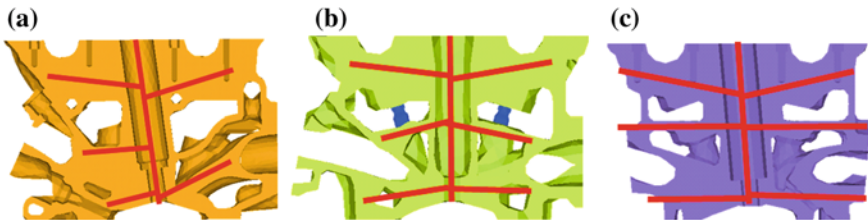


Fig. 5 Heads connection around plug hole. **a** Head A. **b** Head B. **c** Head C

3.2.2 Design Comparison

1. Connection between plug holes and wall.

The upper half part of head is shown in Fig. 4. The plug holes of head A are joined up which helps enhance bending stiffness. For head B, plug holes connect intake and exhaust side wall as one which is benefit for bending stiffness. Head C owns both two designs from head A and B and gets better stiffness than head A and B.

2. Connection around plug hole.

Plug hole is the skeleton of head which owns high stiffness. Side-part connects to skeleton can efficiently enhance these area and make head stiffer. As shown in Fig. 5, these three head have already well connected to plug hole.

3. Closed-design of water jacket.

As we know, closed-design owns good stiffness compared to open-design. As the typical closed-design, water jacket can help head to achieve good stiffness if height of water jacket is sufficient in proportion to head. As shown in Fig. 6, the water jacket height proportion of head B and C is about 53.6, 56.5 %, but head A only gets 36.7 %.

4. Closed-design of bolt boss.

As known, head bolt boss owns high stiffness as well. Specially, when area around bolt boss forms closed-design, the stiffness of bolt boss can be more

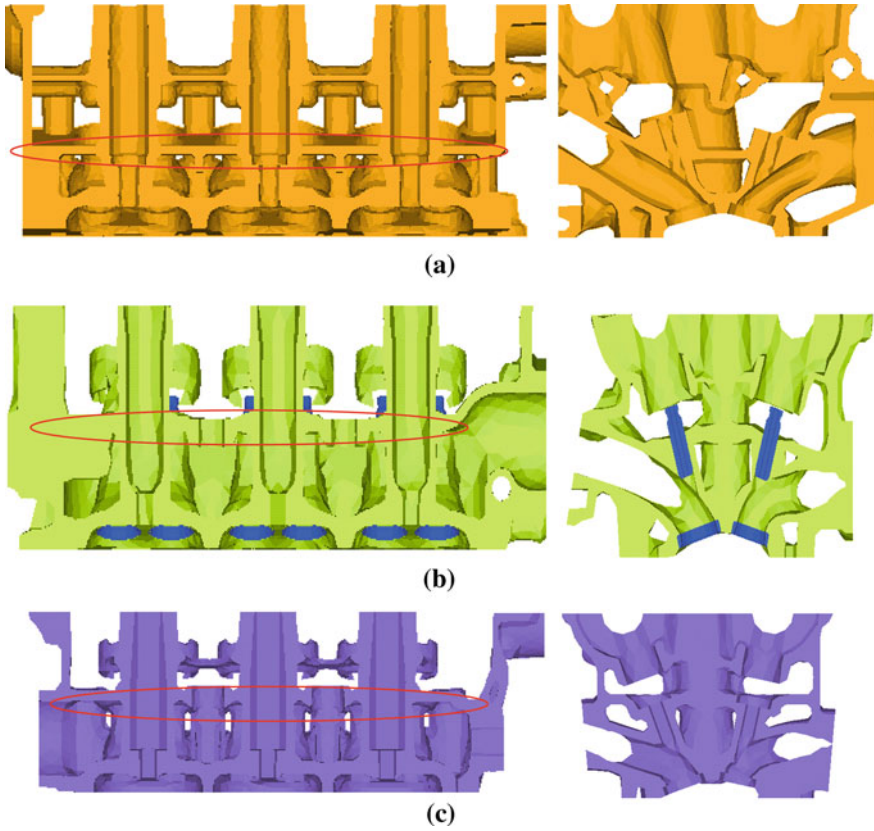


Fig. 6 Water jacket cross section. a Head A. b Head B. c Head C

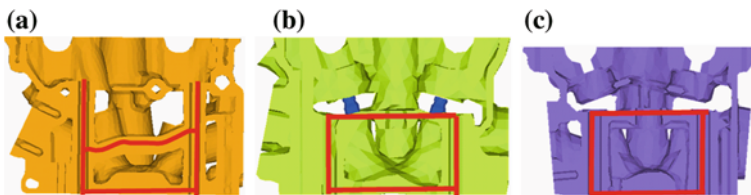


Fig. 7 Heads boss bolt connection. a Head A. b Head B. c Head C

efficiently utilized and will makes this area stiffer than bolt boss with open-design. Figure 7 shows the boss layout of three different heads. Area around bolt boss of head B and C forms closed-design. But for head A, it is design closed at lower side, but open-designed at upper side.

Based on the studies above, some key designs on head is summarized which could be helpful for enhancing head A with good stiffness for turbo charge and direct-inject engine.

1. Connections among plug holes of each cylinder form strong skeleton of cylinder head.
2. Connections from side-part to plug holes make area stiffer.
3. As typical closed-design, water jacket with sufficient dimension in height makes cylinder head stiffer.
4. Closed-designed area around bolt boss can make this area stiffer.

4 Optimization

4.1 Design Changes

Base on the above-mentioned designs discussion, structure of head A should be optimized to meet higher NVH demand for turbo charged and direct injection engine. Considering the engineering limitation and after several design-simulation tuning loops, final design is fixed listing below.

1. Ribs are added from intake and exhaust side to centre to seek support by bolt bosses and plug holes.
2. Ribs are added between bolt bosses and valve stem guides.
3. Rear-end wall cut out to achieve thinner wall and lighter head (Fig. 8).

4.2 Results

4.2.1 Mode Results

Figure 9 shows the mode results of head A after design changes.

1. First torsional mode frequency is 1,880 Hz which means 286 Hz (17.9 %) increased.
2. First bending mode frequency is 2,694 Hz which means 154 Hz (6.1 %) increased.
3. Three modes lost in frequency range up to 6,400 Hz.

4.2.2 Frequency Response Results

Figure 10 shows the frequency response results of head A under three different excitations after design changes.

From Figure 10, it is clear that response peaks caused by resonance move to high frequency and magnitude decrease in narrowband. And the maximum values

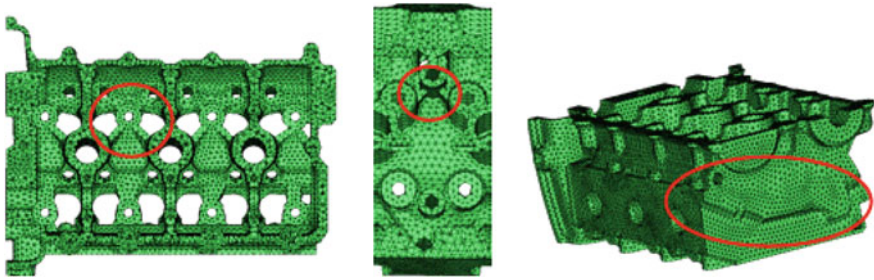


Fig. 8 Head A optimizations

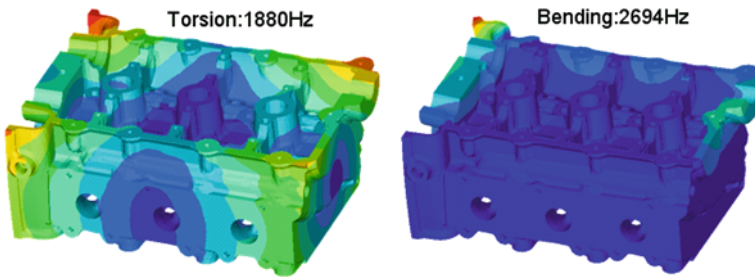


Fig. 9 Head A modal result after optimization

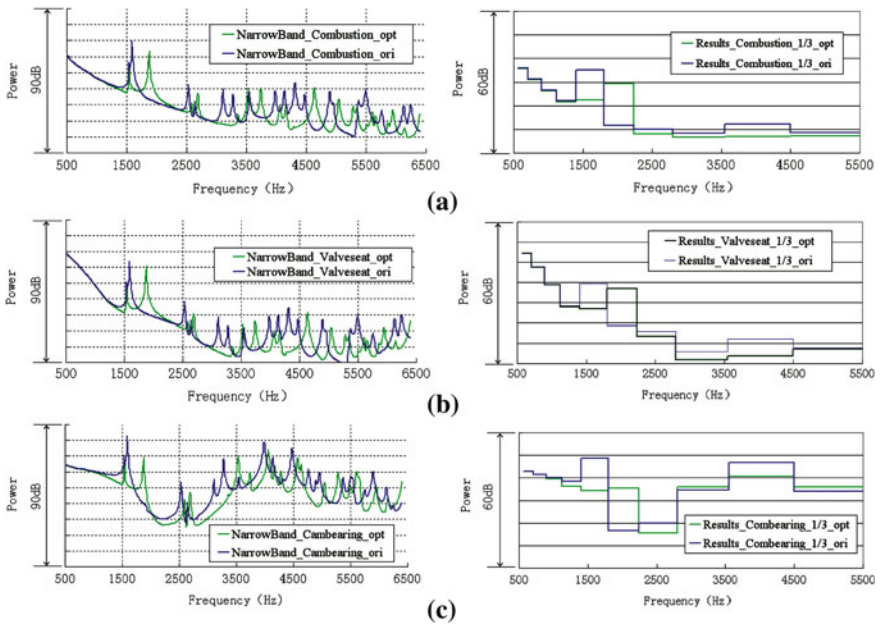


Fig. 10 Head A frequency response. **a** Response by gas force excitation. **b** Response by valve force excitation. **c** Response by cam force excitation

of response power caused by gas force, valve force and cam force excitation drop about 5.6, 2.7 and 8.3 dB respectively in 1/3 octave.

In summary, natural frequencies and response levels under different excitations of head A has been efficiently improved thanks to the stiffness increase by the design changes.

5 Conclusions

1. Cylinder head NVH performance has great relationship with it's global stiffness, so better global structure of cylinder head in concept design phase will be a prerequisite for it's good NVH performance at later design phase.
2. One creditable simulation procedure for cylinder head NVH performance which will applied to engineering practice in concept development stage is established.
3. Cylinder head NVH performance will be under control with this simulation procedure in engine concept development stage, the design failure will be avoided effectively and cylinder head NVH target is met.

Rattle Simulation Analysis of a Manual Gearbox

Xiaoying Ma, Zhan Zhangsong, Guoming Peng, Jun Lan, Bo Yu, Lei Zhang and Xiaofeng Li

Abstract Based on the flexible MBD method, a numerical model is used to study and optimize the gear rattle phenomenon of the manual transmission driveline system. This model simulates the gear meshing influenced by driveline torsional vibration, gear clearance, oil drag damping, friction and other nonlinear factors. The mechanism of these influences on gear rattle noise is summarized through parametric study for the purpose of reducing the transmission rattle noise.

Keywords Gear rattle · MBD simulation · Driveline torsional vibration · Unloaded gear

1 Introduction

For getting lower vehicle noise, transmission noise is one of the main source and has become an important research area. Gearbox rattle and whine, the two main noise sources of transmission, are caused by the gear meshing. Till now, many studies on the gear rattle have been done by using computational model simulations for gearbox and driveline designs and experimental verifications [1, 2]. These approaches are limited in understanding the basic tooth rattle phenomenon because

F2012-J03-005

X. Ma (✉) · Z. Zhangsong · G. Peng · J. Lan · B. Yu · L. Zhang · X. Li
Powertrain Global R&D Center in Chongqing Changan Automobile Co. Ltd,
Chongqing, China
e-mail: sunqiemail@163.com

the gear rattle issue is a transmission system problem influenced by tooth clearance, oil drag damping, gear meshing dynamic contact stiffness and other non-linear factors which bring special difficulties to mathematical model and simulation.

In this paper we discuss the gearbox rattle mechanism study on the gear meshing impulse by making a multi-body dynamics model (MBD). This model uses the commercial software of AVL EXCITE TD considering the driveline torsional vibration, the gear clearance, oil drag damping, friction and other non-linear factors. Through parametric analysis of the gear rattle influence factors, some conclusions are provided as guidance for low-noise design.

2 Gearbox Rattle Mechanism

Gearbox rattle, usually audible in the operating condition of run-up at low speed or at idle speed, is caused by the relative unloaded gear impacts. In Fig. 1, the 4 cylinder inline engine generates a periodical drive torque with the dominant fly-wheel 2nd order angular velocity fluctuation which can be transmitted from the clutch to the gear shafts. The angular fluctuating input shaft causes the unloaded gears to impact and radiate with high frequency broad-band gear rattle by transmitting from the shaft bearings to the gearbox housing [3].

3 Dynamic Modeling of the Contact Gears

In simulating the gear meshing as shown in Fig. 2, the gears are assumed to be rigid bodies with lumped mass and inertia and the gear meshing has non-linear stiffness and damping coupling the two gears [4]. I_1 and I_2 are the inertia of driving gear 1 and driven gear 2. r_1 and r_2 are the pitch radius of the driving and driven gears. θ_1 , $\dot{\theta}_1$, $\ddot{\theta}_1$ and ω_1 , $\dot{\omega}_1$, $\ddot{\omega}_1$ and ω_1 are the angular displacement, angular velocity, angular acceleration and the rotational speed of the driving gear. θ_2 , $\dot{\theta}_2$, $\ddot{\theta}_2$ and ω_2 are the angular displacement, angular velocity, angular acceleration and the rotational speed of the driven gear. Then,

$$\omega_1 = i\omega_2 \quad (i \text{ is the transmission ratio}) \quad (1)$$

The drive torque $T_1(t)$ acting on the driving gear can be seen as a sum of a constant value and a harmonic variable:

$$T_1(t) = T_m + T_b \sin(\omega_b t + \varphi_b) \quad (2)$$

Where, T_m is the torque mean amplitude and T_b is the amplitude of the harmonic variable. ω_b and φ_b are the circular frequency and initial phase angle respectively. $T_2(t)$ is the drag torque as a constant value acting on the driven gear.

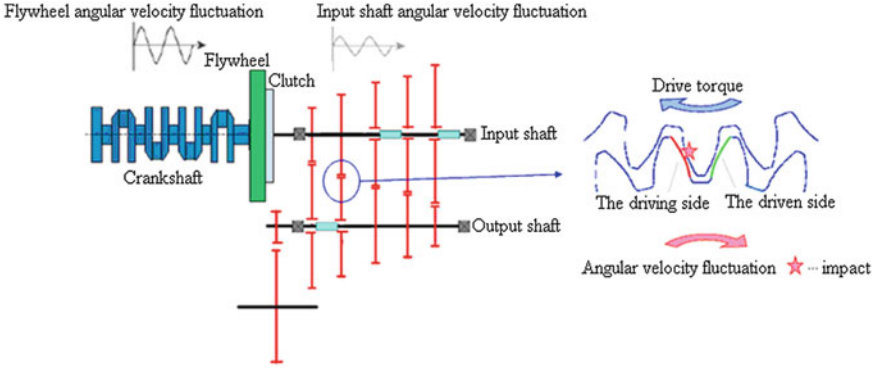


Fig. 1 Gearbox sketch and the rattle mechanism

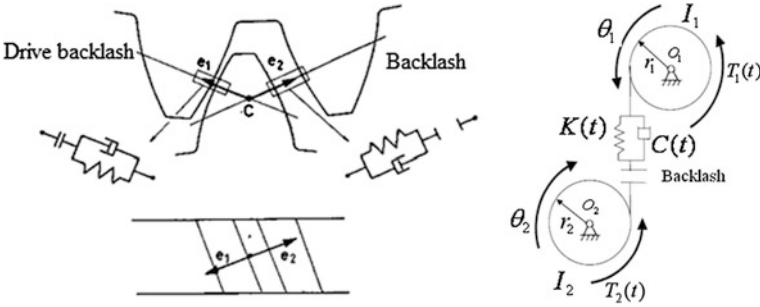


Fig. 2 Gear contact modeling

The dynamic meshing force between the driving gear and driven gears as follows:

$$\begin{aligned}
 F_n &= k(t)f(r_1 \tan \theta_1 - r_2 \tan \theta_2 - \delta(t)) \\
 &\approx k(t)f(r_1\theta_1 - r_2\theta_2 - \delta(t)) \\
 &= k(t)f(t)
 \end{aligned}
 \tag{3}$$

Where, $k(t)$ is the gear mesh stiffness. $\delta(t)$, $f(t)$ are respectively the gear mesh error and the microscopic deformation of the gear. The micro-deformation of the gear is expressed as:

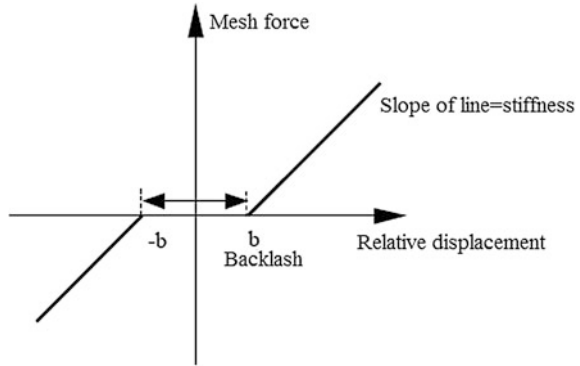
$$f(t) = \begin{cases} r_1\theta_1 - r_2\theta_2 - \delta(t) - b & r_1\theta_1 - r_2\theta_2 - \delta(t) > b \\ 0 & -b < r_1\theta_1 - r_2\theta_2 - \delta(t) < b \\ r_1\theta_1 - r_2\theta_2 - \delta(t) + b & r_1\theta_1 - r_2\theta_2 - \delta(t) < -b \end{cases}
 \tag{4}$$

Where, b is half of the gear backlash. And Fig. 3 show the nonlinear meshing force between the gear pairs.

Gear meshing moment is defined as:

$$F_n r_i = k(t)f(t)r_i \quad (i = 1, 2)
 \tag{5}$$

Fig. 3 The gear meshing force–displacement



Then the gear meshing damping torque is:

$$C(t)\dot{f}(t)r_i \quad (i = 1, 2) \tag{6}$$

$$C(t) = 2\sqrt{m_v k(t)\zeta} \tag{7}$$

Where $C(t)$, m_v are the damping coefficient and the gear equivalent mass respectively. ζ is the damping ratio. The dynamic gear mesh MBD equation is presented as:

$$\begin{cases} I_1\ddot{\theta}_1 + C(t)\dot{f}(t)r_1 + k(t)f(t)r_1 = T_1(t) \\ -I_2\ddot{\theta}_2 + C(t)\dot{f}(t)r_2 + k(t)f(t)r_2 = T_2(t) \end{cases} \tag{8}$$

It can be obtained the gear rattle force and the gear deformation through the dynamic gear mesh MBD equation. Thus a parametric sensitivity study of the influence factor can be done to investigate the transmission gear rattle.

4 Multy-Body Dynamic Model

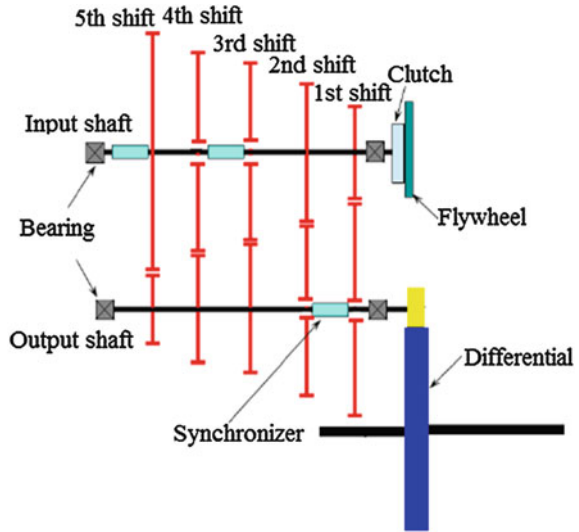
4.1 Layout of the Gearbox Structure

There are three shafts and five shift gear pairs in the gearbox layout shown in Fig. 4. The 1st and 2nd shift synchronizer is located on the input shaft, and the 3rd, 4 and 5th shift synchronizer are located on the output shaft.

4.2 Simulation Modeling

The modeling of gear meshing contact in the gearbox is performed by utilizing AVL EXCITE TD which is a multi-body dynamic software used in gearbox

Fig. 4 Layout of the gearbox



component development of input/output shafts, differential, gears, bearings and the synchronizers as lumped masses and inertias inertia shown in Fig. 5. The gear parameters are also set in the model.

4.3 Boundary Conditions

For a 4 stroke 4 cylinder engine, the 2nd order flywheel torque fluctuation and the 2nd angular velocity are dominant which are mainly caused by the engine gas force and mechanical force [5]. The 2nd order angular velocity fluctuation curve shown in Fig. 6 is loaded into the simulation model. The 2nd order angular velocity fluctuation curve is derived from the angular acceleration obtained in the test.

$$\ddot{\varphi} = A \cos 2\omega t \tag{9}$$

$$\dot{\varphi} = \frac{A}{2\omega} \sin 2\omega t \tag{10}$$

where $\ddot{\varphi}$ and $\dot{\varphi}$ are the 2nd EO angular acceleration and 2nd EO angular velocity. A is the amplitude of the 2nd EO angular acceleration at the input shaft from the measurement. ω is the engine speed.

A constant output torque acquired from test is applied to the differential output shaft of the transmission system in the model with the backlash, the gear meshing stiffness and the drag torque. The gear meshing stiffness is an angle dependent curve as shown in Fig. 7. In the model, the gear drag torque is estimated from the

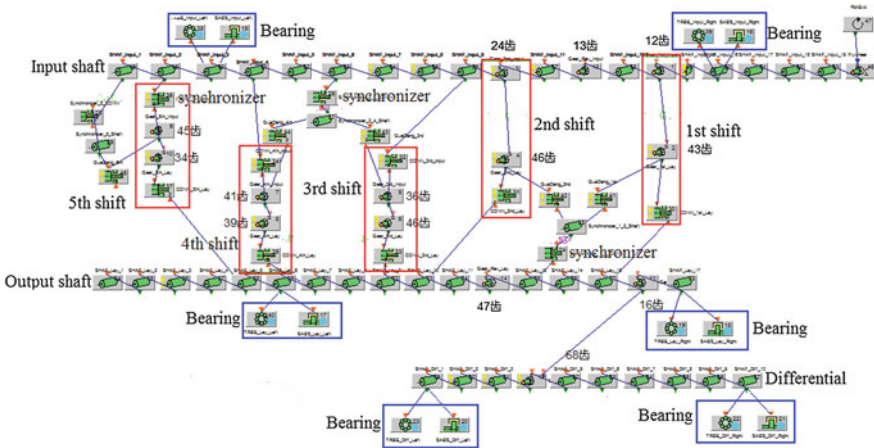
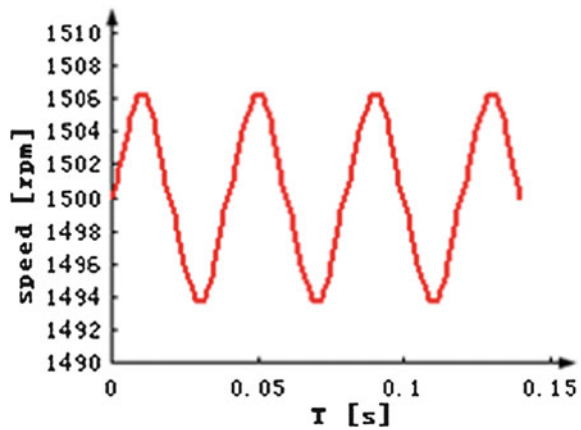


Fig. 5 AVL EXCITE TD model of the transmission

Fig. 6 2nd EO angular velocity fluctuation



empirical formula by a combination of oil-string torque [6] and bearing friction torque [7] and it is relevant to the gear speed, tooth parameters, the gear depth immersed in the oil, and the temperature etc.

4.4 Result Analysis

The force, angular displacement, angular velocity, angular acceleration of the shafts, bearings and gearwheel are obtained from the simulation of the dynamic response of the transmission system. In Fig. 8, the Campbell diagrams of the

Fig. 7 Angle dependent meshing stiffness

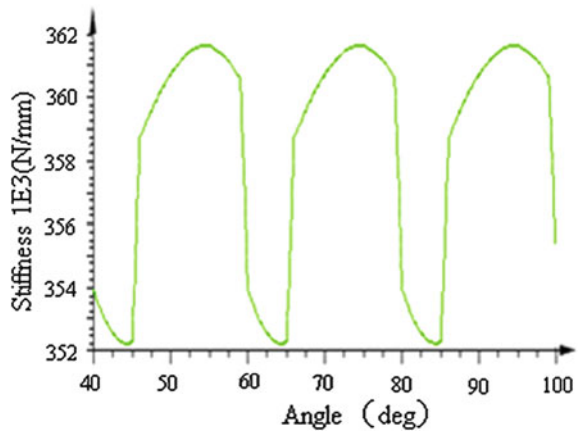
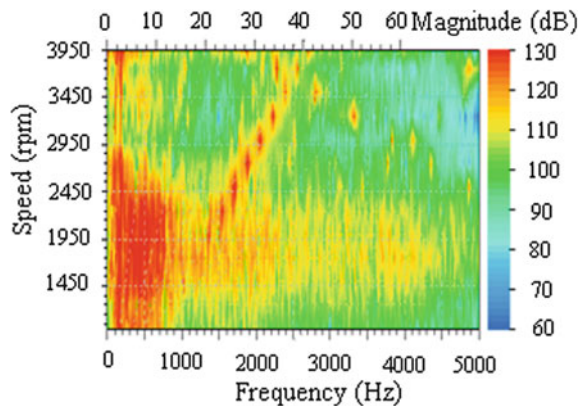


Fig. 8 Campbell diagram of the bearing force

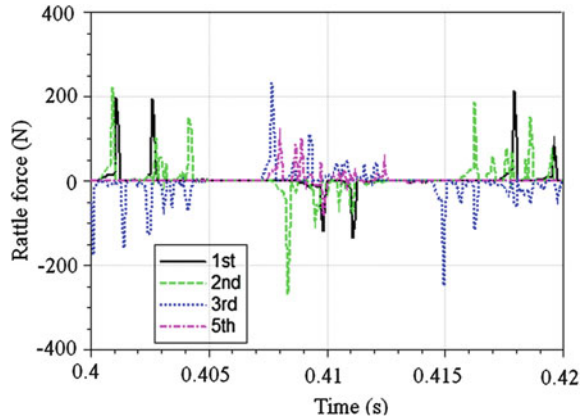


output shaft bearing force is a board band impact force from 1500 to 2200 rpm which can be transmitted to the gearbox housing radiating gear rattle. In order to obtain the rattle mechanism of the transmission, the meshing forces of the unloaded gears is investigated. In Fig. 9, the gear meshing forces of unloaded gears at 2000 rpm are between 200 and 400 N, where the 3rd gear rattle is most serious at 4th shift operating condition.

5 Parameter Study of the Gear Rattle

The parametric studies focus on the gear rattle influence factors such as angular velocity fluctuation, drag torque, the unloaded gearwheel inertia, gear tooth backlash and the gear meshing stiffness for the purpose of better gearbox without rattle.

Fig. 9 Meshing force of unloaded gears at 2000 rpm



5.1 Influence of Torsional Vibration on Gear Rattle

The gear rattle forces are compared under different angular acceleration fluctuation amplitudes of the gearbox input shaft in the condition of 4th shift at engine 2000 rpm with gear lash clearances = 0.1375 mm and full load torque = 365 Nm. The different 2nd EO angular acceleration amplitudes are list in the following Table 1.

From the result of the rattle forces and their 1/3 octave band spectrum in Figs. 10, 11, it can be seen that the larger the angular acceleration fluctuation of the input shaft are, the larger the rattle forces are. The torsional vibration of the transmission input shaft has strong influence on the gear rattle.

5.2 Influence of Drag Torque on Gear Rattle

The gear rattle forces are compared under different gear drag torques in the 4th shift at engine speed of 2000 rpm with 2nd EO angular acceleration = 1000 rad/s², backlash = 0.1375 mm and full load torque = 365 Nm. The drag torque for all unloaded gears are assumed as identical in one simulation case as following (Table 2).

Figure 12 shows the result of rattle forces and the relative displacement of unloaded gears. It's clear that the large the drag torque is, the smaller the rattle impact forces are. In Fig. 13, the results of the relative displacement between contact gears show that there are three kinds of gear impact of double-sided impact, single-sided impact and slight impact without strong tooth contact under different drag torque conditions. The double-sided gear meshing impact happens when the drag torque is below 0.3 Nm. The single-sided impact happens when

Table 1 Different 2nd EO angular acceleration amplitudes

Condition	1	2	3	4
2nd EO angular acceleration (rad/s ²)	500	1,000	1,500	2,000

Fig. 10 Gear rattle force

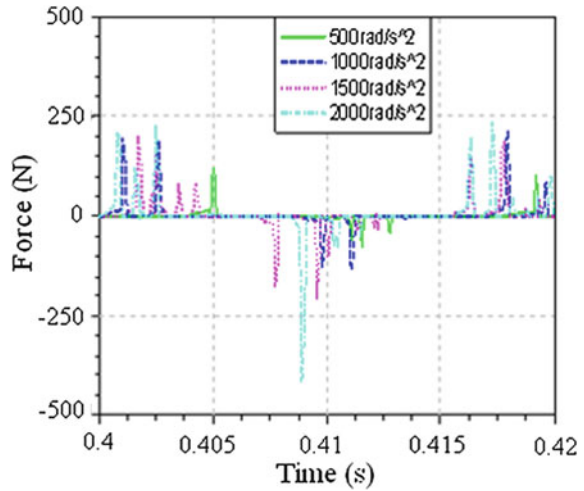
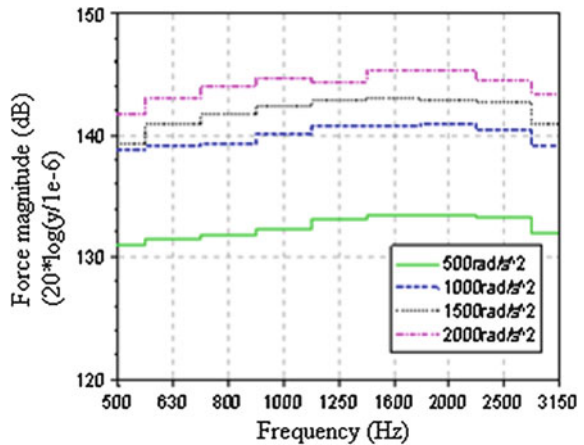


Fig. 11 1/3 octave band spectrum result



drag torque is from 0.3 to 0.6 Nm. The slight impact with very small force happens when drag torque is above 0.6 Nm. Therefore for reducing the gear rattle, we can increase the gear drag torque by several ways such as higher oil viscosity, larger amount of oil and low working temperature in the gearbox.

Table 2 Different gear drag torque

Simulation cases	1	2	3	4	5	6	7	8
Drag torque (N m)	0.04	0.1	0.2	0.3	0.4	0.5	0.6	1

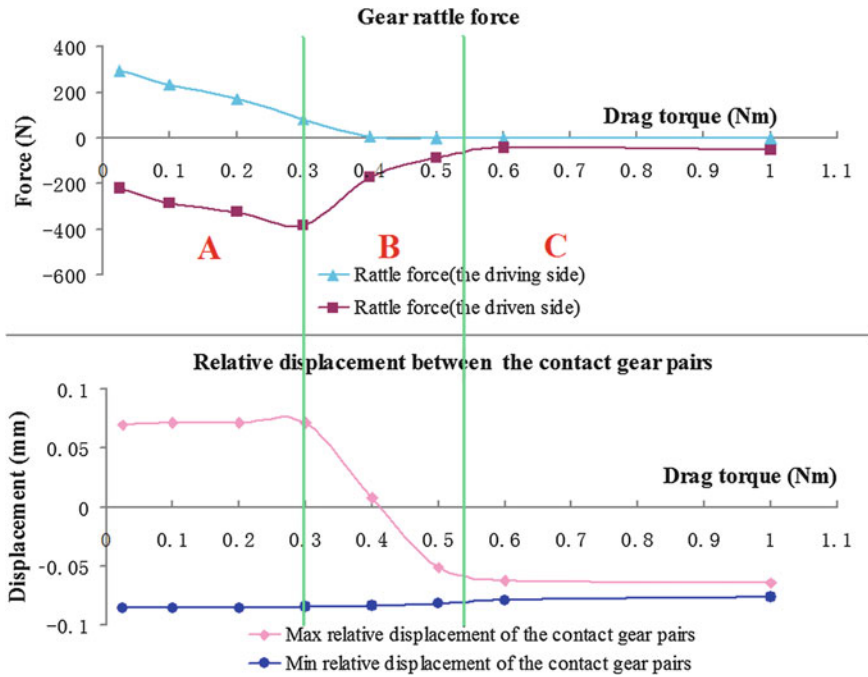


Fig. 12 Gear rattle force and the relative displacement of the unloaded gears

5.3 Influence of Unloaded Gear Inertia on Gear Rattle

The gear rattle forces are compared under different unloaded gear inertia at the 4th shift and engine 2,000 rpm with 2nd EO angular acceleration = 1,000 rad/s², backlash = 0.1375 mm at full load torque = 365 Nm. The variant unloaded gear inertias are list below (Table 3).

Figures 14 and 15 show the result of the rattle forces and 1/3 octave band spectrum in Fig. 16 shows the gear rattle force at the center frequency of 1,000 Hz under different unloaded gear inertia. It can be seen that the larger the unloaded gear inertias are, the larger the rattle forces are. Therefore, it's better to design lighter gearwheel for less rattle force.

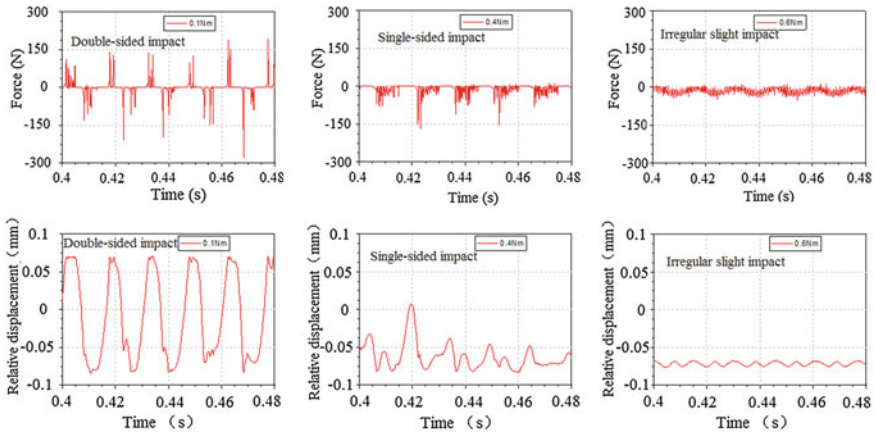
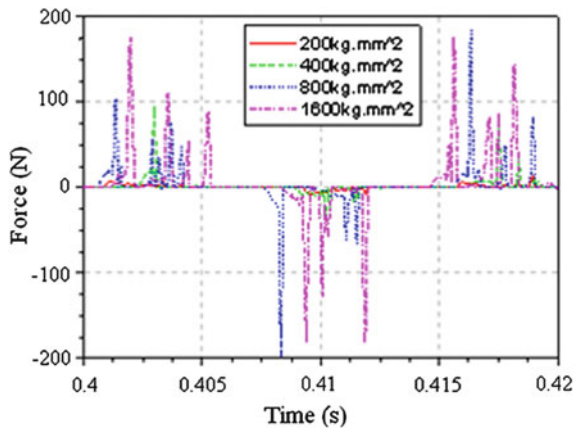


Fig. 13 Three kind of impacts of Gear meshing at 2000 rpm

Table 3 Different gear inertia

Condition	1	2	3	4
Gear inertia (kg mm ²)	200	400	800	1,600

Fig. 14 Gear rattle force



5.4 Influence of Gear Backlash on Gear Rattle

The gear rattle forces are compared under different gear lash clearances at the condition of the 4th shift and engine 2,000 rpm with 2nd EO angular acceleration = 1,000 rad/s² at full load torque = 365 Nm. Assuming the identical lash for all free gears as listed below (Table 4).

Fig. 15 1/3 octave band spectrum

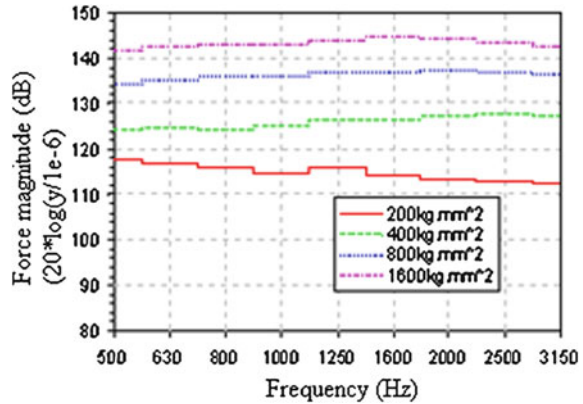


Fig. 16 1/3 octave of gear rattle force at center freq. 1,000 Hz

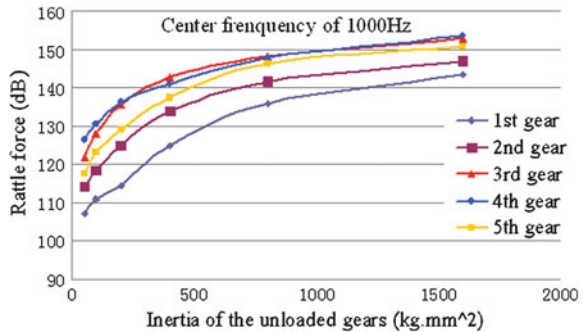


Table 4 Different gear backlashes

Condition	1	2	3	4
Gear backlash (mm)	0.05	0.1	0.15	0.2

Figures 17 and 18 show the calculation result of the rattle forces and their 1/3 octave band spectrum. It can be seen that the larger the backlash there are, the larger the rattle forces are, although the behavior of double-sided or single-sided impacts still exist. Therefore, it’s always better to get small gear backlash clearance for lower rattle noise if permitted.

5.5 Influence of Gear Meshing Stiffness on Gear Rattle

The gear rattle forces are compared under different gear meshing stiffness in the 4th shift at the engine speed of 2,000 rpm with 2nd EO angular acceleration = 1,000 rad/s², backlash = 0.1375 mm and full load torque = 365 Nm.

Fig. 17 Gear rattle force

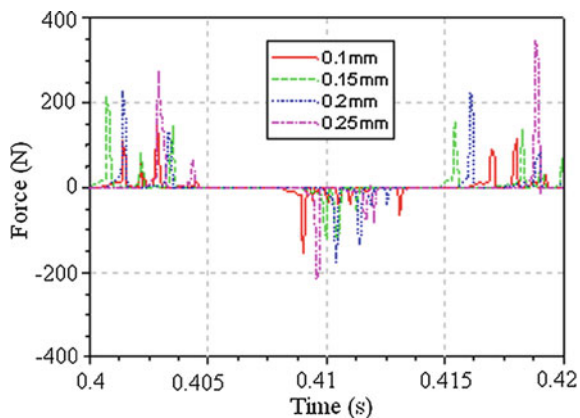


Fig. 18 1/3 octave band spectrum

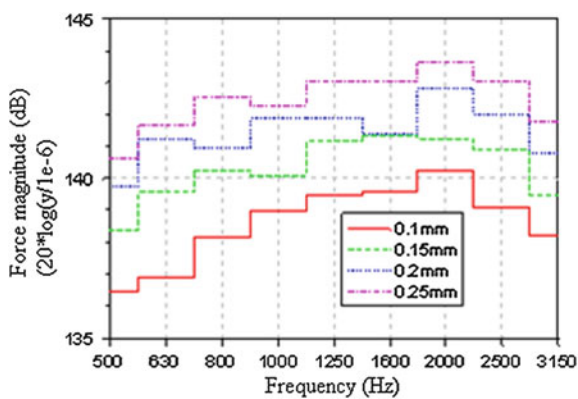


Fig. 19 Gear rattle force

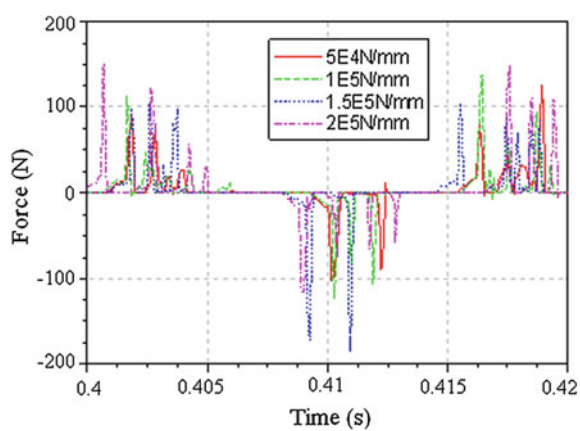


Fig. 20 Gear rattle force magnitude of 1/3 octave band spectrum

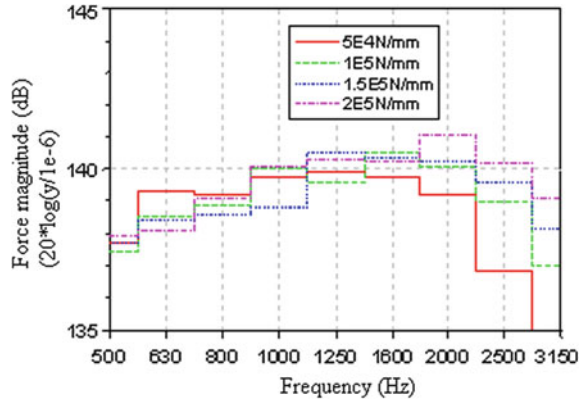


Table 5 Different gear meshing stiffness

Simulation case	1	2	3	4
Gear meshing stiffness (N/mm)	50,000	1,00,000	1,50,000	2,00,000

The gear meshing stiffness is listed below. In Figs. 19 and 20, the unloaded gear meshing stiffness have little influence on the impact force below 1,500 Hz, but have great difference above 1,500 Hz. Therefore, slim and high tooth are often used in the gearbox for lower impact force at high frequency (Table 5).

6 Conclusion

As demonstrated in this paper, a simulation model was set up considering the dynamic gear teeth meshing to predict the rattle phenomenon in the driveline system. The numerical investigation was conducted to understand the gear rattle mechanism.

1. The larger the torsional vibration amplitudes, the higher the meshing impulse force on the driving and backlash side of the teeth. Therefore, attenuating the driveline torsional vibration is a main measure to tackle with the unloaded gear rattle.
2. The higher the drag torques of the oil on the unloaded gears, the lower the rattle forces on the driving side or backlash side. The rattle impulse force has different behaviors according to the dragging torque. The impact behaviors are: double-sided impact, single-sided impact, slight impact of the meshing. The optimization method is to minimize the rattle force of the unloaded gears together with a damping dragging torque.

3. The higher the unloaded gear inertia, the larger the rattle force which also has the form of double-sided impact, single-sided impact, slight impact. Usually there is a critical inertia which leads to slight rattle force.
4. The smaller the teeth side clearance, the lower the rattle force. Usually the smaller or larger side clearance cannot change the impact behavior of the double-sided impact or single-sided impact.
5. Usually making the teeth stiffer cannot get better rattle noise. Slim and high tooth are often used in the gearbox.
6. Utilizing the multi-dynamic simulation in the investigation of gear rattle can quite well predict the meshing impact of unloaded gear meshing. Variant designs and operating conditions such as driveline torsional vibration, drag torque of the oil, unloaded gear pair inertia and lash clearance can be considered in the simulation model. Based on the study, design guidelines are provided for further product designs with improved rattle noise.

References

1. Wang H, Glover R (2005) Analytical and experimental study on gear rattle in supercharger. SAE technical paper Series
2. Morgan JA, Dhulipudi MR (2007) Gear mesh excitation models for assessing gear rattle and gear whine of torque transmission systems with planetary gear sets. SAE technical paper Series
3. Wang MY, Manoj R, Zhao W (2002) Gear rattle modeling and analysis for automotive manual transmissions. Drive System Technique
4. Albers P (2004) A study to oil churning losses in a gearbox. Report number: DCT-2004/35
5. Jian P, Gang C, Hua H (2006) Automotive noise and vibration-principle and application. Beijing Institute of Technology Press, Beijing
6. Noben PFM (2005) Design of a test bench for measuring oil churning losses. Traineeship report
7. Zejiu L (2006) Rolling bearing application handbook. Mechanical industry Press, Beijing

Study about the Relationship Between Power-Train Modal and Connecting-Plane

Yongjiang Xu, Zhangsong Zhan, Wenjun Chen, Yanlin Shi,
Hangkui Lu, Junping Xue and Xin Zhao

Abstract The power train modal is needed to pay attention because it is a main factor to affect vibration. The relationship between power train modal and connecting plane was studied in this paper. The global vertical connecting plane is the main factor to affect power train global bend mode#1, especially the connecting plane between clutch box and engine block. Build a simple approximate model, and find the key factors affect the power train global bend mode#1 with this model. The key factors include connect stiffness 'K', span distance 'L' and inertia 'I'. Then do several testing and CAE analysis, validated some methods to improve connect stiffness and power train modal. At last, applied these conclusions to optimize the modal of a 4 strokes L4 engine and improved the natural frequency of power train global bend mode#1 from 198 to 254 Hz. This study has gotten some useful conclusions, and these conclusions can be used to optimize power train global bend mode effectively.

Keywords Power-train · Modal · Engine · Transmission · Connecting-plane

F2012-J03-007

Y. Xu (✉) · Z. Zhan · W. Chen · Y. Shi · H. Lu · J. Xue · X. Zhao
Powertrain Global R&D Center in Chang an Automobile Co. Ltd, Mainland, China
e-mail: sunqiemail@163.com

Y. Xu · Z. Zhan · W. Chen · Y. Shi · H. Lu · J. Xue · X. Zhao
State Key Laboratory of Vehicle NVH and Safety Technology, Chongqi, China

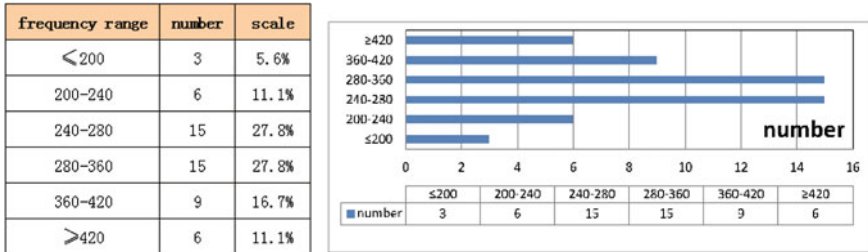


Fig. 1 Statistical data of the power train frequency of global mode#1

1 Introduction

Power train vibration can transmit to the driving room getting across mounting brackets, and bring the NVH problems. The power train modal is needed to pay attention because it is a main factor to affect vibration. Generally, it is recommended that the frequency of power train global mode#1 should above the fire frequency with a safe coefficient 1.4, to minimize the influence of resonance. As showed in Fig. 1, 5.6 % of the power train frequency of global mode#1 are lower than fire frequency (200 Hz), 55.6 % are higher than the safe frequency (280 Hz). Most of the power train frequency of global mode#1 is designed higher than fire frequency [1, 2].

The power train modal can be classed as global bend modal, global torsion modal and local modal. Modal analysis includes natural frequency analysis, mode shape analysis and mode damping analysis. The relationship between natural frequency of power train global bend mode#1 and connecting plane was analyzed in this paper. Some conclusions were obtained after this study, and these conclusions are helpful to optimize power train global bend mode.

There are various connecting planes in power train, as like as showed in Fig. 2. These planes can be classed as global vertical connecting plane (the connecting planes among gearbox, clutch box, block and timing cover), global horizontal connecting plane (the connecting planes among valve cover, cylinder head, cylinder block and oil pan) and local connecting plane (the connecting planes of assistant parts, manifold pipe, brackets and so on). It is proved that the global vertical connecting plane is the main factor to affect power train global bend mode#1. As showed in Fig. 3, it is the compare result of modify the global horizontal connecting plane. After modify the connecting plane, the natural frequency of power train global bend mode#1 increased 5 Hz, it is owe to the change of mass, but not the connecting plane.

This paper started from building a simple approximate model, and found the key factors affect the power train global bend mode#1 with this model. Then did several testing and CAE analysis, validated some methods to improve connect stiffness and power train modal. At last, applied the conclusions to optimize the modal of a 4 strokes L4 engine.

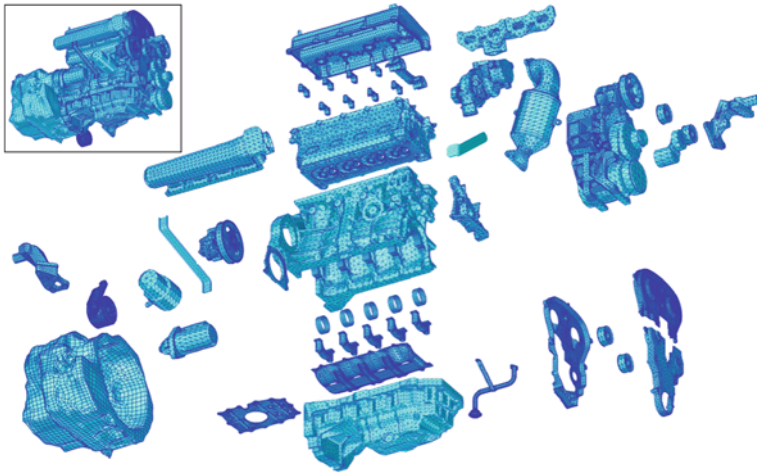


Fig. 2 Connecting plane in the power train

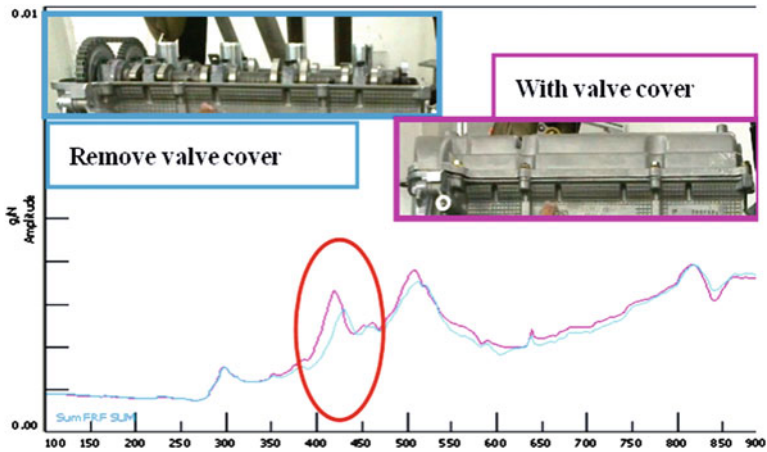


Fig. 3 Results of modify the global horizontal connecting plane

2 Model Building

The connecting planes of power train are complex, and it is difficult to build an exact model. For a theory study, a simple approximate model is enough. Predigest the model as following.

1. Predigest the model to 1D model, component with mass and spring as showed as Fig. 4. It has been proved that the global vertical connecting plane is the main factor to affect power train global bend mode#1, so the model can be

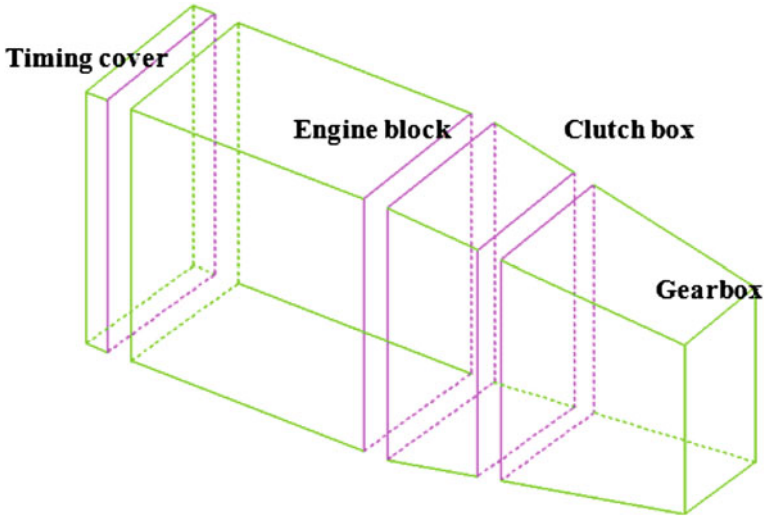


Fig. 4 1D model

predigest to 1D model. In this model, there are some masses (timing cover, engine block, clutch box, gearbox) and springs between the masses;

2. Predigest the 1D model to two masses system. There are two components in this model, engine and gearbox. As showed as left picture in Fig. 5. Owe to mass distribution of power train, the mode shape of global bend mode#1 usually focus the connecting plane between clutch box and engine block. As showed as right picture in Fig. 5, it is mode shape result of power train global bend mode#1 of an Changan's power train, the deformation is focus the connecting plane between clutch box and engine block;
3. Distribute the connect stiffness to several local stiffness and name these local stiffness as K1, K2, K3, K4, K5, K6....in this study, connect stiffness was distributed to 6 area local stiffness. The area local stiffness is interrelated with the distribute area size, connecting plane local stiffness, connecting bolts and so on;
4. Disregard the non-linear ingredient and damping. Usually, the connecting plane's material is aluminum or iron, influence of non-linear and damping is light;
5. Predigest to a single DOF model, as showed as the right picture of Fig. 6. The single DOF is the rotation, and the inertia is 'I'.

After predigesting, the model is a single DOF system, the kinematics differential equation of this model showed as Eq. 1.

$$I\theta + K_1L_1\theta + K_2L_2\theta + K_3L_3\theta + K_4L_4\theta + K_5L_5\theta + K_6L_6\theta = 0 \quad (1)$$

θ Angle displacement

I Inertia

K Area local stiffness

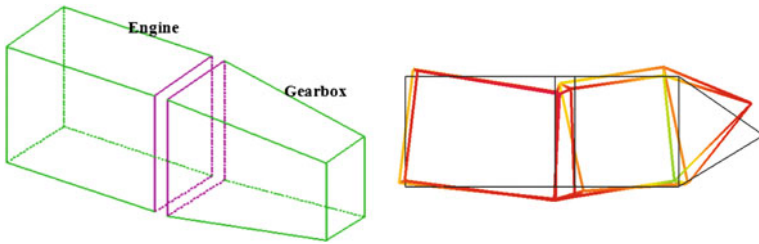


Fig. 5 Two masses system

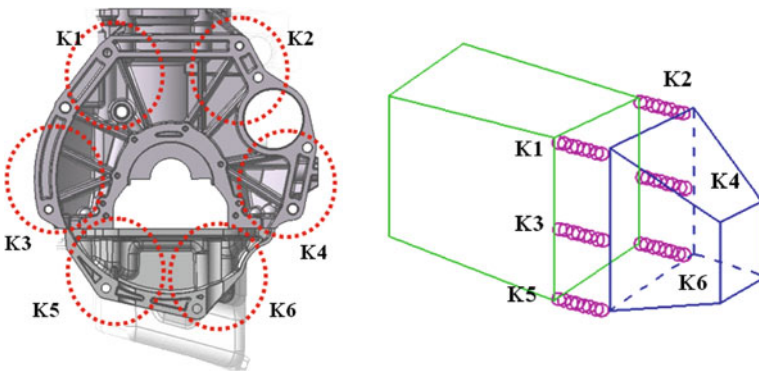


Fig. 6 Distribution of connect stiffness

L Span distance

Give a start value 0, do Laplacian transform to Eq. 1, get Eq. 2

$$IS^2 + K_1L_1 + K_2L_2 + K_3L_3 + K_4L_4 + K_5L_5 + K_6L_6 = 0 \tag{2}$$

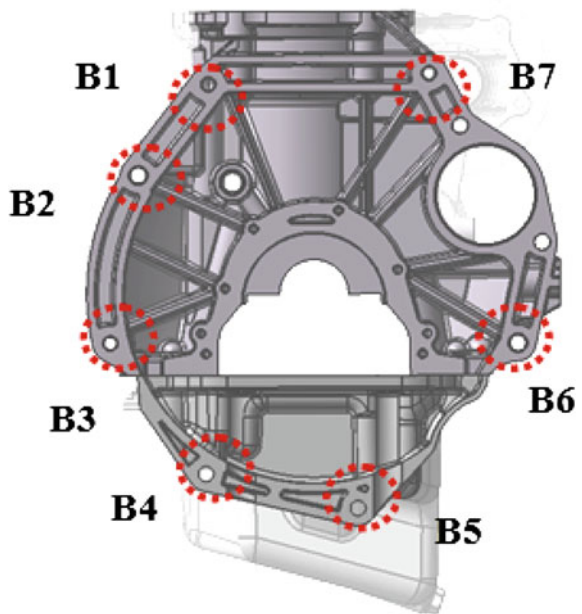
Calculate Eq. 2, get two roots of S, showed as Eq. 3

$$S = \pm \sqrt{-\frac{K_1L_1 + K_2L_2 + K_3L_3 + K_4L_4 + K_5L_5 + K_6L_6}{I}} = \pm j\omega_0 \tag{3}$$

The ω_0 in Eq. 3 means the natural frequency of a non-damping system. It is can know clearly from Eq. 3, the area local stiffness ‘K’, span distance ‘L’ and inertia ‘I’ is the most important parameters related with natural frequency of the system. The natural frequency is increased while the ‘K’ and ‘L’ are increased and the ‘I’ is reduced. As to these parameters, several validations have been done. All of these validations are showed as Table 1.

Table 1 Validation of the parameters

Key parameters	Validate item	Means
Connect stiffness 'K'	Connecting bolt size	Displace the bolts M8–M6
	Connecting bolt amount	Bolts amount reduced from 7 to 5
	Connecting bolt fix torque	Fix bolts with 1/2 torque
		Fix bolts with 1/4 torque
Area size	Area size	Add two bracket to add connect area size
	Connecting plane stiffness	Add some rib on clutch box to strengthen the connecting plane stiffness
Span distance 'L'	Span distance	Compare two span distance's results with two group connecting bolts
Inertia 'I'	Inertia	Add 12 kg mass on the gearbox

Fig. 7 Connecting bolts location

3 Study about the Relationship Between Power Train and Connecting Plane

The validation has been done in a 4 strokes L4 power train of Changan. There are 7 connecting bolts between clutch box and engine block in this power train, as showed as Fig. 7. These bolts are numbered from B1, B2 to B7.

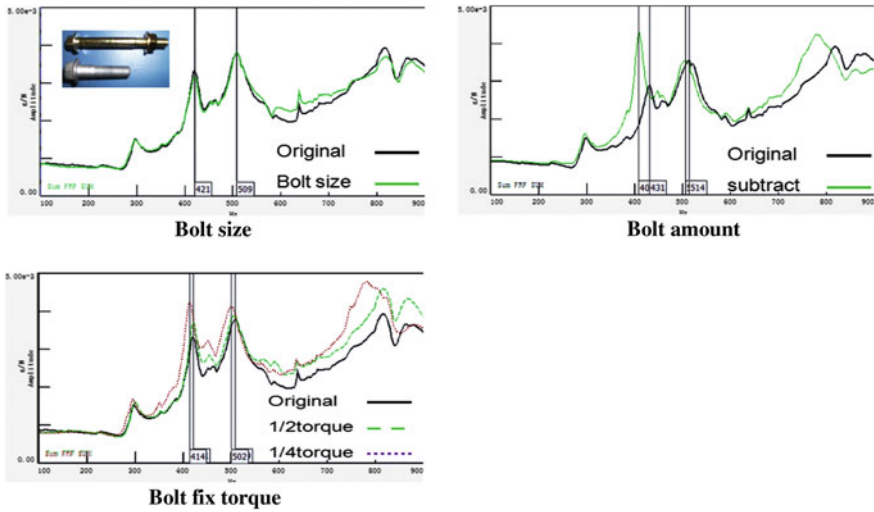


Fig. 8 Validation results of connecting bolt

3.1 Connect Stiffness ‘K’

3.1.1 Validation about Connecting Bolt

Change the Connecting bolt size, Connecting bolt amount and Connecting bolt fix torque one by one, tested and got the modal results, as showed as Fig. 8.

1. Replace the bolts M8 with M6, the natural frequency of power train global bend mode#1 changed little;
2. Remove B4 and B8, bolts amount reduced from 7 to 5, the natural frequency of power train global bend mode#1 reduced 22 Hz;
3. Fix bolts with 1/2 torque, the natural frequency of power train global bend mode#1 changed little;
4. Fix bolts with 1/4 torque, the natural frequency of power train global bend mode#1 reduced 7 Hz.

3.1.2 Validation about Connect Area Size

Add two brackets to add the connect area size between clutch box and engine block, as showed as Fig. 9. After add brackets, the natural frequency of power train global bend mode#1 increases 16 Hz.

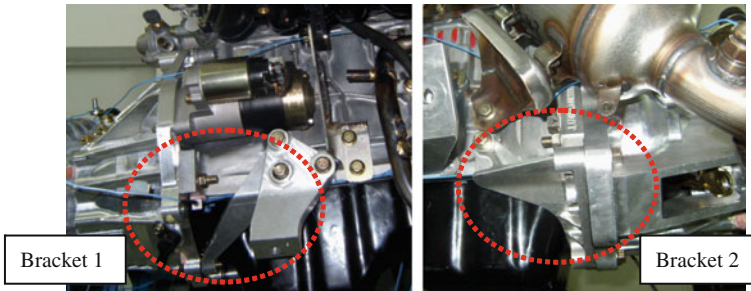


Fig. 9 Brackets between clutch box and engine block

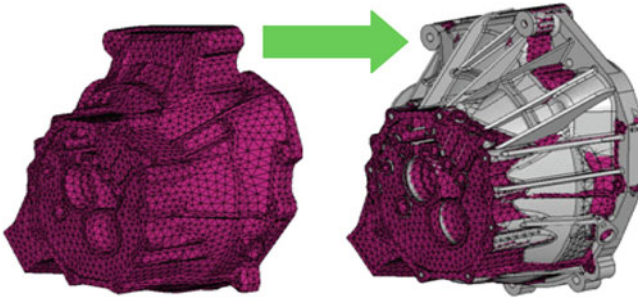


Fig. 10 Add ribs on clutch box

3.1.3 Validation about Connecting Plane Stiffness

Add some ribs on clutch box to strengthen the connecting plane stiffness, as showed as Fig. 10. After add ribs, the natural frequency of power train global bend mode#1 increases 22 Hz.

3.2 Validation Span Distance 'L'

To validate the span distance 'L', classed the bolts to two groups, as showed as Fig. 11. Group A marked with blue circle, and group B marked with green circle, group A have more span distance than group B. Compare the results, with the bolts group A, the natural frequency of power train global bend mode#1 is 22 Hz more than with the bolts group B.

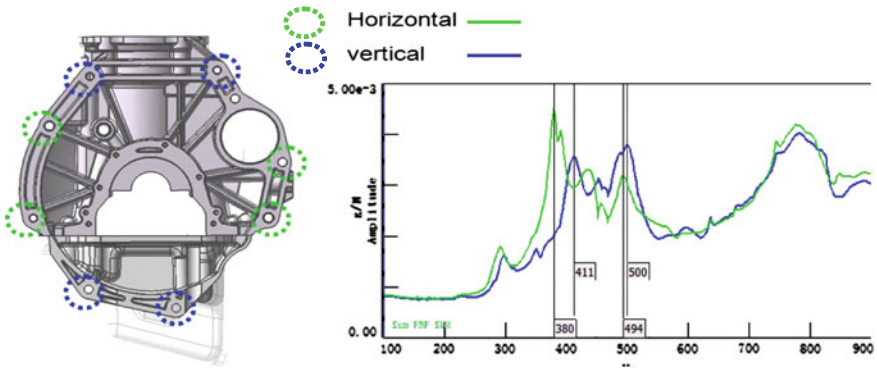


Fig. 11 Validation about span distance ‘L’

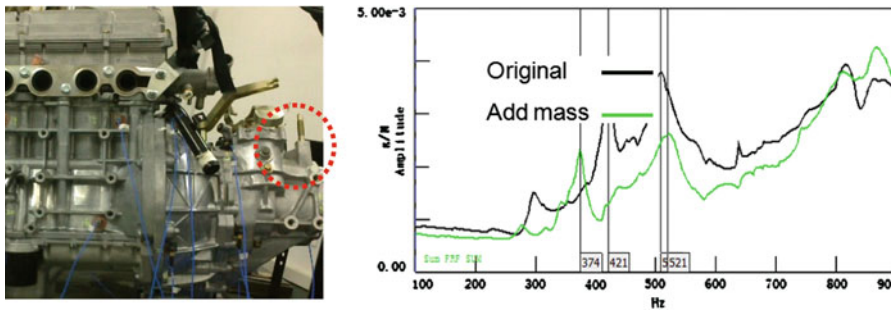


Fig. 12 Validation about inertia ‘I’

3.3 Validation about Inertia ‘I’

Add 12 kg mass on the gearbox, as showed as the Fig. 12. The mass was fixed at the position marked with red circle in the left picture. As showed as the right picture, the natural frequency of power train global bend mode#1 reduced 47 Hz after add the mass.

3.4 Conclusions

After several validations, some results were gained. The results are showed as Table 2.

1. The natural frequency is increased while the ‘K’ and ‘L’ are increased and the ‘I’ is reduced;
2. The connect stiffness is increased while the connect area size and the connecting plane stiffness are increased;

Table 2 Results of validations

Key parameters	Validate item	Means	Influence to natural frequency
Connect stiffness 'K'	Connecting bolt size	Displace the bolts M8–M6	Little
	Connecting bolt amount	Bolts amount reduced from 7 to 5	Reduce 22 Hz
	Connecting bolt fix torque	Fix bolts with 1/2 torque Fix bolts with 1/4 torque	Little Reduce 7 Hz
	Area size	Add two bracket to add connect area size	Increase 16 Hz
	Connecting plane stiffness	Add some rib on clutch box to strengthen the connecting plane stiffness	Increase 22 Hz
Span distance 'L'	Span distance	Compare two span distance's results with two group connecting bolts	The group have more span distance is 22 Hz more than another group
Inertia 'I'	Inertia	Add 12 kg mass on the gearbox	Reduce 47 Hz

3. The decrease of the account of connecting bolt, mean decrease of the connect stiffness;
4. Generally speaking, the connecting bolts' size and the fix torque mean a little with the natural frequency of power train global bend mode#1.

4 Example of Modal Optimization

The aim power train is a 4 strokes L4 gasoline power train, as showed as Fig. 13. Its rate speed is 5500 rpm. It is recommended that the frequency of power train global mode#1 should above 256 Hz. A flow was used in this optimize processing, as showed as in Fig. 14.

4.1 The Modal Parameters of the Original Power Train

There are 4 connecting bolts between clutch box and engine block in the aim power train. And the natural frequency of power train global bend mode#1 was 198 Hz. 198 Hz cannot avoid resonance excited by fire excitation while engine working at rate speed. So the modal of this power train need optimization.

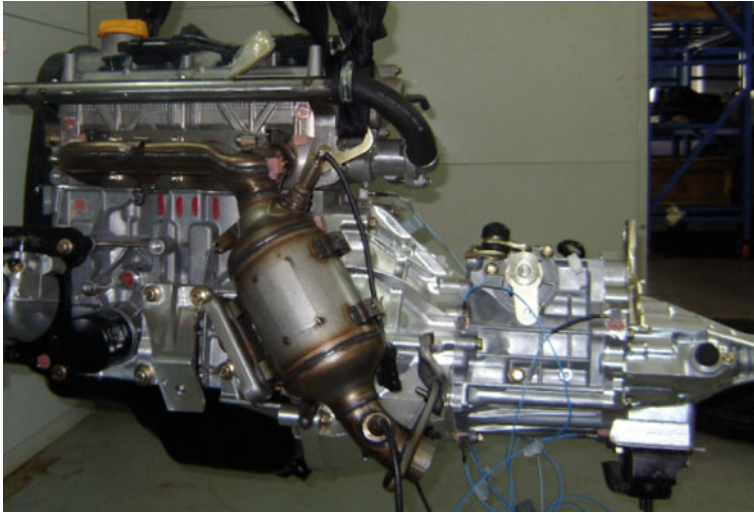
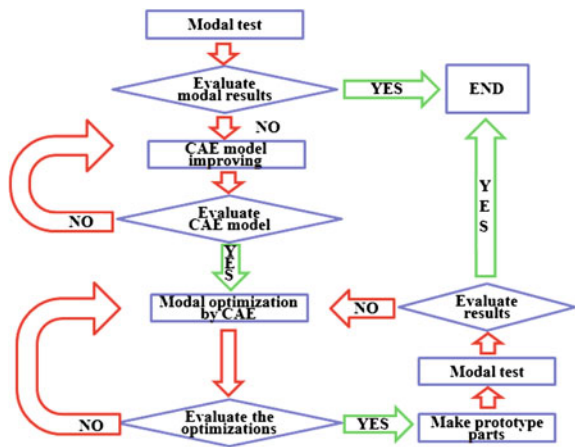


Fig. 13 The aim power train

Fig. 14 Flow of modal optimization



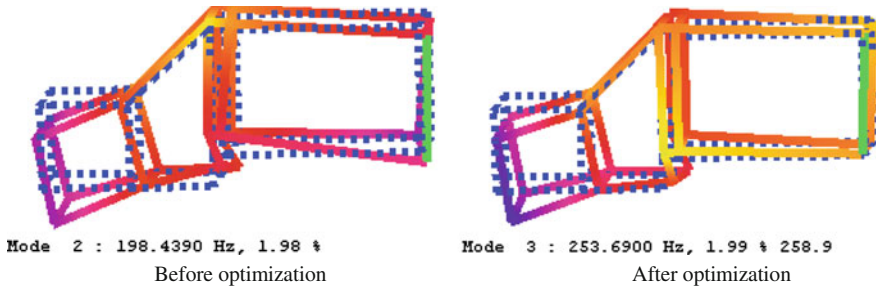
4.2 Modal Optimization

Several means were validated in this process, as showed as Table 3. After evaluated, most of the means were accepted except the one increase span distance, because it was hard to apply in the project.

After modal optimization, the natural frequency of power train global mode#1 increased from 198 to 254 Hz, as showed as Fig. 15. It almost achieved the natural frequency target. And have avoided the venture to get resonance by the engine fire excitation.

Table 3 Means of modal optimization

Optimizations	Means	Effective	Accept
Connecting bolt amount	Increase from 4 to 6	Yes	Yes
Connect area size	Add 2 brackets	Yes	Yes
Connecting plane stiffness	Add some rib on clutch box	Yes	Yes
Span distance	Increase span distance	Yes	No
Inertia	Gearbox reduce weight	Yes	Yes

**Fig. 15** Results compare of modal optimization

5 Conclusions

The global vertical connecting plane is the main factor to affect power train global bend mode#1, especially the connecting plane between clutch box and engine block. The key factors affect the power train global bend mode#1 include connect stiffness 'K', span distance 'L' and inertia 'I'. Validated some methods to improve connect stiffness and power train modal with several testing and CAE analysis, and educed some conclusions as following.

1. The natural frequency is increased while the 'K' and 'L' are increased and the 'I' is reduced.
2. The connect stiffness is increased while the connect area size and the connecting plane stiffness are increased.
3. The decrease of the account of connecting bolt, mean decrease of the connect stiffness.
4. Generally speaking, the connecting bolts' size and the fix torque mean a little with the natural frequency of power train global bend mode#1.

At last, applied these conclusions to optimize the modal of a 4 strokes L4 engine, and improved the natural frequency of power train global bend mode#1 from 198 to 254 Hz. This study has gotten some useful conclusions, and these conclusions can be used to optimize power train global bend mode effectively.

References

1. Pang jian, Zhan gang, He hua (2006) Vehicle vibration and noisetheory and application[M].
Beijing: Beijing Institute of Technology publishing house
2. Balachandran B, Magrab EB (2003) Vibration. Thomson-Engineering

Investigation on the Vibration of the Engine Fead Accessory Driving Belt

Yanping Ding, Yifeng Dong, Hanjie Liu, Jincai Yang, Qingwei Gu and Liang Zhang

Abstract Poly V belt is widely used in automotive gasoline accessory drive system. The FEAD belt vibration usually brings boring noise radiation from the front end of engine and easily causes belt fatigue failure. The reasons and influences on the excessive transverse vibration of the FEAD belt are investigated. By the test and simulation analysis, the belt vibration can be controlled by using OAD or modifying the layout of accessory drive or lowering the torsional vibration of the cranktrain.

Keywords FEAD belt · Transverse vibration · Slip · OAD

1 Introduction

With the increasing requirements of vehicle idle noise control and pass by noise control from the customers, the engine NVH performance vibration and noise become one of the major problems in automobile engineering. After the engine

F2012-J03-009

Y. Ding (✉) · H. Liu · J. Yang · Q. Gu · L. Zhang
State Key Laboratory of Vehicle NVH and Safety Technology, Chongqing, China
e-mail: sunqiemail@163.com

Y. Ding · H. Liu · J. Yang · Q. Gu · L. Zhang
Changan Powertrain R&D Center, Chongqing, China

Y. Dong
Changan Commercial Vehicle R&D Center, Chongqing, China

airborne noise is effectively controlled, the auxiliary noise becomes the main noise source. The accessory drive noise is one of the important sound sources regarding the sound pressure level and sound quality. Research of Dr. Kiran's [1–3], shows that accessory driving belt noise is controlled by changing the belt wrap angle or tension force, controlling the engine speed up/slow down rate, using one-way clutch, ensuring the belt alignment, etc. Anyway, the belt system structure resonance caused by the belt vibration must be controlled.

Poly-V belt is widely used in the engine accessory drive. Till now, the accessory drive noise mainly focuses on the control of misalignment and circumferential belt slip by controlling less pulley misalignment, low slip rate, larger friction coefficient, or even system re-design. The FEAD belt transverse vibration is mainly discussed in this paper.

2 Accessory Driving System Analysis

Figure 1 shows a basic belt driving system consisting of belt and driving/driven pulleys. The belt and pulley contact surface produces contact pressure. Assume the pre-load force in the belt is F_0 at the assembly static condition. When working in Fig. 2, the belt force at the tension side of the driving pulley is F_1 , the force of loose side is F_2 .

Then, the belt driving effective tension force F and the belt driving power P are:

$$F = F_1 - F_2 \quad (1)$$

$$P = F \cdot v \quad (2)$$

Where, v is the belt velocity.

Assuming the material obeys Hooke law, the tight side tension increment and loose side reduction are equal:

$$F_1 - F_0 = F_0 - F_2 \quad (3)$$

when the belt speed $v < 10$ m/s, the centrifugal force qv^2 can be ignored. Then, the relation of F_1 and F_2 can be expressed using the following exponent equation:

$$F_1 = F_2 e^{f\alpha} \quad (4)$$

where, f —friction coefficient, α —belt wrap angle (*rad*)

From Eqs. (1) and (4), we can get F_1 and F_2 :

$$\left. \begin{aligned} F_1 &= F \frac{e^{f\alpha}}{e^{f\alpha} - 1} \\ F_2 &= F \frac{1}{e^{f\alpha} - 1} \end{aligned} \right\} \quad (5)$$

Fig. 1 Belt driving system. 1 driving pulley, 2 belt, 3 driven pulley

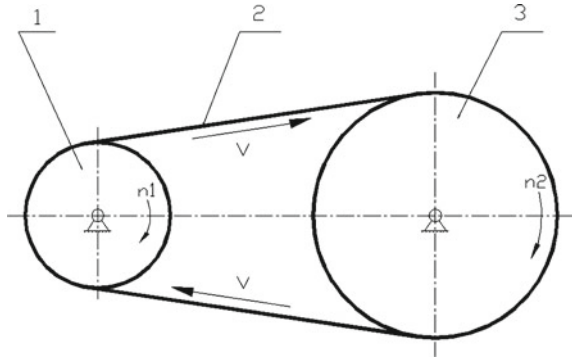
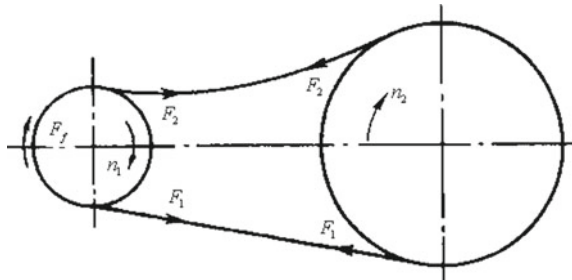


Fig. 2 Accessory belt drive at working state



Therefore from Eqs. (5) and (3), we can get the maximum effective tension force F_{max} , which reflects the belt driving capacity:

$$F_{max} = 2F_0 \frac{e^{f\alpha} - 1}{e^{f\alpha} + 1} \tag{6}$$

When effective tension force exceeds the critical friction force between the belt and pulley, the belt will slip. From the microcosmic viewpoint, the pitch length of the belt is a slightly short than that of pulley due to elasticity of the belt. Therefore, the slight slip can not be avoided but can be controlled by modifying the layout, changing the load of accessory, etc.

3 Transverse Vibration Engine Fead Belt Test and Analysis

The noise level is high at full load 1,000–2,000 rpm in Fig. 3. The FEAD belt has a strong slap at low speed and high load. In order to test the accessory belt transverse vibration, a laser non-contact vibration device was used in engine test bed measurement which was placed below the belt in Fig. 4. The test results in Fig. 5 show that the transverse vibration displacement between AC and crankshaft pulley reaches to amplitude of 16 mm which is beyond the design limit.

Fig. 3 FEAD belt noise at run up condition

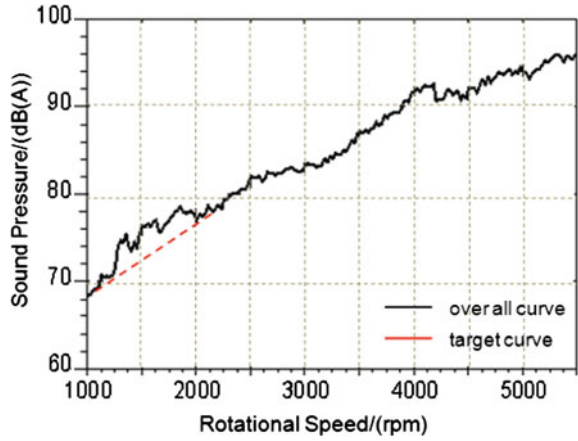


Fig. 4 Vibration laser device positioned under the belt



Simulation analysis of the FEAD accessory belt system was done to analyze the transverse vibration in Fig. 6, the simulation results in Fig. 7 show that the transverse vibration displacement between crankshaft pulley and AC is the greatest.

In order to investigate the noise contribution from FEAD belt transverse vibration, we removed the FEAD belt in the test. Noise level increases during full

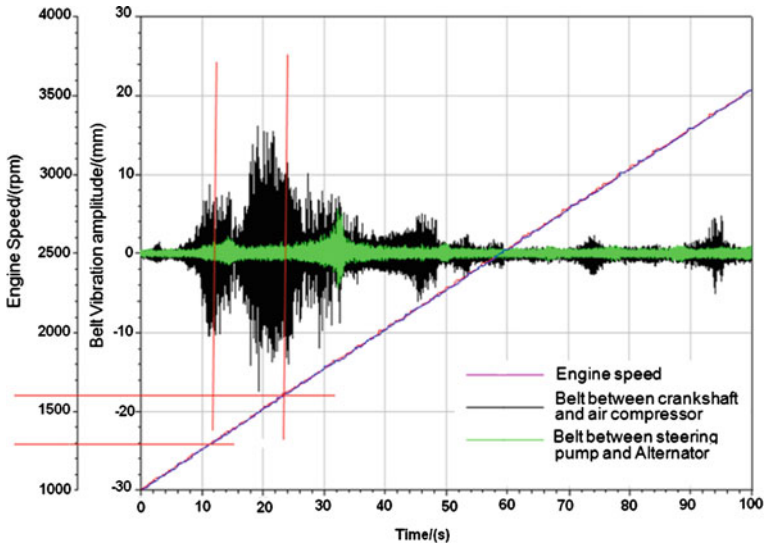
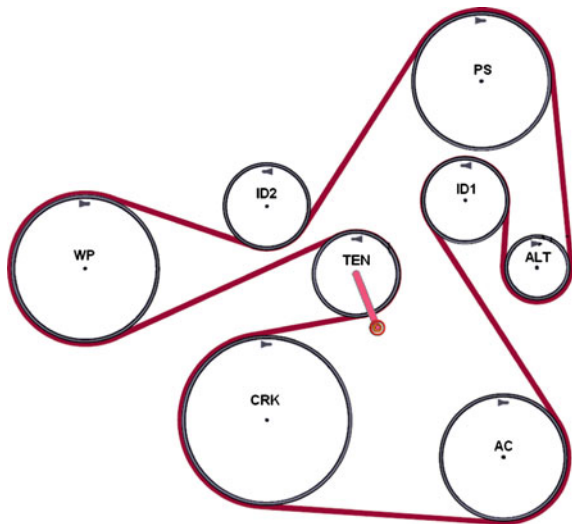


Fig. 5 FEAD belt transverse vibration displacement test result

Fig. 6 Accessory driving system



load run-up operating condition in Fig. 8. The average noise level is lower without belt as several accessories (especially alternator) are not driven. But it is obvious that the noise peaks are related to the belt vibration because such peaks could not originate from any of the accessories. The FEAD belt transverse vibration brings strong noise with poor sound quality.

Fig. 7 Simulation result of FEAD belt transverse vibration

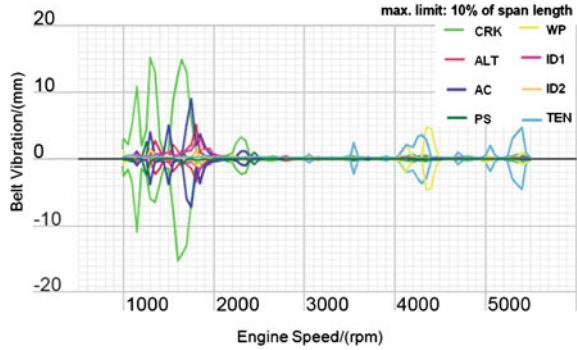
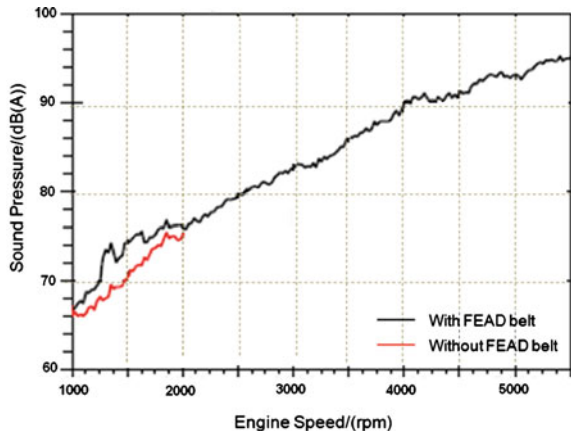


Fig. 8 The belt noise with/without FEAD at running-up operating condition



4 The Main Influences on Belt Transverse Vibration

4.1 Crankshaft Torsion Vibration in Inline-4 Gasline Engine

The simulation result in Fig. 9 shows that the angular displacement of damper hub is 0.21° , so that the torsional vibration is within requirement.

The belt vibration spectrum at full load run-up in Fig. 10 shows that the belt resonances are occurring approximately at 130 and 280 Hz. The resonance frequencies shift slightly with engine speed as the belt tension is reducing with higher engine speed due to the belt dynamics. In the low speed range the belt flap can be seen as a broadband vibration showing amplitudes in several orders. For 1300 rpm the orders 2 (43 Hz) and 4 (86 Hz) are dominant. At 1,600 rpm order 1 (27 Hz) and order 3 (80 Hz) are dominant. The result show that the FEAD belt vibration and noise is not relate to the crankshaft torsion vibration.

Fig. 9 Angular displacement magnitude of damper hub

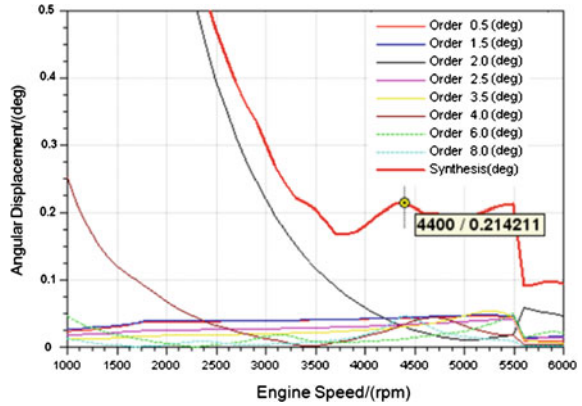
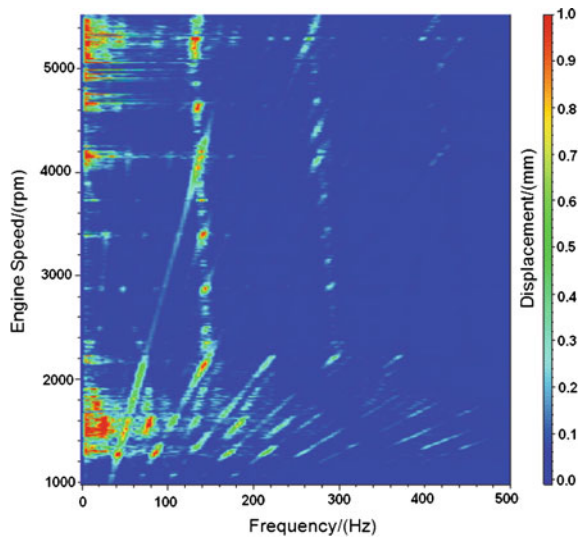


Fig. 10 Spectrum of FEAD belt transverse vibration



4.2 Engine Load

The belt transverse vibration is tested at the engine speed of 1,300 and 1,600 rpm with the engine output torque increasing by the step of 10 %. The results shown in Figs. 11 and 12, when the engine load is larger than 80 % at 1,300 rpm, the FEAD belt transverse displacement increases quickly and the noise level goes up significantly with 5 dB (A). So is the approximately the same results at 1,600 rpm.

Fig. 11 FEAD belt transverse vibration test result at different load

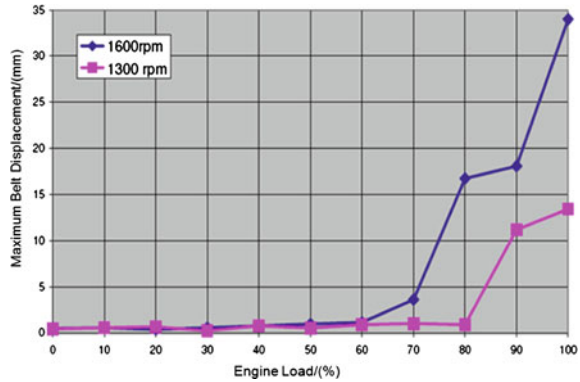
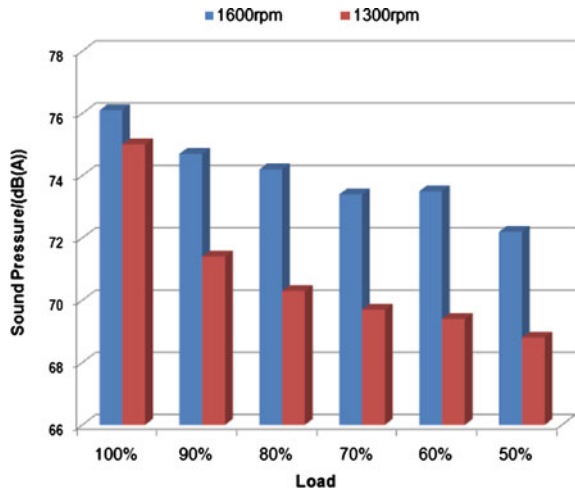


Fig. 12 Engine noise test result at different load



4.3 Optimizations

4.3.1 Idler Pulley

A test for reducing the belt vibration is utilizing of an additional idler pulley in the middle of the belt span between AC and crankshaft pulley in Fig. 13. The effect of the modification on 1 m noise at full load and running up operating condition is shown in Fig. 14. The belt noise from 1,300 to 1,600 rpm is reduced clearly.

4.3.2 OAD

It's necessary to use OAD to control the belt vibration caused by speed irregularity from the crankshaft and the output torque load of alternator. The accessory drive

Fig. 13 Layout of additional idler pulley

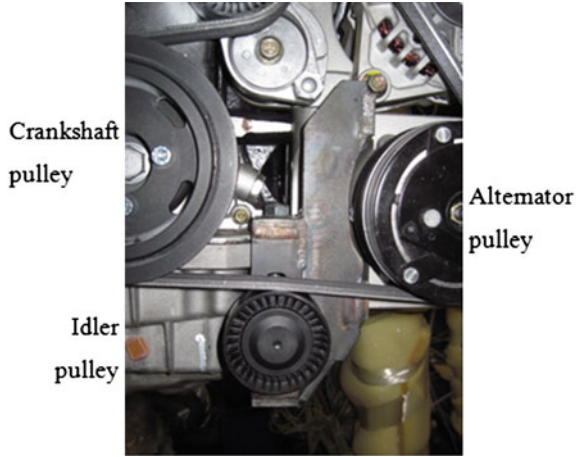
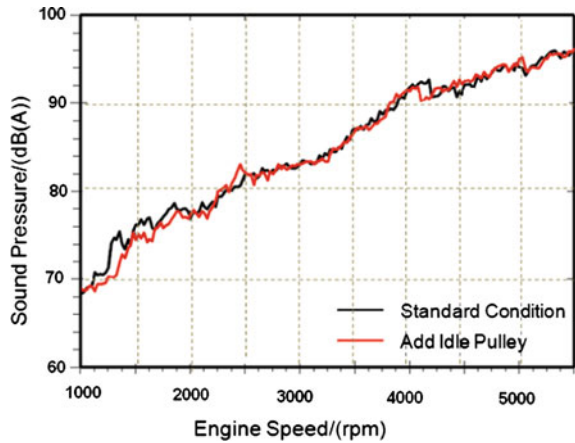


Fig. 14 Noise test result of with/without idler pulley



system, the alternator rotor inertial mass is larger, and the rotational speed is the crankshaft speed 2 ~ 3 times, thus the crankshaft speed fluctuation will amplify the alternator rotor vibration, resulting in large belt tension change, lead to the belt fatigue damage, and bring the noise in the front engine.

A one-way clutch used in the pulley of OAD is shown in Fig. 15. Usually in the accessory driving system, alternator has the maximum inertia. The one-way clutch can isolate the alternator rotor inertia torque and output load torque in one orientation from on the FEAD belt system. Thus, the angular acceleration and running torque fluctuations will be reduced (Fig. 16).

Fig. 15 One-way clutch

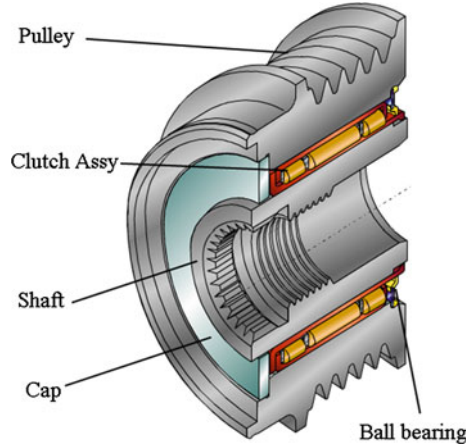
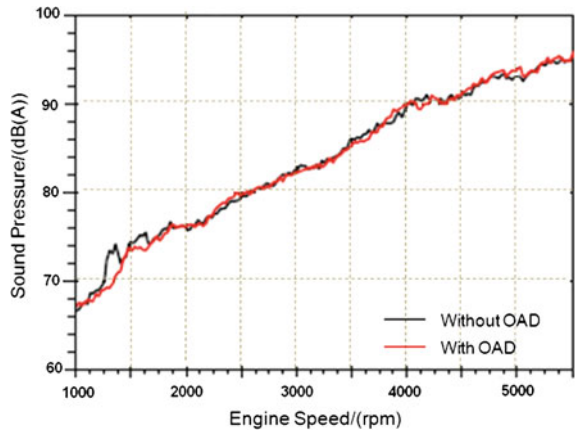


Fig. 16 Noise test result with/without OAD



5 Conclusions

- (1) The speed irregularities of engine crankshaft is a main cause for the FEAD belt vibration with higher noise and boring sound quality.
- (2) Without changing the layout of the accessory drive system, the OAD can isolate the crankshaft speed fluctuation from the effect of alternator rotor torsion vibration.

References

1. Sheng G, Miller LD, Pang J, Qatu MS (2006) Wet belt friction-induced dynamic instability and noise in automotive accessory belt drive systems. *Int J Veh Noise Vib* 2(3):251–252
2. Sheng G, Brown L, Pang J, Qatu MS (2007) Chirp, squeal and dynamic instability of misaligned V-ribbed belts in automotive accessory belt drive systems. *Int J Veh Noise Vib* 3(1):90–91
3. Govindawarry K (2001) NVH seminar component NVH accessories. FEV Engine Technol 1

The Effect of EMS Calibration on Noise Control of Turbocharger for Gasoline Engine

Pengyuan Liu, Shuxia Miao, Hui Zheng, Xianli Hu, Biao Du and Jugang He

Abstract This paper studied a noise problem of turbocharger engine, which results from activation of the dump valve. Lots of vehicle tests have been done to find out that this noise problem always occurs when quickly release the throttle pedal at the end of acceleration. At this condition, EMS opens the dump valve and the turbocharger pressure arises quickly, which results in the noise. After analyzing the control parameters and test data in detail, the control parameters of dump valve duty cycle at transient process and the dump valve opening timing were optimized by calibration. Through EMS calibration, assisted with mechanical optimization, the test results show that the waste gas pressure was reduced by 60 hbar at least, and the noise problem was solved successfully.

Keywords Engine · Turbocharger · Waste gate · Dump valve · EMS · Noise

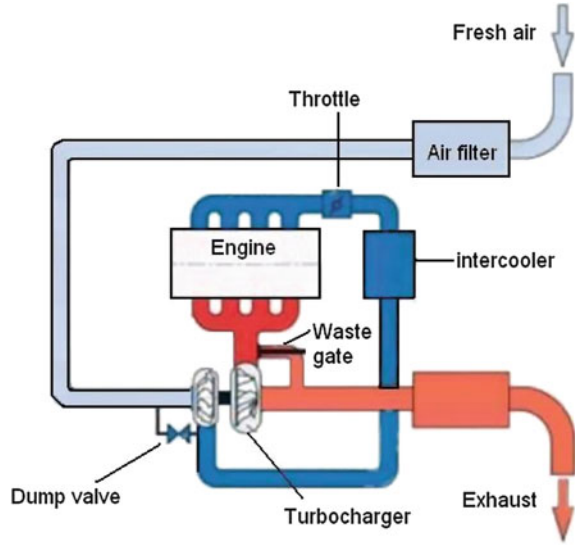
1 Introduction

Recently, as consumer has much more higher expectations to vehicle fuel economy and performances than ever, turbocharger gasoline engine has been applied widely as an effective way of engine downsizing and power boosting. The market share of turbocharged engine application is estimated to reach 36.1 % in 2019 [1].

F2012-J03-010

P. Liu · S. Miao (✉) · H. Zheng · X. Hu · B. Du · J. He
Changan Auto Global R&D Centre of Changan Automobile Co LTD, Chongqing, China
e-mail: miaosx@changan.com.cn

Fig. 1 Schematic drawing of a turbocharger engine



Many researches also focus on the area of gasoline turbocharged system from system design to performance [2–4]. A general gasoline engine turbocharger system is depicted in Fig. 1.

The turbocharger system is much more complex than normal engine and the turbocharger runs at condition of high pressure and high temperature. Because of its complex and severe working condition, more practical application problems have arisen. One of these is that when vehicle accelerates, engine needs much more fresh air and dump valve will be opened by ECU (Engine Control Unit) quickly, which results in sudden changes of charger pressure and noise. This noise will greatly reduce the vehicle performance of comfortability.

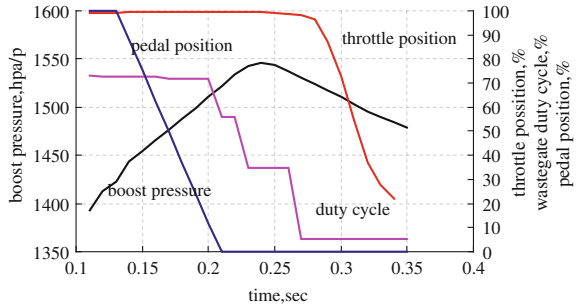
This study focuses on a specific acoustic problem and its optimization during the R&D of a middle size sedan with 1.8 L turbo-charged gasoline engine.

2 Dump Valve Activation Noise Analysis

2.1 The Noise Phenomena

It is well known that there exists a surge limit line in the compression graph (also be referred to as program map in many cases) describing the characteristic of a compressor for a typical turbocharged engine. Such compressor surge limit is the boundary line between stable and unstable operations. When engine running condition changes rapidly, the transient process may fall into an unstable operation range so that cause a surge acoustically.

Fig. 2 Typical parameter and status during noise occurs situation



In order to solve the noise surge problem of turbocharger engine during vehicle R&D, a dump valve is designed and activated open at specific conditions. But unfortunately another noise problem occurred in several conditions. One of the typical conditions is as follow: when engine coolant temperature is over 80 °C, and the vehicle starts to accelerate with a rude 100 % pedal from a static status on a slope road, keep engine running with wide open throttle (WOT) condition till engine reaches around 2,200 rpm, then loose the pedal suddenly, A noise that is often referred to as ‘whoosh’ noise within some SAE papers will occur.

From the above driving condition and the control principle of turbocharger engine, much less engine torque is requested when the acceleration pedal is released suddenly. To reduce the output engine torque quickly, ECU (Engine Control Unit) opens both the wastegate valve and dump valve to reduce the pressure of compressor and inlet manifold, cut down the fresh air that flows into the engine cylinder. When the dump valve opens, the airflow overflows the dump valve and causes the whoosh noise.

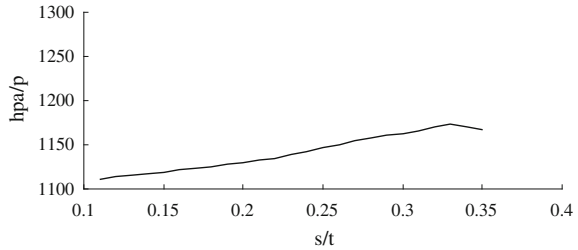
2.2 Root Causes Investigation

In order to find out the causes of this gas noise and an effective way to solve this problem with relatively low cost, an efficient and convenient method, a large number of engine dynamometer and vehicle tests have been done. By analyzing the test data in detail, two main possible causes are located. One is the transient process of dump valve opening and the other is the compensation of the valve inertia. The control parameters associated with the above two aspects are optimized by calibration. The effectiveness of the new control parameters are validated by vehicle tests.

Figure 2 shows the typical parameters and status when whoosh noise occurs.

As it can be seen, when pedal is released quickly and reaches idle position at about 0.22 s and the wastegate is actuated at around 0.2 s, it is expected that the turbocharger pressure decreases quickly as well. However, it is found in this case that the throttle position recovery has a delay and the turbocharger pressure

Fig. 3 Turbocharger pressure with waste gate open



increases to 1550 hpa continuously, which is about 1.5 times of atmospheric pressure. The following two reasons are considered:

1. Mechanical execution delay. The execution of waste gate from close to fully open position needs certain period of time due to mechanical delay or signal handling, so that transient process of the waste gate is slower than that of the throttle. When the throttle closes quickly, the waste gate still remains at a relatively heavier duty cycle.
2. The turbocharger inertia. When turbocharger runs in full load at WOT condition the turbine is running at very high speed and exhaust gas pressure is higher as well, it takes time for the turbine to slow down gradually due to its own inertia even if a sudden pedal release signal has been broadcast. Even after the control duty cycle of the waste gate reaches zero, the turbocharger pressure may still increase continuously.

It is found that under above condition, the dump valve was actuated to further release the pressure and torque request quickly when the pressure is near its peak value, then the unpleasant whoosh noise is heard. Therefore it is believed that the high pressure remained in the turbocharger system may be the cause of the whoosh noise at those typical situation.

2.3 Causes Validation

Now that the possible cause of the noise problem is the improper control principle of the waste gate transient process, a special experiment is designed to further validate this conclusion. During this experiment, the waste gate was kept at the wide open position so that the transient process was cancelled while keeping other conditions same as the above section. The test result is show in Fig. 3.

From the test result, the turbocharger pressure increases slowly during the whole process and the maximum pressure is only 1170 hpa, which is much smaller than that in Fig. 2. The relief noise disappeared at the same time. According the above comparison results, the control principle of waste gate transient may be improved by reducing the turbocharger pressure, which is good for solving the noise problem. Of course, this extreme case only shows some strategy direction

but can not be applied since the turbocharger loses its boost effect totally in the whole process.

3 Calibration Improvement on Noise

From above analysis, it is concluded that the activation of the valve is a key factor of this noise problem. Several methods can be adopted to improve the transient process of the valve activation and solve the noise problem, such as redesigning the control logic of the waste gate transient process, adopting new turbocharger whose response is much faster, redesigning the air flow system, etc. But all these methods need much more time and cost, which can hardly satisfy the requirements of the project. Furthermore, other work package and vehicle performance may be influenced negatively. A low cost, efficient and convenient method should be considered. Obviously, EMS calibration improvement is a much better route.

From the point view of EMS calibration, two types of control parameters may be calibrated to solve this whoosh noise problem. One is to adjust parameters associated with the transient duty cycle control of waste gate and the other is that associated with the compensation for the turbocharger inertia. The details of the calibration improvement are discussed as following.

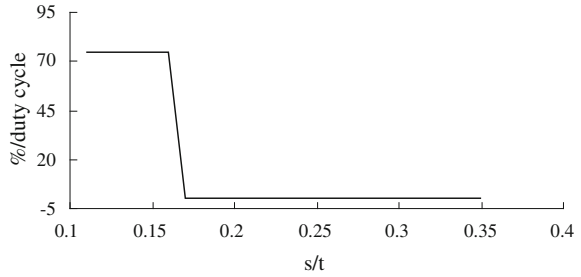
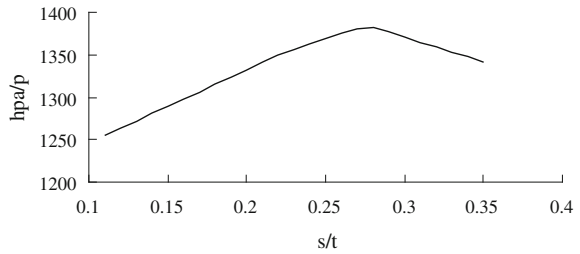
1. *Calibration the dynamic duty cycle of waste gate*

The results show that the turbocharger pressure is greatly reduced, which is at least 60 hbar, and the total engine noise lies in acceptable range. The problem is solved successfully by calibration of control parameters without any modification of hardware and control logic.

In the original calibration, the duty circle of the turbocharger controlling doesn't open 100 % immediately after the accelerate pedal was released. It causes the exhaust pressure to keep rising when the dump valve opened. As a result the reduction of boost pressure will be slow too. When the duty cycle of the waste gate was calibrated to drop down with some slope from 100 to 0 % but without intermediate stages of volume-flow factors, the actual boost pressure is 60 hpa lower than before. Its means the strategy in Fig. 4 is useful to reduce boost pressure to some extent.

2. *Calibration the lowest actual boost pressure*

Since sound noise pressure level becomes higher when the actual boost pressure is much higher. Therefore, it is possible to reduce the noise pressure level from dump valve releasing by calibrating the boost pressure to the lowest level. When the turbocharger is operating, low pressure periods occur at either before boost pressure has not risen to the peak, or holding dump valve till boost pressure has reduced down to certain level. In the first case, the dump valve needs to response quickly right after pedal release; and in the second case, a surge noise must be

Fig. 4 Changed duty cycle**Fig. 5** Actual boost pressure

prevented in the same time. Through numerous tests, two representative proposals were tested:

2.1 The dump valve was hold to the last moment, and the throttle closing velocity is set as half of than original.

After the duty cycle has been improved, the next step needs to consider how to reduce the actual boost pressure. That is useful for the noise control when the dump valve opened at a lower pressure level.

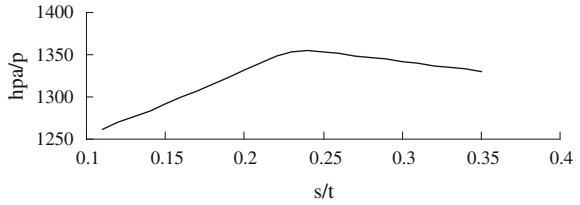
By adjusting the calibration controlling strategy, the dump valve is opened as late as possible, so that most airflow mass is consumed in the combustion when the dump valve is going to open, the pressure can be reduced while ensuring that the surge does not occur at that time. When the dump valve opened, the actual boost pressure is about 1,360 hpa, about 80 hpa lower than before.

2.2 The dump valve opened as soon as possible and the throttle closing velocity is twice of the original (Fig. 5).

This proposal is to validate whether the boost pressure can be reduced anymore when the dump valve opened earlier and keep the throttle closing velocity is same with the last proposal.

As the test data shown in Fig. 6, this strategy can reduce the actual boost pressure more significantly than before. When the dump valve opened, the actual boost pressure is less than 1,300 hpa, lower about 60 hpa than the last proposal. Therefore, this proposal is the most effective to reduce pressure when the dump valve opened.

Fig. 6 The boost pressure when dump valve is actuated as soon as possible



4 Conclusion

High boost pressure can causes the whoosh noise aloud when the dump valve opens after the accelerate pedal released. The dynamic duty cycle of waste gate and actual boost pressure can be optimized through EMS calibration.

1. The EMS can control the waste gate the dump valve and the throttle closing velocity deliberately so that the boost pressure can be adjusted effectively during transient period. Boost pressure can be reduced up to 150 hpa through calibration only.
2. Calibration the duty cycle of the waste gate can improve the actual boost pressure without any negative effects;
3. Reduce the boost pressure can reduce the noise level.

References

1. IHS automotive light vehicle engine forecast: engine production (2012) 1
2. Lin JS (2005) The principle and applications of turbine engine and turbo chargers. Tianjin University Press, Tianjin
3. Li H, Zhou J, Sun Z (2012) NVH mechanism and its control of vehicle turbocharger. Beijing Mechanical Industry Press, Beijing, 1
4. Bernhard schweizer dynamics and stability of turbocharger rotors 6 May 2009

The Method of Accurate Sound Source Localization for the Engine Abnormal Noise

Jincai Yang, Zhangsong Zhan, Hanjie Liu, Liang Zhang, Lingfeng Qian and Yanping Ding

Abstract The multi-source information fusion method with three kinds of signals is given in this paper to identify engine sound sources. The three signals are the wavelet analysis result of engine sound and vibration, the crankshaft rotating angle and the camshaft phase, using these signals can accurately make sure the vibration and noise state of the moving parts of the engine at a certain state. As a result of the limitations of normal continuous wavelet transform (CWT) arithmetic, a frequency correction algorithm of wavelet analysis and an A-Weighted correction algorithm of wavelet analysis are put forward. Thus, the correction wavelet coefficients are more suitable for the sound identification in actual engineering application. An engineering case is studied in this paper and a good identification result is obtained.

Keywords Multi-source information fusion · Engine impact noise · Wavelet analysis · Sound source identification

1 Introduction

With the improvement of people's living standard, the comfort demand of the vehicle is increasingly high, the vehicle NVH performance becomes more and more important. Automobile engine is the power source, is also the largest noise

F2012-J03-011

J. Yang (✉) · Z. Zhan · H. Liu · L. Zhang · L. Qian · Y. Ding
Powertrain Global R&D Center in Changan Automobile Co. Ltd, Mainland, China
e-mail: sunqiemail@163.com

J. Yang · H. Liu · L. Zhang · L. Qian · Y. Ding
State Key Laboratory of Vehicle NVH and Safety Technology, Chongqi, China

and vibration source of the automobile [1]. The vehicle NVH level depends largely on the level of engine NVH. The separation and identification of the engine main noise source is the principal important issue in the noise control. To find the engine main noise sources, to take pertinent measures, and to be able to achieve the desired effect in the noise reduction.

Literature [2, 3] and [4] studied the basic problem of the continuous wavelet transform which was applied to the noise source identification of the internal combustion engine, but it only used a single noise or vibration signal for sound source identification. As an engine has many mechanisms, the movement relationship is complex, hot state and cold state will lead to the large difference, the combustion excitation is very hard and the parts are precision, so, it is difficult to localize the source of vibration and noise, this paper proposes an analytical technique which uses the multi-source information fusion to determine the engine noise source.

Multi-source information fusion analytical technique uses multiple sensors to get the general and correct estimate for the environment, compared to a single sensor, it can get more accurate and reliable conclusions [5]. The multi-source fusion analytical technique mainly is used in military field at first, now it has been successfully used in many disciplines, such as navigation, automatic target recognition, multiple target tracking, robot, small processing and so on. This paper studied the multi-source information fusion analysis technique used for the engine noise source identification, and achieved good results.

2 Multi-Source Information Fusion Analysis Techniques

The multi-source information fusion analysis technique, is to make full use of different time and space multi-sensors information resources, to analyze, integrate and control in certain rules, to get the coincident interpretation and description of the measured object and complete the required tasks, finally, the system obtains the more superior performance than its components. Multi-sensor system is the hardware basis for information fusion analysis technique, multi-source information is the analysis objects of information fusion, coordination, optimization and integrated is the core of information fusion [6].

The structure of the information fusion system hasn't a unified classification, in the functional point of view of information fusion, the information fusion process can be divided into 5 levels, that is detected (judgment) fusion, state (tracking) fusion, attribute (target recognition) fusion, situation assessment and threat assessment. Attributes fusion aims to determine the identity of the target, according to 3 levels of the data abstraction, attribute fusion is divided into: data fusion, feature fusion and decision fusion [5]. According to the engine noise source identification features, using the feature fusion of attribute level is more appropriate, the structure of feature fusion shows in Fig. 1. The following analysis show that how to use the feature fusion to identify the engine noise sources.

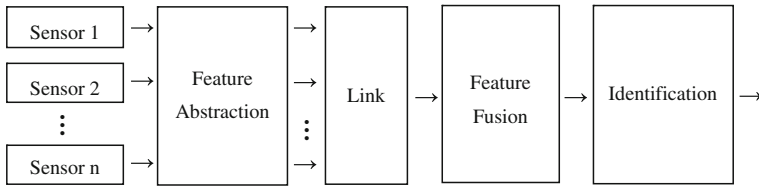


Fig. 1 Fusion structure of the feature level

Vibration and noise signals are the basic signals, applied to the multi-source information fusion technology analysis in the engine noise source identification. At present in the engine vibration and noise analysis, Fourier transform technique still plays an important role, but the Fourier theory cannot get the time domain localization analysis, only get the macro analysis in the entire time course, it is unable to fully reveal the non-stationary signal transient message. The internal combustion engine vibration and noise signal is a typical non-stationary, time-varying signal, and has the local impact signal characteristics. For this type of signals, must adopt the time–frequency analysis method, it is more scientific. In the time–frequency analysis method, wavelet analysis is known as signal analysis mathematical microscope, is a very suitable for the internal combustion engine signals analysis in time–frequency analysis [7]. In this paper, the wavelet analysis result is used as one of multi-source analysis basic signals.

An engine has many institutions, movement relationship is complex, but there is a definite relation between the components of the movement. In the engine development process, generally the crankshaft rotation angle is controlled, which means that through the angle domain to analyze their mutual relations generally. So as knowing the crank angle, we can determine the relative position of each moving parts, thus the engine crankshaft rotation angle as another signal of a multi-source information fusion analysis.

The vehicle engine is generally four-stroke engine, the crankshaft rotates two revolutions, and the engine completes a work cycle. So some parts of the engine (such as a piston) in a work cycle have two times same motion state, but in different work processes. For example, the pistons have two upward movement states, but one in the compression stroke, one in the exhaust stroke, so only the crankshaft rotating angle cannot distinguish which stroke is working, and the work processes have a different impact on the vibration and noise. It is also necessary to separate them by another signal. After research, this paper chose the engine camshaft position signal. With the camshaft position signal, coupled with the crankshaft rotation angle, the engine moving parts state can be uniquely determined.

Of course, there are many methods to uniquely determine the movement state between the engine moving parts, but with the crankshaft rotation angle and the camshaft position is the least signal sources, and is the most easy test method.

Figure 2 shows the specific structure of feature fusion for the engine noise identification.

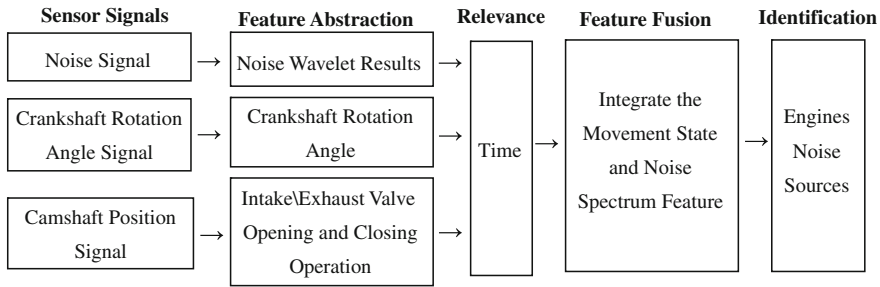


Fig. 2 Feature fusion of the engine noise source identification

In Fig. 2 three signals of the operation engine are: the wavelet analysis result, crankshaft rotation angle and the intake/exhaust valve opening and closing operation. The three signal sources have a connection link: time, through the time can put them together, and accurately find the vibration and noise state of the engine moving parts in a motion, completed noise source identification.

3 The Improved Algorithm of Wavelet Analysis for Noise Source Identification

Wavelet analysis is a very good tool of time–frequency analysis that can accurately extract the information in the time domain and frequency domain of the signal, but there are two limitations if directly applied to the engine noise signal analysis: one is high frequency attenuation of the wavelet coefficients, another one is not a reflection the A-weighted characteristics of the automobile noise. Therefore, wavelet analysis is applied to the engine noise analysis, needs for frequency correction and the A-weighted correction.

3.1 The Frequency Correction Algorithm of Wavelet Analysis

Assume that the signal $f(t) \in L^2(R)$ is a space, $\psi(t)$ is the basic wavelet or mother wavelet function, then the general mathematical definitions of continuous wavelet transform about the signal $f(t)$ is defined [8]:

$$W_x(a, \tau) = \langle x(t), \psi_{a,\tau}(t) \rangle = \frac{1}{\sqrt{a}} \int_R x(t) \overline{\psi\left(\frac{t-\tau}{a}\right)} dt. \tag{1}$$

Formula (1) shows that wavelet analysis is an integral operation, in the change process, if the signal has a component $\sin(2\pi f_i t)$, there will be a factor $1/\sqrt{2\pi f_i}$ via

continuous wavelet transform, therefore, the higher the frequency components of the signal, via the continuous wavelet transform, the amplitude attenuation is more, then the resulting wavelet coefficients, its size can not accurately reflect the strength of the different frequency components in the signal, then for identifying the noise source, that easily leads to miscarriage of justice, so must improve the usual algorithm.

According to the superposition properties and scaling transform properties of wavelet transform properties, taking into account the congruent relationship of the scale and frequency of wavelet transform, to modify Eq. (1) via applying Eq. (2):

$$W'_x(f, \tau) = \sqrt{2\pi f}W_x(f, \tau) \tag{2}$$

A modified wavelet coefficients can accurately reflect the strength of the signal frequency components, these noise source identification results are more reasonable and accurate.

3.2 The A-Weighted Correction Algorithm of Wavelet Analysis

The noise signal analysis and processing, the ultimate goal is to identify noise sources, to distinguish major and minor components in the noise, then to achieve noise control. The current the national compulsory noise standards refers the A-Weighed sound level, which is also the closest to the human hearing reflection. Therefore, starting from the engineering point of view, in order to meet the project needs better, the noise signal processing is not only restricted to reflect the signals in a variety of components, but also to” listen” bases on A-Weighted sound level perspective from the requirements of national standard, and then to analyze the noise signal, on the basis of A-weighted to analyze the major and minor components of the signal, to look for the A-Weighted sound level most contributor of the main noise source, and to provide foundation for noise control.

Generally the A-weighted level is expressed in decibels (dB) (Fig. 3), it can be understood as the noise level on a variety of frequency noise components together with the corresponding weights, in fact, the A-weighted level is a product operations.

Figure 3 shows the weighted data, it converts by formula (3), and A-weighted multiplication can be obtained (Fig. 4).

$$A(f) = 10^{A_1(f)/20} \tag{3}$$

where: $A_1(f)$ is an A-weighted level expressed in decibels, $A(f)$ is A-weighted data converted corresponding multiplication.

Figures 3 and 4 show that the A-weighted is very large impact on various frequency components of the noise. To meet the requirement of national standard

Fig. 3 A-weighting network decibels value

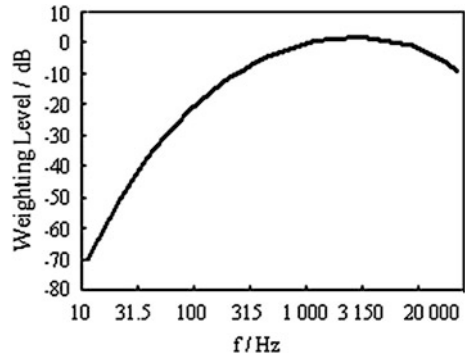
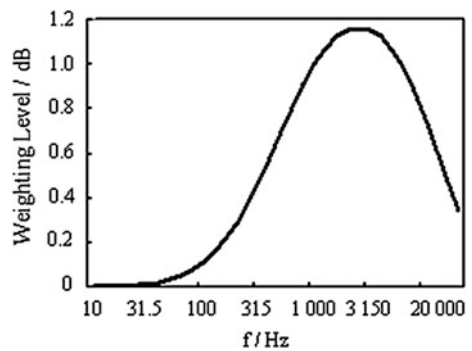


Fig. 4 A-weighting network multiplication weights



in the actual noise control in order, it is very necessary to analyse the principal components of the signal based on A-weighted and to find the main noise source which is the most A-weighted levels contributor.

The size of the wavelet coefficients which transformed by formula (2) can correctly reflect the strength of the various frequency noise components, but to find the main noise source on the most A-weighted levels contributor, also the wavelet coefficient transformed should be A weighted.

A-weighted correction of the wavelet coefficients is achieved by formula (4):

$$W''_x(f, \tau) = W'_x(f, \tau) \times A(f) \tag{4}$$

The noise source identification, based on the A-weighted correction wavelet coefficients, the result is closer to the human ear, on the basis of these result to control noise and can get more obvious effect.

4 Engineering Applications of Multi-Source Information Fusion of Analysis Technique

The valve noise is one of the common engine noise, it can be effectively eliminated by using the roller finger follower (RFF) valve trains with hydraulic valve lash adjustment (HLA), thereby this structure has become choice for more and more high quality engine, but low temperatures will lead to an bad impact for the hydraulic component. The following is the specific application of the information fusion, shows the impact noise identification between the roller finger follower and the cam.

A line-4-cylinder SI engine uses the roller finger follower valve trains with hydraulic valve lash adjustment, in the early development test the engine starting sound is normal, while in the winter as temperatures fall, found that the impact noise existed in vehicles equipped with these engines when cold starting, the abnormal sound duration of varying lengths, some were 1–2 s, and others were more than 3 min, and it disappeared after the heat.

Based on the subjective evaluation and the data character compare between abnormal noise and normal noise, this abnormal noise can be determined from the fourth cylinder and occurred in compression stroke, one time per cycle. In order to accurately locate abnormal sound location and solve the problem, we researched the structure and the motion process of the valve train, and collected the noise and vibration signals, the crank angle signal, the intake camshaft phase signal from existing abnormal noise in the engine cold starting to abnormal sound disappeared after the hot engine, it is the basic preparation for multi-source information fusion analysis methods.

Figure 5 shows the fourth cylinder abnormal noise identification by multi-source information fusion technology, the abnormal noise can be found before the intake valve closed, then can be calculated accurately:

The time of the abnormal noise occurred is: $\frac{71.42766 - 71.42098}{71.47729 - 71.35898} \times 720 = 40.6^\circ\text{CA}$, namely, the camshaft position is: 20.3° .

When the engine was cold starting in the low temperatures, the abnormal sound occurred once a work cycle, and before the intake valve closed, so this impact noise generation mechanism could be inferred:

When the temperature is low, the viscosity of lubricant is increased, thereby the air in the hydraulic valve lash adjustment isn't be discharged smoothly, resulting in the initial operation stage hydraulic pressure is insufficient, then the impact noise occurs between the roller finger follower and the cam, in the other words, in the low temperature cold starting condition, when the valve is fully open state, the cam tip contacts the roller finger follower (Fig. 6), the hydraulic valve lash adjustment is in compression stage; the valve trains keeps on operation, the cam tip departs from the roller finger follower, and the valve starts closes, due to lack of hydraulic, the hydraulic tappet plunger does not bounce, results in the roller finger follower lost touch with the cam, the valves keep on close, when the lift reaches a certain

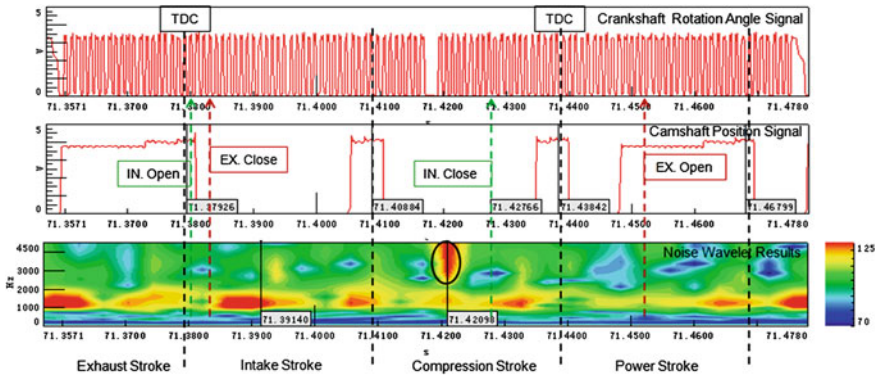


Fig. 5 The fourth cylinder abnormal noise location by multi-source information fusion technology

Fig. 6 Schematic diagram of valve trains



value (in this case the camshaft angle is 20.3°), the valve lifter promotes the roller rocker to hit the cam, then the impact noise occurs.

Based on the above speculation, an oil pressure establishment test was designed, to validate the reasons that the cam hit the roller rocker due to the hydraulic adjustment failure at low temperatures:

The transparent pipe was connected to the hydraulic valve lash adjustment oil duct end, to check the need time that the hydraulic tappet oil pressure reached the design oil pressure at different temperatures.

The results showed that:

1. The hydraulic valve lash adjustment oil duct end pressure set-up time needs $4 \sim 5$ s, so the abnormal sound will exist in startup 5 s.

2. The abnormal noise related to the engine cooling fluid and oil temperature. When the temperature was low, the abnormal noise occurred, and the temperature rose to a certain level the abnormal noise completely disappeared.
3. The air existed in the hydraulic tappet oil passages when the engine started.

The above test validates the accuracy of the impact noise localization and the reason analysis, making use of multi-source information fusion technology between the roller finger follower and the cam.

The above specific application shows the recognition method using multi-source information fusion technology, and it is effective, which can be extensively applied to the engine vibration and noise source identification.

5 Conclusion

1. The engine vibration and noise wavelet analysis result, the crankshaft rotation angle and camshaft position signal to integrate and analyze, can accurately judge the vibration and noise state of the engine moving parts in a motion.
2. In multi-source information fusion analysis, the wavelet analysis algorithm is necessary to carry out the frequency correction and the A-weighted correction.
3. The specific application which the impact noise occurs between the roller finger follower and the cam, confirms the multi-source information fusion analysis technique is accurate, efficient and practical.

References

1. Pang J, Chen G, He H (2006) Automotive noise and vibration-principle and application. Beijing Institute of Technology Press, Beijing
2. Yang J, Hao Z, Jia W (2006) Using continuous wavelet transform to identify internal combustion engine sound source. *J Zhejiang Univ (Eng Sci)* 40(3):404–407
3. Yang J, Hao Z (2006) Using a-weighting CWT to identify internal combustion engine sound source. *J Zhejiang Univ (Eng Sci)* 40(7):1174–1177
4. Yang J, Hao Z, Jia W (2005) The wavelet analysis method of transmission noise source identification of I.C. engine. *Chin Intern Combust Engine Eng* 26(5):74–76
5. Fan X, Su L, Guo J (2005) Summary of multi-sensor information fusion. *J Hohai Univ Changzhou* 19(1):1–4
6. Zhang Y (2008) Research on sensors fault diagnosis approach based on multi-source information fusion. North China Electric Power University, Beijing, p 5
7. Desantes JM, Torrerrosa AJ, Broatch A (2002) Wavelet transform applied to combustion noise analysis in high-speed DI diesel engine. SAE paper, 2002-01-1545
8. Peng Y (1999) Wavelet transform and engineering application. Science Press, Beijing

Sound Source Identification Based on Acoustic Source Quantification by Measuring the Particle Velocity Directly

Byung Hyun Kim, Tae Jin Shin and Sang Kwon Lee

Abstract The sound intensity and airborne source quantification methods were used to estimate the airborne noise radiating from a gasoline direction injection engine and the contribution of gasoline direction injection engine components to such airborne noise. In order to estimate noise contribution using airborne source quantification, the volume velocity for source should be estimated. In the previous method, the volume velocity has been estimated by using the inverse method. In this paper, the volume velocity is estimated directly. For this work, the sources of noise radiating from the engine are first identified by measuring the sound intensity of the noise sources while the car's engine is running at idle condition. The volume velocities of these sources estimated by multiplying the area of that noise source and directly measured particle velocity. In order to validate the proposed method, two speakers with different frequencies were installed in an anechoic chamber and the contribution of each source was estimated. Finally, the proposed method was applied to the identification and contribution of noise sources in a gasoline direction injection engine.

Keywords GDI engine · Sound intensity · Acoustic source quantification · Frequency transfer function

F2012-J03-012

B. H. Kim (✉) · T. J. Shin · S. K. Lee
Inha University, Incheon, Korea
e-mail: sangkwon@inha.ac.kr

1 Introduction

Recently, the development of fuel-efficient, high-powered and environmentally friendly engines has gained prominence. In particular, environmental performance has come under strict legal regulations, rather than being an optional enhancement, and the importance of engines' environmental performance has grown steadily. Due to such circumstances, the GDI (gasoline direct injection) engines have emerged as having significant advantages in fuel economy, output power and environmental performance. However, GDI engines generate increased noise due to inherent requirements for components, such as high-pressure fuel pumps, fuel injectors and fuel rails, and such noise has increasingly become an issue [1]. Therefore it is an import task to identify the noise sources and their contribution in a GDI engine for the refinement of GDI engine. The research in this paper used sound intensity method and ASQ (acoustic source quantification) techniques to identify noise sources among GDI engine components, and expresses the noise contribution of such components. Sound intensity method has been used for sound source identification, visualization of acoustic energy flow and measurement of sound penetration and loss. This method has the advantage of being able to ignore background noise, and therefore, is used frequently to identify noise source, both in labs as well as in the field. Sound intensity at a given point is expressed as a complex quantity obtained by multiplying the sound pressure and particle velocity [2–5]. ASQ technique is used to quantify airborne noise sources and aims to determine the contribution level of each noise transfer path by considering the transfer path between each noise source and response at target point [6, 7]. Generally, in the application of ASQ, an inverse matrix method is mainly used to obtain the volume velocity of the airborne noise sources [8, 9]. However, there is the error inherent in the inverse matrix process of the transfer function. In order to avoid the error, in the paper, the volume velocity of noise sources is directly calculated by multiplying the particle velocity and the area of the noise sources obtained during the measurement of sound intensity. ASQ technology with the volume velocity is used to estimate the sound pressure of response at target point. To identify the noise sources of a GDI engine equipped vehicle while idling, the research first used the 1/2 inch PU-probe of Microflown Technologies Company to map the sound intensity of noise sources. Afterwards, the particle velocity was measured simultaneously with sound intensity. Noise sources were identified using the measured intensities, and the volume velocity of each source was obtained by multiplying the area of that noise source and measured particle velocity. Applying this to ASQ, the noise contribution levels of GDI engine components were analyzed.

2 Theory of Sound Intensity and ASQ

2.1 Sound Intensity

Sound intensity is expressed in vectors that indicate the magnitude and direction of sound energy propagated from a given point. Intensity I_n in a specific direction n equals the energy passing through a unit area of plane perpendicular to the direction of transfer, and is defined by Eq. (1).

$$\vec{I}_n = \frac{dE_n}{dt \cdot dA} \quad (1)$$

where E_n is acoustic energy of a noise source. The sound intensity vector I_n is the average of values derived by multiplying the momentary sound pressure and particle velocity at a specific position, and is defined by Eq. (2) when the signal is stationary.

$$\vec{I}_r = \overline{p(r,t) \cdot \vec{u}(r,t)} \quad [W/m^2] \quad (2)$$

The cross correlation function between the sound pressure and particle velocity is defined by Eq. (3).

$$R_{pu}(\tau) = \lim_{T \rightarrow \infty} (1/T) \int_0^T p(t)u(t + \tau)dt \quad (3)$$

The average of sound intensity values in direction n can be expressed as follows:

$$I_n = \lim_{T \rightarrow \infty} (1/T) \int_0^T p(t)u_n(t)dt = R_{pu}(0) \quad (4)$$

In order to convert the multiplication of sound pressure p and particle velocity u into frequency ranges, Fourier transform must be applied to the cross correlation function. The intensity of cross power spectrum $S_{pu}(\omega)$ is expressed in Eq. (5).

$$S_{pu}(\omega) = \frac{1}{2\pi} \int_{-\infty}^{\infty} R_{pu}(\tau)e^{-j\omega\tau}d\tau \quad (5)$$

This function takes the form of complex quantities that indicate the average phase relation of pressure p and particle velocity u . $R_{pu}(\tau)$ and $S_{pu}(\omega)$ are a pair of Fourier transforms, and can be expressed as below.

$$\begin{aligned} R_{pu}(\tau) &= \int_{-\infty}^{\infty} S_{pu}(\omega)e^{j\omega\tau}d\omega \\ I_n = R_{pu}(0) &= \int_{-\infty}^{\infty} S_{pu}(\omega)d\omega \end{aligned} \quad (6)$$

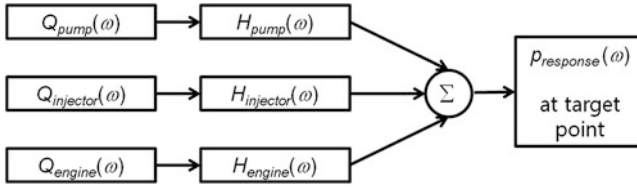


Fig. 1 Modeling of noise transfer path of linear system for ASQ application

Based on this aspect, $S_{pu}(\omega)$ represents the sound intensity in frequency domain. Therefore, the cross power spectrum can be characterized by Eq. (7).

$$\begin{aligned} \text{Re}\{S_{pu}(\omega)\} &= \text{Re}\{S_{pu}(-\omega)\} \\ \text{Im}\{S_{pu}(\omega)\} &= -\text{Im}\{S_{pu}(-\omega)\} \end{aligned} \tag{7}$$

In Eq. (7), $S_{pu}(\omega)$ can have both positive and negative frequencies, but from a signal processing viewpoint, it is more convenient to check using positive values only, so the equation can be rephrased as Eq. (8).

$$\begin{aligned} G_{pu}(\omega) &= 2S_{pu}(\omega) \quad \omega > 0 \\ G_{pu}(\omega) &= S_{pu}(\omega) \quad \omega = 0 \\ G_{pu}(\omega) &= 0 \quad \omega < 0 \end{aligned} \tag{8}$$

where $G(\omega)$ means power spectrum in the only positive side frequency domain. Then, the value of sound intensity by component can be defined by Eq. (9).

$$\begin{aligned} I_r(\omega) &= S_{pu}(\omega) + S_{pu}(-\omega) \\ &= 2\text{Re}\{S_{pu}(\omega)\} \\ &= \text{Re}\{G_{pu}(\omega)\} \end{aligned} \tag{9}$$

Using the above process, the sound intensity can be obtained.

2.2 Airborne Source Quantification

Assuming the noise path as a linear system, the noise transfer path model for a GDI engine noise to predict the sound pressure level at the distance of 0.5 m from the front of engine can be represented, as shown in Fig. 1. Through each transfer path expressed by their respective transfer function corresponding to each noise source, the responses at target points are revealed. To verify the transfer characteristics from each noise source to the response point, the ASQ technology is used. By multiplying the transfer function and the volume velocity from each noise source, the noise contribution level by each component can be calculated [9]. The model expressed in Fig. 1 can be reiterated as equations, as shown in Eq. (10).

$$\begin{aligned}
P_{pump}^{oper}(\omega) &= H_{pump}(\omega) \times Q_{pump}^{oper}(\omega) \\
P_{injector}^{oper}(\omega) &= H_{injector}(\omega) \times Q_{injector}^{oper}(\omega) \\
P_{engine}^{oper}(\omega) &= H_{engine}(\omega) \times Q_{engine}^{oper}(\omega)
\end{aligned} \tag{10}$$

where $Q_{pump}^{oper}(\omega)$, $Q_{injector}^{oper}(\omega)$, and $Q_{engine}^{oper}(\omega)$ are the volume velocities measured at each noise source. This volume velocity can be calculated when measuring sound intensity. $H_{pump}(\omega)$, $H_{injector}(\omega)$ and $H_{engine}(\omega)$ refer to the frequency response function from each noise source to a response point. This can be measured using LMS Q-source and B&K prepolarized Free-field 1/2" microphone type 4189 while the engine is off. Terms $p_{pump}^{oper}(\omega)$, $p_{injector}^{oper}(\omega)$, and $p_{engine}^{oper}(\omega)$ refer to the sound pressure values contributed by each component of GDI engine at target point. These sound pressures are obtained by multiplying the volume velocity and the frequency response function. By summing up the sound pressure values for each component, the total sound pressure at target point is estimated. The estimated total sound pressure is shown in Eq. (11). The magnitude and phase should be considered together when summing up the sound pressure values.

$$P_{est}^{oper}(\omega) = \sum \left[p_{pump}^{oper}(\omega) + p_{injector}^{oper}(\omega) + p_{engine}^{oper}(\omega) + \dots \right] \tag{11}$$

If the sound pressure measured using a microphone at an actual target point exhibits a similar trend to the sound pressure estimated using Eq. (11), the proposed method can be used for the identification of the noise transfer path and the contribution of each noise source. This method can avoid the error occurred by inverse method [9].

3 Validation of the Proposed Method

3.1 Validation Experiments in Laboratory

In order to verify the validity of the proposed method prior to real vehicle testing, a validation experiment was conducted using two speakers being set under laboratory. Assuming the speakers were the noise sources of a GDI engine, they were installed in an anechoic chamber, as shown in Fig. 2. In order to allow for the intensity mapping and analysis of noise contribution level by components, the speakers were located in a 3×6 grid. Then, the left speaker shown in Fig. 2 vibrated with a 400 Hz sine signal, and the right speaker with a 900 Hz sine signal. As the speakers were activated, the sound intensity I_n and volume velocity u were measured for each point of the grid using the PU-Probe. Intensity measurement used the ISO 9614-1 method, which takes individual measurements for each numbered grid, in contrast to the ISO 9614-2 method, which uses continuous scanning. Once the intensity measurements were completed, the speaker vibration stopped and LMS Q-Source was set up at the target point of 0.5 m in front of the

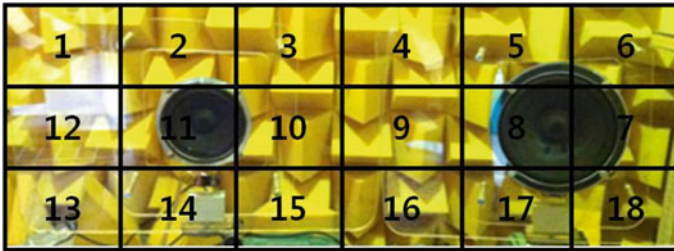


Fig. 2 Area segment for the intensity mapping of the sound that radiated from two loud speakers installed in anechoic chamber

speakers. Then, by installing microphones at each segment of the grid used for intensity I_n measuring, the frequency transfer function $H(\omega)$ for each point was obtained. The volume velocity $Q(\omega)$ of each segment is obtained by multiplying measured particle velocity $U(\omega)$ and area A of each segment. $U(\omega)$ is Fourier transform of particle velocity $u(t)$.

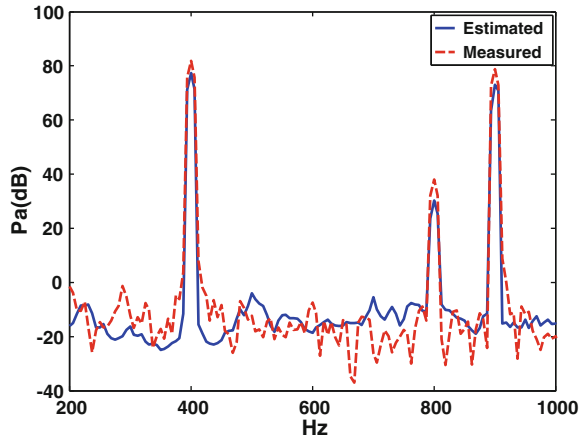
3.2 Analysis of Sound Intensity

The sound intensity measured using speakers that vibrated at 400 and 900 Hz can be analyzed through mapping. Since noise analysis typically uses 1/3 octave bands, the intensity mapping also used 1/3 octave bands. The sound that propagated from the center of the right speaker vibrated at 900 Hz. These results show that the noise source in the 400 Hz range is the left speaker and the source at the 1,000 Hz range is the right speaker. Using the same method, the sound intensity technique to identify noise source components in a GDI engine is applied in the Sect. 4.

3.3 Estimating Sound Pressures of Two Noise Sources

In order to estimate the sound pressure at target point, 0.5 m in front of the speaker, ASQ described in Eq. (10) is used. Therefore, the estimated sound pressure radiating from each grid is calculated by multiplying the frequency transfer function $H(\omega)$ and volume velocity $Q(\omega)$ associated with each segment grid. Then, by summing up the sound pressures due to each grid, the estimated total sound pressures at target point is calculated. Figure 3 shows a graph that compares the sound pressure values measured at target points with two speakers vibrating and the values calculated by summing up the sound pressures estimated at target points. At the 400, 800 and 900 Hz ranges, the measured values and the estimated values exhibit similar trend and magnitude. The sound at 800 Hz is the

Fig. 3 Comparison between estimated sound pressure and measured sound pressure



harmonic component of the noise emitted by the speaker that vibrated at 400 Hz. In theory, for the results of ASQ, the estimated values should be smaller than the measured values. However, the results shown in Fig. 4 show that the estimated values are actually higher for a certain frequency band of the background noise, even when its maximum estimated values are lower than those measured. This is a measurement error due to signal leakage caused by the window effects [10].

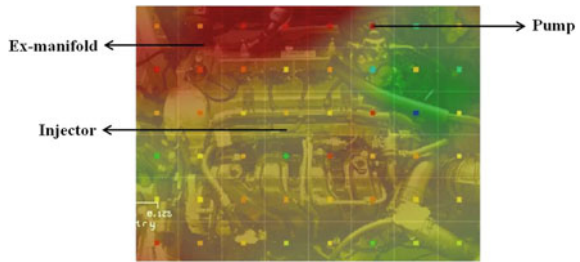
Therefore, the estimated values were validated as reliable. Then, the noise contribution levels were analyzed by dividing the estimated values for each section. Based on these results, the proposed method of incorporating transfer functions to directly measured volume velocities can be used without inverse problem rather than the conventional method of using the inverse matrix method on transfer functions, thus ensuring validity for vehicle testing.

4 Application of the Proposed Method to GDI Engine

4.1 Experiment

With the reliability of laboratory results confirmed through the validation experiment, the proposed method was applied to a vehicle with a GDI engine. The experiment method was identical to the validation experiment, and intensity measurements were taken with the engine at idle. The entire engine was set as the boundary, with the dimensions of the entire engine area set at 0.6×0.45 m and each grid segment set at 0.075×0.075 m. Intensity measurements used the discrete point method using ISO 9614-1, and measurements were taken at 48 points representing each grid segment. Next, microphones were set up at the same points as those during intensity measurements, and the transfer function from the noise

Fig. 4 Mapping of sound intensity for the noise sources of a test GDI engine in frequency



source to target points were measured by installing LMS Q-Source at 0.5 m. This process was carried out in an open free field environment in order to eliminate the effects of reflected sounds.

4.2 Analysis of Sound Intensity

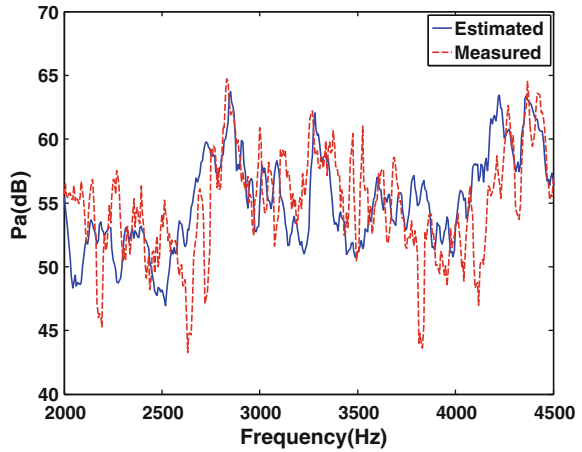
By measuring the sound intensity of each grid, the sound intensity of GDI engine components was obtained. Same as the validation experiment, the intensity was analyzed using 1/3 octave bands. By analyzing the intensity, It can be verified which components have the greatest SIL (sound intensity level) at different frequencies. When performing intensity spectrum analysis, the highest SILs were found in the 2,000–4,500 Hz range. Therefore, the 1/3 octave analysis was also carried out for only three center frequency bands at 2,500, 3,150 and 4,000 Hz. Figure 4 shows the image map for sound intensity level in the frequency range between 2,250 and 2,825 Hz band and the center frequency is 2,500 Hz. The range of SIL is displayed from 20 to 50 dB. Overall, the SIL around the exhaust manifold appear the high SIL, and there is also substantial impact around the injector.

4.3 Acoustics Source Quantification for Engine Noise

4.3.1 Representation Noise Source Components in a GDI Engine

Through sound intensity analysis, major noise sources components of GDI engine are identified. Through analysis of how noise is transferred using intensity mapping, the noise sources of the engine were divided. The representative values were set for each of the noise source sections, and their transfer functions and volume velocities were calculated. By multiplying these two functions, the sound pressure $p(\omega)$ was obtained for each noise source section. The phase was considered when multiplying the two functions.

Fig. 5 Comparison between measured sound pressure and estimated sound pressure radiating from the test GDI engine



4.3.2 Comparison of Measured and Estimated Values at Response Point

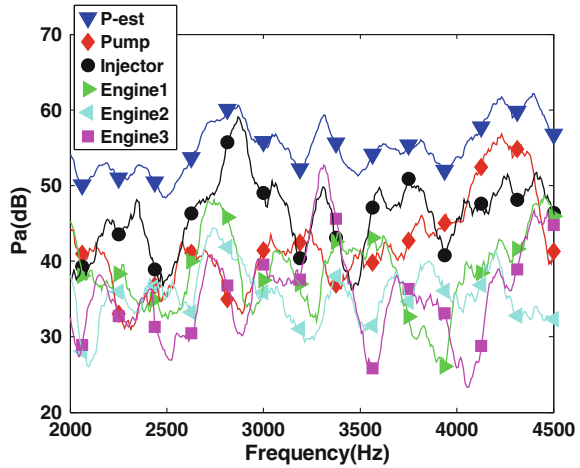
The estimated values and measured values of sound pressure at response points must show similar value and trends. The estimated values shown in Fig. 5 were derived by adding up all the estimated sound pressures from each noise source. As the sound pressure values were minimal under 2,000 and over 4,500 Hz, only the 2,000–4,500 Hz range was analyzed. According to results, the estimated and measured sound pressure at response points exhibited similar trends and values.

Theoretically, estimated values should be lower than measured readings, but the signal leak due to the effects of the window caused estimated values of a certain frequency range to be larger. However, for the frequency bands this test is most concerned with—around 2,800 and 4,200 Hz—the estimated and measured sound pressures were almost identical. Based on this result, the test to analyze noise contribution level by source using estimated values can be confirmed as reliable.

4.3.3 Analysis of Contribution Level by Noise Source

With the reliability of noise contribution analysis secured above, the noise contribution levels based on the estimated sound pressures are analyzed. Figure 6 displays the contribution of each noise source in a spectrum format. Overall, the contribution of the injector appears to be the largest, but the pump's contribution is larger around 4,200 Hz. Since the sound pressure values from the injector and the pump are high in the frequency range with the peak value, it can be concluded that the injector and the pump had a large contribution on the total noise level. To quantify and express the contribution levels by noise source, analysis was carried out using 1/3 octave bands.

Fig. 6 Contribution of major noise sources in the test GDI engine running at idle condition



5 Conclusion

In this research, the engine noise sources were mapped within a near sound field by measuring the sound intensities of an idling vehicle with the PU-Probe. The position of noise sources were identified through this exercise and the engine was divided up according to those sources. Volume velocity of each source is obtained by multiplying the particle velocity and area of these noise sources. After measuring the transfer functions up to the normal point for the divided sections, the volume velocity and transfer function were multiplied with consideration for phase, and the sound pressure for each component was estimated. Based on this method, the noise contribution of components by frequency could be identified. While the injector's contribution was larger around 2,900 Hz, it was confirmed that the pump's contribution is larger around 4,200 Hz. The engine's contribution is the largest around 2,700 and 3,300 Hz. Based on these results, the noise contribution level for each component can be estimated during GDI engine design and this will assist in the noise reduction of specific noise sources in future GDI engine design.

Acknowledgments This work was supported by Mid-career Researcher Program through NRF grant funded by the MEST (No. 2010-0014260).

References

1. Omekanda AM, Geiob T, Buehler DB, Wan K, Lavan LG (2010) Acoustic noise assessment of gasoline direct injection component using taguchi methods-application to GDi high-pressure pumps. SAE international, SAE 2010-01-0586
2. Moschioni G, Saggin B, Tarabini M (2007) Sound source identification using coherence and intensity-based methods. IEEE, vol 56, no 6, pp 2478–2485
3. Yang JJ, Lee DJ (2010) Identification of noise source of the HVAC using complex acoustic intensity method. KSNVE, vol 20, no 11, pp 1089–1096
4. Fahy FJ (1987) Sound intensity. Elsevier Applied Science, New York
5. Kinsler LE (2000) Fundamentals of acoustics. Wiley, New York
6. Byun JH, Kang YJ (2008) The mathematical model on crosstalk effect of airborne noise sources and verification based on comparison between transfer path analysis methods. KSNVE, vol 18, no 9, pp 943–951
7. Fleszar AR, van der Linden PJG, Johnson JF, Grimmer MJ (2001) Combining vehicle and test-bed diagnosis information to guide vehicle development for pass-by noise. SAE, VDI-Berichte, No. 1616, pp 317–327
8. Cheung WS, Suh JG, Eun HJ (1997) Experimental analysis of the sound radiation characteristics of a vibration plate using the reciprocity principle. Asia-Pacific Vibration Conference, pp 876–881
9. Kim SJ, Lee SK (2009) Prediction of structure-borne noise caused by the powertrain on the basis of the hybrid transfer path. In: Proceedings of the institution of mechanical engineers, Part D: J Automobile Eng vol 223, no 4, pp 485–502
10. Shin K, Hammond JK (2008) Fundamentals of signal processing for sound and vibration engineers. Wiley, London

Noise Reduction Potential of an Engine Oil Pan

Tommy Luft, Stefan Ringwelski, Ulrich Gabbert,
Wilfried Henze and Helmut Tschöke

Abstract Considering automobiles with internal combustion engines, the power train represents one of the main noise sources, especially during idling and slow driving speeds. One major contributor to the overall power train noise emission is the engine oil pan. The objective of this paper is to evaluate the noise reduction potential of an oil pan with a combined use of passive and active methods. The passive approach is best suited for a frequency range above 1,000 Hz and is implemented in this study using different substitute materials. Active noise control techniques are efficient in a frequency range below 1,000 Hz. In the present study piezoceramic patches are used as actuators as well as sensors. By means of FE simulations a smart system is designed to reduce passively and actively the structural vibrations and consequently the resulting sound radiation. Therefore, optimal locations of piezoelectric actuators are computed. A control algorithm with respect to a collocated design is used to obtain high active damping effects. With control, attenuations up to 15 dB in vibration level are achieved at the resonance frequency regions of the most dominant modes of the oil pans in laboratory. It is shown that significant reductions up to 4 dB are achieved on the engine test bench in a frequency range up to 1,000 Hz and at engine speeds below 2,000 rpm, where a multi-discrete excitation characteristic exists. Due to the use of a low-mass plastic oil pan, improvements at several engine operating points are

F2012-J03-018

T. Luft (✉) · W. Henze · H. Tschöke
Institute of Mobile Systems (IMS), Otto-von-Guericke University of Magdeburg,
Magdeburg, Germany
e-mail: tommy.luft@ovgu.de

S. Ringwelski · U. Gabbert
Institute of Mechanics (IFME), Otto-von-Guericke University of Magdeburg,
Magdeburg, Germany

measurable. Drawbacks of this material substitution are the higher temperature dependency and the lower electromechanical coupling of the piezoelectric patches due to the elasticity of the plastic ground material. An oil pan made of sheet steel has shown the worst acoustical properties.

Keywords Oil pan · FEM · Material substitution · Active control · Engine test bench

1 Introduction

Over the past years an increasing attention has been paid to acoustic noise control in automotive engineering. The use of light-weight materials in parts of a car has a direct influence on the radiated sound intensity of these parts. There are two different approaches to achieve noise and vibration attenuations. On the one hand, there is the widely used passive approach. Passive control techniques mostly reduce vibration and sound emission of structures by modifying the structural geometry, by applying additional damping materials or by a complete material substitution [1, 2]. These methods are best suited for a frequency range above 1,000 Hz. The active control approach can effectively support passive noise treatments as an alternative way to minimize unwanted structural vibration and noise. This technique is usually employed in a frequency range between 50 and 1,000 Hz. In active noise reduction piezoelectric ceramics can be attached to structures as actuators and sensors. An often used concept for noise reduction is active structural acoustic control (ASAC). In this concept the surface attached actuators are used to change actively the dynamic behavior of the structure in order to reduce the sound radiation from the surface.

One major contributor to the overall power train noise emission is the engine oil pan. Over the past years, researchers have already applied active noise reduction of a car oil pan [2] as well as a truck oil pan [3] by using distributed piezoelectric actuators. However, in these studies the oil pan was treated separately and no attempt was made to consider interactions between the crankcase and the oil pan. Furthermore, no investigations on an engine test bench or with a passenger car were done so far. In recent years, we have studied active noise reduction of a car oil pan on a dynamic acoustic engine test bench [4–7]. In these studies, we have investigated a smart aluminum oil pan. The objective of this paper is to assess the noise reduction potential of an oil pan with a combined use of passive (three different materials) and active (piezoelectric actuators) methods.

The paper is organized in the following way. First, numerical FEM simulations of a smart stripped car engine comprised of a crankcase and two types of oil pans (an aluminum and a plastic one) are performed. After identifying the most dominant mode shapes, suitable actuator and sensor positions at the bottom of the oil

pans are selected. In a next step, the control problem of the smart system is considered. A feedback control technique is chosen to compute input signals for the actuators that are bonded on the outer surface of the oil pan bottoms. Additionally, piezoelectric sensors are placed at the inner surface of the pans. Finally, in order to evaluate the quality of the designed system and to investigate the simultaneous use of passive and active reduction, experimental tests are carried out in laboratory at the stripped car engine and on a dynamic engine test bench. The experiments on the fired engine with different oil pans involve stationary engine operating points and engine running-ups. In the experimental investigations the uncontrolled behavior of a sheet steel oil pan is used as a worst-case reference.

2 Design of a Smart Stripped Car Engine

In the following, the development of a smart stripped car engine is discussed to understand the interactions between the crankcase and the oil pans as well as to prepare an oil pan configuration for entire engine tests.

2.1 *Finite Element Analysis and Definition of Actuator Positions*

In order to design an active system to reduce the vibrations of the stripped car engine in a noise reducing manner, it is essential to identify the most dominant mode shapes. This step is carried out by means of an eigenvalue analysis using a three-dimensional FE model meshed with quadratic 10 node tetrahedral elements. The FE model is refined enough to include the irregular-shaped geometry of the crankcase and the oil pan accurately. The FE formulation for modeling the stationary behavior of the uncoupled stripped car engine is given in [5]. More details about the modeling of the configuration with the aluminum oil pan are also presented in [5]. The detailed modeling approach of the plastic oil pan as well as some additional details regarding the overall configuration is published in [6].

A force excitation by an actuator placed on the inner side panel of the oil pan is chosen to excite all eigenmode in a frequency range up to 1,000 Hz. Figure 1 shows exemplarily the frequency response functions (FRFs) of the aluminum configuration between the structural displacement at the center of the oil pan bottom calculated from an acceleration sensor signal and the excitation force. It can be seen that the measured data and the computational prediction agree very well. Since the FE model is stiffer than the real object, the simulated eigenfrequencies are slightly higher. It can be observed that the first (580 Hz) and the third (960 Hz) eigenmode are pure bending modes of the oil pan bottom [4]. The second mode is a global bending mode of the whole stripped car engine. Under real

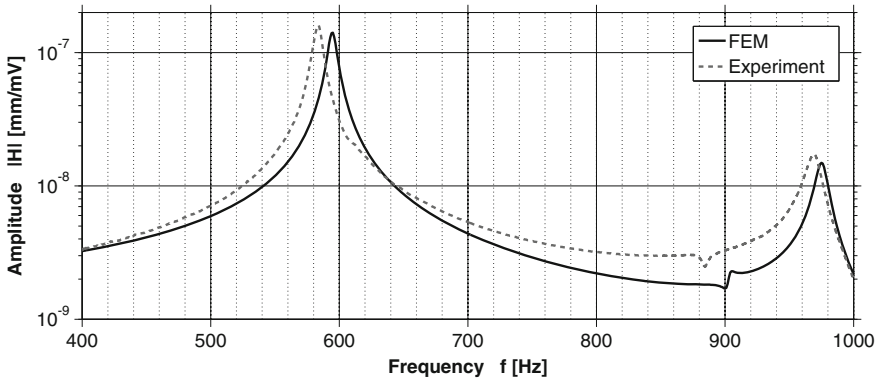


Fig. 1 Frequency response functions (FRFs) of the uncontrolled stripped car engine with an aluminum pan

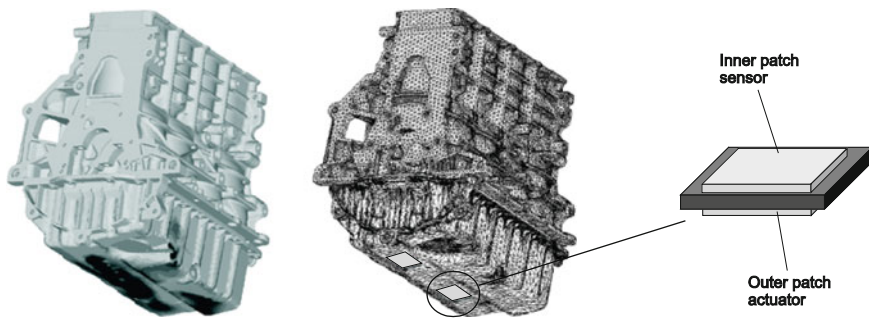
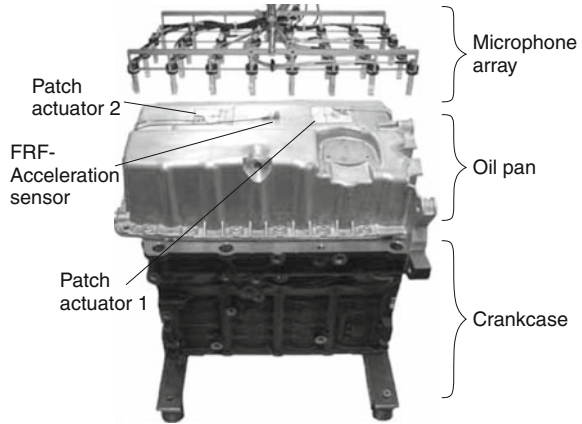


Fig. 2 Contour plot of the superposed modal strain field (*left*) and FE mesh with selected actuator and sensor positions (*right*) of the aluminum configuration

operating conditions the bottom modes are the main contributor to the overall noise emission. Due to this fact, the present approach aims to control these two modes only.

The choice of suitable actuator positions depends on many factors, such as the employed control and the vibrational behavior of the structure. An often used method for the actuator placement is based on the assumption that an actuator is placed well when it is able to influence significantly the shape of the structural modes. This means that an in-plane actuator should be placed at positions on the surface of the structure where the strains and the corresponding electric potentials are the highest. In case of the stripped car engine, the first and the third eigenmode are considered. In contrast to an additive superposition, the multiplicative superposition makes sure that the actuators are not placed on the node line of an eigenmode which should be controlled. A contour plot of the superposed field allows the definition of optimal actuator positions. Two actuator positions have been selected according to the contour plot visible in Fig. 2. The light gray areas of

Fig. 3 Actuators and sensors of the stripped car engine attached to the aluminum pan



the FE mesh mark the two selected positions. Additionally, two sensors are placed on the opposite side of the oil pan. The collocated design of the piezoelectric actuator/sensor pairs guarantees control stability.

It should be noted that also more collocated actuator/sensor pairs could be applied. The method explained has also been applied to choose suitable actuator positions for the plastic oil pan [6].

2.2 *Implementation and Verification of a Suitable Control Strategy*

The design of a smart stripped car engine requires the implementation of a suitable control algorithm. Feedback control has several advantages over feedforward control. For instance, feedback control is able to take into account unexpected disturbances. Another advantage of feedback control is the capability to stabilize unstable processes. For that reason the robust and widely used velocity feedback control is applied [4, 7]. This algorithm combines high performance control with robustness against time variance of the operating parameters such as oil temperature and excitation frequencies. An important requirement for a successful feedback is the availability of appropriate feedback points. Using a separate sensor for each actuator leads to a decentralized feedback control strategy with independent local feedback loops.

The experimental setup, shown in Fig. 3, has been developed to measure the uncontrolled and the controlled behavior of the stripped car engine with the different oil pans. By means of an actuator placed at the inner side panel of the oil pan, the stripped car engine is excited harmonically with white noise and also with real engine spectra resulting from combustion engine measurements. It should be noted that the force amplitudes of the excitation are smaller than under real operating conditions.

Table 1 Material parameters of the crankcase and three types of oil pans

	Density (g/cm ³)	Elastic modulus (N/mm ²)
gray cast iron crankcase	7.2	135,000
Aluminum pan	2.7	70,000
Glass fiber reinforced polyamide plastic pan	1.3	6,000
Sheet steel pan	7.85	210,000

The obtained results show that a significant damping of the dominating resonance frequencies can be achieved with help of the implemented velocity feedback control. Amplitudes are reduced by about 15 dB at 580 Hz and by about 10 dB at 960 Hz on the aluminum configuration [4]. Amplitude reductions up to 6 dB at the dominating resonance frequencies are achieved on the plastic configuration [6]. The active reduction potential of the stripped car engine with the plastic oil pan is lower because of the lower electromechanical coupling of the piezoelectric patches due to the elasticity of the plastic ground material.

2.3 Passive Behavior of the Stripped Car Engine with Three Types of Oil Pans

The passive reduction potential of an engine oil pan is investigated in this study using three oil pans of different type material. The material parameters of the used components of the stripped car engine are shown in Table 1. The die cast aluminum oil pan (see Fig. 3) has a mass of 2,600 g and a wall thickness of 3 mm. In comparison, the low-mass plastic one (1,790 g) with a wall thickness of 3.5 mm has higher passive damping characteristics [1, 6]. By means of reinforcing ribs on the inner surface of the plastic oil pan bottom, improvements of the stiffness have been achieved. The thinnest oil pan of the three examples is the sheet steel one (1.9 mm, 1,950 g) without any reinforcing ribs. The low production costs are the main advantage of the steel oil pan.

For comparison purposes, investigations of the passive behavior of the different oil pans are carried out using the experimental setup, shown in Fig. 3. Only the point force excitation has been realized by means of an impulse hammer at the oil pan flange instead of applying the piezoelectric actuator placed on the inner side panel of the oil pan. Figure 4 shows the frequency responses in terms of the structural displacement at the center of the oil pan bottom due to an excitation force at the flange.

It is clearly visible that the sheet steel configuration has the highest frequency peaks in the presented frequency domain. The amplitudes are also the highest due to the thin wall thickness. The amplitudes of the dominating resonance frequencies of the aluminum and plastic oil pan are at about the same level. Since the plastic pan has superior material damping properties compared to the aluminum pan, wider frequency regions can be seen (blue function graph in Fig. 4).

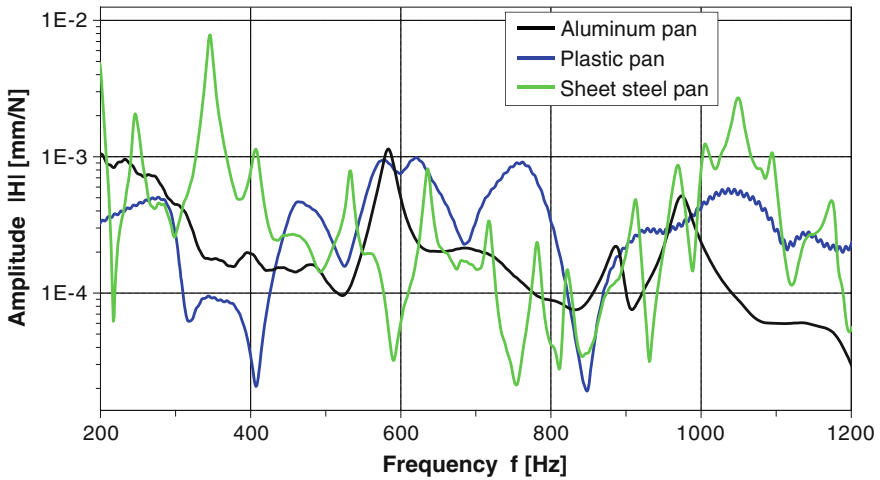


Fig. 4 FRFs measured of the uncontrolled stripped car engine with three different types of oil pans

3 Modification of the Oil Pans for Engine Tests

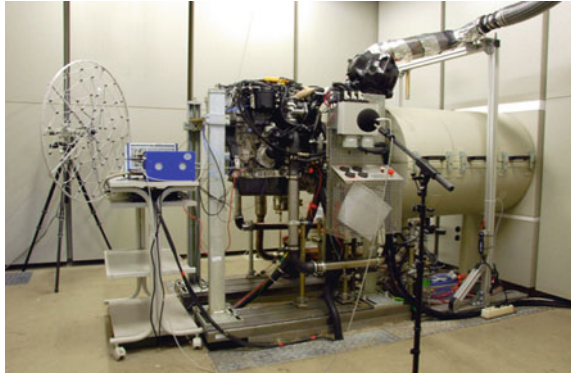
Before analyzing the developed smart car oil pans on a diesel engine, the configuration has to be protected against the oil and the high temperature. The jacket of the cables connecting the piezoceramic patches consists of polyolefin copolymer isolation. This chemical composition is heat- and oil-resistant until 145 . Furthermore, the cables have been fixed with two-component gluten. The single-layer piezoelectric ceramics attached on the inner surface of the oil pan have been protected with elastic packing material [7].

4 Measurements on a Dynamic Acoustic Engine Test Bench

In order to evaluate the quality of the designed oil pans, several experimental tests on an acoustic engine test bench have been carried out. In Fig. 5 the altered four-cylinder common rail diesel engine is shown.

First, investigations of the separately excited engine without combustion are made to determine the potential of the active system. After that, tests of the uncontrolled and controlled behavior of the oil pans on a fired engine have been performed.

Fig. 5 Four-cylinder diesel engine with the polyamide plastic oil pan in an anechoic room



4.1 Analysis of the Separately Excited Entire Engine

By means of an actuator placed at the inner side of the oil pans, the diesel engine has been excited with white noise signal that excites all eigenmode in a frequency range up to 1,000 Hz. Figure 6 exemplarily shows the frequency responses of the aluminum configuration in terms of the structural displacement at the center of the oil pan bottom due to the excitation force. The given results show a damping effect at the dominating resonance frequencies due to the implementation of a velocity feedback control algorithm. Amplitudes are reduced by about 4 dB at 640 Hz and by about 1.5 dB at 880 Hz.

Additionally, it can be observed that the two bending modes of the oil pan bottom have suffered frequency shifts compared to the stripped car engine caused by mass and stiffness variations of the entire engine. The lower amplitude reductions primarily result from the smaller deformation of the pan because of the damping behavior of the sealing between the crankcase and the oil pan. Furthermore, the influence of the oil has also to be taken into consideration. The modified vibrational behavior of the pans due to the presence of oil is discussed in [8, 9]. Nevertheless, it can be seen in Fig. 6 that in spite of frequency shifts and amplitude variations, the velocity feedback control used in collocated design is robust against variances of the real control system.

This study considers also the robustness of the design with respect to the temperature. During the experimental tests it could be noticed that besides the wall thickness, the oil temperature influences the stiffness of the glass fiber reinforced polyamide plastic pan. The elastic modulus of the plastic material is very dependent on the temperature. Increasing the oil temperature, leads to a stiffness reduction. This dependency is shown in Fig. 7. The amplitudes of the hot oil pan have risen (red function graph). Additionally, FRF measured of the uncontrolled stripped car engine with the plastic oil pan without oil is plotted in Fig. 7. Thus it is visible that the oil presence in the pan shifts the frequencies of the system.

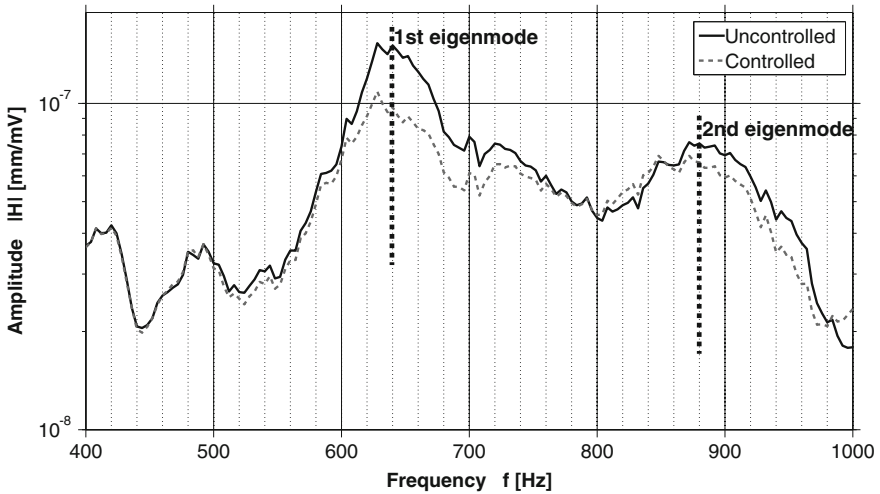


Fig. 6 FRFs measured of the uncontrolled and controlled aluminum oil pan on a diesel engine

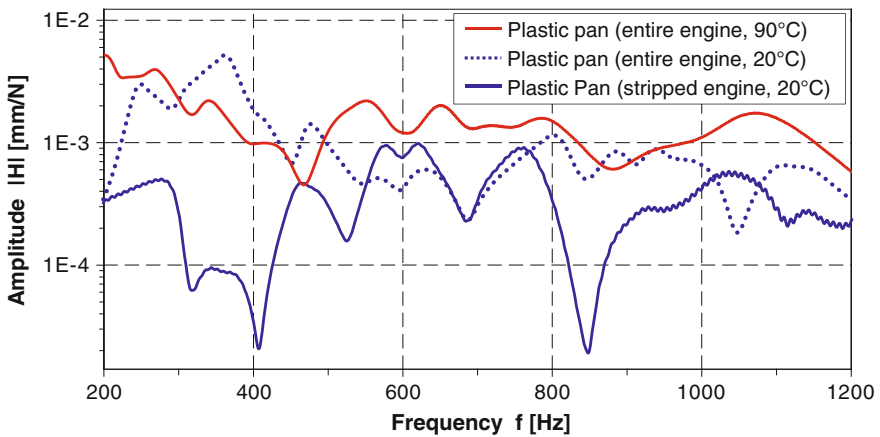
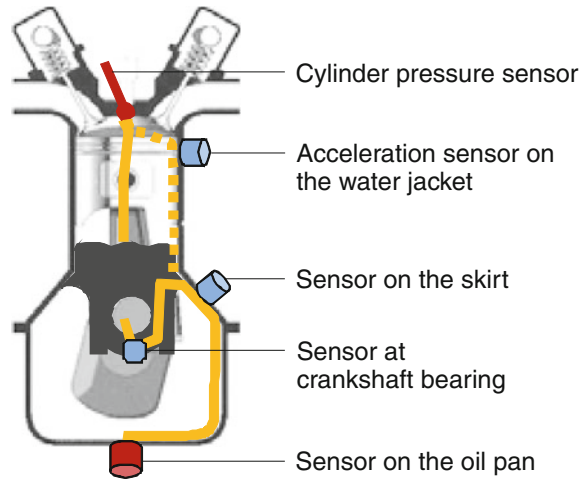


Fig. 7 FRFs measured of the uncontrolled plastic oil pan on a diesel engine at different oil temperatures in comparison to FRF measured of the uncontrolled stripped car engine with the plastic oil pan

4.2 Oil Pan Vibrations on a Fired Engine

The following experimental engine investigations involve stationary engine operating points and engine running-ups (900–4,000 rpm) for different loads (20, 50, 100 and 150 Nm). The four cylinder pressure signals are measured using an indicating system.

Fig. 8 Inner (*solid yellow line*) and outer (*dashed yellow line*) structure-borne noise path of one cylinder



The total combustion noise of a diesel engine which dominates over mechanical noise at low and middle revolutions per minute (less than 3,000 rpm) and at low and middle loads is mainly radiated by the crankcase and the oil pan. To separate the direct combustion noise from the indirect combustion noise, the coherence criterion between combustion pressure and acceleration signals measured at the oil pan bottom is used. To check how the oil pan bottom responds to the excitation of the combustion pressure, all cylinder pressures have to be considered since the excitation is caused simultaneously by each cylinder moved by the particular firing interval. The cylinder pressure signal in the frequency domain has peak amplitudes with a periodicity defined by the cylinder firing. Coherence analyses revealed that in the low frequency region up to 1,500 Hz linear direct combustion noise dominates over the non-linear indirect combustion noise without respect to the engine operating point [7]. Physically, a direct combustion noise source is generated internally. Consequently, the cylinder walls are excited and the sound is transferred into the pan by an inner and outer structure-borne noise path as shown in Fig. 8.

4.2.1 Passive Behavior of the Fired Engine with Three Types of Oil Pans

In order to get an overview of the uncontrolled behavior of the oil pans on a fired diesel engine, engine running-ups were made and evaluated. The acceleration sensor at the center of the oil pan bottom is used to generate the diagram of Fig. 9, because this sensor represents the entire vibration characteristics of the oil pans.

The analysis of these graphs indicates significant improvements in the vibration level by using a polyamide plastic oil pan because of the higher damping properties compared to the other pans. As it can be seen in Fig. 4, the sheet steel oil pan graph shows the highest acceleration levels from 1,300 up to 3,000 rpm because of the thin-walled structure and the missing reinforcing ribs.

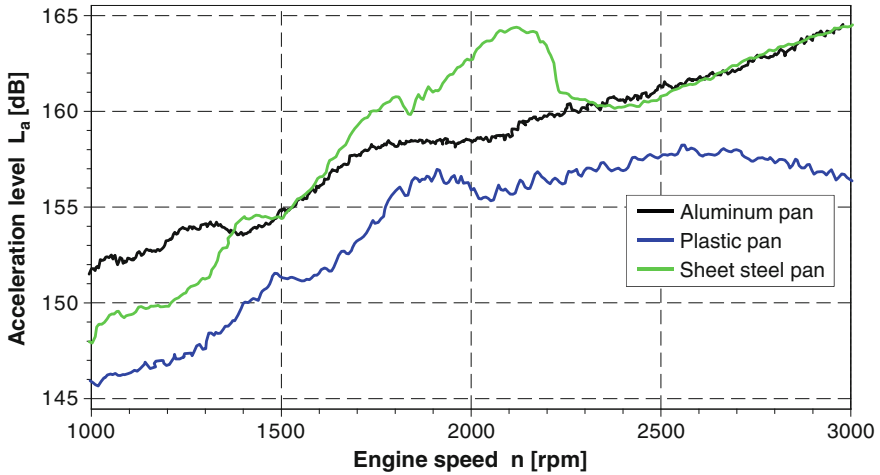


Fig. 9 Acceleration level of the uncontrolled oil pans at engine running-ups (engine load 100 Nm)

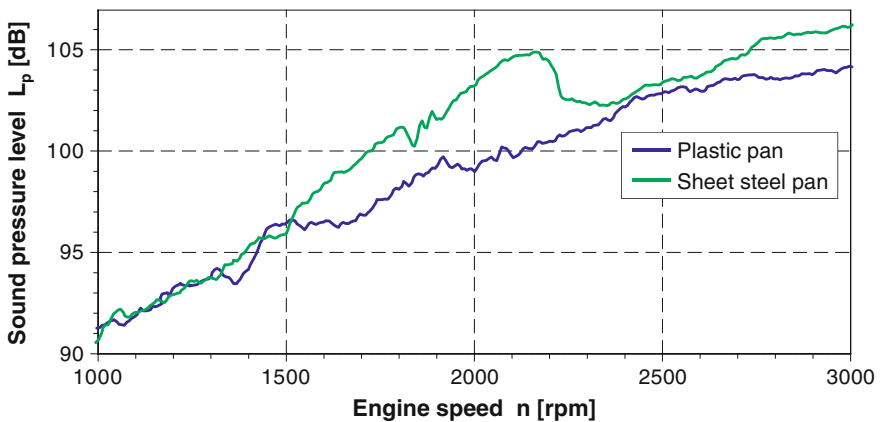


Fig. 10 Sound pressure level of the uncontrolled plastic and the sheet steel oil pan 150 mm apart from the oil pan bottom at engine running-ups (engine load 100 Nm)

A similar trend can be noticed by comparing the sound pressure levels of the plastic and the sheet steel oil pan given in Fig. 10. However, up to 1,500 rpm the sound pressures are at about the same level. It has to be taken into account that the microphone recognizes the surface integral of the vibrational behavior of the oil pan bottoms.

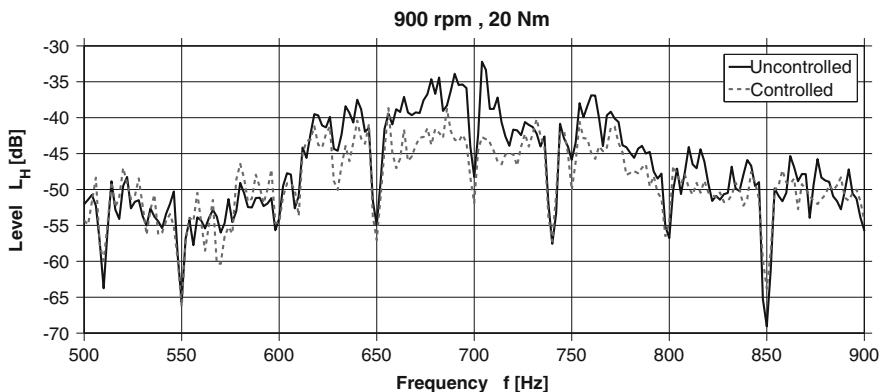


Fig. 11 Transfer functions between the acceleration of the aluminum oil pan bottom and the energetically averaged cylinder pressure

4.2.2 Active Behavior of the Fired Engine

For a further validation of the smart active systems, a stationary engine operating point with minimal real excitation forces is chosen. At 900 rpm, multiples of the half engine order cause excitations in a frequency interval of 7.5 Hz and multiples of the second engine order cause excitations in a frequency interval of 30 Hz.

In Fig. 11, the dependency between the structural vibration and the cylinder pressure in uncontrolled and controlled case can be seen exemplarily for the aluminum pan. Additionally, the results show significant damping effects in the frequency region of the first eigenmode. Amplitudes are reduced up to 8 dB. This demonstrates the advantage of the developed control which benefits from the multi-discrete characteristics of the real excitation signals.

To evaluate the quality of active control of the plastic and aluminum oil pan at higher engine speeds and loads, several engine running-ups are carried out. The measurements, shown in Fig. 12, revealed that the piezoelectric actuators generate counteracting forces which suppress the sound pressure level 150 mm apart from the oil pan bottom of the two pans.

The active reduction potential of the stripped car engine with the plastic oil pan (on the left-hand side of Fig. 12) is lower because of the lower electromechanical coupling of the piezoelectric patches due to the elasticity of the polyamide plastic ground material. As explained, the higher the oil temperature is, the higher the material elasticity becomes. Although the uncontrolled sound pressure level of the plastic pan is slightly better, the aluminum pan shows nearly linear behavior over the speed range. This is an important advantage for the subjective sound perception. In a previous paper [7] it is shown for an aluminum pan that with control, attenuations up to 4 dB are achieved at the resonance frequency regions of the most dominant modes at engine speeds below 2,000 rpm. The main reason for

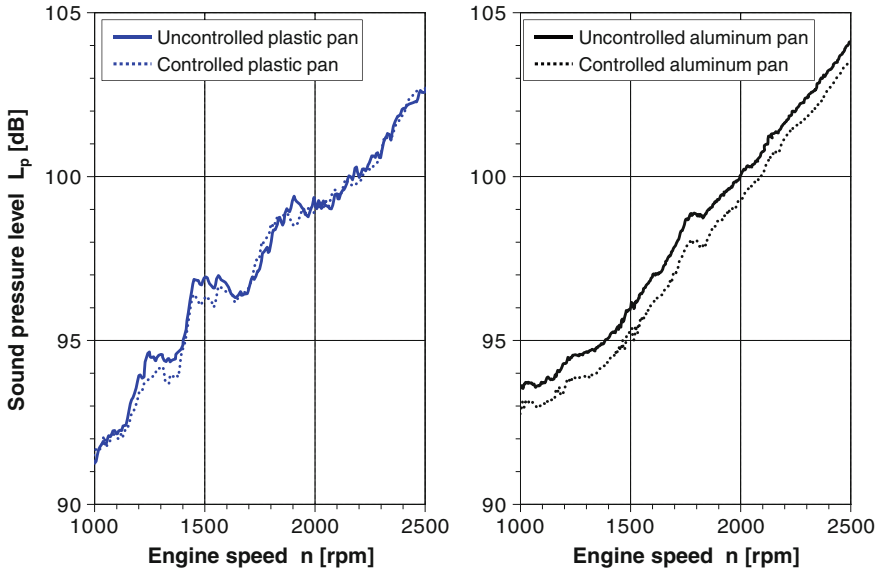


Fig. 12 Sound pressure level up to 10 kHz of the uncontrolled and the controlled plastic (*left*) and aluminum (*right*) oil pan 150 mm apart from the oil pan bottom at engine running-ups (engine load 100 Nm)

performance limits of the developed control system at higher engine speeds is the higher firing frequency at these engine operating points. For that reason, the developed control needs a roughly multi-discrete excitation characteristic.

5 Conclusions

In the paper the application of a combined passive and active vibration control of oil pans on a four-cylinder diesel engine has been presented. The passive approach includes the investigation of different materials of the oil pans. Due to the use of a low-mass glass fiber reinforced polyamide plastic pan, improvements at several engine operating points are measurable. Drawbacks of this material substitution are the higher temperature dependency and the lower electromechanical coupling of the piezoelectric patches. A sheet steel oil pan has offered the worst acoustical properties. The active approach has been implemented by using piezoceramic patches. It is shown that significant reductions up to 4 dB are achieved on the engine test bench if the oil pan is made of aluminum. The performance of the designed control system could be improved by using more efficient piezoceramic patch actuators.

Acknowledgments The work is financially supported by the German Federal State of Saxony-Anhalt and by the European Commission as a part of the research project “Competence in Mobility”. This support is gratefully acknowledged.

References

1. Marburg S (2002) Developments in structural-acoustic optimization for passive noise control. *Arch Comput Methods Eng* 9(4):291–370
2. Redaelli M, Manzoni S, Cigada A, Wimmel R, Siebald H, Fehren H, Schiedewitz M, Wolff K, Lahey H-P, Nussmann C, Nehl J, Naake A (2007) Different techniques for active and passive noise cancellation at powertrain oil pan. In: *Proceedings of the adaptronic congress, Germany*, p 8
3. Heintze O, Misol M, Algermissen S, Hartung CF (2008) Active structural acoustic control for a serial production truck oil pan: experimental realization. In: *Proceedings of the adaptronic congress, Germany*, pp 147–153
4. Luft T, Ringwelski S, Gabbert U, Henze W, Tschöke H (2010) Adaptive controllers for active noise reduction of a stripped engine. In: *Proceedings of World automotive congress FISITA, Budapest, Hungary*, “In CD-ROM” F2010-A-039, p 10
5. Ringwelski S, Luft T, Gabbert U (2011) Piezoelectric controlled noise attenuation of engineering systems. *J Theor Appl Mech (JTAM)*, Warsaw 2011 49(3):859–878
6. Ringwelski S, Luft T, Gabbert U, Henze W, Tschöke H (2011) Numerische Untersuchungen eines Rumpfmotors zur passiven und aktiven Schwingungs- und Schallreduktion. In: *Proceedings of 6. Magdeburger Symposium Motor- und Aggregateakustik, Magdeburg, Germany*, pp 119–128
7. Luft T, Ringwelski S, Gabbert U, Henze W, Tschöke H (2011) Active reduction of oil pan vibrations on a four-cylinder diesel engine. In: *Proceedings of 1st international ATZ automotive acoustics conference with autoneum, Zurich*, “In CD-ROM” paper 7, p 14
8. Li Y, Han S, Pfeiffer T (2010) Simulationsbasierte und experimentelle Sensitivitätsanalysen eines adaptiven Systems. In: *Proceedings of DAGA, Berlin*, , pp 295–296
9. Rimondi M, Ruotolo R, Lomario D (2011) Design optimization of an oil pan for radiated noise reduction. In: *Proceedings of the Aachen acoustic colloquium, Aachen*, pp 61–69

Experimental Investigation of the Pulsation Noise Induced by Automotive Turbocharger Compressors

Ho-il Park, Sungyou Hong, Jubong Seo and Hyeongill Lee

Abstract Automotive turbochargers have become common in passenger cars as well as commercial vehicles. They are an excellent mechanism to effectively increase fuel efficiency and power, but they unfortunately cause several noise problems. The noises are classified as structure-borne noises, generated from the vibration of rotating shaft modules (cartridges), and air-borne noises, from air flow inside turbochargers or their coupling ducts. The structure-borne noises are whine and howling, and the air-borne noises are BPF (blade-passing frequency), blow, pulsation, surge, and hissing noises. These noises bother passengers because their levels are higher, or their frequencies are clearly distinctive from other noises, even at low levels. Since people easily recognize them and complain to car manufacturers about them, car manufacturers as well as turbocharger makers have made a concerted effort to satisfy their customers. The number of noises in an automotive turbocharger increases as other vehicle noises are lowered. The noise investigated in this study is the pulsation noise generated from the compressor wheels, whose frequency is the same as the whine noise. Therefore engineers are often confused about whine and pulsation noises. Although they have the same frequency, their noise sources are absolutely different. The whine noise is induced by unbalanced rotating modules, while the pulsation noise is generated by the wheel's dimensional asymmetry. The asymmetry considered in this study was prepared by partly cutting the compressor wheels' edge in order to remove its unbalance in a semi-circular shape. Since the size of the shapes is limited, the

F2012-J03-019

H. Park (✉) · S. Hong · J. Seo
Keyyang Precision Company, Eungmyeong-dong, Korea
e-mail: hi_park@keyyang.co.kr

H. Lee
Kyungpook National University, Daegu, South Korea

number of cuttings may be greater than one. It was realized through testing that the number was directly related to the level of the pulsation noise, and a specific number had to exist to cause the noise problem. Additional tests were done to investigate the characteristics of the noise by changing the numbers, the size, and the arrangements of the cuttings. Finally, this study concluded that the pulsation noise was related to the three factors of cuttings.

Keywords Automotive · Turbocharger · Noise · Pulsation

1 Introduction

Turbochargers are devices which allow more power to an engine by actively supplying additional air to it. A turbocharger is composed of two main components: a compressor and turbine wheels. The turbine wheels are rotated by the dynamic energy of gas exhausted from the cylinders, and the compressor wheels are run by a shaft directly connected to the turbine wheels. They compress air and then supply the air to the cylinders. Engines can combust more fuel with the compressed air, and generate more power with an engine of a given exhaust volume. Due to this benefit, all diesel engines adopt turbochargers, and car manufacturers have recently started to install them in gasoline engines as well [1].

Since turbochargers spin at very high speeds, even greater than 200,000 rpm, they need robust durability. Unfortunately though, for this same reason, they generate several noise problems. Most noises emanating from turbochargers are pure tones, which bother passengers because they can easily be heard, even at a low level [2, 3]. As the noise quality of cars is very important, automaker engineers and turbocharger makers jointly make a concerted effort to eliminate or reduce the noise so that people cannot perceive it [1–6].

Turbocharger noises can be largely classified into two categories: air-borne and structure-borne noises. The air-borne noises are BPF (blade-passing frequency) noises induced by wheels, blow [6], pulsation [7], surge, and hissing [8], while the structure-borne noises make whine or howling sounds. This chapter investigates pulsation noise, which has the same frequency characteristics of a whine noise. But, the two noises have a different noise generation mechanism. The whine noise is caused by an unbalance of the rotating parts, and its frequencies correspond to the turbocharger speed (marked as 1 N). The pulsation noise was investigated through several combinations of balancing cuttings of compressor wheels, and a countermeasure was found. Through this process, it was found that the noise could be successfully controlled by visual identification of compressor wheels before they are made available to production lines.

2 Pulsation Noise

2.1 Mechanism of Noise Generation

Pulsation noise is known to be induced by air flow around asymmetric compressor wheels. Since the asymmetry is made in the manufacturing or assembly process, it is natural that they all are asymmetric to some degree. However, the deviation from symmetry causes aerodynamic pulsation, corresponding to pulsation noise [7]. A compressor wheel is shown with main blades and splitters in Fig. 1.

It was realized that compressor wheels have geometric asymmetries, which are made in the process of balancing them. Every rotating part should be precisely balanced or machined before assembly, since turbochargers spin at very high speeds and the unbalance of the rotating parts can cause both noise and serious durability problems. A compressor wheel and a turbine rotor (made with a turbine wheel and a shaft) are balanced to two planes. The three methods for balancing compressor wheels are shown in Fig. 2. All of the methods cut the end of the boss at one plane, but they are cut at different positions at the other plane—hub, backside, or edge marked by a circle in Fig. 2, respectively. This chapter considered the pulsation noise generated from the compressor wheel of Fig. 2c. Since the number of cuttings causes the breaking of the symmetry, our tests determined how the number, the size, and the arrangements of balance cuttings are related to the noise.

2.2 Test Facility

Noise tests were done in a semi-anechoic chamber built for turbochargers, which was operated by a control device utilizing air compressed at room-temperature. The boost pressure of the compressors was controlled by a valve installed after the compressor outlet. The facility is shown in Fig. 3.

The pressures of the compressor inlet and outlet were measured for noise and vibration. The noise was measured at 10 cm from the center of the bearing housing, and the vibration was measured on the compressor housing at the axial direction of a rotating shaft. The speed was calculated from the vibration signals without measuring it.

2.3 Characteristics of Pulsation Noise

The turbocharger studied in this chapter was for a small-size diesel engine. The noise characteristics were acquired from several types of tests on cars before this study started in-depth, and the following was observed:

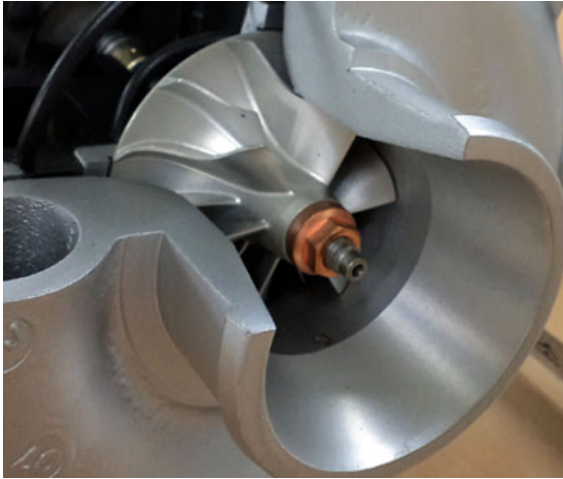


Fig. 1 A compressor wheel

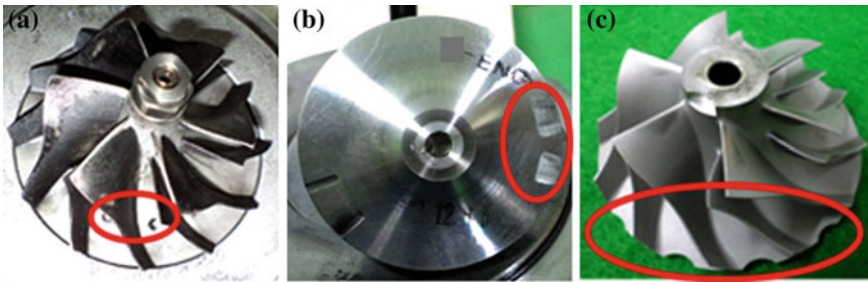


Fig. 2 Three balancing methods for compressor wheels. **a** Hub cutting, **b** backside cutting, **c** edge cutting

- The amplitude of the whine noise generated from the unbalance of the rotating parts of turbochargers might not be related to that of the pulsation noise.
- The strength of the pulsation pressure inside the compressor outlet seemed to be related to the number of balance cuttings of the compressor wheels.

3 Identification of Pulsation Noise Factors

3.1 Whine and Pulsation Noises

Noise, vibration, and pressure were measured in a running car in order to examine the relation among the values, and the 1 N components were compared by dotted-circles as shown in Fig. 4. The vibration of the whine noise is shown in Fig. 4a,



Fig. 3 Semi-anechoic chamber for turbochargers

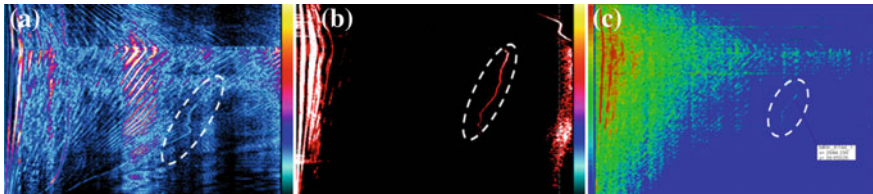


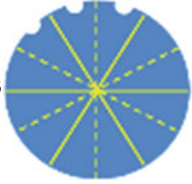
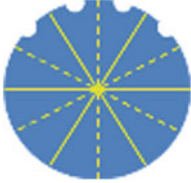
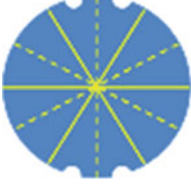
Fig. 4 1 N signals in a running car. **a** Vibration on compressor housing, **b** pressure inside compressor outlet, **c** noise in cabin

and the pressure of the pulsation noise is shown in Fig. 4b. The 1 N noise in the cabin is shown in Fig. 4c, and it should be determined by the superposition of the two noise components. However, they could not be separated by signal processing.

3.2 Test Samples

It was determined by the tests that the pulsation noise was related to the number of balancing cuttings of the compressor wheels. In order to numerically relate the number and their arrangement to the strength of the pulsation noise, the compressor wheels were prepared. They had 0–5 cuttings, and some samples had additional or special cuttings, produced by machining. The test samples, shown in Table 1, were investigated in the semi-anechoic chamber.

Table 1 Summary of test samples

Items	No	Positions	Comments
1. Cuttings	0	–	Ex) No. = 3 
	1–5	–	
2. Positions of cuttings	4	Base: next to each other	
		Evenly spaced by 1	
		180° by 2	
3. Area of cuttings	–	Base, A 1 × 2A 2 × 2A	2 × A, 4 × A Vs. 2 × A Vs. 4 × A

An example of a balanced compressor wheel with 3 cuttings is shown in Fig. 5. The compressor wheel considered in this chapter had 6 main blades and 6 splitters. Hence the edge of the compressor outlet was evenly divided by 12.

3.3 Independence of Whine and Pulsation Noises

In order to ascertain the independence of the whine and the pulsation noises first, the two groups of samples were prepared for the same number of cuttings. The one was passed on a balancing production line (“Pass”), and the other was failed because of a higher unbalance (“Failure”). The vibrations of the whine noise are compared in Fig. 6, showing that the values are clearly dependent upon the evaluation (Pass or Failure) results of the production line. On the other hand,

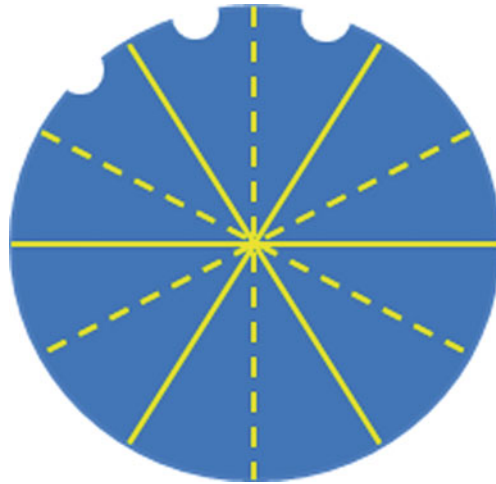


Fig. 5 The number and positions of the balancing cuttings

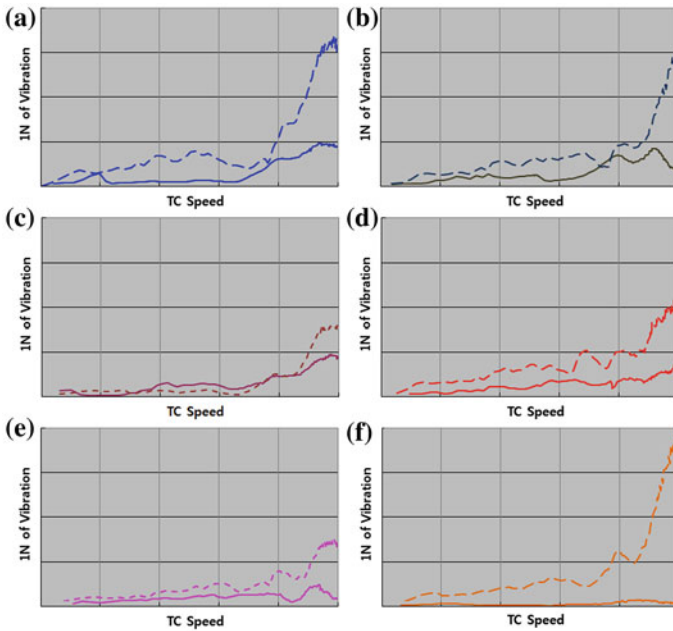


Fig. 6 Vibration comparisons to the number of balancing cuttings of compressor wheels and the balancing results (Pass and Failure) in a production line: *solid* = Pass and *dotted* = Failure in the balancing production line. **a** Cuttings = 0, **b** cuttings = 1, **c** cuttings = 2, **d** cuttings = 3, **e** cuttings = 4, **f** cuttings = 5

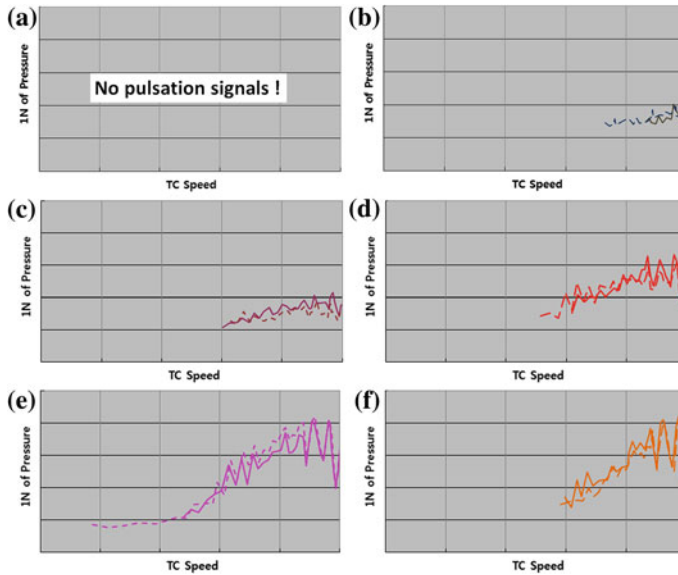


Fig. 7 Pulsation pressures to the number of balancing cuttings and the balancing results (Pass or Failure). **a** Cuttings = 0, **b** cuttings = 1, **c** cuttings = 2, **d** cuttings = 3, **e** cuttings = 4, **f** cuttings = 5

the pressure differences of the pulsation noise were negligible for the vibration differences, as shown in Fig. 7, and the amplitudes of the pressure were globally dependent upon the number of cuttings. This means that the vibrations did not affect the amplitude of the pressures; furthermore, it allowed us to appropriately evaluate the pulsation by changing the compressor wheels even at risk of breaking the balancing.

The maximum values of the vibrations and the pressures are briefly compared in Fig. 8a and b. Figure 8c shows that there is no linear relation between the two factors.

3.4 Test Samples of Different Arrangements and Areas of Cuttings

The cuttings are fundamentally gathered in one area or on opposite sides, next to each other. The size of the cuttings is dependent upon the unbalance of compressor wheels, and its maximum width of one cutting is limited in production lines. The distribution of cuttings was investigated for 4, as shown in Fig. 9.

Additionally, in order to see the influence of its area to the pulsation pressure, different areas of the cuttings were compared to the regular size of 1 cutting. The large one was about twice the regular size, and the wheels are shown in Fig. 10. One of the large cuttings corresponded to 2 regular ones in area, as did the two large cuttings to 4 regular ones.

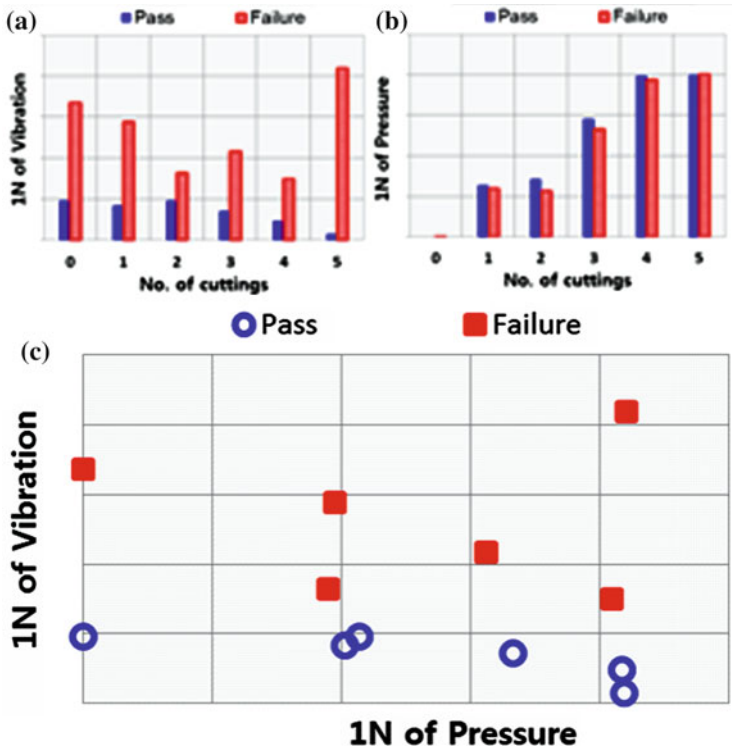


Fig. 8 Comparison of maximum 1 N vibrations and pressures to the number of balancing cuttings and “Pass” and “Failure” in the production line. **a** Max 1 N of vibrations, **b** max 1 N of pressures, **c** relation of max 1 N of vibrations and pressures

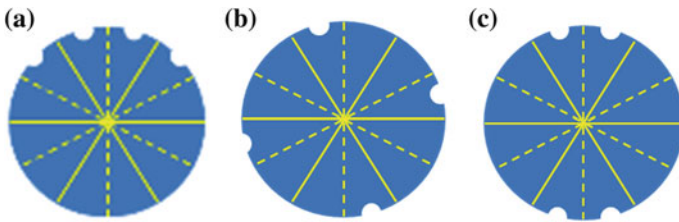


Fig. 9 Three samples of 4 cuttings. **a** Base, **b** evenly spaced by 1, **c** 180° by 2

Fig. 10 Two samples with large cutting areas. **a** One large cutting, **b** two large cuttings

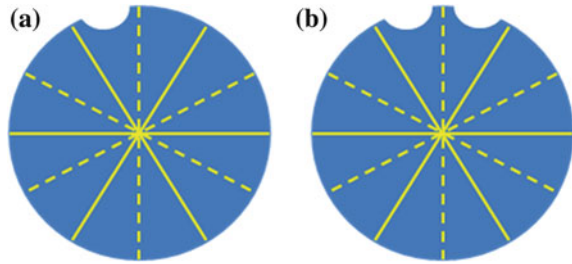
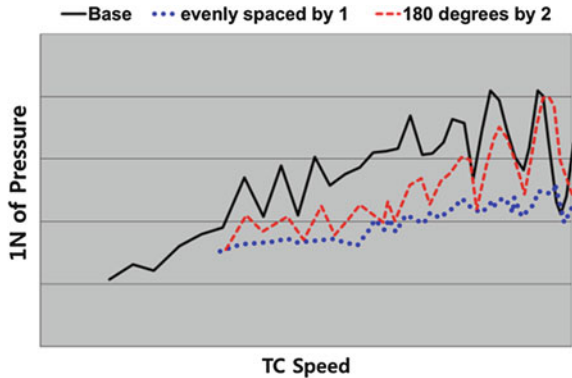


Fig. 11 Pulsation pressures to the three arrangements of 4 cuttings



3.5 Test Results

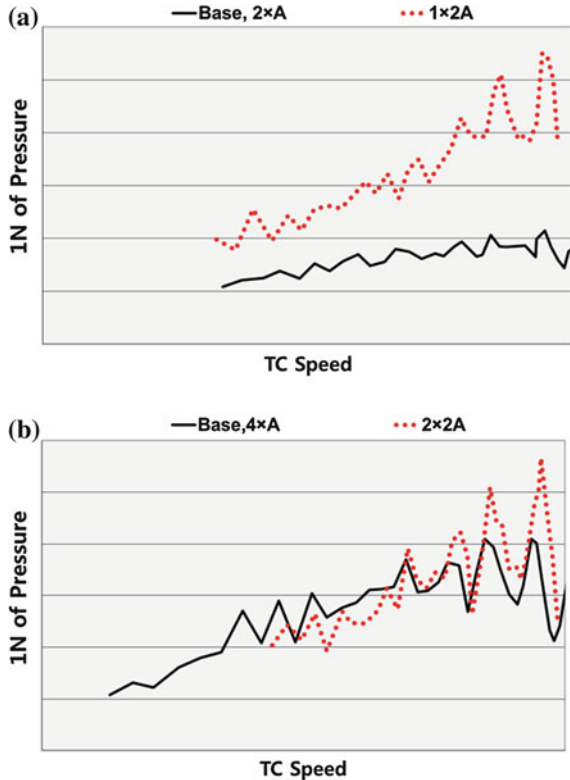
3.5.1 Different Cutting Arrangements

The pressures of the pulsation noise are compared in Fig. 11 for the samples with 4 cuttings, as shown in Fig. 9. It was concluded that the pulsation was stronger the more closely positioned the cuttings were.

3.5.2 Different Cutting Areas

The pressures of the two samples shown in Fig. 10 were compared with those of the 2 and 4 cuttings in Fig. 12, respectively. Figure 12a shows that one large cutting had a much higher pressure than the 2 regular cuttings. On the other hand, the two large cuttings had a higher pressure only at a high speed than the 4 regular cuttings. It seemed that the large cuttings generally had the same effect as the closely positioned cuttings. This indicated that pulsation could be limited by a proper cuttings size as well as the appropriate number of cuttings.

Fig. 12 Pressure comparisons for larger cuttings to regular cuttings with the same total area.
a One large cutting ($1 \times 2A$) to 2 regular cuttings ($2 \times A$),
b two large cuttings ($2 \times 2A$) to 4 regular cuttings ($4 \times A$)



4 Conclusion

The turbocharger pulsation noise, generated by a flow of air inside the compressor blades, was investigated. It was shown that the pulsation noise was not influenced by the vibration induced from the unbalance of the rotating parts. Through tests, this chapter investigated the factors that affect the noise based on the fact that the noise was related to the number of balancing cuttings of the compressor wheels. We concluded as follows:

- The pulsation noise generally increases with the number of cuttings. Thus, the number should be limited in order to control the noise.
- The noise is dependent upon the arrangement of the cuttings. The noise is greater when the cuttings are next to each other.
- One cutting with the same area of two cuttings generates higher pressure than two cuttings. It seems therefore that a proper size of cuttings is desirable, as well as an appropriate number in order to control the pulsation noise.

References

1. Arnold S (2004) Turbocharger technologies to meet critical performance demands of ultra-low emissions diesel engine. SAE technical paper 2004-01-1359
2. Trochon EP (2001) A new type of silence for turbocharger noise control. SAE 2001-01-1436
3. Calvo JA, Diaz V, San Roman JL (2006) Controlling the turbocharger whistling noise in diesel engines. *Int J Veh Noise Vib* 2(1):17–28
4. Kim BH, Hong SS, Song JE (2006) A study on turbocharger noise for passenger powertrains. In: Proceedings of the KSNVE annual spring conference, pp 1707–1712
5. Lee HI (2010) Noise diagram of an automotive turbocharger and its applications. *Trans KSNVE* 20(5):502–509
6. Park HI, Kim HJ, Kang SY, Eom SB (2010) Investigation on engine operation area based on turbocharger noise map. In: Proceedings of the KSAE conference and exposition, Nov 2010, pp 462–467
7. Lee JK, Kim HJ, Kang KT (2007) Development of the evaluation method for aerodynamic noise caused by pressure pulsation in the turbocharged diesel engine. In: Autumn conferences of the Korean society for noise and vibration engineering, pp 918–922
8. Kang W, Kim HJ, Sung HJ (2009) Reduction of flow-induced noise an expansion muffler with lids. *Trans KSME* 33(B)(2):79–84

Rotordynamics for Turbocharger Application Using Matlab Software

Cosmin Boricean, Gheorghe Alexandru Radu and Anghel Chiru

Abstract Analytical modelling involves, generally speaking, a sophisticated mathematical system of equations, that do not always correspond to the exact turbocharger dynamic behavior that occurs during functioning. For a rigorous approach related to the turbocharger dynamic behavior a test rig validation is also necessary besides an analytical estimation [1]. This chapter focuses on highlighting some aspects related to analytical modelling of turbochargers rotors. This modelling is further used to compare the results with the data sets obtained during test rig testing.

Keywords Rotordynamics · Turbocharger · Vibration · Bearing · Dynamic behavior

1 Introduction

For modelling the rolling bearing turbocharger a finite element model that was obtained in accordance with the full scale rolling bearing turbocharger GTB2260V was first established. Figure 1 presents the schematic model of the considered turbocharger, where the exact placement of the connecting nodes could be observed.

The discrete finite element model of the turbocharger presented in Fig. 1 is presented in Fig. 2, in which the main system components: disc type elements, shaft and also bearing type elements can be observed [2].

F2012-J03-021

C. Boricean (✉) · G. A. Radu · A. Chiru
University Transilvania of Brasov, Brasov, Romania
e-mail: cosmin.boricean@gmail.com

Fig. 1 Schematic turbocharger GTB2260V model

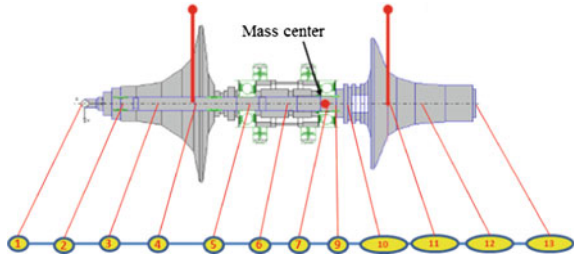
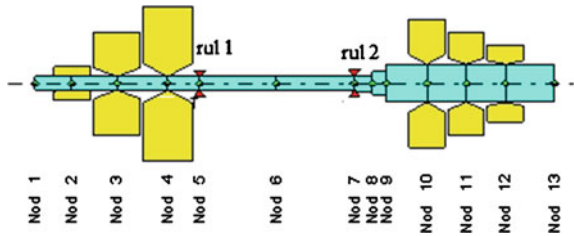


Fig. 2 Finite element model



In Fig. 2 the elements related to the compressor and turbine wheel were considered as rigid disc type elements with mass and geometric parameters in accordance with the real scale turbocharger [2]. The decoupling of each wheel (turbine and compressor) was achieved using three disc type elements. Taking into consideration the fact that the real scale turbocharger compressor, respectively turbine wheel have a trapezoidal shape, by using this approximation, the considered model was in a more exact correlation between the considered model and the real scale one.

The motion equations can be obtained by using the equation of kinetic and potential energy of the composing elements. These equations lead to the stiffness, gyroscopic and inertial matrix [3]. The same equations coupled with Lagrange equations applied for the system imposed degrees of freedom, give the general analytical form of the considered turbocharger. Where the Lagrange equations have the following form [4]:

$$\frac{d}{dt} \left(\frac{\partial E_c}{\partial \dot{q}_i} \right) - \frac{\partial E_c}{\partial q_i} + \frac{\partial E_p}{\partial q_i} = Q_i, \quad i = 1, 2, \dots, N$$

where: N—represents the system degree of freedom number; E_c , E_p —kinetic respectively potential energy of the considered turbocharger system.

In order to study the dynamic behavior of the turbocharger rotor sustained by rolling bearings the variation of three fundamental parameters that influence directly the functioning of the turbocharger rotor was considered. These parameters are: functioning speed, the effect of bearing stiffness and the effect of the bearing damping. On observing the influence that these three parameters have over the turbocharger system, conclusions can be drawn about the dynamic stability of the rotor and also about which is the important factor of the three above-mentioned parameters that influence the stability motion.

Table 1 Data sets

General data	Shaft	Compressor	Turbine
Mass (kg)	0.045	0.055	0.120
Maximum diameter (m)	0.015	0.06	0.0489
Disc height (m)	–	0.0262	0.0276
Mechanical, diametrical and polar J_d , J_p (kgm^2) inertial moments	–	$J_d = 9.29 \cdot 10^{-6}$ $J_p = 13.16 \cdot 10^{-6}$	$J_d = 27.57 \cdot 10^{-6}$ $J_p = 86.58 \cdot 10^{-6}$

2 Simplifying Hypothesis Used in Mathematical Turbocharger Modelling

The mathematical modelling the turbocharger required several approximations introduced with the purpose of simplifying the equations which were implemented by means of MatLab software [2]. The used approximations are related to shaft, bearing and disc elements and are as follows:

- shaft type elements are considered as Timoshenko beam elements;
- bearing type elements are considered as rolling bearing characterized by stiffness and damping elements;
- disc type elements are defined by inertial and mass properties;
- for an more exact approximation of the turbocharger shaft a number of 13 nodes placed on the shaft beam were considered at the level of nodes 5 and 7 are considered rolling bearing elements (Fig. 2).

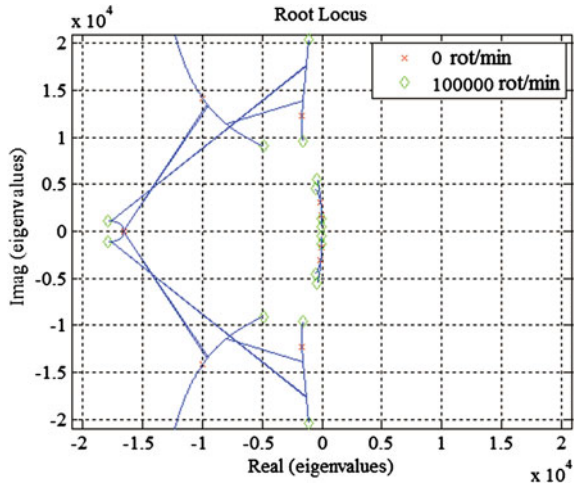
3 General Characteristics of Considered Turbocharger

For the purposes of the turbocharger modelling in the first stage, several measurements of the real scale turbocharger rotor were made. The data sets gathered from the measurements of each component are briefly presented in Table 1.

4 Validation of the Mathematical Model Accomplished for Dynamic Stability Simulations of Turbocharger Rotor

For the theoretical validation of the considered turbocharger mathematical model the Root Locus values corresponding to the entire system equations have been computed [2]. The Root Locus values for two functioning speeds: 100,000 and 200,000 rpm (Figs. 3, 4) were computed for the evaluation of the mathematical stability of the global equation system that models the dynamic behavior of the turbocharger rotor.

Fig. 3 Root locus
100,000 rpm



It can be noticed that even at 200,000 rpm the mathematical model is stable because at the Root Locus values indicate that a certain mathematical model is stable when all the values are placed in the imaginary domain and have negative orders.

4.1 The Effect of Functioning Speed Over the Turbocharger

In order to observe the general dynamic behavior of the turbocharger rotor for each simulation the Campbell diagram was designed [2]. It presents the values of damped natural frequencies over the rotor speed. At the intersection of the forward whirl curves (red color) with the frequencies induced by the functioning speed the values of so called critical speeds could be found. They are speeds where the rotor precession tends to be unstable. Figure 5 presents the Campbell diagram for the rotor at 100,000 rpm.

In Fig. 5 the curve noted with 1 represents the forward whirl and the curve noted with 2 represents the backward whirl. At the intersection of the forward whirl curves with the excitation frequencies given by the functioning speed one could find the critical speeds which in this case have the following values: 15,000, 25,000 and 40,000 rpm. The Campbell diagram represents a frequently used estimation graph of system dynamic stability with high applicability to almost all rotating machines.

In order to observe the rotor behavior at the imposed values of functioning speed, bearing stiffness and damping a response magnitude diagram was accomplished.

Figure 6 presents the motion amplitudes of the considered rotor-bearing system which are measured in various points of the rotating assembly. Curve noted with

Fig. 4 Root locus
200,000 rot/min

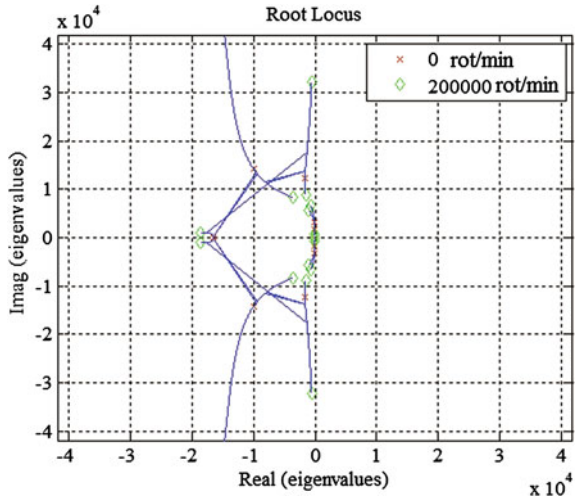
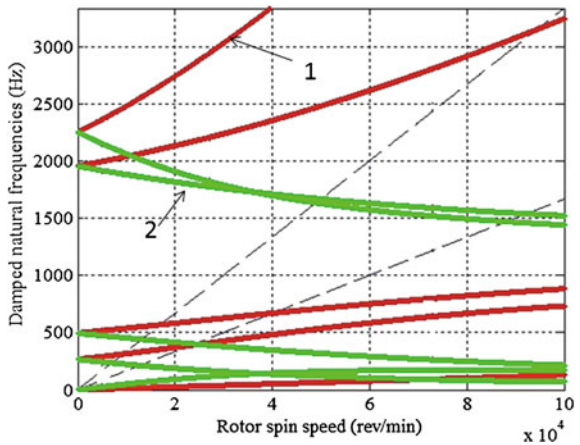


Fig. 5 Campbell diagram for
100,000 rpm



number 3 represents the rotor motion amplitude measured at the level of a point considered placed on the bearing. Considering the fact that the rolling bearing plays the role of an restrictor of shaft motion in radial direction due to its mounting conditions and own length, it can be noticed that the response amplitude, measured on the shaft side where the bearing is mounted has the lowest value which is also sustained by practice. It can be noticed that the highest value of displacement is registered at the level of turbine wheel.

The Campbell diagram for 200,000 rpm functioning speed is presented below in order to discuss the establishment of the values of critical speeds and also the values of damped natural frequencies in Fig. 7.

Fig. 6 Response magnitude for 100,000 rpm

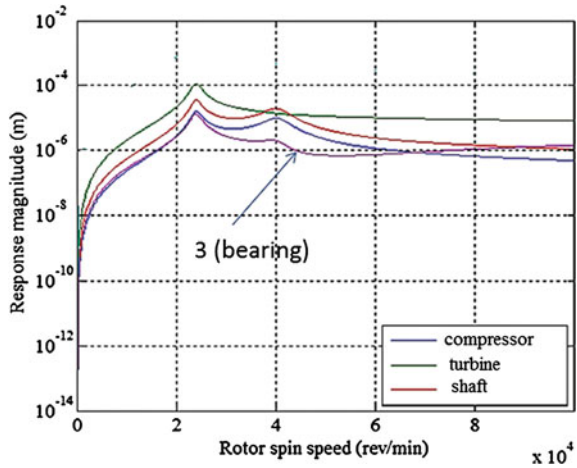
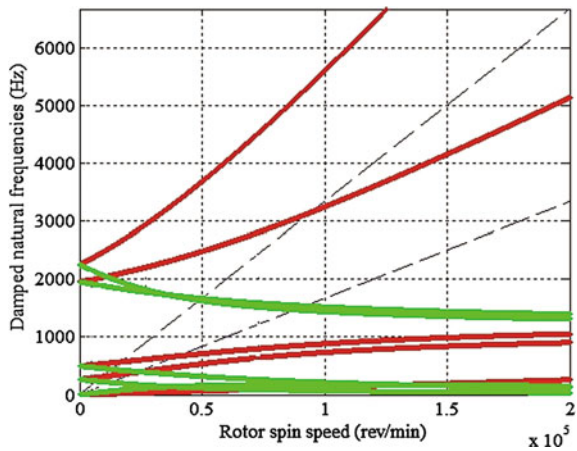


Fig. 7 Campbell diagram for 200,000 rpm

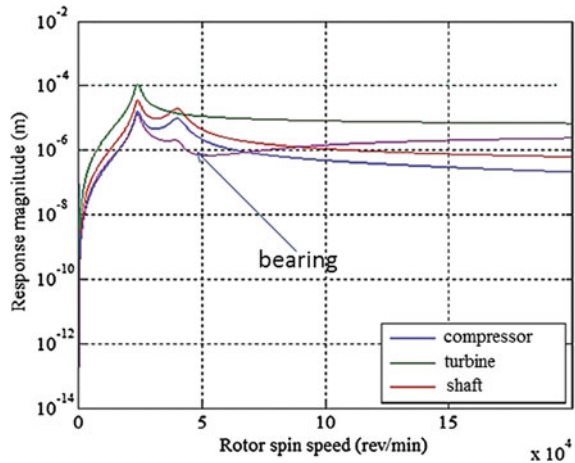


The critical speeds for functioning at 200,000 rpm have the following values: 25,000, 45,000 and 80,000 rpm. It can be noticed that the values of damped natural frequencies are unchanged compared with the ones obtained for 100,000 rpm.

For the study of the dynamic behavior of the rotor system, Fig. 8 shows the amplitude response for the system functioning at 200,000 rpm. In this figure it could be noticed that there are certain values of rotating speed where the rotor has the highest amplitudes. These rotating speeds correspond exactly to the critical speed identified by the Campbell diagram presented in Fig. 7.

It is to be noticed that even if the turbocharger rotor functions at 100,000 or 200,000 rpm the response magnitude amplitudes do not exceed in both cases the value of 10^{-4} m.

Fig. 8 Response magnitude for 200,000 rpm



The effect of self-centering of the rotor takes place in this case at 80,000 rpm in comparison with the previous case (100,000 rpm) where the self-centering phenomena took place at 60,000 rpm.

We can conclude by saying that the functioning speed plays an important role for the dynamic stability of turbochargers rotors, the effect of the functioning speed being a complex one which is difficult to estimate [5].

4.2 The Effect of Bearing Stiffness Over the Turbocharger

The effect of bearing stiffness can provide useful information regarding the type of material that is to be used on bearing manufacture, or in some other cases information regarding its optimization possibilities. The same parameters as in the previous case were studied in order to detail the effect of bearing stiffness over the entire rotor assembly where only the functioning speed varied. Is it to be mentioned that all parameters, excluding the stiffness, remained the same.

For a stiffness value of $k = 10^8$ N/m and a functioning speed of $n = 100,000$ rpm the simulation results are presented in the following diagrams.

The examination of the Campbell diagram in Fig. 9 and its comparison with the diagram in Fig. 5 shows that by modifying the bearing stiffness value from $k = 10^7$ to $k = 10^8$ N/m the dynamic stability of the system slightly changes at the level of damped natural frequencies and also at the level of critical functioning speeds. In Fig. 10, the critical speeds are obtained at 20,000, 30,000 and 50,000 rpm, denoting a certain change from the ones presented in Fig. 5.

Figure 10 presents the response amplitudes diagram by means of which the global behavior of the rotating system can be studied. Also in this case the critical speeds found in the Campbell diagram (Fig. 9) are validated in Fig. 10. By increasing the stiffness value by 10 times from the previous value, it can be

Fig. 9 Campbell diagram

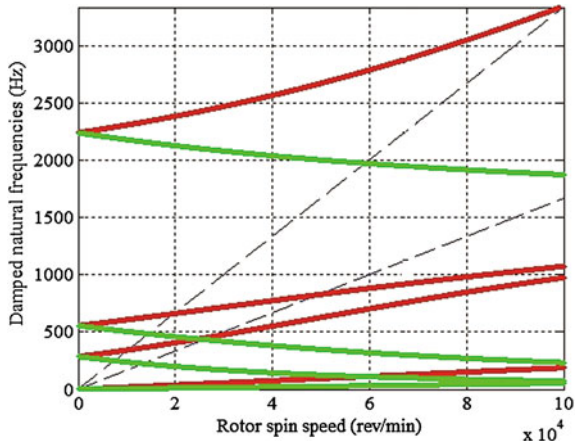
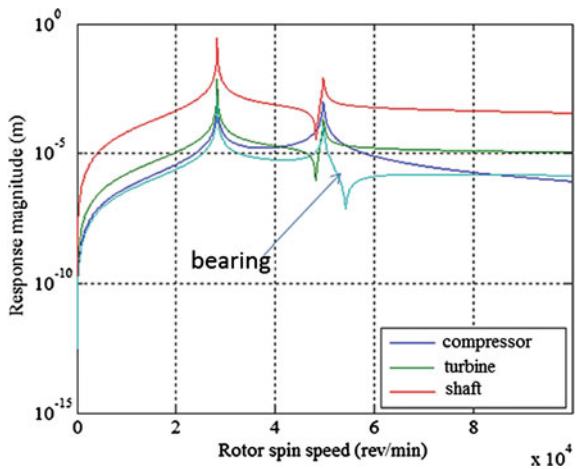


Fig. 10 Response magnitude

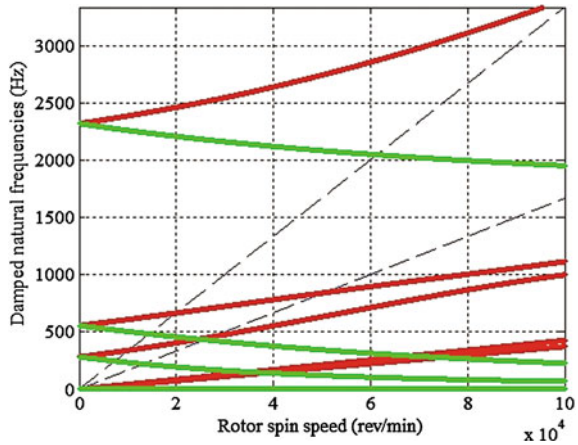


observed that the response amplitude considerably changes from the value of 10^{-4} to 10^{-1} m. The highest values of amplitudes are obtained for the turbocharger shaft being placed at a medium level of $10^{-2.5}$ m. The lowest level of amplitudes are registered at the level of the bearing.

4.3 The Effect of Bearing Damping on the Turbocharger

In all vibrating systems the most important parameter is represented by the damping which is defined by the damping coefficient “c [Ns/m]”. In order to prove the influence of the damping over the dynamical stability of the turbocharger rotor, in the following only the value of bearing damping was varied from the value of

Fig. 11 Campbell diagram



$c = 10^3$ Ns/m (value used in all previous simulations) to the value of $c = 10^4$ Ns/m. The Campbell diagram of the modeled system is presented in Fig. 11 in order to highlight the general behavior of the turbocharger rotor by modifying the value of damping.

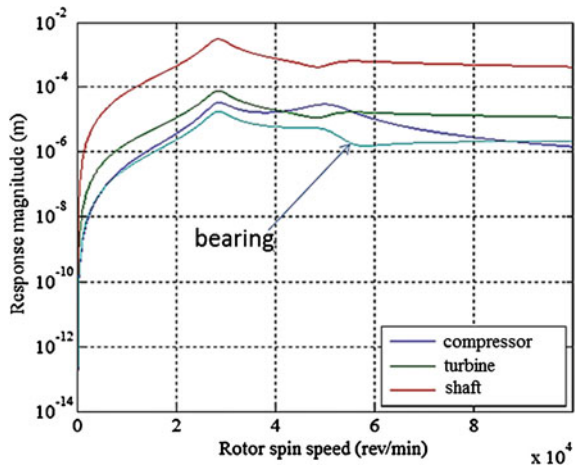
In Fig. 11 it can be observed that even if the value of the damping coefficient was modified, the damped natural frequencies did not change with a major value comparing these results with the ones obtained in Fig. 5. Also the differences between the values of the critical speeds are not significant from the ones obtained with the previous value of the damping coefficient.

For the identification of the amplitudes that the modification of the damping coefficient induces to the system in Fig. 12 the response magnitude diagram is presented. By raising the value of the damping coefficient the system becomes more stable. If the raising of the value of stiffness induces a vibrational character to the system, the raising of the damping coefficient induces a calming character to the system which is also confirmed by practice. Comparing the data obtained in Fig. 12 with the ones presented in Fig. 10 it can be observed that the values of response amplitudes are lower starting from the value of 10^{-1} m to the value of 10^{-3} m in this case. The raising value of the damping coefficient has changed the entire rotor-bearing response with high values, in comparison with previous values.

In order to identify the real dynamic behavior of the rolling bearing turbocharger, several test rig tests were conducted.

5 Vibrational Performances Comparison Between Rolling Bearing and Hydrodynamic Bearing Turbochargers

In order to evaluate the vibrational performances of the rolling bearing turbochargers, a comparison between this model of turbocharger and a turbocharger that uses hydrodynamic bearings was made. The tests were accomplished using a

Fig. 12 Response magnitude

Schenk MBRS 110 test rig and the signal acquisition data platform used was Pulse 12 supplied by Bruel & Kjaer. The tests were accomplished for certain functioning speeds: stabilized regime of 30,000 and 90,000 rpm; deceleration regime of 30,000 and 90,000 rpm and acceleration regime for 30,000 and 90,000 rpm.

5.1 Results Obtained at Stabilized Regimes

It is to be mentioned that in the following diagrams the signals marked in red refer to the rolling bearing turbocharger and the signals marked in green refer to hydrodynamic bearing turbocharger.

Figure 13 represents the signals gathered for a stabilized functioning regime at 30,000 rpm. It is to be observed that the turbocharger with rolling bearings (GTB2260V) has, at this functioning speed, worse vibrational performances (the vibration amplitudes are higher) than the hydrodynamic bearing turbocharger GTV2600.

In Fig. 14 are represented the signals gathered for a stabilized functioning regime at 90,000 rpm. For a stabilized functioning speed of 90,000 rpm the turbocharger with rolling bearings has a higher level of vibration amplitudes than the turbocharger with hydrodynamic bearings, which denotes a poor vibrational behavior.

5.2 Results Obtained at Accelerated Regimes

The functioning regimes of turbochargers are mostly transient regimes of constant acceleration and deceleration. In order to observe the vibrational behavior of the

Fig. 13 Signals at stabilized 30,000 rpm

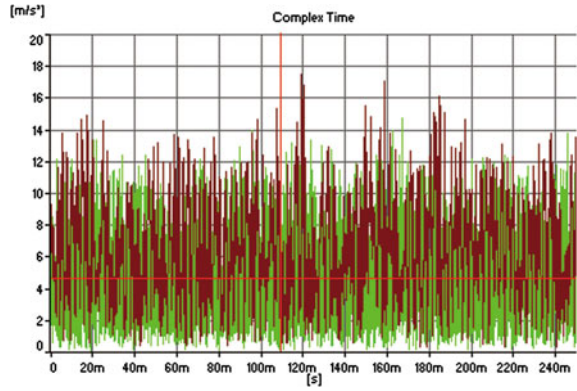


Fig. 14 Signals at stabilized 90,000 rpm

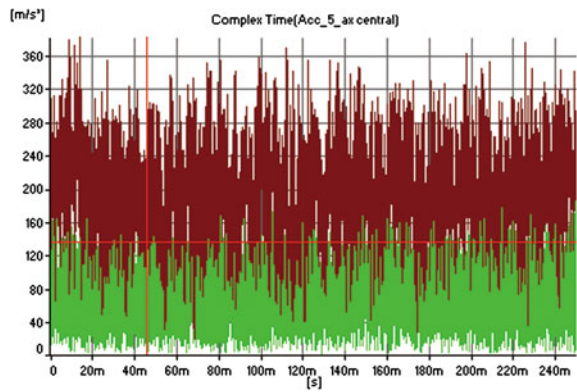


Fig. 15 Signals at accelerated 30,000 rpm

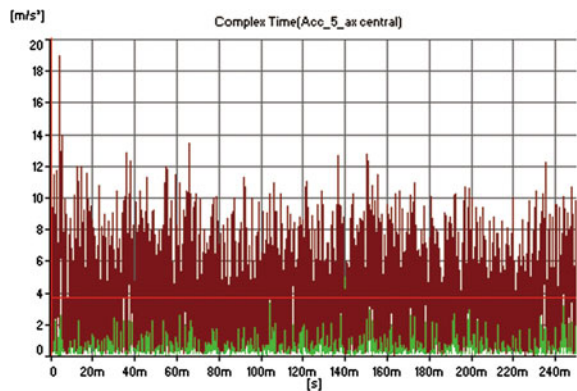


Fig. 16 Signals at accelerated 90,000 rpm

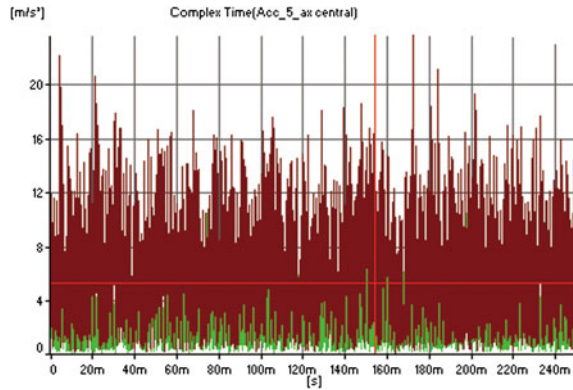
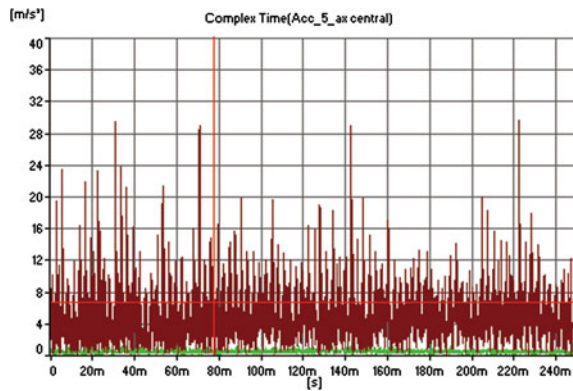


Fig. 17 Signals at decelerated 30,000 rpm



two turbochargers, in the following the data obtained by several tests at two acceleration regimes: 0–30,000 and 0–90,000 rpm will be presented.

Figure 15 presents the signals gathered for an acceleration regime from 0 to 30,000 rpm. It can be observed that the level of vibration amplitudes is higher for the turbocharger equipped with rolling bearings.

Figure 16 shows the signals gathered for an acceleration regime from 0 to 90,000 rpm. It can be observed that the turbocharger with hydrodynamic bearings behaves better.

5.3 Results Obtained at Decelerated Regimes

Maintaining the comparison scale previously described, in the following the data sets obtained for two deceleration regimes: from 30,000 to 0 rpm and from 90,000 to 0 rpm are presented. For each regime the obtained results are shown in Figs. 17 and 18.

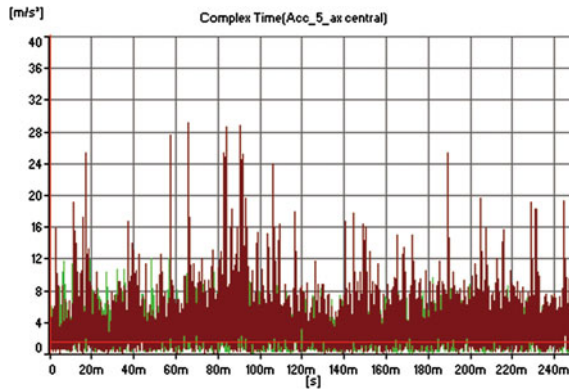


Fig. 18 Signals at decelerated 90,000 rpm

Table 2 Test conclusions

	Functioning speed	Rolling bearing	Hydrodynamic bearing
Stabilized regime	n = 30,000 rpm	–	+
	n = 90,000 rpm	–	+
Acceleration regime	n = 30,000 rpm	–	+
	n = 90,000 rpm	–	+
Deceleration regime	n = 30,000 rpm	–	+
	n = 90,000 rpm	+	+

Figure 17 presents the signals gathered for a deceleration regime from 30,000 to 0 rpm. It can be observed that the level of vibration amplitudes is higher for the turbocharger equipped with rolling bearings.

Figure 18 presents the signals gathered for an acceleration regime from 90,000 to 0 rpm. It can be observed that both turbochargers have an appropriate level of amplitudes.

6 Conclusions

In order to establish an analytical model for the dynamic behavior of a turbocharger, model which describes the exact functioning, it is necessary to use a high complexity mathematical system. By increasing the complexity of the mathematical system, the results in some cases may not be satisfactory. Generally speaking, all mathematical models need certain adjustments that are imposed by test rig measurements. The mathematical simulations accomplished in this study highlight the influence of the main parameters which define the turbocharger.

From the study reported in this chapter it could be observed that the main influence over the dynamic behavior of the turbocharger is given by the phenomena occurring at the level of the bearing. By choosing an optimal value for the damping coefficient in correlation with an optimal value for the stiffness, the vibrational behavior could be decreased or totally dimmed.

The oil film favorably influences the dynamic stability of the rotor by inducing the self-centering phenomena at higher functioning speeds [5].

The high costs of turbochargers equipped with rolling bearings are justified only by the higher rate of durability that these bearings provide to the system. The tests showed that the turbocharger with rolling bearing has a higher level of vibration in almost all of the considered functioning regimes.

Table 2 briefly presents the conclusions of these tests. It also highlights the general performances obtained during test rig tests.

The boxes noted with “+” specify the fact that a certain bearing has higher performances from the vibrational point of view.

The studies reported in this chapter allow for the highlighting of the phenomena and also the functioning parameters that must be studied in depth to assure the rolling bearing turbochargers at same level as the turbochargers equipped with hydrodynamic bearings.

Acknowledgments This chapter is supported by the Sectorial Operational Programme Human Resources Development (SOP HRD), financed from the European Social Fund and by the Romanian Government under the contract number POSDRU/88/1.5/S/59321.

References

1. Ehiric FF (1992) Handbook of rotordynamics. McGraw-Hill Inc., New York
2. Friswell MI (2010) Dynamics of rotating machines. Cambridge University Press, United Kingdom
3. Wu JJ (2007) Prediction of lateral vibration characteristics of a full size rotor-bearing system by using those scale models, vol 43, issue 10. Science Direct, Amsterdam, pp 803–816
4. Lalanne M (1997) Rotordynamics prediction in engineering, 2nd edn. Wiley, New York
5. Nyugen H-S (2012) Rotordynamics of automotive turbochargers. Springer, Berlin

Part IV
Body Vibration and Noise Control

A Systematic Approach for Rattle Problem Detection and Prevention of Seat Belt Retractors

Youmin Guo, Xiaoping Gong, Zhiqiang Tu, Zhonghua Wu, Yangjia She, Peng Xu and Zhigong Li

Abstract Seat belt retractor rattle is one of the most frequently encountered vehicle squeak and rattle problems—a major quality issue. Numerous papers have been published concerning problem detection and design improvements for brand new seat belt retractors. In reality, the rattle performance tends to degrade as vehicle mileage gets accumulated, which would hurt long-term customer satisfaction. None of previously published papers mentioned the performance degradation and prevention strategies of seat belt retractors. The current paper presents a systematic approach for detection of rattle performance degradation of seat belt retractors and design optimization strategies for preventing degradation.

Keywords Seat belt retractor · Rattle noise · Detection · Prevention · CAE analysis

1 Introduction

Squeak and rattle is one of the major concerns in vehicle design and development for customer satisfaction. One of the critical squeak and rattle problems is seatbelt retractor rattle. A number of papers have been published in discussing seatbelt retractor rattle problems. The root causes of retractor rattle problems and a diagnostic procedure using in-vehicle and laboratory test methods were discussed

F2012-J04-002

Y. Guo (✉) · X. Gong · Z. Tu · Z. Wu · Y. She · P. Xu · Z. Li
Changan Auto Global R&D Center of Changan Automobile Co. Ltd, Chongqing, China
e-mail: sunqiemail@163.com

in [1]. A computational method for predicting rattle propensity reduction using theoretical models and a comparison between the computational results and laboratory measured ones were presented in [2]. A correlation between vehicle subjective and laboratory objective evaluations was studied in [3]. A retractor rattle design optimization through material selection and design of the sensor basket was described in [4].

All the papers mentioned above addressed rattle problems of brand new retractors and design improvements in retractors themselves. However, squeak and rattle degradation [5] is also an important issue in customer satisfaction. Retractor rattle degradation depends on not only retractor designs but also body designs at which retractors are attached (a system issue). The current paper presents a systematic approach for rattle degradation problem detection and prevention of seatbelt retractors.

2 Root Cause Analysis of Seat Belt Retractor Rattle Degradation Problems

A systematic approach for detecting seat belt retractor rattle problems using vehicle on-the-road subjective evaluations, component laboratory objective testing and CAE analysis is given in what follows.

2.1 *Vehicle on-the-Road Subjective Evaluations*

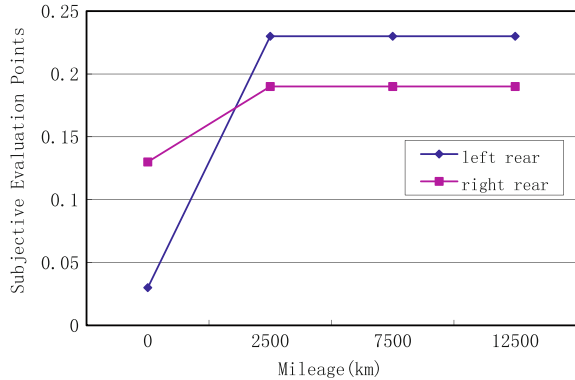
Subjective evaluations are typically a first step in detecting any vehicle squeak and rattle issues if any. To determine rattle degradation level in the useful life of a project vehicle, a production vehicle was selected to go through mileage accumulation on different road segments. Subjective evaluations of rattle level at different mileage stage were conducted. The following rattle subjective evaluation system is used to quantify the rattle performance at each stage.

Total Rattle Index = Summation of (Part Squeak and Rattle Index \times Test Road Index)

Part rattle index: 1.0 (majority of customers can notice and feel annoyed)
 0.3 (50 % customers will notice and feel annoyed)
 0.1 (mild squeak and rattle noise although majority of customers can notice)
 0.0 (no squeak and rattle noise at all)

Test road index: 1.0 (smooth road—roads used by majority of customers)
 0.3 (mildly rough road—roads used by 1/3 customers)
 0.1 (very rough road—roads used by few customers)

Fig. 1 Total rattle index of left rear and right rear seat belt retractors



The total rattle index reflects both the part rattle performance and road excitation conditions. The smaller the index is the better rattle performance of the part is. The project vehicle was driven on different road segments and the total rattle index for the left rear and right rear seat belt retractors was generated at 0, 2,500, 7,500 and 12,500 km, respectively. The results are plotted in Fig. 1. It can be seen in this figure that the rattle index for both retractors shows the same performance degradation trends although the actual performance level is different. The figure also indicates that the most degradation took place in the first 2,500 km.

2.2 Laboratory Objective Testing

To investigate the root causes of the seat belt rattle degradation problems, the (left rear) retractors before and after mileage accumulation were tested in the laboratory using random excitations corresponding to the road segments when the project vehicle was subjectively evaluated. A Zwicker N10 loudness metric in “sones” was used to quantify the rattle noise level and a comparison of this noise level before and after mileage accumulation is given in Fig. 2. The figure indicates that the retractor has 2.2 Sones performance degradation which is consistent with the findings in the subjective evaluations discussed in the earlier section.

2.3 Vehicle Body System Rattle Sensitivity Study

The retractor rattle degradation depends on not only the retractor design itself but also the body designs at which the retractor is attached. The vibration level at the retractor/body attachment point greatly affects the degradation rate of the retractor. Therefore, it is crucial to minimize rattle sensitivity at this location. A CAE-driven body squeak and rattle sensitivity analysis method has been developed at Changan

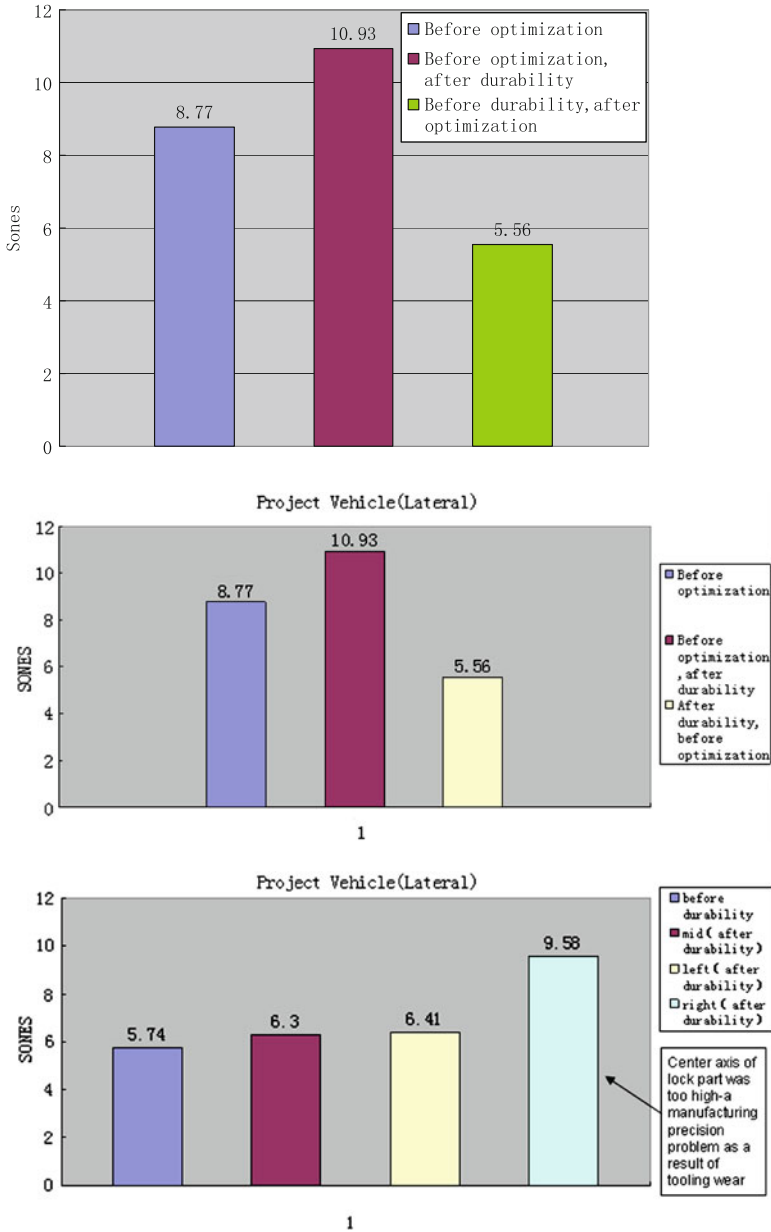


Fig. 2 Loudness level at left rear seat belt retractor (lateral excitation)

which can be used to guide designs for improvement of squeak and rattle performance. To make sure that none of the squeak and rattle sensitive areas experiences high vibration level when a vehicle is driven on the road, a squeak and rattle transfer function analysis is conducted which computes frequency response

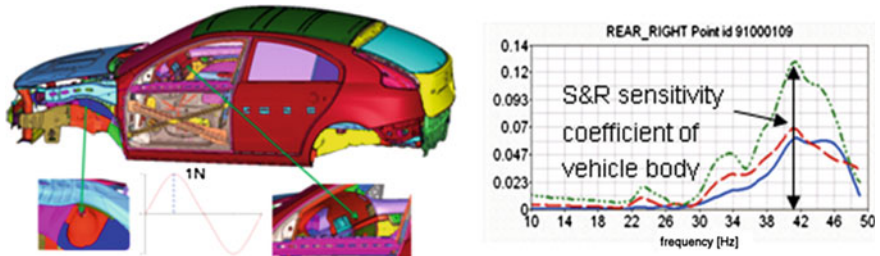


Fig. 3 Body squeak and rattle transfer function analysis, *left* unit load (1N), *right* output velocity

functions at each pre-determined locations in a body due to a unit load applied at each critical body/chassis attachment locations, respectively. This method is illustrated in Fig. 3. The response function at each location in each direction due to each excitation is frequency dependent as shown in Fig. 3. The maximum peak of the responses in three directions is defined as the sensitivity coefficient at that particular location. The maximum value of response functions at all locations in a sub-system (e.g., instrument panel, doors, seatbelt retractor attachment, etc.) is defined as the squeak and rattle sensitivity coefficient of this particular sub-system.

The rattle sensitivity coefficient at the left rear retractor/body attachment location of the project vehicle was computed and is shown in Fig. 4. It can be observed in this figure that the sensitivity coefficient (maximum transfer function in the vertical direction due to rear left excitation) is 0.56 mm/s which is the highest sensitivity coefficient of all sub-systems in the body system. This implies that the root cause of the retractor problem is a combined design problems of both retractor itself and body/retractor attachment point.

3 Prevention Strategies for Seat Belt Retractor Rattle Degradation

To prevent the seat belt retractor degradation problems, structural design deficiency associated with the retractor and body structures are explored and design improvements are made accordingly as described in what follows.

3.1 Seat Belt Retractor Design Improvement

It was discussed in [2] that the sensor, the pool and the lock pawl represent three principal sources of retractor rattle. A retractor rattle design improvement through material selection of the sensor basket can be found in [4]. Following the ideas presented in these two papers, an investigation was made on the sensor basket. It was found that the material of the sensor basket was too hard and also exhibited high

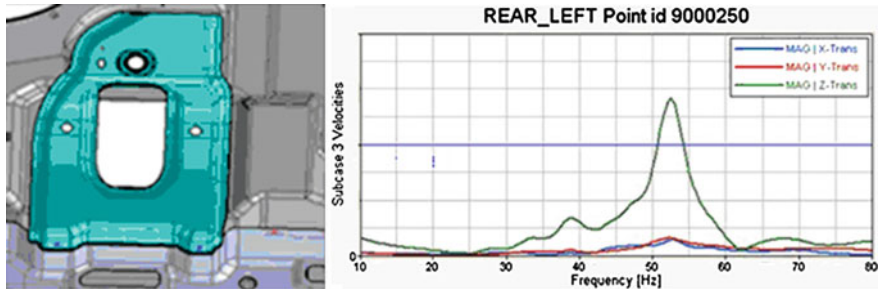


Fig. 4 Baseline retractor attachment design and rattle sensitivity coefficient at left rear retractor/body attachment location

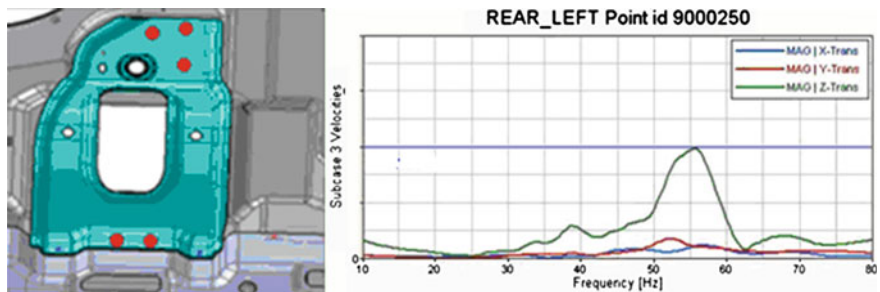


Fig. 5 Optimized retractor attachment design and rattle sensitivity coefficient at left rear retractor/body attachment location

instability in hardness. A new sensor basket made of softer material with high stability in material properties improved rattle noise problems before and after mileage accumulation as shown in Fig. 2. It can be seen in this figure that the sensor basket with material optimization resulted in 3.21 Sones improvement before mileage accumulation and exhibited insignificant performance degradation (0.56–0.67 Sones) after mileage accumulation at the left rear and middle rear retractors. Only the right rear retractor showed significant rattle degradation (3.84 Sones). A further investigation confirmed that the right rear retractor rattle degradation was caused by the fact that the center axis of the lock pawl of that particular part is too high—a manufacturing precision problem as a result of tooling wear.

3.2 Vehicle Body System Structural Design Improvement

As discussed in an earlier section that the seat belt rattle retractor sensitivity study indicated retractor/body attachment design deficiency issue also. To reduce the retractor rattle sensitivity, the stiffness of the local attachment area was increased

by adding a few welds as shown in Fig. 5. This design optimization resulted in 28 % improvement in rattle sensitivity. Most importantly, actual vehicles with both the retractor and body design optimization exhibited no annoying seat belt rattle noise before and after vehicle mileage accumulation anymore.

4 Summary

- A systematic approach for rattle problem detection and prevention of seat belt retractors has been demonstrated.
- Combined retractor and body design optimization proved to be very effective in eliminating retractor rattle problems.

Acknowledgments The authors would like to thank CAE Department in the Changan Auto Global R&D Center for their support in body rattle sensitivity CAE analysis.

References

1. Malinow IG, Perkins NC (1999) "Seat belt retractor rattle: understanding root sources and testing methods", SAE paper 1999-01-1729
2. Morgan CD, Naganarayanan BP, Shanker S (2004) "Comparative evaluation of seat belt retractor websense mechanism rattle noise", SAE paper 2004-01-0391
3. De Oliveira ED, Hualppa B, Reis DB (2005) "Seat belt retractor objective evaluation", SAE paper 2005-01-4164
4. Liu KJ, DeVilbiss T, Freeman M (1999) "Experimental analysis of rattle noise abatement in seatbelt retractor assembly", SAE paper 1999-01-1723
5. Kuo EY, Liaw L "Statistical analysis of vehicle high mileage NVH performance", SAE paper 971912

A Study on Optimization Design of Engine-Room NVH for a Modified Vehicle

Honghua Li, Fengwei Sun, Hao Xu, Jielong Chen,
Aijun Jin and Fuquan Zhao

Abstract The performance test of NVH is first conducted with regard to the original car in this paper. Based on the results, it is extrapolated that this problem mainly attributes to insufficient stiffness of right longitudinal beam of bodywork. By performing cause analysis, it is understood that right longitudinal beam stiffness can be indirectly improved by enhancing the stiffness of radiator frame. The optimized design is performed in respect of the radiator frame structure. Combined with the CAE's analysis results and NVH's test validation, it is concluded that longitudinal beam stiffness can be significantly improved by adjusting the thickness of upper cross member of radiator from 0.8 to 1.5 mm, and increasing eight post reinforcements at the same time, thereby satisfying the NVH's requirements.

Keywords Engine room · Longitudinal beam · Radiator frame · Stiffness · Optimization design

1 Introduction

With the continuous improvement and development of the car, the car's comfort requirements also become higher and higher. The automotive noise, vibration and harshness, referred to as NVH, three important indicators of the evaluation of

F2012-J04-003

H. Li (✉) · F. Sun · H. Xu · J. Chen · A. Jin · F. Zhao
Zhejiang Geely Automobile Research Institute CO. LTD, Hangzhou, China
e-mail: lhh8650@yahoo.com.cn

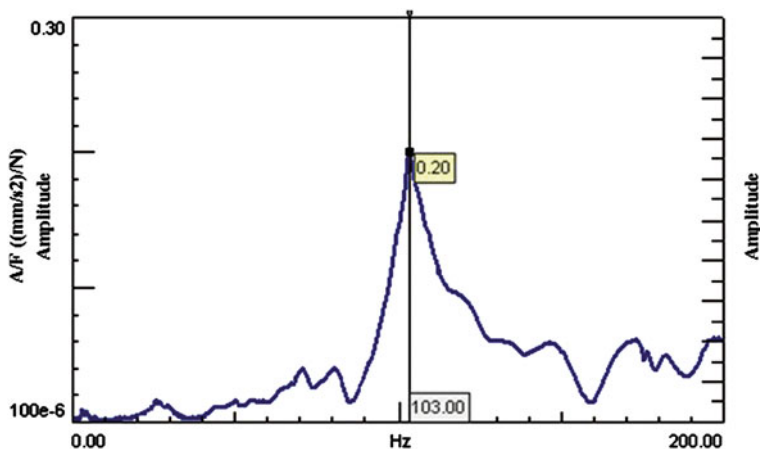


Fig. 1 Y direction bending vibration curve of original vehicle

automotive comfort [1–4]. For NVH performance testing, noise and vibration are the most important two indicators [5–8]. The vibration mainly comes from the vibration of powertrain system and excitation generated by road; the noise mainly comes from the air noises including powertrain system and its nearby noise, tire noise, wind noise and structure noise by passing the vibrations of chassis, body-work and other structures to the crew area inside [9, 10].

At present, each car industry and some research institutes study the performance of NVH more and more deeply and widely. During the development processing of new car, it can be reduced vibration and noise in the early days. And for the modified model, in order to reduce the cost, through the CAE analysis, specific NVH performance improvement is a very effective design method. This article analyzed and resolved particularly the NVH problems encountered in the development processing of a modified vehicle to expound an indirect structure improvement method with reducing vibration noise and improving NVH performance.

2 NVH Performance Testing

In allusion to original vehicle to test NVH performance, the results show that the right carling stiffness of original vehicle is lower, and so that lead to the bigger noise and vibration. Figures 1 and 2 is the original vehicle right carling Y, Z-bending vibration curves. It can be seen from the graph, two vibration curves all show a change trend that it increases at first and then lows, and it shows a peak at the engine speed for 3,100 rpm (frequency 103 Hz). Therefore, considering the NVH performance of this modified vehicle, it can reduce the vibration and noise, eliminate vibration peak by improve the right carling stiffness.

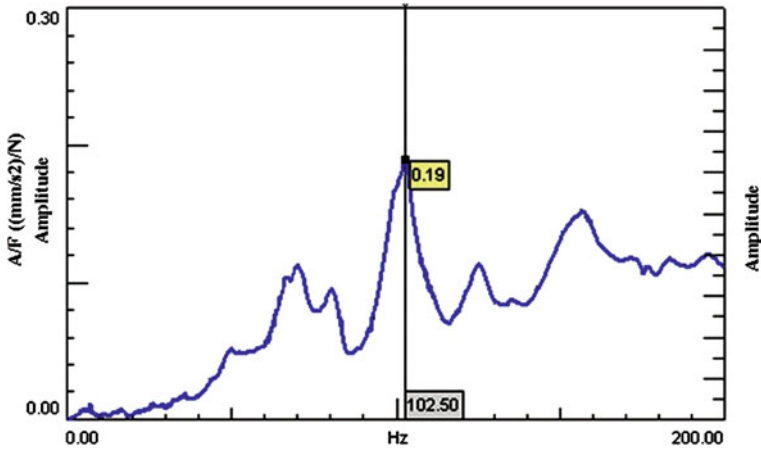


Fig. 2 Z direction bending vibration curve of original vehicle

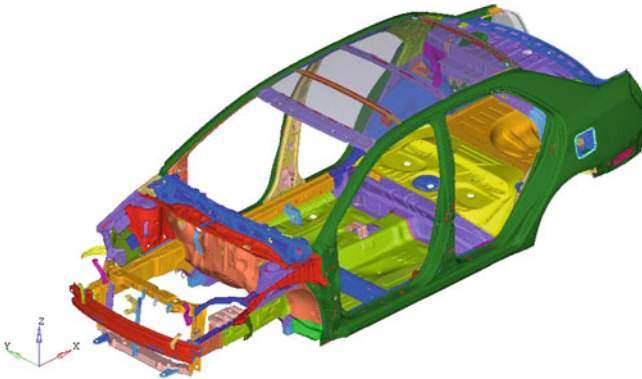


Fig. 3 Modified vehicle right longitudinal beam finite element model

3 Reason Analysis

3.1 Simulation Model

The finite element model of modified vehicle right carling stiffness performance analysis is shown in Fig. 3. This model shows that the welding point adopts CWELD unit simulation, adhesive adopts body unit simulation (with the characteristics) and bolt connection adopts rigid unit simulation. Finally, the established finite element model is composed by 5,10,121 units, including 4,79,577 quadrilateral units, 24,558 triangular units, 444 body units, 4767 CWELD units and 775 rigid units.

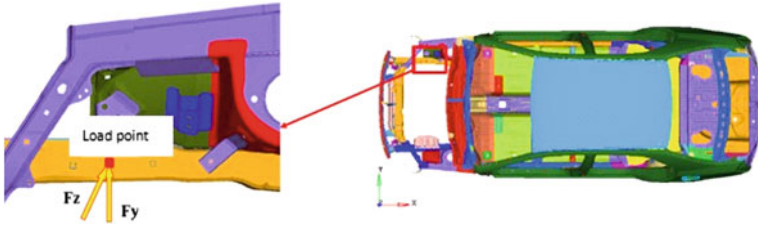


Fig. 4 Loads and restraints

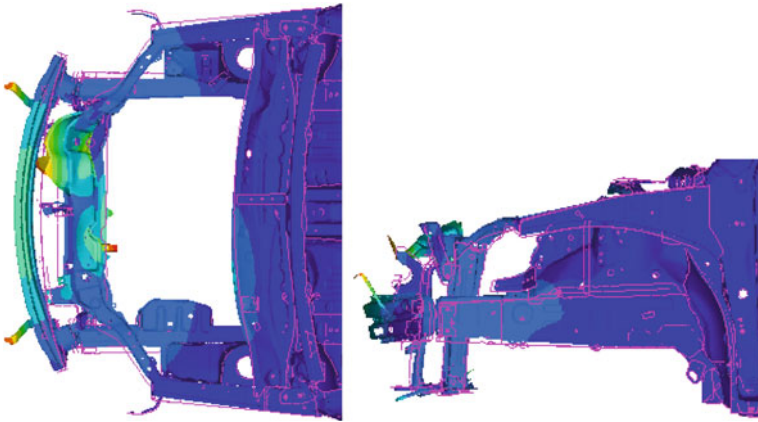


Fig. 5 Schematic drawing to right longitudinal beam vibration mode ($f = 99.5$ Hz)

3.2 CAE analysis

Figure 4 is the scheme that it shows Y, Z direction unit excitation inflicted on the connected point between right mounting and carling. The body in white modal analysis results of modified vehicle is shown in Fig. 5.

Figure 5 is the right carling vibration mode of modified vehicle in 99.5 Hz. It can be seen that the radiator frame, especially radiator crossbeam vibrates seriously in the frequency. Serious vibration of radiator frame can easily cause great Y and Z direction bending vibration to right carling. And compared the simulation result with experimental condition that right carling Y and Z direction bending vibrations are serious at engine speed 3,100 rpm, frequency 103 Hz (Fig. 6), it can be seen that both frequencies are close, vibration modes are similar. This will cause sympathetic vibration to produce bigger vehicle noise. From the Fig. 5, it also can be seen that the larger radiator crossbeam vibration is the main reason for right carling bending vibration. So by improving the radiator crossbeam stiffness, it can indirectly improve the right carling stiffness, and need not directly

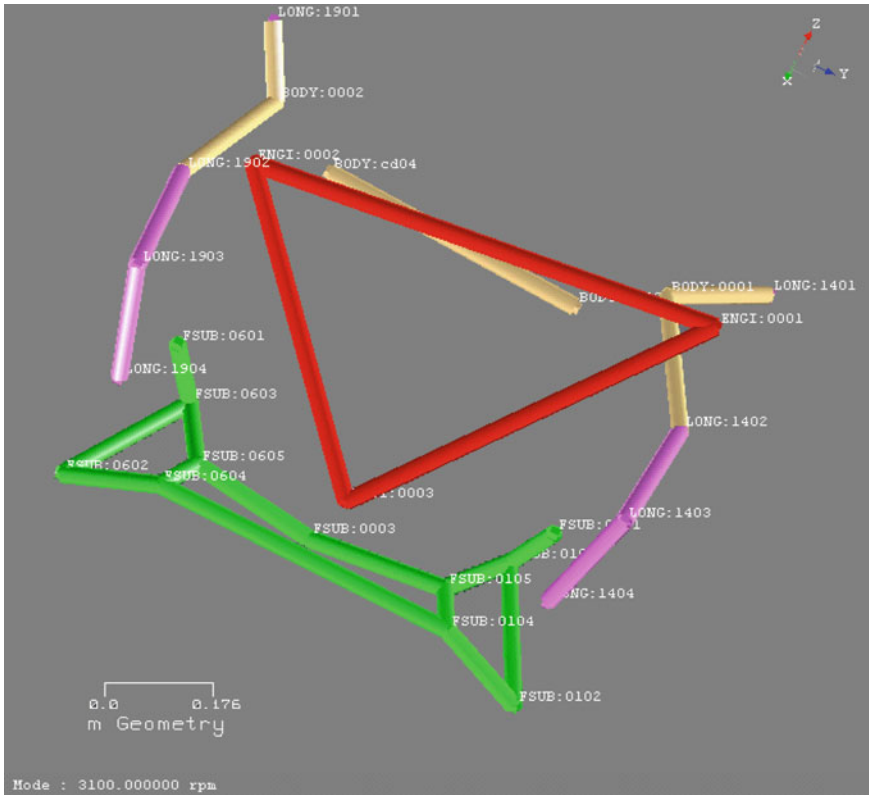


Fig. 6 Deformation drawing to right support carling ($f = 103$ Hz)

increase the right carling stiffness through increasing right carling reinforced plate or right carling thickness. In addition, the different order and frequency radiator beam normal modes are shown in Fig. 7, and it can be seen obviously that frequency vibration is so serious with the inadequate stiffness of radiator crossbeam.

The mounting installation point dynamic stiffness analysis results of modified vehicle right carling are shown in Fig. 8. The reference curve value is 5,000 N/mm, and presents a parabola changed tendency. The Y and Z dynamic stiffness curve fluctuates up and down along the reference curve, and there is a peak value in 100 Hz. The peak value is mainly caused by the larger carling Y and Z bending vibration referring to experimental result (Figs. 1 and 2). In addition, there are some peak values in 28, 36, 46, 5 and 68 Hz of dynamic stiffness curve, respectively. The main reason comes from engine overall and partial mode.

According to above analysis, it is due to the radiator crossbeam stiffness and its connection structure stiffness with surrounding parts are weak so that Y and Z direction bending vibration of right carling are serious in 99.5 Hz. There is a big

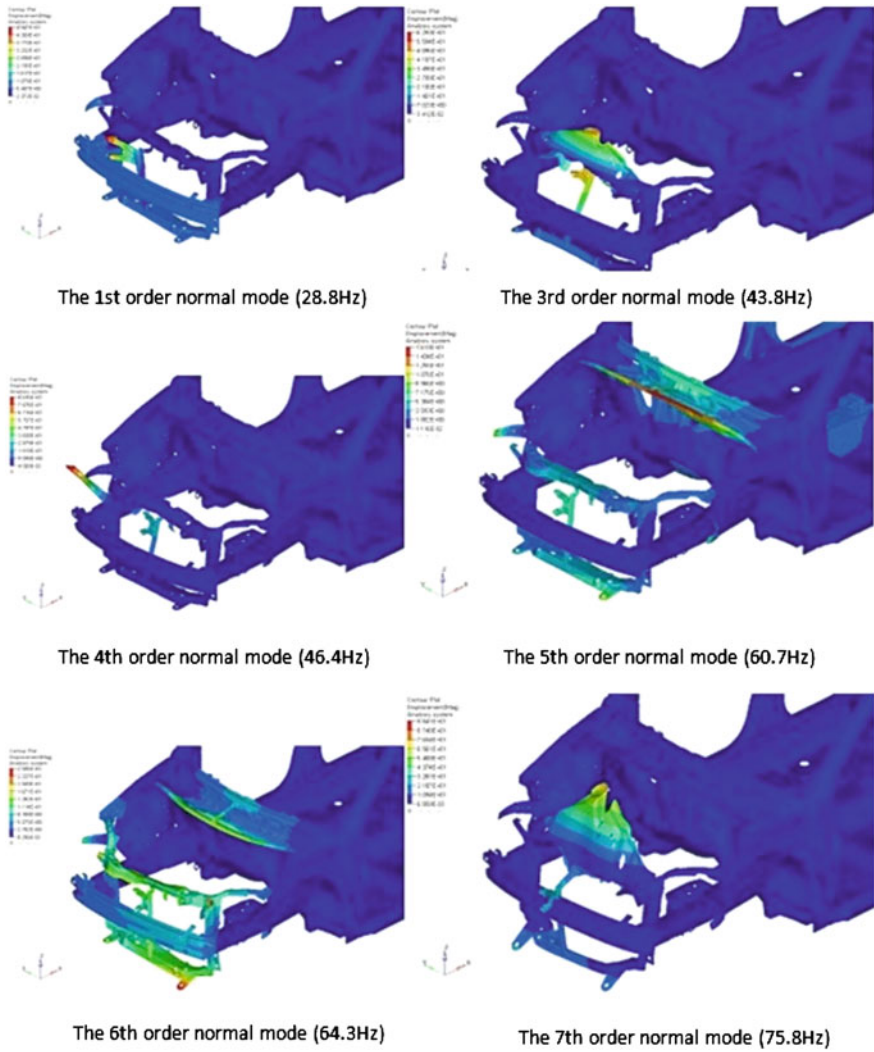


Fig. 7 Radiator crossbeam modal frequency vibration mode

peak value in 100 Hz on the right mounting installation points dynamic stiffness response curve (Fig. 8). The result is close the test result that there is a peak value in 103 Hz. So this is the main reason that modified vehicle can't meet NVH performance requirements. And then to improve the radiator crossbeam stiffness is the main measure to solve the problem.

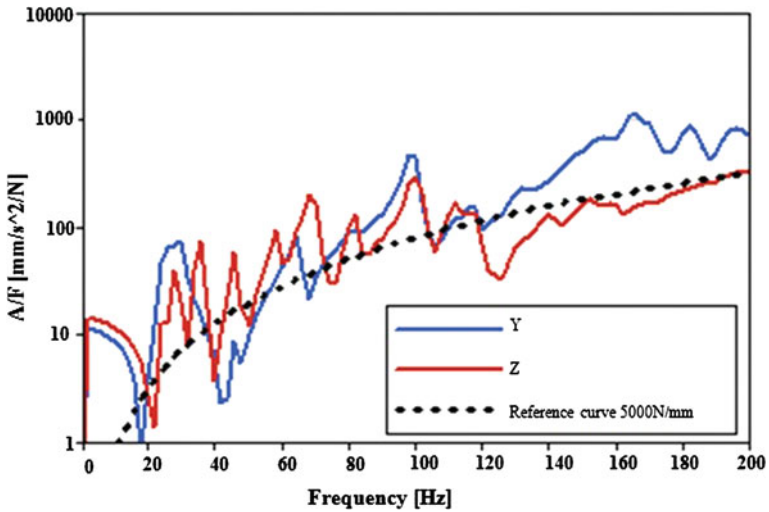


Fig. 8 Y and Z dynamic stiffness curves of modified vehicle right carling

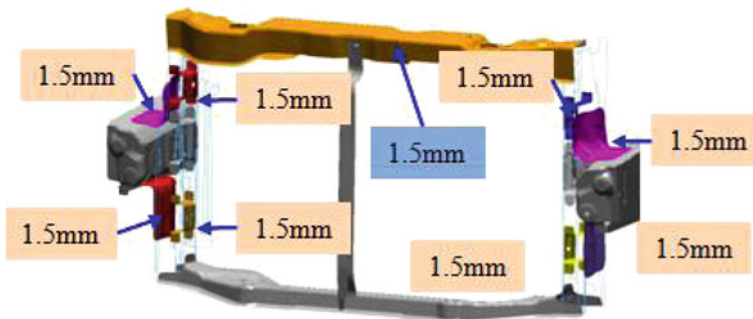


Fig. 9 The first method

4 Optimization Design

4.1 Optimization Methods

Based on the previous reason analysis, it takes three methods to analyze and improve the radiator crossbeam stiffness. The first method is shown in Fig. 9. It can be seen that the thickness of radiator upper crossbeam increases from 0.8 to 15.mm, and at the same time, increasing 8 reinforcing plate on the radiator pillar to halve on the left and right. The thickness of reinforced plate is all 1.5 mm.

As shown in Fig. 10, it is the second method. The Fig. 10 shows that it increases 1.5 mm radiator upper crossbeam inner reinforced plate with keeping radiator upper crossbeam outer plate thickness. Equal to the first method,

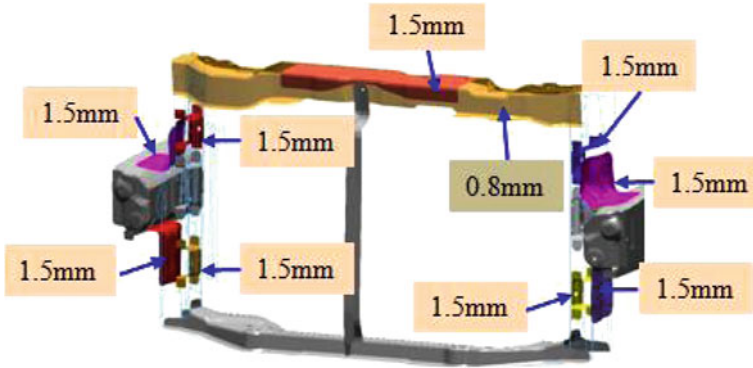


Fig. 10 The second method

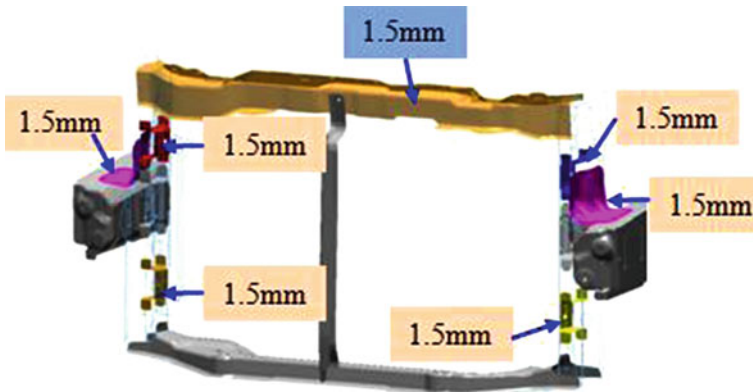


Fig. 11 The third method

the second method also increases 8 reinforced plates on radiator pillar to halve on the left and right.

The third method, as shown in Fig. 11, that it increases radiator upper cross-beam in thickness from 0.8 to 1.5 mm, and at the same time increases 6 reinforced plates on radiator pillar to halve on the left and right.

4.2 Contrast Analysis to CAE Results

Figure 12 is the Y direction dynamic stiffness contrastive curve graph between three optimized methods and original method. It can be seen from Fig. 12 that the improved dynamic stiffness performances of the first method and the second method are more evident comparing to the third method in 100 Hz.

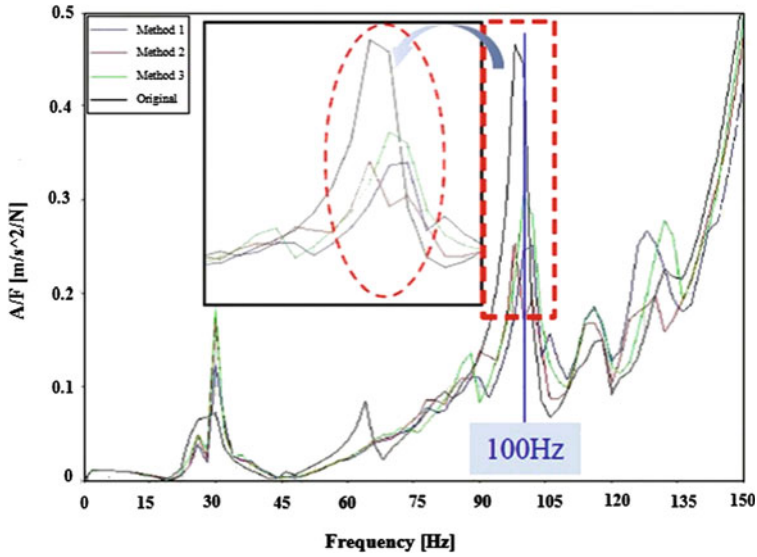


Fig. 12 Y to dynamic stiffness analysis result contrastive curve graph

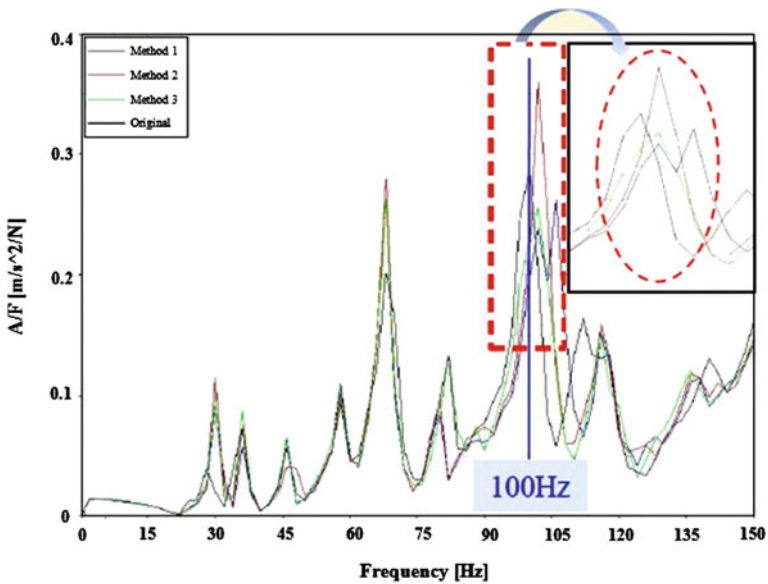


Fig. 13 Z to dynamic stiffness analysis result contrastive curve graph

Figure 13 is the Z direction dynamic stiffness contrastive curve graph between three optimized methods and original method. It can be seen from Fig. 13 that the improvement dynamic stiffness performances of the first method and the third method are more evident comparing to the second method in 100 Hz.

Fig. 14 The improved fore-and-aft peak value contrastive diagram

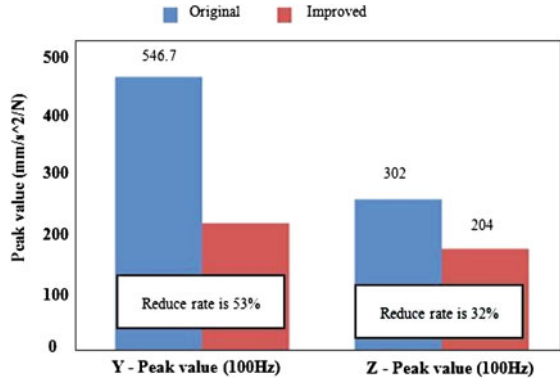


Fig. 15 The test working condition and sensor position schemes



Through the above contrastive analysis results of three methods, it can be seen that the first method, increasing the thickness of radiator upper crossbeam, and 8 radiator pillar reinforced plates, can significantly reduce Y and Z to dynamic stiffness value in 100 Hz.

4.3 Validate to NVH Results

Figure 14 is Y and Z to dynamic stiffness contrastive diagram of the original and first method, as can be seen from the Y to dynamic stiffness peak by 546.7 mm/s² decreased to 254.3 mm/s², and the reduced rate is 53 %; Z to dynamic stiffness peak by 302 mm/s² reduced to 204 mm/s², the reduced ratio is 32 %. This shows that the improved effect is obvious. In addition, in the range of former 200 Hz, the improved fore-and-aft Y to equivalent dynamic stiffness respectively for 2,522 and 2,937 N/mm, it relatively increases about 14 %. Z to equivalent dynamic stiffness

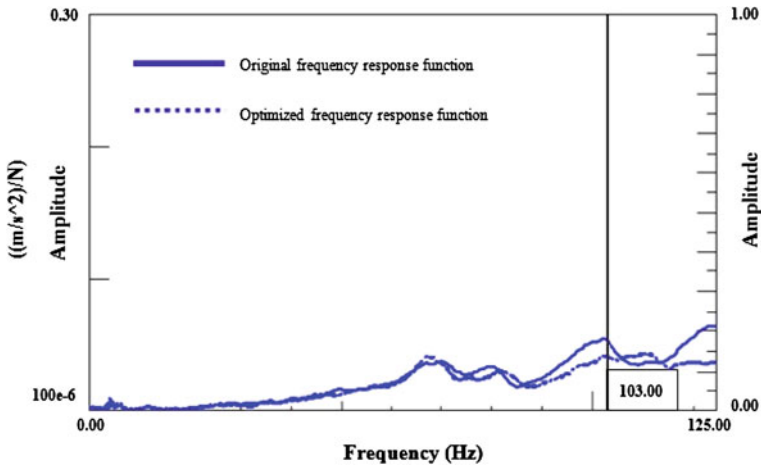


Fig. 16 The contrastive curve of X frequency and response function on right mounting and body connected point

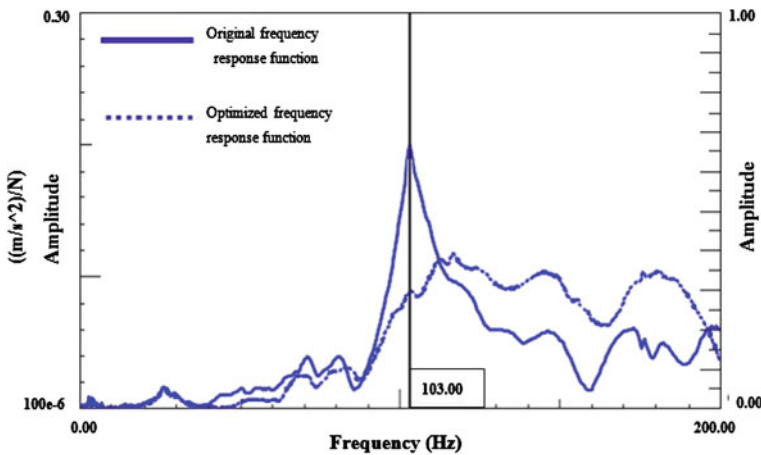


Fig. 17 The contrastive curve of Y frequency and response function on right mounting and body connected point

respectively for 5,049 and 5,074 N/mm, the overall rigidity level has a slightly better, and the whole dynamic characteristics gets improvement.

Figure 15 is the real car test working condition and the sensor position schemes. It makes modal force hammer to incentive the connected point between right engine mounting and body in the chart, the test results as shown in Figs. 16, 17 and 18. It can be seen from the graph that the peak value in 103 Hz eliminates on the connected point between right engine mounts and body. Therefore, the optimized method can improve modified vehicle right carling NVH performance.

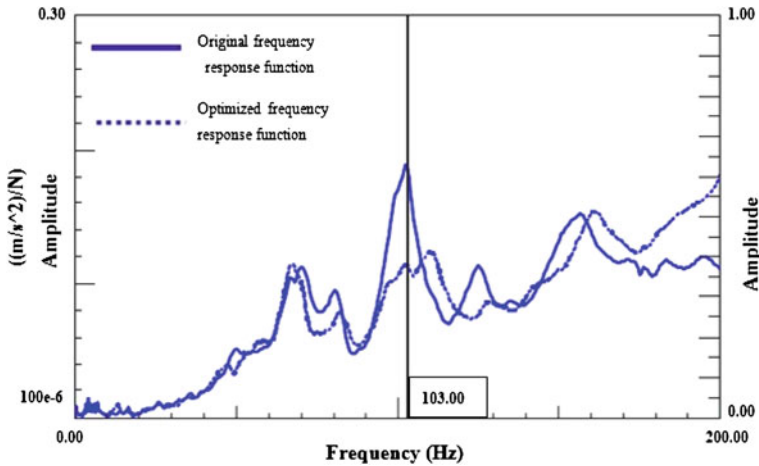


Fig. 18 The contrastive curve of Z frequency and response function on right mounting and body connected point

5 Conclusions

To sum up, through the original vehicle NVH test to provide the direction for the modified vehicle problems, and analyze the reasons, optimize the methods, it draws the following conclusions:

1. Through the original vehicle NVH test, the results shows that it can't meet the vehicle NVH performance requirements, due to the vibration and noise produced by the inadequate stiffness of original vehicle right carling. Aiming at this issue, it performs the reasons analysis, and obtains that the radiator frame stiffness has obvious effect on right carling stiffness, and improving the radiator frame stiffness, it can increase the right carling stiffness, and solve the vehicle NVH performance.
2. Through the three methods optimized design comparison and analysis to the radiator frame, it can draw the first method that increasing radiator upper crossbeam thickness and radiator pillar reinforced plate can solve right carling stiffness problem, and at the same time, the real car NVH verification results show that the method meets vehicle NVH performance requirements.

Based on the original vehicle carling stiffness shortage problem in this article, through the indirect method to improve the carling stiffness, it avoids the direct method that affecting the original model production. For the indirect method, it ensures the original vehicle carling general application, but also provides an effectively design ideas for future vehicles within each platform general lending, improvement.

References

1. Zhang S, Zhang Y, Dai Y (2010) Study on dynamic stiffness analysis of body attachment for NVH performance improvements. *Automobile Technol* 10:26–29
2. Liu C (2008) Car body modal analysis based on noise, vibration, harshness (NVH). *J Fujian Univ Technol* 6(s0):69–71
3. Wang D, Li C, Yao H (2008) Study of car's NVH performance based on finite element analysis of car-body. *Mach Electron* 9:3–6
4. Yang B, Zhu P, Y H (2008) Auto-body NVH structure sensitivity analysis based on modal analysis method. *Chin Mech Eng* 19(3):361–364
5. Chen Y, Yuan H, Chen J (2007) Study on modal and its effect on interior noise in body-in-white of SRV. *Automobile Technol* 5:27–29
6. Yin K, Song X (2011) Analysis of improvement of a bus for suppressing its abnormal vibration and noise. *Noise Vib Control* 4:102–105
7. Yue K (2006) Vibration and noise analysis of vehicle NVH characteristic. *Chin Sci Technol Inform* 23:68–69
8. Guo R, Wan G, Zhao Y (2007) Study on transfer path analysis method of automobile interior noise. *J Vib, Meas Diagn* 27(3):199–203
9. Chen Y, Liu C (2008) Study and analysis on the car body NVH characteristic. *J Guangxi Univ Technol* 19(4):5–9
10. Huang Z, Wang Y (2011) Improving vehicle NVH performance—a new problem encountered by automobile industry. *New Technol New Process* 7:73–77

Mechanism of Vibration Noise Transfer of Trimmed Body

Huimin Zhuang, Shuo Zhang, Xiaofeng Qu and Ye Zhang

Abstract Structure born noise and air born noise are two basic noise sources of a vehicle. Structure born noise, which is mainly determined by the body structure, takes an important role in NVH performance of a vehicle. The mechanism of structure born noise is that the vibration coming from external excitation force (engine, road etc.) is transferred to body by structure parts, and then arose the body vibration. The objective of this chapter is to explore the mechanism of vibration and noise transfer of a trimmed body, introduce the factors that influence the noise transfer function (NTF), and take two examples to explore the methods and give a guidance to reduce noise transfer function (NTF) of a body.

Keywords NTF · Structure born noise · Noise transfer function · Air born noise · NVH

1 Foreword

As the rapid development of vehicle industry, the performance can not reach our requirement at present. It seems more importance to research the vibration and noise to improve the driver and passenger's comfortable feeling. In CAE analysis,

F2012-J04-006

H. Zhuang (✉) · S. Zhang · X. Qu · Y. Zhang
CAE and Vehicle Performance Department, Beijing Automotive Technology Center,
Beijing, China
e-mail: zhuanghuimin@beijing-atc.com.cn

as a specialty subject, the NTF analysis is more perfect. In this chapter, two NTF examples of mechanism and optimization method will be introduced.

2 Mechanism

2.1 NTF Mechanism

During the TB NVH simulation analysis, NTF is one of the important system characteristics. In reality, when frequency is low or mid, the coupling of acoustic mode and body structure vibration are strong, so at that time, the body structure vibration should be considered at acoustic field response analysis, and acoustic mode also is regarded by body structure vibration analysis. That means when the problem is analyzed and calculated, acoustic mode and body structure vibration should be taken as one whole coupling part. The strong coupling of the cavity air with body structure at low frequency comes from the cavity obturation. If compressed, the volume of air will change, and then the air will have a high impedance and will produce strong coupling with body structure vibration. If the body of vehicle has a high response on this situation (low frequency coupling mode), the pulsant pressure will come out, and the passengers will feel uncomfortable.

So by the analysis of NTF, the sound pressure level can be got, and estimating if the unreasonable part which influence on acoustic exists on the body of vehicle, and make the passenger's ear uncomfortable [1].

2.2 Dynamic Stiffness Mechanism

In the mechanism vibration, the definition of dynamic stiffness is the force that can make the structure producing unit amplitude. It expresses the ability that counteracting transmutation under dynamic force. The dynamic stiffness is not a constant, which is the function about frequency, and changed with frequency. For the stiffness of the same structure in different vibration, although the numerical value is the same, depends on body own characteristics, and also during different frequency range, the characteristics have different effects on dynamic stiffness [2].

Generally, during the analysis of TB dynamic stiffness, the input is unit force, the output is acceleration response, and then comparing with the benchmark, to make sure if the local structure is reasonable.

The relationship about acceleration and stiffness is as follows:

$$a = 4\pi^2 f^2 x \quad (1)$$

$$k * x = F \quad (2)$$

a: acceleration, f: frequency, x: displacement; k: local stiffness, F: force;

Table 1 Acoustic mode of considering trim

Fre(Hz)	4	8	16	32	64	128	256	512
Bounce mode	<1> <2> <3>*****							
Lateral mode	<1>*****							
Bounce + Lateral mode	<1,1>*****							
others	*****							

When the force is unit, $F = 1$, and take formula (2) to (1), formula (3) can be got, and then the relationship of acceleration, stiffness, frequency is as follow:

$$a = 4\pi^2 f^2 / k \tag{3}$$

2.3 Acoustic Mode Analysis Mechanism

The vehicle inner space is a close cavity that made of body structure sheet, and full of air. And such as any other system, it has mode frequency and mode shape, that's acoustic mode. The character of acoustic mode is sound pressure distribution, not displacement distribution such as other systems. Acoustic mode frequency is the acoustic resonance frequency. At this frequency, the inner cavity produce acoustic resonance, and enlarge sound pressure. When the sound wave transfer in the interior at one frequency, the incident wave will be reinforced or weakened by the reflected wave of cavity boundary, and then come out different sound pressure at different location, that's we called acoustic mode shape.

The acoustic characteristic of driver's room has large relation with other acoustic mode characteristics. If the cavity of driver's room is excited by a force that has the same frequency, such as some low frequency vibration of body sheet, the driver's room will come out acoustic resonance, and low booming noise that make people uncomfortable. So by using the FEM, the acoustic mode frequency and mode shape can be gained, and it can supply a guidance for the body design, and also the result can be used in frequency response analysis.

The volume of acoustic mode will change a lot in low frequency, mode movement will compress the air and come out high sound pressure.

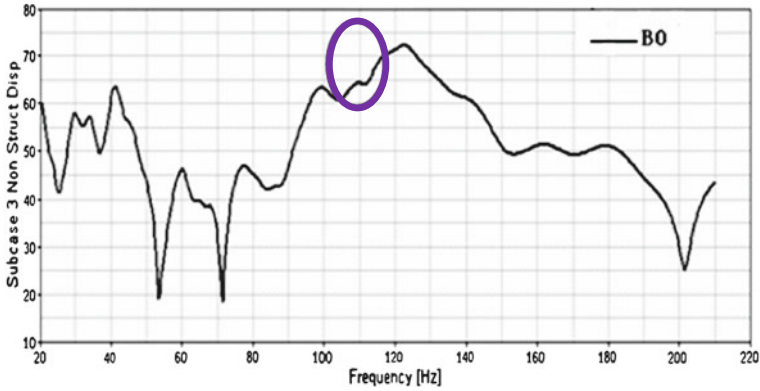


Fig. 1 Driver's ear sound pressure

Table 1 shows a mode frequency distribution of acoustic mode considering interior trim.

3 Methodology and Results

The definition of NTF is the sound pressure of driver/passenger's ear under unit force. The following transfer path is carefully examined: excitation → structure vibration transfer → panel vibration → volume velocity change of adjacent air → air noise transfer → noise around passenger's ears. The effects of the following factors on NTF are addressed: the dynamic stiffness and resonance of excitation points and panels, and acoustic modes, etc.

The following two examples will be introduced the methods which improve the NTF result.

3.1 Dynamic Stiffness

Based on the transfer path of NTF, if the dynamic stiffness of excited node can be improved, that will effectively reduce the vibration that transfer to the system, and then reduce the sound pressure to people's ear.

In this example, the force input node is front mount, and the NTF of driver is more than 70 dB at 122.5 Hz, worse than the target, so we need to modify the structure to improve the NTF peak (Fig. 1).

The Fig. 2 shows that the acceleration has a peak between 90 to 130 Hz, and over the target; And acoustic mode has a second order mode around 116 Hz. Then through evaluation the reason of the NTF peak at 122 Hz is the coupling of the

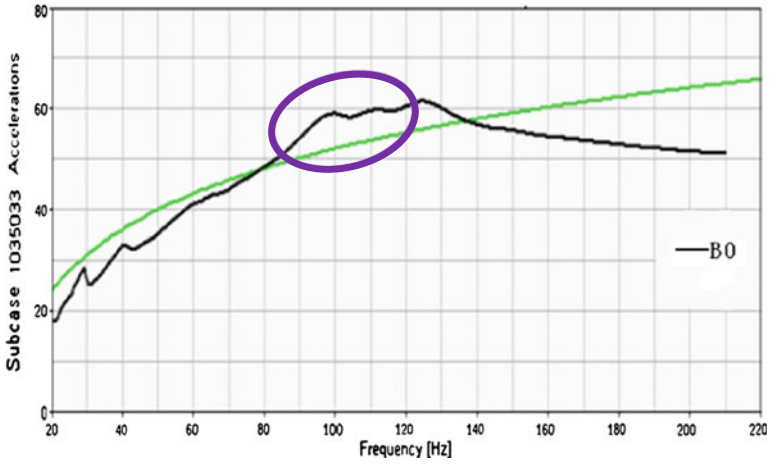


Fig. 2 Front mount Z acceleration curve

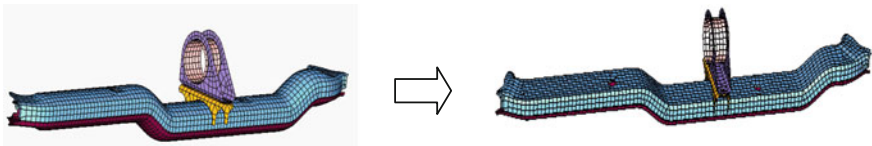


Fig. 3 Front mount structure

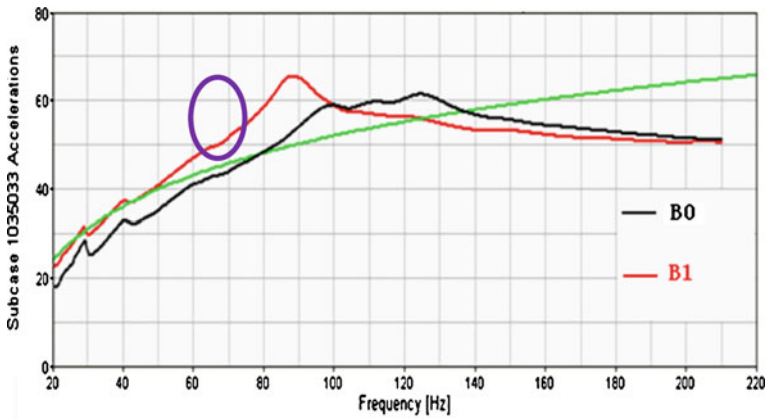


Fig. 4 Front mount Z acceleration curve

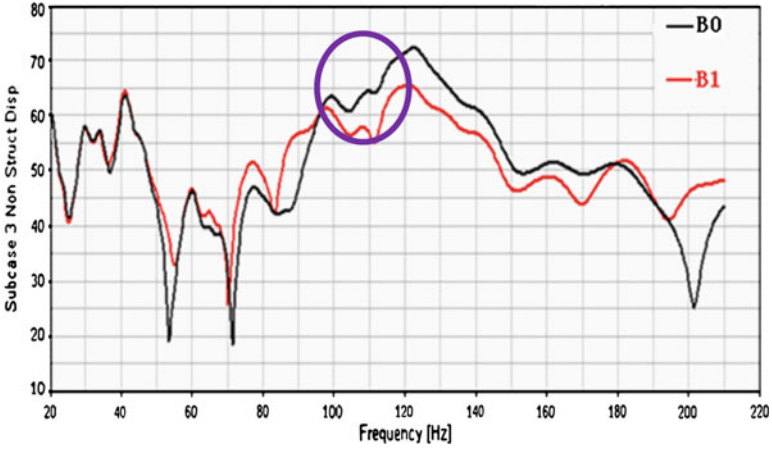


Fig. 5 Driver's ear sound pressure

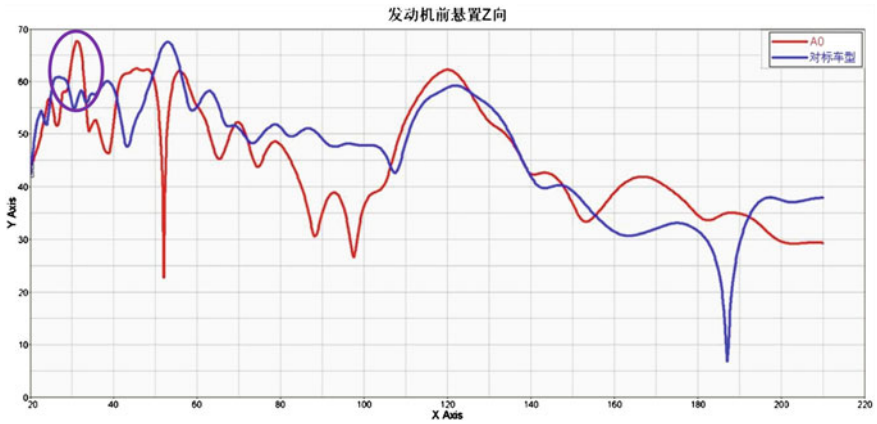


Fig. 6 Driver's ear sound pressure

dynamic stiffness and the second order acoustic mode. So next step the peak frequency of front mount dynamic stiffness will be changed, and decoupled with the second order acoustic mode.

By some optimization, the final structure can be got, just like Fig. 3.

Using the new model, the dynamic stiffness can be calculated, the peak of the acceleration has been changed to 88 Hz, which has missed with second order acoustic mode at 116 Hz Fig. 4.

And then, the NTF should be calculated using new model, the result is as follow (Fig. 5), the NTF has improved from 72.1 to 65.2 dB, decreased 6.9 dB. The effect is so much clearly.

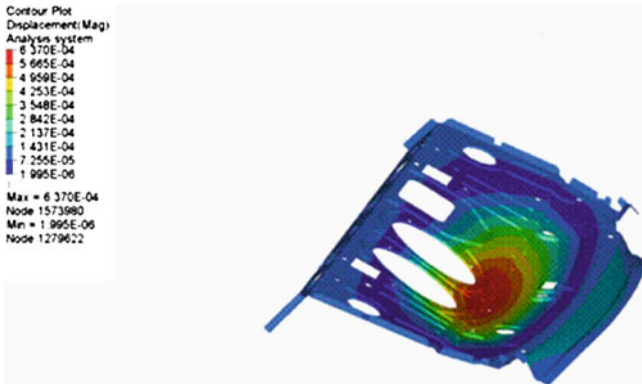


Fig. 7 31.25 Hz running mode

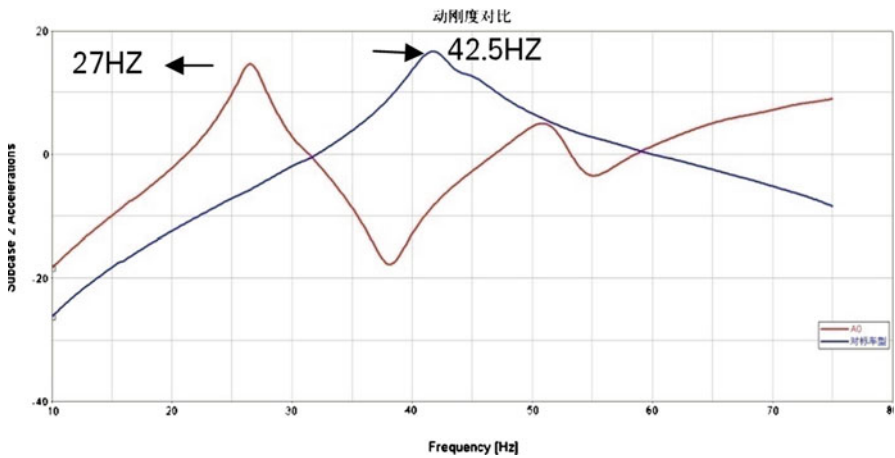


Fig. 8 Parcel shelf acceleration curve

3.2 Panel Response

Based on the theory of NTF transfer path, the sound pressure also can be effectively reduced by controlling the acoustic panel response.

For this example, the problem is that the NTF peak of driver’s ear is worse than benchmark when excited at front mount Z direction at 31.25 Hz (Fig. 6).

Through Fig. 6, comparing with the benchmark vehicle, the sound pressure of the design vehicle A0 is 67.6 dB, 7 dB worse. So the problem should be solved.

Firstly, according to the analysis of panel contribution, the parcel shelf is the most contribution panel to this problem. And then the running mode of A0 at

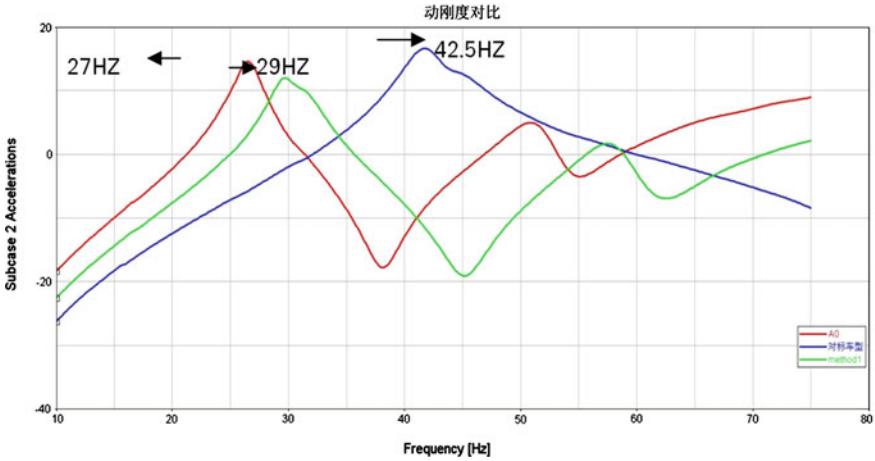


Fig. 9 Parcel shelf acceleration curve

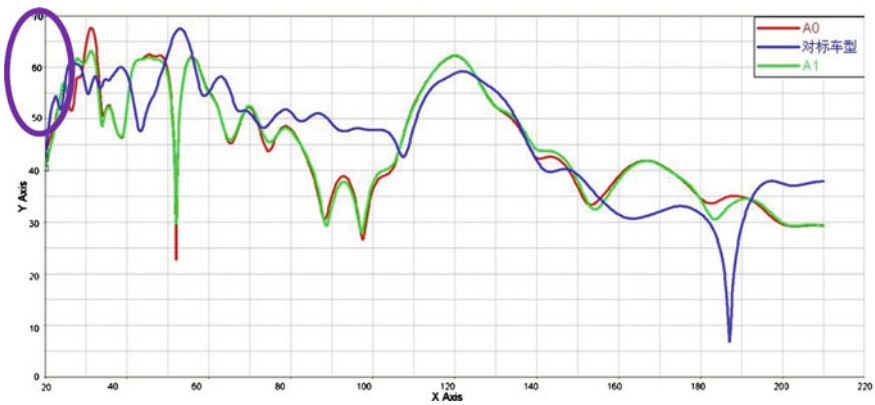


Fig. 10 Driver's ear sound pressure

31.25 Hz has been calculated, like Fig. 7. From the result, the parcel shelf has large displacement at 31.25 Hz.

One node on parcel shelf was picked to calculate the panel response (Fig. 8). From this Figure, it shows that the stiffness of A0 is worse than benchmark, and the peak comes out at 27 Hz. So the conclusion is that the stiffness of parcel shelf is weak, and then produce large displacement, then at last make the NTF peak worse.

Until now, the reason for this NTF problem can be confirmed. Then a new structure which can improve the stiffness must be found out. Finally, a method which make the stiffness peak improve from 27 to 29 Hz was found, (Fig. 9), and through this method the NTF peak was reduced by 4.4 dB (Fig. 10).

4 Limitations and Future Potential Researches

This study is limited to a TB model and finite element analysis by using a simplified model of a trimmed body. For further study, the guidance of NTF reduction need to be illustrated by actual examples, for example, the forced response analysis, which will be given in the accompanying paper. Moreover, the experimental verification need be carried out.

5 Conclusions

The chapter summarizes the effects of the following factors on NTF: the dynamic stiffness and resonance of excitation points, the panels, and acoustic modes, etc. and a guidance to reduce NTF is presented. This is expected to significantly contribute to the design of the car body with excellent NVH performance.

References

1. Pang J, Zhan G, He H (2006) Vehicle noise and vibration: mechanism and applications. Beijing institute of technology, 200606, ISBN 978-7-5640-0749-2
2. Xu X, Wang X, Guo J (2009) The applications research of dynamic stiffness on the design of vehicle body, Altair hyperworks pp: 257–260

Automotive Concept Modelling: Optimization of the Vehicle NVH Performance

Naser Nasrolahzadeh, Mohammad Fard, Milad Tatari
and Mohammad Mahjoob

Abstract The NVH optimization of the BIW and seat structure in the advanced phase of the design demands too much time and cost. On the other hand, developing a reliable NVH concept model in the earliest stage of the design to improve dynamic behaviour of the structure and avoid conflicting designs might be an effective approach. To this end, a practical method for CAE-NVH concept modelling is developed. The developed model utilizes beam elements with standard and arbitrary cross sections for the main load carrying components (namely beam-like structures) of the BIW and seat structure. Also, major joints are approximated from the detailed CAE model by taking static model reduction method into account. Due to the indisputable effects of some panels (e.g., roof) on the BIW structural dynamics characteristics, shell element with rough meshing are exploited to model these components. The developed concept models are verified by comparing their resonant frequencies and mode shapes with counterpart advanced CAE models in low frequency range. Having been validated by dynamic domain indicators, the developed concept model is used to improve the NVH performance of the automotive. In one case, modes interaction between BIW and seat structure is characterized. Then, by examining the influence of the beams properties (both BIW and seat) in conflicting modes, the problem is managed. Having been separated the identified interacting modes, the amplitude of the vibration on the seat-back is

F2012-J04-008

N. Nasrolahzadeh (✉) · M. Tatari · M. Mahjoob
School of Mechanical Engineering, College of Engineering,
University of Tehran, Tehran, Iran
e-mail: n.nasrlh@gmail.com

M. Fard
School of Aerospace, Mechanical and Manufacturing Engineering,
RMIT University, Melbourne, Australia

suppressed about 10 db around corresponding frequency. As a result, by taking advantages of the proposed method in similar cases, the CAE-NVH concept model can be successfully used to lead the right first time design.

Keywords Advanced CAE model · Concept modelling · Modes management · NVH performance · Vibration suppression

1 Introduction

The present highly competitive automobile market demands for cost effective new vehicles with short time to market periods. It is therefore crucial to predict and improve the car performance in various conflicting areas such as NVH and safety in the earliest stage of design. Despite the fact that automotive advanced CAE model is developed by detailed and accurate geometry data, concept model can be created in early design phase where there is no enough detailed and constrained design data. The primary objective of the concept modelling is to investigate the functional performances of the new vehicle such as the structure stiffness and global modes. Furthermore, In order to achieve appropriate results for NVH performance, one needs a fairly simple but reliable concept model to answer lots of what-if questions in a short time to find the best set of component design for developing the new vehicle.

There are totally two distinct areas in concept modelling. The first one that is called from scratch approach is used when the aim of the design is to develop a completely brand new structure for the vehicle. In other words, in this case there is no predecessor FE model and just the outfit style of the new model is available; therefore the designers have to start from scratch to develop the new platform and cabin structure. On the other hand, the second class of the concept modelling is those methods, when the new model is going to be developed on base of an earlier model platform. In these methodologies the predecessor FE model is smartly exploited in order to create the concept model. The first branch of concept modelling includes methods with the purpose of the Topology Design Optimization [1– 3] and the Functional Layout Design [1, 4]. In the latter class, however, the main objective is the improvement of a few functional performances in the previous model. Up until now, in the second class of concept modelling, based on predecessor FE models, there are not practical enough studies. Fard [5] and Sung and Nefske [6] conducted concept modelling only by using beam elements, but the major issue of both works is that they do not have a definite approach to estimate beam properties of the main load carrying components. Lee et al. [7] used beam elements to create the concept model and also the presented method compensates the joints unrealistic stiffness by an optimization measure. Mundo and Donders [8, 9] proposed a concept modelling methodology, in which beam-like structures and joints are replaced by standard beam profiles and concept joints that are extracted from the predecessor FE model. Mundo et al. [10] considered concept

panels by mesh morphing approach. The latter is not developed for full automotive BIW and restricted by static analysis though. The CAE concept modelling method of the automotive body is still an attractive research area for the automotive CAE investigators, because the industry demands for the fast and robust methods to achieve the goal “Analysis Leads Design”.

Due to the fact that the vibration of the structure is thoroughly connected to its dynamic characteristics including natural frequencies and mode shapes, characterization of these features is an important stage for the NVH performance optimization. Taking advantages of a reliable NVH concept model, the structural dynamics of the new products can be analyzed and thus there is the capability to extract a rough dynamic response from the structure in the first step of the process. Consequently, the new product flaws can be identified and managed in the early design phase and leads to approximately right first design. For example, one of the most challenging issues in NVH performance of the vehicle is avoiding modes interaction between BIW and other component which are assembled on. In the industry, usually these kinds of problem are identified in advanced phase of the development process. Therefore, as various restrictions are imposed for any remarkable change in the structure when CAD data has been frozen, extra cost demanding measures such as using a dynamic damper are taken to handle the problem; nevertheless, mode management can be efficiently achieved by the CAE-NVH concept model. Since each run of the concept model is completed very fast, many modification and/or optimization can be accomplished in a short period of time. In fact, it is indisputable that any modification in concept phase of the design can help to reduce extra costs, shorten the vehicle development and time to market process.

In order to analyze and mitigate the vibration transmission to the occupant, one has to consider both BIW and seat structure. A major portion of the vibrations experienced by the occupants of an automobile enters the body from the seat path [11]. In fact, all vibration sources in the vehicle such as road disturbances, power train unbalances, etc. induce their undesired effects through the seat structure. While several studies in the literature [12–14] have been reported in view of considering the seat and automotive cabin as a rigid structures, there is a few, if any, research about optimization of the BIW and seat structure to control the seat vibration. In other words, studies regarding seat vibration did not take BIW and seat structural dynamics into account; however, improvement of BIW and seat dynamic characteristics may have a great influence on vibration transmission to the occupant. A few earlier studies [5, 15] have reported the interaction between the seat torsional mode and BIW global modes. This phenomenon may magnify the vibration level that is experienced by the occupants and can be controlled by optimization of the structures and separating tuned modes. This is worth mentioning that the in order to shift fundamental modes of the structure, usually, remarkable changes are required; so that just in concept phase of the design this optimization sounds practical and can be implemented. As a result, to predict and handle this issue, it is inevitable to develop a consistent concept model for the vehicle body and seat.

In this paper, a practical method for CAE-NVH concept modelling is developed. The BIW and seat are modelled using concept beams, joints and panels. Having been validated by dynamic domain indicators, the developed concept model is used to improve the NVH performance of the automotive when modes interaction exists. Modelling the structure with simple elements allows quickly probing the influence of the basic components such as BIW main members, pillars and also seat-back frame, in the dynamic behaviour of the vehicle in low frequency range and search for the practical improvements. Therefore, by using the sensitivity of the beams properties in conflicting modes, the modes are detuned and problem is managed. Finally, the conspicuous findings of the conducted work are presented in a few conclusions.

2 Method

2.1 Concept Modelling

In order to create a concept model, the first step is to decide about the layout and functional components of the structure. Generally, in concept modelling three major parts should be simplified and modelled. The most primary parts are beam like structures or main members that define the frame body of the vehicle. Joints are in secondary order of importance and they connect beam like structure to each other. Panels are other major components that perfect the layout of the structure.

Beam like components are those members that have small cross-section in comparison with their lengths. Main members of the BIW such as doorsill, pillars and the frame of seat structure are modelled using beam elements. Since the shape of the cross sections are considered similar to the corresponding sections at the physical model, therefore, calculated properties of the beam elements such as bending and torsional moments of inertia reflects good approximation in accordance with real members. It is worth mentioning that this just can be achieved when arbitrary cross section (e.g., PBRSECT in Nastran [16]) are utilized for complex cross sections such as BIW pillars along with standard beam library (Box, Tube, etc.) for simple cross section components like back-rest of the seat structure.

In NVH concept modelling, preparing the concept joints is a crucial issue. Usually, model reduction methods (static or dynamic) are exploited to reduce the FE model computation time and cost. According to the characteristics of the model and analysis requirements, an appropriate model reduction method [17] such as Guyan, CMS, SEREP, etc. has to be selected. Then the large FE model is condensed in a few degrees of freedom by the method specified transformation matrix (T_c) according to Eqs. (1–3); where subscripts A is representative of all DOFs, subscripts i stands for the DOFs that are going to be omitted and subscripts b are those that will be kept after model reduction. Since the concept joints connect the concept beam like structures (1D beam elements) to each other in their terminal

nodes, the detailed joints are condensed into a reduced description of the stiffness and mass matrices at the boundary nodes.

$$\{x_A\} = \begin{Bmatrix} x_i \\ x_b \end{Bmatrix} = [T_{Condensation}]\{x_b\} \quad (1)$$

$$[K_C] = [T_C]^T [K_A] [T_C] \quad (2)$$

$$[M_C] = [T_C]^T [M_A] [T_C] \quad (3)$$

Here, both Guyan [18] and CMS¹ [19] model reduction are tested for reducing and generating concept joints; the results for both have a little discrepancy in low frequency range. Therefore, as the aim of the concept modelling is focusing in global modes of the structure, that are usually below 100 Hz, Guyan method is used to prepare concept joints. Neglecting the inertia effects in calculating reduced model, Guyan method is also called static condensation. Equation (4) is the general form of the static finite element model, in which the internal and boundary DOFs are reordered to make the calculation process straightforward. Then by a little manipulation on block rows of this equation [17], the Guyan condensation matrix (T_G) can be extracted according to Eq. 5.

$$\begin{bmatrix} K_{ii} & K_{ib} \\ K_{bi} & K_{bb} \end{bmatrix} \begin{Bmatrix} x_i \\ x_b \end{Bmatrix} = \begin{Bmatrix} F_i \\ F_b \end{Bmatrix} \quad (4)$$

$$[T_G] = \begin{bmatrix} [-K_{ii}^{-1}K_{ib}] \\ [I_{bb}] \end{bmatrix} \quad (5)$$

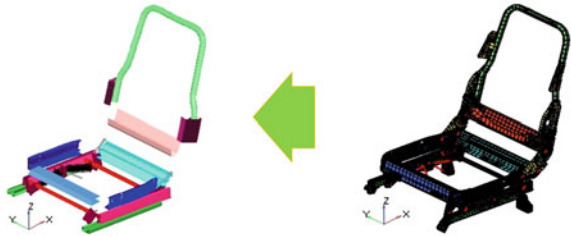
Concept model of panels are created using rough shell elements. Although it is not required to involve all panels of the BIW in the concept modelling, a few effective panels are identified to have significant role in BIW global modes. Roof, platform tunnel, windshield and rear glass are those that dramatically affect the stiffness and mass distribution of the BIW. In the developed NVH concept model, these panels are simplified and modelled by coarse 2D elements (e.g., CQUAD4 and CTRIA3 in Nastran [16]) such that the shape of the panel are kept as similar as possible to the physical model and available CAD data. In addition, it is important to note that these panels are linked to the beam like structure by simple connector elements (e.g., RBE2 and RBE3 in Nastran [16]) to avoid increasing local stiffness of the interface regions. Having performed the presented process, the CAE-NVH concept model of the BIW and seat are developed. The advanced and concept model of the BIW and seat structure are illustrated in Figs. 1 and 2 respectively.

¹ Component mode synthesis.



Fig. 1 Advanced and concept CAE models of the BIW

Fig. 2 Advanced and concept CAE models of the seat structure



2.2 Experimental Test

Experimental modal analysis is utilized to characterize the structural resonant frequencies and their corresponding mode shapes [19]. In order to excite and extract the response of the BIW and seat an electromagnetic shaker and a number of accelerometers are used. The other equipment of the conducted modal test consisted of the LMS testing system (hardware and software for DAQ), force transducer and power amplifier. In addition, air cushions are used to provide Free–Free boundary condition for the BIW; also the seat structure was suspended by elastic ropes to allow the seat system to be nearly free in six axes. The accelerometers are mounted in various locations to clearly reflect the harmonic motion of the structure in desired mode shapes (low frequency range). The test setup for the BIW and seat modal test is depicted in Fig. 3.

3 Model Validation

Due to the fact that the developed concept model is going to be used for NVH performance improvement, so that it is firstly required to be validated in dynamic domain. To this end, the natural frequency and corresponding mode shapes of the developed concept model are compared with the results of the advanced CAE model as well as conducted experimental modal tests. The error percentage ($\Delta \%$) between corresponding resonant frequency and Modal Assurance Criterion (MAC) [19] of the similar mode shapes are used to show the accuracy of the developed model. Here, at first, the concept model of the seat is verified and the results are



Fig. 3 Experimental set up for BIW and seat modal testing

reported in Table 1. Then the seat is assembled to the BIW and the comparison is performed for the combined BIW-seat structure and results are presented in Table 2 (Fig. 4).

Also, knowing that the advanced CAE model has been completely correlated with the physical model, the Δ and MAC is calculated for advanced and concept CAE models. For example, the second mode of the seat (fore-aft motion) and the fifth mode of the combined BIW-seat (BIW torsion) are illustrated for concept, advanced and physical models in Figs. 5 and 6 respectively. It is worthwhile to note that the key nodes of the structures are used for Eigen-Vectors comparison. These nodes are selected in various main locations of the models in a way that the desired mode shapes can be perfectly distinguished (e.g., 50 nodes for the BIW and 10 nodes for the seat)

According to the presented results in Tables 1 and 2, one can infer that the concept models have a satisfactory accuracy to predict desired dynamic characteristics of the seat only ($MAC > 0.9$ and $\Delta < 5\%$) and combined BIW-seat structures ($MAC > 0.8$ and $\Delta < 5\%$). Therefore, the developed model can be reliably used for NVH performance improvement.

4 Optimization of the Vehicle NVH Performance

By a consistent and correlate concept model in hand, examining numerous design ideas can be accomplished in a short time. Despite the time consuming process to scrutinize the result after a change in advance CAE model, one of the most important benefits of the concept modelling is that the analysis results can be extracted in a few minutes. In addition, modelling the structure with simple elements allows quickly probing the influence of the basic components such as BIW main members, pillars and also seat-back frame, in the dynamic behaviour of the vehicle in low frequency range.

Table 1 Comparison of the resonant frequencies and mode shapes for the concept model, advanced model and experimental test of the seat only structure

No.of mode	Mode shapes nature	Resonant frequencies			Accuracy	
		Concept CAE	Advanced CAE	Experiment	MAC _{A,C}	$\Delta_{A,C}\%$
1	First torsion	24.75	25.98	26.1	0.99	4.73
2	Fore- aft	56.15	56.97	57.2	0.98	1.43

Table 2 Comparison of the resonant frequencies and mode shapes for the concept model, advanced model and experimental test of the combined BIW- seat structure

No of mode	Mode shapes nature	Resonant frequencies			Accuracy	
		Concept CAE	Advanced CAE	Experiment	MAC _{A,C}	$\Delta_{A,C}\%$
1	Seat lateral (rigid like)	16.83	17.54	17.5	0.88	4.04
2	Seat fore-aft (rigid like)	19.91	20.90	21.0	0.85	4.74
3	BIW floor	34.75	35.48	35.5	0.90	2.06
4	Seat first torsion	39.5	38.9	39.0	0.86	1.54
5	BIW lateral bending (mostly engine compartment)	41.98	41.36	41.5	0.96	1.50
6	BIW roof	45.46	45.75	46.0	0.84	0.63

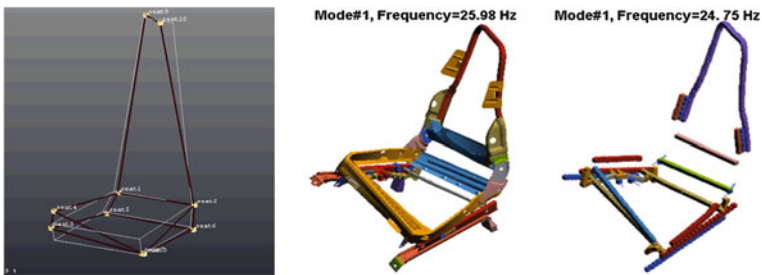


Fig. 4 First torsion of the seat only structure (results from concept model, advanced model and experiment)



Fig. 5 The BIW torsion mode coupled with the seat torsion (results from experiment and concept model)

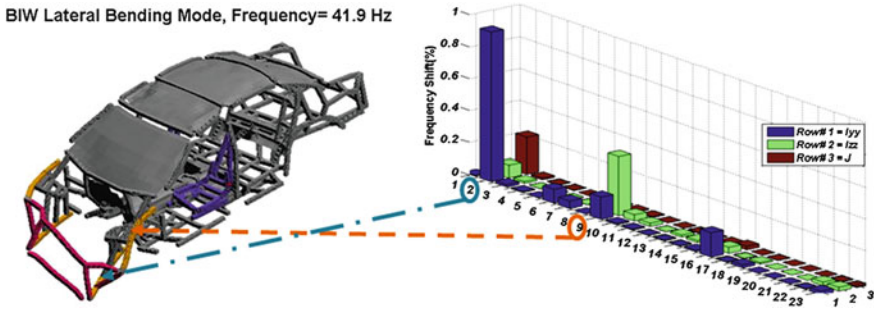


Fig. 6 Results of the sensitivity analysis for properties of the BIW beam components by the objective to shift BIW second structural mode

As it can be observed from Tables 1 and 2, after mounting of the seat to the BIW, the seat-only first torsion resonance frequency (25.9 Hz) has shifted up to around 40 Hz that is near to the BIW second structural mode. This phenomenon may magnify the vibration level that is experienced by the occupants and have to be controlled by optimization of the structures and separating tuned modes. In fact, it is important to solve these sorts of problem in early stage of design because in order to detune structural mode shapes and mode management, sometimes considerable changes in sensitive components are required. In order to find major components in conflicting modes and changing their characteristics for modes separation, sensitivity analysis is conducted. In other words, the effects of beams properties such as area and moments of inertia are investigated. This has done when these parameters are increased by 20 % of their original values; then the influence of changes in shifting the interacting natural frequencies are read and tabled. The results of this analysis for combined BIW-seat structure are presented for BIW and seat components in Fig. 6 and Table 3 respectively.

According to Fig. 6, the most sensitive components of the BIW are the engine compartment main members. These members are very important in crashworthiness of the vehicle. So that, changing their characteristics may affect the safety of the vehicle. On the other hand, by analyzing the result of the Table 3, one can infer that seat component are generally more sensitive, and also modifying their simple beams characteristics are much more practical rather than the BIW complex members. Therefore, the characteristics of the seat sensitive beams (components No. 1, 2 and 7) are modified and the first torsion of the seat is shifted to around 37 Hz, where it is appropriately far away from the BIW lateral bending mode.

In order to probe the impact of modes separation on vibration level suppression, the frequency response function (FRF) of the combined BIW-seat is utilized. The FRF are calculated according to Fig. 7 input-output configuration, when the combined structure is excited in front main member by a vertical force. Also, the acceleration output is considered on the back rest of the seat where seatback vibration is transmitted to the occupant. The FRF graphs in the case of conflicting

Table 3 Results of the sensitivity analysis for the seat components by the objective to shift seat first torsion

J	I ₁₂	I ₂	I ₁	A	Components no.
0.67	0	0.65	0.62	-2.30	1
1.04	0.06	0.14	0.02	-0.19	2
0.01	0	0	0	-0.18	3
0	0	0	0	-0.04	4
0.24	0	0.07	0.04	-0.13	5
0.08	0	0.14	0.03	-0.11	6
0.39	0	0.37	0.37	-0.06	7
0.02	0	00	0	-0.11	8

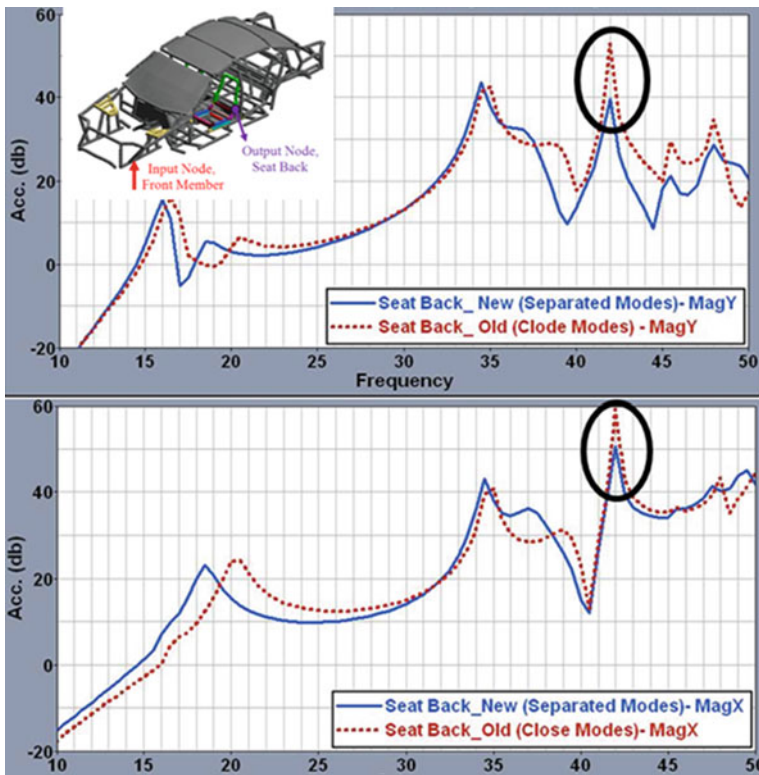
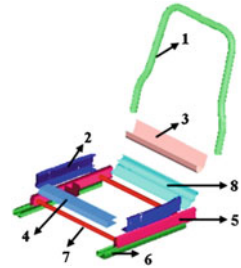


Fig. 7 The influence of modes separation in vibration level suppression on the seat back

and detuned modes are compared in Fig. 7. As it can be observed from the results, management of the interacting modes has caused 10 dB reduction of the vibration in frequency around 41 Hz.

5 Conclusion

A practical method for CAE-NVH concept modelling was presented. The developed model used beam elements with standard and arbitrary cross sections for the beam-like structures of the BIW and seat. In this method, main joints are approximated from the detailed CAE model by reducing their size into boundary nodes. Since the influences of effective panels such as roof and platform tunnel are really vital on the resonant frequencies of the BIW, coarse 2D shell element were utilized to model them. The error percentage ($\Delta\%$) and Modal Assurance Criterion (MAC) of the similar modes between the concept and advanced models are used to examine the validity of the developed models. The created concept models had a satisfactory accuracy to predict desired dynamic characteristics of the seat only (MAC > 0.9 and $\Delta < 5\%$) and combined BIW-seat structures (MAC > 0.8 and $\Delta < 5\%$).

Having been validated by dynamic domain indicators, the developed concept model is used to improve the NVH performance of the automotive. In one case, modes interaction between BIW and seat structure was identified. This phenomenon had magnified the vibration level that is experienced by the occupants and had to be controlled by optimization of the structures. In fact, it is important to solve these problems in concept phase of the design, because in order to separate structural modes, sometimes significant changes in sensitive components are obligatory. Having been examined the influence of the main beams in conflicting modes, the close modes were detuned. The FRF graphs revealed that the management of the interacting modes might decrease the level of vibration up to 10 dB.

By a consistent and correlated concept model in hand, examining various design ideas can be accomplished in a short time. Despite the time consuming process to scrutinize the result after a change in advance CAE model, one of the most important benefits of the concept modelling is that the analysis results can be extracted in a few minutes. As a result, by taking advantages of the proposed method, the CAE-NVH concept model can be successfully used to lead the right first time design.

References

1. Lee S et al (2007) Integrated process for structural-topological configuration design of weight-reduced vehicle components. *Finite Elem Anal Des* 43:620–629
2. Reed C (2002) Applications of optistruct optimization to body in white design. In: *Proceedings of Altair engineering event, Coventry*
3. Wang L et al (2004) Automobile body reinforcement by finite element optimization. *Finite Elem Anal Des* 40:879–893
4. Chapman CB, Pinfold M (2001) The application of a knowledge based engineering approach to the rapid design and analysis of an automotive structure. *Adv Eng Softw* 32:903–912
5. Fard M (2011) Structural dynamics characterization of the vehicle seat for NVH performance analysis

6. Sung SH, Nefske DJ (2001) Assessment of a vehicle concept finite-element model for predicting structural vibration, SAE noise and vibration conference and exposition, 30 April–3 May, Traverse City, Michigan
7. Lee S et al (2002) Numerical approximation of vehicle joint stiffness by using response surface method. *Int J Autom Technol* 3:117–122
8. Donders S et al (2009) A reduced beam and joint concept modeling approach to optimize global vehicle body dynamics. *Finite Elem Anal Des* 45:439–455
9. Mundo D et al (2009) Simplified modelling of joints and beam-like structures for BIW optimization in a concept phase of the vehicle design process. *Finite Elem Anal Des* 45:456–462
10. Mundo D et al. (2010) Concept modelling of automotive beams, joints and panels. April 20–22
11. Van Niekerk J et al (2003) The use of seat effective amplitude transmissibility (SEAT) values to predict dynamic seat comfort. *J Sound Vib* 260:867–888
12. Liu X, Wagner J (2002) Design of a vibration isolation actuator for automotive seating systems-Part I: modelling and passive isolator performance. *Int J Veh Des* 29:335–356
13. Liu X, Wagner J (2002) Design of a vibration isolation actuator for automotive seating systems-Part II: controller design and actuator performance. *Int J Veh Des* 29:357–375
14. Gundogdu O (2007) Optimal seat and suspension design for a quarter car with driver model using genetic algorithms. *Int J Ind Ergon* 37:327–332
15. Nasrolahzadeh N et al. (2012) Automotive NVH performance characterization using concept modelling
16. Nastran MD (2010) R3 quick reference guide. Msc. software corporation, USA
17. Guyan RJ (1965) Reduction of stiffness and mass matrices. *AIAA J* 3:380
18. Craig RR, Bampton MCC (1968) Coupling of substructures for dynamic analyses. *AIAA J* 6(7):1313–1319
19. Ewins DJ (2000) Modal testing: theory, practice and application. Research Studies Press Ltd, Baldock

Part V
Vehicle Vibration and Noise Control

Improvements of Steering Wheel's Idle Shaking

Wenku Shi, Guangming Wu, Shichao Wang and Zhiyong Chen

Abstract Vehicle steering wheel's idle shaking has negative effect on driving comfort. The cause of steering wheel's idle shaking was recognized through vibration test and modal analysis method. It was found that steering system's operational modal was close to the 2nd order excitation frequency of the engine, and steering wheel resonated. To relief this problem, five improvements were presented, including structure reinforcement, lightweight design of steering wheel, installing of dynamic vibration absorber, matching of power train mounts and increase of engine idle speed. The effectiveness of each improvement was proved through experiments.

Keywords Steering wheel · Idle shaking · Structural optimization · Lightweight design · Dynamic vibration absorber

1 Introduction

As the increasing demand on the safety and comfort of vehicles, vehicle manufacturers pay more and more attention to vehicle's drive comfort.

F2012-J05-002

W. Shi (✉) · G. Wu · S. Wang · Z. Chen
State Key Laboratory of Automobile Simulation and Control, Jilin University,
130022 Changchun, China
e-mail: cleverwgm@gmail.com

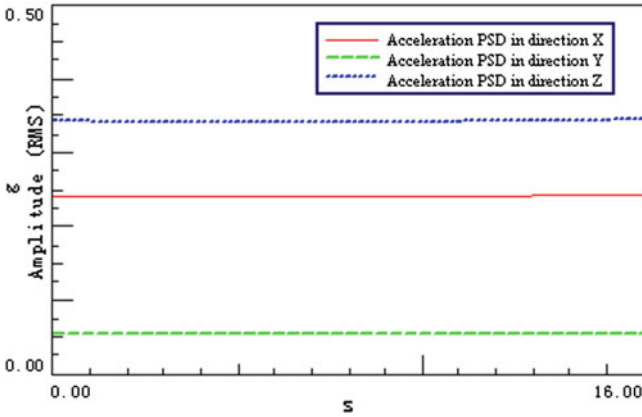


Fig. 1 Acceleration RMS of steering wheel in each direction

Steering wheel's shaking make trouble to the driver, especially on urban roads where there are many traffic lights, and the vehicle stops and starts frequently; and paralysis feeling of driver's arms and negative emotion will generate.

Steering wheel's idle shaking was researched and analysed in this chapter; improvement was brought out to inhibit idle shaking.

2 Cause Analysis of Steering Wheel's Idle Shaking

2.1 Vibration Testing of Steering Wheel

The most important excitation source of vehicle was the engine vibration in idle condition. Steering wheel's idle shaking was caused by the vibration generated by power train and transferred through frame and vehicle body.

In idle condition, acceleration RMS of steering wheel in each direction was shown in Fig. 1. The vibration in X direction and Z direction was much more serious than in Y direction.

Acceleration PSD of steering wheel in idle condition was shown in Fig. 2. The vibration frequency of steering wheel, which was equal to 26.67 Hz, was same to the 2nd order ignition excitation frequency of the engine idle speed (800 rpm). Therefore, the excitation of steering wheel's idle shaking was the 2nd order excitation of engine.

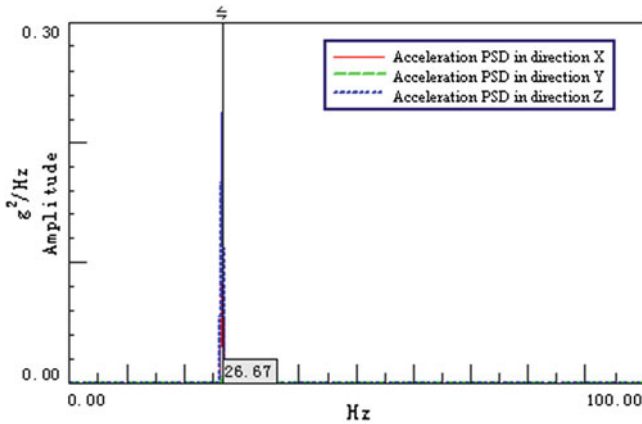


Fig. 2 Acceleration PSD of steering wheel in each direction

2.2 Modal Analysis of Steering System

FEM modal analysis of steering system in constraint condition was carried out, and verified through modal tests.

2.2.1 FE Modal Analysis

3D model of steering system and instrument beam was built with CATIA, and then imported into software Hyper mesh. All the combinations were set as practical condition; and all the boundary conditions and constraints were set as practical condition, too. The FE model was shown in Fig. 3.

The FE model was analysed in software Optistruct with Lanczos method [1, 2]. The first five order FE modal frequency of steering system in constraint condition were shown in Table 1. The 2nd order modal frequency (25.45 Hz), of which the mode shape was steering column rotating around Y axle relative to instrument beam, shown in Fig. 4, was very close to peak frequency of accelerating of engine speed in parking condition; steering system resonated and steering wheel shook seriously. The 3rd order modal shape (33.43 Hz) was steering column rotating around X axle relative to instrument beam, as shown in Fig. 5.

2.2.2 Experiment Mode Analysis

During the processing of building FE model, steering system was simplified a little; and the model was not the same with the practical structure. The reliability of FE analysis should be validated through steering system modal test.

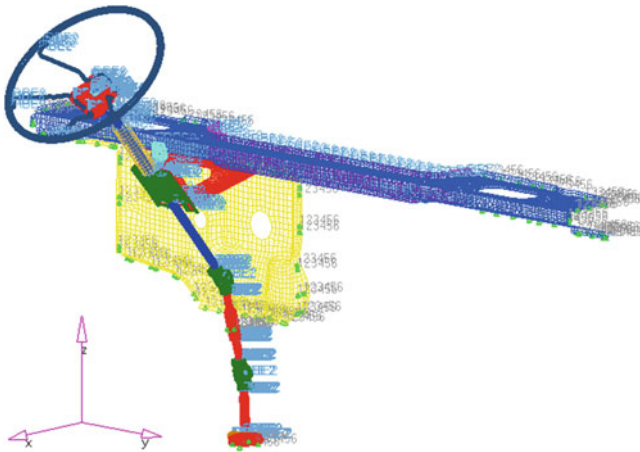


Fig. 3 FE model of steering system

Table 1 Mode frequency of steering system

Order	FE mode frequency (Hz)	Test mode frequency (Hz)	Relative difference (%)
1 st order	14.22	15.62	8.96
2 nd order	25.45	25.73	1.09
3 rd order	33.43	33.10	1.00

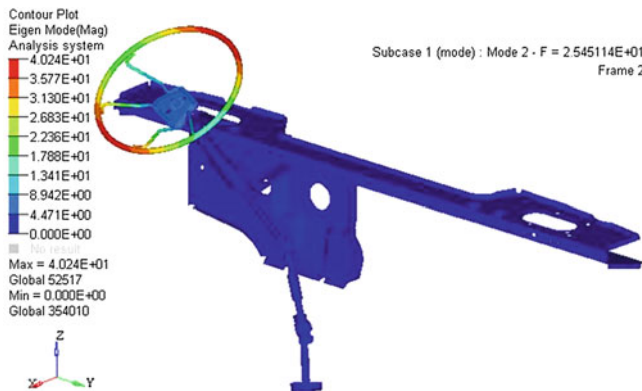


Fig. 4 The 2nd order FE mode shape

Hammering method was used in the experiment to test acceleration response of measure points; and mode parameters were extracted. The arrangement of measure points was shown in Fig. 6 the hammer exciting point was shown in Fig. 7.

The first three order mode frequencies of steering system in constraint condition were shown in Table 1. The mode shapes and vibration directions of FE analysis were very similar to of experiment analysis; the natural frequencies of FE analysis

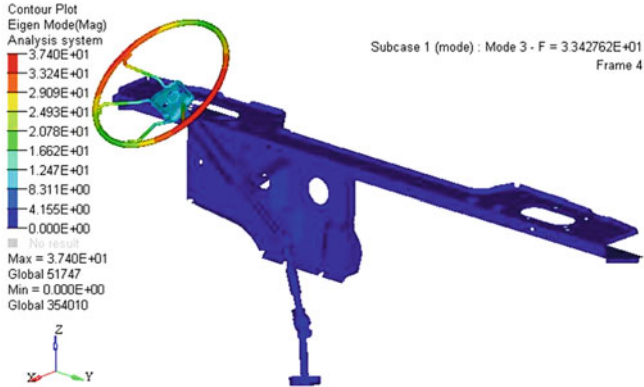


Fig. 5 The 3rd order FE mode shape

Fig. 6 Arrangement of measure points

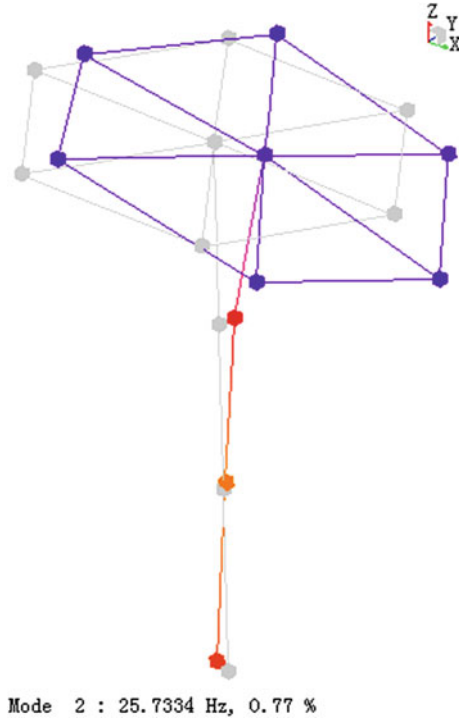


Fig. 7 The hammer exciting point



were very close to of experiment analysis. The 2nd order mode shape (steering column rotating around Y axle relative to instrument beam, as shown in Fig. 8) and frequency of experiment analysis were very close to of FE analysis. The 3rd order mode shape was shown in Fig. 9.

Fig. 8 The 2nd order test mode shape



The results showed the correctness of FEA and experiment analysis. The 2nd order modal frequency of steering system in constraint condition was very close to the 2nd order ignition frequency of engine, which caused steering wheel's resonance and idle shaking.

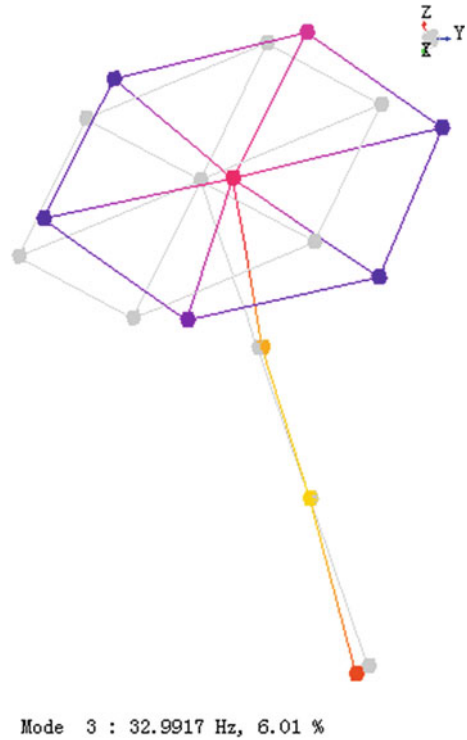
3 Improvements of Steering Wheel's Idle Shaking

To relief steering wheel's vibration from engine, the most effective resolutions were vibration isolation, vibration attenuation and avoiding resonance frequency range.

3.1 Reinforcement of Combination Between Steering Column and Instrument Beam

The combination between steering column and instrument beam was reinforcing [3, 4]. The thickness of triangular bracket and connector panel became 2.5, 3 mm

Fig. 9 The 3rd order test mode shape



separately from 1.7 to 2 mm, and then FE analysis of reinforced steering system was carried out. The 2nd order mode frequency of reinforced steering system was 34.74 Hz, which was far from engine's 2nd ignition frequency (26.7 Hz); and the idle resonance of steering system could be avoided. The mode shape was shown in Fig. 10.

3.2 *Lightweight Design of Steering Wheel*

According to vibration theory, lightening the steering wheel will raise the natural frequency of steering system [5]. By changing the density of steering wheel's FE model, the weight of steering wheel decreased from 2.8 to 1.8 kg; and FE analysis was carried out. Lightening the steering wheel raises the steering system rigid mode frequency to 32.02 Hz, which was far from engine's 2nd ignition frequency (26.7 Hz); and the idle resonance of steering system could be avoided. The mode shape was shown in Fig. 11.

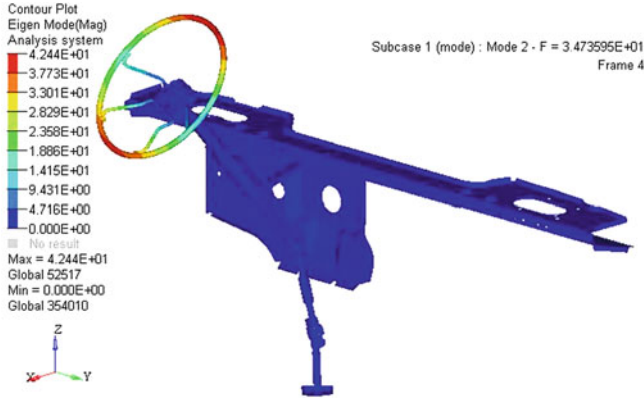


Fig. 10 The 2nd order mode shape of reinforced steering system

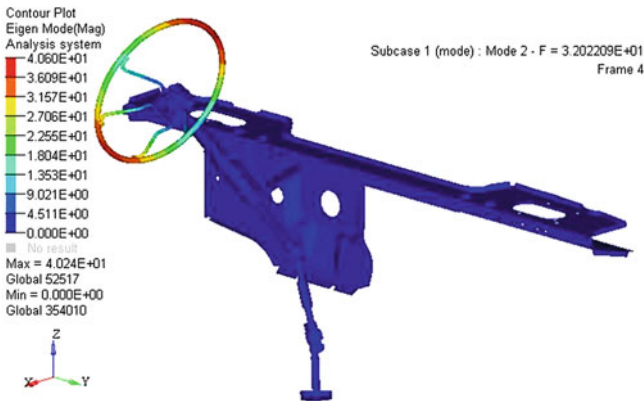


Fig. 11 The 2nd order mode shape of steering system with lightened steering wheel

3.3 Installing Dynamic Vibration Absorber

Dynamic vibration absorber (DVA) could damper vibration in specific frequency range. DVA is simple and practical. Dynamic vibration absorber could be installed in the steering wheel to relief idle shaking of steering wheel [6, 7].

As shown in Fig. 12, dynamic vibration absorber consisted of three parts: mount panel, damped rubber and mass panel. The three parts were pasted together through rubber vulcanization. Mount panel was attached to steering wheel; damped rubber provided elasticity stiffness; mass panel was the mass block of vibration system. The installation of DVA was shown in Fig. 13.

According to the theory of DVA, excitation frequency ω has the following relationship with DVA natural frequency ω_0 .

Fig. 12 Structure of DVA

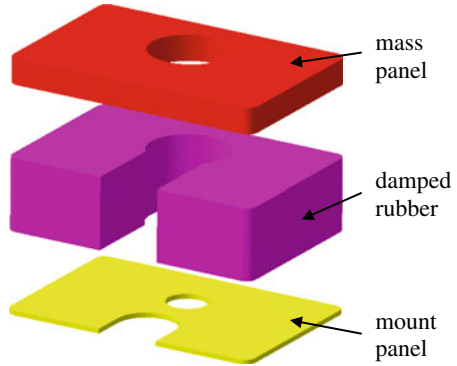
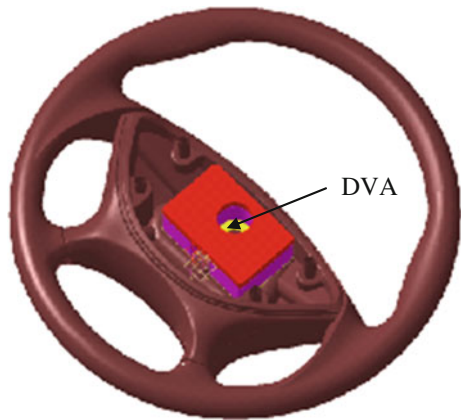


Fig. 13 Installation of DVA



$$\omega = \omega_0 = \frac{1}{2\pi} \sqrt{\frac{k}{m}}$$

As shown in Fig. 3 idle vibration frequency of steering wheel was 26.7 Hz. A DVA was designed to damp the vibration of idle frequency. The stiffness k and mass m of DVA were shown in Table 2.

The model of steering system with DVA was built with software ADAMS. Sine wave excitation of 26.7 Hz was applied at combination of steering column and instrument beam. Acceleration responses of steering wheel before and after installation of DVA were shown in Figs. 14, 15.

The result showed effectiveness of DVA. RMS value and PSD peak value of acceleration of steering wheel were shown in Table 3.

Table 2 Structure designing of DVA

	Project 1	Project 2	Project 3	Project 4
Design mass of DVA (kg)	0.3	0.4	0.5	0.6
Design stiffness of DVA (N/m)	8000	11000	13000	16000

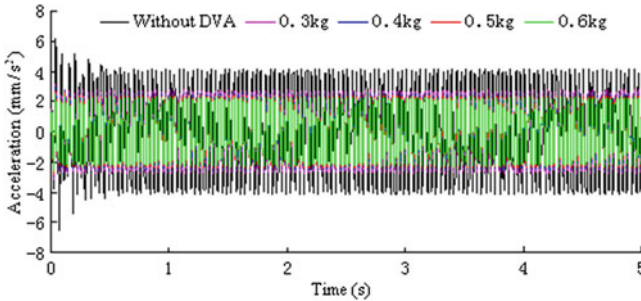


Fig. 14 Acceleration response of steering wheel in time domain

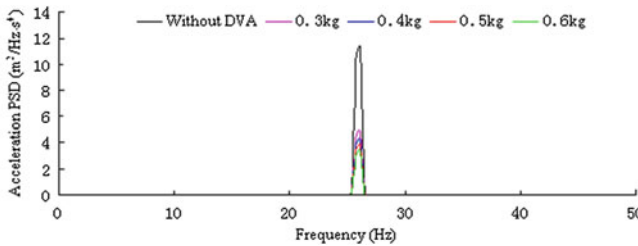


Fig. 15 Acceleration response of steering wheel in frequency domain

Table 3 Simulation results of projects

	Without DVA	Project 1	Project 2	Project 3	Project 4
Design mass of DVA (kg)	0	0.3	0.4	0.5	0.6
Acceleration RMS value (m/s ²)	2.96	1.93	1.81	1.71	1.61
PSD value (m ² /Hz·s ⁴)	11.31	4.91	4.28	3.87	3.41

3.4 Matching of Power Train Mount

Power train mount system with good vibration isolation performance could damp most vibration of power train in idle condition, and decrease the energy transported to steering system. Therefore, power train mount system should be matched appropriately.

6-dof vibration of power train coupled with each other, which caused large vibration amplitude and wide range of vibration frequency domain of power train.

Table 4 Energy distribution matrix of power train before optimization

Vibration direction	X	Y	Z	RX	RY	RZ
Natural frequency (Hz)	5.8779	6.4800	8.8901	11.5526	13.6536	9.2317
Energy distribution						
X	84.2424	2.0188	7.6233	0.0760	3.9745	2.0651
Y	0.8656	57.9026	11.2587	2.9874	0.0000	26.9857
Z	4.3087	0.0006	55.1397	0.5791	17.7548	22.2172
RX	0.2585	4.5268	11.0599	68.7432	0.0104	15.4012
RY	9.2570	0.1599	8.0505	0.1801	78.2606	4.0918
RZ	1.0678	35.3914	6.8678	27.4342	-0.0003	29.2390

So the vibration energy of power train mount system should be decoupled. Energy decoupling method, aimed at energy decoupling of power train, indirectly improved NVH performance of vehicle [8, 9].

3-direction stiffness of rubber mounts were optimized with energy decoupling method while installation angle and location of mounts were not changed. The energy distribution matrix of power train before optimization was shown in Table 4 the energy distribution matrix of power train after optimization was shown in Table 5.

As shown in Table 4 original power train mount system coupled seriously, especially in Z and RX direction; other directions coupled at different degree. As shown in Table 5 decoupling effect of power train mount system was better after being optimized, especially in Z and RX direction.

3.5 Increase of Engine Idle Speed

As shown in Fig. 3 steering wheel idle frequency was 26.7 Hz, which was the same with the 2nd order excitation frequency in idle condition (800 rpm). With the improvement of increase of engine speed, excitation frequency was far away from steering wheel natural frequency and shaking of steering wheel was avoided.

4 Experiment Validation

To relief steering wheel idle shaking, five improvements were presented:

1. Structure reinforcement of combination between steering pillar and instrument panel bar. Thickness of bracket and connector were separately changed to 2.5 and 3 from 1.7 to 2 mm.
2. Lightweight design of steering wheel. According to redesign, the weight of steering wheel decreased to 2.0 from 2.8 kg.

Table 5 Energy distribution matrix of power train after optimization

Vibration direction	X	Y	Z	RX	RY	RZ	
Natural frequency (Hz)	5.8779	6.4800	8.8901	11.5526	13.6536	9.2317	
Energy distribution	X	5.9841	6.6697	9.1580	14.8751	11.2465	8.8146
	Y	49.0592	0.1298	5.6345	0.0072	45.1240	0.0453
	Z	0.0773	84.8389	0.2379	11.4907	0.0003	3.3549
	RX	2.4437	0.1680	93.7637	0.1238	3.3505	0.1503
	RY	0.0598	12.4240	0.0231	88.6705	0.0138	-1.1912
RZ	48.2800	0.0238	0.0419	0.0435	51.2502	0.3606	

Fig. 16 Arrangement of acceleration sensor

3. Installing of DVA. As shown in Fig. 11 DVA was installed in the steering wheel. The stiffness and mass were separately designed as 11000 N/m and 0.4 kg.
4. Matching of power train mount system. 3 direction stiffness of rubber mounts were optimized with energy decoupling method.
5. Raising engine idle speed. Idle speed of engine was recalibrated to 850 from 800 rpm.

The effectiveness of five improvements should be separately tested through experiments. As shown in Fig. 16 an acceleration sensor was arranged to collect vibration acceleration signal of steering wheel. and vibration of steering wheel test points is evaluated with ISO 5349-1:2001 standard, the results were shown in Table 6. Compared to original design, vibration amplitude and acceleration PSD value of steering wheel with improvements decreased at a large degree; steering wheel idle shaking is greatly relieved.

Table 6 Evaluation of improvements

	Acceleration RMS value (m/s ²)	Acceleration PSD value (m ² /Hz·s ⁴)
Original	1.48	11.31
1st improvement	0.59	1.02
2nd improvement	1.11	4.38
3rd improvement	0.84	4.00
4th improvement	1.33	8.72
5th improvement	0.85	2.61

5 Conclusion

To relief steering wheel's idle shaking, five improvements were brought out: structure reinforcement of combination between steering pillar and instrument panel bar, lightweight design of steering wheel, installing of dynamic vibration absorber, matching of power train mount system, increase of engine idle speed. Experiments were separately carried out to verify effectiveness of these five improvements; and good results were achieved. Steering wheel's idle shaking decreased at a great degree.

References

1. Rudroju S, Gupta A, Yandamuri S (2007) Operational modal analysis of aluminium beams. *J Lest* 50(1):74–85
2. Qi Keyu, He Zhengjia, Li Zhen et al (2008) Vibration based operational modal analysis of rotor systems. *Measurement* 41(7):810–816
3. Chiang SL (1985) Using experimental modal modeling techniques to investigate steering column vibration and idle shake of a passenger car. SAE paper 850996
4. Kim K-C, Choi I-H, Kim C-M (2007) A study on the advanced technology analysis process of steering system for idle performance. SAE paper 2007–01-2339
5. Shim YJ, Shin CS (1999) The study for the reduction of idle vibration of steering system through the use of a weight reduction method. SAE paper 1999-01-0393
6. Swayze JL, Rivin ER (1997) Improvements in the optimization of dynamic vibration absorbers. SAE paper 971934
7. Yoshimori K, Morimura H, Yoshimura Y (1984) Dynamic-shock-absorber-effect of engine mounting system on the power-train vibration. SAE paper 840255
8. Park J-Y, Singh R (2007) Effect of engine mount damping on the torque roll axis decoupling. SAE paper 2007-01-2418
9. Johnson SR, Subhedar JW (1979) Computer optimization of engine mounting systems. SAE paper 790974

Squeak and Rattle Performance Degradation and Prevention in a Vehicle Design and Development Process

Youming Guo, Zhonghua Wu, Yangjia She, Peng Xu, Xiaoli Duan, Yun Zhang and Li Tang

Abstract Squeak and rattle is one of the major quality concerns in vehicle designs for customer satisfaction. Although a significant amount of work has been conducted in squeak and rattle detection and prevention for new (low mileage in service) vehicles, relatively little work has been done in squeak and rattle degradation and prevention for high-mileage-in-service vehicles. This paper is a first attempt in the automotive industry to systematically address root cause analysis of both low-mileage (or short-term) and high-mileage (or long-term) vehicle squeak and rattle degradation and corresponding prevention strategies.

Keywords Squeak and rattle performance · Degradation · Prevention · Vehicle design and development process · Vehicle body system design

1 Introduction

Traditionally, vehicles have been designed intentionally to have good squeak and rattle performance when they are new (i.e., good first-impression vehicles or low-mileage-in-service vehicles). A significant amount of work has been done in this area and an excellent survey paper can be found in [1]. Vehicle high-mileage-in-service squeak and rattle performance [2] is becoming more crucial for long term

F2012-J05-003

Y. Guo (✉) · Z. Wu · Y. She · P. Xu · X. Duan · Y. Zhang · L. Tang
Changan Auto Global R&D Center of Changan Automobile Co. Ltd, Chongqing, China
e-mail: sunqiemail@163.com

customer satisfaction as a result of strong competition in the automotive industry. The improvement in vehicle long-term squeak and rattle performance will increase residual values (or re-sale prices) of used vehicles from business point of view.

The current paper discusses root causes of vehicle squeak and rattle degradation from the viewpoint of vehicle operational conditions and corresponding degradation modes. Prevention strategies are presented which involves vehicle body CAE analysis and test methods for squeak and rattle critical parts provided by suppliers. The effectiveness of the prevention strategies is then demonstrated with actual vehicles.

2 Root Cause Analysis of Vehicle Squeak and Rattle Performance Degradation Problems

Vehicle squeak and rattle degradation can be grouped in two categories: low-mileage-in-service (or short term) degradation associated with relatively brand new vehicles and high-mileage-in-service (or long term) degradation observed on vehicles with high mileage or relatively old vehicles.

2.1 Vehicle Short Term Squeak and Rattle Degradation

Vehicle short-term squeak and rattle degradation is mainly due to the following reasons:

- Manufacturing issues such as missing welds, part-to-part variation and inadequate clearance, etc.
- Assembly issues such as improper installation of fasteners or bolts (e.g., insufficient clamp load or missing fasteners, etc.)
- Material incompatibility issues (frictional coefficients between two parts are not compatible with each other).
- Design or manufacturing defects associated with parts provided by suppliers such as glove box, CD/DVD players, etc.

2.2 Vehicle Long-Term Squeak and Rattle Degradation

Vehicle long-term squeak and rattle degradation is mainly due to design deficiencies of vehicle body systems and squeak and rattle critical parts. A vehicle experiences road excitations, temperature and humidity changes and corrosion due

to salt and dust in its useful life. Road excitations will cause vibrations of vehicle parts which in turn could cause fatigue damage, gap changes, loosening of parts, mechanical aging of non-metallic parts and wear and tear. Fatigue damage is caused by excessive stress induced in a part which is an issue of strength design and is beyond the scope of squeak and rattle design. Squeak and rattle performance design and development are an issue of stiffness designs which will be elaborated in what follows.

Vehicle parts with a gap in between could contact each other and cause rattle noise because of gap changes. Fasteners which attach two parts together could become loose because of continual excessive vibration and cause squeak problems between two parts with relative motion. Mechanical aging could cause stiffness changes in non-metallic parts such as door seals, bumper in a latch/striker system and bushings and mounts in suspension systems. Change in door seal stiffness could cause seal squeak. Change in bumper stiffness in a latch/striker system could cause latch/striker chucking noise. Change in suspension bushings and mounts will change excitations transferred from roads to body structures and result in higher squeak and rattle sensitivity in a body. Tear and wear could cause fading of seal coating which in turn causes seal squeaking noise. It could also cause degradation of weld integrity which results in higher diagonal distortions at body closure openings. Excessive diagonal distortions typically accelerate squeak and rattle degradation rate of a latch/striker system and door seals. Tear and wear could also result in squeak and rattle problems associated with many parts with a mechanism such as window regulators, seats, moon roofs, seat belt retractors and shock absorbers, etc.

Temperature change could cause changes in parts dimensions and gaps between parts which in turn cause squeak and rattle problems. One of the major root causes for squeak and rattle problems is material incompatibility (i.e., the frictional coefficients between two parts are not compatible with each other, especially metal to non-metal or non-metal to non-metal contact). A few typical papers in this area can be found in [3–6]. Non-metallic materials are very sensitive to temperature and humidity changes. Two parts which are originally compatible with each other (without squeak and rattle issues) may become incompatible with squeak and rattle issues because of temperature and humidity changes.

Another effect of temperature and humidity change is thermal aging of non-metallic parts. Thermal aging could cause stiffness changes in door seals and bumpers in a latch/striker system which in turn result in squeak and rattle problems associated with these parts, respectively. Thermal aging could also cause stiffness changes in suspension bushings and mounts. The stiffness changes in suspension elastomeric components will affect the excitations transferred from roads to body which may increase the body squeak and rattle sensitivity.

A body structure exposed to salt and dust for a long period of time may exhibit corrosion problems. The effects of the corrosion problems are thinning of parts and fading of weld integrity which may result in excessive diagonal distortions at body closure openings. These excessive distortions then impose excessive burden on

door seals and the latch/striker system which can accelerate squeak and rattle degradation.

3 Prevention Strategies for Vehicle Squeak and Rattle Degradation

As discussed in an earlier section that many long-term squeak and rattle problems are caused by excessive vibrations in squeak and rattle sensitivity areas in a body structure coupled with design deficiencies of some critical parts. Therefore, the key concept in prevention strategies is to minimize vibration sensitivity in critical body areas and optimize designs of squeak and rattle critical parts with respect to squeak and rattle performance.

3.1 Vehicle Body System Design Optimization Strategies

To minimize body squeak and rattle sensitivity, two key performance parameters are employed to guide body designs: (a) diagonal distortions at closure openings of a body-in-prime structure under static torsion load; (b) squeak and rattle sensitivity coefficients in a full body system. The significance of body-in-prime diagonal distortions with respect to squeak and rattle TGW's (things-gone-wrong) can be found in [7]. The rationale behind using squeak and rattle sensitivity coefficients to guide instrument panel designs for squeak and rattle robustness was also discussed in [7]. This up-front CAE driven design process is modified and extended to guide designs for all body parts such as doors and seat belt retractor, etc. at Changan. The concept of this method is described in what follows.

To make sure that none of the squeak and rattle sensitive areas experiences high vibration level when a vehicle is driven on the road, a squeak and rattle transfer function analysis is conducted which computes frequency response functions at each pre-determined locations in a body due to a unit load applied at each critical body/chassis attachment locations, respectively. This method is illustrated in Fig. 1. The response function at each location in each direction due to each excitation is frequency dependent as shown in Fig. 1. The maximum peak of the responses in three directions is defined as the sensitivity coefficient at that particular location. The maximum value of response functions at all locations in a sub-system (e.g., instrument panel, doors, etc.) is defined as the squeak and rattle sensitivity coefficient of this particular sub-system.

A data base of the above-mentioned squeak and rattle sensitivity coefficients was constructed after the method had been applied to a number of vehicle programs. Targets of squeak and rattle sensitivity coefficients are established at a very early design stage (prior to vehicle prototype build) for each vehicle program.

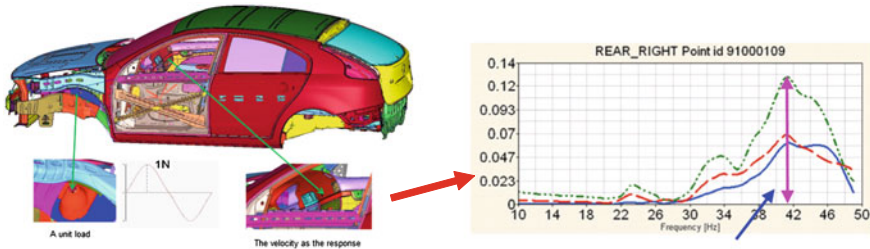


Fig. 1 Body squeak and rattle transfer function analysis

These targets are used to drive body designs favorable for squeak and rattle performance.

3.2 Structural Design Optimization Strategies of Squeak and Rattle Critical Parts

As mentioned earlier that designs of many parts provided by suppliers also affect long term squeak and rattle degradation rate. OEM's like Changan do not design and manufacture suppliers' parts. However, it is very crucial for OEM's to develop and provide performance parameters which can be used to guide part designs favorable for squeak and rattle performance. Fasteners are widely used in the instrument panel and doors and past experiences indicate that many vehicle squeak and rattle problems are associated with loosening of fasteners. Hence, design optimization of fasteners is selected to illustrate the squeak and rattle prevention strategy of critical parts.

Fasteners are used to attach two parts together to prevent relative motion between the parts. The key performance parameters for squeak and rattle designs are insertion and extraction forces in a laboratory test. It is crucial to have an insertion force below a certain target value to avoid any potential initial damage when first installed in a vehicle. On the other hand, the extraction force needs to be above a certain target value to avoid any potential loosening in the long run when used in a vehicle. These target values are normally jointly developed by Changan and suppliers based on vehicle squeak and rattle degradation tests and fasteners insertion and extraction force tests in a laboratory. To demonstrate the design optimization process, one of the fasteners employed by Changan went through three stages design optimization before it is selected as a standard part used by all vehicle programs.

Stage 1: Identification of fastener squeak and rattle problems

Vehicle on-the-road testing was conducted before and after mileage accumulation and fastener degradation was confirmed. An insertion/extraction force test of a new fastener was conducted in a laboratory. It was found in the test (Fig. 2) that the extraction force meets the target value but the insertion force is larger than the

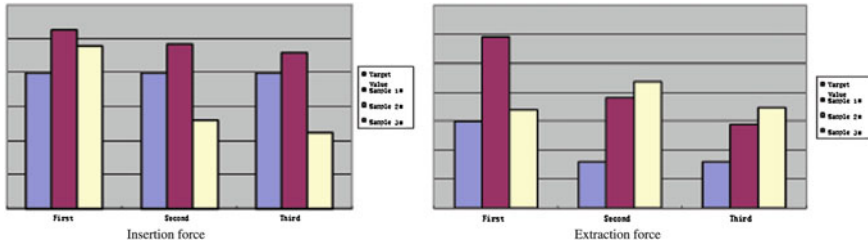
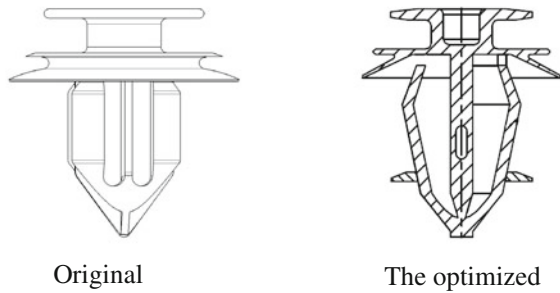


Fig. 2 Test results of insertion/extraction force of the original fastener before mileage accumulation

Fig. 3 The geometry of the fastener before and after optimization



target value and most fasteners already induced some damage when first installed in the vehicle.

Stage 2: Design optimization with respect to geometry

To improve the performance, the geometry of the fastener was optimized as shown in Fig. 3. Then another fastener insertion/extraction force test was conducted in the laboratory and the results are shown in Fig. 4. It can be found in this figure that both the insertion and extraction forces meet the target values before artificial thermal aging. However, the extraction force of some specimens fails to meet the target value after thermal aging. In other words, this design has a high risk of long-term squeak and rattle degradation.

Stage 3: Design optimization with respect to material properties

To further improve the performance, the same fastener in Stage 2 went through material optimization. To determine the effectiveness of this optimized fastener design, a vehicle installed with these fasteners went through a laboratory artificial aging process (4-poster with durability excitations and temperature cycles in an environmental chamber). An insertion/extraction force test of fasteners before and after vehicle artificial aging was then conducted and the results are shown in Fig. 5. It can be seen in this figure that both insertion/extraction forces meet target values before and after vehicle artificial aging. This implies that the design-optimized fastener has no short-term and long-term squeak and rattle degradation risk.

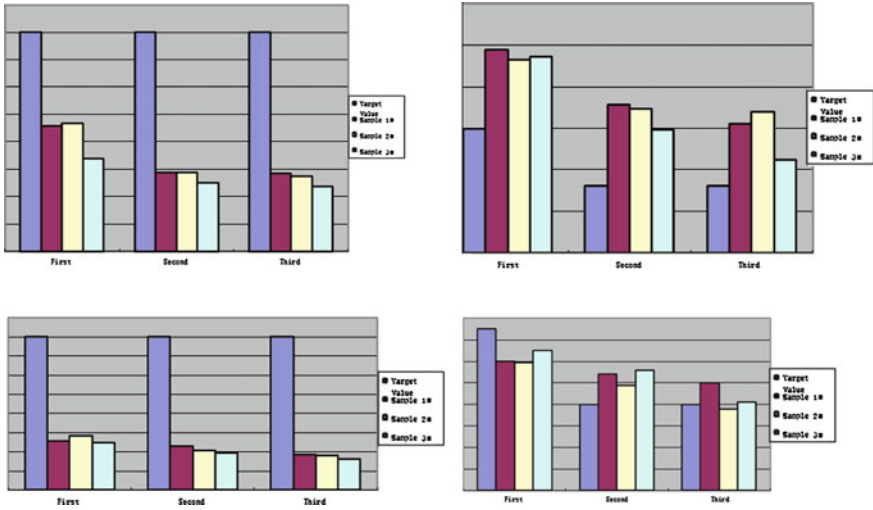


Fig. 4 Test results of insertion/extraction force of the geometry-optimized fastener before and after components artificial thermal aging

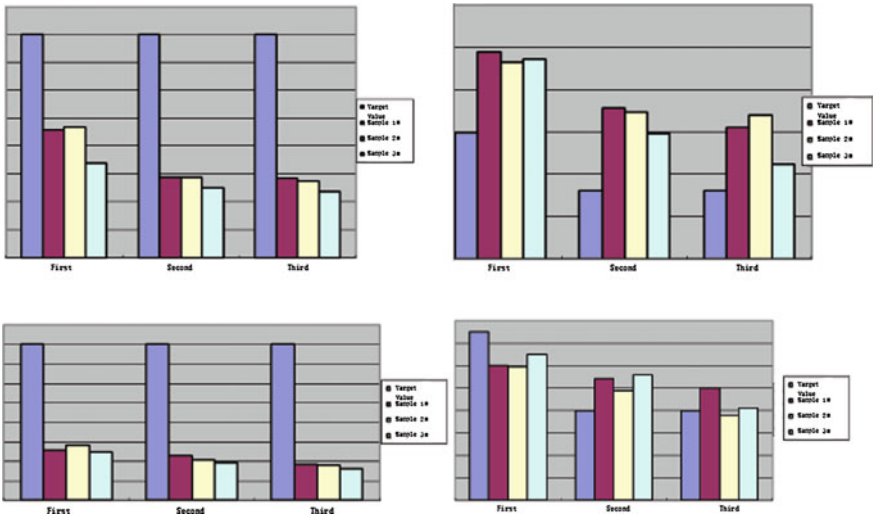


Fig. 5 Test results of insertion/extraction force of fasteners with geometry and material optimization before and after vehicle artificial aging

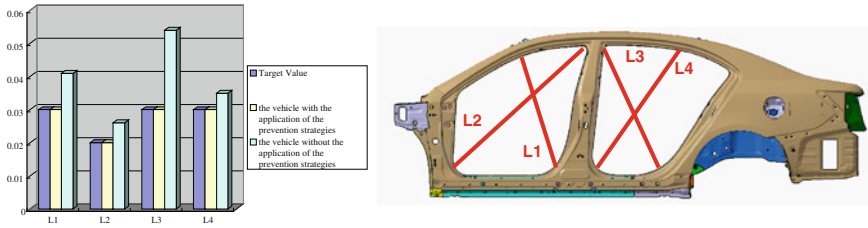


Fig. 6 Comparison of diagonal distortions at body closure openings

4 Case Studies

To demonstrate the effectiveness of the above-mentioned prevention strategies, two project vehicles (one without applying prevention strategies and one with applying prevention strategies) were selected for a design and performance comparisons study.

4.1 Design and Performance Comparisons

A comparison of diagonal distortions at body closure openings is given in Fig. 6. A comparison of the body squeak and rattle sensitivity coefficients for the instrument panel, doors and seat belt retractor is shown in Fig. 7. A comparison of the designs of three types of most critical parts (fasteners, latch/striker and seat belt retractors) is summarized in Fig. 8. Figures 6 through 8 indicate design and performance improvements at both body and component levels.

4.2 Vehicle on-the-Road Subjective Evaluations Comparison

Subjective evaluations are typically a first step in detecting any vehicle squeak and rattle issues if any. To determine squeak and rattle degradation level in the useful life of a project vehicle, project vehicles were selected to go through mileage accumulation on different road segments. Subjective evaluations of squeak and rattle level at different mileage stage were conducted. The following squeak and rattle subjective evaluation system is used to quantify the squeak and rattle performance at each stage.

- Total Squeak and Rattle Index = Summation of (Part Squeak and Rattle Index × Test Road Index)
- Part Squeak and Rattle Index 1.0 (majority of customers can notice and feel annoyed)

The body squeak and rattle sensitivity coefficients (mm/s)		
Sensitive Area	The vehicle without the application of the prevention strategies	The vehicle with the application of the prevention strategies
Doors	0.19	0.22
Instrument panel	0.46	0.34
Rear seat belt retractor	0.56	0.14

Fig. 7 Comparison of the body squeak and rattle sensitivity coefficients for the instrument panel, doors and seat belt retractor

	0.3 (50 % customers will notice and feel annoyed)
	0.1 (mild squeak and rattle noise although majority of customers can notice)
	0.0 (no squeak a rattle noise at all)
Test Road Index	1.0 (smooth road—roads used by majority of customers)
	0.3 (mildly rough road—roads used by 1/3 customers)
	0.1 (very rough road—roads used by few customers)

The total squeak and rattle index reflects both the part squeak and rattle performance and road excitation conditions. The smaller the index is the better squeak and rattle performance of the part is.

A comparison of the subjective evaluations between the two project vehicles before and after mileage accumulation is given in Fig. 9. It can be observed that the vehicle with the application of the prevention strategies has significantly better squeak and rattle performance than the one without it.

5 Summary

Vehicle squeak and rattle performance degradation can not be completely eliminated. But it can be minimized through up-front design optimizations of both body systems and critical parts.

Acknowledgments The authors would like to thank various departments in the Changan Auto Global R&D Center for their support during the course of this research work. They would also like to thank Shanghai ITW Plastic & Metal Co., Ltd for their support in fasteners laboratory testing.

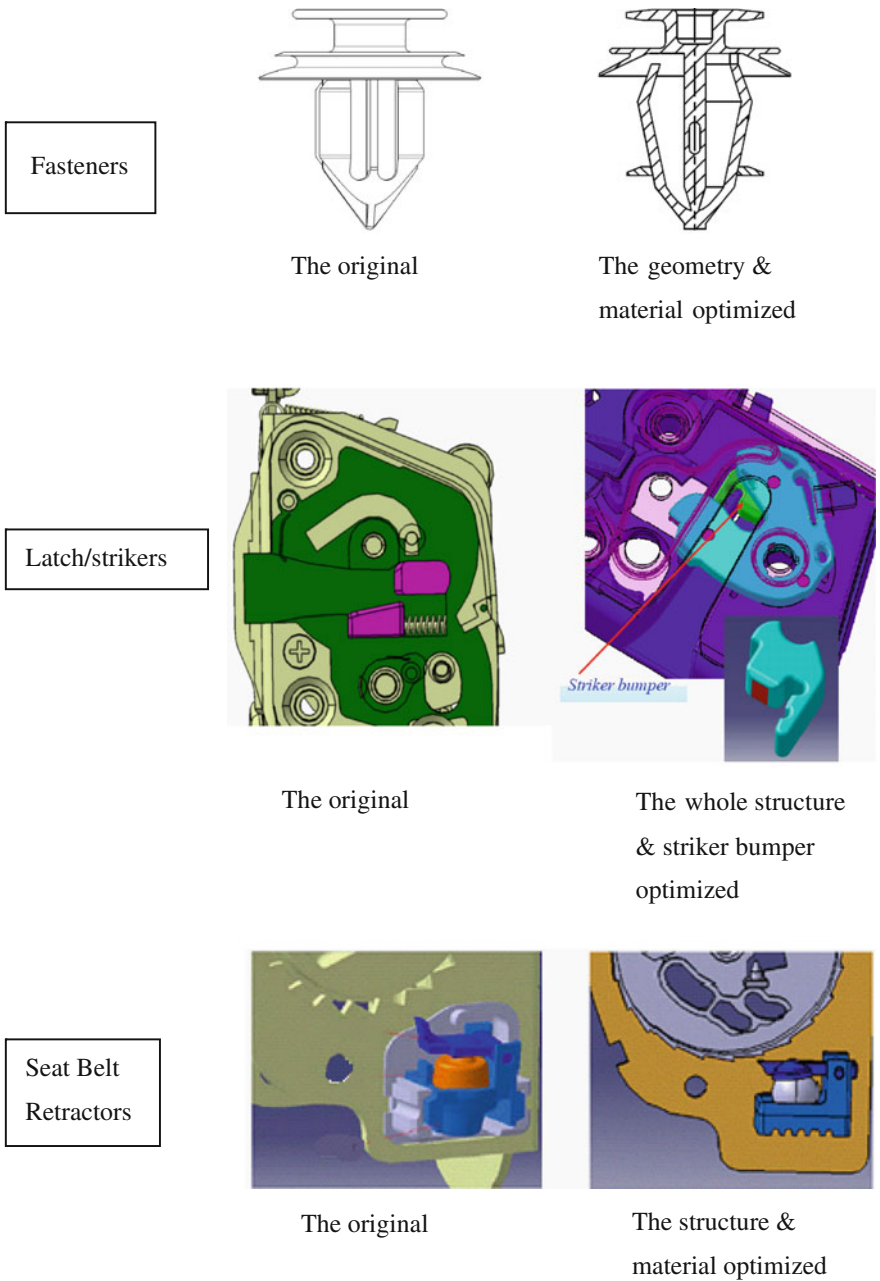


Fig. 8 Comparison of the designs of three types of most critical parts (fasteners, latch/strikers and seat belt retractors)

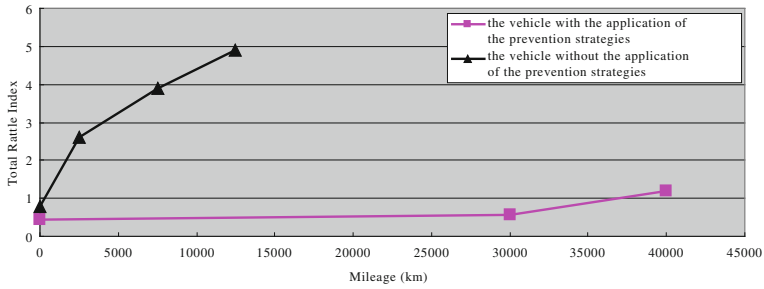


Fig. 9 Comparison of the subjective evaluations between the two vehicles before and after mileage accumulation

References

1. Kavarana F, Rediers B (1999) Squeak and rattle—state of the art and beyond. SAE paper 1999-01-1928
2. Kuo EY, Liaw L (1997) Statistical analysis of vehicle high mileage NVH performance. SAE paper 971912
3. Juneja V, Rediers B, Kavarana F, Kimball J (1999) Squeak studies on material pairs. SAE paper 1999-01-1727
4. Peterson C, Wieslander C, Eiss NS (1999) Squeak and rattle properties of polymetric materials. SAE paper 1999-01-1860
5. Lee P, Rediers B, Hunt K, Brines R (2001) Squeak studies on material pair compatibility. SAE paper 2001-01-1546
6. Hunt K, Rediers B, Brines R, McCormick R, Leist T, Artale T (2001) Towards a standard for material friction pair testing to reduce automotive squeaks. SAE paper 2001-01-1547
7. Kuo EY (2003) Up-front body structural designs for squeak and rattle prevention. SAE paper 2003-01-1523 SAE noise and vibration conference, May 5–8, 2003

Test and Simulation Integrated Transfer Path Analysis and Optimization of the Steering Wheel Vibration in Idle

Ran Xie, Zhifeng Liu, Shucheng Long and Zilong Tian

Abstract To decrease the steering wheel vibration in idle, the test and simulation integrated transfer path analysis and optimization method is proposed. First the contributors to the steering wheel vibration are studied, including the vibrational excitation sources, the transmission channels, and the steering wheel itself. Then a series of improvements are carried out, including lowering the engine idle speed with AC ON, tuning the engine mounts to decrease the engine vibration, improving the body structure and the support brackets of the steering column, etc. Results show that the steering wheel vibration in idle drops over 70 %.

Keywords Transfer path analysis · Steering wheel · Idle · Body structure · Engine vibration

1 Introduction

In the process of a new car development, drivers complain about NVH problems such as the excessive vibration of the steering wheel in idle. There are many factors that may cause the vibration in idle including the vibrational excitation sources, such as the engine and its mounts; the transmission channels, such as the body structure and suspension; and the steering wheel itself. Thus it becomes a very complex problem [1].

F2012-J05-009

R. Xie (✉) · Z. Liu · S. Long · Z. Tian
Guangzhou Automobile Group Co. Ltd, Automotive Engineering Institute, Guangzhou
510640, People's Republic of China
e-mail: ran_xie@126.com

The Transfer Path Analysis (TPA) method can be used to determine the proportion of the excitation energy transmitted in each transmission channel, to find out the major contributors to the vehicle vibration and to improve the NVH performances [2]. Usually the test based TPA is applied to these problems, which needs a lot of testing work and costs money and time, while the final effects can only be evaluated after making a new prototype vehicle. The simulation based TPA can overcome this shortcoming, and be well integrated with the test based method. Therefore, this paper proposes a test and simulation integrated TPA method to deal with the steering wheel vibration problem.

2 TPA Method for NVH Problems

All NVH system models can be simplified as “excitation source–transfer path—acoustic & vibration receptor”. Take the engine idle vibration problem for example. The engine loads on the engine mounts travel through the suspension system, tires and body structure, and finally act on the steering system, causing the steering wheel to vibrate. In the process of TPA, the single response of a specified transfer path is shown in Eq. (1), where P_i , H_i , F_i represent the response, transfer function and coupling excitation force of the i th transfer path.

$$P_i = H_i(\omega) \cdot F_i(\omega) \quad (1)$$

In a general way, the system is assumed to be linear, and the overall response can be considered as the linear sum of all the transfer path contributions, shown in Eq. (2), where P_{stru} represents the overall response, N is the total number of the transfer paths [3].

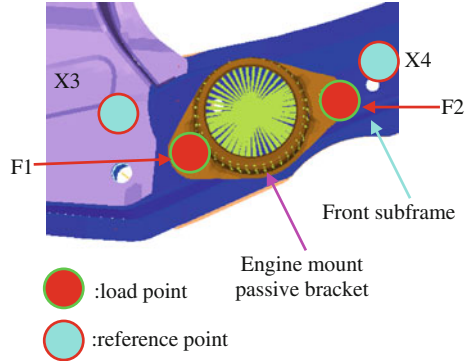
$$P_{\text{stru}} = \sum_{i=1}^N H_i(\omega) \cdot F_i(\omega) \quad (2)$$

In order to later predict the structure borne vibration response induced by the engine, the sensitivities of these responses towards the engine loads are needed, which are the transfer functions of the acceleration divided by force that provide the partial acceleration response for unit loads acting on the engine mounts. Transfer functions can be acquired by test or simulation. However, the former requires a lot of test work, so this paper uses the finite element simulation method.

Moreover, the matrix inverse method is used in the load identification. Take a simple model for example. Figure 1 demonstrates this, where x_1 , x_2 , x_3 , x_4 represent the acceleration of the measurement points, and F_1 , F_2 represent the operational input forces which are close to the mount passive side and in a line with the mount center. T_{ij} represents the measured transfer function from point i to point j . x_3 , x_4 can be expressed as Eqs. (3) and (4).

$$x_3 = f(F_1, F_2) = T_{13} \cdot F_1 + T_{23} \cdot F_2 \quad (3)$$

Fig. 1 Matrix inverse force identification model



$$x_4 = f(F_1, F_2) = T_{14} \cdot F_1 + T_{24} \cdot F_2 \tag{4}$$

Then the loads F_1, F_2 can be identified in matrix form as Eq. (5).

$$\begin{bmatrix} F_1 \\ F_2 \end{bmatrix} = \begin{bmatrix} T_{13} & T_{23} \\ T_{14} & T_{24} \end{bmatrix}^{-1} \begin{bmatrix} x_3 \\ x_4 \end{bmatrix} \tag{5}$$

Finally the engine load F is determined to be the average of F_1 and F_2 .

3 Full Vehicle FEM Modeling and Verification

The full vehicle FEM model are divided into subassemblies like tires, sub frames, suspensions, engine, steering system and body, as shown in Fig. 2. To assemble the full vehicle model, it is needed to provide the structural dynamic characteristics in the form of transfer functions or modes for each subsystem, and also to define the connection stiffness property between these subsystems. Then the modal coupling and transfer function synthesis method can be used for the assembled vehicle dynamic characteristics, such as the full vehicle modes.

First it is needed to calculate the modal properties of various subsystems, then to define the rigid or flexible connections between these subsystems. Through the modal synthesis method, for the front suspension HOP modal frequency, the simulation value is 11 Hz, and the test result is 12.5 Hz; for the trimmed body overall bending modal frequency, the simulation value is 28.5 Hz, and the test result is 27.8 Hz, as shown in Fig. 3.

The test accelerations on the passive side of the engine mount bracket and other test data on the reference points are measured during operational conditions. Combined with frequency response functions measured between these points, the forces on the engine mount attachment points of the body side can be obtained by the inverse force identification method. The response of the steering wheel locating at 12 o'clock position in X/Y/Z directions in idle is shown in Fig. 4, when

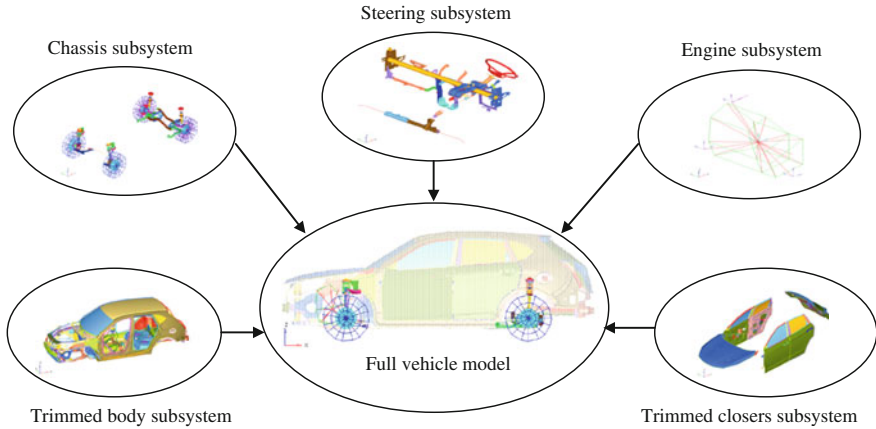


Fig. 2 Full vehicle FEM model

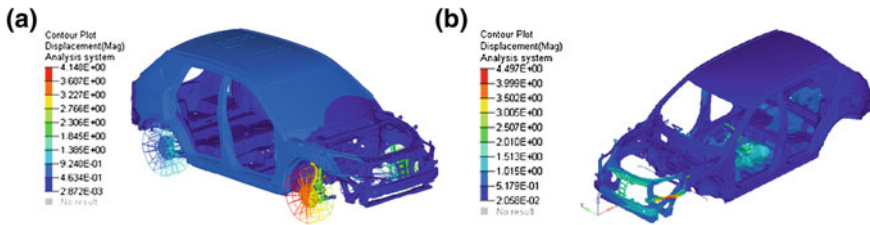


Fig. 3 Assembly mode simulation results. **a** Front suspension HOP mode. **b** Trimmed body overall bending mode

the air condition (AC) is turned off. The simulation and test values of the resonance frequency are close, and although the peak amplitude of vibration is a little different, the result curves are basically the same.

The arrangement of the steering wheel sensor is shown in Fig. 5.

4 Idle Vibration Problem Analysis

From the computed response curves, it is known the problem frequency is at 25 Hz, which is just the engine operation frequency. From the operational deflection shapes (ODS) simulation result in Fig. 6, it is known that at the frequency 25 Hz, the body and steering wheel show large vibration deformation, and it is possible that their modal frequencies are close to that of the engine excitation.

The 12 o'clock response of the steering wheel in X direction under individual X/Y/Z direction excitations are shown as the color bar in Fig. 7. At the roll restrictor mount, only direction X considered; while the other three mounts, all three translation force in X/Y/Z direction considered. There are ten paths in the problem for the force transmission.

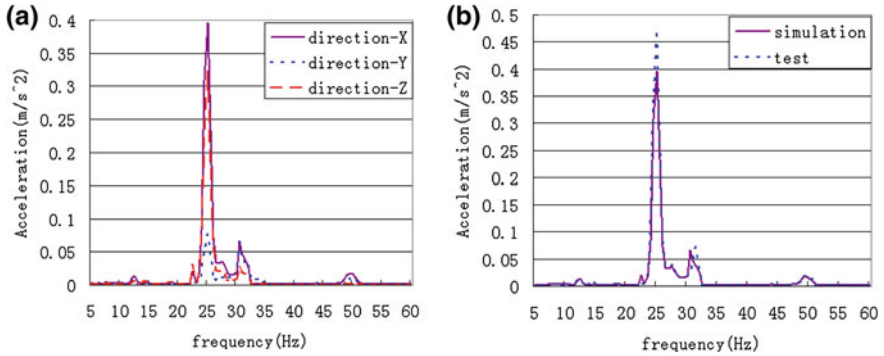
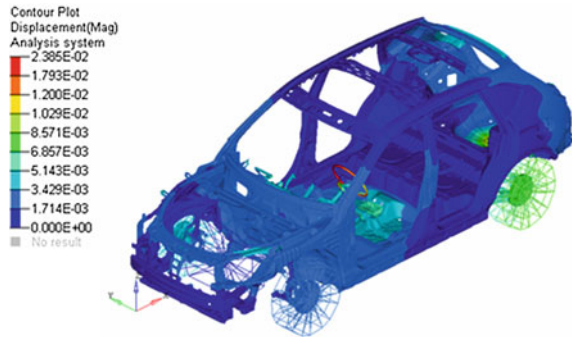


Fig. 4 The steering wheel response in X/Y/Z directions in idle (AC OFF). **a** Simulation results in three directions. **b** Comparison between simulation and test result in direction X

Fig. 5 Measurement points of the steering wheel in test



Fig. 6 Operational deflection shapes (ODS) at 25 Hz



From the above results, it can be seen that the load on the rear engine mount in X direction provides an important contribution at near 25 Hz for the response. The vibration peak is at about 31 Hz, which may be induced by the steering wheel itself resonance. As the engine idle speed is at a stable condition, the contribution of energy is concentrated in a certain frequency.

Figure 8 shows the other path contribution analysis result.

It is important to find out whether the peak responses are coming from the sensitivity around problem frequencies in the vibration transfer functions between

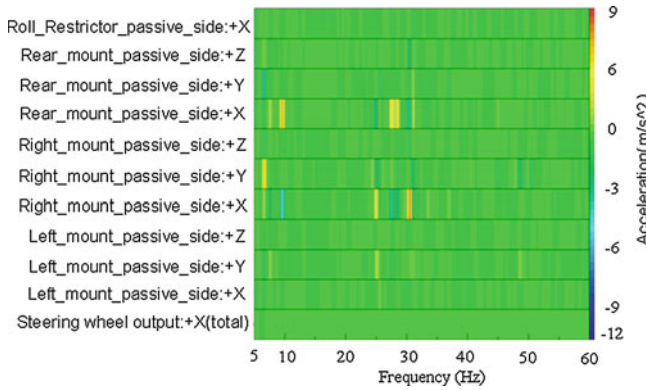


Fig. 7 Color bar contribution display of the steering wheel response in direction X

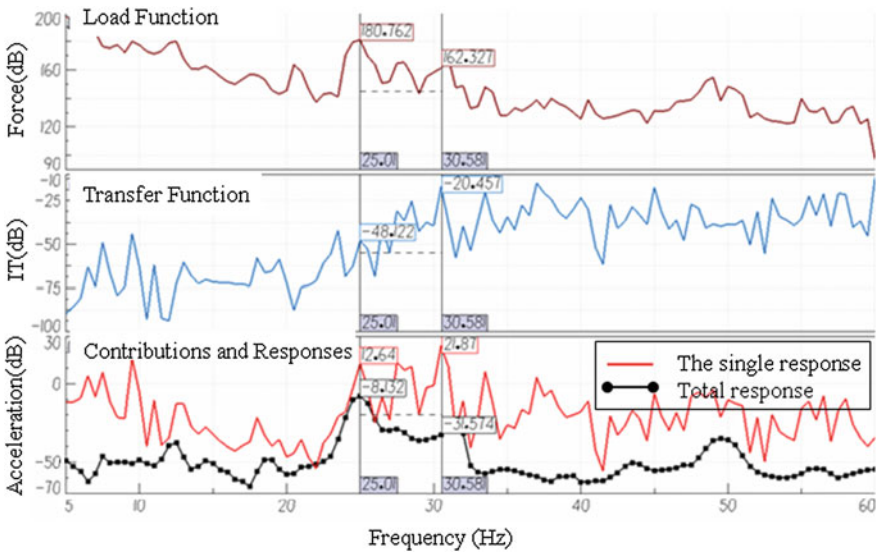


Fig. 8 Path related contribution display of the steering wheel response in direction X

engine mounts and the steering wheel response points or from the big forces at the engine mounts. The final response is the vector sum of different transfer path responses, but because of the phase differences, some reinforce each other, and some are weakened. From Fig. 8, it can be seen that the single response is greater than the total response in the single excitation point in direction X, which means that the other points weakened the effect of this point.

Because the structure borne vibration is composed of all excitation forces and vibration transfer functions, the two aspects are considered in the transfer path

Table 1 Operation test method to the vibration source identification

	Condition	Result (acceleration: m/s ²)
Step 1	AC off, engine 750 rpm	0.64
Step 2	Step 1 + cool fan on(high speed mode)	0.68 (+6 % compare to step 1)
Step 3	Step 2 + generator on	0.91 (+34 % compare to step 2)
Step 4	A Step 3 + compressor on,engine 750 rpm	1.19 (+30 % compare to step 3)
	B Step 3 + compressor on, engine 800 rpm	1.83 (+101 % compare to step 3)
Step 5	Step 4B + AC on	2.19 (+84 % compare to step 4A) (+20 % compare to step 4B)

analysis. From Fig. 8, the engine mount force shows an actual peak at 25 Hz, which the engine itself is responsible for it, and needed to tune the engine force and mount stiffness. Also it can be seen that the high sensitivity and a rather high load are at about 25 and 31 Hz, which may need to improve the body and steering wheel structure.

From numerical simulation results above, the engine loads and body structure transfer functions have become the main cause of the problem. In the further study, the operation test method is applied to the vibration source identification, and the excitation sources are studied under different engine idle speeds and with different working subsystem by compulsive switch on or off. It comes to the conclusion that the rough engine vibration and the idle speed variation rank the top two, however whether the cooling fan is turned on or off has limited effect. Table 1 presents the steering wheel test results in idle, which show the acceleration of the steering wheel increases sharply from 0.64 to 2.19 m/s² after AC ON. So it’s necessary to control the engine idle speed with AC on.

5 The Idle Vibration Optimization

5.1 Engine Mounts Stiffness Tuning and Engine Idle Speed Adjustment

The optimization of the engine rigid modal decoupling rate can decrease the transfer of engine operational forces to the body structure [4]. The engine vibration frequency and mode decoupling rate simulation model is shown in Fig. 9, where BUSH elements are instead of the mount rubbers and the dynamic stiffness values are given in three translational directions for it, and RBE2 and CONM2 elements are for engine rigid body. The BUSH element is fixed in one end, and the other end connected to the engine. A DMAP language subprogram is included in the NA-STRAN FEM program code to extract the corresponding frequency and modal shape, and to calculate the decoupling parameters. Then the engine mount stiffness is optimized to meet the engine rigid modal decoupling requirement.

Fig. 9 Mode decoupling rate simulation model

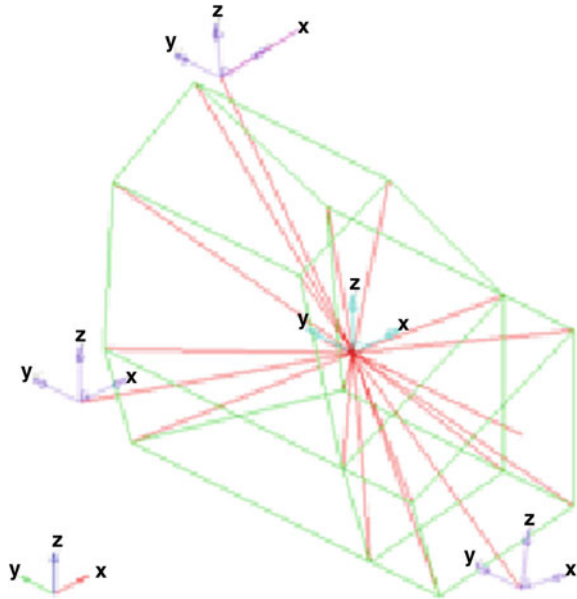


Table 2 gives the engine rigid modal decoupling optimization results, which shows that the modal decoupling rate is improved, and the modal frequency distribution is more reasonable.

The other way to decrease the engine loads is to change the idle speed with AC on from 800 to 780 rpm. It brings the largest improvement, and does not add weight or cost. The test results of the steering wheel vibration under the engine idle speed variation are shown in Fig. 10. The engine management system (EMS) needs to be refreshed, in order to avoid engine from stopping work caused by the idle speed drop and power lost.

5.2 Body and Steering Wheel Structure Optimization

A variety of the body structure and steering wheel structure improvements and results are shown in Table 3. With the body bending mode frequency increases, the vibration transfer function between engine mount and the steering wheel measuring point in the peak amplitude also decreases.

The steering wheel structure improvement is illustrated in Fig. 11, including making the capsule and bracket and sliding ring stiffer, and improving the steering column pipe welding technology. Table 4 shows the steering wheel improvement results. The modal frequency of the steering wheel increases and is separated from the engine excitation and body mode frequency for more than 2 Hz.

Table 2 Engine rigid modal decoupling rate (MDR) optimization results

		Fore/Aft	Lateral	Bounce	Roll	Pitch	Yaw
Freq (Hz)	Baseline	5.6	8.0	9.6	14.7	17.2	11.9
	Optimization	8.5	6.6	9.2	17.8	13.1	15.4
MDR (%)	Baseline	61.4	70.6	93.6	74.4	46.1	58.1
	Optimization.	95.8	91.8	96.9	64.1	60.9	79.4

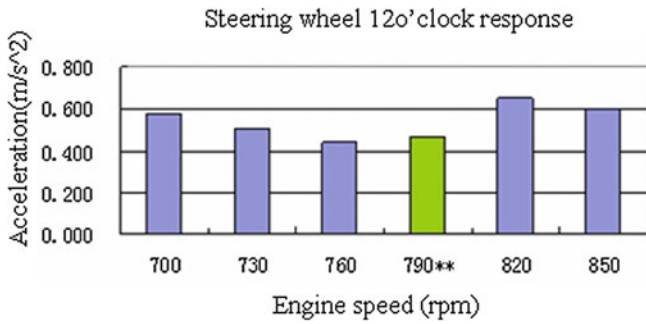


Fig. 10 Steering wheel vibration versus idle speed (AC OFF)

Table 3 Body structure and wheel structure optimization

	Joint under A pillar and seat crossbeam	Adding a crossbeam on tunnel end
Bending mode frequency	+0.4 Hz	+0.3 Hz
VTF peak amplitude	-7 %	-6.1 %

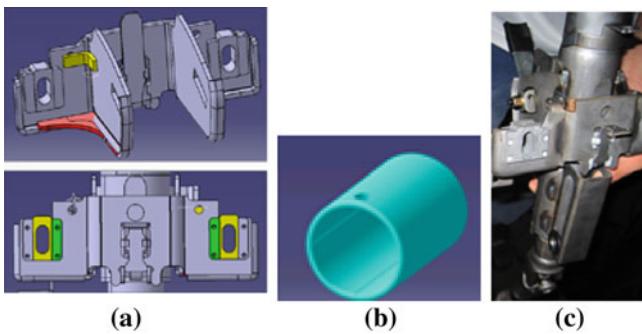


Fig. 11 Steering wheel structure improvement **a** Capsule and bracket **b** sliding ring **c** steering column pipe welding technology

Table 4 Steering wheel improvement results

	Steering wheel only test	Steering wheel on the car	
		CAE	Test
Baseline	40.6	30.8	27.4
Optimization	43.9	32.7	31.2

Table 5 Final results before and after improvement

Condition	State	Steering wheel(m/s ²)		
		Direction-X	Direction-Y	Direction-Z
AC OFF	Baseline	0.64	0.13	0.28
	Optimization	0.31	0.06	0.17
AC ON	Baseline	2.19	0.62	0.77
	Optimization	0.49	0.07	0.23

5.3 Final Optimization Results

Through the improvement, the prototype test results are shown in Table 5. With AC on, the engine idle speed is 800 rpm and the corresponding frequency is 26.7 Hz, while the vibration frequencies of the body structure and steering wheel are over 27 Hz with a large engine excitation force, which shows an extremely bad vibration condition with AC on. From Table 5, the direction X acceleration decreases from 0.64 to 0.31 m/s² with AC OFF and from 2.19 to 0.49 m/s² with AC on. This demonstrates that the conditions are greatly improved under both AC off and AC on conditions.

6 Conclusions

The test and simulation integrated transfer path analysis and optimization method is applied to decrease the steering wheel vibration in idle. The following conclusions are drawn:

1. The optimization of the engine rigid modal decoupling rate and tuning of engine speed with AC on can decrease the amplitude of engine operational forces to the body structure and suppress the vibration from excitation sources.
2. Trimmed-Body 1st bending modal frequency and the steering column vertical modal frequency are reciprocally coupled with the idle vibration frequency, so resonance phenomenon happens. Through structure optimization, the two frequencies are increased and properly separated from the engine excitation frequency.

3. The test and simulation integrated transfer path analysis and optimization method can be an effective way to find out the major contributor to the NVH problem, and the steering wheel vibration in idle drops over 70 %, thus the subjective evaluation of the real vehicle performance is remarkably improved.

References

1. Krishna RD, Frederick JZ, Shan UH (2003) Application of noise path target setting using the technique of transfer path analysis. SAE Paper 2003-01-1402
2. Antonio V, Herman VA, Peter K et al (2005) Experimental transfer path analysis of hybrid bus. SAE Paper 2005-01-2335
3. Juha P (2005) Finding and fixing vehicle NVH problems with transfer path analysis. Sound Vib 2005 (11):12–16
4. Hamid RK (2006) Optimal vibration control of vehicle engine-body system using haar functions. Int J Control Autom Syst 4(6):714–724

Study on Mount Matching Optimization for Removing Powertrain Abnormal Low Frequency Vibration

Feili Dai, Wei Wu, Hailin Wang, Qiang Liu,
Fangwu Ma and Fuquan Zhao

Abstract *Research Objective* For abnormal engine vibration due to hidden engine design defects, manufacturing error or mount mismatching, the priority should be to re-match the mount, which is the easiest way to solve this hard problem. In this study, it focuses on engine mount matching research, and the torque roll axis (TRA) decoupling method is applied to remove low-frequency intermittent traverse of an engine model. *Methodology* With the measured inertia characteristics of the engine powertrain, the TRA theory is used to calculate the direction of TRA. It is indicated in the TRA complete decoupling theory that it is theoretically possible if a pure TRA mode is implemented, torque vibration along crankshaft only produces roll vibration along TRA. However, other loads exist on engine-mounts system. So, a large decouple rate along TRA with acceptable decouple rate in other directions is a priority in guiding further adjustment on installation location, installation angle and stiffness of the four engine mounts. Then, energy decoupling theory is used to calculate the decouple rate after optimization, to validate whether the vibration direction with large excitation energy has been decoupled to the greatest extent. *Results* According to TRA decoupling calculation with experimental results, slight adjustments on the engine mount installation location, installation angle and stiffness can remove the abnormal low-frequency vibration Phenomenon tremendously, and promote NVH performance of the vehicle. *Limitations of this study* It is found that multiple hydraulic mounts can remarkably improve the performance of low frequency vibration isolation, but worsen the vehicle noise performance. If active mount control method can be applied jointly, it is prospective that the mount matching performance could be

F2012-J05-012

F. Dai (✉) · W. Wu · H. Wang · Q. Liu · F. Ma · F. Zhao
Zhejiang Geely Automobile Research Institute CO. LTD, Hangzhou, China
e-mail: daifeili@163.com

optimal. *What does the paper offer that is new in the field including in comparison to other work by the authors?* A new optimization idea for engine-mounts decoupling method is applied. With a large decouple rate along TRA and acceptable decouple rate in other directions, the phenomenon of abnormal low-frequency vibration can be eliminated. *Conclusion* TRA Mount Matching Optimization Methods can greatly improve the abnormal low frequency vibration of the powertrain system.

Keywords Mount matching · Low-frequency · Vibration · Torque roll axis · Decouple

1 Background

Abnormal low-frequency vibration phenomenon was found in the development of a powertrain mounting system, which lowered the driving comfort of the vehicle. Time-spectrogram waterfall diagram in Fig. 1 shows a broadband low-frequency vibration with frequency between 8 and 20 Hz, which is just near the rigid body modal frequencies of the engine-mount system.

Early computing report for this mounting system is illustrated in Table 1 [1]. According to isolation performance curve of mounting system, the rigid body modal frequencies of the engine along the crankshaft direction (Pitch) has exceed the frequency upper limit, which will reduce the vibration isolation rate of mounting system directly, and increase the transfer of vibration to the seat. The calculation report also showed that modal decouple rate along the direction of the crankshaft is low, which can cause coupled vibration problem of the engine mounting system. (If the input vibration in one direction leads to the response vibration mode in another direction, it is claimed that the two vibration modes are coupled. If the coupling is separated, that is called decoupling.)

Two coupled vibration modes may stimulate each other, which will results in a series of troubles:

1. Vibration amplification.
2. Widen natural vibration frequency.
3. Stiffer Mount needed in order to restrict the amount displacement of the engine, which deteriorates the vehicle NVH characteristics.
4. With coupled vibration of different directions, it is difficult to improve the individual vibration performance without affecting the isolation performance of others.

Therefore, in-depth study in powertrain mounting system is implemented in the paper for powertrain abnormal vibration caused by probable mount matching errors, and the optimization method for improving the powertrain abnormal low-frequency vibration is given.

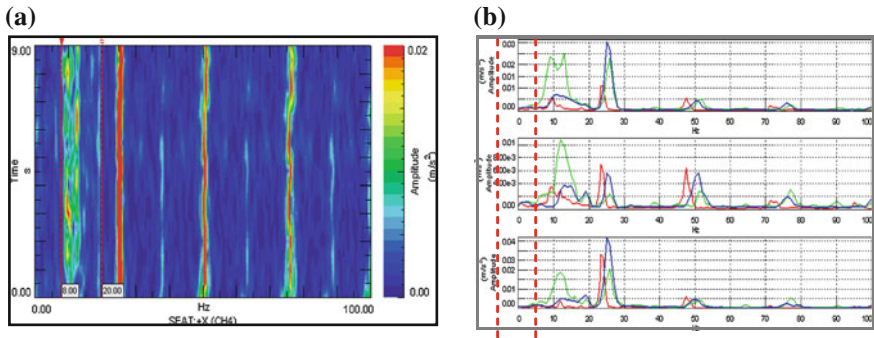


Fig. 1 Powertrain abnormal indoor seats to low-frequency jitter. **a**Waterfall diagram. **b**Spectrogram

Table 1 Decoupling calculating report of mounting system

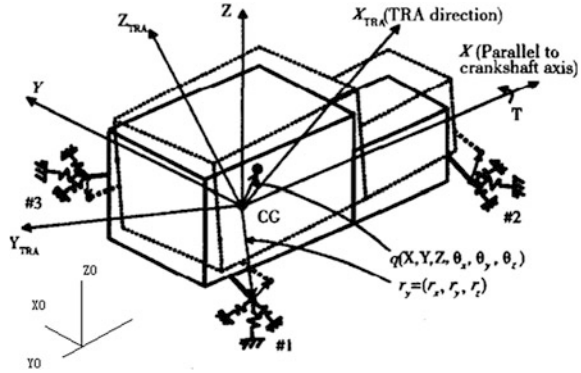
6DOF decouple	Fore/Aft	Lateral	Bounce	Roll	Pitch	Yaw
Freq lower limit (Hz)	7	7	8	8	8	8
Freq upper limit (Hz)	13	15	11	18	12	18
Freq calc (Hz)	8.3	9.0	10.1	15.4	13.7	12.0
Decouple rate(%)	80	60	90	80	90	60
Fore/Aft	80.78	5.69	0.01	0.04	10.45	3.03
Lateral	4.30	79.08	2.95	12.13	0.00	1.54
Bounce	0.20	2.46	96.50	0.57	0.02	0.25
Roll	0.68	11.37	0.03	87.66	-0.34	0.59
Pitch	13.95	-0.05	0.17	-0.54	72.58	13.89
Yaw	0.09	1.45	0.33	0.15	17.29	80.69

2 Theoretical Basis

Domestic vehicle factories traditionally take optimization measurements for powertrain low frequency vibration in the vehicle coordinate or in the inertial coordinate. Optimization parameters usually include the mount stiffness, mount location and mount installation angle. However, the rigid body of the powertrain is not symmetrical, so when the engine is working, the torsional vibration along the direction of the crankshaft will drive the powertrain rotate along a straight line called torque axis [2]. Mounting system optimization in the torque axis coordinate is more practical significance. This article will describe the general method in establishing the dynamic mechanical model of mounting system in the torque-axis coordinate, and deduce the target parameters for mounting system optimization.

Figure 2 shows a simplified mechanical model of the powertrain with six degrees of freedom fixed in the approximated rigid frame using four components containing three elastic parameters. The vehicle coordinate system X0Y0Z0 is constructed with the origin of the coordinates picks up randomly on the car body.

Fig. 2 Mechanical model of powertrain mounting system



X0-axis is defined from front to rear. Z0-axis is vertically upward. Y0-axis is determined in terms of the right-hand rule. The powertrain centre of mass coordinate system XYZ is constructed with Centroid CG of the powertrain as the origin. The X-axis is passing through the origin and parallel to the crankshaft. The Z-axis is vertically upwards. The Y-axis is determined using right-hand rule. Besides, $q(X, Y, Z, \theta_x, \theta_y, \theta_z)$ represents small displacement of CG. Local coordinate of each mount is established along principal axes of elasticity respectively, and $r_i = (r_x, r_y, r_z)$ is the location vector of the origin of the coordinate of each mount. The powertrain torque roll axis coordinate system $X_{TRA}Y_{TRA}Z_{TRA}$ is established with CG of the powertrain as the origin. X_{TRA} is parallel to the TRA, and the other two axes are arbitrary and mutually orthogonal with TRA.

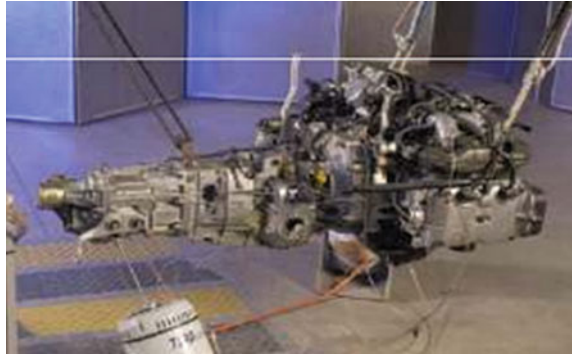
To establish the mechanical model of the mount system, the mass of the engine is obtained initially and the location of CG and moment of inertia tensor is measured using a modal impact mass line method [3] in the vehicle coordinate system shown in Fig. 3.

$$S = \begin{bmatrix} J_X & -J_{xy} & -J_{xz} \\ -J_{xy} & J_y & -J_{yz} \\ -J_{xz} & -J_{yz} & J_z \end{bmatrix} \tag{1}$$

Symbol S in Eq. (1) represents tensor matrix of the rotational moment of inertia. Diagonalize the matrix in XYZ coordinate, and get the principal moment of inertia and the principal axis of inertia. Then calculate the direction of the TRA with Eq. (2)

$$\begin{cases} l = \left[\frac{u_1^2}{J_1} + \frac{u_2^2}{J_2} + \frac{u_3^2}{J_3} \right] / P \\ m = \left[\frac{u_1 v_1}{J_1} + \frac{u_2 v_2}{J_2} + \frac{u_3 v_3}{J_3} \right] / P \\ n = \left[\frac{u_1 w_1}{J_1} + \frac{u_2 w_2}{J_2} + \frac{u_3 w_3}{J_3} \right] / P \end{cases} \tag{2}$$

Fig. 3 Measurement of rigid body inertial properties using modal impact mass line method



where $P = \sqrt{\frac{u_1^2}{J_1^2} + \frac{u_2^2}{J_2^2} + \frac{u_3^2}{J_3^2}}$ is related to properties of inertia, and $J_i (i = 1, 2, 3)$ represent the principal moment of inertia, $u_i, v_i, w_i (i = 1, 2, 3)$ represent the cosine of the angle of the i -th principal axis of inertia with three axes X, Y, and Z in the XYZ coordinate.

According to the Lagrange dynamic equation [Eq. (3)], it is easy to get mass matrix [Eq. (4)] and stiffness matrix [Eq. (5)] in TRA coordinate.

$$\frac{d}{dt} \left(\frac{\partial T}{\partial \dot{Q}_i} \right) - \frac{\partial T}{\partial Q_i} + \frac{\partial U}{\partial Q_i} + \frac{\partial D}{\partial \dot{Q}_i} = \{F_i\} \tag{3}$$

$$[M] = \begin{bmatrix} m & & & & & \\ & m & & & & \\ & & m & & & \\ & & & J_x & -J_{xy} & -J_{xz} \\ & & & -J_{xy} & J_y & -J_{yz} \\ & & & -J_{xz} & -J_{yz} & J_z \end{bmatrix} \tag{4}$$

$$[K] = \begin{bmatrix} k_{11} & k_{12} & k_{13} & k_{14} & k_{15} & k_{16} \\ k_{21} & k_{22} & k_{23} & k_{24} & k_{25} & k_{26} \\ k_{31} & k_{32} & k_{33} & k_{34} & k_{35} & k_{36} \\ k_{41} & k_{42} & k_{43} & k_{44} & k_{45} & k_{46} \\ k_{51} & k_{52} & k_{53} & k_{54} & k_{55} & k_{56} \\ k_{61} & k_{62} & k_{63} & k_{64} & k_{65} & k_{66} \end{bmatrix} \tag{5}$$

Eigenvalue solution of kinematic Eq. (6) is implemented, and rigid body modal circular frequency ω_r and modal vector ϕ_r of powertrain mounting system is calculated, which are shown in Eq. (8).

$$[M]\{Q\} + [K]\{Q\} = 0 \tag{6}$$

$$\det([K] - \omega^2[M]) = 0 \tag{7}$$

$$([K] - \omega_r^2[M])\{\phi_r\} = \{0\}, r = 1, \dots, 6 \quad (8)$$

After getting the six intrinsic vibration mode of the engine-mount system, mode shapes are used to get the energy distribution of the engine-mount system, and the energy distributions are applied to determine whether decoupling degree is enough or not. Energy decoupling method of engine-mount system is basically out of shackle about the characteristic of the type and arrangement of powertrain with general applicability, and can fit in any complex shape of the rigid body, which has become a primary method of decoupling design. Energy decouple rate calculation equation: when the system vibrates with the j -th natural frequency, energy assigned to k -th generalized coordinates share percentage of the total energy is shown below.

$$DIP_{kj} = \frac{\sum_{i=1}^6 ((\phi_j)_k m_{ki} (\phi_j)_i)}{\sum_{k=1}^6 \sum_{l=1}^6 ((\phi_j)_k m_{kl} (\phi_j)_l)} \quad (9)$$

Mode decouple rate and mode frequency will behave a major factor in evaluating the performance of the mounting system.

3 Optimization

If the TRA direction and the direction of one of the natural vibration modes comes across coincidence, regardless of excitation frequency, torque force along the crankshaft results in the response only exist around the TRA. In this situation, energy decouple rate in TRA direction reaches 100 %. With reasonable mount layout, if a pure mode is achieved in the TRA, torque along crankshaft will produce a pure torsional vibration around the TRA, without producing the vibration of the other directions [2]. Because the incentive of the engine is not only exist along the crankshaft, there are incentives in other directions, so it is considered to optimize the torque axis decouple rate, while ensuring decouple rate in other directions are not bad, this approaches the realization of TRA mode decoupling in an engineering way.

Gaps exist between initial design values and measured values of powertrain rigid body inertial properties, and the same mount layout is for these two powertrain mentioned above. In this paper, these two situations will be treated respectively with different initial optimization values. Then design variables, objective function and constraints, accompanying with a multi-objective quadratic programming optimization algorithm (10) [4], will be used to optimize the engine-mount system parameters.

Table 2 Centroid location and TRA

Centroid location	Test value			Design value		
	Xcog Ycog Zcog (m)	-0.555	0.0587	0.185	-0.553	0.0361
Mass (kg)	203			194		
Mass moment of inertia						
Ixx Iyy Izz (m ² * kg)	18.655	77.172	72.590	21.375	72.445	73.335
Ixy Ixz Iyz (m ² * kg)	4.748	-21.977	-1.234	-5.440	-19.263	3.423
Cosine orientation of TRA	-0.181	0.976	0.126	-0.105	0.982	0.159

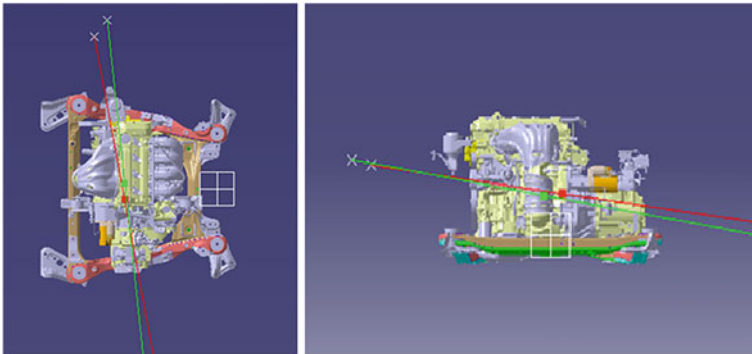


Fig. 5 Designed TRA vs. measured TRA (Note The green line is the designed TRA, the red line is the measured TRA)

position is calculated according to the moment of inertia and is shown in Table 2 and shown in Fig. 5.

3.2 Optimization of the Powertrain with Designed Inertial Parameter and TRA

3.2.1 Constraint Condition

Tables 3, 4.

3.2.2 Mount Optimization Requirement

Table 3 Mount displacement constraint (In Vehicle Coord.)

Mount displacement	X0	Y0	Z0
Engine mount	[-3, 3 cm]	0	0
Transmission mount	0	0	0
Rear mount	0	0	0
Front mount	0	0	0
Mount Angle	Around x [0, 360]	Around y [0, 360]	Around z [0, 360]
Mount Stiffness	Stiffness vary allowance [-200, 200 N/mm]		

Table 4 Frequency constraint (In TRA Coord.)

Degree of freedom	X_TRA	Y_TRA	Z_TRA	RX_TRA	RY_TRA	RZ_TRA
Freq. lower limit (Hz)	7	7	8	8	8	8
Freq. upper limit (Hz)	13	15	11	18	12	18

3.2.3 Optimization Result

3.3 Optimization of the Powertrain with Measured Parameter and TRA

3.3.1 Constraint Condition

3.3.2 Mount Optimization Requirement

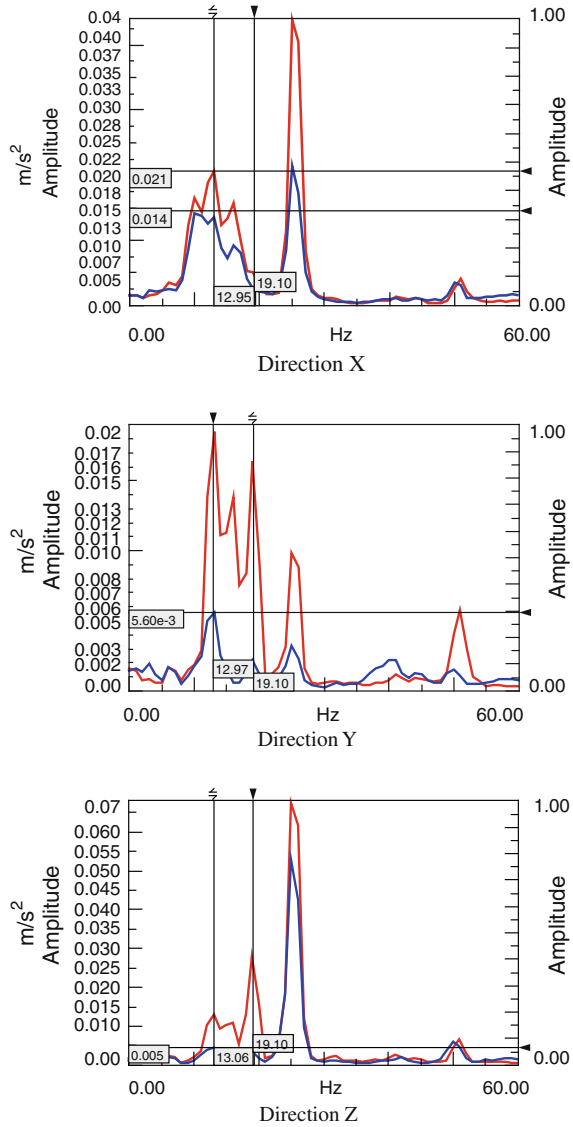
Mount installation angle and mount rates are not sensitive parameters to improve the decouple rate, and these values stay unchanged during optimization.

3.3.3 Optimization Result

3.4 Mount Optimization Improve the Vibration Considerably

Figure 6.

Fig. 6 Seat vibration before and after mount optimization with measured inertial parameter



3.5 Analysis

Mount stiffness and mount installation angle adjustment is enough to attain a high decouple rate, and no demand is necessary for changing mount location, when Optimization process applied is design situation [Shown in (Tables 5, 6, 7, 8)] (Tables 9, 10).

Table 5 Mount location before and after optimization (In Vehicle Coord.)

Location before optimization (mm)	X0	Y0	Z0
Engine_MT	-610.5	500.4	415
Trans_MT	-518.38	-396.35	304.9
Rear_MT	-180	-85	135
Front_MT	-836.78	-88	56.7
Location After optimization (mm)			
Engine_MT	-613.5934	500.4	415
Trans_MT	-518.38	-396.35	304.9
Rear_MT	-180	-85	135
Front_MT	-836.78	-88	56.7

Table 6 Mount angle before and after optimization (In Vehicle Coord.)

Angle before optimization (deg)	ui			vi			wi		
Vehicle coord.	x	y	z	x	y	z	x	y	z
Engine_MT	0	90	90	90	0	90	90	90	0
Trans_MT	0	90	90	90	0	90	90	90	0
Rear_MT	30	90	120	90	0	90	60	90	30
Front_MT	30	90	60	90	0	90	120	90	30
Angle after optimization(deg)									
Vehicle coord.									
Engine_MT	0	90	90	90	0	90	90	90	0
Trans_MT	0	90	90	90	0	90	90	90	0
Rear_MT	5.4	94.5	92.9	87.5	29.7	119.5	85.1	60.7	29.7
Front_MT	26.9	83.6	116.0	90.4	13.3	76.6	63.0	101.6	29.7

Table 7 Mount rates before and after optimization (In Mount Coord.)

Rates before optimization(N/mm)	Ku*	Kv*	Kw*
Engine_MT	217.5	217.5	259.5
Trans_MT	100.5	465	253.5
Rear_MT	180	60	115.5
Front_MT	180	36	135
Rates after optimization(N/mm)			
Engine_MT	113.1463	217.5363	259.581
Trans_MT	100.3757	464.9501	253.537
Rear_MT	179.8366	59.8492	112.3997
Front_MT	179.9369	35.735	133.4365

However, mount stiffness and mount installation is no longer sensitive in improving decouple rate for the measured situation, and the only valid way is focused on mount location shift [Shown in Tables (11, 12)]. To get an optimal value of TRA decouple rate, measurement like re-design of mount location arrangement have to be taken. It is proper to move the engine mount ahead as well as lower the location of the very mount.

Table 8 Mounting subsystem modal & decouple rate before and after optimization (In TRA Coord.)

6DOF	X_TRA	Y_TRA	Z_TRA	RX_TRA	RY_TRA	RZ_TRA
Frequency and decouple rate before optimization						
Freq. calc. (Hz)	8.3	9.0	10.1	15.3	13.6	12.0
Decouple rate (%)	83.9	85.1	99.4	85.3	57.1	66.7
Frequency and decouple rate after optimization						
Freq. calc. (Hz)	8.1	9.1	9.8	15.3	12.0	11.0
Decouple rate (%)	83.9	83.9	88.9	85.2	89.6	83.9

Notes RY_TRA is parallel to TRA, the corresponding decouple rate is most important

Table 9 Mount displacement constraint (In Vehicle Coord.)

Mount displacement	X0	Y0	Z0
Engine mount	[-6, 6 cm]	0	[-6, 6 cm]
Transmission mount	[-6, 6 cm]	0	[-6, 6 cm]
Rear mount	0	0	0
Front mount	0	0	0
Mount angle	Around x [0, 360°]	Around y [0, 360°]	Around z [0, 360°]
Mount stiffness	Stiffness vary allowance [-200, 200 N/mm]		

Table 10 Frequency constraint (In TRA Coord.)

Degree of freedom	X_TRA	Y_TRA	Z_TRA	RX_TRA	RY_TRA	RZ_TRA
Freq. lower limit (Hz)	7	7	8	8	8	8
Freq. upper limit (Hz)	13	15	11	18	12	18

Table 11 Mount location before and after optimization (In Vehicle Coord.)

Location before optimization (mm)	X0	Y0	Z0
Engine_MT	-610.5	500.4	415
Trans_MT	-518.38	-396.35	304.9
Rear_MT	-180	-85	135
Front_MT	-836.78	-88	56.7
Location after optimization (mm)			
Engine_MT	-658.5518	500.4	355
Trans_MT	-514.6199	-396.35	295.2998
Rear_MT	-180	-85	135
Front_MT	-836.78	-88	56.7

Table 12 Mounting subsystem modal and decouple rate before and after optimization (In TRA Coord)

6DOF	X_TRA	Y_TRA	Z_TRA	RX_TRA	RY_TRA	RZ_TRA
Frequency and decouple rate before optimization						
Freq. calc. (Hz)	8.1	9.0	9.8	18.0	12.1	15.3
Decouple rate (%)	83.4	89.6	94.9	82.1	68.4	86.7
Frequency and decouple rate after optimization						
Freq. calc. (Hz)	8.4	9.1	9.8	17.4	11.9	15.1
Decouple rate (%)	81.8	85.4	88.5	81.8	82.2	88.8

Notes RY_TRA is parallel to TRA, the corresponding decouple rate is most important

4 Summary

In this paper, we focused on the problem of abnormal low-frequency vibration in the driveline. Under the premise to avoid the engine itself, optimization method for the mounting system is proposed. Through optimizing rigid body modal frequencies as well as rigid mode decouple rate of the mounting system, it is efficient to enhance vibration isolation and reduces engine vibration passes to the seat.

The accuracy of measured TRA location affects the powertrain decouple rate largely. In other words, whether the line connection between engine mount and transmission mounts parallel to the TRA is crucial to increase the decouple rate. In the above premise, adjustment of installation angle of the rear mount and front mount is enough to get a high decouple rate. Otherwise, unless installation location adjustment is applied for engine mount and transmission mount, it will be a futile effort.

References

1. Ningbo Tuopu Vibro-Acoustics Technology Co., Ltd (2009) Calculation report for the powertrain mounting subsystem. Issue date: 16 May 2009
2. Jeong T, R Singh (2000) Analytical methods of decoupling the automotive engine torque roll axis. *JSound Vibr* 234(1):85–114
3. 朱石坚 施引, 利用加速度FRF的质量控制区段求测刚体质量分布特性, 测试设备与技术, 1994-10-25
4. MATLAB—Documentation, www.mathworks.com/help/techdoc/

Study on Influence of High-Performance Acoustic Materials on a Vehicle's NVH Performance

Yang Yue, Qiang Liu, Yu Xie, Meng Zhang and Fuquan Zhao

Abstract The application of acoustic materials is not only an important method of improving NVH performance of vehicle, but also the main work of acoustic packaging. The improvement effect of high-performance acoustic materials on vehicle NVH performance is discussed in this paper. Through experimental data this subject research different influence on NVH performance with three type material, including acoustical material, acoustic insulating material and damping material, and with variety of material or different specification, so that will helpful for selection material. Two solutions of different materials are obtained based on different application positions and materials combination. And then the effect is evaluated on the vehicle. The effects of two solutions are compared with the original vehicle's performance. The influence of material performance and application position difference on the NVH performance of vehicle body is also studied. The objective of this study is to provide reference for development on performance of material package.

Keywords NVH performance · Acoustic materials · Acoustic packaging

F2012-J05-013

Y. Yue (✉) · Q. Liu · F. Zhao
Zhejiang Geely Automobile Research Institute Co., Ltd, Hangzhou, China
e-mail: yueyang@rd.geely.com

Y. Xie · M. Zhang
Tianjin Haicheng Industry & Trading Co., Ltd, Tianjin, China

1 Introduction

Noise, vibration and comfort is a comprehensive technical indicators to measure the level of modern car manufacturing, especially for passenger car, interior noise condition is one of the important criterion to measure the grade and brand of car. The NVH performance of vehicle body improved through the active control and passive control [1], active control is to control from the source of noise, including improving the machining accuracy and assembly quality of each component, improving engine structure, improving body structure and so on; passive control is to control from car body. Acoustic packaging as the primary means of car passive noise reduction, play a crucial role in vehicle NVH performance improvement. The core of acoustic packaging technology is the application of acoustic material [2], and the material application level largely determines the effect of acoustic packaging [3, 4]. About the improvement of material on interior noise, has had related documents study on this at home and abroad [5–8]. The paper focuses on the acoustic performance of damping material, sound-absorption material and sound insulation material, and acoustic effect of the related parts, the influence of material type and application position difference on NVH performance of vehicle body.

2 Performance of Damping Material

According to the method specified in GB/T 18258-2000 standard (test metal plate is 0.8 mm thickness steel plate), test structural damping factor of damping material in different temperature range. Study the impact of different structure, different material on damping performance.

2.1 Performance of Variety of Damping Material

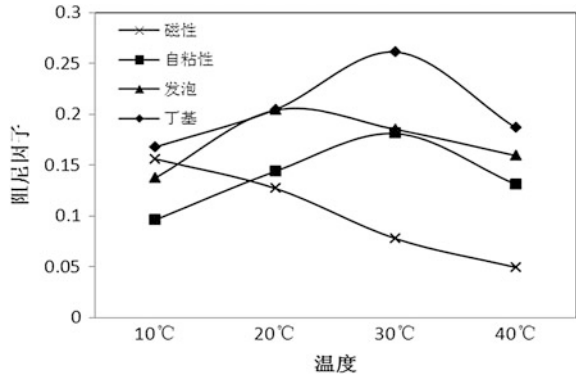
Examine the damping performance of different kinds of vehicle damping material. The specifications of specimens are as follows:

1. Asphalt base damping material with magnetic, thickness 2 mm;
2. Asphalt base damping material with self-adhesion, thickness 2 mm;
3. Asphalt base damping material with expanding foam, thickness 2 mm;
4. Butyl rubber damping material, thickness 2 mm;

Damping factor curve of four kinds of material (see Fig. 1).

Through the damping factor curve of variety of material in Fig. 1, it can be seen that the damping performance of asphalt base damping material with magnetic is relatively poor, its damping performance didn't play in a reasonable temperature range, this is due to the large amounts of iron magnetic particle which is caused by

Fig. 1 Damping factor curve of four kinds of material



magnetic bituminous material contains large amounts of iron magnetic particle, occupied the content of the additives. The peak temperature and range of damping performance for self-adhesive bituminous material, asphalt foam material and butyl damping materials are relatively appropriate, but judge from the size of damping absolute value, the peak value of damping factor for butyl rubber damping material can reach more than 0.25, damping performance is relatively excellent. The peak temperature of damping for damping material with expanding foam also can reach more than 0.2, and its damping performance is better than asphalt base damping material with self-adhesion. Thus choose butyl rubber damping material as acoustic packaging of vehicle body.

2.2 Performance of Different Structure Damping Material

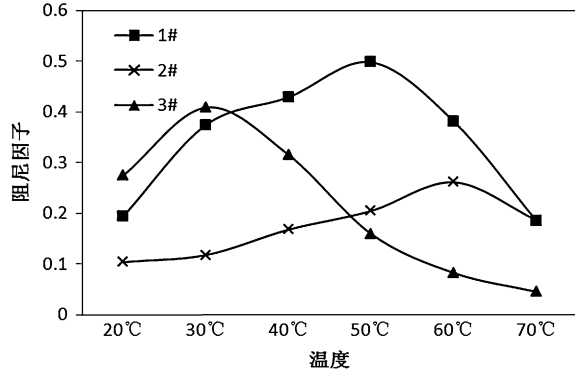
Examine the damping performance of different structure vehicle damping material; the specifications of specimens are as follows:

1. High stiffness of the composite damping material (petroleum resin 2 mm + epoxy resin 0.2 mm + Hot melt asphalt 2 mm);
2. High stiffness of the composite damping material (petroleum resin 2 mm + Hot melt asphalt 2 mm);
3. Asphalt base damping material with expanding foam, with 3 mm thickness.

Damping factor curve of three samples (see Fig. 2).

As shown in Fig. 2, the peak temperature range of damping factor for high stiffness composite damping material is higher than monolayer material. The main reason is the massive existence of petroleum resin in high stiffness composite damping material, that makes the temperature of whole glass transition surface promoted; From the high-stiffness composite material with or without adhesive middle layer damping factor curve, shows that the use of adhesive have a significant impact on composite damping factor value. Due to the existence of adhesive,

Fig. 2 Damping factor curve of three samples



improved the bond strength between two layers of petroleum resin and asphalt material, allow petroleum resin constraint level to play its role to the full, thus increased the shear consumption of the vibration energy. For the practical application, as the body floor is effected by external factor such as powertrain and surface temperature in the running process of vehicle, the surface temperature will higher than inside. Therefore, the application of high-stiffness composite damping material in body floor area, make the damping effect of sheet metal more apparent.

3 Performance of Sound-Absorption Material

3.1 Performance of Different Fiber Sound-Absorption Material

Measured and compared with sound absorption coefficient of variety of fiber sound-absorbing material, examine the level of sound-absorbing performance.

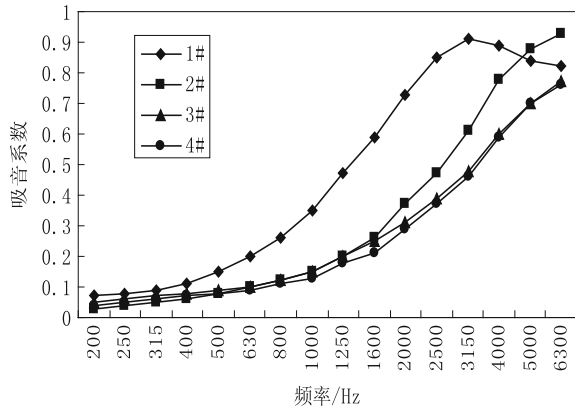
Test instrument: B&K Model 4206 (Impedance Measurement Tube with 2 sensor).

Test standard: ASTM E1050.

The size of test sample is each piece of disc-type specimen with 99 and 29 mm diameter. The 99 mm diameter sample used for sound absorption curve of test material on the low-frequency (125–1600 Hz) noise, The 29 mm diameter sample used for sound absorption curve of test material on the high-frequency (500–6300 Hz) noise. The full frequency sound absorption curve of material is fitted by the two curves.

To compare with sound-absorbing performance of PET + PP fiber, PET + PP fiber, PET fiber material and regenerated fiber with same surface density and

Fig. 3 Sound-absorbing curve of variety of fiber material



different thickness, test the sound-absorbing coefficient of four kinds of material. Test sample:

1. PET + PP fiber (surface density 200 g/m², thickness 26 mm);
2. PET + PP fiber (surface density 200 g/m², thickness 13 mm);
3. PET fiber (surface density 350 g/m², thickness 10 mm);
4. regenerated fiber (surface density 400 g/m², thickness 10 mm).

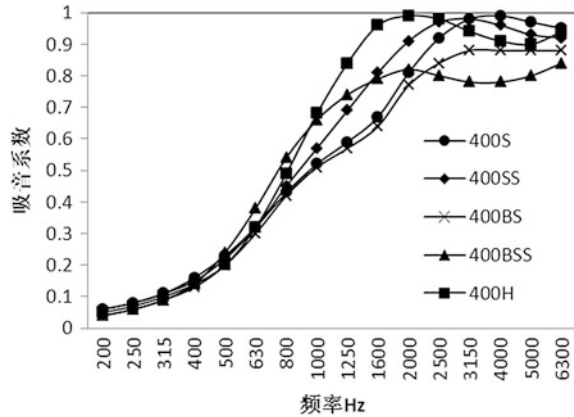
The test result of sound-absorbing coefficient, as shown in Fig. 3:

With Sound-absorbing coefficient curve analysis in Fig. 3, for PET + PP fiber with same surface density, the sound-absorbing coefficient increases with the increasing of material thickness. Due to the increasing of thickness that makes the obstacle of sound waves through material enhanced, and the acoustic energy consumption on materials increased, so that the material sound-absorbing performance is strengthened. Besides, compared with sound-absorbing curve of PET + PP fiber, PET fiber and regenerated fiber, PET + PP fiber shows greater sound-absorbing effect at smaller surface density. The sound-absorbing coefficient for PET + PP material with 200 g/m² surface density is higher than PET fiber with 350 g/m² surface density and regenerated fiber with 400 g/m² surface density. The application of PET + PP fiber material in vehicle can not only ensure good sound-absorbing effect, but also conducive to the lightweight of the vehicle acoustic interior; Compared PET fiber with 350 g/m² surface density with regenerated fiber with 400 g/m² surface density, their sound-absorbing curve are similar, just the sound-absorbing performance for PET fiber is slightly better than regenerated fiber. So select PP + PET fiber as acoustic packaging of vehicle body.

3.2 Performance of PP + PET Fiber Material

Research the effect of process surface and surface density on sound-absorbing performance of PP + PET fiber material, and select the best material.

Fig. 4 Sound-absorbing curve for fiber material with variety of process surface



1. PET + PP fiber, surface density 400 g/m², single sided non-woven(400S);
2. PET + PP fiber, surface density 400 g/m², double sided non-woven(400SS);
3. PET + PP fiber, surface density 400 g/m², single sided black non-woven (400BS);
4. PET + PP fiber, surface density 400 g/m², double sided black non-woven (400BSS);
5. PET + PP fiber, surface density 400 g/m², double sided embossed non-woven (400H);

The test result of sound-absorbing coefficient, as shown in Fig. 4:

With sound-absorbing coefficient curve analysis in Fig. 4, different process surface of PP+ PET fiber material have their advantages for noise-absorbing performance of different frequency band. In the frequency band of below 1000HZ, the sound-absorbing performance for double sided black non-woven PP + PET fiber material is the best. The main reason is the surface density of black non-woven material is higher than other non-woven that can increase the acoustic effect of material on the low frequency noise; in 1000–2500 Hz frequency band, the embossed PP + PET fiber material has excellent sound-absorbing performance. You can see that embossed surface gives a special structure to material surface, and this structure has significant effect for the absorption of frequency noise. In the frequency band of above 2500 Hz, the sound-absorbing performance of single sided non-woven PP + PET fiber material is the best. One side without non-woven material state is conducive to high-frequency noise into inside of material; also it plays a greater role in the energy consumption of three-dimensional structure for the high frequency sound energy.

When applied PP + PET fiber in acoustic packaging of vehicle body, should choose different surface process material according to the noise characteristic of applied parts. When the material used to absorb low-frequency noise, then should choose double-sided black non-woven material, such as the engine compartment, the front wall parts and others; When the material used to absorb middle-frequency noise, then should choose double-sided embossed material, such as

floor, wheel covers and others; When the material used to absorb high-frequency noise, then should choose single-sided non-woven material, such as interior panels, ceiling and others.

4 Performance of Sound-Insulation Material

According to ISO 140 standard, testing sound-insulation PVB film, and by contrast front windshield glass of sound insulation PVB films with ordinary PVB films, study acoustic performance differences between sound insulation PVB films and ordinary PVB films. Specimens are as follows:

1. Ordinary PVB films windshield, glass/ordinary film/glass thickness: 2/0.76/2 mm;
2. sound-insulation PVB film windshield, glass/sound-insulation film/glass thickness: 2/0.76/2 mm;

Glass sound insulation curve for different film material, see Fig. 5:

From Fig. 5, we can get that sound insulation of acoustic PVB films windshield glass in 1000–4000 Hz frequency range have more obvious advantages than ordinary PVB film. Material sound insulation can reach to 35 dB in this frequency range, the average sound insulation effect increased 2–8 dB. In 3000 Hz or so, its sound insulation is the best; achieve more than 40 dB, sound insulation increased 8 dB. Thus, the acoustic performance of sound insulation films has obvious advantages than ordinary film.

5 Materials Application Effect

5.1 Test

(1) Test vehicles and material program

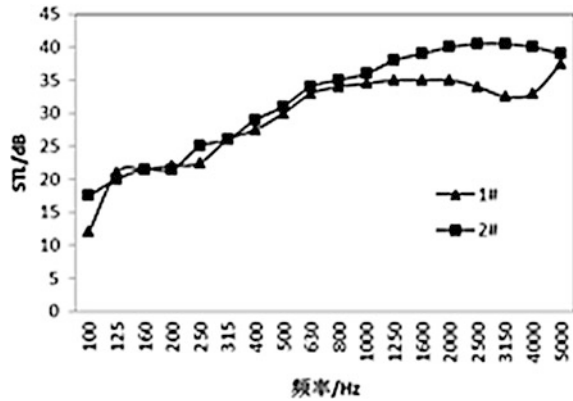
In order to study the improvement effect of acoustic encapsulation material on vehicle noise, select a vehicle as testing vehicle. Firstly, test initial state vehicle's NVH performance, and then disassemble the vehicle, implement and restore the material program in vehicle. To make the test results comparable, before testing, check vehicle sealing performance to ensure the consistency in the state before and after the implementation of material program.

Option one:

Test information is as follows:

B grade model, manual transmission, engine displacement of 2.4L, front wheel drive

Fig. 5 Sound insulation curve of front windshield glass



The application program content of acoustic packaging material:

1. Use hot melt asphalt base damping material (material thickness 2 mm) in the front left, front right, left rear, right rear of the front floor and spare sheet metal parts.
2. Use Butyl rubber damping material in auto doors outboard and front wheel package sheet metal parts. Each one of these auto doors outboard should use two pieces of material in up and down of door beam, the size is 150 mm * 400 mm; and the material size in front wheel package parts is 150 mm * 200 mm, used to weaken local vibration energy.
3. Use PP + PET fiber material with surface density 400 g/m² in lining board, front wall parts. The additional material in lining board is double sided embossed non-woven, used for absorbing middle-frequency noise, and material covers the whole lining board area; The front wall parts material is double sided black non-woven, it with the 2 mm thickness EVA material comprise the front sound-insulation mat, replaced EVA + PU structure sound-insulation mat of the original state of vehicle.

Implement option 1 on the basis of option 2:

1. Use high stiffness of the composite damping material instead of asphalt damping material in the front left, front right, left rear, right rear of the front floor and spare sheet metal parts (petroleum resin 2 mm + epoxy resin 0.2 mm + Hot melt asphalt 2 mm).
2. Use PP + PET fiber material with surface density 400 g/m² in door trim parts, material covers the whole door trim area, replaced regenerate fiber sound-insulation mat of the original state of vehicle.
3. Use sound-insulation front windshield glass to replace ordinary sound-insulation glass at the original state.

(2) Test condition

In order to study the improvement effect of material on NVH performance of vehicle body, testing the vehicle interior noise, the detailed test conditions are as follows:

1. Test vehicle idling noise in the open spaces.
2. Test vehicle uniform noise on the smooth asphalt pavement, the test vehicle's speed is 60, 80, 100, and 120 km/h.

(3) Data acquisition

Test equipment is LMS mobile noise tester, LMS Test.Lab8A software. Placed a microphone in the right ear position of the main driver's seat of car front to collect test data, the sampling frequency is 1.25 Hz, ensure that each microphone placed in the same position and direction each test runs. After the testing acoustic signal is enlarged, recorded by the digital recorder for subsequent analysis and decoding. During the interior noise testing, turn off air conditioning, audio equipment and all the window glass, so as to minimize the impact of other factors on interior noise. In each condition, all collected four sections of independent data and each acquisition time is 15 s. If there is other noise interference in the data collection process, then the collection data will be cancelled and need recollect. The collection of data signal after spectrum analysis to draw the curve of the frequency and decibel values, all acoustic sound pressure level measured values are A-weighted.

5.2 Test Result and Analysis

(1) Sound Pressure Level in Prototype Idling Condition

Figure 6 shows the driver's right ear sound pressure level contrast of the original state vehicle and in idle state; Fig. 7 shows that after the implementation program 2 on the basis of program 1, the driver's right ear sound pressure level in idle state.

After the implementation of program 1, the driver's right ear sound pressure level decreased about 1.5 dB (A), thus it can be seen that program 1 has a significant improvement. The figure shows that the decrease relatively in low frequency range below 200 Hz and the reason is the main source for vehicle idling noise is the engine and powertrain, low frequency high energy. The good damping performance of butyl damping material effectively weakened the noise of low-frequency noise. Besides, the application of damping material on the floor and wheel cover parts can not only reduce the vibration noise of sheet metal, but also the large surface density can play a certain sound insulation effect, by cutting off the entering of powertrain noise into car from this part. But the excellent sound absorption performance of PP + PET fiber material in the middle and high

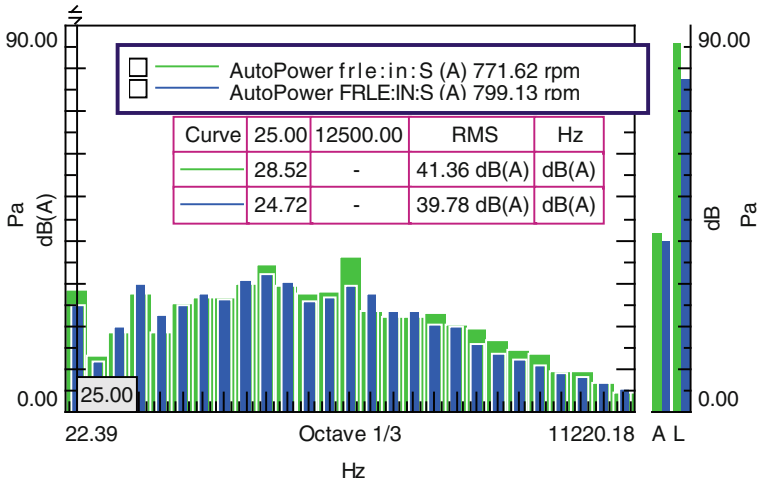


Fig. 6 Comparison of driver’s right ear sound pressure level (option 1)

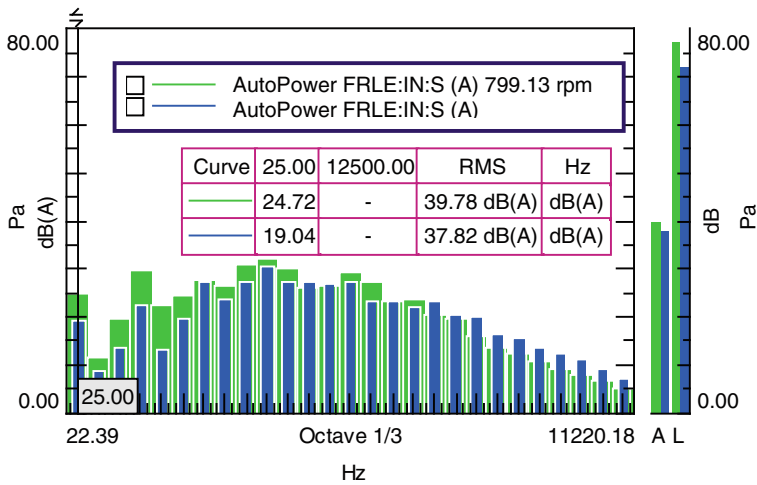


Fig. 7 Comparison of driver’s right ear sound pressure level (option 1)

frequency band can effective weaken the middle and high frequency part in sound pressure level.

The implementation program 2 on basis of program 1 make the vehicle’s sound pressure level decrease about 2 dB(A).The figure shows that program 2 decline is particularly evident in the center frequency of below 300 Hz, which is contributed by the application of high stiffness damping material. In addition, in 1000–4000 Hz frequency range, the sound pressure level data also has certain decline; this frequency range is coupled with the sound insulation PVB films.

Table 1 Comparison of driver's right ear sound pressure level (option 1)

Constant speed condition (km/h)	Origin vehicle dB (A)	Modified vehicle dB (A)	Improvement dB (A)
60	59.78	57.44	2.34
80	62.35	60.88	1.47
10	65.47	63.75	1.72
120	68.40	66.71	1.69

Table 2 Comparison of driver's right ear sound pressure level (option 2)

Constant speed condition (km/h)	Origin vehicle dB (A)	Modified vehicle dB (A)	Improvement dB (A)
60	57.44	55.67	1.77
80	60.88	59.94	1.06
100	63.75	63.37	0.38
120	66.71	66.20	0.51

(2) Sound Pressure Level in Vehicle Constant Speed Condition

The test data in Table 1 shows that the driver's right ear sound pressure has a certain reduction in constant speed range 60–120 km/h. The application of acoustic packaging can obviously improve the driver's right ear sound pressure in constant speed 60 km/h condition, and the improvement is 2.34 dB (A). With the uprising speed of vehicle, the improvement effect of sound pressure level is gradually reduced. When the speed reaches 120 km/h, the improvement of sound pressure level reduces to 1.69 dB (A). In addition to powertrain, tyre and wind also makes a significant contribution to noise in constant speed condition. The noise improvement in vehicle constant speed condition mainly originates from the application of the PP + PET fiber material in material program.

Table 2 shows, after the implementation of program 2, the driver's right ear noise sound pressure level have a further reduction, but decreased degree reduced. The further reduction of vehicle sound pressure level is mainly contributed by the application of sound insulation PVB films windshield and PP + PET fiber in the door trim panels; And sound insulation film has a weaken effect on wind noise in the running process of a vehicle. Besides, because the door area is relatively large in the interior parts, the application of PP + PET fiber material further increases the sound absorption area of car reverberation space, thus the middle and high frequency sound pressure level decreased in a certain degree. However, because program 1 has a significant impact on the reduction of full frequency sound pressure level, and the reduction of interior noise is limited, thus the improvement result of program 2 is less obvious than program 1.

6 Conclusion

By comparing the performance of different types and structure of damping material, butyl rubber has better damping performance than other material in single-component material; but for composite damping material, high stiffness damping material is suitable for the application in automobile body floor. By comparing the performance of different types and surface of fiber sound-absorbing material, PP + PET material with double-sided black non-woven has the best low-frequency noise absorption performance; embossed non-woven material has the best middle-frequency noise absorption performance; PP + PET material with single-sided non-woven has the best high-frequency noise absorption performance. Through analysis and evaluate the improvement of acoustic packaging material program to the improvement effect of vehicle interior noise, high-performance acoustic material has a remarkable result. After applied the material, the decrease of sound pressure level in idling and constant speed condition is more than 3 dB (A), and up to more than 4 dB (A). In future, during the application of vehicle acoustic packaging material, the in-depth study in correlation of vehicle noise spectral characteristics and material program is meaningful.

References

1. Miki Y (1990) Acoustical properties of porous materials—modifications of Delany-Bazley models. *J Acoust Soc Japan* 11(5):19–25
2. Bosch (2007) *Automotive handbook*. Robert Bosch GmbH, Germany, pp 950–951
3. Harrison M (2009) *How to Make the Car to be Good QualityAutomobiles Noise and Vibration Control* [M]. Beijing: China Machine Press
4. Xing shikai,Wen desheng,Pan jingsheng (2003) Research on the Reduction of Car Interior Noise [J]. *Noise and Vibration Control* 23(4):28–30
5. Saha P (2002) Application of noise control materials to trucks and buses. In: SAE paper 2002-01-3063
6. Charles T, Polce III, Saha P, James A (2003) Groening, ray schappert. A data analysis approach to understand the value of a damping treatment for vehicle interior sound. In: SAE paper 2003-01-1409
7. Sophiea D, Kathawate G (1997) Performance benefits of a new spray applied automotive damping material. In: Presented at the IBEC automotive body materials conference
8. Sophiea D, Xiao H (1999) A New light weight, high performance, spray applied automotive damping material. In: SAE paper 1999-01-1674

The Identification and Countermeasure Analysis of Vehicle Idle Vibration

Ye Zhang, Hui Wang, Qingjun Zhu, Yanghui Xu
and Lie Wu

Abstract The Automotive industry of China is at big rapid development stage, each independence domestic OEM have paid more attention to independent brand vehicle, especially passenger vehicle development. As increasing of vehicle comfortableness requirement from the customer and technology input from domestic OEM, the vehicle Noise, Vibration, Harshness (NVH) performance has be regarded as one important symbol which reflects internal performance quality and outside characters, and taken more and more attention. The idle vibration is one common problem in independent brand vehicle development, because this issue is related to the powertrain system, powertrain mounts system, trimmed body system, steering wheel—steering column—Cross car beam (CCB) system etc., the control is very difficult.

Keywords Idle vibration · Control mechanism · Frequency distribution · Powertrain mounts · Trimmed body

1 The Control Mechanism of Idle Vibration

There are two aspects which are the basic control mechanism need to be considered, one is how to as much as reduce the transfer load from the powertrain to the body by mounts system. The other is how to as much as reduce the vibration transfer function (VTF) from the mounts to the steering wheel and seat rail.

F2012-J05-014

Y. Zhang (✉) · H. Wang · Q. Zhu · Y. Xu · L. Wu
Beijing Automotive Technology Center, Beijing, China
e-mail: zhangye@beijing-atc.com.cn

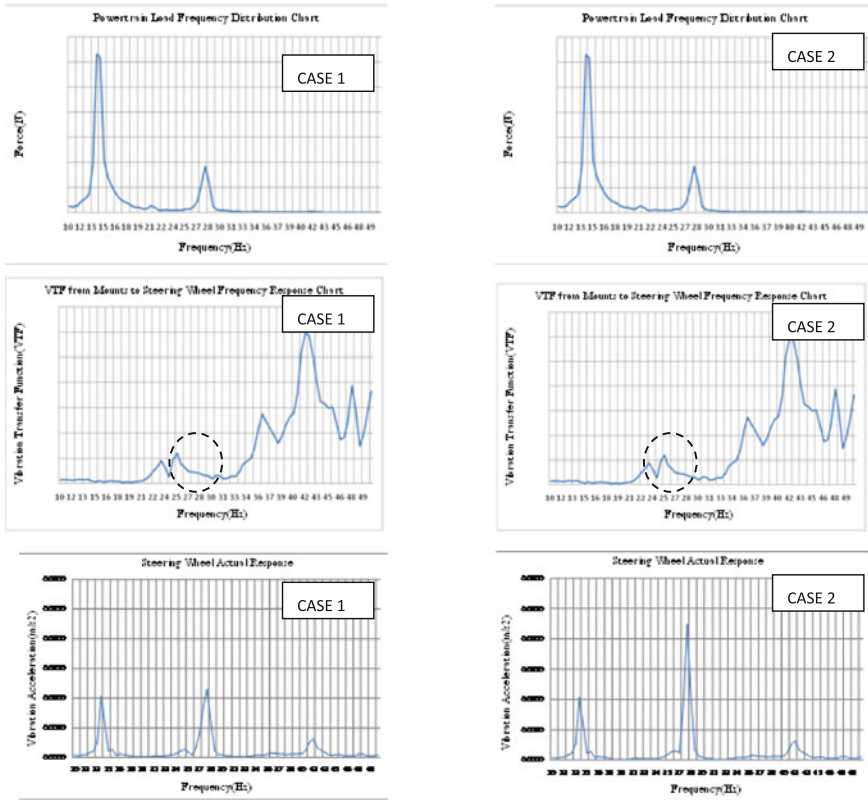
$$a_{jb} = \sum_{l=1}^n \left(\sum_{a=x,y,z} F_{ia} \times VTF_{iajb} \right) \quad (1)$$

a_{jb} : the acceleration response of point j direction b (m/s^2); F_{ia} : the load force of point i direction a (N); VTF_{iajb} : the vibration transfer function from point i direction a to point j direction b ($m/s^2/N$). The formula means the vibration response is the load force of each driver point and each direction products the VTF from the driver point to the response point. If want to reduce the vibration acceleration of response point, the following three aspects need to be controlled.

1.1 Logically Distribute the Sparking Frequency and Subsystems Inherent Frequency in the Transfer Road

For four cylinder engine vehicle, the main force of idle is the 2nd order harmonic force (20–40 Hz) caused by the unbalance inertia force and the fluctuating of air pressure torque [1] and 1st order harmonic force caused by crank unbalance (10–20 Hz) (See Picture 1 Powertrain load distribution). There are several subsystem modes in the transfer road from powertrain mounts to steering wheel, include trimmed body 1st swing mode, trimmed body 1st bending mode, steering wheel 1st swing mode, steering wheel 1st vertical mode, those mode will produce related response peak in the VTF frequency response curve (See Picture 1-powertrain mounts to steering wheel VTF frequency response curve). Logically distribute the sparking frequency and subsystems inherent frequency in the transfer road, when the powertrain idle speed is decided, the sparking frequency is fixed. So the design of subsystems inherent frequency, on the one hand, need to be apart from the sparking frequency, on the other hand, the inherent frequency of each subsystem need to be away one another. If the frequency is overlap between sparking source and subsystem, the result is vibration response at that frequency will magnify obviously. Just like Picture 1, considering the 2nd order frequency of idle speed is at 27.5 Hz, if the trimmed body 1st bending mode is 25 Hz, from the vibration response point of view, the amplitude is very low, but if put trimmed body mode to 27.5 Hz, the amplitude is one time more than original.

Considering the increasing of vehicle fuel economy and vehicle durability requirement and new body technology application, the idle speed of engine is reduced, and the stiffness of body is enhanced. Just due to this trend, the mode map in allusion to vehicle idle performance is changing (See Picture 2), the 1st order frequency of trimmed body is changed from under the idle frequency to above it, usually set it above 28 Hz, and the 1st order frequency of steering wheel on vehicle is increased to above 35 Hz, and even above 40 Hz.



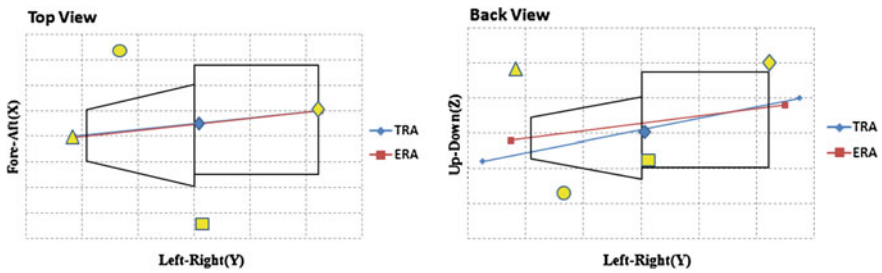
Picture 1 The steering wheel influence contrast figure of distribution the sparking frequency and subsystems inherent frequency

1.2 Reduce Transfer Load from Powertrain to Body

The powertrain mounts is the key control parts to reduce the load and vibration from powertrain to body, its design quality will influence the NVH performance of vehicle idle load case, key on and key off load case, and acceleration and deceleration load case, etc. For idle small movement load case and four points mounts system(left and right mount bear the weight, front and rear mount to control the movement of engine torque), the position of left and right mount elastic center point need to be especially controlled, the preload of front and rear mounts and mode distribution and decoupling.



Picture 2 The mode map of main subsystem in the transfer road



Picture 3 Logically distribute powertrain torque axle and elastic axle

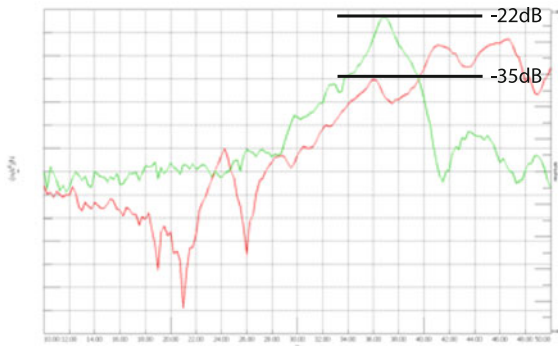
1.2.1 Logically Design Powertrain Torque Axle and Elastic Axle

If imagine the powertrain is supported on “very soft spring”, when input torque on the center line of crank, powertrain will rotate along one axle, this axle is defined torque axle (TRA). When the elastic center points of mounts are put on the TRA axle, the load from powertrain to body will be reduced [2]. If powertrain is supported on mounts system, when input static torque on the center line of crank, powertrain will rotate along spacial axle, this axle is called elastic axle(ERA) [3]. Adjust mounts stiffness, the TRA and ERA can be close each other, this will reduce the preload of front and rear mount, enhance the mode decoupling, powertrain will not be restricted by mounts, and not produce redundant load. The distribution of the elastic center point of mounts, torque axle and elastic axle showed in Picture 3 is reasonable.

Table 1 Logically distribute powertrain rigid mode and requirement of mode decoupling

Mode distribution and decoupling map						
Freq	Fore/Aft	Lateral	Bounce	Roll	Pitch	Yaw
5.7	0.0	100.0	0.0	0.0	0.0	0.0
7.2	1.7	0.2	91.4	3.0	3.5	0.2
8.3	84.4	0.0	0.3	0.4	6.9	8.0
10.5	5.0	0.0	2.0	5.0	86.4	1.6
12.2	1.4	1.2	4.6	91.6	0.8	0.4
13.5	1.2	0.0	0.0	2.4	6.4	90.0

Picture 4 VTF from mounts to steering wheel contrast figure



1.2.2 Logically Design Powertrain Rigid Mode and Decoupling

There are six rigid modes of Powertrain and Mounts system, the frequency distribution and mode decoupling of those six modes are very important to avoid mode resonance and reduce the transfer load from powertrain. The rigid modes of four cylinder powertrain and mounts system usually are put from 5 to 20 Hz [4]. Among them, the most important two modes are the vertical mode (Bounce mode) and rotate vehicle Y mode (Pitch mode). Considering idle 1st order frequency and, avoid front suspension inherent frequency Bounce mode is controlled around 8–10 Hz, and in order to separate Bounce mode and Pitch mode, Pitch mode is set around 10–12 Hz. Usually the other rigid modes are distributed between 6 and 17 Hz, and the interval frequency is controlled above 1 Hz [5]. The other important factor need to take care is the mode decoupling. The general decoupling requirement for Bounce and Pitch mode is above 90 %, the other mode decoupling is above 80 %. The following powertrain rigid mode distribution and decoupling map shows in Table 1 is reasonable.

1.3 Reduce the Amplitude of Vibration Transfer Function

Logical distribution of the sparking frequency and subsystems inherent frequency in the transfer road is discussed in Sect. 1.1, This is talked about from avoiding structure mode resonance, but considering the inherent frequency of each subsystem always exist, the system stiffness will influence the amplitude on the resonance frequency. Picture 4 shows the VTF from mounts to steering wheel, although, 1st vertical order of steering wheel in two vehicle are both around 36 Hz, but because the amplitude of VTF are different greatly, when the sparking force is same, the actual response will have much difference. So it is also very important for improving idle vibration performance to effectively control VTF and reduce the amplitude.

2 Problem Investigation of Idle Vibration

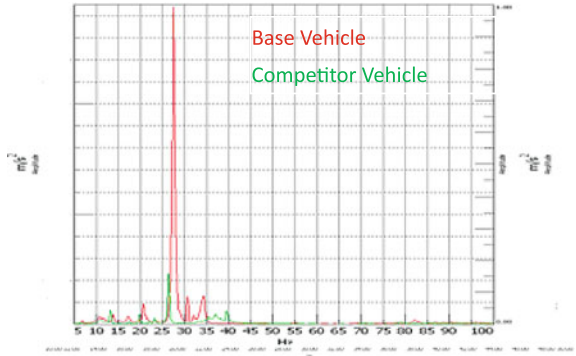
The actual project is based on control mechanism of idle vibration, investigate the problem and propose the count measure. The following is one example to show the draft procedure. Pictures 5 and 6 shows the steering wheel and seat rail vibration acceleration frequency response curve, from the curve, you can see the main different is concentrated on engine 2nd order frequency between base vehicle and competitor vehicle. Because the problem of two transfer roads (road from mounts to steering wheel, and road from mounts to seat rail), powertrain mounts need to be confirmed firstly, and then, the important subsystems in the transfer road need to be checked, and make clear if there are amplificatory structure elements in the transfer road.

2.1 Reduce the Transfer Load from Powertrain to Body

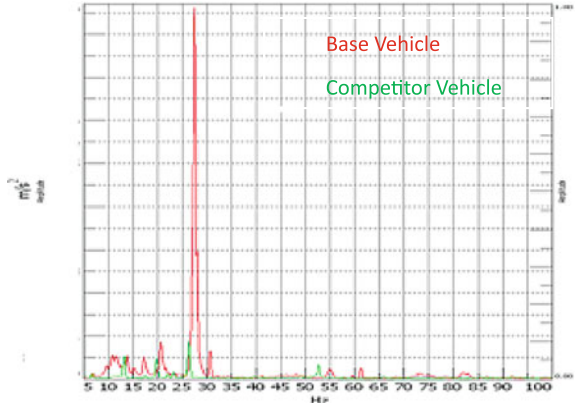
Based on the test result of mass center and inertia moment of powertrain system (include the main accessories), the ideal TRA axle is calculated again, the elastic center of transmission mount is found not on the TRA axle, the difference is 28 mm, and the line between left mount and right mount can not pass through mass center (see Picture 7). After checked the powertrain rigid mode on the base vehicle, the Bounce mode shape is not pure, there is much coupling with Pitch mode (Picture 8).

After calculating the preload distribution of each powertrain mount on the base vehicle, the rear mount has the preload, the preload is 85.9 N (See Table 2). The main reason is the elastic points of left and right mounts are not put on the TRA which cause the preload of rear mounts. If the elastic points are put on the TRA axle, Table 2 shows the preload is very small. In the actual design, the preload of

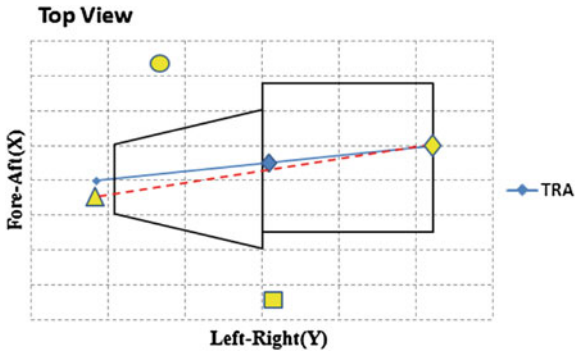
Picture 5 Steering wheel vibration curve contrast



Picture 6 Seat rail vibration curve contrast



Picture 7 powertrain mounts elastic center and TRA contrast



front and rear mount need to be reduced as much as possible, the preload on the one hand will increase dynamic force of front and rear mounts in idle load case, on the other hand, will increase the dynamic stiffness of rubber mounts.

In order to confirm the conclusion above, two sensitivity test are prepared on the base vehicle, include the vehicle test to move the elastic point of transmission mount to the TRA axle and the vehicle test disconnect the rear mount

Picture 8 Powertrain bounce mode shape on base vehicle

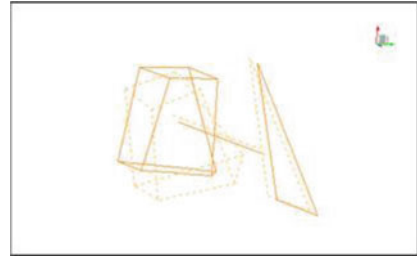
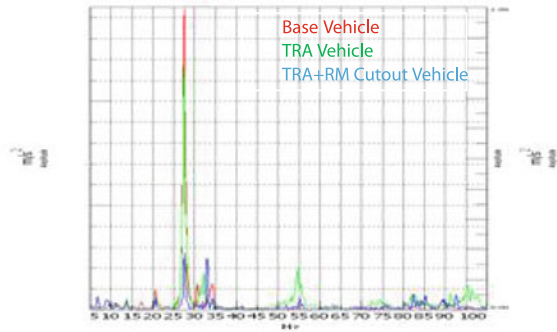


Table 2 Mounts preload distribution contrast

Preload distribution (CAE result) (N)				
PT mounts position	RHM	LHM	FM	RM
Original position	-1200.0	-1417.0	0.7	85.9
TRA position	-1159.0	-1371.0	-1.2	1.0

Picture 9 Steering wheel vibration autopower curve

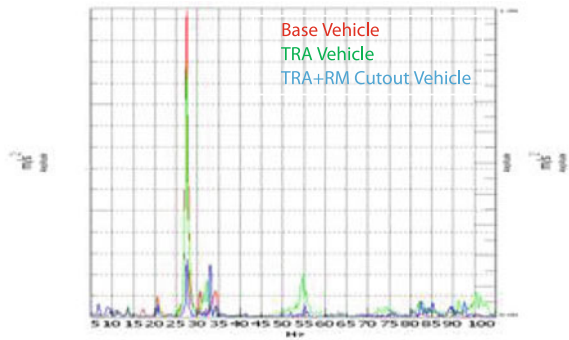


based on that, furthermore, the Pictures 9 and 10 show the problem of original mounts system, and give us two modification direction for the next mounts system design, one is the elastic center of transmission mount need to be put on the TRA, the other is the vertical stiffness of rear mount need to be reduced as much as possible during mount system matching design.

2.2 Logically Distribute the Sparking Frequency and Subsystems Inherent Frequency in the Transfer Road

As reducing the transfer force from Powertrain to body as much as possible, which need to be confirmed if it is reasonable for the distribution of the sparking frequency and subsystems inherent frequency in the transfer path. Considering the

Picture 10 Seat rail vibration autopower curve



idle speed of base vehicle is 825 rpm, the 2nd order frequency is 27.5 Hz, the 1st bending mode of trimmed body is 24.5 Hz, 1st bending frequency is low, but already separated around 3 Hz with idle frequency, from the frequency distribution point of view, this can meet requirement, but because the stiffness is low, maybe have risk on the amplitude of VTF. For 1st order of steering wheel, Table 3 shows the test result on the vehicle, the 1st swing mode is low and close to the sparking frequency, so from the considering the logical distribution the sparking frequency and 1st swing mode frequency and stiffness points of view, the swing mode need to be improved.

3 Count Measure and Result

According to the problem above, the counter measure can be discussed at the beginning of design. Frankly speaking, the control of vehicle vibration need to be considered at the beginning of vehicle development, because the phenomena is related to the package of engine compartment, powertrain mounts, steering system and body structure, if the control is not well done at the design phase, at the vehicle tuning phase, it is very hard to modify.

3.1 Optimize the Elastic Center position of Powertrain Mounts

Re-design the elastic center position of powertrain mounts, put them on the TRA axle as much as possible, reduce the static preload of front and rear mount and the dynamic force from powertrain to body (See Picture 3).

Table 3 Steering wheel 1st order on base vehicle

Steering wheel position	Steering wheel 1st order freq on base vehicle(Hz)	
	1st vertical mode	1st swing mode
Height direction: lowest Length direction: longest	33.5	29.5
Height direction: lowest Length direction: middle	34.0	31.0
Height direction: middle Length direction: shortest	35.0	31.0

Table 4 Base vehicle PT rigid mode and decoupling

Base vehicle PT rigid mode and decoupling result						
Freq	Fore/Aft	Lateral	Bounce	Roll	Pitch	Yaw
6.4	75.3	0.2	13.0	0	11.5	0
7.3	6.8	35.4	18.9	4.1	9.7	25.1
8.0	17.2	26.4	34.8	0	11.3	10.3
11.5	0	20.4	5.5	15.9	11.0	47.2
14.4	0.7	13.1	12.5	14.7	41.6	17.4
15.1	0.1	6.4	13.8	72.2	7.4	0.1

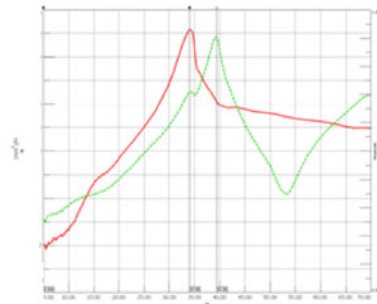
3.2 Optimize the Static and Dynamic Stiffness of Powertrain Mounts

Based on meet the requirement powertrain movement and mounts durability, re-optimize static and dynamic stiffness of powertrain mounts, logically distribute six rigid mode of powertrain and mounts system, enhance the decoupling of mode shape, especially Bounce and Pitch mode, as like the contrast between Tables 4 and 5, the decoupling of Bounce and Pitch mode of new vehicle are much better than the Base vehicle, and the pitch mode is controlled to below 11 Hz, from the separation from the 1st order frequency of engine, the new design is better than base design. As the same time, The ERA axle of new vehicle is closer to the TRA axle and the dynamic force will be reduced greatly. As the same time, when the dynamic stiffness is reduced as much as possible, attenuation of vibration will be enhanced at the idle and acceleration load case.

Picture 11 shows the powertrain transfer load contrast between base vehicle and new vehicle. You can see after the position and stiffness optimization of powertrain mounts system, the transfer load from powertrain to body is greatly reduced.

Table 5 New vehicle PT rigid mode and decoupling

New vehicle PT rigid mode and decoupling result						
Freq	Fore/Aft	Lateral	Bounce	Roll	Pitch	Yaw
6.6	83.6	0.1	3.4	0.1	11.8	1.2
7.4	0.4	82.2	1.2	5.9	1.0	9.3
8.7	3.8	2.4	92.9	0.1	0.6	0.3
10.9	9.9	2.2	0.1	1.9	85.2	0.7
13.0	0.0	9.6	0.7	1.8	0.1	87.8
13.8	0.0	0.2	0.0	92.6	6.0	1.2



Picture 11 a PT mounts transfer load contrast. b Steering wheel frequency response curve

Picture 12 Steering wheel vibration contrast

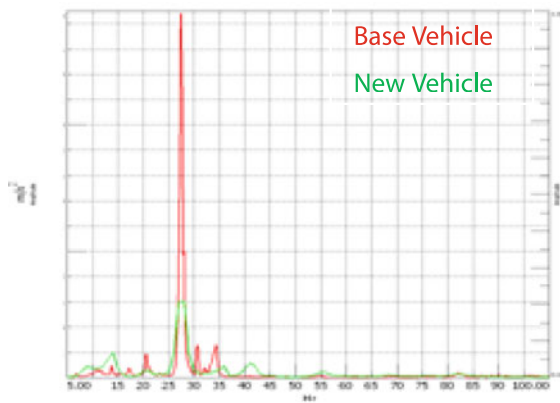


Table 6 Steering wheel and seat rail vehicle vibration contrast

Idle vibration(m/s ² RMS 5–100 Hz)				
Vehicle	Gear	Condition	Steering Wheel	Seat Rail
Target	N Gear	AC-OFF	X,Y,Z RMS <=0.2	Z<=0.03
Base vehicle			0.48	0.10
New vehicle			0.14	0.02

3.3 Enhance the 1st Order of Steering Wheel on Vehicle

After the structure optimization of steering column and cross car beam, the 1st order frequency of steering wheel on vehicle are increased greatly, can meet the 35 Hz requirement of vehicle. Picture 11 shows the swing mode of steering wheel is 35 Hz, and the vertical mode is 39 Hz.

3.4 The Vehicle Vibration Contrast Between Base Vehicle and New Vehicle

By the counter measure above, the vibration of steering wheel and seat rail in idle load case is greatly reduced, Picture 12 shows the steering wheel acceleration frequency response contrast, the amplitude on 2nd order frequency is just 20 % of base vehicle. Table 6 shows the overall target of steering wheel and seat rail, and the contrast between base vehicle and new vehicle, the vibration of new vehicle can meet the target requirement.

4 Limitations and Future Potential Researches

Because the project timing, the body structure can not be modified greatly, so the 1st bending of trimmed body and stiffness is a bit low which need improve. And how to set up vehicle CAE model which include powertrain mounts, Steering system, IP system, suspension system and body system, to accurately predict vehicle idle vibration performance at the design phase of vehicle development will become one important direction in the future potential research.

5 Contribution of Knowledge

This paper analyzes the mechanism and identification method of vehicle idle vibration problem, summarize the important performance requirement of key control subsystems from the source of vibration and transfer paths, which has been applied in engineering project.

6 Conclusions

Vehicle idle vibration phenomenon relates to the matching of many key subsystems. At the beginning of vehicle development, the key factors of key subsystems should be paid more attention. The paper is based on an actual project as an

example, to analyze the mechanism of vehicle idle vibration and show the key control countermeasures. The comparison of test results of the steer idle vibration before and after taking the countermeasures are presented in the paper.

References

1. Wang L, Zhenhua L (2001) A Survey of research and development of hydraulically damped rubber mount of automotive powertrain. *Automot Eng* 23:323–328
2. Brach RM (1997) Automotive powerplant isolation strategies. SAE paper 971942
3. Wu I (2010) The improvement of A SUV vehicle NVH performance. The sixth China and foreign countries automotive design and engineer conference 5–10
4. Seonho C (2000) Configuration and sizing design optimization of powertrain mounting system. *Int J Veh Des* 24(1):34–47
5. Yong H, Tao Z (2007) A study on decoupling design of engine mounting system. *Automot Eng* 29:12

Study on Automotive Interior Structure-Borne Sound Based on TPA

Lingyun Yao and Guangrong Zhang

Abstract *Research and/or Engineering Questions/Objective* The inertia excitation and the unbalanced force is one of main excitation sources, which induce the vehicle interior structure-borne noise. The research on the optimization of the PT mounting system is very common, but the research on how to modify the vehicle panel to reduce the structure-borne noise induced by engine is very few. The paper utilizes CAE technology and transfer path analysis for identifying the main transfer path, and the control of the vehicle interior structure-borne noise excited by engine excitation is well implemented. *Methodology* A new TPA method based on the CAE technology is proposed to analyze the vehicle interior structure-borne noise in present work. This method can implement the control of the vehicle interior structure-borne noise excited by engine excitation through the control of the transfer function of subsystem on the main transfer path. In present method, the finite element method is used to establish the dynamics model of vehicle PT-Body coupled system is establish, and the prediction of vehicle interior structure-borne noise is investigated, then the main transfer path is identified by using TPA method on the basis of subsystem response. Finally, the Panel contribution Analysis (PCA) techniques can be implemented on the structure- acoustic transfer function of body-subsystem in the uppermost transfer path, and the dominant panel contributions can be identified. *Results* This paper considers a problem of micro-car interior structure-borne noise generated by engine excitation. The micro-car is simply treated with a coupled system composed with two subsystems, namely

F2012-J05-015

L. Yao (✉)

China Automotive Engineering Research Institute, mainland, China
e-mail: 19831022y@163.com

G. Zhang

Pan Asia Technical Automotive Center Co., Ltd, mainland, China

body-subsystem and PT-subsystem. In the light of above method, the prediction on vehicle interior structure-borne noise induced by the engine second excitation is obtained. As the main transfer path then is found out. The PCA technology is utilized to analyze the special structural acoustic transfer function. The result shows the main panels are the dash panel and the roof, respectively. The topography technology is applied to optimize the main panel to improve the performance. The result shows the proposed method reduce the vehicle interior structure-borne noise effectively. *Limitations of this study* The vehicle interior structure-borne noise induced by the chassis subsystem is not studied and the chassis transfer path analysis is also not carried out in present work. This paper has not studied the influence due to the error of CAE model. There are some others TPA methods such as Fast TPA, multilevel TPA, presently. These ideas in other TPA methods should be used for reference in present method. *What does the paper offer that is new in the field in comparison to other works of the author* A new TPA method based on the CAE technology is proposed to analyze the vehicle interior structure-borne noise induced by engine excitation in present work. The CAE technology will be introduced to improve the range and effect of TPA. This paper introduces the PCA techniques into TPA method, and synergies the strengths of PCA and TPA methods. The proposed method improves the optimization efficiency compared with classical CAE technology. Compared to the classical TPA, the present method provides the NVH design directions at detailed engineering phase even at the concept phase. *Conclusion* The new TPA method synergies the strengths of CAE and TPA methods, is feasible to analyze the interior structure-borne noise induced by engine excitation. The PCA technology is well applied into the optimization of vehicle interior structure-borne noise. The present method is applicable and can provide broad guidance for interior noise control in the design process.

Keywords Structure-borne noise • Subsystem • Finite element method • The transfer path analysis (TPA) • Optimization

1 Introduction

The NVH performance is one of the important vehicle design targets, and is also the customers concerned vehicle performance. As we all known, the engine excitation is the main excitation sources of the vehicle vibration. The NVH problem caused by engine excitation has always been the focus of the study of domestic and foreign scholars [1, 2]. Literature [3] established the finite element (FE) model coupling the powertrain-subframe system and trim-body system. The frequency response function analyses of subsystem, as well as the sensitivity analysis to optimize the stiffness parameters of the mount system, are implemented

effectively, and the vehicle structure-borne noise caused by engine excitation is well controlled. A nonlinear dynamic model for complete vehicle as an acoustic-structure interaction system is established by using free-interface component modal synthesis for substructures with linear and nonlinear link, and a numerical simulation is performed on interior noise generated by the excitation of engine using the model. The simulation results is verified by test under same conditions [4]. In Literature [5], the automotive powertrain mounting systems was looked as subsystem attached to the body, and the direct quantitative relationships between the interior noise pressure and the stiffness, damping characteristic parameters of elastic mounting components were revealed, and the response surface methodology was used for approximate treatment. For the sake of reducing vehicle interior noise pressure, an acoustic optimization design model was established for well matching of the stiffness and damping parameters of the elastic mounting components. The above-mentioned research work is mainly concentrated on the prediction and control of the vehicle structure-borne noise caused by engine excitation, as well as the mount stiffness sensitivity optimization.

On the basis of the interior structure-borne noise transfer path identification, this paper proposed a novel method to control the interior noise caused by engine excitation by controlling the structure-borne noise transfer function of subsystem. This method firstly utilizes the FE method to establish the dynamics model coupling the PT-body subsystem, and forecast the vehicle interior structure-borne noise generated by engine excitation through the mounting system to the body. The most significant transfer path impacted on the interior noise is identified by the transfer path analysis (TPA) on the basis of the responses of subsystem. According to the vibration and noise mechanism, we can choose the significant transfer path, then the panel contribution analysis (PCA) is implemented on the structure-borne noise transfer function of this path. Through the above-mentioned analyses, the greater influential panels to the interior noise are identified, and the structural modifications to reduce the interior structure-borne noise are proposed by the analysis. So, this method can be used for powertrain-body (PT-body) structure noise transfer path identification at the automotive design and development phase, and provide guidance for interior noise control in the automotive design process.

2 Transfer Path Analysis Method

The vehicle is a complex system, composed of multiple subsystems, such as powertrain, mount, body, etc. The vibration performance of the vehicle is integrated the dynamic characteristics of the various systems, so the sub-structure synthesis techniques can be studied and described the overall performance of the vehicle.

The interior structure-borne noise transfer path analysis method based on frequency response function (FRF), is start from the frequency response function of the sub-structure. The noise and vibration characteristics of the systems are

described in frequency domain, and a quick, effective analysis method is provided to predict the vehicle NVH performance. The proposed method divide the whole system into several independent sub-structures, and each sub-structure dynamic characteristic is described by the substructure frequency response function, respectively; these substructure frequency response functions are assembled to describe the dynamic characteristics of the entire structure [6–10].

2.1 The Subsystem Coupling Based on FRF

The dynamic characteristics of a complex system are composed by the dynamic characteristics of each subsystem, and the subsystem can be formulated by corresponding frequency response function. In general, the frequency response function of a subsystem can be described with the vibration energy transmissions between the excitation points to the specific response points.

Now assume that we composed the subsystem A and subsystem B into a new coupling system C through a flexible connection, and the $[k_S]$ is defined as the flexible coupled matrix, as shown in Fig. 1.

The dynamics equation of the flexible coupling system C

$$\{X_S\} = [H_S]\{F_S\} \quad (1)$$

Where, the vectors $\{X_S\}$ and $\{F_S\}$ are comprised with vectors of responses and exaction vectors comes from the sub-systems A and B, respectively; the $[H_S]$ is the transfer function matrix of system C, then the frequency response function matrix $[H_S]$ of coupled system C can be simplified

$$\begin{bmatrix} [H_S]_{o(a)i(a)} & [H_S]_{o(a)c(x)} & [H_S]_{o(a)i(b)} \\ [H_S]_{c(x)i(a)} & [H_S]_{c(x)c(x)} & [H_S]_{c(x)i(b)} \\ [H_S]_{o(b)i(a)} & [H_S]_{o(b)c(x)} & [H_S]_{o(b)i(b)} \end{bmatrix} = \begin{bmatrix} [H_A]_{o(a)i(a)} & [H_A]_{o(a)c(x)} & [0] \\ [H_X]_{c(x)i(a)} & [H_X]_{c(x)c(x)} & [H_X]_{c(x)i(b)} \\ [0] & [H_B]_{o(b)c(x)} & [H_B]_{o(b)i(b)} \end{bmatrix} \\ - \begin{bmatrix} [H_A]_{o(a)c(a)} \\ \alpha[H_X]_{c(x)c(x)} \\ -[H_B]_{o(b)c(b)} \end{bmatrix} \left([H_A]_{c(a)c(a)} + [H_B]_{c(b)c(b)} + [K_S]^{-1} \right)^{-1} \begin{bmatrix} [H_A]_{c(a)i(a)} \\ \alpha[H_X]_{c(x)c(x)} \\ -[H_B]_{c(b)i(b)} \end{bmatrix}^T \quad (2)$$

Where, x is A and B, when x is A, the $\alpha = 1$. when x is B, the $\alpha = -1$. If the coupled stiffness tends to infinity, the term disappears, and the expression of the flexible coupling system will become the expression of the rigid coupling system.

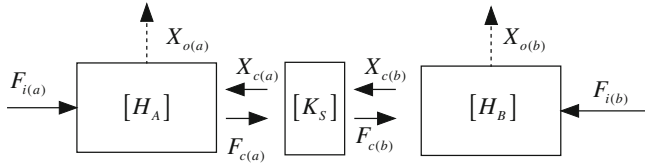


Fig. 1 The flexible coupling system

2.2 The Coupled Excitation

In order to apply the frequency response of the subsystem to the transfer path analysis, the user must know the coupled forces. Take the two adjacent substructures as the example, impose the external excitation in a certain direction and the coupling force between the two substructures appear. If the two substructures are connected by elastic element, then the coupling transfer force is formatted by the elastic element stiffness matrix and the both connection point displacement difference, is defined as

$$f_i = k \cdot (x_i - x_t) \tag{3}$$

where, f_i is the transfer coupled force in the transfer path i . x_i is the displacement of the elastic element input. x_t is the displacement of the elastic element terminals.

2.3 The TPA Based on Subsystem Response

In the transfer path analysis, the excitation source and response points is regarded as two different systems, two subsystems is connected through the coupling element, and each coupling point can be seen as a transfer path. So each transfer path is defined as the vibration energy transmission from the excitation source to the response point. The energy of each path can be expressed as the contribution of the transfer path, and we can obtained the response of target point by superimposing these energy of every path. For example, the engine is connected to the body through three mounts, and each mount has three coupled directions (X-direction, Y-direction, Z-direction), so there are nine transfer paths between the engine and body, each excitation force and the corresponding path can obtain a response component, as shown in Fig. 2.

The vehicle interior noise as the system responses can be defined as

$$p_i = H_i(\omega) \cdot F_i(\omega) \tag{6}$$

where $H_i(\omega)$ is the transfer function between the mount connect point to interior response field; $F_i(\omega)$ is the coupled force transferred from engine to body via

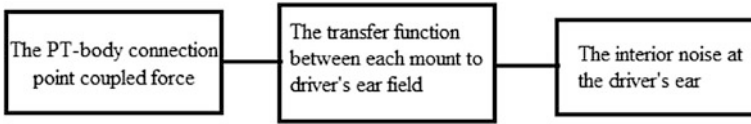


Fig. 2 The TPA functional scheme

mount. The overall interior noise induced by all excitation transferred from the engine can be defined

$$p = \sum_{i=1}^9 p_i = \sum_{i=1}^9 H_i(\omega) \cdot F_i(\omega) \tag{7}$$

Through contrast of the noise contribution of all the paths, we can identify the greatest contribution to the transfer path of interior noise, and find out the reasons of the excessive noise by comprehensive analysis. In order to compare noise contribution of each the transfer path, we defined the formula of average energy of the frequency band. For a frequency-dependent function curve $H(f)$, the formula of average energy of the frequency band is defined as

$$\Pi_r = \frac{\sum_{i=1}^N |H(f_i)|^2 \Delta f}{N} \tag{8}$$

Where Π_r , average energy between the frequencies is ranges $f_1 \sim f_2$; N is the spectral line in assigned frequency ranges. In this way, a single value is obtained to evaluate this frequency response function curves in the specified frequency range contribution.

Now, on the basis of the Eq. (8), we can assess the overall contribution as defined

$$\Gamma = \sum_{i=1}^n \Pi_r(i). \tag{9}$$

3 The Control of Vehicle Interior Noise Based on TPA

This section take the interior structure-borne noise transfer path analysis between the engine mount connection point to the driver’s right ear as example, and introduce the control step of vehicle interior noise based on TPA. The steps can be defined as

1. The response (sound pressure level) at the driver's right ear point is measured and the structure-borne noise transfer functions of three DOFs direction in each mount connect point;
2. Calculating force of each mount connect point;
3. Based on the structure-borne noise transfer functions and connect point of each transfer path, the contribution of each transfer path is analyzed and the main transfer path is identified;
4. According to the Eq. (8), the contribution of each transfer path is calculated and the contribution of each mount is obtained according to Eq. (9).
5. On the basis of the analysis of the transfer path contribution, the PCA is investigated on the main path of noise contribution, then the main influence panel is identified.
6. Choosing the panels which mainly influenced the structure-borne noise transfer function, and reduced the amplitude, then the control of vehicle interior noise is implemented.

4 Applied Example

This section applies the proposed method for a micro car and researches on the control of interior structure-borne noise. The calculation process is introduced as follows.

4.1 The Transfer Path Computation Analysis

As we all known, the Vehicle interior noise has many of transfer paths and the paths generally are complex, and the model should be simplified appropriate combined with the actual situation. This paper views the automobile as a system, and divides the subject into two sub-structures, the vehicle body structure, A, and the powertrain substructure, B, as shown in Fig. 3. The output of the vehicle system is noise pressure of the driver's right ear. These two substructures are connected by various engine mounts, and these mounts transfer the energy from the powertrain to the body, then the body panels vibrates and radiate noise in the interior. The engine mount combined with the left mount, the right mount and rear mount, and each mount has three translational directions (X-direction, Y-direction, Z-direction), so there are nine transfer path in powertrain vibration.

By calculating the structure-borne noise transfer function between the mount connection points to the driver's right ear, as well as the coupling force of mount point, we can obtained the pressure of the driver's right ear. The noise contribution of nine transfer paths between the engine mount connection points to the driver's

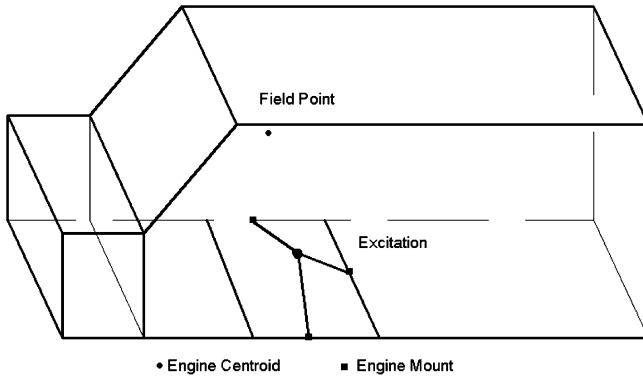


Fig. 3 The simply micro car's TPA model

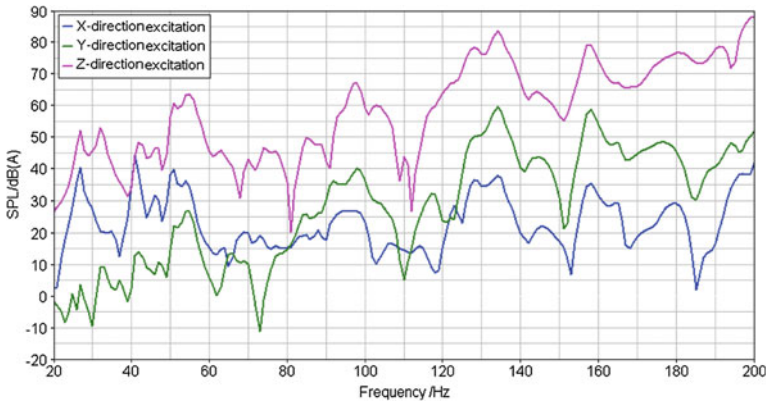


Fig. 4 Right mount X/Y/Z direction transmission path commutation

right ear are calculated, then the main path of noise contribution is identified through the contribution analysis of each transfer path. Figure 4 shows that three noise functions of transfer path in the right mount.

With the analyzing the overall noise pressure level of interior noise, it can be found that A-weighted noise pressure is bigger in the frequency range 100 ~ 200 Hz. So this section research on the frequency band 100 ~ 200 Hz. In this band, we can calculate the noise contribution of each transfer path by utilizing the formula (8), and also calculate the noise contribution of each mount by utilizing the formula (9). The results are shown as in Fig. 5.

According to the transfer path noise contribution analysis, as well as the interior structure-borne noise in 100 Hz-200 Hz frequency range, it can be concluded from Fig. 5 that, the transfer path noise of right mount path is the biggest one in these transfer paths, and the greatest contribution is the Z-direction.

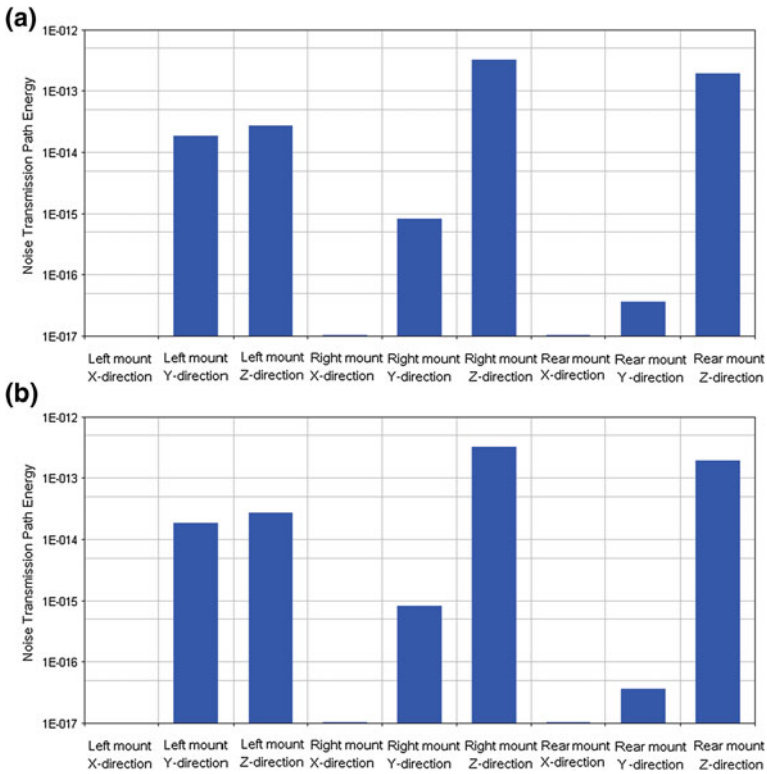


Fig. 5 The noise contribution of the transfer path. **a** Each transmission path computation (100–200 Hz) **b** The noise commutation of three mount transmission path (10–200 Hz)

4.2 Interior Structure-Born Noise Control

According to the transfer path analysis, we can find that the largest contribution of transfer path is the right mount point. The reason is that the transferred coupling force is greater, as well as the structure-borne noise transfer function. We can reduce the structure-borne noise transfer function by reducing the noise contribution of transfer path. On the basis of TPA, as well as select the right mount transfer path, we can implement the panel contribution analysis to identify structure with greater effect to the transfer function. With the panel contribution analysis, the main influence panels are the roof, front floor, dash panel, etc. According to the vibration and noise mechanism, we have chosen to optimize these main influence panels, and some modification is implemented to improve their local stiffness to control its vibration, thereby reducing the noise pressure level of in the interior.

This paper implements the morphology optimization method to modify panel local structure. In this method, the panel thickness and material doesn't change and

Fig. 6 The cross-section of the line type stiffener

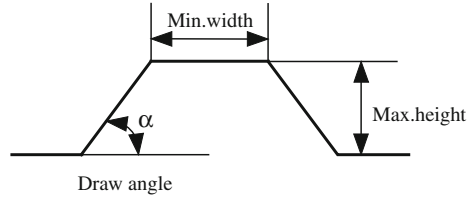
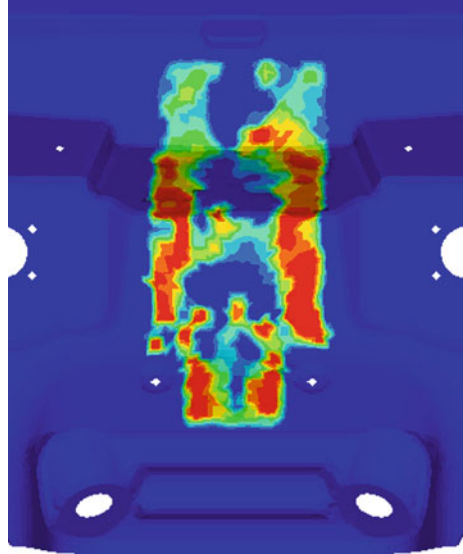


Fig. 7 The cloud map of optimized results for dash panel



the location and the shape and size of stiffeners are optimized according to the fluctuations of the nodes in the design area, thereby increasing the panel stiffness [11]. The optimization objective is the first natural frequency, and the HyperWorks the OptiStruct module are used to optimize the location, shape and the size of stiffener in the body panels. Taking into account the craft, the stiffeners is selected the linear type. The original ribs in the front floor and dash panel are removed, and the stiffeners are redesigned. The minimum width of the redesigned stiffener cross-section is 25; the maximum height of that is 8.5 mm; the draft angle of the cross-section is 60° , as shown in Fig. 6.

As the dash panel taken out and appropriate structure cut out, the 1st constraint mode is optimized in this sub-section. The optimize parameter settings of stiffeners cross-section are shown as previously mentioned. In order to simplify the optimization process, the layout stiffeners arranged on the panel geometry midline symmetry. The optimization the results are as shown in Fig. 7, and the trimmed structure is shown in Fig. 8.

The comparative of three natural frequencies between the origin model and optimized model is shown in Table 1. The comparative results showed that these

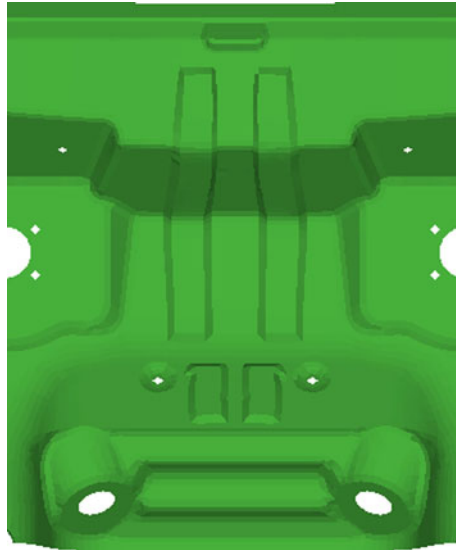


Fig. 8 The optimized structure of dash panel

Table 1 The comparative of three natural frequencies between the origin model and optimized model

Natural frequency	1st	2st	3st
Oral model	119	147	181
The optimized model	194	234	262

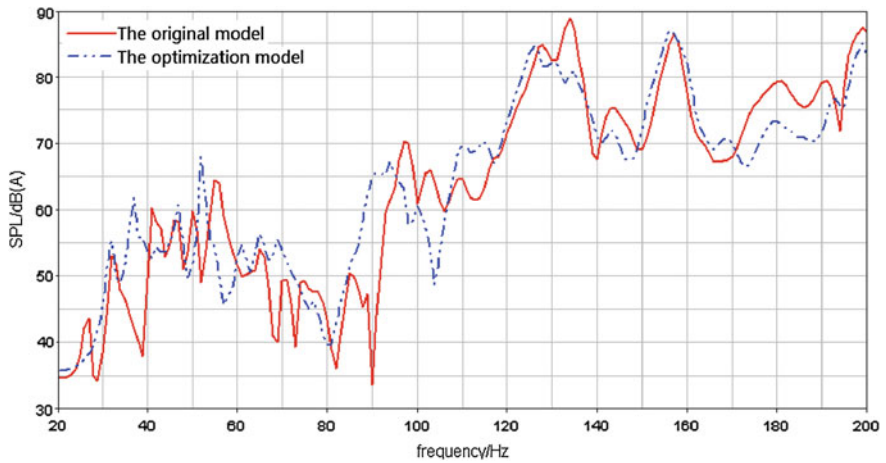


Fig. 9 The contrast of interior noise shape optimization of panel

nature frequencies are improved obvious after the optimization of the morphology, especially the first natural frequency increase rate of 63 %.

The front floor morphology optimization is basically the same with the dash panel. This point is no longer described here in detail. After these panel morphology optimizations, the interior noise caused by engine excitation is shown in Fig. 9. It can be concluded from the results that, the panel optimizations have a significant role to reduce the noise of the micro-car, the noise reduction amount is 2.2 dB (A).

5 Conclusion

In this paper, finite element method is used to establish the predicted model of vehicle interior structure-borne noise caused by engine excitation. The most significant impact on the interior noise transfer path is identified by the transfer path analysis (TPA) on the basis of the responses of subsystem. The obvious contribution panel is determined according to the panel contribution analysis. Then the optimization is implemented and the noise caused by the engine excitation is reduced. This paper proposes a complete method to predict, analyze and control the PT-body structure-borne noise, and the method has important engineering guidance value to reduce automobile interior structure-borne noise, as well as to improve vehicle NVH performance.

References

1. Junhong Z, Jun H (2006) CAE process to simulate and optimize engine noise and vibration. *Mech Syst Sig Proc* 20:1400–1409
2. Lijun Z, Hong Z, Zhuoping Y (2001) Research on control of car interior noise due to engine vibration. *J Vib Meas Diagn* 21(1):59–63
3. Lee DH, Hwang WS, Kim CM (2002) Design sensitivity analysis and optimization of an engine mount system using an FRF-based sub-structuring method. *J Sound Vib* 255(2):383–397
4. Mingxia F, Jianghong C (2005) A research on interior noise of vehicle as a nonlinear acoustic-structure interaction system. *Automot Eng* 27(5):598–601
5. Yong W, Weiping D, Du S (2009) Acoustic optimization design for powertrain mounting system based on the method of dynamic subsystem modification. 28(5):180–183
6. Pang J, He H (2006) *Automobile noise and vibration—theory and application*. Beijing Institute of Technology, Beijing
7. JianTie Z (2001) Development of a spectral-based sub-structuring technique for modeling vibratory response of complex vehicle structures [Doctor Dissertation]. The University of Alabama, Tuscaloosa, pp 17–32
8. Lei L (2002) A frequency response function-based inverse sub-structuring approach for analyzing vehicle system NVH response [Doctor Dissertation]. The University of Alabama, Tuscaloosa

9. Li J, Lim TC (1990) Application of enhanced least square to component synthesis using FRF for analyzing dynamic interaction of coupled body-subframe system. SAE paper 1999-01-1826
10. Tonghang Z (2008) Vehicle interior noise identification and control based on transfer path analysis [Doctor Dissertation]. The University of Jilin, Changchun
11. Zhaoxiang D, Shuna G, Yumei H (2008) Low noise design of car body based on topology optimization analysis. *J Vib Shock* 27(11):168–172

The Vibration Analysis of Eco-Friendly Vehicle Based on the Electric Motor Excitation

Peicheng Shi and Yuan Shang

Abstract Using the Switched Reluctance Motor (SRM) as the excitation source, the authors established a five degree-freedom multi-body dynamics model of the eco-friendly electric vehicle on ADAMS software platform; given out the body-chair's steady-state response simulation curve, thought analyzing the vibration degree of the vehicle vibration system which was brought by the electric motor. The research results can provide a theoretical reference for the electric vehicle drive system development and operation stability study.

Keywords Switched reluctance motor · Electric vehicle · Vibration analysis · Multi-body dynamics

In recent years, as a new generation of eco-friendly electric vehicle's research and development, it has been already paid more attention of the countries all over the world. Motor is the power source of the electric vehicle, and it is the first choice to choose the motor of the electric vehicle because of its simple and powerful structure, high power, high efficiency and well tolerated, especially it can meet requirements in constant torque when the electric vehicle is in low speed, and in constant power when the electric vehicle is in high speed. However, due to its strong vibration of switched reluctance motor is the main shortcoming, directly affects the ride comfort for passengers. Therefore, it is significant to improve the performance of vehicle to improve the vibration characteristics of switched reluctance motor and the pertinent design of vibration isolation system.

F2012-J05-016

P. Shi (✉) · Y. Shang
Anhui Polytechnic University, Wuhu 241000, China
e-mail: shipeicheng@126.com

Once scholars had discussed how to solve its own vibration problem in the motor design and control theory, and he had made some achievements [1, 2]. But they had not considered the specific environmental application and work characteristics of the motor. This chapter will apply the motor in pure eco-friendly electric vehicle, and research the influence of vibration system in particular direction (vertical) on the torque ripple of vibration force, so as to accurately describe vehicle vibration system incentive of the motor, it provides the basic reference of drive system development and stable operation of electric vehicle.

Firstly, the chapter analyses the torque fluctuations of switched reluctance motor, and get the curve of the motor excitation force changed with time in vertical direction; Secondly, it can be established five dof multibody dynamics model of electric vehicle based on ADAMS software, and motor excitation force in vertical direction as a model of the vibration excitation force intuitively shows the dynamic characteristic of vibration motor of the electric vehicle seats, and gives the electric vehicle seats curve changed with time in the vertical displacement, velocity and acceleration.

1 Vibration Model

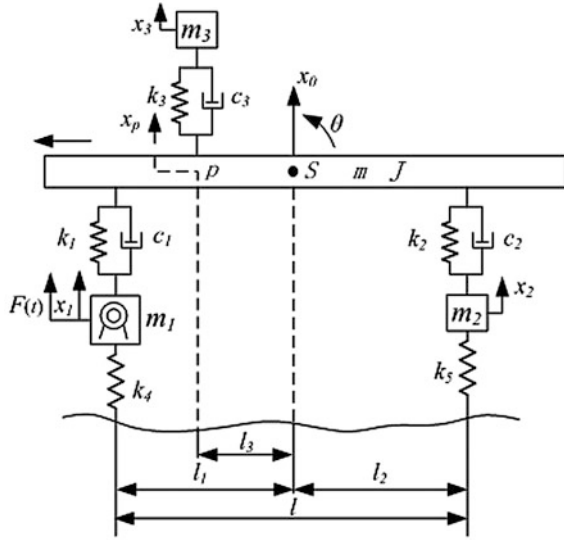
1.1 Model Analysis

Electric vehicle is similar to the traditional vehicle, and is also a more complex multiple degree of freedom vibration system, but the driving system structure is different from the general fuel vehicle, typically the vehicle structure of drive motor and integral front drive axle. Therefore, in the research of the system vibration, it should be differentiated according to different drive form. This chapter illustrates that new switched reluctance motor as a drive source establishes a drive system of five dof multibody dynamics model with a switched reluctance motor in the viewpoint of electric car vehicle, and research the response of body and the vibration of vehicle with motor incentive.

According to the emphasis of the research problems and the special structure of the electric vehicle, in this chapter, the modeling process is on the assumptions:

1. The road has the same incentive to auto left and right wheels, and vehicle structure and quality distributions are symmetrical. Thus, vehicle does not have horizontal angle of vibration, and vibration of the vehicle can be simplified as vibration problems in a vertical plane.
2. Due to the stiffness of the frame and the body is strong enough, each order modes caused by frame elastic can not be under consideration, the frame and body can be regarded as rigid bodies.
3. The suspension quality of front axle and rear axle and the distributed mass of body is instead of lumped mass respectively.

Fig. 1 Five degrees of freedom vibration model

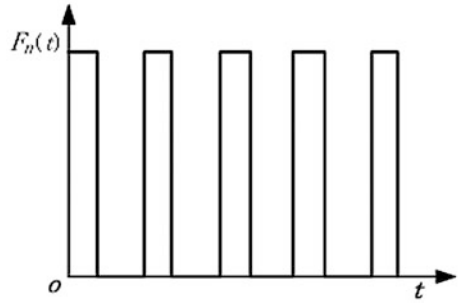


4. The mechanical properties of wheels are simplified to a massless spring, regardless of the damping.
5. Elastic force of frame and wheels and the damping force of vibration-damper is a function of displacement and speed, respectively, namely, vibration system is linear.

Thus, simplified five degrees of freedom vibration model is shown in Fig. 1, the parameters of the model are as follows:

- x_0 vehicle vertical displacement of the center;
- x_1 the vertical displacement of the front axle non-suspension quality;
- x_2 the vertical displacement of the rear axle non-suspension quality;
- x_3 the vertical displacement of the human body and the seat quality;
- x_p the vertical displacement under the seat body;
- θ the displacement of angle of pitch;
- K_1 front suspension stiffness;
- K_2 rear suspension stiffness;
- K_3 seat stiffness;
- K_4 front wheel stiffness;
- K_5 rear wheel stiffness;
- m body quality;
- m_1 the front axle non-suspension quality(including motor quality);
- m_2 the rear axle non-suspension quality;
- m_3 the human body and the seat quality;
- c_1 damping factors of front suspension vibration-damper;
- c_2 damping factors of rear suspension vibration-damper;
- c_3 damping factors of seat;
- l the distance between front and rear axle;

Fig. 2 Relationship between tangential force and time



- 11 the distance of front axle to vehicle center;
- 12 the distance of rear axle to vehicle center;
- 13 the distance of vehicle center to seat;
- J moment of inertia of vehicle around vehicle center;
- F (t) torque incentive of SR drive motor.

1.2 Motor Excitation Force Analysis

The iron core of stator and rotor is made of stacked silicon steel sheet in SR Drive motor, large teeth and slots are distributed evenly on the circumference inside of the stator core and circumference outside of the rotor core, teeth also known as salient, and this is the “double salient-pole” structure, the concentrated winding is installed on each salient pole of the stator core, the windings on the two opposite salient poles turn into a set of series (forward) windings. Since the switching of the electronic circuit, saturation, nonlinearity of the magnetic circuit, usually the total magnetic energy inside the motor (refer to the energy which is turned into mechanical energy from motor magnetic energy) or the inductance will be lineared by pieces, according to the specific research purposes, the simplified electromagnetic torque is [3]:

$$T_e = \frac{1}{2} K i^2 \quad (1)$$

K is the change rate of position angle of the winding inductance, i is phase current of the motor winding.

For the SR drive motor of eco-friendly electric vehicle, its vibration is effected by the rotor between the tangential and radial forces result. According to the actual operation of the motor, the electromagnetic torque is fluctuated, therefore the relation of tangential force and time is shown in Fig. 2, the specific expression is as followed.

Fig. 3 Relationship between radial force and time



$$F_n = \begin{cases} \frac{T_e}{R}, & nT \leq t \leq (n + \frac{7}{20})T \\ 0, & (n + \frac{7}{20})T \leq t \leq (n + 1)T \end{cases} \quad (n = 0, 1, \dots) \tag{2}$$

R is the stator inner radius, period $T = \frac{1}{f} = \frac{60}{a} N_r$, f is the fundamental frequency of torque ripple, a is the motor speed, N_r is the rotor series, t is the motivating force in the role of a period of time.

Since the nonlinear magnetic saturation SRM, the precise analytical expression of radial force is very difficult. Starting from the qualitative analysis, it can be assumed as follows: (1) the magnetic circuit is linear; (2) concentrated radial force is acting on the stator poles, and assuming that phase current is constant. Considering the same period of radial force and tangential force, after simplified the role, the radial force can be obtained over time as shown in Fig. 3, the specific expression is as followed.

$$F_r = \begin{cases} \frac{i^2(L_{Min} + \frac{a\pi K}{30}(t - nT))}{2\sqrt{b^2 + (\frac{\pi ar}{30})^2(\frac{7T}{20} - (t - nT))^2}}, & nT \leq t \leq (n + \frac{7}{20})T \\ 0, & (n + \frac{7}{20})T \leq t \leq (n + 1)T \end{cases} \quad (n = 0, 1, \dots) \tag{3}$$

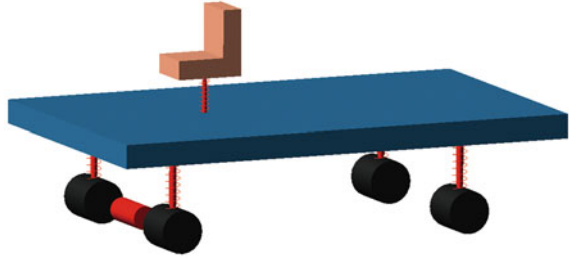
Minimum air gap length $b = R - r$, r is the rotor radius; L_{min} is the minimum inductance of windings; i is the winding current.

In the normal operation of electric vehicles, the direction of the motor tangential and radial forces is changed with the rotor angular displacement (or time), and this study centers on vehicle vibration excitation in the vertical direction response. Based on the synthesis and decomposition of principle force, the resultant force of motor excitation in the vertical direction is as followed.

$$F(t) = \begin{cases} \frac{T_e}{R} \cos(\frac{a\pi}{30}t + \varphi) - \frac{i^2(L_{Min} + \frac{a\pi K}{30}(t - nT))}{2\sqrt{b^2 + (\frac{\pi ar}{30})^2(\frac{7T}{20} - (t - nT))^2}} \sin(\frac{a\pi}{30}\pi t + \varphi), & nT \leq t \leq (n + \frac{7}{20})T \\ 0, & (n + \frac{7}{20})T \leq t \leq (n + 1)T \end{cases} \quad (n = 0, 1, \dots) \tag{4}$$

This force is the vertical vibration exciting force of SR motor drive system, φ is the initial phase of the rotor.

Fig. 4 Multi-body vehicle dynamics model



1.3 The Multi-Body Simulation Model

Based on these modeling assumptions, the five dof multibody dynamics vibration analysis model is established by ADAMS software as shown in Fig. 4. Model includes seven moving objects, a cylindrical pair, three moving pairs, three fixed pairs. Auto left and right wheels of the front axle and rear axle are connected with fixed pairs; seats and wheels only allow to move up and down, and the body allows to move up and down and to turn around the centroid. Thus, it forms five dof vehicle model, that is, front axle and rear axle wheels, seats and body move up and down in vertical direction [4, 5].

2 Examples of Simulation Analysis

First of all, according to the formula (4), the simulation parameters substitute into it (such as Table 1); the curve of resultant force of Motor excitation F in vertical direction with the time of change by using MATALAB programming, as shown in Fig. 5; Second, taking some coordinates in Fig. 5 curve of ADAMS software, according to the circulation course of motor excitation, the spline curve can be shown in Fig. 6. Then, the curve in Fig. 6 shows in vertical direction of motor excitation force, which is applied to the vehicle multibody dynamics model of the motor, so as to produce vertical incentive in the vibration system. Finally, vehicle multi-body dynamics simulation is competed based on the ADAMS software platform. Vibration characteristics can be made in the displacement, velocity and acceleration of the human body and seat equivalent quality with changed time, the curves as shown in Figs. 7, 8 and 9 respectively.

As shown in Fig. 7, litter displacement is in motor excitation of seat vertical vibration; however, according to Figs. 8 and 9, the vertical vibration velocity and acceleration of the seat is high, especially when the acceleration achieves more than 10 m/s^2 , it causes the ride comfort. Therefore, in the given vehicle, it should be to optimize the design of seat vibration absorber system or motor dampening cushion, if necessary, to optimize the automobile suspension system, in order to improve the ride comfort for drivers and passengers.

Table 1 Simulation parameter table

Parameter name	Parameters (units)	Parameter name	Parameters (units)	Parameter name	Parameters (units)
m	1454.5 (kg)	k_1	186 (k N/m)	J	64.3 (kg m ²)
m_1	120 (kg)	k_2	17 (k N/m)	R	0.05 (m)
m_2	68.5 (kg)	k_3	52.8 (k N/m)	b	0.001 (m)
m_3	102 (kg)	k_4	118 (k N/m)	a	1,500 (r/min)
l	2.4 (kg)	k_5	118 (k N/m)	N_r	6
l_1	1.1 (m)	c_1	0.6 (kN s/m)	i	1 (A)
l_2	1.3 (m)	c_2	0.55 (kN s/m)	K	82.5
l_3	0.2 (m)	c_3	0.4 (kN s/m)	L_{\min}	4.95 (H)

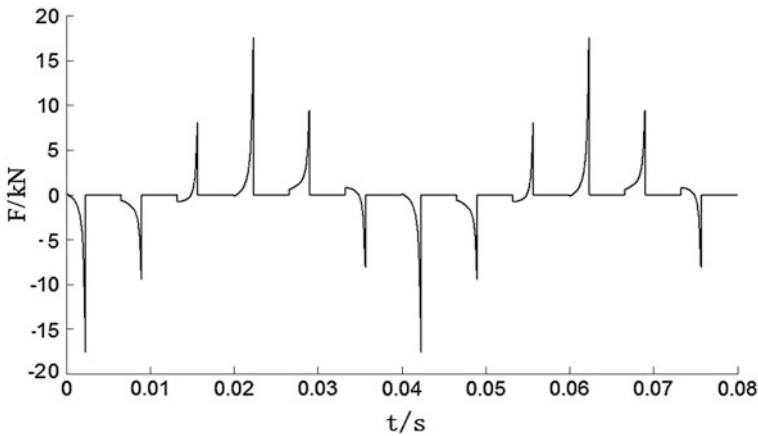


Fig. 5 Motor vertical excitation force

In conclusion, the traditional research analysis method has failed to meet the requirements of the modern vehicle, virtual prototype technology as a new technology, has been used in various fields. This chapter is to study the drive comfort influence of the vibration of the eco-friendly electric vehicle using dynamic simulation software ADAMS. It is clear that virtual prototype technology can be well used in automobile prophase development. In the study based on SRM drive system of electric vehicle vibration process, first, it should be started from the vehicle, the author analyzes the vehicle vibration including drive motor, regards the drive motor as excitation source, and analyses the steady state response of vehicle body, human body and seat. For this reason, it is an important reference for the design of vehicle.

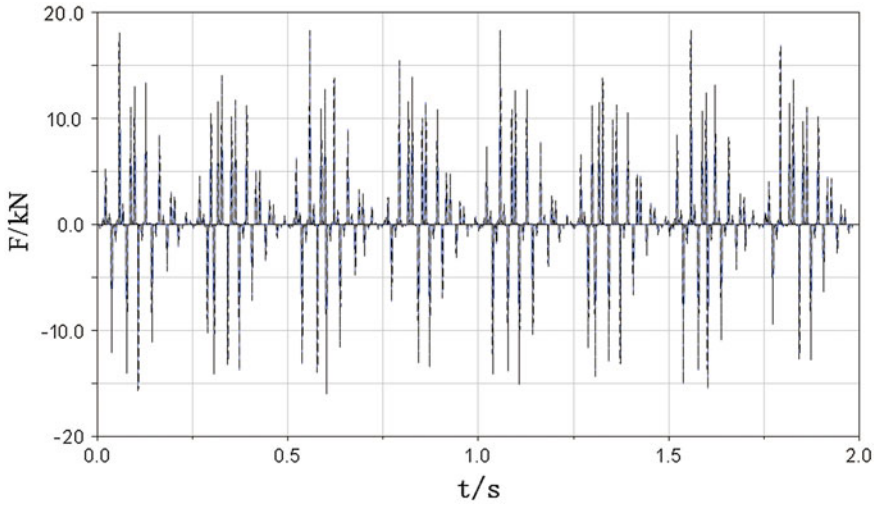


Fig. 6 Vertical direction of motor excitation force

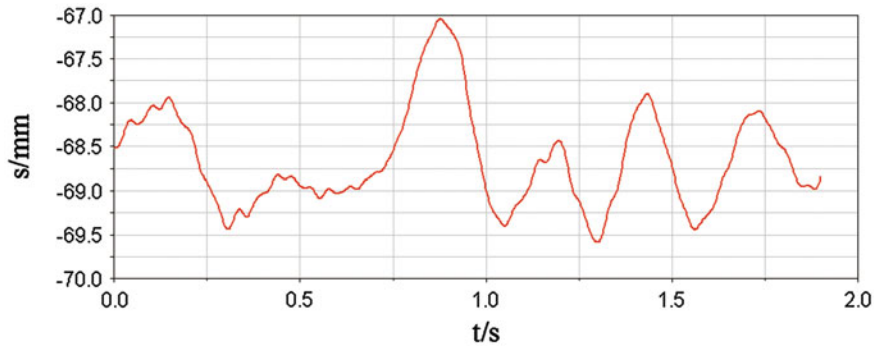


Fig. 7 Displacement of the human body and seat equivalent quality with changed time

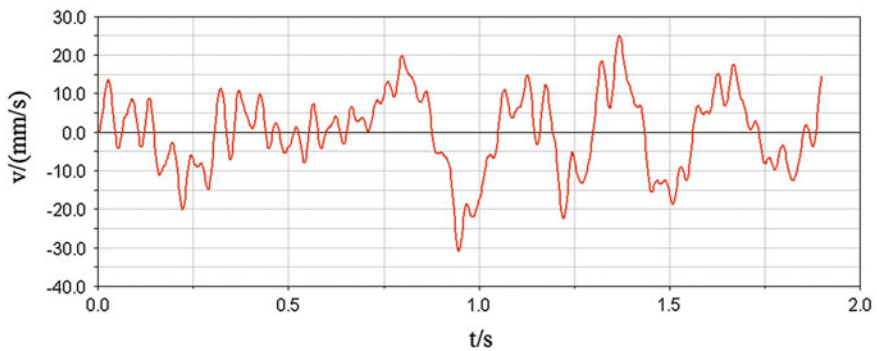


Fig. 8 Velocity of the human body and seat equivalent quality with changed time

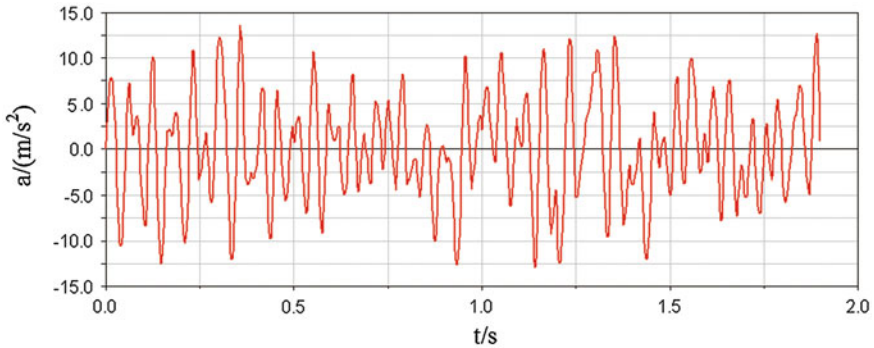


Fig. 9 Acceleration of the human body and seat equivalent quality with changed time

3 Conclusions

This chapter is to study the vibration of the eco-friendly electric vehicle using dynamic simulation software ADAMS. According to the vibration characteristic of switched reluctance motor, it regards the drive motor as excitation source, and derives analytical expressions of radial force and tangential force with the change over time. The author chooses the electric vehicle based on SRM drive system to analyse the vehicle vibration. Five dof vehicle vibration system model have specific aim to research the motor incentive as vibration source, and displacement, velocity and acceleration of the dynamic simulation “body-seat” with the change over time. The results for the electric vehicle drive system development and the operation stability study provide the theory basis and the method which can simplify the electric the design of the vehicle product and shorten the construction cycle of product.

Acknowledgments The authors would like to thank the financial supports of Anhui Provincial Education Department Natural Science Foundation (Grant No. KJ2011A036), of the An Hui Key Laboratory of Advanced Numerical Control & Servo Technology, of the Mechanical Manufacturing & Automation AnHui Provincial Key Subject and of Anhui Provincial Natural Science Foundation (Grant No. 11040606M144).

References

1. Cajander D, Le-Huy H (2006) Design and optimization of a torque controller for a switched reluctance motor drive for electric vehicles by simulation. *Math Comput Simul* 71:333–344
2. Faiz J, Moayed-Zadeh K (2005) Design of switched reluctance machine for starter/generator of hybrid electric vehicle. *Elect Power Syst Res* 75:153–160
3. YiMin Z (2007) *Mechanical vibration* [M]. Tsinghua University Press, Beijing, p 3

4. Chen QS (2007) Advanced electric vehicle technology [M]. Beijing Chemical Industry Press, Beijing, p 7
5. (Japan) Electrical Society, (2008) The electric car latest technology [M] (trans: Kang LY). Mechanical Industry Press, Beijing, p 9

Author Biographies

Shi Pei-cheng Male, born in 1976, Ph.D., associate professor. Research Direction: automobile systems dynamics, vehicle vibration analysis and testing technology. More than 10 chapters have been published, including six chapters in EI; eight national patents have been applied in Automobile direction. He has obtained one provincial scientific and technological achievements and published some materials as a deputy editor.

Shang Yuan Female, born in 1989, a undergraduate in Anhui Polytechnic University.

Apply Near-Field Acoustic Holography to Identify the Noise Source of Pass-by Vehicles

Lingzhi Li, Jun Li, Bingwu Lu and Yinjie Liu

Abstract When using Near-field Acoustic Holography (NAH) to identify the noise source of a pass-by vehicle in a test—room, the hologram aperture must be at least as large as the source aperture, requiring a large element array. The reconstruction of NAH is an ill-posed inversion problem that requires a regularization procedure. The commonly used Tikhonov regularization procedures require a significant amount of computing time for a large hologram array. In this work, a fast and robust regularization procedure is developed for NAH on the basis of a statistical energy constraint equation (SECE) that links the hologram and the reconstruction sound pressures. This procedure is able to identify the optimal cutoff wave number for an existing exponential filter in a single measurement event without a prior knowledge of the noise. It is tested via numerical simulation for an exponential filter function in an NAH at various sound frequencies, hologram distances and signal-to-noise ratios (SNR). The SECE procedure is applied to identify the noise source on the right side of a vehicle in a semi-anechoic chamber. The results are compared with those obtained with the Far-field filter, generalized cross validation (GCV), L-curve and the Morozov discrepancy principle (MDP) methods.

Keywords Pass-by noise · Noise source identification · Near-field acoustic holography · Error analysis · Regularization procedure

F2012-J05-021

L. Li (✉) · J. Li · B. Lu · Y. Liu

State Key Laboratory of Comprehensive Technology on Automobile Vibration and Noise and Safety Control, Mainland, China

L. Li · J. Li · B. Lu · Y. Liu

China FAW Co., Ltd. R & D Center, Mainland, China

1 Introduction

Developed by Williams and Maynard [1, 2], nearfield acoustic holography (NAH) is a method for reconstructing and predicting sound pressure, particle velocity and sound intensity in the entire sound field with the hologram sound pressure in the nearfield of a radiator. Owing to its simplicity and reliability, NAH has been widely applied in noise and vibration identification and diagnosis.

In a NAH backward reconstruction process, relatively small measurement errors [3, 4] in the hologram sound pressure can lead to large errors in the reconstruction sound pressure through the exponentially increasing inverse Green's function. According to the analysis of Nam and Kim [3], only the random noise errors will be significantly amplified in NAH. In addition, NAH has intrinsic algorithm errors due to the transformation of the infinite and continuous convolution integrals to finite and discrete values, and the Gibbs and aliasing effects pertaining to the finite and discrete measurement apertures [5]. Therefore, a regularization procedure (i.e., a wave number filter) must be used in NAH to overcome the ill-posedness [6]. For example, an exponential wave number filter can be used to reduce the reconstruction errors, and consistently good results can be obtained if the cutoff wave number k_c and decay factor α are properly selected [7]. When the variance of the hologram noise is available, k_c can be reasonably estimated. Although lacking of a rigorous theoretical explanation, empirically it is found that $\alpha = 0.1 \sim 0.2$ can consistently give relatively good results. Other regularization methods or filters, such as Tikhonov regularization, have been proposed in the literature. The selection of the regularization parameters is crucial in all regularization methods and requires constraint equations. The Morozov discrepancy principle (MDP), L-curve [8] and generalized cross validation (GCV) are the commonly used constraints for determining regularization parameters [8]. These regularization procedures start to give erroneous and inconsistent results if the hologram sound pressure has a large edge discontinuity [6, 9]. Evidences show that exponential filter is probably the most efficient and effective one if its parameters can be determined properly and automatically [10]. As pointed out by Williams [6], a constraint equation may be necessary for determining k_c when the variance of the hologram noise is unavailable. However, no constraint equation has been proposed in the literature for exponential filter.

Inspired by the work of Nam and Kim [3], we analyzed the relations between the hologram sound pressure and reconstruction sound pressure in terms of mean values and variances using the continuous NAH theory. We assumed Gaussian noise for phase and amplitude, and used random process theory to treat the random spatial distribution in the derivation of the expressions of rigorous bias and random errors on the hologram and prediction planes. A statistical energy constraint equation (SECE) linking the measured and reconstruction pressures, their variances, the energy of the inverse Green's function, and the wave number filter, is established based on the assumption that the average signal-to-noise ratio of the

reconstruction pressure is equal to that of the hologram pressure. The simulation test and application to a pass-by vehicles show that SECE can be used to optimize exponential filter parameters.

2 Theoretical Formulation

2.1 Review of Planar NAH

For planar NAH, if the acoustic sources are confined to the half space $z \leq z_s$, and if the pressure is known on a plane $z = z_h \geq z_s$ the pressure on any other plane is given as [5]

$$P(k_x, k_y, z) = P(k_x, k_y, z_h) e^{ik_z(z-z_h)}, \quad (1)$$

where k_z is defined by $k_z = \sqrt{k^2 - k_x^2 - k_y^2}$ within the radiation circle, and by $k_z = i\sqrt{k_x^2 + k_y^2 - k^2}$ outside of it, $P(k_x, k_y, z)$, $P(k_x, k_y, z_h)$ is the sound pressure spectrum in the wave number domain. The pressure spectrum and the spatial sound pressure form a Fourier transform pair [5]

$$P(k_x, k_y, z) = \int_{-\infty}^{\infty} dx \int_{-\infty}^{\infty} dyp(x, y, z) e^{-i(k_x x + k_y y + k_z z)}, \quad (2)$$

$$p(x, y, z) = \frac{1}{4\pi^2} \int_{-\infty}^{\infty} dk_x \int_{-\infty}^{\infty} dk_y P(k_x, k_y, z) e^{i(k_x x + k_y y + k_z z)}. \quad (3)$$

The relation between the reconstruction and hologram sound pressures in the space domain is [2]

$$p_z(x, y) = \int_{-\infty}^{\infty} \int_{-\infty}^{\infty} p_h(x', y') G(x - x', y - y', z - z_h) dx' dy', \quad (4)$$

where $G(x - x', y - y', z - z_h)$ is the inverse Green's function in the space domain.

In these formulas, when $z \geq z_h$ the solution is a forward prediction problem. When $z < z_h$, the solution is a backward reconstruction problem.

2.2 General Errors of Measured Pressure

There are various sources of errors in the measured hologram sound pressure, such as those due to the mismatch of the sensors and positions [3, 4] and those due to the background noise. Let $\varepsilon_p(\omega, r)$ represent uncorrelated measurement errors at

position $r(x, y, z)$ with angular frequency ω . If phase errors are not considered, the measured pressure $\hat{p}(\omega, r)$ is the true pressure $p(\omega, r)$ plus $\varepsilon_p(\omega, r)$,

$$\hat{p}(\omega, r) = p(\omega, r) + \varepsilon_p(\omega, r). \quad (5)$$

In the following discussion, (ω, r) will be omitted for brevity, such as $\varepsilon_\phi = \varepsilon_\phi(\omega, r)$.

Since phase errors are not considered, ε_p has zero mean value, so

$$E[\hat{p}] = E[p] + E[\varepsilon_p] = p, \quad (6)$$

where $E[\]$ represents the mean value of the quantity in the brackets.

However, if phase errors are considered, such as in the work of Nam and Kim [3], the measured pressure \hat{p} should contain the true pressure p and both the magnitude errors ε_a and phase errors ε_ϕ ,

$$\hat{p} = (1 + \varepsilon_a)e^{i\varepsilon_\phi}p. \quad (7)$$

The mean value of \hat{p} is:

$$E[\hat{p}] = [(1 + E[\varepsilon_a])E[e^{i\varepsilon_\phi}]]p. \quad (8)$$

In this paper, the noise expression in Eq. (7) is used for general derivation and discussion. The noise expression in Eq. (5) is used for comparison.

2.3 Gaussian Type Errors of Measured Pressure

Since normal (Gaussian or random) distribution is the natural distribution arisen from thermal motion, it is reasonable to assume that the measurement errors are in Gaussian distribution and spatially uncorrelated.

Nam and Kim [3] assumed that the microphones' magnitude errors and phase errors are small, and expressed the error-contained hologram sound pressure as a Taylor series. By further assuming these errors are randomly distributed and spatially uncorrelated, they derived the expressions of the discrete second-order approximated bias and random errors on the hologram and prediction planes, in both the space and wave number domains. However, the random errors are not always small, thus cannot be always well expanded in a Taylor series. For example, the phase error for a monopole sound source with a frequency of 5,000 Hz is about 52° when the position error is 1 cm under standard atmosphere conditions. In the following, another expression is derived.

If the amplitude and phase errors $\varepsilon_{a,\phi}$ are in Gaussian distribution with a zero mean value and variance $\sigma_{a,\phi}^2$. The probability density function of a Gaussian distribution is $f(\varepsilon_{a,\phi}) = (1/\sigma_{a,\phi}\sqrt{2\pi})e^{-\varepsilon_{a,\phi}^2/2\sigma_{a,\phi}^2}$. The mean values of $\varepsilon_{a,\phi}$ and ε_a^2 are

$$E[\varepsilon_{a,\phi}] = 0, \quad (9)$$

$$E[\varepsilon_a^2] = \int_{-\infty}^{\infty} \varepsilon_a^2 f(\varepsilon_a) d\varepsilon_a = \sigma_a^2. \quad (10)$$

Since $\varepsilon_{a,\phi}$ are spatially uncorrelated, the mean value of $\varepsilon_a(x, y)\varepsilon_a(x', y')$ is

$$E[\varepsilon_a(x, y)\varepsilon_a(x', y')] = \sigma_a^2 \delta(x - x')\delta(y - y'). \quad (11)$$

The mean value of $e^{i\varepsilon_a\phi}$ is a Moment-Generating Function, [11] and can be expressed as

$$E[e^{i\varepsilon_a\phi}] = \int_{-\infty}^{\infty} e^{i\varepsilon_a\phi} f(\varepsilon_a) d\varepsilon_a = \frac{1}{\sigma_a \sqrt{2\pi}} \int_{-\infty}^{\infty} e^{i\varepsilon_a\phi - \varepsilon_a^2/2\sigma_a^2} d\varepsilon_a = e^{-\sigma_a^2\phi^2/2}. \quad (12)$$

Using Eqs. (9) and (12), the mean value and bias error of \hat{p} can be expressed as

$$E[\hat{p}] = (1 + E[\varepsilon_a])E[e^{i\varepsilon_a\phi}]p = e^{-\sigma_a^2\phi^2/2}p, \quad (13)$$

$$b[\hat{p}] = E[\hat{p}] - p = (e^{-\sigma_a^2\phi^2/2} - 1)p, \quad (14)$$

where $b[\]$ represents bias error in the brackets. Using Eqs. (9) and (10), the mean value of $|\hat{p}|^2$ can be expressed as

$$E[|\hat{p}|^2] = E[\{(1 + \varepsilon_a)e^{i\varepsilon_a\phi}p\}\{(1 + \varepsilon_a)e^{i\varepsilon_a\phi}p\}^*] = E[(1 + \varepsilon_a)^2|p|^2] = (1 + \sigma_a^2)|p|^2. \quad (15)$$

The variance of \hat{p} is

$$\text{Var}[\hat{p}] = E[|\hat{p}|^2] - |E[\hat{p}]|^2 = (1 + \sigma_a^2)|p|^2 - |e^{-\sigma_a^2\phi^2/2}p|^2 = (1 - e^{-\sigma_a^2\phi^2} + \sigma_a^2)|p|^2, \quad (16)$$

where $\text{Var}[\]$ represents variance in the brackets. Equations (13) and (16) show that the mean value of \hat{p} is determined only by the phase error, but the variance is determined by both the magnitude and phase errors. Clearly, when $\mu_{a,\phi} = 0$ and σ_a^2 is small, the first-order Taylor expansions of Eqs. (13) and (16) are the approximate formulas of Nam and Kim [3].

3 The Propagation of Hologram Errors

Assuming $\varepsilon_{a,\phi}$ is in Gaussian distribution and spatially uncorrelated, the expressions of the mean values and variances of the hologram and reconstruction sound pressures and sound pressure spectra can be derived (see Appendix). In practice, a finite discretization aperture is used to measure the hologram sound pressure. The following formulas are the finite and discrete versions of the formulas in the Appendix. For brevity, the hologram and reconstruction planes are

denoted by subscript labels h and z , such as $p_h(x, y) = p(x, y, z_h)$ and $P_z(k_x, k_y) = P(k_x, k_y, z)$. In addition, integer numbers $(m, n), (r, s)$ are used to replace continuous variables $(x, y), (k_x, k_y)$.

For hologram sound pressure, Eqs. (13), (14) and (16) can be written as

$$E[\hat{p}_h(m, n)] = e^{-\sigma_\phi^2/2} p_h(m, n), \tag{17}$$

$$b[\hat{p}_h(m, n)] = (e^{-\sigma_\phi^2/2} - 1) p_h(m, n), \tag{18}$$

$$Var[\hat{p}_h(m, n)] = (1 - e^{-\sigma_\phi^2} + \sigma_a^2) |p_h(m, n)|^2. \tag{19}$$

Similarly, for the hologram sound pressure spectrum, Eqs. (A2), (A3) and (A6) can be written as

$$E[\hat{P}_h(r, s)] = e^{-\sigma_\phi^2/2} P_h(r, s), \tag{20}$$

$$b[\hat{P}_h(r, s)] = (e^{-\sigma_\phi^2/2} - 1) P_h(r, s), \tag{21}$$

$$Var[\hat{P}_h(r, s)] = (1 + \sigma_a^2 - e^{-\sigma_\phi^2}) \sum |P_h(r, s)|^2. \tag{22}$$

Eq. (20) shows that the mean value of $\hat{P}_h(r, s)$ is approximately equal to the true value $P_h(r, s)$ when σ_ϕ is small. Eq. (22) shows that the dispersion of the $\hat{P}_h(r, s)$ values about their mean value is a constant in the entire wave number domain.

For reconstruction sound pressure spectrum, Eqs. (A7), (A8) and (A10) can be written as

$$E[\hat{P}_z(r, s)] = e^{-\sigma_\phi^2/2} G(r, s, z - z_h) P_h(r, s), \tag{23}$$

$$b[\hat{P}_z(r, s)] = (e^{-\sigma_\phi^2/2} - 1) G(r, s, z - z_h) P_h(r, s), \tag{24}$$

$$Var[\hat{P}_z(r, s)] = |G(r, s, z - z_h)|^2 (1 + \sigma_a^2 - e^{-\sigma_\phi^2}) \sum |P_h(r, s)|^2. \tag{25}$$

Equations (23) and (25) show that the mean value of $\hat{P}_z(r, s)$ is approximately equal to the true value $P_z(r, s) = G(r, s, z - z_h) \cdot P_h(r, s)$ when σ_ϕ is small. However, the variance of $\hat{P}_z(r, s)$ is distorted by the inverse propagator $|G(r, s, z - z_h)|^2$ in the entire wave number domain.

Using Eqs. (4) (13) and (14), the mean value and bias error of the reconstruction pressure in the space domain are

$$E[\hat{p}_z(m, n)] = \sum_{m=1}^M \sum_{n=1}^N E[\hat{p}_h(m, n)] \cdot G(m - m', n - n', z - z_h), \tag{26}$$

$$b[\hat{p}_z(m, n)] = \sum_{m=1}^M \sum_{n=1}^N b[\hat{p}_h(m, n)] \cdot G(m - m', n - n', z - z_h), \tag{27}$$

where m and n run over the row and column numbers (M and N , respectively) of microphones in the array. Clearly, the relation between the bias errors in the reconstruction and hologram sound pressures is a two-dimensional circular convolution.

If the square aperture is L , and spacing is Δ , using Eq. (4) and (A10), the variance of the reconstruction sound pressure is:

$$\begin{aligned} \text{Var}[\hat{p}_z(x, y)] &= \text{Var}\left[\frac{1}{4\pi^2} \int_{-k_{\text{Max}}}^{k_{\text{Max}}} dk_x \int_{-k_{\text{Max}}}^{k_{\text{Max}}} dk_y \hat{P}_z(k_x, k_y) e^{i(k_x x + k_y y + k_z z)}\right] \\ &= \frac{1}{4\pi^2} \int_{-k_{\text{Max}}}^{k_{\text{Max}}} dk_x \int_{-k_{\text{Max}}}^{k_{\text{Max}}} dk_y \text{Var}[\hat{P}_h(k_x, k_y)] |G(k_x, k_y, z - z_h)|^2 e^{i(k_x x + k_y y + k_z z)}, \end{aligned} \quad (28)$$

where $k_{\text{Max}} = \pi/\Delta$. As shown in Eq. (A6), $\text{Var}[\hat{P}_h(k_x, k_y)]$ is a constant in the entire wave number domain, so Eq. (28) can be rewritten as

$$\begin{aligned} \text{Var}[\hat{p}_z(x, y)] &= \text{Var}[\hat{P}_h(k_x, k_y)] \\ &\quad \times \frac{1}{4\pi^2} \int_{-k_{\text{Max}}}^{k_{\text{Max}}} dk_x \int_{-k_{\text{Max}}}^{k_{\text{Max}}} dk_y |G(k_x, k_y, z - z_h)|^2 e^{i(k_x x + k_y y + k_z z)}. \end{aligned} \quad (29)$$

Equation (29) shows that the relation between the variance of the reconstruction sound pressure and the hologram pressure spectrum. It is complex due to the integral of Green's function. But the relation between the sum of the variance of the reconstruction sound pressure and the hologram pressure spectrum and the Green's function is simple [3]:

$$\begin{aligned} \int_{-L/2}^{L/2} dx \int_{-L/2}^{L/2} dy \text{Var}[\hat{p}_z(x, y)] &= \text{Var}[\hat{P}_h(k_x, k_y)] \\ &\quad \times \int_{-L/2}^{L/2} dx \int_{-L/2}^{L/2} dy \left[\frac{1}{4\pi^2} \int_{-k_{\text{Max}}}^{k_{\text{Max}}} dk_x \int_{-k_{\text{Max}}}^{k_{\text{Max}}} dk_y |G(k_x, k_y, z - z_h)|^2 e^{i(k_x x + k_y y + k_z z)} \right]. \end{aligned} \quad (30)$$

Using Eq. (A6) and Parseval's theorem, Eq. (30) can be rewritten

$$\begin{aligned} \int_{-L/2}^{L/2} dx \int_{-L/2}^{L/2} dy \text{Var}[\hat{p}_z(x, y)] &= (1 + \sigma_a^2 - e^{-\sigma_\phi^2}) \int_{-k_{\text{Max}}}^{k_{\text{Max}}} dk_x \int_{-k_{\text{Max}}}^{k_{\text{Max}}} dk_y |P_h(k_x, k_y)|^2 \\ &\quad \times \int_{-L/2}^{L/2} dx \int_{-L/2}^{L/2} dy |G(x - x', y - y', z - z_h)|^2 = \int_{-L/2}^{L/2} dx \int_{-L/2}^{L/2} dy \text{Var}[\hat{p}_h(x, y)] \\ &\quad \times \int_{-k_{\text{Max}}}^{k_{\text{Max}}} dk_x \int_{-k_{\text{Max}}}^{k_{\text{Max}}} dk_y |G(k_x, k_y, z - z_h)|^2. \end{aligned} \quad (31)$$

Using finite and discrete variables, the integral equation in Eq. (31) can be transformed to an approximate summation equation. However, in practice the

hologram array only consists of a relatively small number of points, such as 32 by 32. Therefore, the finite and discrete version of Eq. (31) should have a wave number filter $W(r, s)$,

$$\sum_{m=1}^M \sum_{n=1}^N \text{Var}[\hat{p}_z(m, n)] = \sum_{m=1}^M \sum_{n=1}^N \text{Var}[\hat{p}_h(m, n)] \times \sum_{r=1}^M \sum_{s=1}^N |W(r, s)G(r, s, z - z_h)|^2, \quad (32)$$

Equation (32) shows that the sum of the variance of the reconstruction pressure can be expressed as the sum of the variance of the hologram pressure multiplied by the sum of the squares of the absolute values of the Green's function. Eq. (32) is applicable for both the noises described in Eqs. (5) and (7).

4 Regularization and Parameter Selection

4.1 A Statistical Energy Constraint Equation

Equation (32) shows a relationship between the variances of the hologram and the reconstruction sound pressures. Using Eq. (5), $\text{Var}[\hat{p}_h(m, n)]$ in Eq. (32) can be rewritten as

$$\text{Var}[\hat{p}_h(m, n)] = \text{Var}[\varepsilon_p] = E[|\varepsilon_p|^2] - |E[\varepsilon_p]|^2 = E[|\varepsilon_p|^2]. \quad (33)$$

Although this relationship is rigorous, it cannot be used to directly predict the relationship between the actual hologram pressure and the reconstruction sound pressure in one measurement.

Fortunately, the variance of the hologram sound pressure can be obtained from one measurement if the number of microphones in a hologram array meets the statistical requirement. In this case, Eq. (33) can be rewritten as

$$\sum_{m=1}^M \sum_{n=1}^N |\varepsilon_p(m, n)|^2 = MN \cdot \text{Var}[\hat{p}_h(m, n)] = \sum_{m=1}^M \sum_{n=1}^N \text{Var}[\hat{p}_h(m, n)] \quad (34)$$

where m and n run over the row and column numbers (M and N , respectively) of microphones in the array. In the following discussion, the subscript labels m, n, M and N will be omitted. The left side of Eq. (34) is the sum of the noise energy in the hologram plane with a mean value of $\sum |\varepsilon_p|^2 / (MN)$. Similarly, the mean energy of the hologram sound pressure is $\sum |p|^2 / (MN)$. Using Eq. (34), the average signal-to-noise ratio, $\overline{\text{SNR}}$, can be written as

$$\overline{\text{SNR}} = 10 \log_{10} \frac{\sum |p|^2 / (MN)}{\sum |\varepsilon_p|^2 / (MN)} = 10 \log_{10} \frac{\sum |p|^2}{\sum \sigma^2}, \quad (35)$$

where $\sum |p|^2$ and $\sum \sigma^2$ are the energies of the signal (hologram or reconstruction sound pressure) and the noise, respectively.

Substituting Eq. (35) into Eq. (32), a relationship between the true reconstruction sound pressure $p_z(m, n)$ and the true hologram sound pressure $p_h(m, n)$ is obtained

$$\sum |p_z(m, n)|^2 = 10^{\frac{\overline{\text{SNR}}_z - \overline{\text{SNR}}_h}{10}} \sum |p_h(m, n)|^2 \times \sum |W(r, s)G(r, s, z - z_h)|^2, \quad (36)$$

where $\overline{\text{SNR}}_h$ and $\overline{\text{SNR}}_z$ are the mean SNRs of the hologram and reconstruction sound pressures.

In one measurement, the mean square of the noise-contained hologram or the reconstruction sound pressure is

$$E[|\hat{p}|^2] = |\hat{p}|^2 = E[|p + \varepsilon_p|^2] = E[|p|^2] + E[|\varepsilon_p|^2] = |p|^2 + \sigma_p^2. \quad (37)$$

Since σ_p^2 is spatially uncorrelated and randomly distributed, Eq. (37) can be written as

$$\sum [|\hat{p}|^2] = \sum [|p|^2] + \sum \sigma_p^2. \quad (38)$$

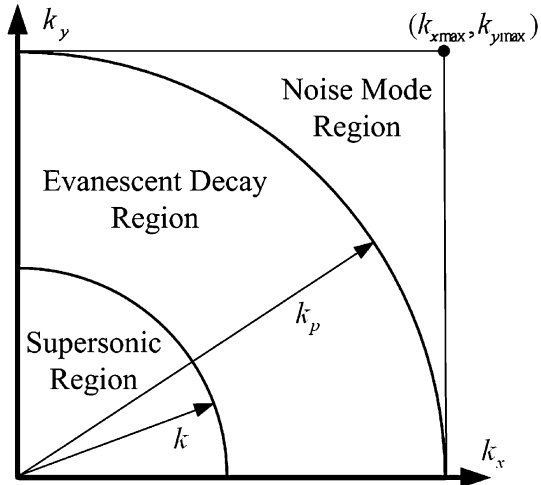
Substituting Eqs. (38) into Eq. (36), and using Eq. (32), we obtain a statistical energy constraint equation (SECE) for the measured $\hat{p}_h(m, n)$, the measured $\hat{p}_z(m, n)$, the filter function, and the inverse propagator factor:

$$\begin{aligned} & \sum |\hat{p}_z(m, n)|^2 - \sum \sigma_h^2 \times \sum |W(r, s)G(r, s, z - z_h)|^2 \\ & = 10^{\frac{\overline{\text{SNR}}_z - \overline{\text{SNR}}_h}{10}} \left(\sum |\hat{p}_h(m, n)|^2 - \sum \sigma_h^2 \right) \times \sum |W(r, s)G(r, s, z - z_h)|^2. \end{aligned} \quad (39)$$

In Eq. (39), σ_h^2 is the variance of hologram sound pressure, which can be estimated in the noise mode region (Fig. 1, which is a redrawing of a similar figure in a paper of Williams Ref. [6]) using the measured $\hat{p}_h(m, n)$. In addition, $\overline{\text{SNR}}_h$ can be estimated with Eq. (36). Of course, in a NAH backward reconstruction, $\hat{p}_z(m, n)$ will be independently determined by $\hat{p}_h(m, n)$ and the filter $W(r, s)$ according to Eq (4). When these three quantities are fixed, there is a one-to-one relation between $\overline{\text{SNR}}_z$ and $W(r, s)$. Therefore, one can adjust $W(r, s)$ to achieve a desired $\overline{\text{SNR}}_z$.

Then the question is: what is the desired or the best $\overline{\text{SNR}}_z$ one should achieve in NAH? This can be answered by the following analysis. In general the noise and the complex Gibbs energy leakage effect due to the finite hologram aperture are both in the entire wave number domain, it is impossible to selectively remove the noise without touching the useful contents. So, the best filter is the one that has the cutoff wave number somewhere in the evanescent decay region. If such a filter is used, the noise in the entire wave number domain will be amplified, and the noise level on the reconstruction plane will be higher than that on the hologram plane. Therefore, although there is a higher signal level on the reconstruction plane as

Fig. 1 A quadrant of the k-space



compared to the hologram plane, the difference between $\overline{\text{SNR}}_z$ and $\overline{\text{SNR}}_h$ should not be very large. It is very likely that an $\overline{\text{SNR}}_z$ equal or close to $\overline{\text{SNR}}_h$ is the desirable one in NAH because it implies that the best $W(r, s)$ has been selected. In other words, the optimal $W(r, s)$ is the one that can lead to $\overline{\text{SNR}}_z = \overline{\text{SNR}}_h$.

In NAH, only a finite number of points are used. Therefore, there is no true but a statistical equality as described in Eq. (39). Statistically, the optimal $W(r, s)$ can be obtained by minimizing the following objective function $|E^b|$,

$$E^b = \frac{\sum |\hat{p}_z(m, n)|^2 - \sum \sigma_h^2 \times \sum |W(r, s)G(r, s, z - z_h)|^2}{\sum |\hat{p}_h(m, n)|^2 - \sum \sigma_h^2} - 10^{\frac{\overline{\text{SNR}}_z - \overline{\text{SNR}}_h}{10}} \times \sum |W(r, s)G(r, s, z - z_h)|^2. \tag{40}$$

Assuming $\overline{\text{SNR}}_z = \overline{\text{SNR}}_h$, Eq. (40) can be written in a simpler form:

$$E^b = \frac{\sum |\hat{p}_z(m, n)|^2}{\sum |\hat{p}_h(m, n)|^2} - \sum |W(r, s)G(r, s, z - z_h)|^2. \tag{41}$$

Numerical simulations (Fig. 2) are performed using an exponential filter to demonstrate that $|E^b|$ can be practically minimized. In these simulations, four point sources are located at (18.75, 18.75), (18.75, -18.75), (-18.75, -18.75), (-18.75, 18.75) cm at the $z = 0$ cm plane. The reconstruction plane is 1 cm and hologram plane is square with a width of 1 m. The lattice spacing is 3.125 cm and the hologram is 32 by 32 points. The standard exponential filter in the k-space [7] is used,

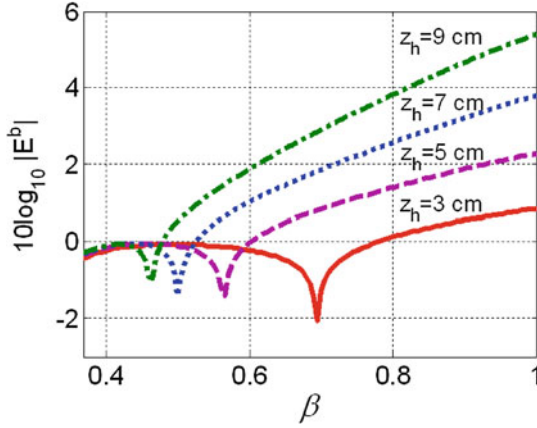


Fig. 2 Numerical simulation shows that unique minimum $|E^b|$ [see Eqs. (40) and (41)] can be found for various hologram distances and cutoff wave number factors β ($k_c = \beta\pi/d$). In the simulation, the reconstruction distance is 1 cm, the decay factor $\alpha = 0.1$, the sound source frequency is 2 kHz. The fact that $|E^b|$ is close to zero proves that the statistical energy constraint equation, Eq. (39), is correct

$$W(k_x, k_y) = \begin{cases} 1 - \frac{1}{2}e^{-(1-|k_r|/k_c)/\alpha}, & |k_r| \leq k_c, \\ \frac{1}{2}e^{(1-|k_r|/k_c)/\alpha}, & |k_r| > k_c, \end{cases} \quad (42)$$

where W is the exponential window function with a cutoff wave number k_c and decay factor α , $k_c = \beta k_{x\max}$, $k_{x\max}$ is the maximum number wave number, $k_{x\max} = \pi/d$, d is the array spacing, $k_r^2 = k_x^2 + k_y^2$. When $k_c = k$ and $\alpha = 0$, Eq. (42) is a Far-field filter.

$$W(k_x, k_y) = \begin{cases} 1, & |k_r| \leq k, \\ 0, & |k_r| > k. \end{cases} \quad (43)$$

Figure 2 plots $10 \log_{10}|E^b|$ for different hologram distances ($\beta = k_c d/\pi$, d is the spacing distance, k is the wave number, 0.37 is the value of radiate circle, kd/π), with $\alpha = 0.1$. Clearly, there exists a unique minimum $|E^b|$ in each of these cases. The fact that $|E^b|$ is close to zero proves that Eq. (39) is correct.

5 Numerical Results

In the following simulations, four point sources are located at (18.75, 18.75), (18.75, -18.75), (-18.75, -18.75), (-18.75, 18.75) cm at the $z = 0$ cm plane. The reconstruction plane is $z = 1$ cm. The hologram plane is a 1×1 m square at

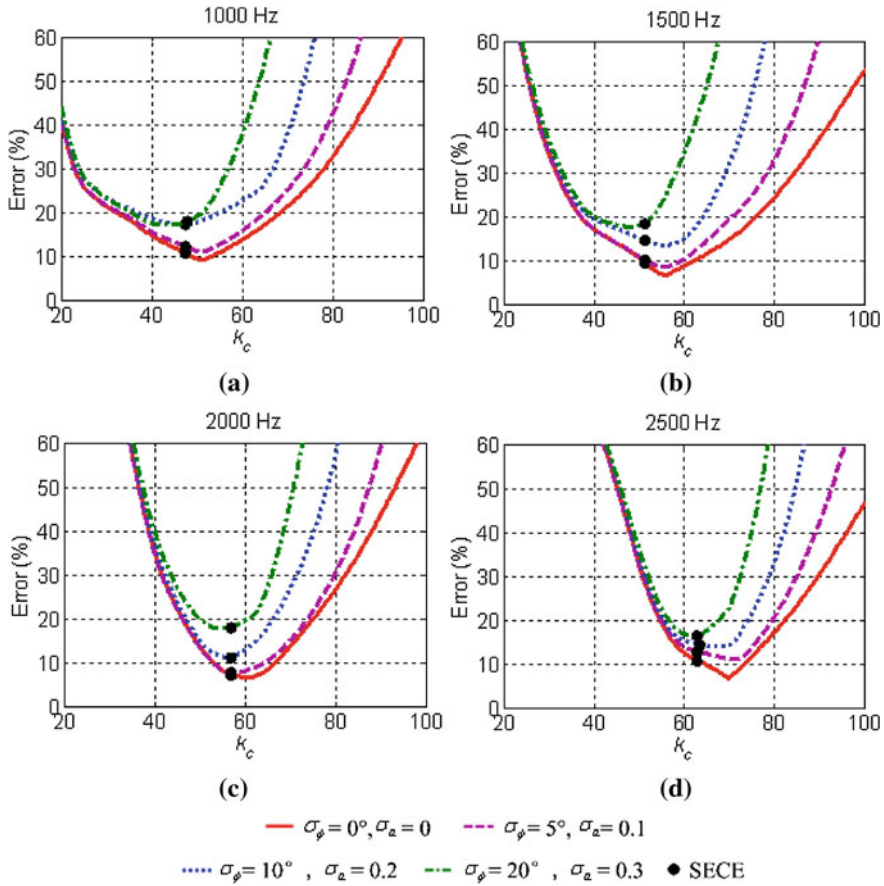


Fig. 3 Simulated error E^z as a function of cutoff wave number k_c for different source frequencies and noise levels. The reconstruction distance is 1 cm and the hologram distance is 5 cm. The optimal k_c values obtained with Eq. (41) are indicated as *black dots*

various distances from the source. The lattice spacing is 3.125 cm and the hologram is 32 by 32 points. The frequency changes from 1 to 2.5 kHz in 500 Hz steps.

The error E^z between the reconstructed pressure \hat{p}^z and the true pressure p_{ex} is defined as

$$E^z = \frac{\|p_{ex} - \hat{p}^z\|}{\|p_{ex}\|}, \tag{44}$$

where $\| \cdot \|$ represents the L2 norm.

Figure 3 shows the simulated error E^z as a function of cutoff wave number k_c for different source frequencies and noise levels. The reconstruction distance is 1 cm and the hologram distance is 5 cm. The optimal k_c values correspond to the minimum E^z values. The optimal k_c values obtained from Eq. (41) are also

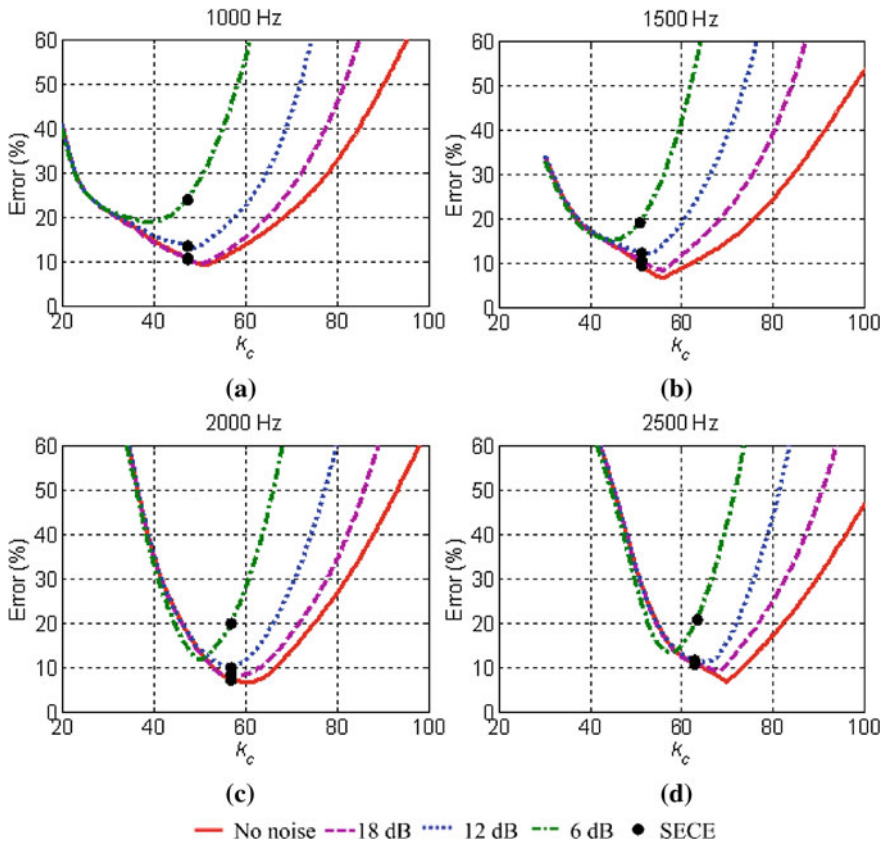


Fig. 4 Simulated error E^z as a function of cutoff wave number k_c for different frequencies and noise levels. The reconstruction distance is 1 cm and the hologram distance is 5 cm. The optimal k_c values obtained with Eq. (41) are indicated as *black dots*

indicated. Clearly, the k_c values obtained via minimizing E^z are very close to those found with Eq. (40) for all frequencies and almost all noise conditions.

Figure 4 shows the simulated error E^z as a function of cutoff wave number k_c for different source frequencies and noise levels [noise described in Eq (5)], with $SNR = \infty, 18, 12$ and 6 dB.

Figure 5 shows that the SECE is valid when the measurement distances are relatively large. The simulation is performed with frequency = 2 kHz and $SNR = 15$ dB. As the hologram distances increases from 3 to 11 cm, although the minimum percent error increases, SECE is able to determine the best cutoff wave numbers.

Figure 6 compares the SECE results with the standard Tikhonov regularization (MDP and L-curve parameter selected methods) results for different hologram

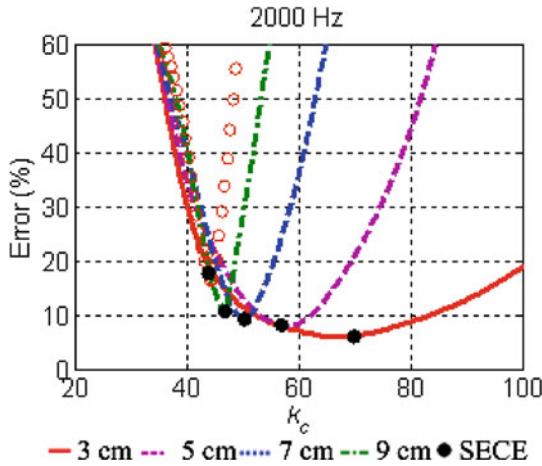


Fig. 5 Simulated error E^z as a function of cutoff wave number k_c for different hologram distances at frequency = 2,000 Hz and SNR = 15 dB. The reconstruction distance is 1 cm. The optimal k_c values obtained with Eq. (41) are indicated as *black dots*

distances (3, 5, 7, 9 cm) at frequency = 2 kHz and SNR = ∞ and 6 dB. At high SNR, Tikhonov and exponential filters exhibit similar minimum errors. For all the distances, SECE is able to find the optimal cutoff wave numbers, and is the best method. MDP is able to give relatively good results, especially at short distances. L-curve is not good for any of these distances, presumably due to the fact that the shape of the “L-curve” is not an “L”.

6 Test Results

In the following tests, the SECE regularization procedure is applied to identify the noise source on a passenger car. The reconstruction results of SECE are compared with the results of Far-field, GCV, L-curve and MDP methods.

As shown in Fig. 7a, the passenger car is put on the chassis dynamometer in a semi-anechoic test chamber. On the right side of the car, a vertical line microphone array is fixed by a robot, with 28 array elements and a spacing of 5 cm. The array is horizontally scanned by the robot. In the scanning procedures, a reference microphone is placed in front of the right-front-wheel to provide phase information for the scanning hologram sound pressure. The microphones are type 4958 of Brüel and Kjær, the front-end is 3560D of Brüel and Kjær.

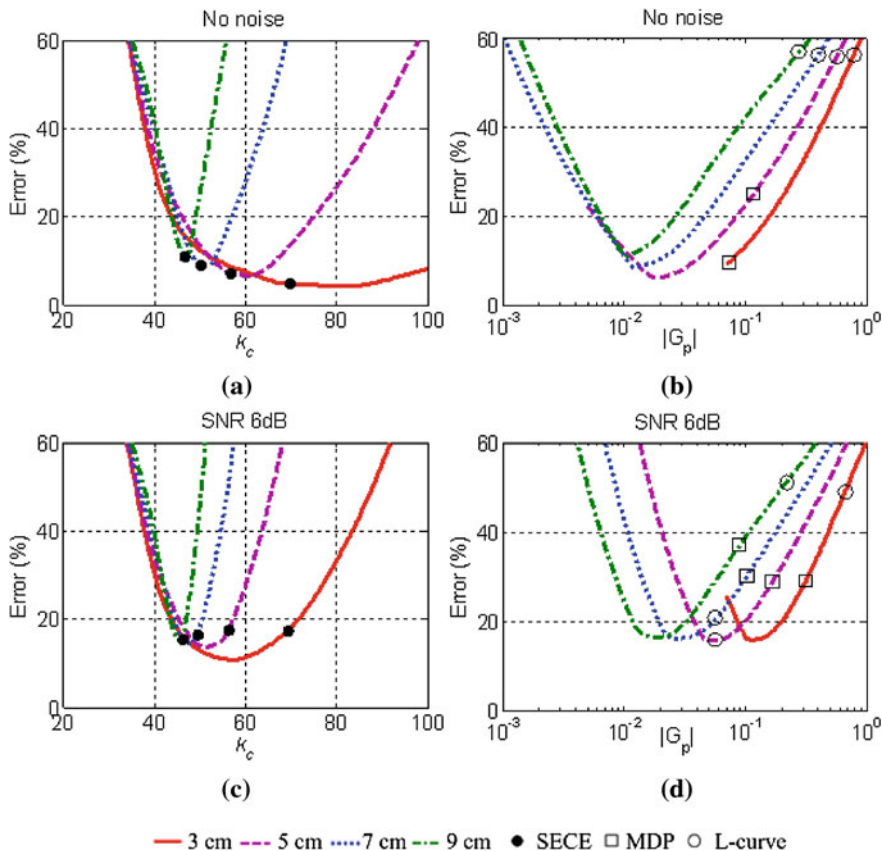


Fig. 6 Simulated error E^z as a function of cutoff wave number k_c for SECE, and as a function of G_p for the MDP and L-curve methods. Simulation is performed for different hologram distances at frequency = 2,000 Hz, SNR = ∞ and 6 dB. G_p is the eigenvalue in the planar case $G_p = [\rho ck / (\sqrt{k_r^2 - k^2})] \exp[-(z_h - z) \sqrt{k_r^2 - k^2}]$. The optimal k_c values obtained with Eq. (41) are indicated as black dots. The optimal G_p values obtained with MDP and L-curve methods are also indicated

6.1 Sound Leakage Measurements

To test the sound leakage of the car door and window, as shown in Fig. 7b, an omnidirectional reference loudspeaker is placed on the rear seats, and a microphone is installed at driver’s right ear to monitor the stability of the loudspeaker. In this test, a pink noise were used, the sound pressure level at driver’s right ear is 100 dB (A) during the entire scanning process. We have a total of 40 scans with a stepsize of 5 cm at distances 2 and 12 cm from the rearview mirror. Consequently, the hologram is 40 by 28 points and hologram plane is 2 by 1.4 m.



Fig. 7 The photos of test, a line array on right side of the car, b loudspeaker in the car

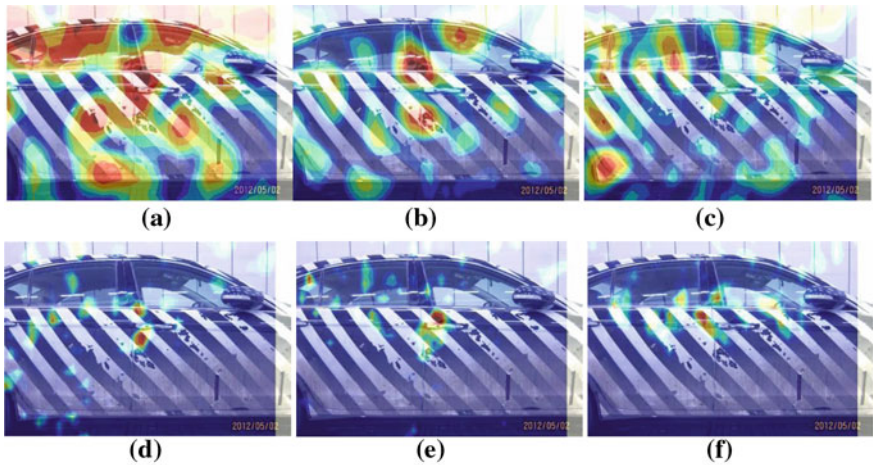


Fig. 8 The measured sound pressure at hologram distance 2 cm for frequency a 525 Hz, b 681 Hz, c 681 Hz, d 1,668 Hz, e 2,175 Hz, and f 3,431 Hz

Table 1 The reconstruction percent error for five regularization parameter selected methods at different frequencies

Frequency (Hz)	Far-filed	GCV	L-curve	MDP	SECE
400	36	124	28	250	28
525	30	118	31	310	29
681	33	68	49	280	20
850	35	70	36	235	17
1,194	30	48	27	201	17
1,668	32	27	27	31	23
2,175	42	23	33	30	23
3,431	73	59	32	45	32

The reconstruction distance is 2 cm and the hologram distance is 12 cm. The loudspeaker is on

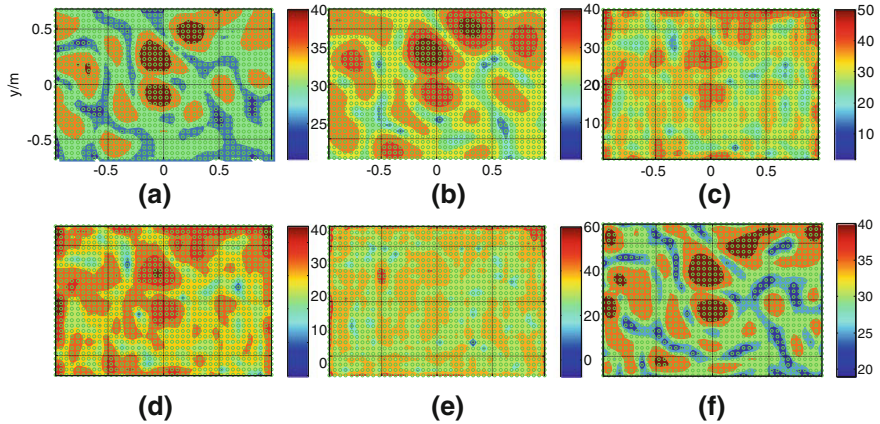


Fig. 9 Comparison of **a** measurement sound pressure at 2 cm with the reconstruction sound pressure of, **b** Far-field, **c** GCV, **d** L-curve, **e** MDP and **f** SECE at frequency 681 Hz

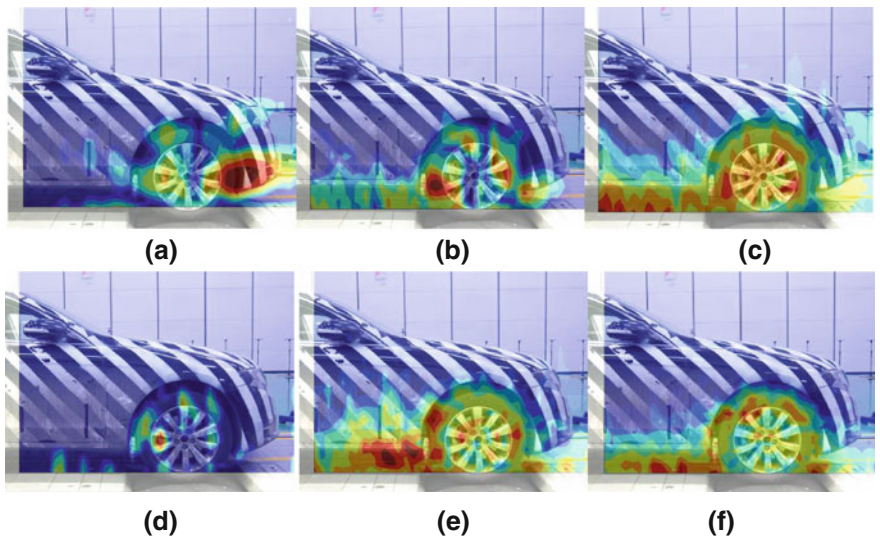


Fig. 10 The measured sound pressure at hologram distance 2 cm for frequencies **a** 550 Hz, **b** 1,160 Hz, **c** 1,312 Hz, **d** 1,531 Hz, **e** 2,056 Hz, and **f** 3,287 Hz. The engine is in idle operation condition

Figure 8 shows the measured sound pressure level at hologram distance 2 cm for frequencies 400, 525, 681, 850, 1,194, 1,668, 2,175 and 3,421 Hz. The sound sources of lower frequencies (400 and 525 Hz) are mainly located at the seams of car door and window. As the frequency increases, there is always sound leakage at the front door handles.

Table 2 The reconstruction percent errors for the five regularization parameter selected methods at different frequencies

Frequency (Hz)	Far-filed	GCV	L-curve	MDP	SECE
550	52	189	30	416	34
1,160	38	41	258	827	31
1,312	43	42	32	1177	61
1,531	64	52	112	1,107	64
2,056	47	39	140	26	34
3,287	58	62	24	62	37

The reconstruction distance is 2 cm and the hologram distance is 12 cm. The engine is in idle operation condition

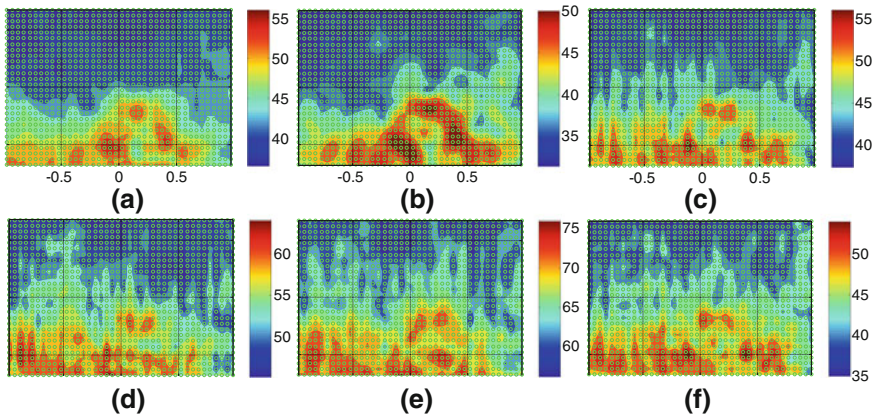


Fig. 11 Comparison of **a** measurement sound pressure at 2 cm with the reconstruction sound pressure of **b** far-field **c** GCV **d** L-curve **e** MDP and **f** SECE in the frequency band 1,120–1,200 Hz with a stepsize 6.25 Hz. The reconstruction distance is 2 cm and the hologram distance is 12 cm. The engine is in idle operation condition

Table 1 shows the reconstruction percent errors for the five regularization methods at different frequencies. The reconstruction distance is 2 cm, and the hologram distance is 12 cm. The results show that SECE always leads to the smallest reconstruction error among the five regularization methods, while GCV and MDP tend to give inconsistent or erroneous results at lower frequencies. The relative computation time in the Far-field, SECE, MDP, GCV and L-curve methods are 1, 19, 162, 921 and 947, respectively. SECE is the second fastest method.

Figure 9 shows the reconstruction sound pressures of the Far-field, GCV, L-curve, MDP and SECE methods at frequency 681 Hz. Obviously, at 2 cm, the reconstruction sound pressure of SECE is the closest to the measurement values.

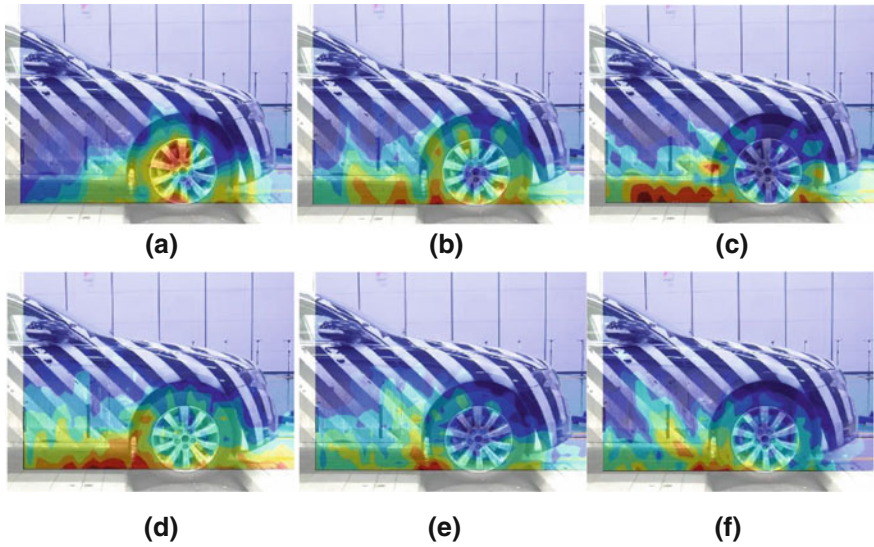


Fig. 12 The measured sound pressure at hologram distance 2 cm for frequencies **a** 550 Hz, **b** 1,160 Hz, **c** 1,312 Hz, **d** 1,531 Hz, **e** 2056 Hz, and **f** 3287 Hz

Table 3 The reconstruction percent errors for the five regularization methods at different frequencies

Frequency(Hz)	Far-filed	GCV	L-curve	MDP	SECE
550	38	90	49	460	55
1,160	46	50	106	766	52
1,312	39	43	58	441	28
1,531	44	32	36	95	30
2,056	50	26	40	28	32
3,287	78	61	27	61	86

The reconstruction distance is 2 cm and the hologram distance is 12 cm. The car is run at a steady speed 50 km/h

6.2 Idle Operation Condition

The car is in the idle operation condition during this scanning procedure. In this test, the reference loudspeaker in the car is turned off.

Figure 10 shows the measured sound pressure levels at hologram distance 2 cm for frequencies 550, 1,160, 1,312, 1,531, 2,056 and 3287 Hz. The noise sources are mainly located at the front wheel, which are driven by the engine.

Table 2 shows the reconstruction percent errors for the five regularization methods at different frequencies. SECE and Far-filed always lead to robust results with small reconstruction errors at all frequencies. GCV, L-curve and MDP tend to give inconsistent or erroneous results at some frequencies.

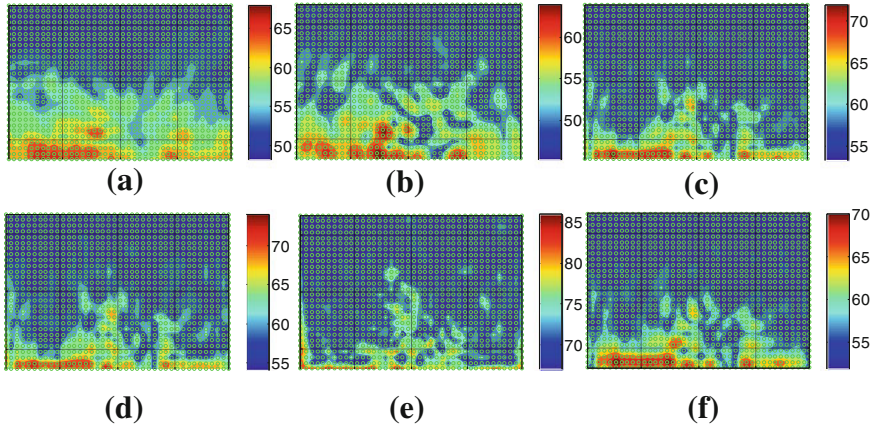


Fig. 13 Comparison of **a** measurement sound pressure at 2 cm with the reconstruction sound pressure, **b** Far-field, **c** GCV, **d** L-curve, **e** MDP, and **f** SECE at frequency 1,312 Hz. The reconstruction distance is 2 cm and the hologram distance is 12 cm. The vehicle is run at a steady speed 50 km/h

Figure 11 shows the reconstruction sound pressures of the Far-field, GCV, L-curve, MDP and SECE methods in the frequency band from 1,120 to 1,200 Hz, with a stepsize of 6.25 Hz. The reconstruction percent errors are 39, 24, 200, 1,083 and 19 %, respectively.

6.3 Steady Speed 50 km/h

The car and the chassis dynamometer are run at a steady speed 50 km/h during this scanning procedure.

Figure 12 shows the measured sound pressure levels at hologram distance 2 cm for frequencies 550, 1,160, 1,312, 1,531, 2,056 and 3,287 Hz. The noise sources are mainly located at the front wheel, which are driven by the engine and gearbox.

Table 3 shows the reconstruction percent errors for the five regularization methods at different frequencies. SECE and Far-field always lead to robust results with small reconstruction errors at all frequencies. GCV, L-curve and MDP tend to give inconsistent or erroneous results at some frequencies.

Figure 13 shows the reconstruction sound pressures of the Far-field, GCV, L-curve, MDP and SECE methods at frequency 1,312 Hz. The reconstruction percent errors are 39, 24, 200, 1,083 and 19 %, respectively.

7 Conclusions

We analyzed the relationships between the measured hologram and reconstruction sound pressure in terms of mean value and variance for planar nearfield acoustic holography, and found that if the measured noise is spatially uncorrelated and randomly distributed, a simple statistical formula linking the energy of reconstruction, hologram planar sound pressure variance, and the energy of inverse Green's function, can be obtained. The formula is continuous, rigorous, and needs no prior knowledge about the magnitude of the hologram noise. Numerical simulations verified the relationship.

The intrinsic statistical properties of a hologram array allows the HSP variance be acquired in a single measurement. In this work a simple statistical energy constraint equation (SECE) between the actual RSP, actual HSP and their average signal-to-noise ratios (SNR) is derived. Using the constraint equation, the appropriate filter parameter can be found in a fast and automatic program in one-measurement event with no prior knowledge of measurement noise. The comparisons of different frequency, SNR and hologram distance with exponential filter show that this method is able to find the appropriate filter parameter for a wide range of signal-to-noise ratios (from no-noise to 6 dB) and a relatively larger hologram distance (~ 10 cm). The application to a pass-by vehicle proved that SECE is the fastest and most robust method as compared to GCV, L-curve and MDP methods.

Appendix

Using Eqs. (10), (11) and (12), the correlation between the hologram and measured pressure $E[\hat{p}_h(x, y)\hat{p}_h^*(x', y')]$ can be derived as

$$\begin{aligned}
 E[\hat{p}_h(x, y)\hat{p}_h^*(x', y')] &= E[\{(1 + \varepsilon_a(x, y))e^{i\varepsilon_\phi(x, y)}p_h(x, y)\}\{(1 + \varepsilon_a(x', y'))e^{-i\varepsilon_\phi(x', y')}p_h^*(x', y')\}] \\
 &= E[e^{i\varepsilon_\phi(x, y)}e^{-i\varepsilon_\phi(x', y')}p_h(x, y)p_h^*(x', y')] + E[\varepsilon_a(x, y)\varepsilon_a(x', y')e^{i\varepsilon_\phi(x, y)}e^{-i\varepsilon_\phi(x', y')}p_h(x, y)p_h^*(x', y')] \\
 &= E[e^{i\varepsilon_\phi}]E[e^{-i\varepsilon_\phi}]p_h(x, y)p_h^*(x', y') + (1 - E[e^{i\varepsilon_\phi}]E[e^{-i\varepsilon_\phi}])p_h(x, y)p_h^*(x', y')\delta(x - x')\delta(y - y') \\
 &\quad + E[\varepsilon_a^2]p_h(x, y)p_h^*(x', y')\delta(x - x')\delta(y - y') \\
 &= e^{-\sigma_\phi^2}p_h(x, y)p_h^*(x', y') + (1 + \sigma_a^2 - e^{-\sigma_\phi^2})p_h(x, y)p_h^*(x', y')\delta(x - x')\delta(y - y').
 \end{aligned} \tag{A1}$$

Equations (2) and (3) show that the angular spectrum $P(k_x, k_y)$ and spatial sound pressure $p(x, y)$ form a Fourier Transform pair. Using Eq. (13), the mean value of the measured hologram angular spectrum $\hat{P}_h(k_x, k_y)$.

$$\begin{aligned}
E[\hat{P}_h(k_x, k_y)] &= E\left[\int_{-\infty}^{\infty} dx \int_{-\infty}^{\infty} dy \hat{p}_h(x, y) e^{-i(k_x x + k_y y)}\right] \\
&= \int_{-\infty}^{\infty} dx \int_{-\infty}^{\infty} dy E[\hat{p}_h(x, y)] e^{-i(k_x x + k_y y)} = e^{-\sigma_a^2/2} P_h(k_x, k_y).
\end{aligned} \tag{A2}$$

The bias error of the measured hologram angular spectrum $\hat{P}_h(k_x, k_y)$ is

$$b[\hat{P}_h(k_x, k_y)] = E[\hat{P}_h(k_x, k_y)] - P_h(k_x, k_y) = (e^{-\sigma_a^2/2} - 1)P_h(k_x, k_y). \tag{A3}$$

Using Eq. (A1), the mean value of $|\hat{P}_h(k_x, k_y)|^2$ can be derived as

$$\begin{aligned}
E\left[|\hat{P}_h(k_x, k_y)|^2\right] &= E\left[\left|\int_{-\infty}^{\infty} dx \int_{-\infty}^{\infty} dy \hat{p}_h(x, y) e^{-i(k_x x + k_y y)}\right|^2\right] \\
&= E\left[\left(\int_{-\infty}^{\infty} dx \int_{-\infty}^{\infty} dy \hat{p}_h(x, y) e^{-i(k_x x + k_y y)}\right) \left(\int_{-\infty}^{\infty} dx' \int_{-\infty}^{\infty} dy' \hat{p}_h^*(x', y') e^{i(k_x x' + k_y y')}\right)\right] \\
&= \int_{-\infty}^{\infty} dx \int_{-\infty}^{\infty} dy \int_{-\infty}^{\infty} dx' \int_{-\infty}^{\infty} dy' E[\hat{p}_h(x, y) \hat{p}_h^*(x', y')] e^{-i(k_x x + k_y y - k_x x' - k_y y')} \\
&= \int_{-\infty}^{\infty} dx \int_{-\infty}^{\infty} dy \int_{-\infty}^{\infty} dx' \int_{-\infty}^{\infty} dy' \{E[e^{i\epsilon_a}] E[e^{-i\epsilon_a}]\} p_h(x, y) p_h^*(x', y') \\
&\quad + (1 + E[\epsilon_a^2] - E[e^{i\epsilon_a}] E[e^{-i\epsilon_a}]) p_h(x, y) p_h^*(x', y') \delta(x - x') \delta(y - y') \} e^{-i(k_x x + k_y y - k_x x' - k_y y')}.
\end{aligned} \tag{A4}$$

Using Parseval's theorem, $E\left[|\hat{P}_h(k_x, k_y)|^2\right]$ is finally derived as

$$\begin{aligned}
E\left[|\hat{P}_h(k_x, k_y)|^2\right] &= E[e^{i\epsilon_a}] E[e^{-i\epsilon_a}] |P_h(k_x, k_y)|^2 \\
&\quad + (1 + E[\epsilon_a^2] - E[e^{i\epsilon_a}] E[e^{-i\epsilon_a}]) \int_{-\infty}^{\infty} dk_x \int_{-\infty}^{\infty} dk_y |P_h(k_x, k_y)|^2 \\
&= e^{-\sigma_a^2} |P_h(k_x, k_y)|^2 + (1 + \sigma_a^2 - e^{-\sigma_a^2}) \int_{-\infty}^{\infty} dk_x \int_{-\infty}^{\infty} dk_y |P_h(k_x, k_y)|^2.
\end{aligned} \tag{A5}$$

Using Eqs. (A2) and (A5), the variance of $\hat{P}_h(k_x, k_y)$ is

$$\begin{aligned}
\text{Var}[\hat{P}_h(k_x, k_y)] &= E\left[|\hat{P}_h(k_x, k_y)|^2\right] - |E[\hat{P}_h(k_x, k_y)]|^2 \\
&= (1 + \sigma_a^2 - e^{-\sigma_a^2}) \int_{-\infty}^{\infty} dk_x \int_{-\infty}^{\infty} dk_y |P_h(k_x, k_y)|^2.
\end{aligned} \tag{A6}$$

Next, the mean value and variance of the reconstruction angular spectrum

$\hat{P}_z(k_x, k_y)$ are derived. Using Eq. (1) and (A2), the mean value of $\hat{P}_z(k_x, k_y)$ is:

$$\begin{aligned} E[\hat{P}_z(k_x, k_y)] &= E[\hat{P}_h(k_x, k_y)G(k_x, k_y, z - z_h)] \\ &= e^{-\sigma_\phi^2/2}G(k_x, k_y, z - z_h)P_h(k_x, k_y). \end{aligned} \quad (\text{A7})$$

The bias error of $\hat{P}_z(k_x, k_y)$ is:

$$b[\hat{P}_z(k_x, k_y)] = E[\hat{P}_z(k_x, k_y)] - P_z(k_x, k_y) = (e^{-\sigma_\phi^2/2} - 1)G(k_x, k_y, z - z_h)P_h(k_x, k_y). \quad (\text{A8})$$

Using Eqs. (A5) and (A6), the mean value of $|\hat{P}_z(k_x, k_y)|^2$ is

$$\begin{aligned} E[|\hat{P}_z(k_x, k_y)|^2] &= E[|\hat{P}_h(k_x, k_y)G(k_x, k_y, z - z_h)|^2] = E[|\hat{P}_h(k_x, k_y)|^2|G(k_x, k_y, z - z_h)|^2] \\ &= |G(k_x, k_y, z - z_h)|^2\{e^{-\sigma_\phi^2}|P_h(k_x, k_y)|^2 + (1 + \sigma_a^2 - e^{-\sigma_\phi^2}) \int_{-\infty}^{\infty} dk_x \int_{-\infty}^{\infty} dk_y |P_h(k_x, k_y)|^2\} \\ &= e^{-\sigma_\phi^2}|P_z(k_x, k_y)|^2 + |G(k_x, k_y, z - z_h)|^2 \text{Var}[\hat{P}_h(k_x, k_y)]. \end{aligned} \quad (\text{A9})$$

Using Eq (A7) and (A9), the variance of $\hat{P}_z(k_x, k_y)$ is

$$\begin{aligned} \text{Var}[\hat{P}_z(k_x, k_y)] &= E[|\hat{P}_z(k_x, k_y)|^2] - |E[\hat{P}_z(k_x, k_y)]|^2 \\ &= |G(k_x, k_y, z - z_h)|^2 \text{Var}[\hat{P}_h(k_x, k_y)] \\ &= |G(k_x, k_y, z - z_h)|^2 (1 + \sigma_a^2 - e^{-\sigma_\phi^2}) \int_{-\infty}^{\infty} dk_x \int_{-\infty}^{\infty} dk_y |P_h(k_x, k_y)|^2. \end{aligned} \quad (\text{A10})$$

References

1. Williams EG, Maynard JD (1980) Holographic imaging without the wavelength resolution limit. *Phys Rev Lett* 45:554–557
2. Maynard JD, Williams EG, Lee Y (1985) Nearfield acoustic holography: I. Theory of generalized holography and the development of NAH. *J Acoust Soc Am* 78(4):1395–1413
3. Nam KU, Kim YH (1999) Errors due to sensor and position mismatch in planar acoustic holography. *J Acoust Soc Am* 106(4):1655–1665
4. Carroll GP (1999) The effect of sensor placement errors on cylindrical near-field acoustic holography. *J Acoust Soc Am* 105(4):2269–2276
5. Williams EG (1999) *Fourier acoustics: sound radiation and near field acoustical holography*. Academic Press, London, pp 1–306
6. Williams EG (2001) Regularization methods for near-field acoustical holography. *J Acoust Soc Am* 110(4):1976–1988
7. Veronesi WA, Maynard JD (1987) Near-field acoustic holography (NAH): II. holography reconstruction algorithms and computer complementation. *J Acoust Soc Am* 81(5): 1307–1322

8. Hansen PC, Jensen TK, Rodriguez G (2007) An adaptive pruning algorithm for the discrete L-curve criterion. *J Comp Appl Math* 198(2):483–492
9. Lingzhi L, Li J, Lu B, Liu Y, Liu K (2010) The determination of regularization parameters in planar near field acoustic holography. *Acta Acustica* 35(2):169–178
10. Wu SF (2008) Methods for reconstructing acoustic quantities based on acoustic pressure measurements. *J Acoust Soc Am* 124(5):2680–2697
11. Bendat JS, Piersol AG (1986) *Random data: analysis and measurement procedures*. Wiley, New York, Chap. 3, p 66

Part VI
Analysis and Evaluation
of In-Car Vibration and Noise

Application Research of Statistical Energy Analysis on Vehicle Sound Package

Xiaoxuan Zhang, Xingrang Wu, Yuhu Cheng,
Hongying Jin and Jun Zhang

Abstract A whole vehicle SEA model is established by hybrid method combining body structure and sound package. Modal density, damping loss factor and sound package material parameters are obtained by testing and then applied into the vehicle model. The vehicle acoustic performances are tested at both ideal running condition and operating condition, and the tested results at ideal running condition are used to correct the SEA model. The outer cavity sound pressure tested in vehicle at operating condition is used as the excitation for prediction of the interior noise. The difference between the predicted interior noise and the tested results is less than 3 dB(A), which shows good correlation. Two optimized methods are proposed to reduce a vehicle interior noise by 1 ~ 3 dB(A) without the changes of weight.

Keywords Statistical energy analysis · Sound package · Noise · Modal density · Damping loss factor

F2012-J06-003

X. Zhang (✉) · X. Wu · Y. Cheng · H. Jin · J. Zhang
Changan Auto Global R&D Center, Mainland, China
e-mail: sunqiemail@163.com

X. Zhang · X. Wu · Y. Cheng · H. Jin · J. Zhang
State Key Laboratory of Vehicle NVH and Safety Technology, Chongqing, China

1 Introduction

With the living standards improved, people has higher demand on the comfort. As an important role in transportation, automobile comfort is gradually becoming a major consideration for the persons desiring to buy a car. As one of the most important factor of comfort, NVH (Noise Vibration and Harshness) impacts directly on the vehicle's comfort [1]. Statistical Energy Analysis (SEA) is a noise analysis method used in middle and high frequency range. SEA is originally used in the aerospace field, and in recent years it has a widely application and development in the automotive industry. Figure 1 shows the history of SEA application in automotive industry [2, 3].

Wenlung Liu et al. [4] predicted the STL of dash mat using SEA. The results had good tendency at mid and high frequency range, and also matched closely with test results at low frequency range. James A. Moore et al. [5] condensed a SEA model of passenger vehicles to 30–50 subsystems. The results of their research provided great convenience for model construction and calculation. Denis Blanchet and Andrew Cunningham [6] developed SEA models building using templates. And a set of tools were developed to further automate the SEA model building process. A. Galasso et al. [7] obtained the loss factor of models by testing and verified the vehicle model accuracy using the tested results.

This paper establishes a vehicle SEA model, and the physical properties including modal density, damping loss factor and materials parameters are applied into the model. This paper also verifies the accuracy of the model, and predicts the interior noise at operating running condition. Last section in this paper proposes two kinds of optimized methods for the interior noise reduction based on the analysis of noise path contributions.

2 SEA Basic Theory

The SEA is a modeling analytical method, which can predict the theoretical assessment of dynamic characteristics, vibration response level and sound radiation using the energy flow relationship. The SEA has a statistical characteristic in time domain and space domain. These energy flow relationships have a simple thermal analogy between various coupled subsystems (such as plate, shell, etc.). In the application of SEA theory, the vehicle is divided into several subsystems, and the energy flow between subsystems is assumed to be caused by resonance between structural modes and acoustic modes. Usually, the SEA is the energy or power flow analysis between a group of resonance oscillators.

Each subsystem of the model has the energy levels in steady state, which are proportioned to the mean-square vibration velocity [v_i^2] (or mean-square sound pressure [p_i^2]) averaged in time domain and space domain, i.s.

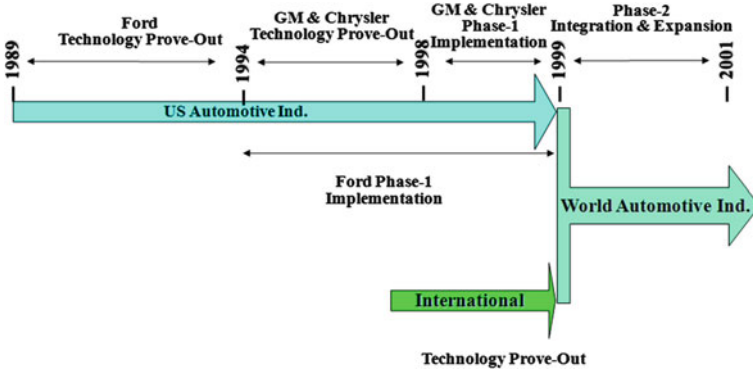


Fig. 1 The application history of SEA in automotive industry

$$E_i = M_i \cdot [v_i^2] E_i = \frac{V_i}{\rho c^2} \cdot [p_i^2] \tag{1}$$

where E_i is the energy of subsystem. M_i and V_i are equivalent masses and volumes for the structural and acoustical subsystems, respectively. ρ and c are the density and speed for the acoustic medium. A subsystem is defined as a certain group of the same type energy resonant modes, and its response with the assumption of equal energy for same type n_i modes in the frequency band Δf .

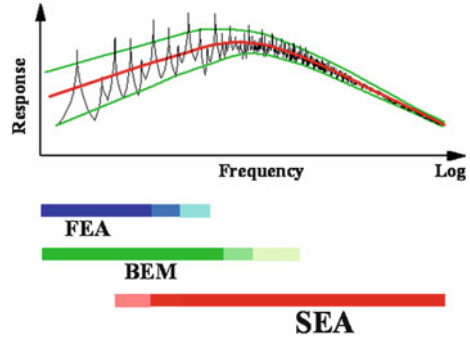
The band-limited energy of subsystem is estimated by the concept of power balance. The distinctive coupling between subsystems is considered, the mean modal energy of subsystem is determined by the following balance equation:

$$\begin{bmatrix} \left(\eta_1 + \sum_{j \neq 1}^k \eta_{1j} \right) n_1 & -\eta_{12} n_1 & \cdots & -\eta_{1k} n_1 \\ -\eta_{21} n_2 & \left(\eta_2 + \sum_{j \neq 2}^k \eta_{2j} \right) n_2 & \cdots & -\eta_{2k} n_2 \\ \cdots & \cdots & \cdots & \cdots \\ -\eta_{k1} n_k & -\eta_{k2} n_k & \cdots & \left(\eta_k + \sum_{j \neq k}^k \eta_{kj} \right) n_k \end{bmatrix} \begin{bmatrix} \bar{E}_1/n_1 \\ \bar{E}_2/n_2 \\ \cdots \\ \bar{E}_k/n_k \end{bmatrix} = \frac{1}{\omega} \begin{bmatrix} \bar{P}_1 \\ \bar{P}_2 \\ \cdots \\ \bar{P}_k \end{bmatrix} \tag{2}$$

where \bar{E}_i is the mean energy, \bar{P}_i is the mean input power, n_i is the modal density, η_i is the damping loss factor, all for subsystem i , and η_{ij} is the energy transfer (coupling) loss factor from subsystem i to j .

Based on the above theory, SEA can be used to predict the average sound pressure level of vehicle interior space in some specific frequency band. The acoustic radiation caused by the vibration modal response excitation is mainly

Fig. 2 The application range of different analytical methods



concentrated in the lower frequency band. In general, the sound radiation due to structural vibration plays a dominant role below 100 Hz. The sound response above 400 Hz has multi-mode characteristics and airborne noise plays a dominant role. Accordingly, the SEA with statistical feature is suitable for airborne noise analysis. In the frequency range between 100 and 400 Hz, the structure-borne and airborne sound energy appear simultaneously, so both structure and air transfer paths should be considered. In fact, the interior acoustic materials and panel trims have limited impact on the noise below 400 Hz. Therefore, SEA is effective in airborne noise analysis above 400 Hz. And the noise below 400 Hz can be analyzed by finite element and boundary element methods. Figure 2 illustrates qualitatively the application range of different analytical methods in noise prediction [2, 8, 9].

3 Vehicle SEA Model Creation

3.1 Structure Subsystem Modeling

The vehicle structure subsystems model is established based on the existing finite element model in trim body. As analysis of the existing model, the model is divided into two groups, one includes the supported beams, reinforcements etc., other one includes the main body cover panels which are necessary for SEA modeling, as illustrated in Fig. 3.

According to its physical characteristics (material, thickness, etc.) and geometric characteristics (flat plates, curved plates, etc.) for the existing geometric model, the vehicle structure subsystem model is established, as shown in Fig. 4. The model has 72 subsystems totally, which consist of 564 elements in plates or shell.

Fig. 3 Vehicle geometry model analysis

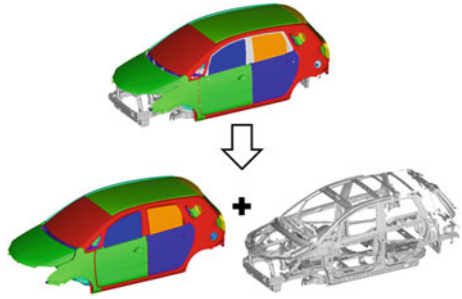


Fig. 4 Vehicle structure SEA model

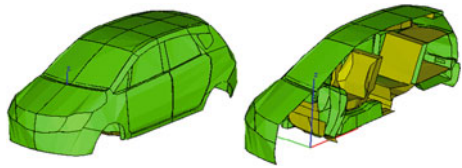
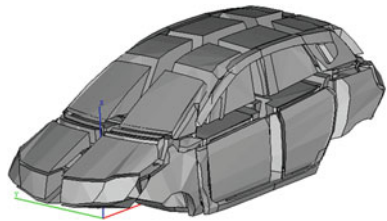


Fig. 5 Inner acoustic cavity subsystem model



3.2 Acoustic Cavity Subsystem Modeling

Acoustic cavity subsystem is divided into two parts of the inner acoustic cavity and the outer acoustic cavity. Once the structure subsystem modeling has been done, both the inner and outer acoustic cavity subsystem modeling are to be proceed, respectively, according to the car interior and exterior room features, and the general principles of the SEA prediction. The models are shown in Figs. 5 and 6.

3.3 Interior Trim Modeling

For the vehicle interior trim acoustic material, due to the complex shapes, unequal cover area, diverse layers, non-uniform thickness and other attributes, so it's difficult of the model establishment using conventional methods. This paper will present the method to simulates the interior trim acoustic material, in which the bare panel creates MNCT (Multiple Noise Control Treatment). Figure 7 intuitively shows the general MNCT creation process.

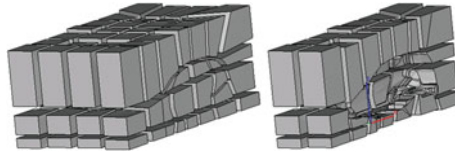


Fig. 6 Outer acoustic cavity subsystem model

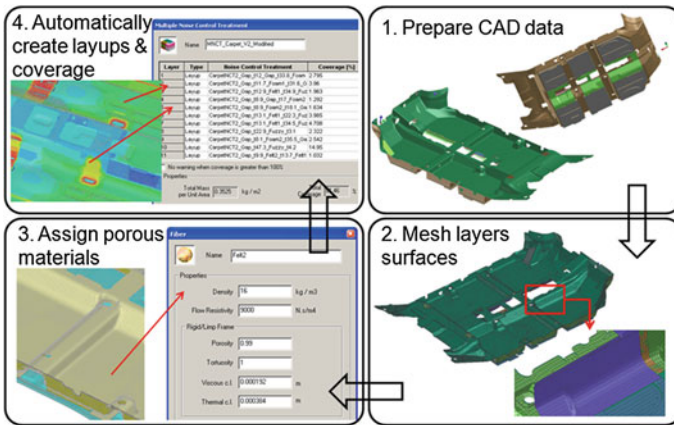


Fig. 7 Creation process of carpet MNCT

According to the division of the body structure subsystems, and the consideration of the fact of the interior trim acoustic materials distributed inside vehicle, the model has 120 MNCTs created totally.

4 Vehicle SEA Model Parameter Obtainment

4.1 Modal Density

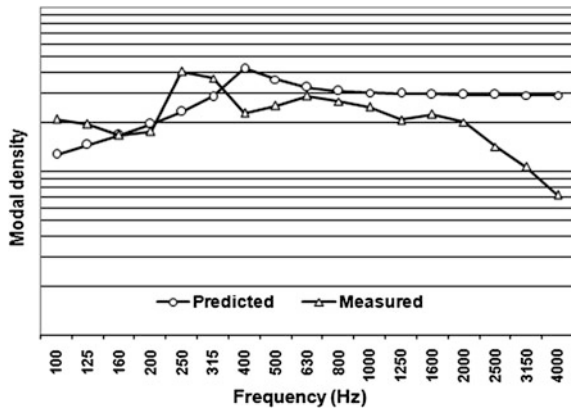
Modal density is the number of modes of the subsystem per unit frequency in a certain frequency range, is a physical quantity to describe the size of stored energy of the vibration system. In order to get the more accurate modal density of structure subsystems, each structure subsystem is tested using experimental approach.

The locations of measured points are determined by the area size and shape complexity of the subsystem. General requirements: Each subsystem has at least five measured points. Measured points should not be selected at the edge or in discontinuous area. The points excited and the points picked up should be close each other as much as possible. Figure 8 shows the distribution of the measured

Fig. 8 Front side glass modal density tests



Fig. 9 Front side glass modal density results



points of the front side glass. In order to avoid both the double-hit and the excitation frequency too lower, the tester should pay attention to the observation of excitation force spectrum and the coherence function during the tests. The general requirements of the overall coherence function reaches above 0.85. The tester should record time signal, coherence function and transfer function. Then the model density curve of the subsystem can be obtained by the data post process. Figure 9 shows the comparison of experimental data and simulation data of the front side glass modal density.

4.2 Damping Loss Factor

Damping loss factor is a ratio of energy loss to average stored energy per unit frequency and per unit time. It is an important parameter of measuring the damping characteristics and determining the vibration energy dissipation. Usually,

Fig. 10 Spare tire curved panel damping loss factor tests

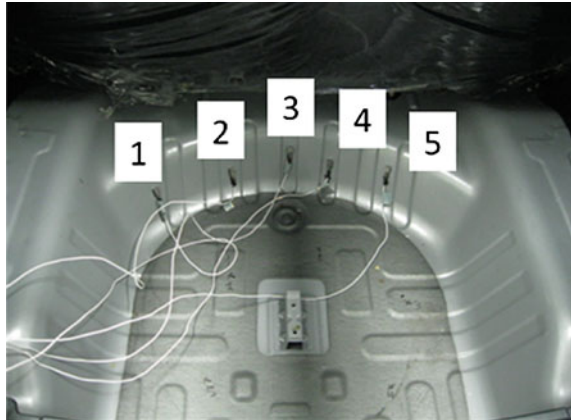
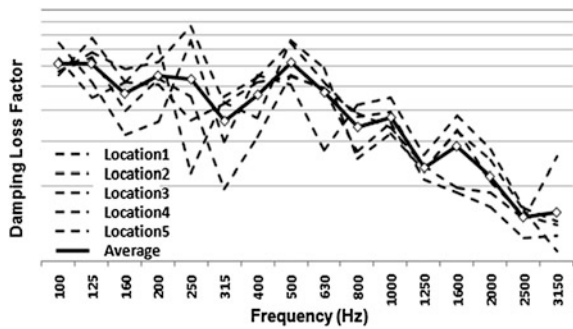


Fig. 11 Spare tire curved panel damping loss factor results



there are two methods for measuring the structural loss factor. One is steady state energy flow. Second one is transient state decay. In this paper, using the method of transient state decay, the average loss factor of the structure is obtained in 1/3 octave band based on the Hilbert Transform [10].

For this test, the principle of selecting measured points and excited points is as same as in modal density test. In the test of spare tire curved panel, according to the size and shape of the panel, five accelerometers are laid in all, as illustrated in Fig. 10. The points closed to measured points are hit by impact hammer in turn around, and the transfer function of the measurements is picked up one by one.

Matlab is used to process the collected data. One curve of damping loss factor can be obtained at one measured point, then the overall damping loss factor for the curved panel can be obtained in averaging all of the curves, as shown in Fig. 11.

Table 1 Material parameters of seat cushion

Material parameter		Number of tests	Mean value	Standard deviation
σ	Airflow resistivity (Ns/m ⁴)	4	24,024	2,727
Φ	Open porosity	4	0.96	0.01
ρ	Bulk density (kg/m ³)	4	57.3	0.5
E	Young's modulus (Pa)	4	180,000	21,000
ν	Poisson's ratio	4	0.031	0.024
η	Damping loss factor	4	0.121	0.011
α_∞	Geometrical tortuosity	4	2.25	0.5
\wedge	Viscous length (m)	4	80e-6	42.7e-6
\wedge	Thermal length (m)	4	348.7e-6	219.4e-6

4.3 Porous Material Parameters Identification

In order to define the interior trim acoustic material properties of the model accurately, there are more than 20 kinds of porous materials to be identified for their parameters and the relevant database. To identify the material parameters most relies on testing method using the impedance tube plus the other testing sets. Some parameters still cannot be identified due to the limitation of the existing test equipments. These parameters may be aided by the simulation in FOAM-X. Table 1 shows the results of seat cushion material parameters.

5 Vehicle SEA Model Excitation Test

5.1 Ideal Running Condition Test and Model Validation

The ideal running condition test is a simulation test as the engine shut-off, which replace the engine and tire real noise sources with acoustic point sources, respectively, to get the responses of the inner and outer cavities at the same time. The test results of ideal running condition are used for model validation mainly, since the point source is relatively simple and the regularity of the inner and outer cavities response is relatively clear in the ideal running condition test.

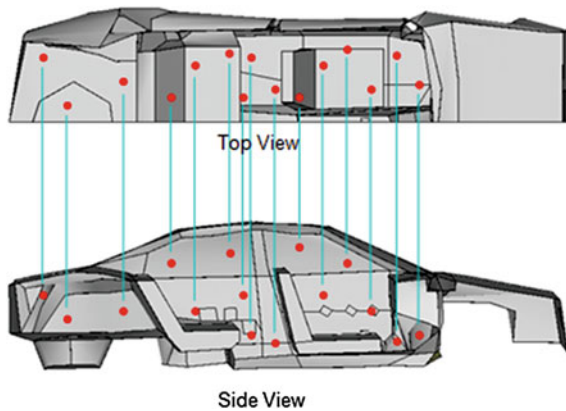
According to the different positions of the point sources layout, the tests are planned with five excitation conditions, four conditions for tire excitations and one condition for engine excitation. The point sources layout is shown in Fig. 12.

The distribution of microphone locations and the number of microphones is determined by the division of cavities and the symmetry of structures. The general principle of measurement points distribution: three points are laid uniformly for each cavity. For outer cavity, the exterior microphones are set away from the body about 20–40 cm. Figures 13 and 14 shows the measurement points distribution diagrams for inner and outer cavities.



Fig. 12 Source locations of ideal running condition tests

Fig. 13 Measurement locations of inner cavity



In the test, operator needs to record both the response and the background noise for each load condition, and check the consistency of the recorded data, the ratio of signal to noise and the acoustic symmetry of cavities.

The results in the simulation and in testing are checked and compared one by one. To find out if the errors or mistakes happened in SEA model or in testing setup according to the noise contribution analysis. Repeating the method mentioned above for model validation, the good model will be available. As shown in Fig. 15, the simulation results of the inner cavity has reached the desired accuracy after the model validation, namely, the result discrepancy between the prediction and the testing is less than 3 dB(A) in 1/3 octave band.

Fig. 14 Measurement locations of outer cavity

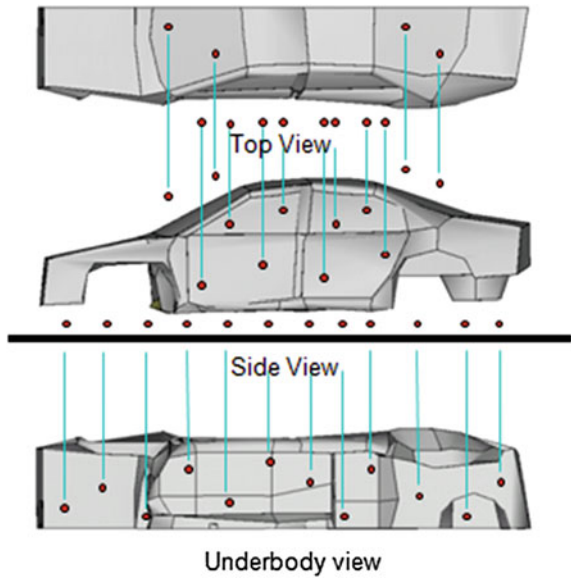
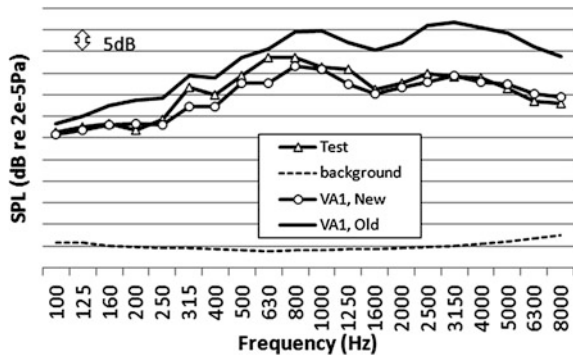


Fig. 15 The result of model correction



5.2 Operating Condition Test

The operating condition test is the measurements for the inner and outer cavity responses under the vehicle real running condition, which includes three conditions: one is the engine running only, the second is single tires running counted, and the third one is the mixed condition, i.e. the combination of the engine and tires running at same time. As shown in Fig. 16, the operating condition test is operated in semi-anechoic chamber with chassis dynamometer, and the distribution of measurement points are the same as in ideal running condition test.

Both the response spectrum and the background noise are recorded for each load condition in the tests, The requirements for this are the same as in the ideal running condition test. The accurate data is output after the data checking.



Fig. 16 Operating condition load tests

Using the tested sound pressure spectrum of the outer cavities as three operation load conditions, it is preparation that for the interior noise prediction and optimization in the next steps.

6 Interior Noise Prediction and Optimization

For the interior noise prediction, the three load cases have been selected as model excitation sources in prior section. These three load cases are loaded respectively into the model, then the model is run for the calculation. Figure 17 shows the predicted results of driver head cavity noise performance in the mixed condition. Above 500 Hz, the results in prediction and in test are mostly consistent, and the discrepancy is within 3 dB(A). But below 500 Hz, the discrepancy between the predicted and test results is quite big, mainly due the model prediction only considers the airborne noise, not the structure-borne noise.

The noise contribution analysis for one particular cavity can determine the main noise sources and the main transmission paths to the cavity. Figure 18 shows the result of noise contribution analysis for driver head cavity. The most noise contributions for driver head cavity came from the dash, front doors and floor.

Based on the noise contribution analysis results, two optimized methods are proposed to reduce the vehicle interior high-frequency noise. One proposal is replacement of the single layer glass of the front doors with the sandwich glass, which improves the thickness and damping of glass, but increases the vehicle weight about 3 kg. Another proposal is replacement of the rubber layer of the dash insulator with high impedance felt, which improves the sound absorption and reduces the vehicle weight by 2.7 kg. As consideration of two kinds of optimized proposals, the interior noise reduces 1 ~ 3 dB(A) in the main frequency range without the changes of vehicle weight, as shown in Fig. 19.

Fig. 17 The prediction result of interior noise performances

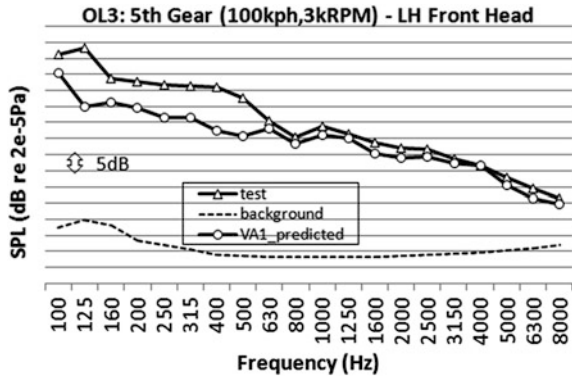


Fig. 18 The result of noise contribution analysis

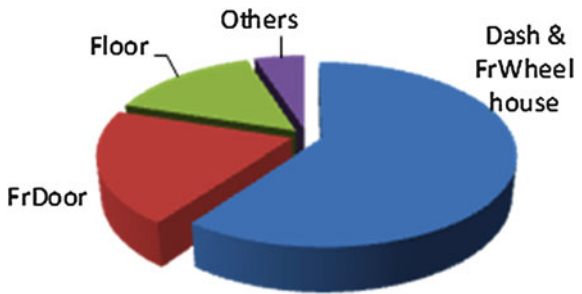
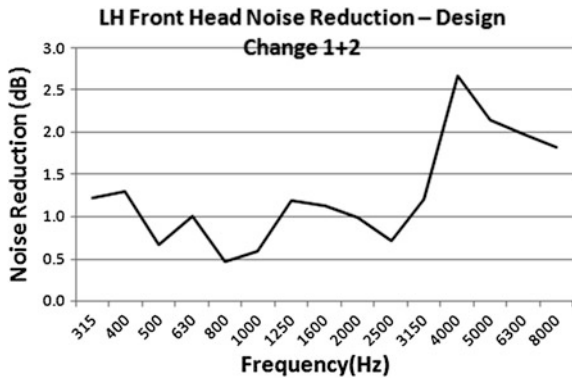


Fig. 19 Noise reduction after design change



7 Conclusions

This paper describes the theory of SEA, one vehicle SEA model established, the vehicle MNCT created based on interior trim acoustic materials CAD model and metal panels finite element model, the panel model density, the damping loss factor and the basic parameters of interior trim acoustic materials obtained by

testing, the vehicle interior high-frequency noise tested and predicted under different load conditions. The following conclusions were obtained:

1. The vehicle model is validated by the simulation on ideal running conditions. The simulation results of inner cavity has reached the engineering accuracy requirements after the model validation, namely, the interior noise discrepancy between prediction and testing is less than 3 dB(A) in 1/3 octave band.
2. The results in operating loads analysis shows that the SEA model after validation can be applied to the operating loads simulation. Namely, the validity of the SEA model is proved.
3. Through the noise contribution analysis for driver head cavity, the most noise contribution for driver head cavity came from the dash, front doors and floor.
4. As consideration of two kinds of optimized proposals, the interior noise had been reduced by 1 ~ 3 dB(A) in the main frequency range without the changes of vehicle weight.

Acknowledgments The authors would like to thank the following individuals for their assistance and support: Dr. Pang Jian, Frank WU, and other colleagues all from Changan Auto Global R&D Center.

References

1. Pang J, Chen G, He H (2006) Automotive noise and vibration-principle and application. Beijing Institute of Technology Press, Beijing
2. Liu T, Gu Y (2006) SEA application in vehicle interior noise analysis. *Noise Vibr Control* 4:66–69
3. Wang D, Chen S (2009) Car interior noise prediction and experimentation using statistical energy analysis. *J Jilin Univ* 39(3):68–73
4. Liu WL, Tao D, Kathawate G (1999) Use of statistical energy analysis method to predict sound transmission loss of sound barrier assemblies. SAE: 1999-01-1707
5. Moore JA, Powell R, Bharj T (1999) Development of condensed SEA models of passenger vehicles. SAE: 1999-01-1699
6. Blanchet D, Cunningham A (2003) Building 3D SEA models from templates-new developments. SAE: 2003-01-1541
7. Galasso A, Montuori G, Rosa S D, Franco F (2003) Vibroacoustic analyses of car components by experimental and numerical tools. SAE: 2003-01-14
8. Huang LY, Krishnan R, Connelly T, Knittel JD (2003) Development of a luxury vehicle acoustic package using SEA full vehicle model. SAE: 2003-01-1554
9. Zhenpo W, Hongwen H (2001) Study on prediction of vehicle vibration and noise by using SEA method. *Automobile Sci Technol* 6:10–34
10. Ning F, Zhang J (2002) Hilbert transform in loss factor measurement. *J Shandong Inst Technol* 16(1):17–20

Optimization of Subframe Mounting System to Reduce the Interior Booming

Jianghua Fu, Xiaomin Xu, Jingbo Li, Dongzheng Ma
and Debin Yu

Abstract To study the influence of the subframe mounting system on vehicle interior NVH performance, to optimize a subframe mounting system in order to reduce the interior booming in the early development phase, are the research purpose. An analysis method including both CAE simulation and testing is used to establish the subframe mounting system model in this chapter. Impact of the subframe mounting system on interior noise and vibration is analyzed in the aspects of the subframe mounting stiffness and the added mass, as well as the subframe structure is optimized simultaneously. The optimized subframe mounting system is validated by the testing, and the results show that the interior booming and vibration are significantly reduced. Subframe mount stiffness and the added mass have influence on the interior NVH performance. Matching the subframe mount appropriately would improve the NVH performance.

Keywords Subframe · Mount · NVH · Booming · Optimization

F2012-J06-004

J. Fu (✉) · X. Xu · J. Li · D. Ma · D. Yu
Changan Auto Global R&D Center, Chongqing, China
e-mail: sunqiemail@163.com

J. Fu · X. Xu · J. Li · D. Ma · D. Yu
State Key Laboratory of Vehicle NVH and Safety Technology, Chongqing, China

1 Introduction

Subframe is usually connected to the body with four mounts. Subframe and these mounts constitute the subframe mounting system, which is mainly used to attenuate the vibration and to improve the connection stiffness of suspension system.

To investigate the relationship between the subframe system and vehicle interior NVH performance, the subframe mounting system is optimized, combined with a vehicle interior booming problem. At present the studies on the subframe mounting system mainly focus on the subframe [1–4], such as subframe modal analysis [5], strength analysis [6], lightweight research [7], durability [8, 9] and topology optimization [10], and so on. There is little study on the influence between subframe mounting system and vehicle interior NVH performance.

A simple subframe mounting system is established in this chapter, combined with the CAE simulation and test method [11]. Parameters of the subframe mounting system including the mount stiffness and added mass of the subframe are studied and optimized, to reduce the interior booming and improve the NVH performance.

2 Modeling of Subframe Mounting System

Establishing a simple CAE model combined with test data could predict the interior NVH performance when the parameter of subframe mounting system is changed.

2.1 Introduction of the Model

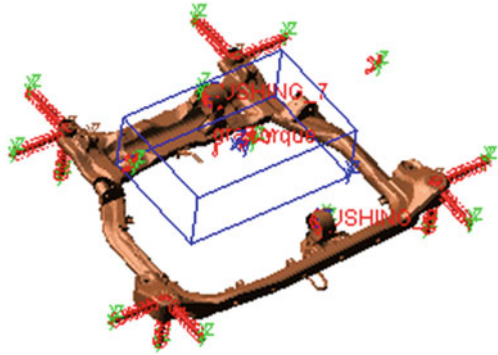
A dynamic model of the subframe mounting system is set up as shown in Fig. 1. The model is consist of subframe, subframe mount, powerplant and powerplant mount. Subframe is a flexible body, which is connected to the ground through 4 subframe mounts in the model. The left and right mounts of powerplant are connected to the ground as well while the other two mounts i.e., front and rear mounts are connected to the subframe.

The transfer function from the input to the output could be considered as the effect of all the sub paths. Therefore the vehicle interior vibro-acoustic transfer function P_{int}/F_{sub} is expressed as follows [12]:

$$\frac{P_{int}}{F_{sub}} = \frac{P_{int}}{F_{body}} \times \frac{F_{body}}{F_{sub}} \quad (1)$$

Where P_{int} is the sound pressure of the interior point; F_{sub} indicates the excitation force in the subframe side of the subframe mount; F_{body} represents the response

Fig. 1 Model of Subframe mount system



force of the body side. As we can see, F_{body}/F_{sub} is the vibration transmissibility of the subframe mount.

The vibration transmissibility of the subframe model could be obtained according to the Fig. 1 while the transfer function from the vehicle side of subframe mount to the vehicle interior point would be measured by test. According to the Eq. (1), the interior noise level could be predicted. Using both simulation and test data, the simple subframe mounting system model could predict the interior noise instead of full vehicle model.

Similarly, the vehicle interior vibration transmissibility a_{int}/F_{sub} could represent as

$$\frac{a_{int}}{F_{sub}} = \frac{a_{int}}{F_{body}} \times \frac{F_{body}}{F_{sub}} \tag{2}$$

Where a_{int} indicates the vehicle interior vibration acceleration; F_{sub} is the excitation force in the subframe side of the subframe mount; F_{body} represents the response force in the body side of subframe mount. According to the Eq. (2) can predict the in-car vibration level.

2.2 Model Verification

In order to ensure the precision of the simulation, the test data is used to verify the model. The model is checked from the aspect of transfer characteristics, i.e., simulation transfer performance is compared with the test data.

Taking the left side of the front subframe mount for example, the vibro-acoustic transfer function of subframe mount from the subframe side in x, y and z direction to the driver’s right ear is shown in Figs. 2, 3 and 4 respectively. The red dashed line is the simulation results while the blue solid line indicates the test data.

All the simulation curves of the transfer function from subframe to driver’s right ear in each direction match well with the test curves. Thus the model can accurately represent full vehicle performance. If there is a big difference between

Fig. 2 Vibro-acoustic transfer function from subframe to driver's right ear in x direction

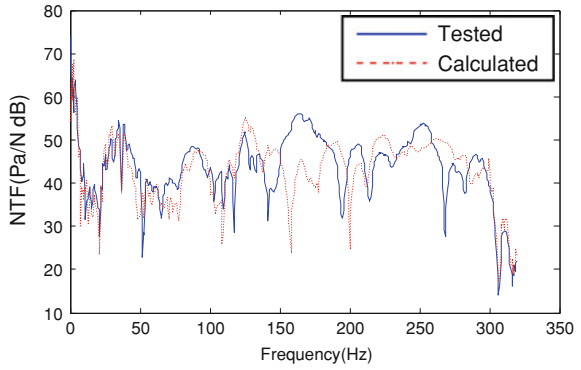


Fig. 3 Vibro-acoustic transfer function from subframe to driver's right ear in y direction

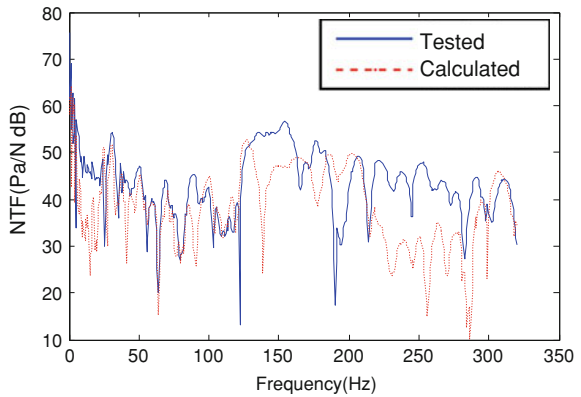
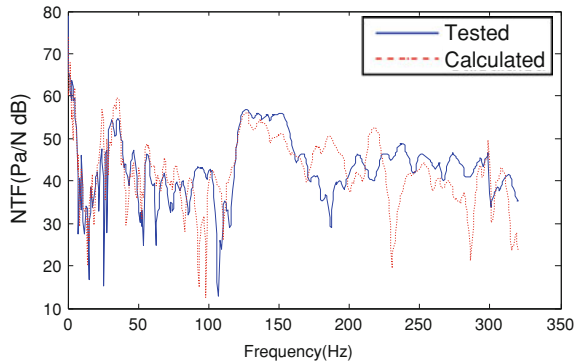


Fig. 4 Vibro-acoustic transfer function from subframe to driver's right ear in z direction



the test value and the simulation one, the stiffness of the subframe mount should be adjusted accordingly. That's because the subframe model with subframe mounts connect to the ground directly, whose boundary condition is different from the real vehicle.

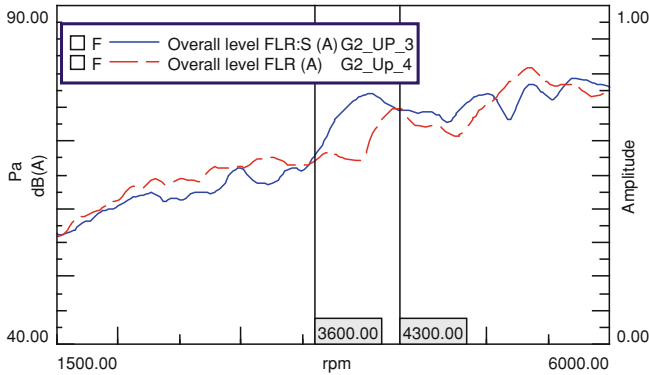
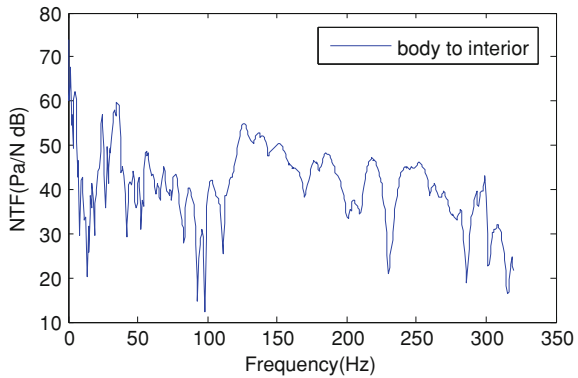


Fig. 5 Driver’s right ear noise

Fig. 6 Vibro-acoustic transfer function from body side of subframe to driver’s right ear in z direction



3 Interior Booming Analysis

There is a serious interior booming in the range of 3,600–4,300 rpm when the car speed up in gear 2. As shown in Fig. 5, the blue solid line is the noise level at driver’s right ear, and the red dashed line is responding data of the benchmark. There is an obvious peak at the driver’s right ear during 3,600–4,300 rpm.

Noise can be divided into structural booming and air booming, which are caused by different reasons. A unit excitation force is applied at the center of gravity (COG) of the engine in the model as shown in Fig. 1 and the vibration transmissibility of each subframe mount could be obtained. According to Eq. (1), the vibration transmissibility multiplies the vibro-acoustic in Fig. 6, then the whole transfer function, as shown in Fig. 7, could be obtained. Similarly, we can get the vibration transfer curve in x and y direction, as shown in Figs. 8 and 9 respectively.

Vehicle interior booming takes place around 3,900 rpm, corresponding to the excitation frequency 130 Hz. From Figs. 7, 8 and 9, it is known that there is a peak

Fig. 7 Vibro-acoustic transfer function from engine to driver's right ear in z direction

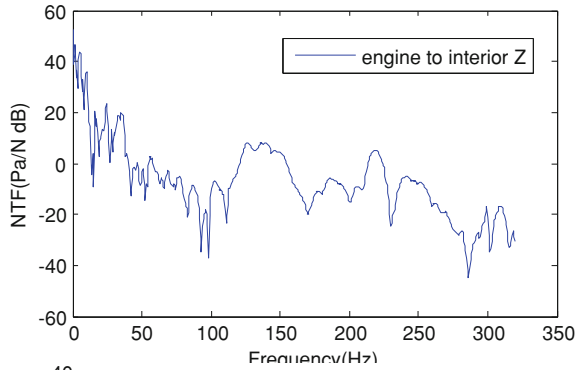


Fig. 8 Vibro-acoustic transfer function from engine to driver's right ear in x direction

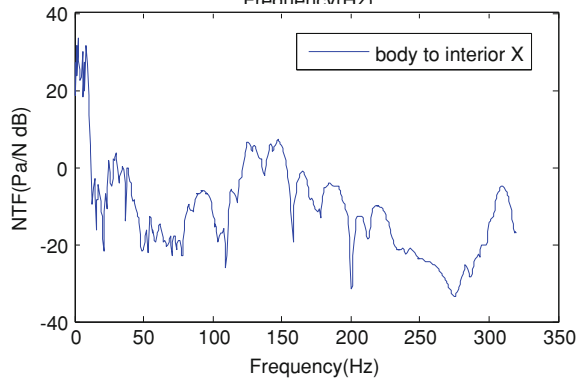
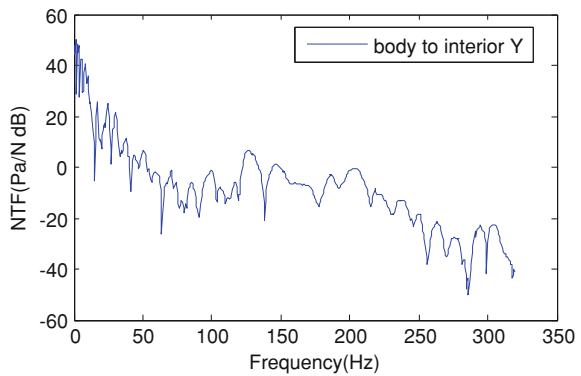


Fig. 9 Vibro-acoustic transfer function from engine to driver's right ear in y direction



near 130 Hz in the vibro-acoustic transfer function from the engine to driver's right ear. Thus the booming in 3,600–4,300 rpm may be caused through this transfer path.

Compared the 2nd order content of driver's right ear with its overall noise in above speed range, as shown in Fig. 10, it can be determined roughly that the 2nd order interior vibration may be the main cause of booming. The 2nd content rises up sharply from 3,300 rpm, which induces the resonance booming of high speed.

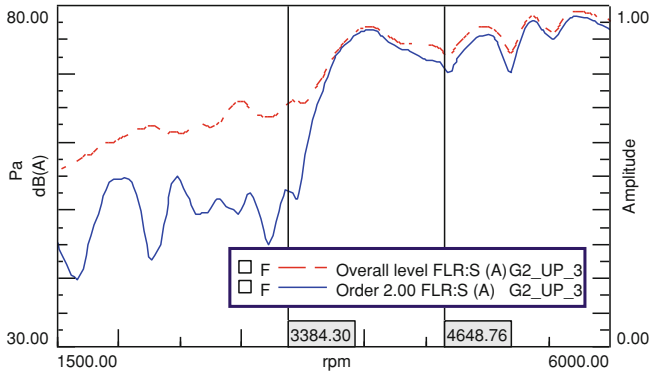
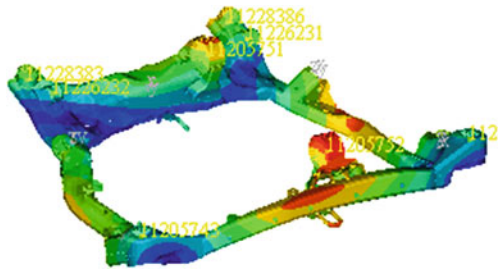


Fig. 10 Noise analysis of driver’s right ear

Fig. 11 Subframe modal shape in 132 Hz



The 2nd order content and the overall of the noise are almost the same in 3,600–4,300 rpm. Therefore, the interior booming is mainly caused by the 2nd order vibration of engine, which transfers through subframe to body.

At the same time the calculated modal analysis of the subframe is performed, whose modal shape is shown in Fig. 11. The modal frequency is 132 Hz, which is corresponded to the frequency of interior structural booming.

It shows that there is a resonant coincidence between engine and subframe at the 3,900 rpm in Fig. 11, which cause the interior booming. To overcome above booming problem, changing the parameter of subframe could improve the interior NVH performance.

4 Optimization

According to the Eq. (1), when the transfer function from the body to vehicle interior point is not changed, the vibration transmissibility only be considered for predicting the interior noise. The subframe mounting system is optimized from the

Fig. 12 Vibration transmissibility from engine to body side of subframe mount in x direction

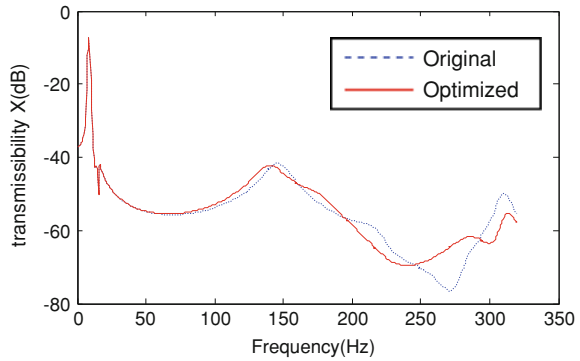
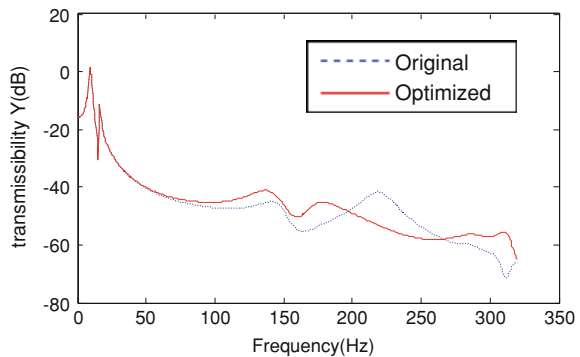


Fig. 13 Vibration transmissibility from engine to body side of subframe mount in y direction



aspects of adding a mass on the subframe and altering the stiffness of subframe mount. Simultaneously, the effect of above solution is verified by test.

4.1 Optimization Solution with Added Mass

Adding a mass at the joints between the front mount of powerplant and subframe where is a bigger vibration according to Fig. 11, could change the transfer characteristics of subframe effectively. With the transfer function in 130 Hz as the optimization objective, the mass of the added mass is optimized. During the optimization, the size of the mass block is constrained in view of the installation space available.

The mass of the mass block is 1.62 kg according to the optimization result. Subframe mounting system is simulated after the optimization and the result is compared with that before optimization. The unit excitation force is applied in the COG of engine again and the vibration transmissibility from the engine to the body side of subframe mount is shown in Figs. 12, 13 and 14.

Fig. 14 Vibration transmissibility from engine to body side of subframe mount in z direction

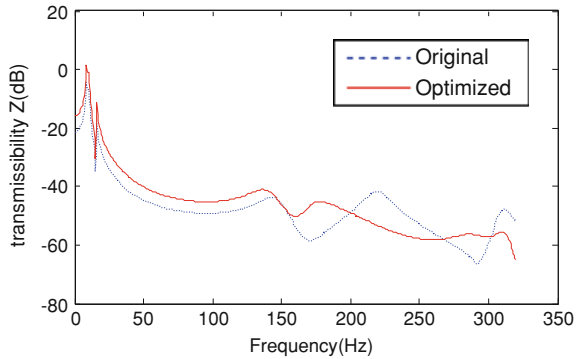
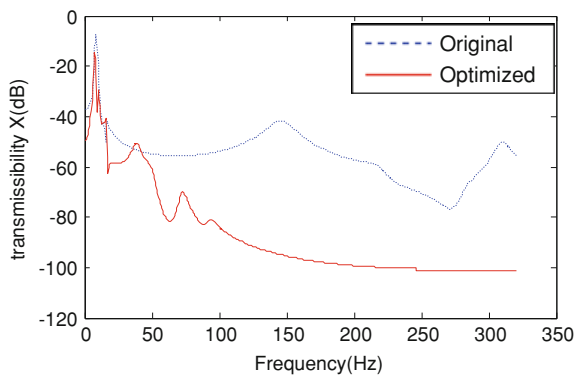


Fig. 15 Vibration transmissibility from engine to body side of subframe mount in x direction



It can be known that all the vibration transmissibility curves have been improved in different extent according to Figs. 12, 13 and 14 and all the peak in 130 Hz move to lower frequency. Therefore this optimization solution could improve interior booming.

4.2 Optimization Solution with Different Subframe Mount Stiffness

With the vibration transmissibility of subframe mounting system as the optimization objective, the stiffness of subframe mount in each direction is optimized. During the optimization, all the subframe mounts have the same stiffness and the mount stiffness ratio of pressure to shear is controlled to ensure the feasibility of optimization results.

The unit excitation is applied in the COG of engine, and the vibration transmissibility curve is shown in Figs. 15, 16 and 17.

Fig. 16 Vibration transmissibility from engine to body side of subframe mount in y direction

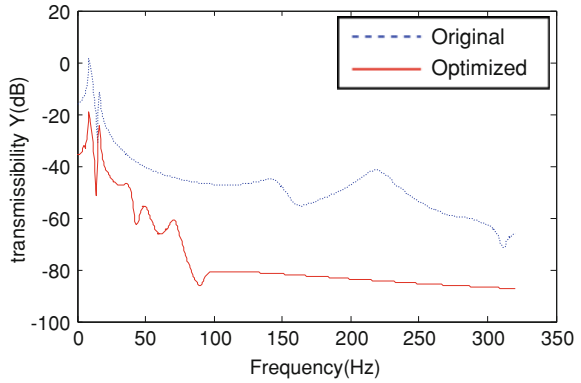
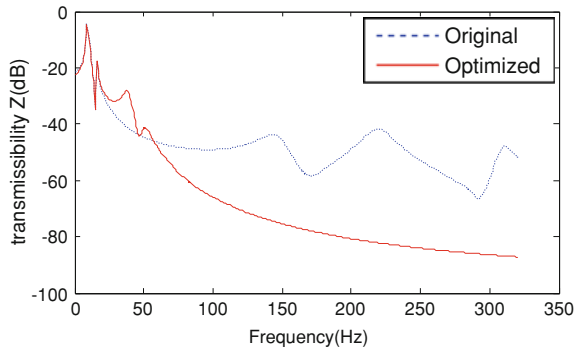


Fig. 17 Vibration transmissibility from engine to body side of subframe mount in z direction



There is a big improvement in vibration transmissibility after optimization according to Figs. 15, 16 and 17. Thus optimizing the stiffness of the subframe mount could ameliorate the interior booming.

4.3 Test Validation

It's convenient to verify the effect of the solution adding a mass on the subframe, meanwhile it takes time to make a sample with new stiffness. Therefore only the added mass solution is validated in this chapter.

As shown in Fig. 18 a 1.5 kg mass is attached in the point corresponding to the CAE indication, i.e., the place between subframe and front mount of engine. Driver's right ear noise and the NTF from body side of powerplant mount to driver's right ear are tested.

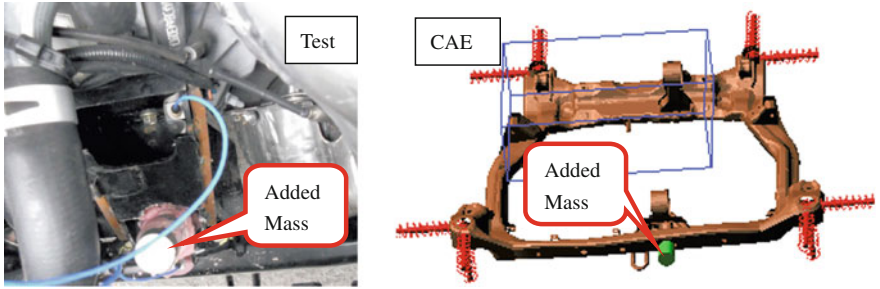


Fig. 18 Subframe with added mass

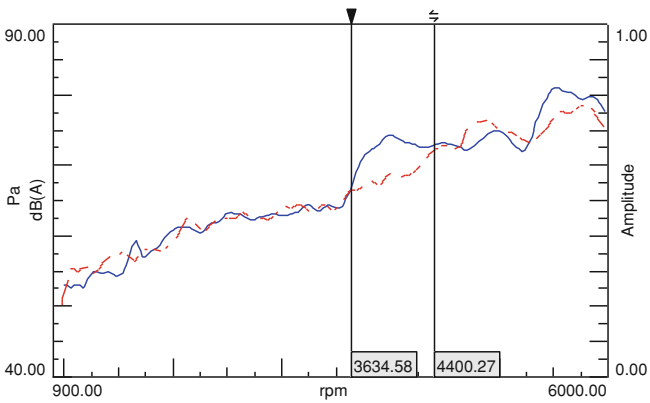


Fig. 19 Overall noise of driver's right ear

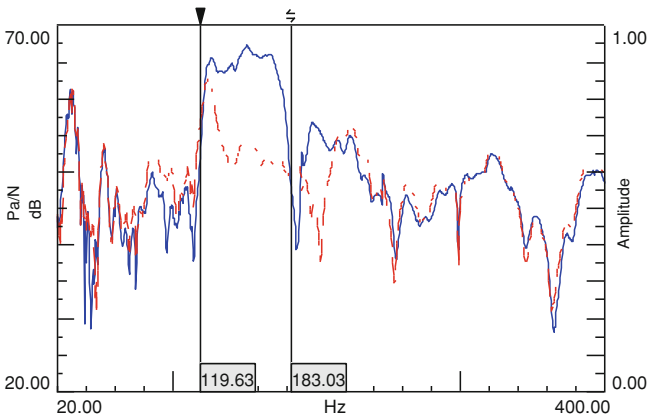


Fig. 20 NTF from powerplant mount to driver's right ear

The overall interior noise and NTF curve is shown in Figs. 8 and 9 respectively. Blue solid line is the original state, while the red dashed line for the improved state.

The peak in 3,600–4,300 rpm has been suppressed with added mass as shown in Fig. 19, and there is no booming noise when subjective evaluation. The NTF level from body side of powerplant mount to driver's right ear has been reduced as well in Fig. 20. NTF has been reduced 12 dB from 120 to 180 Hz. Thus adding a mass resolve the booming in 3,600–4,300 rpm successfully.

5 Conclusion

The interior booming problem has been resolved by optimizing the parameter of the subframe mount system. The interior vibration is reduced and consequently the interior NVH performance is improved.

The stiffness of subframe mount and the added mass have influence on interior NVH performance. Match subframe mount system reasonably could improved the NVH performance. In addition, this method has some limitations, i.e., not all the booming problems can be overcome through the optimization of subframe mount system.

Acknowledgments In the process of writing this chapter, doctor PANG Jian, vice president of Changan Auto Global R&D Center, and WU Guo-ming deputy chief engineer give me much guidance. Thanks for their help!

References

1. Nakagawa T, Nishigaki H et al.(2004) First order analysis for automotive body structure design—Part 4: noise and vibration analysis applied to a subframe. SAE:2004-01-1661
2. Park SY, Park DC et al.(2009) A study of front subframe system optimization for improving vehicle nvh performance. SAE:2009-01-2097
3. Murali MR, Krishna, Carifo J (2000) Optimization of an engine cradle in frequency domain. SAE:2000-01-0599
4. Xin T, Gan C, Jian-peng S (2009) The FM simulation of structure improvement of a car subframe. *Automobile Sci Technol* 5:49–51
5. Yun W, Hong Z, Haijian M (2007) Modal test and fea modal analysis of subframe. *China Sci Technol Inf* 3:87–89
6. Song-lin Z, Yun-yi W et al (2009) The structural strength and modal analysis of the rear subframe in the passenger car. *Shanghai Auto* 11:20–22
7. Li-ling Z, Li H, Zi-qing YE, Yi L (2010) Research and application of lightweight technology for passenger car subframes. *J Plast Eng* 17(5):71–75
8. Cheng-long W (2005) Car cradle durability design based on finite element analysis. *Shanghai Auto* 4:32–34
9. Jun Tan (2009) The car subframe assembly durability adapting rapid development research. *Shanghai Auto* 3:18–21

10. Jun L, Jing-zhong L, Wang-yue HU (2010) Topology-optimization of the fuel-cell-car's vice-frame structure. Bull Sci Technol 26(4):628–632
11. Qatu M, Sirafi M (2003) Accurate modeling for the powertrain and subframe modes. SAE:2003-01-1469
12. Daly MA (2003) Influence of mount stiffness on body/subframe acoustic sensitivities. SAE:2003-01-1714

Disturbing Noise Identification and Sound Quality Research on Car Generator

Yanfang Hou, Guohua Han, Yaozhen Zhao and Xueying Xu

Abstract As cars become more and more quiet, the customer's perception for the acoustic comfort increases. Therefore the sound quality of cars interior noise has become a very important task for the acoustic engineers. Because the noise level of cars major components such as motor reduces more and more, the noise of cars auxiliary equipments like generator are paid much attention. This chapter on one hand analyzed one car auxiliary equipment generator's disturbing noise source through the whole car acoustic test, found the generator main order problem, and on the other hand studied the generator's psychoacoustic metrics. In this chapter the countermeasure of solving this problem was also given, and then noise level and psychoacoustic parameters are compared. Both objective evaluation and subjective evaluation showed that the generator with the solution not only reduced the sound pressure level, solved the disturbing noise problem, but also improved the car sound quality greatly.

Keywords Generator · Sound quality · Psychoacoustic metrics

1 Introduction

With the development of vehicle industry technology, noise of car accessories is paid much attention because it plays a more important role in the passenger comfort. Accessories of car includes the accessories not only engine-powered

F2012-J06-010

Y. Hou

College of Electronics and Engineering, Tongji University, Shanghai, China

G. Han (✉) · Y. Zhao · X. Xu

Shanghai Volkswagen Corporation, Shanghai, China

e-mail: hanguohua@cswv.com

accessories driven by the engine through a serpentine belt-alternator, power steering pump, air conditioning compressor, but also power windows, windshield wipers, seat adjustment [1]. Today's customers not only expect vehicles to be quiet, but also importantly to sound comfortable. It is necessary in sound quality research to address the components that are related both to sound and human cognition [2]. Sound quality of accessories is becoming ever more significant in today's vehicle manufacturing industry. This leads sound quality engineers focus their attention not just for low noise level but also for better sound quality in the consumer and appliance industries, and not only for engine, tire, but also for accessory components, including generator, etc. Generator noise is one of the accessories component noises which can be heard and perceived in passenger compartment when engine works. The complexity of generator sounds gives them a multidimensional character from both acoustic and human perceptual points of view.

In this chapter, first subjective evaluation was done, and it found the abnormal noise of car generator sounds like mental click with rpm increasing. Through exchanged the different supplier's generator of the same rated parameter, the abnormal noise is gone. Second the measurement results of generator with complaint and generator without complaint were compared on the same car, and the main problem of noise complaint was found out. Finally, the countermeasure to optimize the generator was given; through optimizing the complained generator, the noise complaint problem was solved, and sound quality was improved a lot. Subjective evaluation and objective measurement both verified this point.

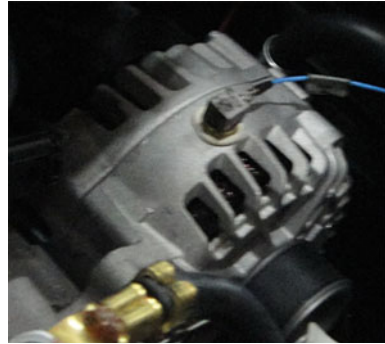
2 Method

2.1 Subjective Evaluation of Generator Noise

The subjective evaluation of the complained car was made in a semi-anechoic room at Shanghai Volkswagen Corporation. It found the noise has something to do with the rpm, and it sounds likes mental click. To make sure the noise source is generator, exchanging the different supplier's generator at the same rated parameter was done. It found the problem of the abnormal noise was solved when using another supplier's generator.

The objective evaluation was also done using Head System and one microphones placed on driver seat and one three direction accelerator was placed on the generator. Measurements of the noise were made for both inside and outside of the car. The accelerator position was showed in Fig. 1. Another supplier's generator without complaint is showed in Fig. 2.

Fig. 1 Accelerator position on the generator



2.2 Objective Evaluation of Generator Noise

The result of the test noises are presented in Fig. 3. It is very clear that the noise complaint comes from electromagnetic noise main order 36 order.

AC electrical generator can be called an alternator. The task of the alternator is generation of electrical energy, and supplies direct current to the battery and the electrical consumers. Alternators generate electricity by the same principle as DC generators, namely, when the magnetic field around a conductor changes, a current is induced in the conductor. Typically, a rotating magnet called the rotor turns within a stationary set of conductors wound in coils on an iron core, called the stator. The field cuts across the conductors, generating an electrical current, as the mechanical input causes the rotor to turn [3].

2.3 Countermeasure for the Complained Generator

There are five countermeasures for the complained generator. Table 1 showed the contents of the rotor improvement (Table 1).

3 Results and Discussion

3.1 Generator Electromagnetic Noise

Car generator noise includes three parts, electromagnetic noise, aerodynamic noise and mechanical noise. The complained generator noise comes from main order 36 order. It is electromagnetic noise problem. Through optimizing the rotor, the noise problem was solved. It can be clearly find in the Fig. 4.

Fig. 2 Another supplier's generator w/o complaint

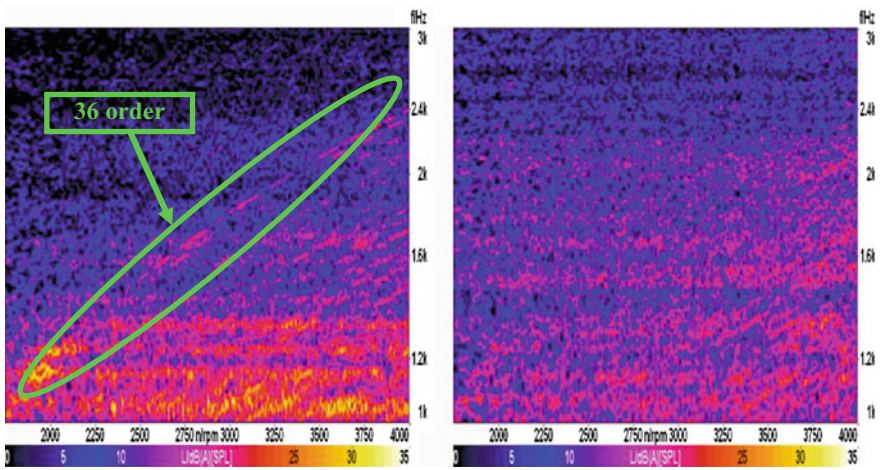
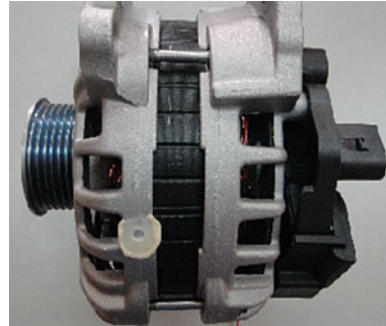


Fig. 3 Colormap comparison of two supplier's generators at driver's ear

Table 1 Countermeasure for the complained generator

Rotor improvement		After improvement	Before improvement
1	Rotor structure Shape of claw	Front & rear different	Front & rear same
2	Single claw Refer claw as centre	Right & left dissymmetrical	Right & left symmetrical
3	Enter interface of electromagnetic	Large arc as gradual	Small arc as straight
4	Exit interface of electromagnetic	Large arc as roundness	Small arc as straight
5	Width	Wider	Normal

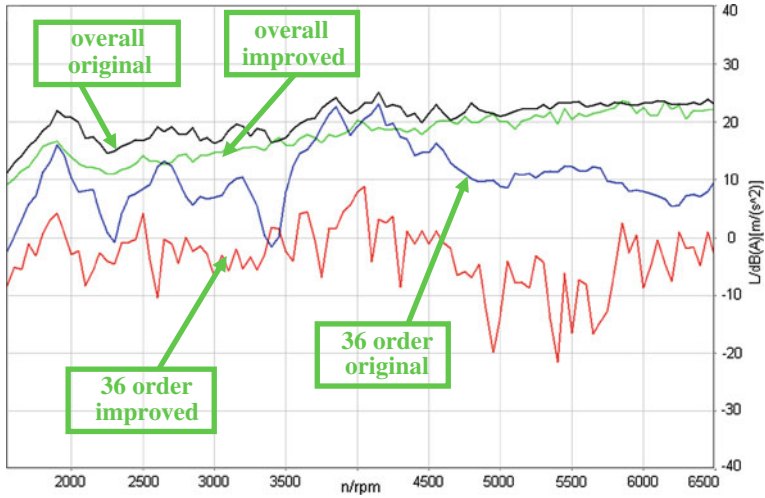


Fig. 4 Order comparison of generators

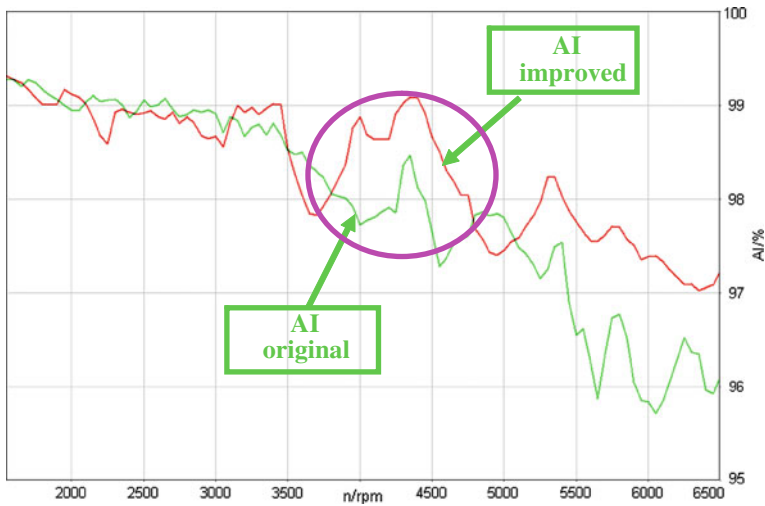


Fig. 5 AI comparison of generators

3.2 Articulation Index

An articulation index of 100 % means that all speech can be understood, 0 % means that no speech can be understood. Articulation Index is calculated from the 1/3 octave band levels between 200 and 6300 Hz centre frequencies. Figure 5 showed after optimizing the generator, AI has a great improvement in the complained rpm area.

4 Summary

This chapter analyzed the abnormal noise of car generator, find the noise comes from the electromagnetic noise. By means of optimizing the generator, the abnormal noise problem was solved. The countermeasures mainly focus on the rotor's performance improvement. The efforts not only reduced the generator electromagnetic main order noise, but also improved the generator's sound quality greatly. This point was both verified by subjective evaluation and objective measurement.

Acknowledgments Shanghai Rising-Star Program (B Type) (11QB1401100).

References

1. Cerrato G (2009) Automotive sound quality: accessories, BSR, and brakes. *Sound and Vibration* 43:10–16
2. Susini P, Mcadams S, Winsberg S, Perry I, Vieillard S, Rodet X (2004) Characterizing the sound quality of air-conditioning noise. *Appl Acoust* 65:763–790
3. <http://en.wikipedia.org/wiki/Alternator>

Characterization of the Automotive Seat Structural Dynamics

Milad Tatari, Mohammad Fard, Naser Nasrolahzadeh
and Mohammad Mahjoob

Abstract Many researches have discussed the dynamics of the vehicle seat structure in response to vibration. The structural dynamics of the seat is linked to the seat noise, vibration and harshness (NVH) quality. The interaction of the vehicle seat resonances with the seat mounting points or the floor resonances may considerably increase the transmission of the vibration into the seat and cause either vibration discomfort or the rattle noise. The vehicle seat rattles or, in general, buzz, squeak, and rattle (BSR) noises are one of the major issues which are directly linked to the NVH of the vehicle. Predicting and improving the seat BSR noise in early design phase is still challenging. This is mainly due to the complexity, nonlinearity and uncertainty of the impact mechanism at joints contributed to the rattle. In this research, two experiments are designed. The first experiment is set up to characterize the seat resonant frequencies and its corresponding structural mode-shapes. The second experiment is designed to measure the seat radiated noise when it goes under vibration excitation. Alternatively, a concept Computer Aided Engineering (CAE) model of the seat is developed and the seat structural dynamics is characterized by using this analytical model. Comparisons of the results of the simulation and experiment validate the developed CAE model. The seat structure demonstrated two major torsion and fore-aft bending structural modes in low vibration frequencies (<50 Hz) where the structure have more potential to be rattled. We have confirmed that the occurrence of the rattle noise is

F2012-J06-013

M. Tatari · N. Nasrolahzadeh · M. Mahjoob
School of Mechanical Engineering, College of Engineering,
University of Tehran, Tehran, Iran

M. Fard (✉)
School of Aerospace, Mechanical and Manufacturing Engineering, RMIT University,
Melbourne, Australia
e-mail: mohammad.fard@rmit.edu.au

related to the seat structural dynamics and it can be controlled and managed by modifying the structure. Two modifications are designed using the seat CAE model. One modification is designed to increase the seat torsion resonance nearly 4 Hz, and the second modification is conducted to decrease the seat torsion resonance nearly 4 Hz. The designed modifications are then implemented on the test seat and the rattle noise is measured on the two modified seats. The results confirm that by changing the seat resonant frequency, the rattle noise and in general BSR noise can be improved or controlled accordingly. Consequently, characterization of the seat structural dynamics led to control and improve the seat BSR noise in early design phase by using the seat CAE model.

Keywords Vehicle seat · Resonant frequency · NVH performance · Rattle noise

1 Introduction

The vehicle seat is one of the major components that have potential to be a source of annoying buzz, squeak, and rattle (BSR) noise [1]. Controlling BSR is becoming essential with the trend toward using lightweight materials combined with the increase in number of the seat sub-components such as electronic gadgets [2]. Moreover, in the quiet cabin of the modern vehicles, BSR has become more prominent as customers perceive BSR as direct indicators of vehicle build quality and durability [3]. According to a market survey, squeaks and rattles are the third most important customer concern in cars after three months of ownership [3]. Furthermore, upcoming electric cars will highlight the importance of the BSR issues [4]. BSR is generally caused by loose or overly flexible elements under excitation. BSR is originated from frictional movement between two parts or from the impact between two parts. The rattle noise is caused when surfaces close to each other move perpendicular to each other due to insufficient attachments or insufficient structural strength [4]. In general, the main causes of the BSR are structural deficiencies, incompatible material pairs, and poor geometrical design [4–6].

Modern advances in the vehicle noise and vibration control engineering have reduced the transmission of the vibration or noise from different sources such as powertrain or road into the passenger cabin [1]. This is mainly due to the development and innovations in virtual or analytical techniques for the structure-borne or airborne noise control in early design phase [7, 8]. Despite the importance of the BSR noises, many of them are detected after production phase of the components, or some even after the vehicle is launched. Therefore, predicting and controlling BSR in the early design phase is important to be investigated [9, 10]. This chapter shows that the seat rattle noise can be predicted and controlled in early design phase by characterizing and controlling the seat structural dynamics. The structural dynamics of the seat is also characterized by using the developed Computer Aided

Engineering (CAE) model of the seat [11–13]. The concept modelling method is used for the CAE modelling of the seat structure [11, 12]. The model is developed to allow us to probe the effects of seat-structure modifications on the rattle noise. Comparisons of the results of the simulation and experiment validate the developed CAE model. The experiment and simulation results show that the seat has two structural resonances in low frequency range (<50 Hz); one at around 31 Hz, which is the seat torsion and the other at around 48 Hz, which is the seat fore-aft bending. The noise measurement result reveals that the seat generates high level of the rattle noise when the seat excitation vibration is close to the seat structure torsion resonance (31 Hz). We have further confirmed that the occurrence of the rattle is related to the seat structural dynamics and it can be controlled and managed by modifying the structure. Two modifications are designed by using the seat CAE model. The designed modifications are then applied on the test seat and the rattle noise is measured on the two modified seats. The results show no more high level of the rattle noise for the two modified seats. Consequently, for the seat system which has an identifiable structural dynamics, the BSR noise can be managed and controlled in early design phase by using the seat CAE model. Furthermore, such early phase modifications of the seat structure are more robust than merely tuning the joints associated with BSR. In fact, the proposed modifications of the structure control the seat resonances and therefore transfer less vibration into the sub-components which are vulnerable to rattle.

2 Method

2.1 Seat Modelling

A selected vehicle seat (Fig. 1) is modelled by using FE methods and CAE techniques. The model of the seat must be correlated with its corresponding test data and it will be used instead of the seat. In other words, the model is developed to characterize the major seat structural dynamic behaviors such as resonant frequencies and corresponding mode shapes. Hence, a concept model which characterizes the main attributes of the system is developed for the seat. It is worthwhile to mention that due to the need of the industry for the fast and high performance computations, the CAE concept modeling method of the automotive body is still an attractive research area for the automotive CAE investigators [15]. According to the CAE concept modeling, the FE model of the seat structure is created via concept beams and joints. The detailed method of CAE modeling or concept modeling is extensively discussed in the literature [11–13]. Altair HyperWorks and MSC Nastran softwares are used for modeling and processing of the seat. The seat frame is made from steel and the steel properties have been used for the structure of the CAE model.

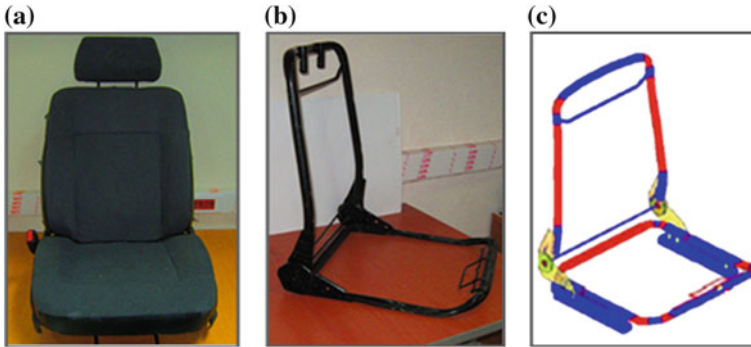


Fig. 1 The vehicle seat used in this research (a) the main frame of the seat structure (b) and its CAE concept model (c)

In CAE concept modelling method, creation of a simple and reliable model for the joints is very important. Extensive researches are reported in the literature about the concept modelling of the main joints in the structure. In this research, Guyan method [14] is used to create simple and reliable concept joints. Guyan Reductionism a method to condense the FE model of structures into a reduced description in terms of the stiffness and mass matrices at the end nodes where the joints connect to the corresponding members. Neglecting the inertia effects in calculating reduced model, Guyan method is also called static condensation. Equation (1) is the general form of the static finite element model.

$$[K]\{X\} = \{F\} \quad (1)$$

Where K is the stiffness matrix, F and X are the force and the displacement vectors, respectively. By identifying boundary degrees of freedom (index b), which must be retained in the solution, and internal degrees of freedom (index i), which are to be removed by static condensation, the system of Eq. (1) can be partitioned as follows:

$$\begin{bmatrix} K_{ii} & K_{ib} \\ K_{bi} & K_{bb} \end{bmatrix} \begin{Bmatrix} x_i \\ x_b \end{Bmatrix} = \begin{Bmatrix} F_i \\ F_b \end{Bmatrix} \quad (2)$$

By substitution of $G_{ib} = -K_{ii}^{-1}K_{ib}$ into the first row of Eq. (2), the Eq. (3) is derived:

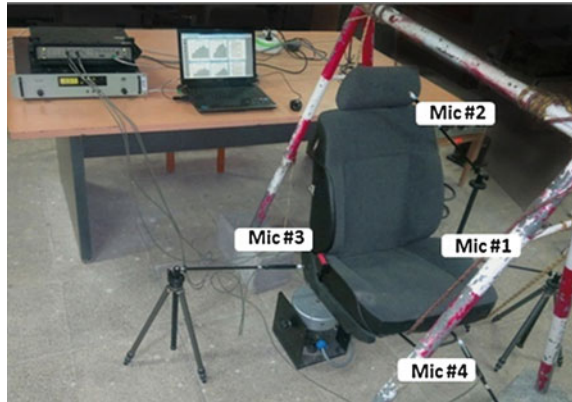
$$x_i = -K_{ii}^{-1}(F_i - K_{ib}x_b) = K_{ii}^{-1}F_i + G_{ib}x_b \quad (3)$$

Finally static condensation matrix is obtained as:

$$K_{bb,red}x_b = F_{b,red} = K_{bi}G_{bi} + K_{bb} \quad (4)$$

The details about Guyan method can be found in the literature [14]. After modelling the seat structure; cushion mass effects are added to the structure using non-structural mass. In other words, the foam cushions are not modelled in

Fig. 2 Test setup and four selected points for measuring the sound pressure level



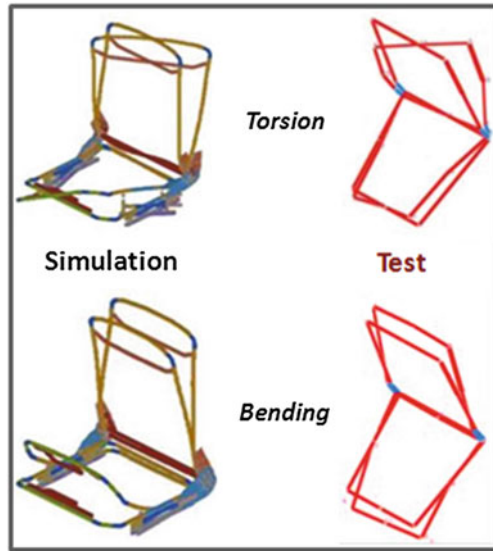
detailed as their stiffness contribution to the seat structure are negligible in low frequencies (<80 Hz). The total mass of the seat cushion,—in the selected vehicle seat, is 6.0 kg.

2.2 Experimental Method

Experimental modal analysis is utilized to characterize the seat structural resonant frequencies and its corresponding mode shapes. Impact hammer test, which is a common method in modal testing, was used to extract the seat structural resonances and mode shapes. The modal test setup consisted of a hammer (Rion PH-51), charge amplifier (B&K 2786), three axial accelerometers, data logger (B&K 3560C) and Pulse 12 software. The seat structure was suspended from bungee cords (elastic ropes) to allow the seat system to be nearly free in six axes. Therefore, the seat modal characteristics were measured in the free boundary condition. The mounting of the accelerometers to the different parts of the seat frame were done using adhesive wax [13]. To obtain proper mode shapes, thirteen points of the seat frame were measured.

In order to measure the BSR noise, the seat is excited by single sine inputs with frequencies between 10 and 60 Hz. Note that we have applied sweep sine inputs to the seat to tune the test frequencies. The generated noise is measured at four points near right and left sides of the seat. The noise measurement system consisted of B&K microphone (B&K 2669), electromagnetic shaker (B&K 4808), amplifier (B&K 2719), data logger (B&K 3560C) and Pulse 12 software. During the experiment, background noise was retained below 36 dB (A) at the running condition of the vibration shaker. The temperature and humidity were kept at 22.5 °C and 35 % respectively. The test setup for noise measurement points at four selected points are illustrated in Fig. 2.

Fig. 3 Seat structural dynamics: torsion modes (*top*) and bending modes (*bottom*) from simulation (*left*) and experiment (*right*) are similar



3 Results

3.1 Simulation and Experiment Results

As already mentioned, to identify the seat rattle noise mechanism and its relation with the seat structure, it is required to characterize the seat structural dynamics. In addition to the experiment the model based simulation results are also required for tuning and controlling the seat rattle noise. The seat structure exhibited two major torsion and fore-aft bending structural modes in low vibration frequencies (<50 Hz) where the structure have more potential to be rattled. The two obtained mode shapes are illustrated in the Fig. 3. As it is shown in Fig. 3, the results of the experiments and corresponding model-based simulation are consistent, so that both have exhibited two torsion and fore-aft shapes. Note that the experimental mode shapes are obtained from the thirteen tri-axial accelerometers.

Following the comparison of the experiment and simulation results, the values of the resonant frequencies and the values of Modal Assurance Criteria (MAC) have been compared (Table 1) between the experiment and the simulation. The MAC index between similar modes of two models is calculated by Eq. (5), in which Φ_E and Φ_C are the Matrix of Eigen vectors for the experimental results and concept model, respectively, and superscript T denotes the transpose of a vector. The Eigen vectors are constructed by using main structure nodes in the test and corresponding nodes in the concept model (a total thirteen nodes).

$$MAC_{E,C}|_k = \frac{(\{\Phi_E\}_k^T \{\Phi_C\}_k)^2}{(\{\Phi_E\}_k^T \{\Phi_E\}_k \{\Phi_C\}_k^T \{\Phi_C\}_k)} \quad (5)$$

Table 1 Comparison of the seat resonant frequencies and corresponding mode shapes between the experiment and simulation

Mode number	Mode nature	Res. freq. experiments (Hz)	Res. freq. simulation (Hz)	Error (Δ) %	MAC
1	Torsional	31	31.9	2.9	0.96
2	Fore-aft bending	48	47.2	1.6	0.91

A MAC value equal to unity indicates a 100 % similarity between the vibration mode shape obtained from the simulation and that of obtained from the experiment. The MAC values, in the Table 1, for the two seat torsion and fore-aft bending modes are found to be above 0.9 (Table 1), which indicates a good consistency between the modes of the developed model and the test data. Comparison of the values of torsion and fore-aft bending resonant frequencies indicate very low discrepancies ($\Delta < 3$ %).

3.2 Noise Source Identification

The radiated sound pressure levels (SPL) are measured when the seat is under the excitation, at four points, which has already been numbered 1–4 in Fig. 2. The results show that when the excitation frequency approaches to the seat torsion resonant frequency (31 Hz), the sub-components of the seat near the seat belt buckle starts rattling. Accordingly, comparison of the SPLs measured by four microphones indicates that the microphone #3, shown in Fig. 2, received higher SPL than other three microphones. Figure 4 compares the SPLs obtained from the four microphones when the seat is excited by a single sine input with 31 Hz frequency (equal to the seat torsion resonance). As it is observed, the rattle causes higher noise level (here 70 dB SPL) mainly at frequencies below 2500 Hz.

By decreasing or increasing the excitation frequency from 31 to 25 or 35 Hz, the rattle noise is also considerably decreased (Fig. 5). In other words, a wide band rattle noise is seen when the seat is excited at its resonance frequency. This confirms that the occurrence of the seat sub-components rattle is linked to the seat resonant frequency, so that by changing the excitation frequency away from the seat structural resonance, the rattle noise can be managed.

3.3 The Effects of the Seat Structure Optimization on the Rattle Noise

Here we have used two strategies to change the seat resonant frequencies and examine the changes of the seat rattle noise. One strategy is based on increasing

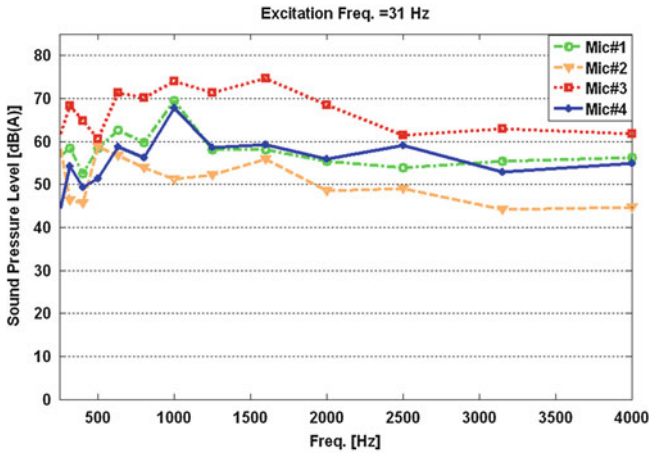


Fig. 4 SPL at four selected points when the seat excited at its 31 Hz resonant frequency

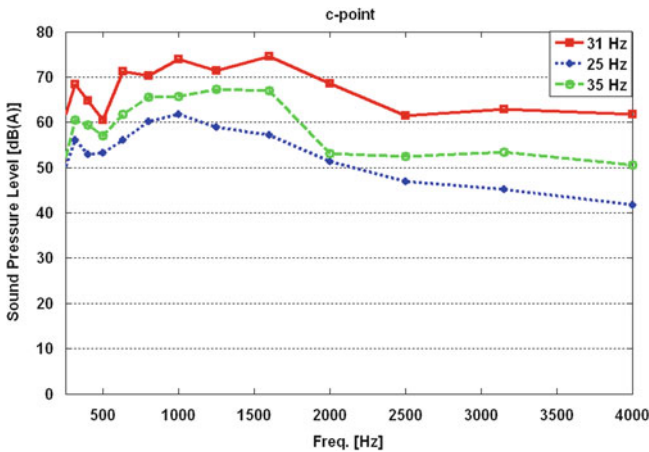


Fig. 5 Comparison of the seat radiated SPLs with those of neighbouring frequencies (25 and 35 Hz) when excitation frequency is equal to seat resonance frequency (31 Hz)

the stiffness of the structure and the other strategy is addition of a lumped mass (called mass/damper) to the structure (Fig. 6). For these purposes, we have first used the developed seat CAE concept model and changed the seat resonant frequency. The designed modifications are then implemented in the physical model. Finally, the modifications effects are investigated on the rattle noise. The modifications of the model are examined to demonstrate the effectiveness of the concept modeling and its advantages to improve and control the rattle or in general BSR noise in the early design phase.

For increasing the stiffness of a part of the seat structure in the model, we increased the young module of the specified part (Fig. 6) to change the torsion

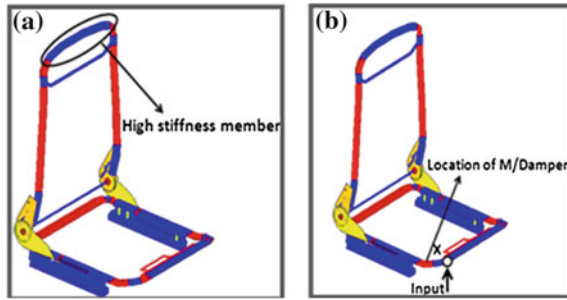


Fig. 6 Modifications of the seat CAE model for changing the resonant frequency by increasing the stiffness (a), and addition of a mass/damper (b)

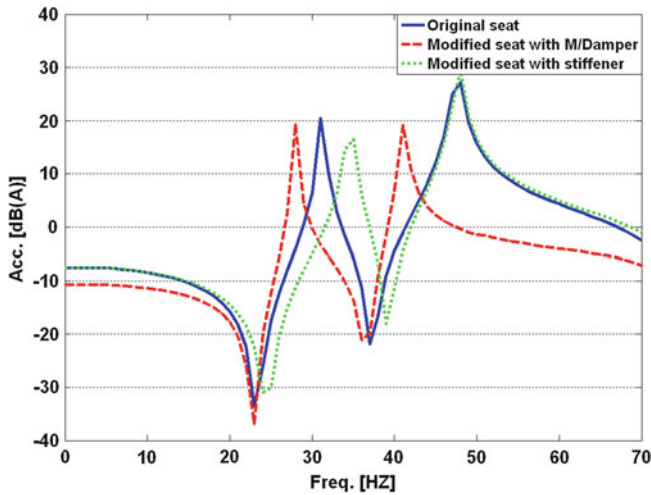


Fig. 7 Effectiveness of the seatback stiffener and mass damper on the frequency shifting

resonant frequency to 34.5 Hz. For modification of the structure by adding mass, we have added a 1 kg lumped mass on the specified (Fig. 6) point of the structure. Having used the proposed mass damper, the simulated seat torsion resonant frequency has decreased to 27.2 Hz. Comparison of the inertance FRF of the original seat CAE model with those of the modified models are shown in Fig. 7. The original torsion resonant frequency (first peak) is shifted in accordance with each modification (Fig. 7).

After confirming the sufficient effects of the modifications on the CAE model, the test seat is modified accordingly. For increasing the stiffness, we have welded a beam on the same part as it has done on the CAE model. For modification by mass/damper, a 1 kg mass is also added fixed (bolted) on the seat. The shifts of the

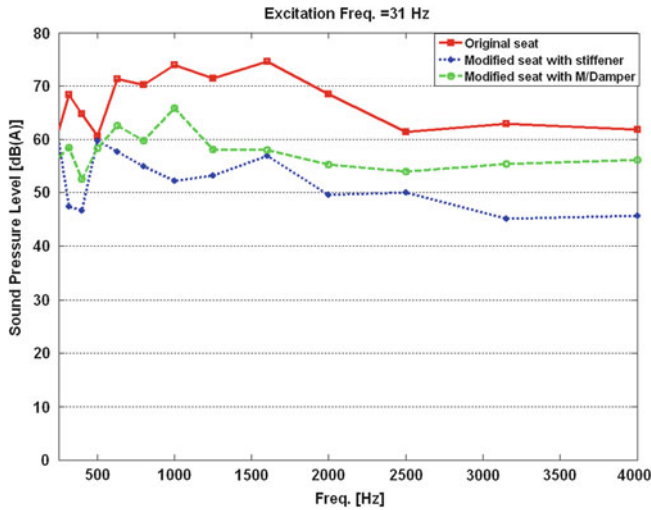


Fig. 8 Experiment results: comparison of the original seat (before modification) radiated SPLs with those of modified seats when the seat excitation frequency is equal to resonance frequency (31 Hz)

torsion resonant frequency, due to the modifications, have become similar to the CAE model. The original 31 Hz torsion resonant frequency, obtained from experiment, has changed to 33.2 and 28.5 Hz for modified seats.

Measurements of the original and the two modified seats radiated noises confirm that by controlling the seat structural dynamics, the rattle noise can be managed accordingly (Fig. 8). When the original and the two modified seats have been excited with a 31 Hz sinusoidal input frequency, despite the original seat, the modified seats have not exhibited any significant radiated rattle noise (Fig. 8). In the frequency range from 500 up to 1500 Hz SPL is decreased nearly 10 dB (Fig. 8).

4 Conclusion

The vehicle seat is one of the major components that have potential to be a source of annoying rattle noise. A possible analytical design method minimizes find-and-fix physical tests and provides an upfront solution for the rattle noise. Some vehicle components such as door trims exhibit a wide range of critical frequencies with no proper global mode shapes and their BSR may happen in a wide excitation frequency band. Nevertheless, the vehicle seat structure has a robust structural dynamics with identifiable vibration resonances and mode shapes. Accordingly, this paper demonstrated that controlling the seat structural dynamics is a robust

upfront solution for improving the seat rattle and, in general, the seat BSR. The concept CAE model of the seat was developed to allow designing the seat-structure modifications as well as predicting the effects of the modifications on the rattle noise. Comparisons of the results of the simulation and experiment validated the developed CAE model. The seat structure exhibited two major torsion and fore-aft bending structural modes in low vibration frequencies (<50 Hz) where the structure have more potential to be rattled. The results of the experiments and corresponding CAE model-based simulation were consistent, so that both have exhibited two torsion and fore-aft shapes. We have further confirmed that the occurrence of the rattle noise is related to the seat structural dynamics and it can be controlled and managed by modifying the structure. Two modifications were designed using the seat CAE model. One modification was designed for increasing the seat torsion resonance nearly 4 Hz, and a second modification was done for decreasing the seat torsion resonance nearly 4 Hz. The designed modifications were then applied on the test seat and the rattle noise is measured on the two modified seats. The results confirmed that by changing the seat resonant frequency, the rattle noise can be changed accordingly. Consequently, for the seat system which has an identifiable structural dynamics, the rattle noise can be managed and controlled in early design phase using the seat CAE model.

References

1. Rao MD (2003) Recent application of viscoelastic damping for noise control in automobiles and commercial airplanes. *J Sound Vib* 262:457–474
2. Cerrato-Jay G et al (2001) Automatic detection of buzz, squeak and rattle events, SAE Paper 2001-01-1479. SAE noise and vibration conference & exposition, Traverse City, Michigan
3. Kavarana F, Reiders B (1999) Squeak and Rattle-state of the art and beyond, SAE Paper 1999-01-1728. SAE noise and vibration conference & exposition, Traverse City, Michigan
4. Gosavi SS (2005) Automotive Buzz, Squeak and Rattle (BSR) detection and prevention. TATA technologies Ltd, Pune, pp 661–667
5. Broo F, Derico J (1995) Silicon elastomer reduces noise, vibration, and squeaks in vehicle instrument panels, SAE Paper 1995-06-35. Proceedings of the noise and vibration conference
6. Nolan S et al (1996) Instrument panel squeak and rattle testing and requirements. IMAC-XIV, SEM, pp. 490–494
7. Eiss N et al (1997) Frictional behaviour of automotive interior polymeric material Pairs, SAE Paper 1997-20-56. Proceedings of the 1997 noise and vibration conference, pp. 1479–1496
8. Shin S, Cheong C (2010) Experimental characterization of instrument panel Buzz, Squeak, and Rattle (BSR) in a vehicle. *J Appl Acoust* 71(12):1162–1168
9. Hagiwara I, Ma Z-D (1992) Development of Eigen mode and frequency response sensitivity analysis methods for coupled acoustic-structural systems. *JSME Int J Series III* 35(2):229–235
10. Ma Z-D, Hagiwara I (1992) Sensitivity calculation method for conducting modal frequency response analysis of coupled acoustic-structural systems. *JSME Int J Series III* 35(1):14–21
11. Donders S et al (2009) A reduced beam and joint concept modelling approach to optimize global vehicle body dynamics. *Finite Elem Anal Des* 45:439–455

12. Mundo D et al (2009) Simplified modelling of joints and Beam-like structures for BIW optimization in a concept phase of the vehicle design process. *Finite Elem Anal Des* 45:456–462
13. Fard M (2011) Structural dynamics characterization of the vehicle seat for NVH performance analysis. SAE paper, 01-0501
14. Guyan R (1965) Reduction of stiffness and mass matrices. *AIAA J* 3(2):380–387

Part VII
Wind Noise Control Technology

The CFD and Noise Simulating Research of Fan Based on the Dipole Noise Theory

Qing Zhu, Zhaocheng Yuan, Chong Liu and Jiayi Ma

Abstract In order to study the actual work of the car fan, the cooling fan and condensing fan models were established by PRO/E, models were meshed by the GAMBIT and the boundary conditions were set by FLUENT, and the flow and noise were simulated to compare with the experimental result which showed the availability. Most of the fan noise belong to dipole noise, therefore, according to the dipole generating mechanism of the sound source, the windshield was set on the axis of the model to reduce eddy current noise. Simulation results show that the distance of windshield and fans have a direct effect on optimization. Three plans were considered in the thesis, finally, we got the result the noise was reduced by 2.6 dB at most after optimization. It was showed that an optimal distance exists between windshield and fan that could reduce noise to a minimum. This method is an indirect method, which could reduce noise without changing the process, and has the advantage of low cost, applicability and high feasibility. Automobile has become very important traffic tool in People's daily life, when it brings convenience to our life, it also have had a profound impact on our environment. Noise pollution and air pollution have influenced people healthy living environment, and fan noise is one of the main components of automobile noise. According to the noise separation experimental data shows, when the car is at the first and second gear, the percentage of fan noise is 24.7 % [1] in the engine acceleration noise. The main noise frequency concentrated in the 100 ~ 4,000 Hz, with the speed increased, the percentage of fan noise will rise sharply [2]. So it is premised on ensuring the flow of fan, the study on reducing fan noise is very important to the influence of vehicle noise.

F2012-J07-001

Q. Zhu · Z. Yuan (✉) · C. Liu · J. Ma

State Key Laboratory of Automotive Simulation and Control, Jilin University, Changchun, 130025, People's Republic of China

e-mail: yuanzc@jlu.edu.cn

Keywords Fan of car · Radiator · CFD · Noise · Simulation

1 The Generating Mechanism of Fan Noise

1.1 The Classification of Fan Noise

The cooling fan of vehicle belongs to axial flow fan, and the noise is composed of the broadband noise and the discrete noise. According to the characteristics of the generation of fan noise, it can be divided into the rotating noise and the eddy current noise [3].

Rotating noise is formed by pressure fluctuation around the blades when the blade blow the surrounding air. After the blade rotating, the blades disturb the surrounding air to generate pressure fluctuation, it makes the surrounding air occur asymmetric alterations and generate metronome. The fundamental frequency is

$$f_i = \frac{nz}{60}i \quad (1)$$

z —leaf number, n —fan speed, (r/min), i —harmonic number ($n = 1, 2, 3\dots$)

Eddy noise is formed by fan blades which cutting the air in flow field to generate eddy current, that make the air flow disturbance. The frequency is [4]

$$f_i = 0.185 \frac{V}{D}i \quad (2)$$

v —blade speed(m/s), D —width of fan in projective plane (mm), i —harmonic number ($n = 1, 2, 3\dots$)

The noise of fan blades is mainly about eddy noise in low speed and rotating noise in high speed. In this paper, it's rotating noise because the speed is more than 1,000 r/min.

1.2 The Classification of Sound and Dipole Noise Reduction Method

Air dynamic noise is produced by high speed air flow, turbulence and airflow interacting with objects. Aerodynamic noise source can be divided into: single level subsidiary sound source, dipole source and four sub sound source [5].

It's considered that existing strong disturbance at near field of the fan and laminar noise fluctuations characteristics at the far field, and there is only solid and fixed boundary in flow field, the following equation is derived by Lighthill equation:

$$\begin{aligned}
 4\pi p(x_i, t) = & \int_V \frac{1}{r} \left[\frac{\partial q'}{\partial t} \right] dV - \frac{\partial}{\partial x_i} \int_V \frac{1}{r} [F'_i] dV \\
 & + \frac{\partial^2}{\partial x_i \partial x_j} \int_V \frac{1}{r} [\rho v_i v_j] dV - \int_V \frac{1}{r} \frac{\partial}{\partial t} \left[\left(\frac{1}{c^2} - \frac{1}{c_0^2} \right) \frac{\partial p}{\partial t} \right] dV + \frac{\partial}{\partial x_i} \int_S \frac{1}{r} [F'_i] ds
 \end{aligned}
 \tag{3}$$

$p(x_i, t)$ —point x_i at t moment sound pressure level, r —the distance of point x_i and volume V or source point y_i on the boundary s , F_i —vector force acting on the boundary s per unit area, F'_i —the external force per unit volume, q' —new fluid mass flow rate in unit volume, c_0 —uniform medium velocity, c —local velocity

The fan noise is composed of rotating noise and turbulence noise in wind tunnel experiments, according to the generating mechanism of dipole source, wind tunnel experiments noise is mainly about dipole noise.

According to (1–3) and removed the interference of monopole and four sub sound source,

$$4\pi p(x_i, t) = \frac{\partial}{\partial x_i} \int_V \frac{1}{r} \left(\rho \vec{v} \times r \sigma t \vec{v} \right) dV
 \tag{4}$$

$p(x_i, t)$ is point x_i at t moment sound pressure level, determined by the vortex vorticity $r \sigma t \vec{v}$ and local speed of vortex \vec{v} .

According to (1–4) can obtain the control method and way of dipole noise source [6]:

1. To reduce the speed of flow \vec{v}
2. To reduce the vortex vorticity $r \sigma t \vec{v}$
3. To reduce the obstacles near the rotation system

According to the above analysis, it can be seen that the direct optimization method commonly most belong to reducing vortex vorticity of noise control methods (the optimization of technical parameters of the fan blades), this paper used the indirect optimization method that control the speed of the flow for noise optimization.

2 Wind Tunnel Experiments of Fan

2.1 Equipment and Methods

Equipment: wind tunnel (Cross-sectional area is 0.2 m^2 , length is 5 m), automotive battery.

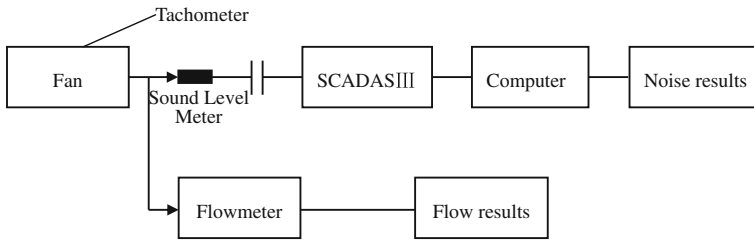


Fig. 1 Experimental system

Instrument: PCB microphone, flowmeter, LMS vibration noise test system, computer, the hand-held tachometer.

Specimen: automotive cooling fan and condensing fan (Fig. 1).

According to the *Cooling System—Fan Noise Test Method* of China Faw Group Corporation R&D Center, arranged the sound level meter in front of the fan work face at 1 m 45° direction, and recorded noise values by the vibration noise test system. It's can measured the flow of the fan simultaneously by this experiment system, and need to measured the background noise of environment before collecting.

Rated rotation speed of cooling fan and condensing fan are both 2210 r/min.

2.2 Result

Table 1.

3 CFD Model of Fan and Simulation Analysis

The performance of the fan is determined by the flow and noise. Measuring of three-dimensional flow could difficultly achieve in ordinary methods, and the result of fan noise detection is affected by environment background noise. In order to test the performance of the fan completely, the data need to be analysed by computer simulation on the base of the experiment. In this paper, the flow field and sound field of the fan was simulated accurately by FLUENT software.

3.1 Wind Tunnel Model

The fan structure have to appropriately simplify when creating the simulation model. Fan wheels could simplify entity and fan leaves fillet could appropriately

Table 1 Result of experiment [background noise of environment is 47.29 dB(A)]

	Cooling fan	Condensing fan
Noise (dB(A))	74.15	73.23
Flow (m ³ /s)	0.79	0.49

Table 2 The fan parameter

	Cooling fan	Condensing fan
Rated rotation speed (rpm)	2,210	2,210
Leaves number	8	6
Leaves width (mm)	60	60
Wheel diameter D1 (mm)	148	148
End diameter D2 (mm)	360	360
Root angle (°)	44	44
Radius of curvature (mm)	120	120

simplify. Table 2 is the model parameter. Figures 2 and 3 are the simplified fan model.

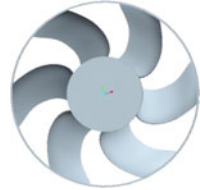
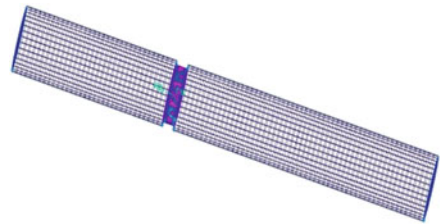
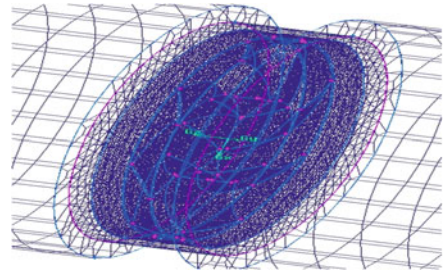
The model was built into GAMBIT software, and established the simulation model of wind tunnel. The wind tunnel included four areas: import pipe area, link area, rotating fluid area and export pipe area. According to the rule of wind tunnel experiment, the import pipe length is greater than six times the diameter of import pipe and export pipeline length is greater than 10 times the diameter of the export pipe line. Link area was used to connect the rotating fluid area and the import and export pipe area. Transition grid can reduce computation. Rotating fluid area could be as close as possible to the outer diameter of the fan blades. Axis of rotation of the fan was the z-axis, import located at the z-axis positive and the origin located at the geometric center of the fan.

The methods of established cooling fan model and condensing model were same (Figs. 4, 5).

3.2 The Flow Field Simulation Process and Result

3.2.1 Setting the Boundary Conditions

The boundary conditions of wind tunnel model is: fans rotating around the Z axis, the boundary conditions of the wind tunnel inlet and outlet were set to pressure, and the initial value is 0. The internal flow field of wind tunnel is incompressible gas, the turbulence intensity is 0.5 %, the boundary condition of fan surfaces and wind tunnel wall were set to the walls, other boundary conditions were set to internal, and rotating area adopted the moving reference frame. The heat exchange had been ignored, so that only considered the continuity equation and the

Fig. 2 Cooling fan model**Fig. 3** Condensing fan model**Fig. 4** Cooling fan wind tunnel simulation grid**Fig. 5** The cooling fan rotating fluid area to enlarge the grid

three-dimensional N–S equations. Internal flow was a steady-state flow, and the velocity and pressure coupling had been solved by SIMPLE pressure correction algorithm.

3.2.2 Simulation Result

In this paper, the cooling fan and the condensing fan had been simulated at speed 2210 rpm, flow monitoring surface was set in outlet face of rotation area. Figures 6 and 7 show the fans simulation results.

Fig. 6 Cooling fan flow simulation result

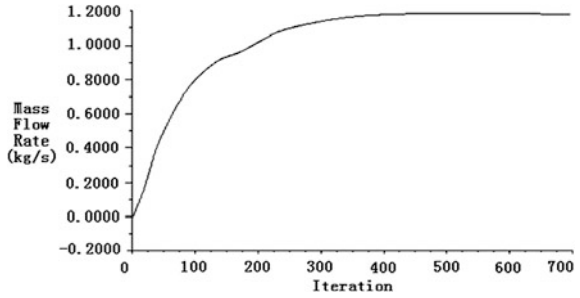
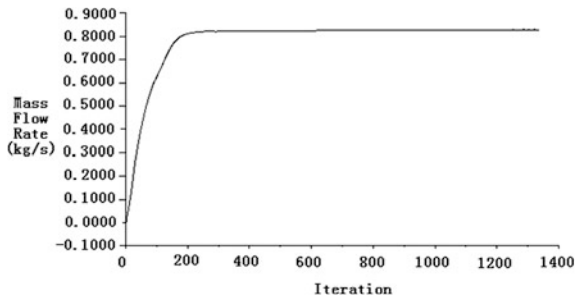


Fig. 7 Condensing fan flow simulation result



The flow simulation results of the cooling fan and condensing fan respectively is 1.18 and 0.81 kg/s, the volumetric flow rates were 0.94 m³/s and 0.67 m/s. Because there are some errors in fan modeling and experimental measurement, rotating areas need to wrap the entire fan. The high-speed rotation region is larger than the actual blade region, which led to flow simulation results slightly larger than the experimental results, but the simulation and experimental results were same trend and reflected the experimental situation basically.

3.3 Simulation Results and Experimental Results of the Sound Field

The simulation models and grid division of sound field as the same as flow field simulation. The surface of rotation area and convergence zone were set to interface, and rotation area adopted the moving mesh, in that the calculation model selected LES Large Eddy Simulation. The sound field of the fan had been simulated only under the rated speed, and noise band is mainly concentrated in the 20 to 2,000 Hz. The collection points of experimental results was set at 1 m from the fan center, and deviate from 45°. Comparative analysis of experimental results and simulation results as follows (Figs. 8, 9).

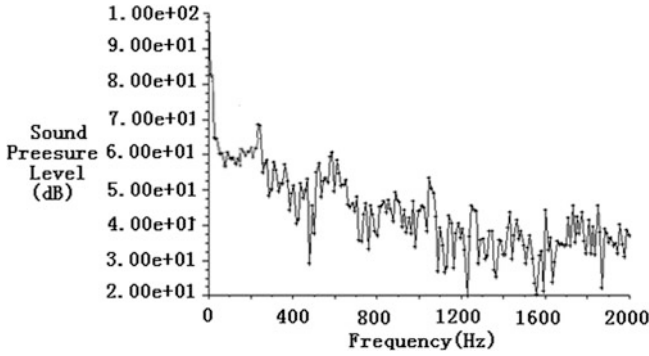
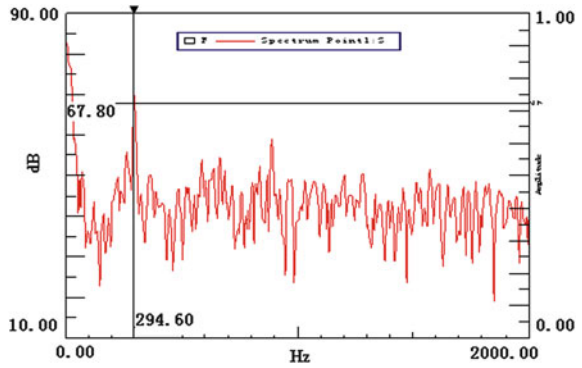


Fig. 8 Spectrogram of the simulation sound field of the cooling fan

Fig. 9 Spectrogram of the experimental sound field of the cooling fan



The maximum noise corresponding frequency that experimentally measured of cooling fan in 2210 r/min is 294 Hz, the maximum noise frequency that simulated is 270 Hz, according to Eq. (1), the fundamental frequency is 294.67 Hz, so the maximum noise frequency is also the fundamental frequency. Simulation and experimental noise results were 77.6 and 76.2 dB (Figs. 10, 11).

The fundamental frequency of condensing fan that experimentally measured in 2210 r/min is 221 Hz, the simulation results appear a cusp near the 220 Hz. The maximum noise corresponding frequency of this fan that experimentally measured is 450 Hz, due to the low frequency noise simulated is bigger, the simulation noise result is 78.8 dB, and the experimental noise result is 73.2 dB, so the larger error mainly concentrated in the low frequency band.

Fig. 10 Spectrogram of the simulation sound field of the condensing fan

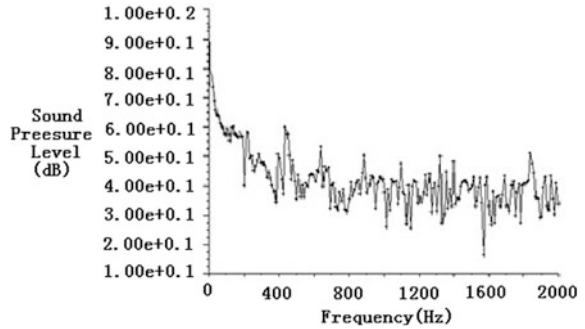


Fig. 11 Spectrogram of the experimental sound field of the condensing fan

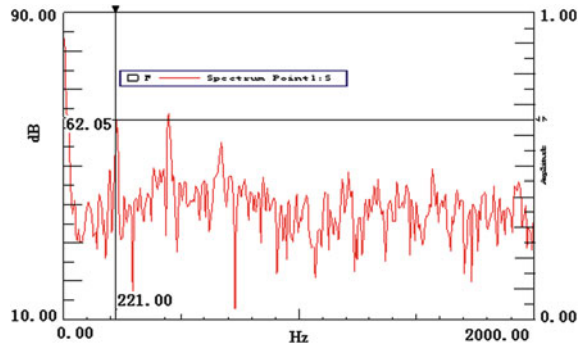
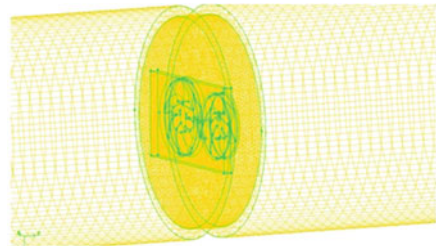


Fig. 12 The double fans wind tunnel grid model



4 The Simulation of Double Fan Flow Filed and Sound Field

4.1 Wind Tunnel Model and Boundary Conditions

Because the radiator and the condenser stacked together in this study, the cooling fan and the condensing fan had been mounted side by side, as shown in Fig. 13. The model of the cooling fan and the condensing fan established had been input GAMBIT to establish the rotation of the wind tunnel and the radiator model, the radiator size is X:800 mm, Y:400 mm, Z:40 mm. The model, the parameters and

Fig. 13 Double fans model added windshield ($Z = 0$)

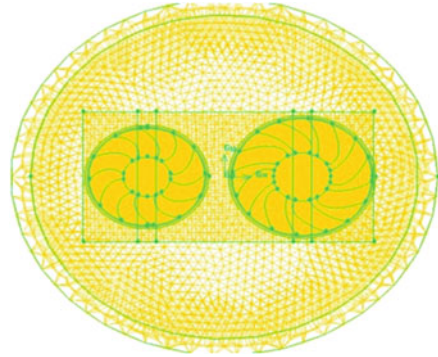
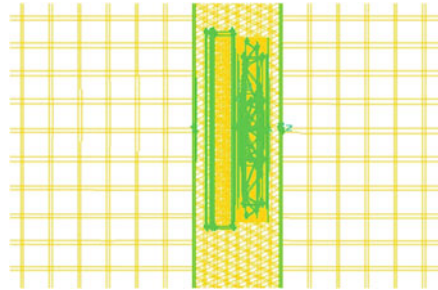


Fig. 14 Scheme 1 side view



the type of grid of double fans with the single fans were essentially the same. Figure 12 shows the double fans wind tunnel grid model.

Because of the radiator structure was complex, it was simplified as porous media in FLUENT. And ignored the temperature field and heat loss. The simulation noise result of double fans is 96.7 dB.

4.2 Analysis of Double Fans Schemes that Added Windshield

This thesis applied dipole noise generating mechanism and noise reduction theory to optimize. The windshield was placed in the axis of the model to optimization to reduce eddy current noise in the purpose of reducing the noise.

The model had been transformed through the double wind tunnel model, and adopted the indirect noise reduction method. The windshield that wide 48 mm and thick 10 mm had been installed in front of the radiator and in the axial direction of the cooling fan and condensing fan. There are three programs in this paper, scheme 1 is the distance of the windshield and the fan is 40 mm, scheme 2 is the distance of the windshield and the fan is 50 mm, scheme 3 is the distance of the windshield and the fan is 60 mm. Figures 13, 14, 15 and 16 show the grid model.

Fig. 15 Scheme 2 side view

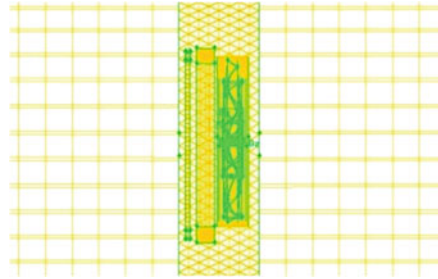


Fig. 16 Scheme 3 side view

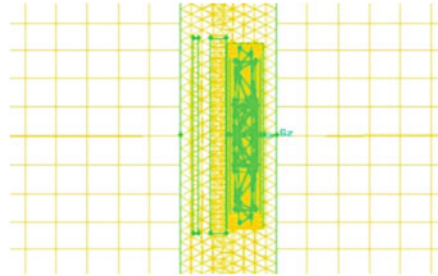
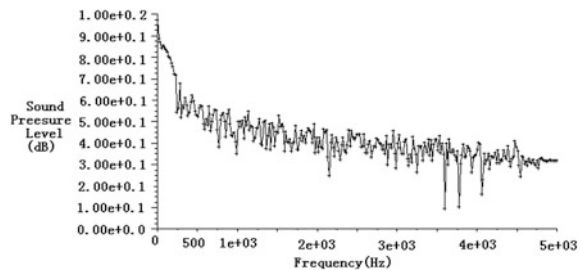


Fig. 17 The original field spectrogram



4.3 The Simulation Analysis of Each Schemes

The simulation of two fans after superposition is 82 dB without radiator (Figs. 17, 18, 19). After installing the radiator, sound pressure level is larger than the noise value without radiator, and the value is 96.7 dB. Figure 20 shows the distance of the windshield and the fan is 60 mm, there is a convex at high frequencies, the noise could have be weakened. It was showed that an optimal distance exists between the windshield and the fan that could reduce noise to a minimum.

It can be seen the noise is smallest when the distance of the windshield and the fan is 50 mm. The best results after the optimization is 94.1 dB, the noise fell down 2.6 dB at most (Table 3).

Figures 21 and 22 show there is a low velocity zone in the import area of the wind tunnel due to the obstruction of the radiator. The diameter and performance ability of the cooling fan are larger than the condensing fan, so the axial direction

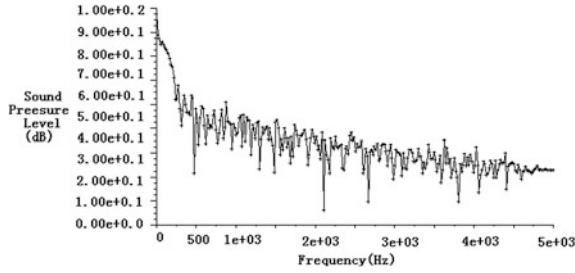


Fig. 18 Scheme 1 spectrogram

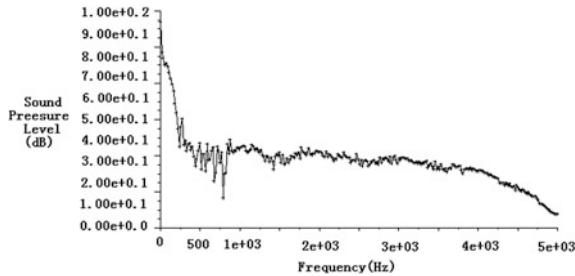


Fig. 19 Scheme 2 spectrogram

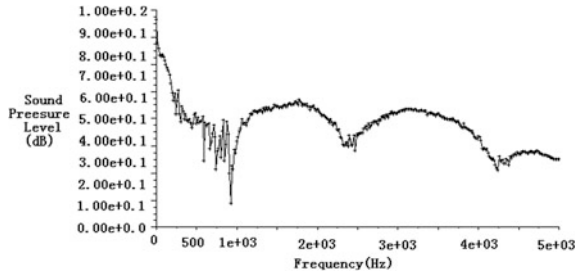


Fig. 20 Scheme 3 spectrogram

Table 3 Noise results contrast

	Original model	Scheme 1	Scheme 2	Scheme 3
Noise simulation results (dB)	96.7	94.9	94.1	94.6

speed of the cooling fan is higher than the condensing fan. Double fans flow rate are 14.8 and 10.5 m/s, they are lower than the single fan that flow rate are 18.9 and 14 m/s, this shows that the fan flow rate decreased due to the obstruction of the radiator (Figs. 23, 24).

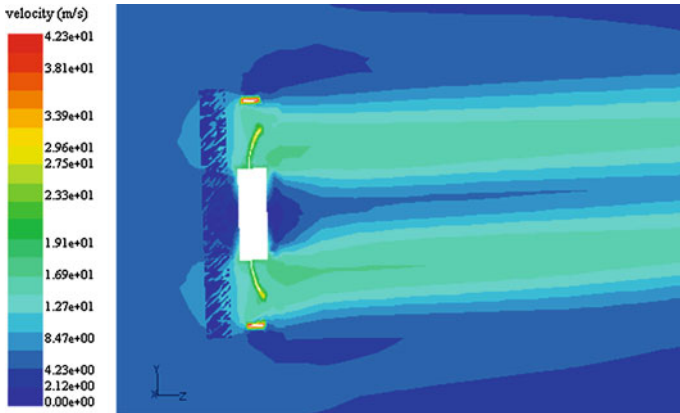


Fig. 21 The original model cooling fan section velocity field ($x = 0$)

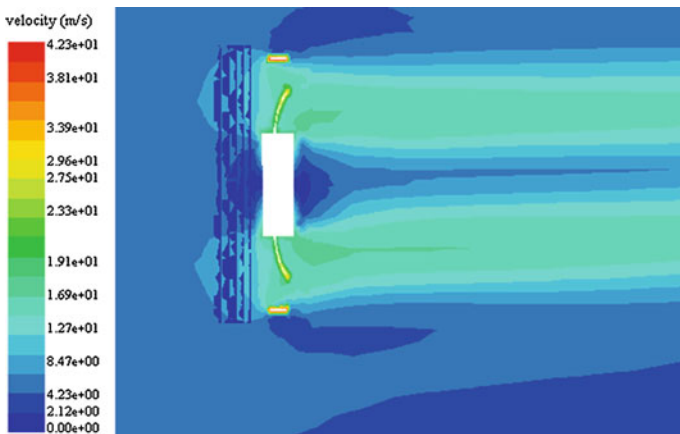


Fig. 22 Scheme 2 cooling fan section velocity field ($x = 0$)

It can be seen that the low velocity zone in front of the fan was significantly wider in scheme 2. The speed that the cooling fan of original model in front of the radiator is 6.4 m/s, correspondingly, the speed of scheme 2 in front of the radiator is 2.2 m/s. The speed that the condensing fan of original model in front of the radiator is 5.6 m/s, and the speed of scheme 2 in front of the radiator is 2.0 m/s. This shows that the windshield reduce the flow velocity in front of the fan, thus the eddy current noise had been reduced.

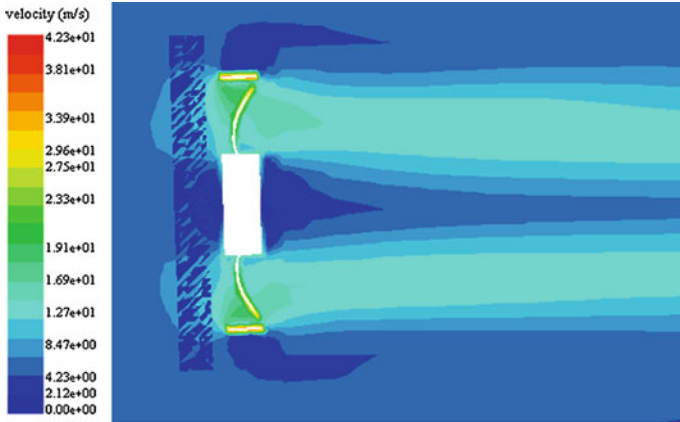


Fig. 23 The original model condensing fan section velocity field ($x = 0$)

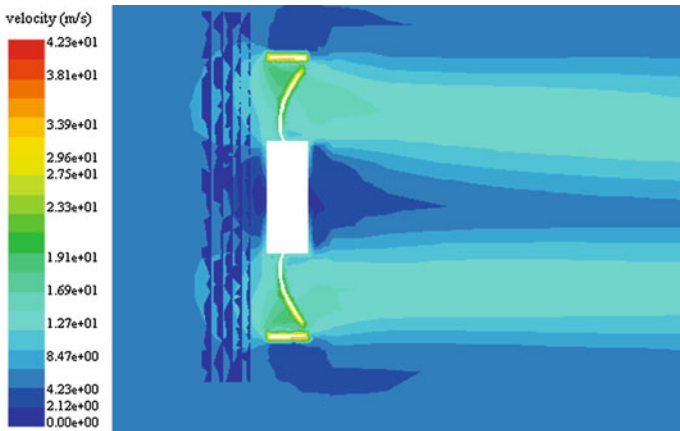


Fig. 24 Scheme 2 condensing fan section velocity field ($x = 0$)

Fig. 25 The original flow diagram

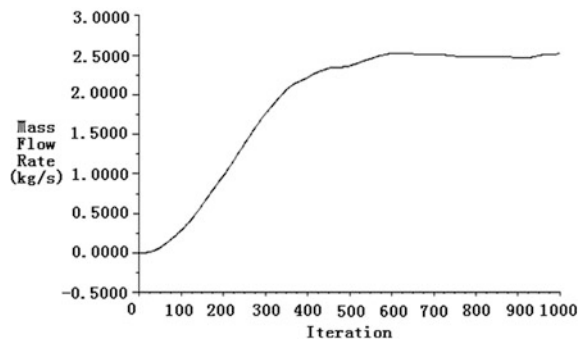
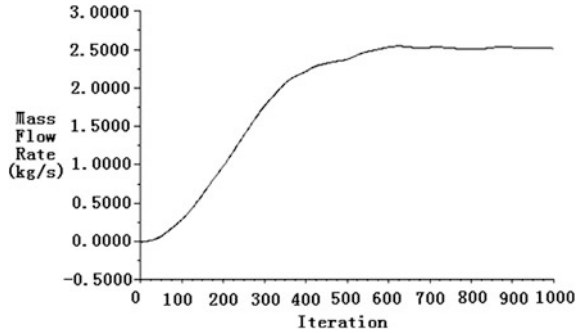


Fig. 26 Scheme 2 flow diagram



Figures 25 and 26 show the flow optimized 2.63 kg/s is slightly lower than the flow of original model 2.72 kg/s, the noise reduction method had little influence on flow field.

5 Conclusions

1. According to dipole noise generating mechanism and noise reduction theory to optimize, the windshield was placed in the axis of the model to optimization to reduce eddy current noise in the purpose of reducing the noise.
2. Simulation noise results show that the distance of windshield and fans have a direct effect to optimization, and an optimal distance existed between windshield and fan that could reduce noise to a minimum.
3. Noise reduction and flow decreased at the same time, but the range of the flow decreased is smaller than the range of noise reduction, and does not have influence on the performance of the engine.
4. This method is indirect method, it could reduce noise without changing the process, and has the advantage of low cost, applicability and high feasibility.

References

1. Henner M, Kessaci S, Moreau S (2002) Latest improvements of CFD model of engine cooling axial fan systems. SAE.2002-01-1205
2. Srun Ap N, Guerrero P, Jouanny P (2002) Influence of front end vehicle, fan and shroud on the heat performance of A/C condenser and cooling radiator. SAE.2002-01-1206
3. Suzuki A (2005) Study on the fan noise reduction for automotive radiator cooling fans. SAE.2005-01-0601
4. Lizhen G (2007) CFD simulation analysis of vehicle engine cooling fan and aero-acoustic reduction research. Jinlin University, Jinlin

5. Kim H-J, Lee S, Fujisawa N (2006) Computation of unsteady flow and aerodynamic noise of NACA0018 airfoil using large-eddy simulation. *Int J Heat Fluid Flow* 27:229–242
6. Maaloum A, Koudri S, Rey R (2004) Aeroacoustic performance evaluation of axial flow fans based on the unsteady pressure field on the blade surface. *Appl Acoust* 65:367–384

Wind Noise Testing at Shanghai Automotive Wind Tunnel Center

He Yinzhi, Zhigang Yang and Yigang Wang

Abstract As wind speed goes up, aerodynamic noise makes more and more contribution to vehicle interior and exterior noise. So it is of great importance to investigate wind noise separately in an exclusive test platform called wind tunnel. But in conventional wind tunnels the isolated representation of aerodynamic noise of vehicles has proven to be difficult or impossible, particularly for aerodynamic exterior noise. Even measurements of aerodynamic interior noise can be severely influenced by the noise generated by the wind tunnel itself. So it is necessary to do the investigation in wind tunnels with low background noise. The full-scale aeroacoustic wind tunnel of Shanghai Automotive Wind Tunnel Center (SAWTC) is such a wind tunnel first of all in China and one of the quietest wind tunnels worldwide. There exist special difficulties for wind noise test when using conventional test techniques due to airflow around measuring object, for example pseudo noise, self-induced noise at the microphones themselves and their supports *etc.* So there is a need for alternative test techniques. In this chapter, after a brief introduction of aerodynamic noise generation mechanisms, the full-scale aeroacoustic wind tunnel of SAWTC is presented, especially the acoustic measures to achieve very low background noise. Furthermore, some special test techniques for vehicle interior, exterior noise and body surface pressure fluctuations are presented. Sound source localization techniques suited to the full-scale aeroacoustic wind tunnel of SAWTC are also listed both for vehicle interior and for exterior out-of-flow.

Keywords Wind noise · Measurement techniques · SAWTC · Interior noise · Exterior noise

F2012-J07-002

H. Yinzhi (✉) · Z. Yang · Y. Wang
Shanghai Automotive Wind Tunnel Center, Tongji University, 201804, Shanghai, People's Republic of China
e-mail: heyinzhi@tongji.edu.cn

1 Introduction

Noise produced from motor vehicles basically comprises drivetrain noise, road-tire noise, and aerodynamic noise. At speed up to 50 kph, the drivetrain noise dominates; between 50 kph and approximately 100 kph, road-tire noise also becomes important. As speed goes up further, aerodynamic noise plays more and more important role. For a typical mid-class sedan, when the speed exceeds 130 kph, aerodynamic noise becomes the dominant noise source [1]. The reason is that aerodynamic noise level increases at about 6th power of speed, while road-tire noise normally only increases at 3rd–4th power [2].

When several noise generating mechanisms are superimposed, it is of great advantage to perform isolated measurements of the individual sources. The isolated representation of aerodynamic noise of vehicles in conventional wind tunnels has proven to be difficult or impossible, particularly when determining the aerodynamic exterior noise. Even measurements of aerodynamic interior noise are severely interfered by the noise generated by the wind tunnel itself. Therefore, special aeroacoustic wind tunnel with low background noise is of great importance for investigating such questions. But due to the huge cost for the construction of such a wind tunnel and test expense, full-scale aeroacoustic wind tunnels exist worldwide up to now only in several large companies and institutes, for example, BMW owns such a modern wind tunnel first of all in 1987 [3]. The completion of the full-scale aeroacoustic wind tunnel of Tongji University in 2009 in China provides a very good test platform for the study of aerodynamic noise for vehicles marketed in the Chinese market.

Due to the airflow around measuring object, there exist special difficulties as conventional measurement techniques are used, for example, Pseudo noise, self-induced noise by microphones themselves and their supports, etc. Therefore, it is necessary to apply alternative techniques especially for vehicle exterior noise measurements.

In this chapter after a brief introduction about aerodynamic noise generation mechanisms and components of vehicle wind noise, some specific interior and exterior aerodynamic noise measurement techniques at the full-scale aeroacoustic wind tunnel of SAWTC (Shanghai Automotive Wind Tunnel Center) are described.

2 Aerodynamic Noise Generation Mechanisms and Components of Vehicle Wind Noise

According to aeroacoustic theory, aerodynamic noise is basically caused by three different excitation mechanisms [4]:

Monopole source is generated due to unsteady volumetric flow. At low air velocity (Mach number small compared with 1, sound radiation efficiency is

proportional to the 1st power of the Mach number. In comparison with dipole or quadrupole sources, the sound radiation efficiency of monopole source is the highest, so normally it is the main source of interior aerodynamic noise, if it exists. Referring to the automobile interior wind noise, noise of monopole source is mainly generated due to the unsteady volume flow through small openings or gaps. The typical appearance is the sealing leaks of joints between different parts of vehicle body due to design or manufacture and assembling error.

Dipole source is generated due to unsteady pressure or force acting on a rigid surface by the flow. Sound radiation efficiency of this type of source is proportional to the 3rd power of the Mach number. Dipole noise is also important for vehicle interior aerodynamic noise. This type of source is active everywhere where a separate flow is impinging on a surface. Typical example is flow over Antenna, A-Pillar, underbody etc. The separated flow induced pressure fluctuation can excite body panels to vibrate, which further causes noise radiation into vehicle interior.

Quadrupole source is generated due to shear stress acting on the flow. Sound radiation efficiency of this type of source is proportional to the 5th power of the Mach number. Due to the low radiation efficiency, noise of quadrupole source is normally ignored for the automobile wind noise analysis.

3 Aeroacoustic Wind Tunnel Description

The full-scale aeroacoustic wind tunnel of SAWTC is a Goettingen type wind tunnel, as Fig. 1 illustrates as a sketch. This wind tunnel is equipped with a $\frac{3}{4}$ open-jet, closed test section with nozzle area 27 m^2 . The maximum wind speed can reach 250 kph. Background noise measured out-of-flow is less than 61 dBA at the wind speed 160 km/h. To achieve this goal, sound attenuation measures were taken, for example, before and after the fan, on four corner turning vanes, by the collector and first diffuser, especially by the test plenum just as a semi-anechoic room. Figure 2 shows a test vehicle on the turntable in the test plenum. In addition, the main parameters of this wind tunnel are as follows:

Nozzle dimensions (W * H)	$6.5 \times 4.25 \text{ m}$
Test section dimensions	$22 \times 17 \times 12 \text{ m}$
Length of open-jet test section	15 m
Static pressure gradient	$<0.001/\text{m}$

In comparison with some other aeroacoustic wind tunnels existed worldwide today, the full-scale aeroacoustic wind tunnel of SAWTC is first of all in China and one of the quietest wind tunnels worldwide.

Fig. 1 Plan view of the full-scale aeroacoustic wind tunnel at SAWTC

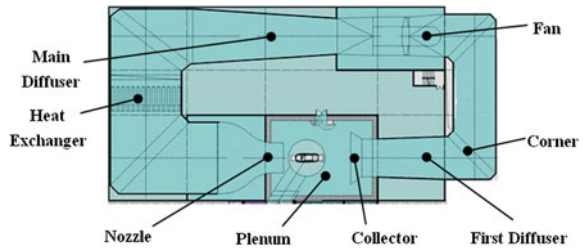


Fig. 2 Test vehicle on the balance turn table in the plenum



4 Wind Noise Measurement Techniques

4.1 Measurement of Interior Noise

For interior noise measurements, normal sound measurement techniques such as microphones, artificial heads, intensity probes are used. In addition, PU probe and relevant scan and listen device are developed in recent years, which are also applied at SAWTC as a relatively new technology.

4.1.1 Microphones

Microphones are used not only generally in machine acoustics but also in aero acoustics. Their employment is especially advantageous when measurements are to be carried out at points of noise entrance, where artificial heads frequently are impractical due to their larger volume, or when many measuring positions are to be recorded.

4.1.2 Artificial Heads

Figure 3 shows interior noise measurements with digital artificial heads made from HEAD Acoustics GmbH. Measurements with artificial head basically are also measurements with microphones, however in a special arrangement. Since 1980s this technology has become increasingly established for the measurement of noise in vehicles and for the subjective assessment of the acoustic environment there. An

Fig. 3 Artificial heads applied for vehicle interior noise measurement

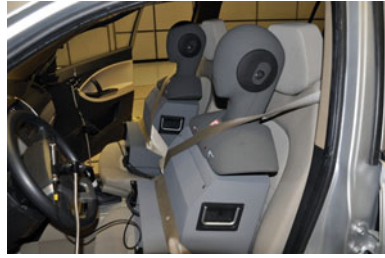
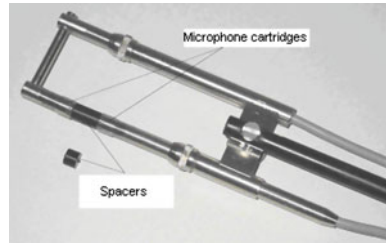


Fig. 4 Intensity probe with two spacers of varying length for adaptation to the frequency range



artificial head consists of a model of a human head, with microphones built into the auricles. When listening to the recorded sound signals with headphones, this set-up permits a spatial (binaural) auditory impression. In this way, the assessment of noise is more realistic than with normal microphone recordings.

4.1.3 Sound Intensity Probe

For the middle to high frequency range, where the sound field in a vehicle can be described as almost anechoic, sound intensity measurements can be used in order to estimate the radiation pattern of the compartment surfaces. In most cases the intensity probe is moved hand held from one measurement position to another. Figure 4 shows one example of a commercially available intensity probe.

4.1.4 Scan and Listen Device Based on PU Probe

Figure 5 shows PU probes made from Microflown company for interior sound source detection. The Scan and Listen device is designed to make the PU probe or Scanning probe signals audible. In comparison with traditional sound intensity probe, PU probe comprises two sensors, one is pressure microphone to measure sound pressure, the other is a Titan sensor element to measure the particle velocity directly. However, for the sound intensity probe, the particle velocity must be calculated through two microphones' test results and microphone distance.

Fig. 5 PU probe and Scan and Listen device used for interior sound source detection



Fig. 6 Surface microphones were used to measure surface pressure fluctuations



4.2 Measurement of Vehicle Body Surface Pressure Fluctuations

Surface microphone is developed in recent years for measurement of the true surface pressure with relatively small size. It is exceptionally well-suited for mounting directly on the vehicle surface in wind tunnel tests. Figure 6 shows an example that surface microphones were taped on the vehicle side window glass to measure the pressure fluctuation distributions (also called pseudo noise) of this area. The test results could be used to verify the accuracy of simulation results.

4.3 Measurement of Exterior Noise

Sound pressure waves which are emitted from the vehicle wind noise sources can be propagated into far-field, so in the wind tunnel out-of-flow, normal free-field microphones can be used to measure sound pressure.

Except single microphones, microphone array are frequently used when measurements in close proximity to the measuring object are not possible or only with great difficulty. With regard to the full-scale aeroacoustic wind tunnel of SAWTC, microphone array based on Beamforming technique is a suitable solution for the sound source localization of vehicle exterior noise. Due to the positioning of such an array out-of-flow normally relative far from the test vehicle, it is thus referred to as “acoustic telescope”. It can consist of a number of microphones set up on a plane surface. How the array is arranged can be principally arbitrary. There can be

Fig. 7 Principle of evaluation technique for microphone array

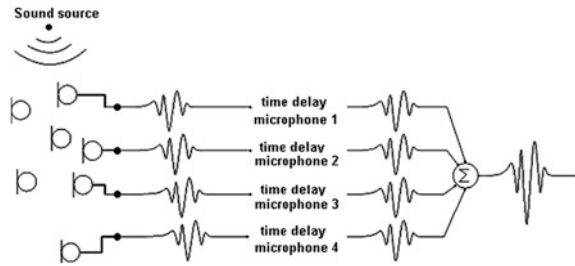


Fig. 8 Microphone array measurement system demonstrated at SAWTC

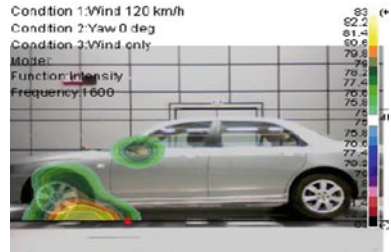


quasi-random distributions, ring-shaped, cross-shaped, linear arrays, spiral shaped etc.

The principle of measurement is to “focus” the array on the various measuring points of the object under investigation. This is achieved by applying a time shift on each measured signal corresponding to the propagation delay from the point of measurement to the respective microphone. The time-corrected signals of all microphones are then added. This results in a curve for the respective point of measurement, as is shown schematically in Fig. 7. With this ‘delay-and-sum’ method the sound emitted by other sources is mostly eliminated (by forming the average). However, the sound emitted by the individual measuring point (focus point) is reinforced.

The key performance parameters of an array are as follows: system dynamic range, spatial resolution, analysis frequency range. If system dynamic range is set greater than its maximum limitation, the pseudo noise sources (namely side lobes) will appear. In addition, if the distance of two sound sources is shorter than array spatial resolution in a certain frequency range, especially in low frequency range, the second sound source will not be detected. Furthermore, the frequency range of microphone array is limited in the lower range by array size: the larger the array, the lower its cut-off frequency. Measurement errors occur more frequently in the upper frequency range—especially in array with a regular set up—due to pseudo sound sources (aliases), which can lead to misinterpretations. One example of modern microphone array displayed in Fig. 8, is available as series production device, which is adapted to use in the wind tunnel. Figure 9 shows an example of sound source localization result of a test vehicle at a certain frequency range. It is clear that the main sound source is the front wheel housing, the second source is side view mirror.

Fig. 9 Sound source localization result of a test vehicle under certain test condition



Part VIII
Vibration and Noise Testing Technology

An Analysis of Vehicle Engine Vibration Signals with Digital Order Tracking Approaches

Wei Shao, Xiaofeng Wang, Dapeng Liu and Zong-an Shao

Abstract This chapter presents an application of Digital Order Tracking to vibration signal analysis of automobile engines. By using a tacho probe to detect the variation of engine speeds and an accelerometer to collect the vibration signals of the engine, the FFT-based analysis are performed in order spectra. Data processing is implemented by digital manipulation—adding zeros, interpolations, oversampling and resampling. Zoom factor \mathbf{D} and decimation \mathbf{d} are thoughtfully selected. A comparisons between tracking and non-tracking spectra is made and the order spectra are plotted in different forms. Referring to the analyzed results, a successful engine diagnoses have been presented.

Keywords Order tracking · Zoom factor · Decimation · Interpolation · Resampling

1 Principles

The noise and vibration generated by the automobile engine are mostly performed as non-stationery signals. In normal FFT analysis of these signals, where the fixed sampling frequencies are used, the “smearing” of frequency components may

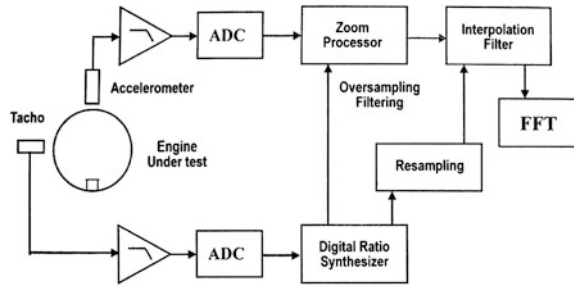
F2012-J08-001

W. Shao
Sany Group, Changsha, China

X. Wang (✉) · D. Liu
Shaanxi Automobile Group, Chang'an, China
e-mail: wangxiaofeng@sxqc.com

Z. Shao
Xian Siyuan University, Xi'an, China

Fig. 1 Block diagram of digital order tracking



appear in its FFT spectrum due to the variation of the engine speeds and, under this situation, the work of analysis becomes difficult. But this problem is eliminated by the technique Order Tracking which analyzes the noise and vibration signals in terms of “Order Spectra” instead of frequency spectra. An order spectrum gives the amplitude or the phase of the signal as a function of harmonic order of the rotation frequency and the harmonic or sub-harmonic order components remains in the same analysis lines independent from the speed of the engine.

In normal FFT analysis the time records are measured in seconds (S) and the FFT spectra are scaled with frequency (Hz), the resolution of frequency spectrum Δf (Hz) equals $1/T$, where T is time record length. Whereas, for order tracking analysis the time records are measured in revolution (REV) and the FFT order spectra are illustrated in (ORD), the resolution of order spectrum Δord equals $1/\text{rev}$, where rev is revolution record length. A tacho probe is adopted to detect the variation of the rotating speed of the engine under test, recording it in revolution per minutes (RPM).

Nowadays, the technique of Digital Order Tracking has been proved to be much more efficient over the previous analogue one. The process of this technique is shown in Fig. 1 [1].

2 Measurement System of Order Tracking Analysis

The noise and vibration of automobile engines are generated by the rotating and reciprocating parts of them. The rotating parts are crankshaft and camshaft. The reciprocating parts are pistons, connecting rods as well as valves. Since the rotating parts are well balanced and move harmonically, the vibration generated by these parts are then low harmonics of the rotating speed of the engine. But the valves are excited in a transient-like way. It makes the valve mechanism of the engine to emit clicking or clanging noise. So, the frequency or order spectra of the impact vibrations are wide band spectra, that means the high frequency or high order components are caused by the activation of the valves.

The layout of the measurement system is shown in Fig. 2. An accelerometer is placed on the top of the engine under test, collecting the vibration signals and

Fig. 2 Layout of measurement system of digital order tracking

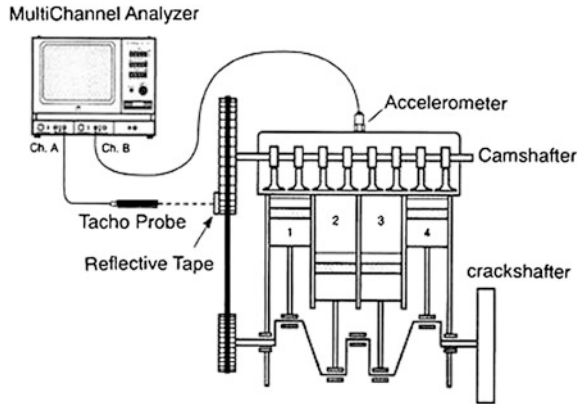
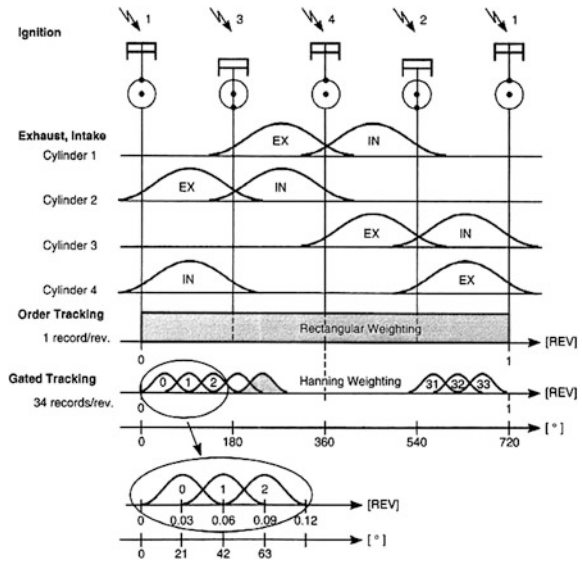


Fig. 3 Valve timing and record definition for order tracking measurements



feeding them to the channel B of the FFT analyzer. Against the tacho probe a piece of reflective tap is placed on the end of the camshaft. The tacho signals generated by the tacho probe are then forwarded to channel A of the FFT analyzer.

The valve timing during one cycle of the crankshaft of the engine under test is illustrated in Fig. 3, together with the sequence of ignition, position of pistons, intake and exhausted valve lifts, angle of crankshaft as well as the weightings [2]. To make a comparison between the frequency and order analyses, two measurements of the vibration signals are made with either Rectangular or Hanning weighting. For order analysis with one record per one revolution of the camshaft, rectangular weighting of the vibration signal is leakage free for the order components and gives best order resolution. For ordinary frequency analysis in an FFT analyzer, since the analysis frequency spans are only a few fixed selection, such as

3.2, 6.4, 12.8 kHz, and the harmonic vibration signals are difficult to match the record length, Hanning weighting is used to minimize the leakage. This operation is so-called Gated Tracking Analysis. Even though, the results of analyses have shown that the order tracking analysis gives better resolution and good selectivity (see Fig. 7).

3 Digital Manipulation with Zooming and Decimation

Since the line numbers of the spectra for FFT analyzer are limited within, for example, 800, 400, or less, the resolution of frequency spectrum Δf have always been a problem of unsatisfactory to the researchers. The higher the upper limit of the analysis frequency span, the lower the resolution of frequency spectrum Δf in lower frequency range—this would result in low analysis accuracy in FFT analyses [3].

To solve this problem, zoom technique is adopted in most of the FFT analyzers and is implemented by selecting a suitable analysis frequency span from a sequence of “stepping” ones such as: 3.2, 6.4, 12.8 kHz.....etc. The approach of “Zooming” is performed by selecting the “zoom factor D ” via switching the analysis frequency span from one to another and that means the changing of time record length. This function is introduced in the present work as “tracking” the rotating speed variation of the engine under test and the principle is illustrated in Fig. 4.

According to the theory of digital signal processing, when the sampling frequency is changing to track the variation of machine speeds, whenever it is in “run up” or “coast down” modes, the FFT analyzer is actually conducting the zoom process with towards or backwards direction. In the present work a dual channel FFT analyzer with 25.6 kHz input module plus analogue anti-aliasing filter is used. Figure 4 shows the block diagram of sampling and zoom processing for the input vibration signals. After the input signal is sampled at 65.536 kHz (2.56 times 25.6 kHz to follow the sampling law) the sampling frequency is artificially doubled by adding an extra sample with a value of zero in between the samples from ADC. Figure 5 is an explanation of oversampling and low-pass filtering in both time and frequency domains corresponding to the process illustrated in Fig. 4. Also, the block diagram visualizes how the zoom process is carrying out and how the measurement parameters are changing when $D = 1, 2, 4$ respectively. Notice that the sampling frequency for order tracking measurement is 10.24 times the maximum frequency span, for example, when it is $\text{max.freq.span} = 12.8$ kHz, the sampling frequency is $f_D = 131.072$ kHz. For present work the automobile engine under test is running within a speed range from 800 to 4000 RPM, the analysis results have shown that the zooming of $D = 4$ is a suitable choice.

Then the data of sampled signals are recorded in the memory. Since the sampling frequencies are remained “step by step” so far such as $f_D = 131.072$ kHz, $f_D = 65.536$ kHz, $f_D = 32.768$ kHz....., to track the whole variation process of

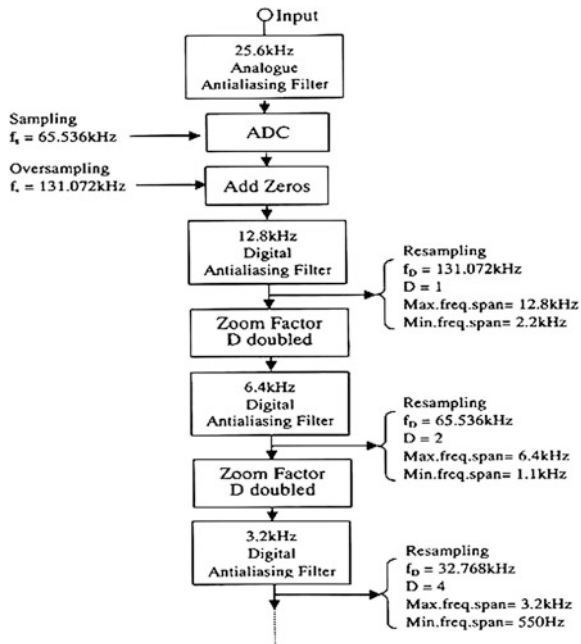


Fig. 4 Block diagram of zoom process with factor D

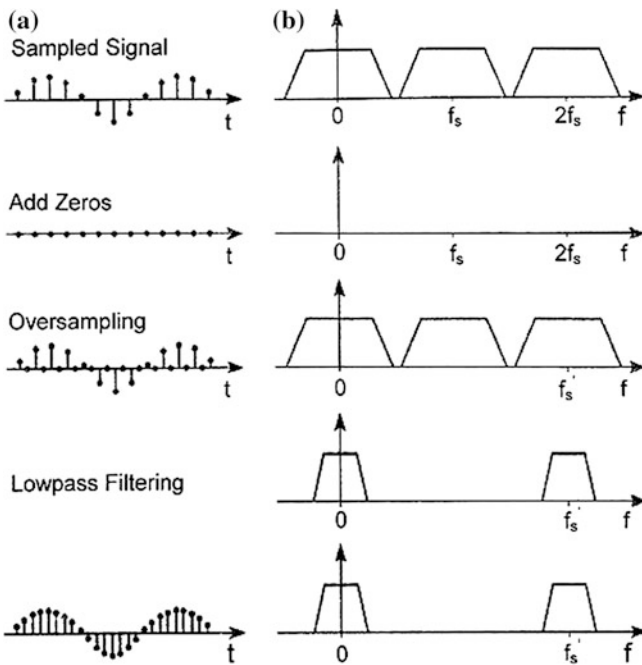
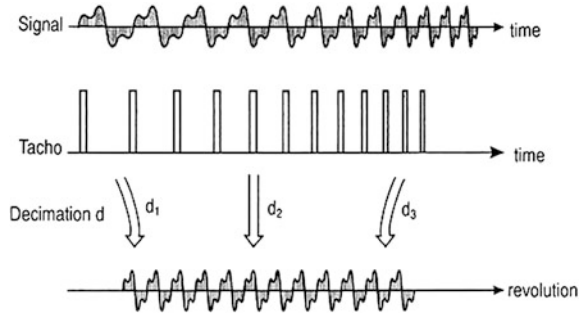


Fig. 5 Oversampling and low-pass filtering **a** time domain **b** frequency domain

Fig. 6 Decimation \mathbf{d} by interpolation and resampling



the engine speed the sampling frequency need further “fine tuning” by the decimation \mathbf{d} so that it could vary to follow the measured tacho signals which are reflecting the variation of the engine speed. Decimation \mathbf{d} is performed by interpolation and resampling. It varies continuously and visualizes in Fig. 6. This process is controlled by the measured tacho frequency along the record and the specified number of order. The decimation \mathbf{d} , can therefore vary along the record and it is a non-integer. In the present work with zoom factor $\mathbf{D} = 4$, decimation \mathbf{d} takes the value of 1–5.92 within each record. This selection can ensure the analysis data train to be managed without any gaps as well as any aliasing problems.

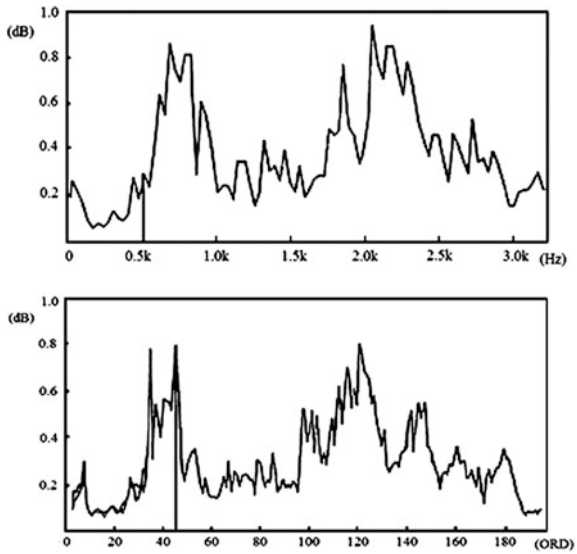
4 Analysed Results and Enlightenments

A few of automobile engines are tested and analyzed. They are model EQ6100, CA6102 made in China and some Japanese engines. The typical measurement system is illustrated in Fig. 2. An accelerometer is fixed on the top of the valve chamber to pick up the vibration signals and feed them to ch.B of the FFT analyzer. The tacho probe signals are input to ch.A of this analyzer. In both ch.A and ch.B the power supplies are available for tacho probes. The measurement setups are: upper limit of order line numbers of the spectra, speed ratio of tacho probe, voltage level of the tacho probe, weighting etc.

If an integer number of revolutions per record is selected, i.e., the orders are perfectly matching up with calculated FFT lines, rectangular weighting can be used since the analysis of the orders are leakage free. If there are considerable non-order related components it may be advantageous to apply Hanning weighting to minimize the leakage effect of them.

A comparison between the spectra measured under both non-tracking and tracking modes for the engine EQ6100 is illustrated in Fig. 7. The upper trace is the non-tracking vibration spectrum with 3.2 kHz frequency span and the “smearing” of the frequency components can be observed at many places on it.

Fig. 7 Non-tracked and tracked spectra of automobile engine model EQ6100



The lower trace is the tracking spectrum of 0–200 (ORD) and all the peaks of it are very clear as there is no frequency “smearing”.

Figure 8 is an order auto-spectrum analyzed from one record of the vibration signals of the engine model CA6102. The horizontal axis (X-axis) scaled by orders and the vertical axis (Y-axis) indicates the magnitude of the auto-spectrum by dB. The plotting of this figure shows that the peaks of the magnitude of the spectrum are clearly distributed on the spectrum lines of the orders, i.e., harmonic components, and the highest value is located at the point of ORD = 3, three times of the fundamental harmonic. This figure visualizes the characters of the order spectrum that is the peak values of magnitude of the spectrum are clearly distributed at the places where the harmonic and sub-harmonics of the fundamental frequency of the machine are located.

In order to look into the process of speed run-up or coast-down of the tested engines, it is necessary to use the three-dimensional (3D) waterfall plotting as shown Fig. 9 as well as the Δ -slides as shown in Fig. 10. In above 3D waterfall plotting, the X-axis order scale has been redefined to the corresponding mean frequency by unit (Hz), still Y-axis indicate the magnitudes of the order spectrum but the Z-axis is the vertical to the plane X-Y and is scaled to indicate the rotating speed RPM or the revolution REV of the engine under test. The Δ -slide is the cut-off profile parallel to the plane of Z-Y or Z-X which enables the order tracking analysis to be conducted from more than one point of view [4].

Since the interest of analysis is focused on the high frequency region where the valve mechanism plays the leading actor, so the Δ -slides are cut-off between 13.5 and 20.4 kHz corresponding to 982–1484 (ORD) from this water fall plotting. These Δ -slides are parallel to the plane Z-Y and, at the same time, along side the X-axis. Figure 10 is one of these Δ -slides but cut-off at the point of 13.5 kHz in

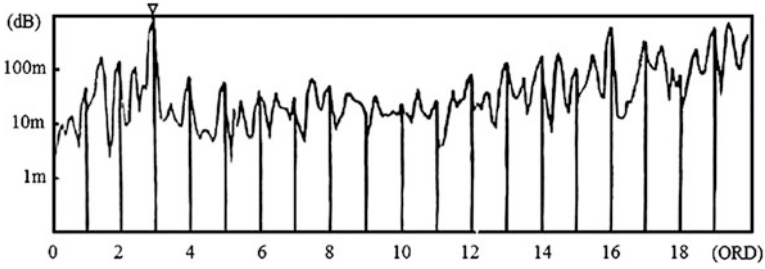


Fig. 8 Order spectrum of 0–20 ORD analysis on automobile engine CA6102 in run-up mode

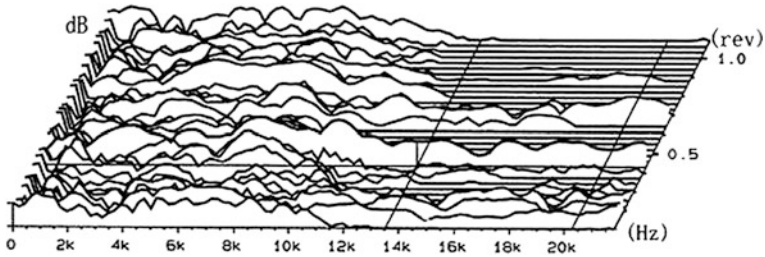


Fig. 9 3D waterfall plotting of gated tracking analysis for engine made in Japan

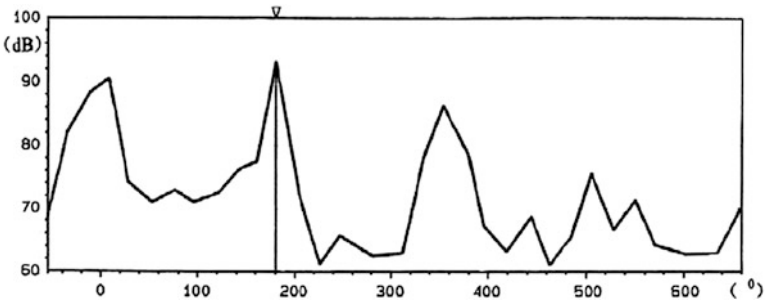


Fig. 10 Δ -slide of the order spectrum of gated tracking analysis for the engine made in Japan

Fig. 9. In Fig. 10 the Y-axis indicates the roots of mean square (RMS) of the order spectrum magnitudes and is scaled with dB (100 dB ref 1.00U, full scale 40 dB). Besides, the X-axis of Fig. 10 is redefined from the revolution of camshaft (0–1 revolution) to the angular displacement of the crankshaft (0–720°) of the engine under test. There are obvious peak values in Fig. 10 corresponding to the angular displacements of 0, 180, 360, and 540° on the X-axis, which in turn indicate the moments of so-called “valve overlap” (both inlet and exhausted valves open) of the cylinder from No. 1–4 respectively. Notice that the highest peak value is at the angle of 180°, that means valve mechanism of cylinder No. 2 devotes the impact energy of the engine more than others. This implies some problems exist in the

valve mechanism of cylinder No. 2. Thus, it can be suggest that more efforts should be put in here to solve the malfunctions. So, it can be seen that the order analysis is helpful to automobile engine diagnosis and trouble shooting.

5 Conclusion

1. The analysis work of this chapter shows that the Digital Order Tracking has obvious advantages over the traditional FFT technique in analysis of non-stationary vibration/noise signals due to its ability to avoid the frequency smearing and to gain better analysis results.
2. Nowadays, more and more efforts have already been put into the problems concerning the automobile NVH and the authors of this chapter believe that the Digital Order Tracking technique will find its better use in this aspect.
3. Both zoom factor **D** and decimation **d** in this chapter are actually mean an operation of “decimation”—selecting a few data from a numerical sample by some laws. But the former is done step by step and the latter is done continuously. This chapter has paid the attention to this situation.

References

1. SHAO W, ZHANG SL(1998) “Digital order-tracking on vibration signals of automobile engines” [J], JSAE spring convention. pp: 221–224
2. Gade S, Herlufsen H (1995) “Order tracking analysis” [J]. Bruel & Kjaer, technical review, No. 2, pp: 5–10
3. S.Zhang (1992) “Vibration measurement and analysis techniques”. [M].Beijing: Publish House of Qinghua University
4. Shao ZA (1994) “Advanced techniques for acoustic noise measurements”. [M]. Xi’an: Publish House of Xi’an Jiaotong University

A New Approach to the Presentation of Vibration Phenomena in Vehicles

Thomas Berberich, Peter Gebhard, Stephan Bohlen,
Oliver Danninger and Markus Lienkamp

Abstract Virtual development is an inherent part of the product development process. To put virtual development into effect the simulated vehicle has to be experienced and rated. Simulators are established to rate the virtual vehicles. A method is presented that demonstrates how the requirements for a comfort simulator can be satisfied. The main part is the realisation of the excitation of the steering wheel. The results that can be achieved with this simulator are discussed and the validity is proven.

Keywords Comfort simulation · Virtual development · Vibration phenomena · Subjective comfort rating · Comfort test bed

1 Introduction

With even more different vehicle models in a company, it is evident that the time to develop new vehicles has to be reduced. This is only possible with computer-aided engineering. Using simulation, the variation of parameters is faster to realize than in real vehicles. The number of prototypes and prototype parts can be

F2012-J08-002

B. Thomas (✉) · L. Markus
Institute of Automotive Technology, Technische Universität München, München, Germany

G. Peter · B. Stephan ·
D. Oliver
AUDI AG, Ingolstadt, Germany

reduced, so that the cost and the time for development will also be reduced. To guarantee the behaviour and the quality of the new vehicle, the virtual vehicles have to be analyzed in the same way like real vehicles. The challenge is that the virtual vehicle cannot be driven.

The comfort impression of a car is highly influenced by the subjective impression. This means, there are many different variables that affect the driver. One of them is acceleration at comfort points. These are the points, where the driver is in touch with the vehicle. Namely the steering wheel, the seat and the foot contact point.

The common way of rating the comfort impression of a vehicle is to drive it on different roads. The roads are characterized by their surfaces, so that the diverse phenomena of the secondary ride are mimicked. The aim is to reduce the influence of the phenomena to the driver that the behaviour of the vehicle is comfortable. That implies the whole impression of the vehicle blends well with the acceleration at the comfort points.

If virtual development is used for vehicles, the subjective rating is only possible in a late phase of the project. In this phase modifications of the vehicle are rather expensive. For this reason the new vehicle has to be rated early in the product development process.

Till now it is not possible to get objective criteria for comfort phenomena, so it is not possible to translate the behaviour of a simulated vehicle into a subjective rating. This is the point, where the impression of a vehicle can be experienced with a simulator. With this tool the gap between virtual development and the experiment can be closed.

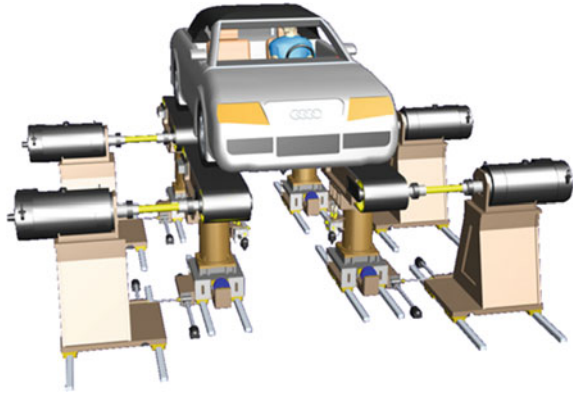
2 The Comfort Simulator

Variable requirements claim specialized solutions. In the comfort category a simulator has to reproduce low and high frequencies in vertical and longitudinal directions [1]. The low frequencies in vertical direction are the natural frequencies of the chassis. This low frequency range has to be simulated, because the simulation should feel like a ride. The higher frequencies, the secondary ride, are frequencies that should be rated. In the next chapter the phenomena of this frequency range will be described.

It is obvious that the whole frequency range has to be presented in such a quality, that the simulation corresponds exactly to real acceleration.

Previous options of representation are Stewart platforms or hydropulse test benches.

Stewart platforms have the possibility of forcing motion in all directions. The challenge of this simulator is the low natural frequency of the platform, more precisely the natural frequency of the piston of the cylinder. The pistons have to have a certain length to realize the high amplitudes. The moving mass has to be as low as possible to realise high accelerations. On the other hand, the natural

Fig. 1 Comfort test bed

frequency has to be higher than the frequency range that should be simulated. This conflict of objectives cannot be solved so that all criteria are fulfilled at the same high level. Results of this simulator are shown in [2].

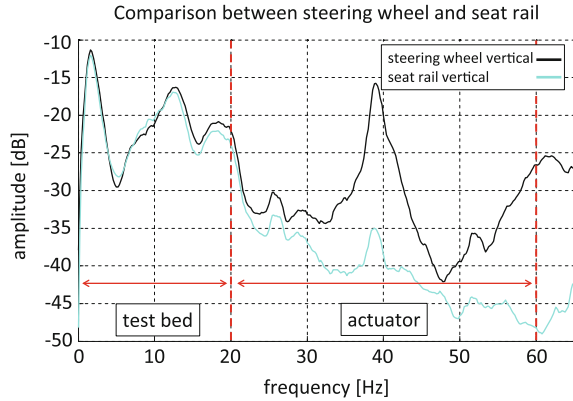
The hydropulse test bench has only the vertical direction to generate acceleration. Based on the high diameter of the pistons of the cylinders, the natural frequency of the test bench is out of the range of the range of the simulated frequency. If a street is represented by the hydropulse test bench for a subjective rating of a vehicle, the natural frequencies of the vehicle on the test bench shifts because of the changing stiffness of a rolling and a standing tyre. In [3] the results of such a simulation can be seen.

A new approach of the comfort simulation is the comfort test bench [4]. This system is a hydropulse test bench with flat track units, shown in Fig. 1. The advantage of this system instead of a normal hydropulse is its ability to generate vertical and longitudinal accelerations. So the system combines the high natural frequency of a hydropulse, that is higher than the simulated frequencies, and the ability of the Stewart platform to generate longitudinal vibrations. The shift of the natural frequency in the vertical direction in this simulator does not exist because of the rotating wheel. In [4] the advantage and results of this system are discussed.

3 Phenomena

The phenomena, which should be rated are these of the secondary ride [3]. These are the stutter, the body shake, the rotational vibration, axle bouncing, engine start and the steering wheel vibration. All of these phenomena have influence on the steering wheel and the interaction between the steering wheel and the seat. Therefore, the behaviour between the seat and the steering wheel has to be shown in the simulator.

Fig. 2 Relationship of the steering wheel and the seat rail



4 Requirement of the Excitation of the Steering Wheel

The different phenomena show diverse movements of the steering wheel. The largest percentage of motion is vertical, lateral and rotary motion. Therefore, three actuators have to be used to realize the movement of the steering wheel.

The subjective rating requires a driver in the simulator. To get a realistic impression, it is necessary that the driver has the same posture in the simulator as in a real vehicle. Thus the actuators of the steering wheel should not influence the driver to take his accustomed position.

Another point is the range of frequency. The range has to start from the body vibrations till the high frequency roughness. So the steering wheel has to fulfil a wide operating range in the presentation. To reach the whole range of frequency, the movement of the steering wheel and the body of the vehicle has to be analyzed. In Fig. 2, the two spectra are shown. It can be seen, that in the field of low frequency the steering wheel and the chassis act like a rigid body.

In the low frequency domain the movement of the steering wheel is realized by the test bed. Because of this reason the actuators of the steering wheel do not need to provide a wide motion. Therefore, smaller ones can be used.

To get a modular simulator, it is decisive that the modification of the simulation medium, the vehicle that is used on the simulator, can easily be undone. So it is possible to use every vehicle as the simulation medium. This is useful, if different segments of vehicles have to be simulated.

The point of application of the force is also very important for the size of the actuators. There are different possibilities to fix the actuator. The options are on the one side near to the revolute joint of the steering wheel or to itself. The centre of rotation of the steering wheel in vertical direction is the revolute joint. The aim is to reproduce a motion at the steering wheel, which is at the outmost position of the steering column. Looking at the different applications of force at the steering column, it is comprehensible, that the lowest amount of energy is necessary, when the actuators are at the steering wheel.

The modularity of the excitation is granted, if the modification is easily installed. With the aim not to influence the test driver and an easy installation, an excitation at the steering column is not possible. The only position for the actuators can be at the steering wheel.

The requirements are summarized as follows:

- Three modes of motion
- No influence to the test driver
- The range of frequency is from 20 till 60 Hz
- Easy installation of the actuators

To solve this problem with these conflicting requirements, have a look at the available actuators and the needed space for them.

5 The Actuator

Common shakers are installed on a solid body to support the force that is induced in the test body. Transferring this behaviour to the problem of this case implies that the shaker for the steering wheel has to be fixed in the vehicle. Following the principle “action equals reaction”, the reaction can be felt at other points in the vehicle. For this reason an actuator is needed, that works with its inertial mass.

A possible solution is a small actuator with a force of 10 N. These actuators are rather small compared to common actuators.

To install this actuator a possible position is the space for the airbag. In a simulator it is not necessary to have a fully functional airbag.

To fulfil the requested modularity a prepared steering wheel is used. The fixing is equal in every Audi so it can be used for the whole model range. To get the perfect profile to install three actuators a 4-spoke wheel is used. Two actuators are fixed at the bottom of the space for the airbag. These two actuators are installed in a way that the force of the actuators do not cross the center of the steering wheel. The principle of this system is shown in Fig. 3. If the two actuators are operating in phase, the steering wheel moves vertical. If there is a phase shift of 180° the steering wheel is turning. With these two actuators, the vertical and turning motion is realized. The lateral motion can be provided with the third actuator at the side of the space for the airbag.

The driver does not recognize the additional actuators at the steering wheel when the airbag cover is on the steering wheel, so there he is not influenced by this solution. The installation of the active steering wheel is done by changing the steering wheel. So a fast installation of this system is guaranteed.

This solution also fulfils the requirement of the requested frequency range. In Fig. 4 the different spectra for every mode of motion are shown. The results of the representation show a good correlation in the observed frequency range. It can be seen, that the simulation follows the real vehicle over a wide frequency range.

This solution fulfils all requirements of the excitation of the steering wheel that a simulation can be realized without influencing the driver.

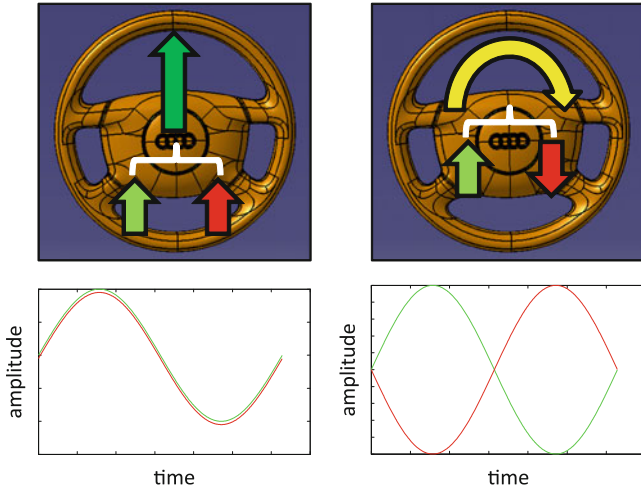


Fig. 3 Function of the steering wheel

6 Validity of the Simulation

The subjective impression of the simulator is ensured with a study. The aim is to guarantee the same impressions in the simulator as on the street.

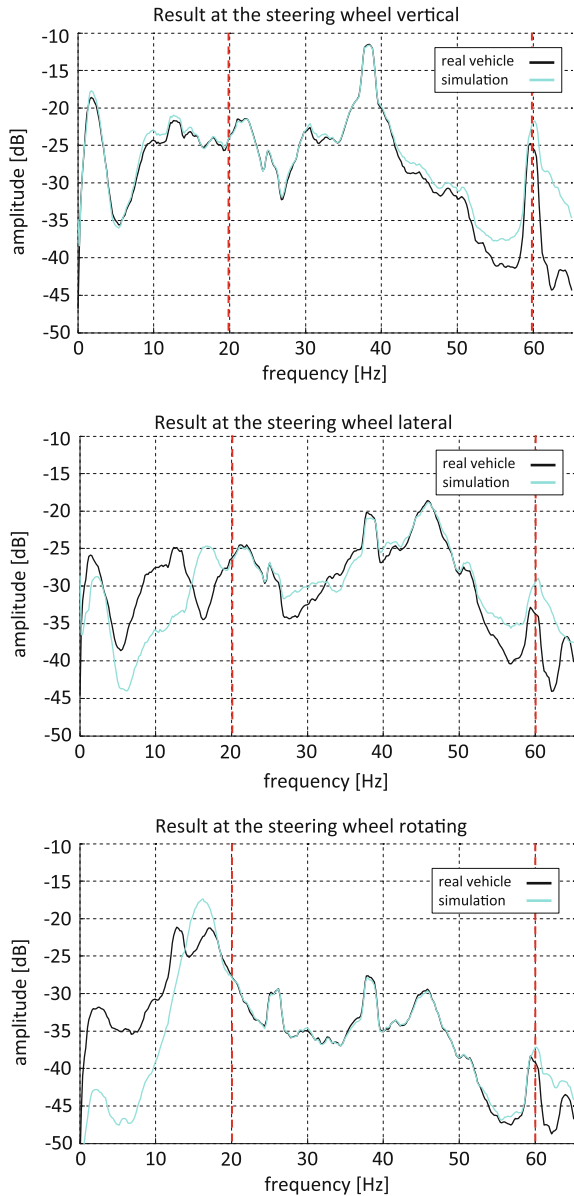
The test is based on four vehicles that are simulated. The test persons drive three of them on the road and generate a list of criteria of which phenomena are characteristic for the vehicle and in which way they detect the phenomena. In the next step the test persons drive these vehicles in the simulator without the knowledge of which vehicle is actually simulated. With the help of their description, they have to identify the different phenomena. If they cannot identify a phenomenon, it is the vehicle they did not drive on the street.

Simulated are one convertible sportscar, a small SUV, a premium compact vehicle and medium sized vehicle. All these vehicles have the engine, a 2.0 l TDI, in common, except the medium sized vehicle. This vehicle has a 1,4 l turbo-charged gasoline engine. The different amplitudes of the seat rail and the steering wheel in the vertical direction of the vehicles are shown in Fig. 5.

The drivers differentiated the following phenomena:

Phenomena	Body vibrations	Bumpiness	stutter
	Body shake	Copying	Steering wheel disturbance
	Way of starting body vibrations		post-pulse oscillation
Categories	Amplitude and frequency of the vibration		
	Ratio of the seat and the steering wheel		

Fig. 4 Spectra of the steering wheel motion modes



With these categories, the phenomena could be separated on the road. In the simulator the drivers were able to identify and rank the phenomena in the same way as on the road. This implies, that it is possible for comfort experts to get the same rating of the phenomena in the simulator and on the road. The other point is the quality of the presentation method of the phenomena. The presentation achieved the needs of the experts to identify the phenomena.

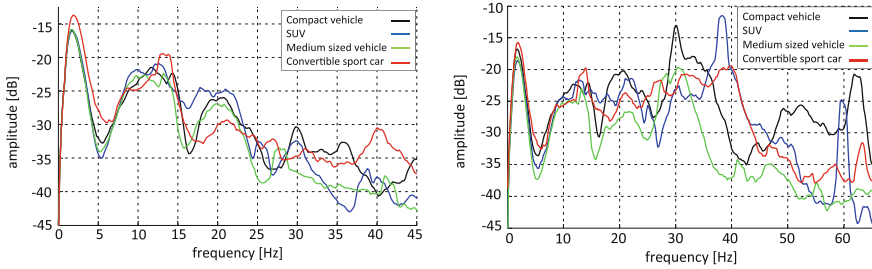


Fig. 5 Spectra of the seat rail and the steering wheel

7 Conclusion

The results show that it is possible to generate all necessary accelerations at the comfort points with this simulator. This is on the one hand the low frequency of the body of the vehicle and on the other hand the high frequency of the comfort phenomena. A decisive role for the comfort phenomena has the active steering wheel. This wide frequency range and the quality of the simulation afford the subjective comfort rating. As shown even small differences can be demonstrated and rated. Therefore virtual development with viewer prototypes is possible.

References

1. Jürgen NH (2007) Anwendungsgerechte Konzipierung von Fahrsimulatoren für die Fahrzeugentwicklung. Dissertation Technische Universität München: 113 – 114
2. Simone L (2009) Zur Objektivierung von Schwingungskomfort in Personenkraftwagen— Untersuchung der Wahrnehmungsdimensionen. Fortschritt-Berichte VDI Reihe 12, Nr.698: 118–137
3. Fernandes CG (2005) Ride comfort measurement. In: SAE technical paper series 2005-01-4026, 2005: 5
4. Thomas B (2012) Subjective ride evaluation—a new approach for the illustration of oscillation phenomena in vehicles. Springer chassis.tech plus 2012, pp 119–131

Research on Noise Testing and Analysis of an Automatic Transmission

Wenfeng Zhan, Jian Wu, Fake Shao and Chuhua Huang

Abstract Nowadays, as the increasing competition on the market, customers and OEMs pay more and more attentions to vehicle's NVH. NVH will be one of the most important performances as power and safety in the future. Engines are downsized but vehicles are more powerful than ever before because of new technology such as turbo GDI hybrid and so on. Transmission noise is becoming more distinct in the power train noise. How to separate the transmission noise from the whole vehicle noise is the first step to improve the NVH performance farther. We research on testing and analysis the noise for an automatic transmission.

Keywords Gear · Noise · Order tracking · Analysis · Frequency

1 Theory of the Order Analysis for Gears

Almost all the transmissions are mainly consisted of gears. The basal principle of gear-drive is teeth mesh, where crash and friction occur between tooth and tooth while both sliding and rolling happen. On the other hand, the teeth mesh have noise and vibration because of the tolerance from machining and assemble and torsional vibration form axis, which will influence the natural mesh of the teeth [1].

The periodic crash while teeth engage and separate alternately make the periodic noise, whose basal meshed frequency is F_m .

F2012-J08-003

W. Zhan (✉) · J. Wu · F. Shao · C. Huang
Guangzhou Automobile Group Co., Ltd. Automotive Engineering Institute,
Guangzhou, China
e-mail: zhanwenfeng@gaei.cn

$$F_m = n Z / 60.$$

Where

n is the rotation speed of the axis;

Z is the teeth number of the gears.

Normally, Mass force because of the eccentric from machining or assemble will bring noise. Furthermore, the engage force will change because of the changed distance between gears according to the rotary angle in eccentric gear, which will make high frequency noise and vibration. At the same time, low frequency noise which caused by pitch tolerance accumulation of the gears happen one time during one circle.

Figure 1 is a simplified structural principle of an automatic transmission. There are three parallel axles in the automatic transmission (AT), main shaft, secondary shaft, counter shaft. Main shaft connect to the hydraulic torque converter and counter shaft connect to the final gears. 4th and 5th gear are assembled on the main shaft with needle bearings and can connect to main shaft by their clutches. Reverse gear used the same gear and clutch with the 4th. Idle gear assembled on the main shaft by spline hub engage the idle gear on the idle shaft. 1st, 2nd, 3rd and 5th gears are assembled on the counter shaft by spline hub directly. 4th and R gears are assembled on the counter shaft by needle bearing, which can connect to the shaft by a slider hub. 1st, 2nd and 3rd gears are assemble on the secondary shaft by needle bearings and can connect to the shaft by their clutches, besides, there is an idle gear on the secondary shaft which can get the power from main shaft by the idle shaft.

Power from engine went through the hydraulic torque converter to the main shaft, then went to the secondary shaft through the idle shaft and then went back to the counter shaft at 1st, 2nd and 3rd. The power went to the counter shaft directly from the main shaft at 4th and 5th. The power transfer path almost is the same as 4th expect going through a reverse idle gear in order to change the rotary direction. The red arrow line in Fig. 2 showed the power transfer line at 1st gear.

Every gear has their own power transfer path, but most of the gears meshed and rotated all the time and even if they were not need to transfer the power because of the structure of the transmission.

We have two rotary speed sensors at this AT. One is assembled on the secondary shaft used to get the speed of the main shaft. The other one is assembled on the counter shaft used to get the speed of the counter shaft. The sensors can get an impulse signal when a tooth passed, so we can know the rotary speed of the shaft if we know the teeth number of the gear. All the teeth numbers was written on the Fig. 1 also. Then, we can make a table including the tooth number according to the shaft, gear ratio and vehicle speed according to the tire type as we can see in Table 1.

Base on the teeth numbers we can calculate the noise frequency of 1st gears:

$$F_m = 28 * n/60 \text{ (Hz);}$$

The first idle gears:

$$F_m = 34/30 * 44 * n/60 \text{ (Hz);}$$

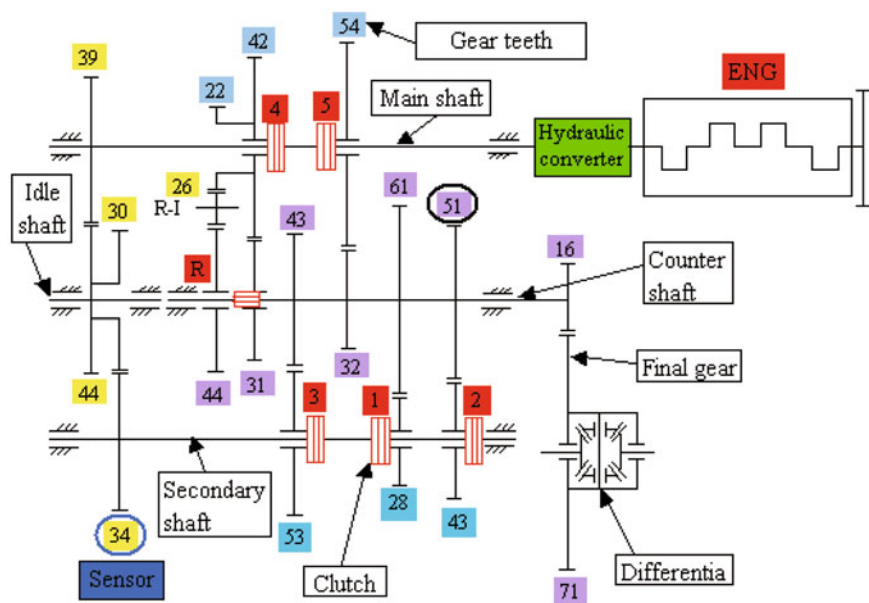


Fig. 1 Structural principle of an automatic transmission

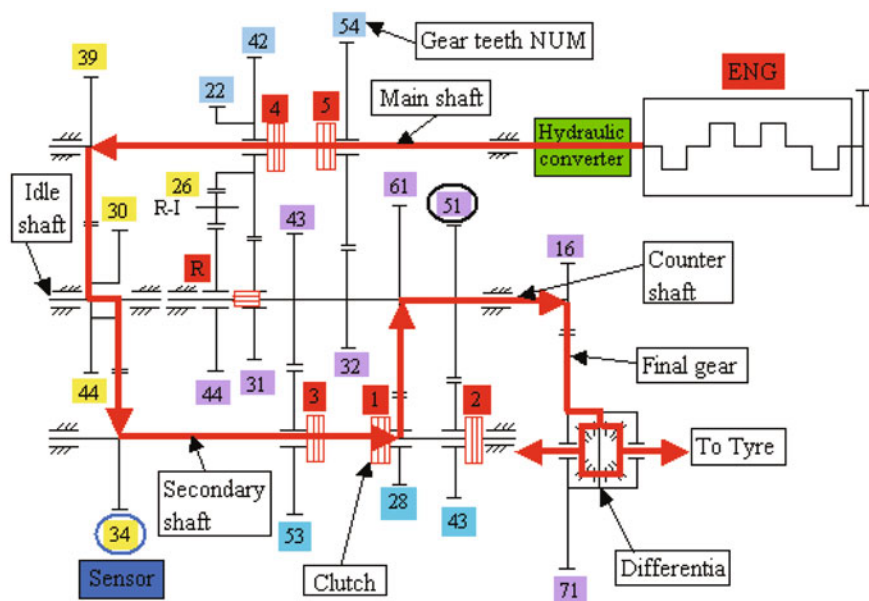


Fig. 2 Power transfer path at 1st

Table 1 Gears ratio and teeth number list

		1ST	2ND	3RD	4TH	5TH	RVS	Idle-A	Idle-B	Final
Gear tooth Number	Main shaft				42	54	22	39		
	Counter shaft	61	51	43	31	32	44			16
	Secondary shaft	28	43	53					34	
	Idle shaft							44	30	
	RVS idle shaft						26			
	Final shaft									71
Ratio	Idle ratio	1.278632	1.278632	1.278632						
	Ratio	2.785592	1.516518	1.037381	0.738095	0.592593	2			
	Final ratio					4.4375				
	Total Ratio	12.36107	6.729547	4.603378	3.275298	2.62963	8.875			
Tyre	Tyre	215	60	R	16	98	H			
	Tyre diameter					0.6644				
Speed	km/h @1000rpm	10.13153	18.60994	27.20533	38.23666	47.62513	14.11115			

Table 2 Order list base on secondary shaft speed

Pulse	S-I	34					
		1st	2nd	3rd	4th	5th	RVS
Order	Idle-A	49.87	49.87	49.87	49.87	49.87	49.87
	Idle-B	34.00	34.00	34.00	34.00	34.00	34.00
	1st	28.00	51.43	75.19	105.67	131.62	39.00
	2nd	23.41	43.00	62.86	88.35	110.04	32.61
	3rd	19.74	36.25	53.00	74.49	92.78	27.49
	4th	14.23	26.14	38.21	53.70	66.89	19.82
	5th	14.69	26.98	39.44	55.43	69.05	20.46
	RVS	7.45	13.69	20.01	28.13	35.04	28.13
	Final 1	7.34	13.49	19.72	27.72	34.52	10.23
Final 2	14.69	26.98	39.44	55.43	69.05	20.46	
Final 3	22.03	40.47	59.16	83.15	103.57	30.69	
Speed	km/h@1000 rpm	12.95	23.80	34.79	48.89	60.90	18.04

The second idle gears:

$$F_m = 34 * n/60 \text{ (Hz);}$$

The final gears:

$$F_m = 28/61 * 16 * n/60 \text{ (Hz).}$$

These are all the gears engaged and transfer the power at 1st gear. So we can calculate frequency for all the meshed gears without power transfer as below:

2nd gear without power load, $F_m = 28/61 * 51n/60 \text{ (Hz)}$

3rd gear without power load, $F_m = 28/61 * 43n/60 \text{ (Hz)}$

4th gear without power load, $F_m = 28/61 * 31n/60 \text{ (Hz)}$

5th gear without power load, $F_m = 28/61 * 32n/60 \text{ (Hz)}$

R gear without power load, $F_m = 28/61 * 31/42 * 22n/60 \text{ (Hz)}$

Considering secondary shaft's speed as the base frequency, the frequency of 1st gears is 28 multiply with base frequency, so it means the order about 1st gear is 28. All the orders for all the gears were calculated out and shown as below in Table 2.

Table 3 Order list base on counter shaft speed

Pulse	C-2	51.00					
		1st	2nd	3rd	4th	5 th	RVS
Order	Idle-A	108.64	59.14	40.46	28.79	23.11	78.00
	Idle-B	74.07	40.33	27.58	19.63	15.76	53.18
	1st	61.00	61.00	61.00	61.00	61.00	61.00
	2nd	51.00	51.00	51.00	51.00	51.00	51.00
	3rd	43.00	43.00	43.00	43.00	43.00	43.00
	4th	31.00	31.00	31.00	31.00	31.00	84.00
	5th	32.00	32.00	32.00	32.00	32.00	32.00
	RVS	16.24	16.24	16.24	16.24	16.24	44.00
	Final 1	16.00	16.00	16.00	16.00	16.00	16.00
	Final 2	32.00	32.00	32.00	32.00	32.00	32.00
	Final 3	48.00	48.00	48.00	48.00	48.00	48.00
Speed	km/h@1000 rpm	12.95	23.80	34.79	48.89	60.90	18.04

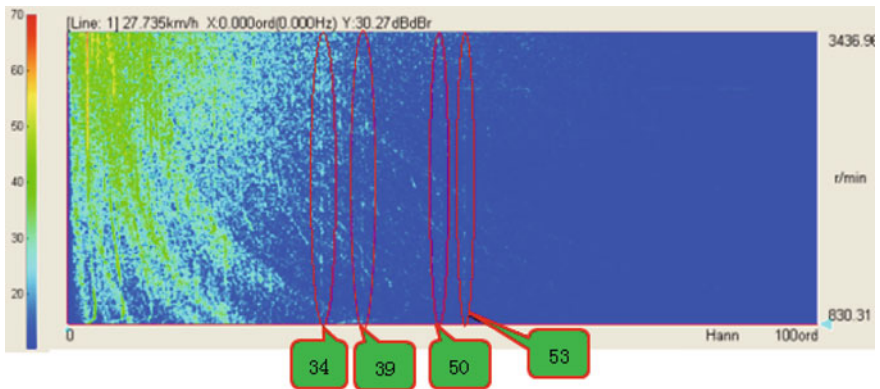


Fig. 3 Contour of order noise

We can calculate the orders based on the counter shaft speed with the same method, shown in Table 3.

2 Test in Vehicle

We used ONO SOKKI DS2000 analysis system, used two microphones, one in the front seat center used to test the air born noise, the other on the top of the shift bar which is used to test structure transfer noise. Take the signal from one of the speed sensor for basal speed input to the instrument. We used the sensor on the secondary shaft in this test.

We need to test every gear’s noise at almost all the speed range. Usually, if the AT has a menu mode, we can easily accelerate or decelerate the car at any normal

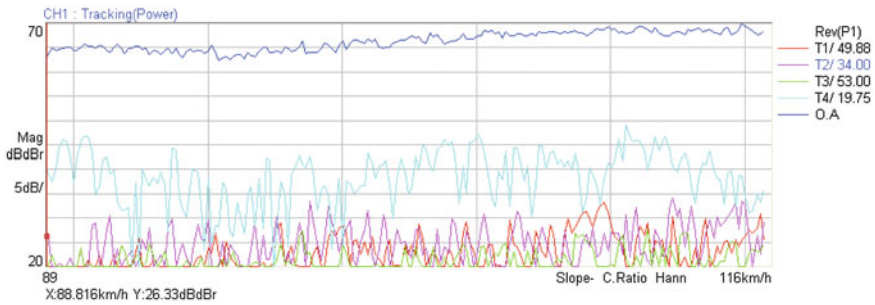


Fig. 4 Noise pressure by order tracking

speed at any gear we want. Some AT has no menu mode to shift the gear but have 2 and 1 which can lock the gear at 2 or 1, So we can't directly shift the gear to gear 3 and higher, but control the gear by the accelerator pedal only and know what gear we are by the vehicle's speed and engine's speed without gear information shown. For example, when we want to test the AT at 4th gear, we should try to accelerate the vehicle at 4th from 30 to 100 km/h. It will kick down to 3rd gear by wide pedal or shift to 5th gear by small pedal at higher speed when we try to accelerate the vehicle by step on the gas pedal. We know the relation between vehicle speed and engine speed at any gear from the Table 1, which can help us to confirm the test is at the right gear we want.

3 Data Analysis

After the test, we analysed the original data by FFT method at the software system. The result base on the speed of secondary shaft was shown in Fig. 3. Axis X is order, axis Y is basal speed while the color means the pressure of the noise. In the Fig. 3, Engine noise which we don't focus on in this test is strong at low order. We can also find the order 34, 39, 49.9, 53 obviously through all the speed range in the figure. With the order list in Table 2, we know where each order from in the figure. For example, order 34 came from the idle gears, order 53 came from 3rd gears and order 39 means the second harmonic of final gear. Order 19.7 made by final gears are difficult to read out because it mixed together with engine noise. Order tracking method was used in order to separate the noise from all the gears. The result of order tracking for noise pressure is shown in Fig. 4.

4 Conclusion and Further Work

In this test and analysis, we knew the basal structure of the transmission at first, and then we worked out a way to test and analysis the gear noise based on the order analysis method.

By this method, we have finished noise test and analysis for a lot of transmission including AT and MT. We can not only use this method for all the gear box, but also we can analysis the rolling bearing noise with the same method in the future, where the order will be more complicated because of the compound movement of the roller.

Reference

Pang J, Shen G, He H (2006) Automobile noise and vibration—principle and application [M].Beijing Institute of Technology Press, Beijing

The Application of Doppler Laser Vibrometer in the Engine NVH Dynocell Test

Jin Yang, Jun Lan, Xu YongJiang, Jin Cai, XiaoNan Zhang,
HanJie Liu and YanLin Shi

Abstract In the engine NVH Dynocell test, the Doppler laser vibrometer can be used in the non-contact measurement of the engine surface vibration. The relative error of these results and the main influence factors can be investigated by comparing the result of the different measurement ways. The test results show that the response characteristic of the Doppler laser vibrometer can satisfy the requirement without any signal distortion, and the mean relative error of 5 % is permitted in the test. The two main external factors affecting accuracy are the reflex capability of the test object surface, and the relation between optical distance and the length of laser pipe. If the reflex capability of the measured surface is strong enough and the optical distance and the laser pipe length has linear relation, the reflex signal will be stronger which leads to the smaller optic noise for the higher Signal-To-Noise and more accurate measurement.

Keywords Doppler laser effect · Engine vibration · Test technology · Relative error

F2012-J08-004

J. Yang (✉) · J. Lan (✉) · X. YongJiang · J. Cai · X. Zhang · H. Liu · Y. Shi
Powertrain Global R&D Center in Chang an Automobile Co. Ltd, Chongqing, China

J. Yang · J. Lan · X. YongJiang · J. Cai · X. Zhang · H. Liu · Y. Shi
State Key Laboratory of Vehicle NVH and Safety Technology, Chongqing, China

1 Introduction

Generally speaking, The engine low or high frequency vibration, for example the vibration and noise of the engine exhaust system and the FEAD, are mainly caused by the periodical gas pressure and the mechanical forces of the crank train or valve train [1]. When the modal frequencies of the exhaust system including the brackets are low without reaching to the requirement, the manifold resonances can easily happen with loud radiation noise or abnormal exhaust noise. Another example is the serious FEAD belt vibration which can cause the abnormal engine FEAD noise problem. To solve these NVH problems, we need to measure the vibration on these parts such as the pulley belt and exhaust manifold for analyzing the resonance frequencies, the orders, the peaks of vibration data in order to find the root causes and optimization methods.

Due to the limitation of the conventional contact measurement equipments, it is impossible to measure the surface vibration of the high-temperature and the rotational components. Therefore, the Doppler laser vibrometer for the non-contact test of the engine vibration will be studied. This paper mainly introduces the vibration measurement on the surface of the exhaust system and the pulley belt. In order to validate the accuracy of the amplitude error relative to frequency of Doppler vibrometer, the intake manifold surface vibration results using the conventional contact measurement and non-contact measurement are compared.

2 Test Equipments and Measurement Theory

In this research, we use the portable digital vibrometer (PDV-100 of Polytec company, the frequency resonance is shown in following Table 1), data sampling device (LMS), and some electric charge amplifiers.

Figure 1 shows the Helium–Neon laser measurement theory [2]. The vibrometer send out two beam lasers, in which one is a reference laser and the other is the object test laser. When the test laser beam points perpendicularly at a vibrating object surface and reflects back, the reflected laser and the reference laser will interfere at the photoelectric diode. The test laser will generate a small frequency shift which is called Doppler frequency f_D by the Doppler effect.

The Doppler frequency equals the difference of two laser beam's frequencies [3]. The object surface normal vibration velocity is a function of Doppler frequency shown in Eq. 1 [4, 5]. The differentiation or integration can be used mathematically to get the vibration acceleration or displacement. The deduction of Eq. 1 is as following:

$$f_D(t) = f_c(t) - f_B = \frac{c + v}{c - v} * f_B - f_B = 2v * \frac{f_B}{c - v}$$

usually, $c \gg v$, $c = \lambda * f_B$, therefore,

Table 1 The frequency character of PDV filter

Filter setting	Pass band (0.1 dB)	Stop band (Attenuation > 40 dB)
1 kHz	0.5 Hz ~ 1 kHz	>4.3 kHz
5 kHz	0.5 Hz ~ 5 kHz	>8.4 kHz
22 kHz	0.5 Hz ~ 22 kHz	>25 kHz

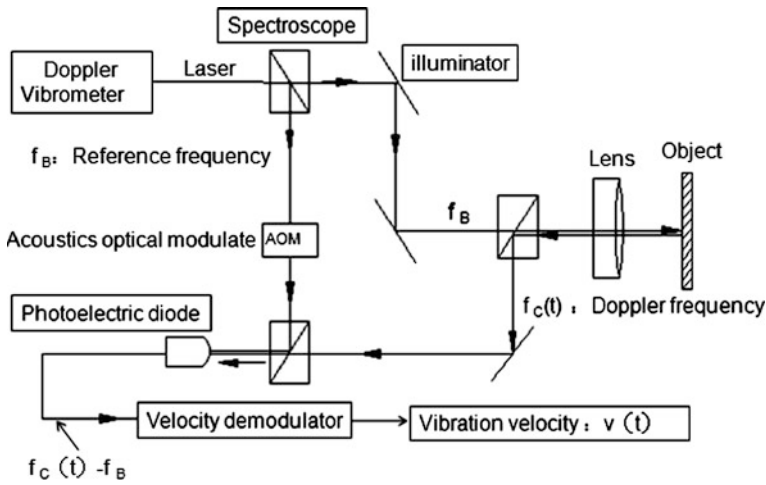


Fig. 1 Helium-Neon laser measurement theory

$$f_D(t) = 2v * \frac{f_B}{c} = \frac{2v}{\lambda} \tag{1}$$

where, c is the laser speed, $f_D(t)$ is the Doppler frequency, f_B is reference laser frequency, $f_c(t)$ is reflecting laser frequency, v is the object surface normal vibration velocity, λ is the Helium–Neon laser wave length ($\lambda = 632.8 \text{ nm}$).

3 The Analysis of Relative Error

In order to compare the amplitude relative error of two approaches of non-contact Doppler laser vibrometer and conventional acceleration sensor, we measure the vibration on an engine component and a standard vibrator. The relative error in speed range or in spectrum can display the accuracy of these two approaches.

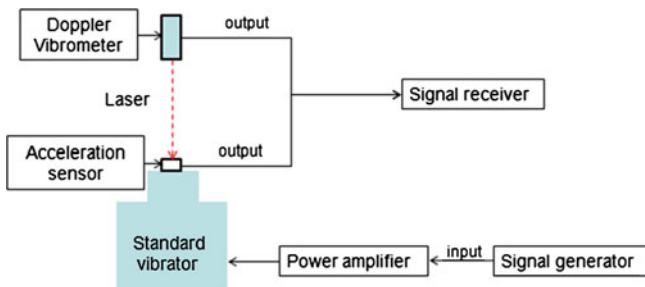
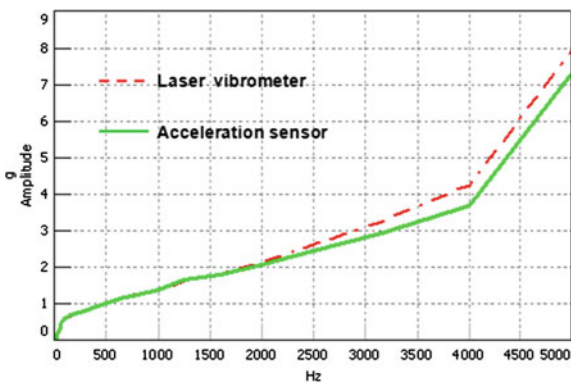


Fig. 2 Test on the standard vibrator

Fig. 3 The 1/3 Octave spectrum of laser vibrometer and acceleration sensor



3.1 Vibration on a Standard Vibrator

In order to have an ideal one direction vibration source, a standard vibrator was used to get the relative error of the laser and the accelerometer in Fig. 2. The standard vibrator has an input excitation frequency bandwidth from 0 up to 6400 Hz. The velocity measurement range of the laser vibrometer is set to 500 mm/s. The LP frequency is set to 5 or 22 kHz respectively.

In Fig. 3, the acceleration results of these two approaches are almost the same in the frequency range of 0 ~ 2000 Hz. Whereas, above the frequency of 2000 Hz, the amplitude by the laser vibrometer is larger than that by the acceleration sensor, and the mean relative error of 8.9 % above 3000 Hz is not permitted.

In order to avoid test random errors at most, we made 16 repetitive measurements and made average of these data at each frequency from 200 to 5400 Hz by the step of 400 Hz. These results consist of the mean relative errors between acceleration sensor and laser vibrometer. In Fig. 4, the mean relative error is less than 5 % when the excitation frequency is below 3000 Hz, and the mean relative error is more than 5 % when the excitation frequency above 3000 Hz.

Fig. 4 The mean relative error at filter setting at 5 and 22 kHz

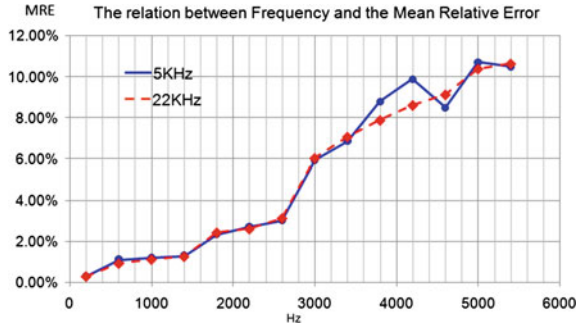
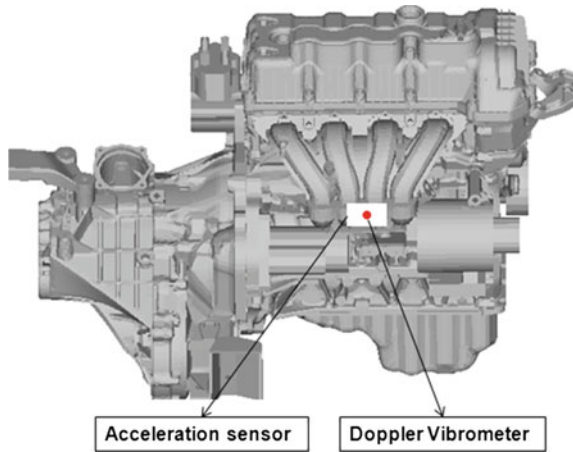


Fig. 5 The test location on an engine intake manifold



3.2 Vibration on an Engine Intake Manifold

In Fig. 5, we measure the same location on the intake manifold using an acceleration sensor close to the laser point shown as. In Fig. 6, the acceleration results are almost the same in the range of 0–2500 rpm. Whereas, above the speed of 2500 rpm, the amplitude by the laser vibrometer is 1.9 g larger at most than that by the acceleration sensor. Figure 7 shows that the average amplitude of the laser vibrometer is 6.0 % larger than that of the acceleration sensor in idle condition. The difference of these two approaches is larger especially at high frequency of 3,000–5,000 Hz in the 1/3 octave spectrum Fig. 8.

4 The Influence Factors on the Measurement Accuracy

Many influence factors on accuracy, classified as exterior factors and interior factors, come from Doppler laser vibrometer. The interior factors in Doppler laser vibrometer consists of uncertainty of direct current gain and offset [6, 7].

Fig. 6 The overall acceleration of the intake manifold in run up operating condition

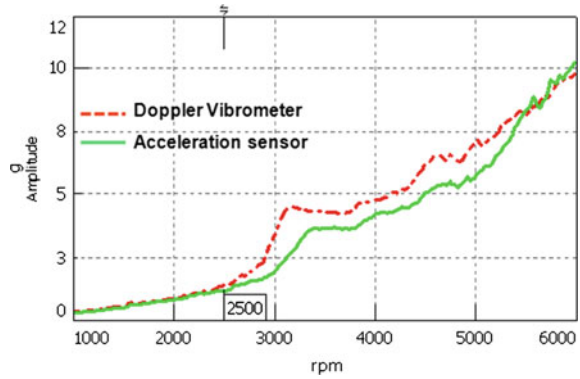


Fig. 7 The vibration spectrum of the intake manifold in idle condition

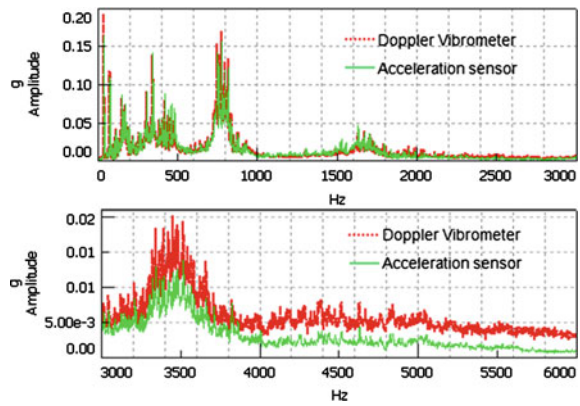
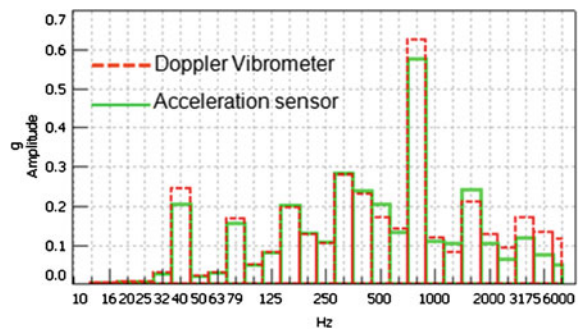
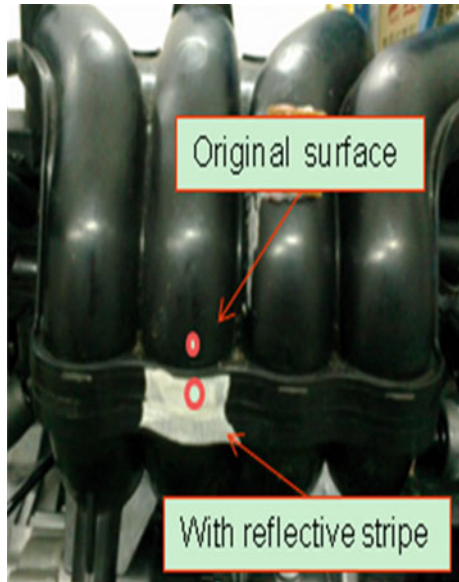


Fig. 8 The 1/3 octave spectrum



The exterior factors mainly consists of the reflex ability of object surface, the measurement distance, and the environmental temperature. In the engine NVH Dynocell test, we have to control the reflex ability of the object surface and the measurement distance when using the Doppler laser vibrometer.

Fig. 9 The object surface

4.1 The Reflex Ability of the Object Surface

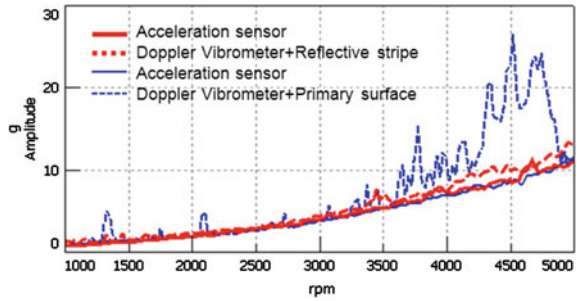
In order to compare the influence of surface reflection ability on the vibration results, we do the test on a low temperature surface on the intake manifold. In Fig. 9, one measurement location surface has a reflective stripe whose signal reflective intensity is 10, the other location has no reflective material whose smaller signal reflective intensity of 6. The results of these two locations by laser and accelerator are shown in Fig. 10.

Without the reflection strip at the measurement point, the blue dotted acceleration curve by Doppler laser vibrometer is less accurate than that by the acceleration sensor especially above the engine speed of 3,000 rpm. When the signal reflective intensity is 10 with reflection strip, the acceleration curves by the Doppler laser vibrometer is almost the same as by the acceleration sensor in whole speed range. Therefore, we should require that the reflection intensity of the measured surface must be 10 in order to get higher Signal-To-Noise and more accurate measurement results in engine test.

4.2 Measurement Distance

The two laser beams having the same phase and wavelength are sent out by the laser pipe in the laser head. When the peaks (or valleys) of the two laser beam waves meet, the laser energy gets the maximum at every integer multiple distance

Fig. 10 The effect of the reflect signal to the test result



of the laser pipe length [8]. Then the reflection signals are strong enough to have high Signal-To-Noise. The measurement distance L must satisfy the Eq. [2].

$$L = a + n * d \quad (2)$$

In the Doppler laser vibrometer we used, $a = 96$ mm, $d = 138$ mm, $n = 0, 1, 2, 3, \dots$

4.3 Summary of the Test Requirement

Some measures has to be taken into account for the measurement accuracy in engine test.

1. Check the reflection intensity of the tested surface:
 - a. Make sure that the laser beam reflects perpendicularly at the tested surface.
 - b. Make the measured surface smoothly otherwise use the reflection strip to be pasted on the surface.
 - c. Use paste reflection strip or spray silver colored reflection material on the measured surface.
2. The optic distance must meet Eq. 2.
3. The working environment temperature of Doppler laser vibrometer should meet the requirement of lower than 40°C .
4. Make sure that there is no disturbing from the engine ignition system or other strong electric device in the engine Dynocell. Check the signal before the test.

5 Laser Vibrometer Application in NVH Measurement Engine Dynocell

In Fig. 11, the surface vibration velocity of an exhaust manifold and catalysis were measured respectively using the laser vibrometer. Figure 12 shows the surface normal vibration acceleration results (after differentiation).

Fig. 11 Test points on exhaust manifold

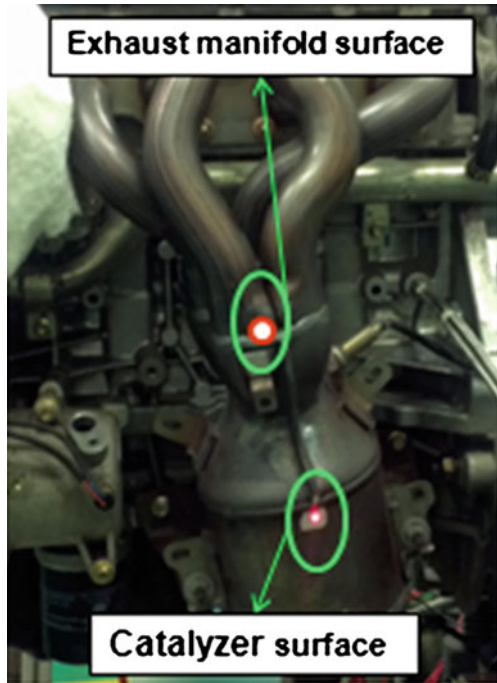
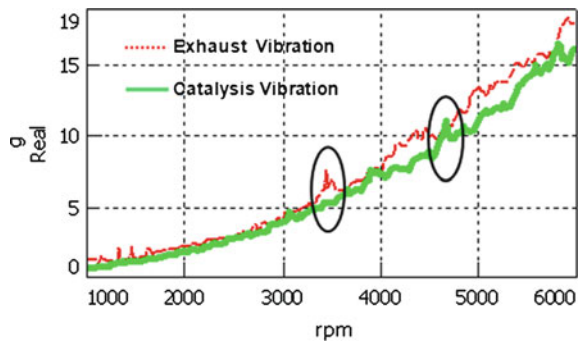


Fig. 12 Test results in run up condition



1. The surface vibration acceleration curve shows a small peak at 3,500 rpm on the exhaust manifold. The acceleration doesn't increase smoothly especially above the speed of 4,000 rpm.
2. The acceleration curve shows a peak at 4,700 rpm on the catalysis surface.
3. Anyway, these results are reasonable in engineering evaluations and optimizations.

In Fig. 13, the noise and normal vibration displacement curve of FEAD pulley belt are displayed in which two belts were used in the experiment of testing vibration on the belt. One is a new belt and another is a used belt in a passenger car

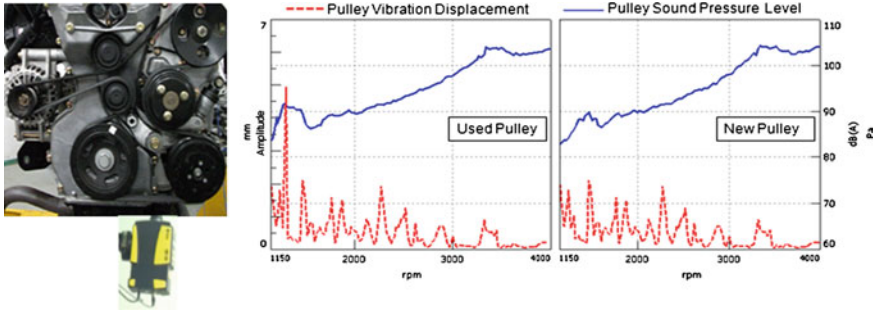


Fig. 13 The noise and vibration displacement curve of different FEAD pulley belt

of 40,000 km running condition. The used FEAD pulley belt transverse vibration displacement has a resonance at 1,300 rpm with a peak value of 5 mm, while the acoustic curve also shows a peak at 1,300 rpm with boring goose noise leading to worse engine sound quality. It's reasonable that the unusual noise peak are caused by the excessive belt wobble and slippage for the belt material aging, stiffening and distortion after running 40,000 km.

Whereas, a new belt can improve the noise with a better sound quality by reducing the transverse vibration. When using a new belt, the peak at 1,300 rpm has decreased greatly and the unusual goose noise is almost inaudible.

The two examples indicate that the Doppler vibrometer can measure the vibration of high-temperature components or belt of the engine in NVH Dynocell test. And then optimizations can be carried out to improve the engine vibration and sound quality by analyzing the resonances or excessive vibration from these components.

6 Conclutions

1. In the engine NVH Dynocell test, the Doppler laser vibrometer is a good non-contact tool for the vibration measurement of hot surface or a specific point vibration on the auxiliary belt.
2. For accurate application, signal reflection intensity of the surface must meet the requirement of 10. The reflection angle and the measurement distance must be meet to the test requirement in the test.
3. The accuracy of the Doppler laser vibrometer can be controlled to get reasonable results within the whole engine speed of 6,000 rpm and within the frequency up to 3,000 Hz.

References

1. Pang J, Zhan G, He H (2006) Automotive Noise and Vibration-Principle and Application. Beijing Institute of Technology Press
2. Portable Digital Vibrometer User Manual. Polytec
3. Zhang D, Zhang D, Liu C, BoYu M, Guo J (2010) Research of All-fiber Single-mode Velocity Interferometer. China Academic Journal Electronic Publishing House
4. 熊诗波,黄长艺.机械工程测试技术基础.机械工业出版社, 2006

Judder Test and Analysis for Electric Vehicle

Xiumin Shen, Yong Wang, Bin Li and Lei Cai

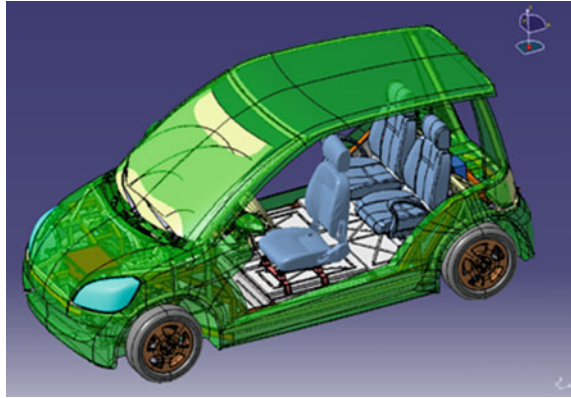
Abstract The electric vehicle appears judder phenomenon while emergent accelerating and then loosing the pedal, especially at lower speed. This paper carried out vibro-acoustic test at conditions of emergent accelerating and then loosing the pedal with different velocities, found that: the electric vehicles' judder frequency primarily focuses on lower frequency band from 10 to 20 Hz, which keeps stable in variable speeds. In addition, all major frame, motor, reducer, differential, tires have varying degrees of judder mutation; the connection between the main and sub-frame mount vibration within the frequency band in the vibration performance is not effective; what's more, the partial correlation coefficient between tire and the main frame is 0.93. It is proved that the vibration of tire is the main reason causing the electric vehicle judder, while the poor isolation performance of mounts between the main and sub-frame is another main reason. Finally, the author put forward to suggestion for mounts optimization, which is not taken measure on the vehicle, so unable to verify the suggestion is validity. But the study of this paper provides significant guiding for eliminating and improving the electric vehicle judder phenomenon.

Keywords Electric Vehicle · Judder · Vibro-acoustic test · Main-frame · Transfer path

F2012-J08-005

X. Shen (✉) · Y. Wang · B. Li · L. Cai
State Key Laboratory of Vehicle NVH and Safety Technology, Chongqing, China
e-mail: xiuminshen@126.com

Fig. 1 Structural diagram of the new electric vehicle



1 Introduction

With the advantages of lower pollution, lower noise and environmental protection, Electric vehicle has been gotten more and more attention in many countries, which can effectively alleviate energy resources tense [1]. Electric vehicle refers to vehicle powered by electric energy, which consists of power driving system, controlling system, transmission system and some other working devices [2]. Because there is no internal combustion engine, electric vehicle has no waste gas and no pollution while working. That is benefit for environmental protection and air cleaning. Electric vehicle has a good name of “zero pollution” [3].

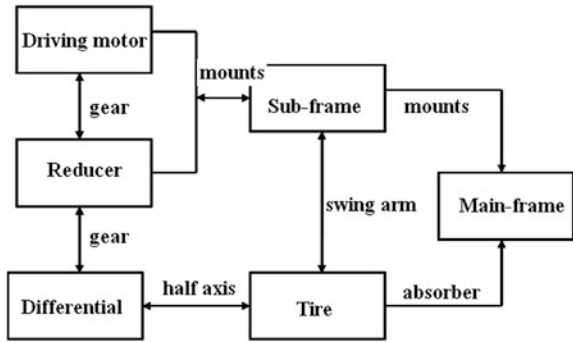
Recently a new type of electric vehicle has been launched, which appears judder phenomenon while emergent accelerating and then loosing the pedal. That makes subjective feeling extremely uncomfortable. In this paper, in view of this phenomenon studied judder phenomenon of this new type electric vehicle.

2 Vibration Sources Analysis of Electric Vehicle

The structure of the new type electric vehicle is shown as Fig. 1. From appearance, there is no difference with traditional vehicle, but the power assembly of electric vehicle is composed by battery, driving motor and controlling system. Where the driving motor is equivalent to the engine, and the battery is equivalent to the fuel tank. The battery provides electricity to the motor, to make motor operate, and then promotes the vehicle forward [4].

In this paper, the new type electric vehicle is Front-motor-Front-driving. The power driving system lies in front of the cabin, including driving motor, reducer and differential. The power driving system is connected to the sub-frame by mount, while the sub-frame is connected to the main frame also by mount.

Fig. 2 New type electric vehicle vibration sources and transmission path



The main vibration sources of electric vehicle include driving motor, reducer and differential, as well as tire vibration caused by road roughness. The new type electric vehicle vibration transmission path is shown as Fig. 2.

3 Vibro-Acoustic Test of Electric Vehicle

Controlling system of electric vehicle is worked by receiving driver’s pedal signal. Electric vehicle appears judder phenomenon while loosing pedal which is the suddenly losing of the vehicle power source, especially under the condition of emergent accelerating and then loosing pedal.

In response to this phenomenon, this paper carried out vibro-acoustic test under conditions of emergent accelerating and then loosing the pedal with different velocities, in order to find the vibration sources and transmission paths. The test did in semi-anechoic chamber in Tongji University, and the test equipment is SQLAB with 34 channels, acceleration sensors are ICP piezoelectric acceleration sensor produced by the U.S. PCB company, microphones are produced by Danish B&K Company.

3.1 Test Conditions

In order to test and analysis judder phenomenon electric vehicle objectively, simulate test did with drum tester. Electric vehicle is separately accelerated to 10 km/h, 20 km/h, 30 km/h, 40 km/h, and then loosed pedal till stopped.

3.2 Test Points Arrangement

For accurately analysis the causes of electric vehicle judder phenomenon, it is necessary to arrange test points reasonably:

- (1) Vibration test points: vertical acceleration of driver seat, acceleration of main frame in front of electric vehicle in three direction, acceleration of sub-frame in middle of the vehicle in three direction, acceleration of driving motor in three direction, acceleration near junction between reducer and driving motor in three direction, acceleration near junction between reducer and differential in three direction, acceleration of reducer in three direction, acceleration of tire in three direction.
- (2) Torque test points: test the speed of driving motor, as well as output torque characteristics of driving motor and differential.

4 Test Results and Analysis

People can feel the judder is derived from mutation of main frame vibration. So this paper focuses on analysis vibration characteristic and sources of main frame while emergent accelerating and then loosing the pedal. Considering that the test signals are not stationary, while handling with the test signals mainly through wavelet analysis [5], as well as coherent/partial coherence analysis, transfer function and some other methods.

4.1 Judder Phenomenon Analysis

- (1) Vibration image of main frame with different velocities

Figure 3 is Vibration image of main frame with different velocities. It is clearly that with different velocities: (1) Judder phenomenon occurred at the moment of loosing pedal; (2) Vibration mutation of main frame frequency focus on the low frequency band from 10 to 20 Hz; (3) Judder intensity reducing while vehicle velocity increasing, i.e. judder phenomenon is much more obviously at lower velocity.

- (2) Transfer path image analyses

Vibration images are used to represent vibration energy transfer between all components, shown as Fig. 4. It is clearly that: (1) Components include tire, driving motor, reducer, sub-frame and main-frame all occurred vibration mutation while emergent accelerating and then loosing the pedal. (2) As for vibration

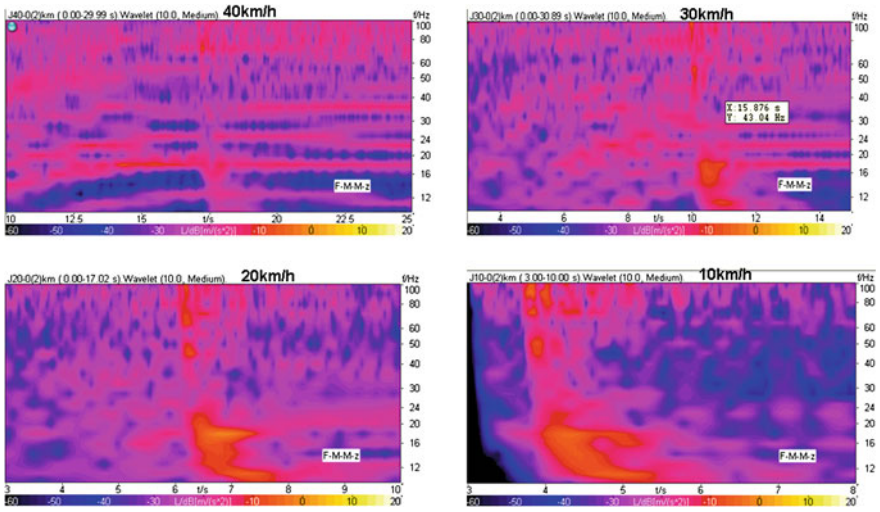


Fig. 3 Vibration image of main frame with different velocities

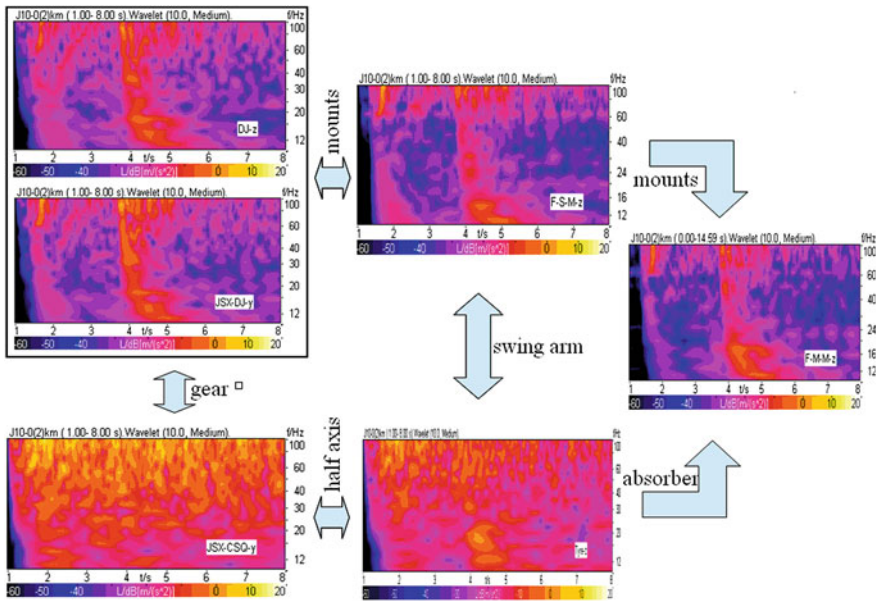


Fig. 4 Vibration transfer path image

intensity, tire judder is the most serious, followed by driving motor, reducer, main-frame, and sub-frame. (3) Vibration mutation focuses on lower frequency band from 10 to 20 Hz.

Table 1 Correlation/partial correlation analysis on test signals of main-frame with sub-frame and tire

		Sub-frame	Tire
Main-frame	Coherent coefficient	0.93	0.99
	Partial coherence coefficient	0.04	0.93

By anglicizing vibration image of main frame and transfer path image under condition of emergent accelerating with different velocities and then loosing the pedal, shown that: (1) Electric vehicle appears judder phenomenon while emergent accelerating and then loosing the pedal. (2) The lower velocity, the more obvious of judder phenomenon. (3) Judder frequency primarily focuses on lower frequency band from 10 to 20 Hz.

The following will analysis the causes of judder phenomenon of electric vehicle while emergent accelerating and then loosing the pedal in detail.

4.2 Judder Causes Analysis

By anglicizing vibration transfer path of electric vehicle, we can see that there are two direct excitation sources affected on main-frame: one is the vibration of motor and reducer transmits to sub-frame and then to main-frame through mounts, the other is the vibration of tire transmits to main-frame through suspension and reducer.

(1) Coherent/partial coherence analysis

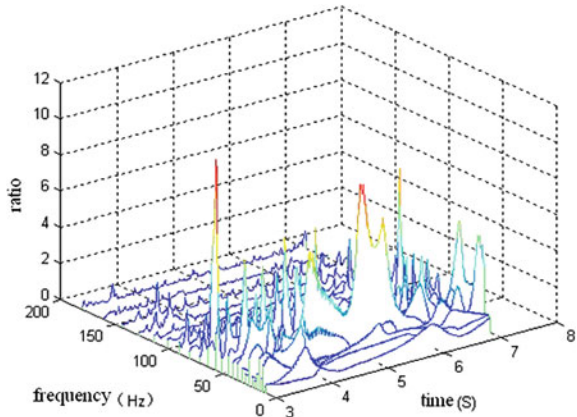
In order to make sure the main causes of the main-frame judder, the author did coherent/partial coherence analysis with vibration signals, main-frame to sub-frame and main-frame to tire, shown as Table 1.

Did not consider vibration interaction between sub-frame and tire, the author did coherent analysis between main-frame and sub-frame, as well as main-frame and tire, shown that: the coherent coefficient between main-frame and sub-frame is 0.93, while the coherent coefficient between main-frame and tire is 0.99.

Because the two main excitation sources are not independent, sub-frame and tire bracket are connected by swing arm. It is necessary to consider vibration interaction between sub-frame and tire. Then did partial coherence analysis between main-frame and sub-frame, as well as main-frame and tire, shown that: the partial coherence coefficient between main-frame and sub-frame is 0.04, while the partial coherence coefficient between main-frame and tire is 0.93.

The above indicated that the main-frame judder is mainly caused by tire vibration, followed by sub-frame. While the contribution of tire vibration to sub-frame is also very large, then vibration of sub-frame transmits to main-frame by mounts.

Fig. 5 Transmission characteristics of mounts between main-frame and sub-frame



(2) Mount performance analysis between main-frame and sub-frame

Main-frame and sub-frame of electric vehicle are connected through mounts. So mounts' performance directly determines vibration transmission from sub-frame to main-frame. This paper analyzed the transmission characteristic of mounts between main-frame and sub-frame, shown as Fig. 5.

Mounts' transmission characteristic between main-frame and sub-frame is shown as Fig. 5. It is clearly that the mounts' isolation performance is poor in judder frequency band from 10 to 20 Hz. Vibration is enlarged while transmitting from sub-frame to main-frame. So the mounts between main-frame and sub-frame have little effect on vibration isolation in judder frequency band.

(3) Torque characteristic of driving motor

Torque characteristic curve of new type electric vehicles' driving motor is shown as Fig. 6, which is obtained by fitting test data with different velocities.

From vibration transfer path image, it is clearly that vibration energy of driving motor, reducer and tire is larger in judder frequency band. At the moment of loosing pedal, it is equivalent add an opposite torque to the driving motor, while tires will generate an opposite torque, so driving motor, reducer and tire judder serious while emergent accelerating and then loosing the pedal.

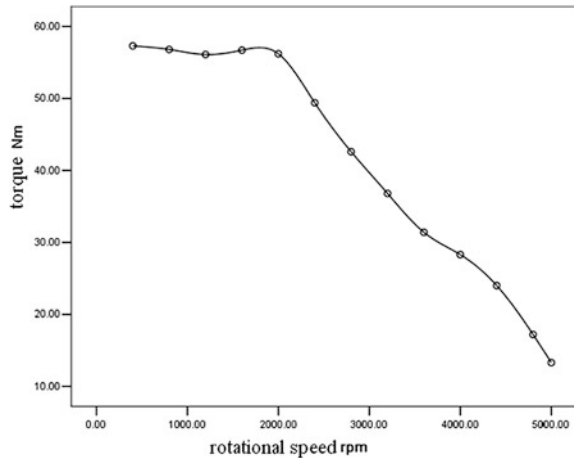
The conversion formula between electric vehicles' running velocity and driving motors' rotational speed as followed:

$$v = \frac{2\pi rn/i}{60} \tag{1}$$

where:

- v running velocity of electric vehicle km/h;
- i transmit ratio $i = 11.8$;
- r wheel radius $r = 0.269m$,
- n rotational speed of driving motor r/min;

Fig. 6 Torque characteristics curve of new type electric vehicle driving motor



From Fig. 6 and formula (1), it is concluded that: while electric vehicles' running velocity < 17 km/h, output torque of driving motor is remain constant, while electric vehicles' running velocity > 17 km/h, with running velocity increases, output torque of driving motor decreases. It is agreement with test results that judder phenomenon more obvious while electric vehicles' running velocity lower than 17 km/h.

5 Conclusions

Based on vibro-acoustic test and analysis of new type electric vehicle under condition of emergent accelerating and then loosing the pedal, conclude:

- (1) Judder phenomenon appears with different running velocities; the lower velocity, the more obvious judder appears; judder frequency primarily focus on lower frequency band from 10 to 20 Hz, which keeps stable while running velocity varying.
- (2) Components include tire, driving motor, reducer, sub-frame and main-frame all occurred vibration mutation while emergent accelerating and then loosing the pedal. As for vibration intensity, tire judder is the most serious, followed by driving motor, reducer, main-frame, and sub-frame.
- (3) Main-frame vibration directly affects people's subjective feelings. Through coherence/partial coherence analysis with vibration signals, main-frame to sub-frame and main-frame to tire, found that tire vibration is the main source that caused main-frame judder.
- (4) Though analyzing mount performance between main-frame and sub-frame, found that the mounts' isolation performance is poor in judder frequency band.

Tracking Algorithm and Its Implementation of the Vehicle BSR Noise Location

Choi Sung Uk, Kang Jun-Goo, Lee Tae-Woong and Mog Mu Gyun

Abstract It is hard to estimate the location of BSR noise and quantify BSR noise due to three main reasons as the followings: ambiguity of representation of BSR noise, quantification of evaluation, and reproduction experiment. To resolve these problems, companies depend on the experienced engineer. In this chapter, we would like to propose a method for categorizing BSR and an algorithm for tracking BSR noise location and evaluating BSR noise.

Keywords BSR · Vehicle · Categorization · Noise source · Tracking algorithm

1 Introduction

Since a suppression NVH technology has been developed rapidly, many kinds of running noises e.g., road noise, wind noise were revealed. BSR noise is also revealed besides these noises [1–4]. BSR becomes an issue because it makes customers uncomfortable. In real world, if there is a trouble with BSR, vehicle maintenance office should change the suspicious part of vehicle when the BSR becomes inaudible. It is time consuming process and takes a lot of money, because

F2012-J08-008

C. S. Uk (✉) · M. M. Gyun
Hyundai-Motor, Seoul, Korea
e-mail: inspace0@hyundai.com

K. Jun-Goo · L. Tae-Woong
SM Instruments, Seoul, Korea

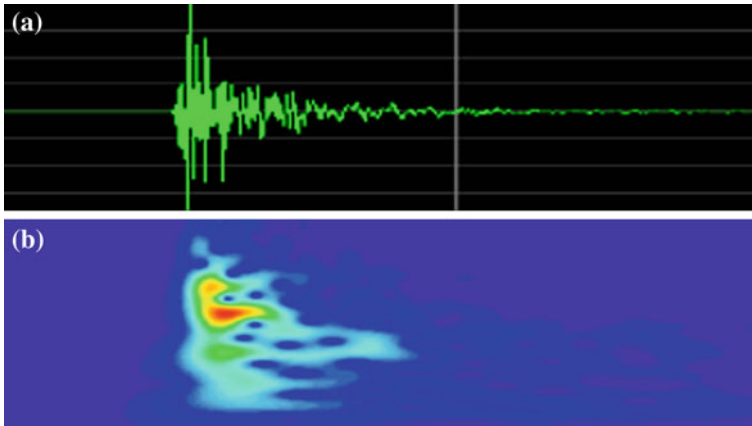


Fig. 1 Conceptual diagram. **a** Time signal which x axis represents time and y axis represents amplitude, **b** Spectrogram which x axis represents time and y axis represents frequency

many parts will be replaced and this process strongly depends on the experience engineer. A proper solution, therefore, is required.

BSR is buzz, squeak, and rattle which can be caused by vibration between adjacent parts of vehicle. It can occur at interior, exterior or underbody of vehicle. It does not represent failure of vehicle, intent of vehicle developer but makes customer become annoying. If BSR occurs in early part of vehicle mass production, it not only deteriorates the vehicle's brand but also may be a major factor of black mark of Initial Quality Study (IQS) and Vehicle Dependability Study (VDS).

In this chapter, we would like to propose a method for categorizing over 3,000 samples BSR with respect to some rules, quantifying BSR, and tracking BSR algorithm.

2 BSR

2.1 Pattern of BSR

Since vehicle is comprised of many complicate parts, it is hard to estimate the position of BSR which occurs at the vehicle without long experience. We, therefore, would like to pattern and categorize BSR for estimating the position of BSR without long experience.

As BSR occurs various positions in the vehicle, BSR varies considerably in measured and processed signal. Furthermore, it is hard to analysis BSR by using only time signal because more information is needed such as frequency. If we introduce spectrogram as shown in Fig. 1b, we can pattern BSR as a certain figure which is comprised of time and frequency. Frequency band of interest in our

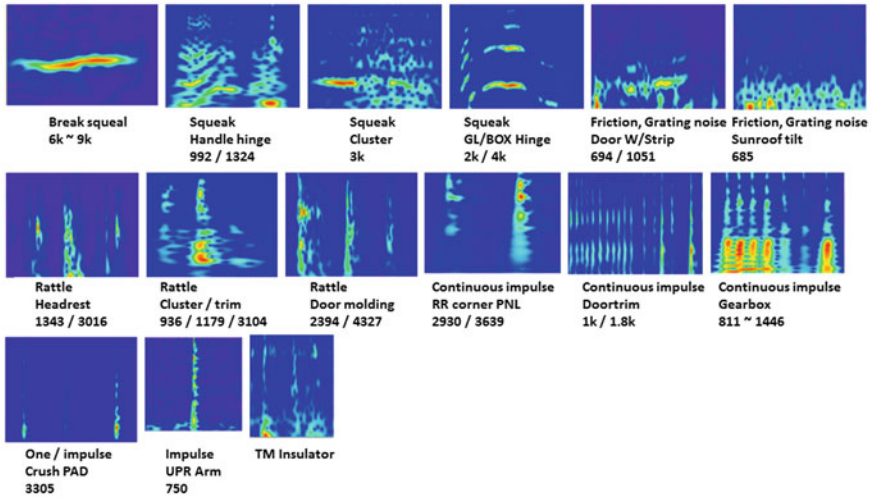


Fig. 2 Spectrograms of BSR

research can be set between 100 Hz ~ 6 kHz which belongs to audible frequency range, because BSR becomes an issue when customer feels uncomfortable.

Since 2003 we have been measuring time signal over 3,000 BSR samples and building a database of their own spectrogram for patterning BSR. For example, a squeal noise which is often occurring from break has a certain frequency range and long time period relatively.

Impulse noise, however, which can be measured from vehicle’s underbody has different pattern from a squeal noise. Figure 2 depicts some spectrograms of BSR which was patterned before. Next chapter, we would like to propose a method for categorizing this result.

2.2 Categorization of BSR

Let us introduce a circle for categorizing BSR patterns. This circle has two parameters i.e., a radius, and a clockwise rotation. The radius represents frequency that increases far from the origin. The clockwise rotation represents continuity of BSR signal that decreases far from the reference axis as shown in Fig. 3.

Furthermore, if we categorize the vehicle part of each BSR same as proposed method, we can draw a diagram as shown in Fig. 4. This will be used to estimate the part of own BSR.

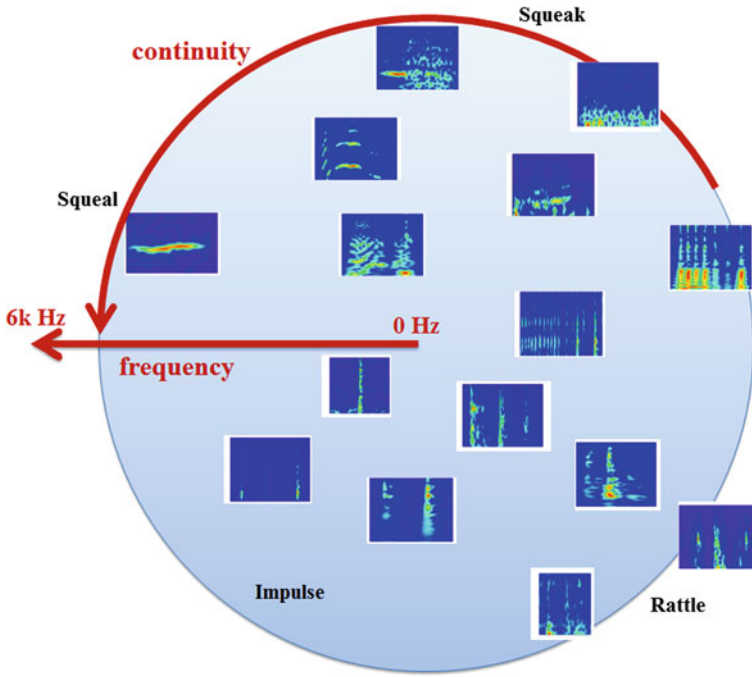


Fig. 3 Categorization of various BSR

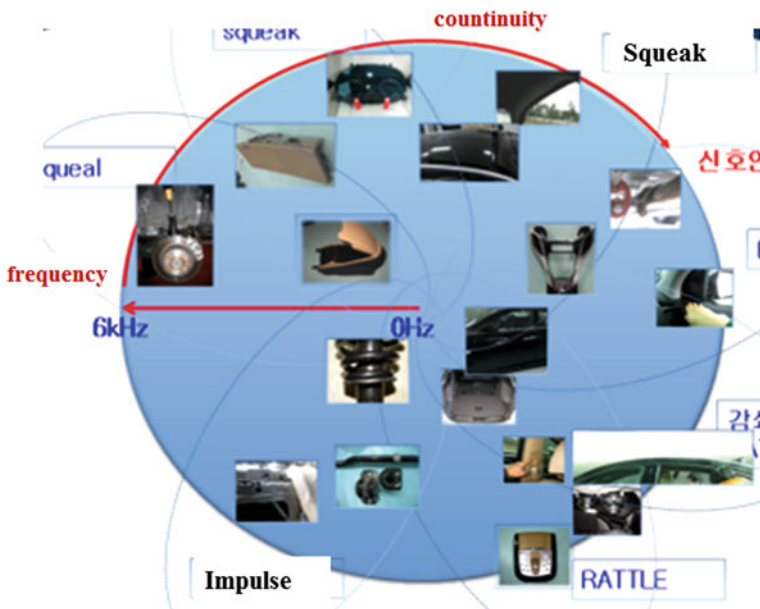


Fig. 4 Vehicle parts of various BSR

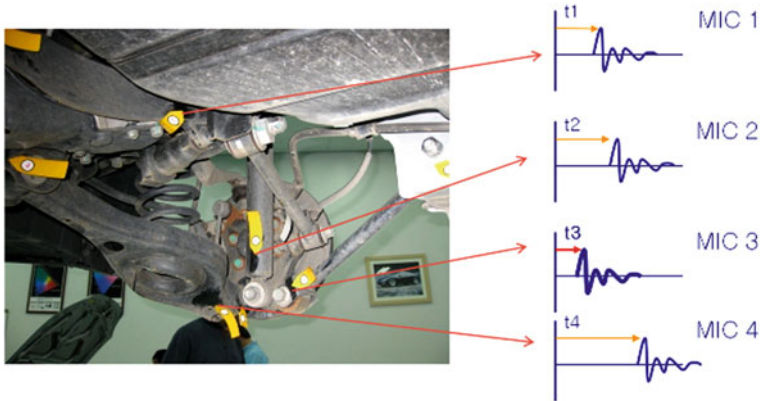


Fig. 5 Measurement positions of microphones

3 Tracking Algorithm

3.1 Experimental Setup

It is hard to estimate the position of BSR at the complicate and narrow part e.g., crush pad intuitively. In this situation, we introduce the sensor and DAQ equipment for measuring time signal and categorizing BSR. We estimate and change the part of BSR for fixing the problem. Let us make a situation that a number of microphones for estimating BSR as shown in Fig. 5 are set around the parts. If a BSR occurs, the signal is firstly measured the closest microphone. Therefore, we can estimate that the position of the BSR may be located around the microphone which is measured the time signal firstly. However, ambient noise is always loud, it is hard to use microphones in real situation. We, therefore, introduce a number of accelerometers instead of microphones in this research. Our experimental setup is comprised of four PCB accelerometers, DAQ board NI-9234 for the measuring convenience [5].

3.2 Simple Trigger Method

To measure the impulsive BSR, simple trigger method is one solution method. Signal exceeds trigger level as shown in Fig. 6a, measuring signal is started. We estimate the part of BSR from the categorized diagram by using measured signals. However, if it is hard to distinguish the starting point of the signal, simple trigger method tend to be misconceived the position of BSR.

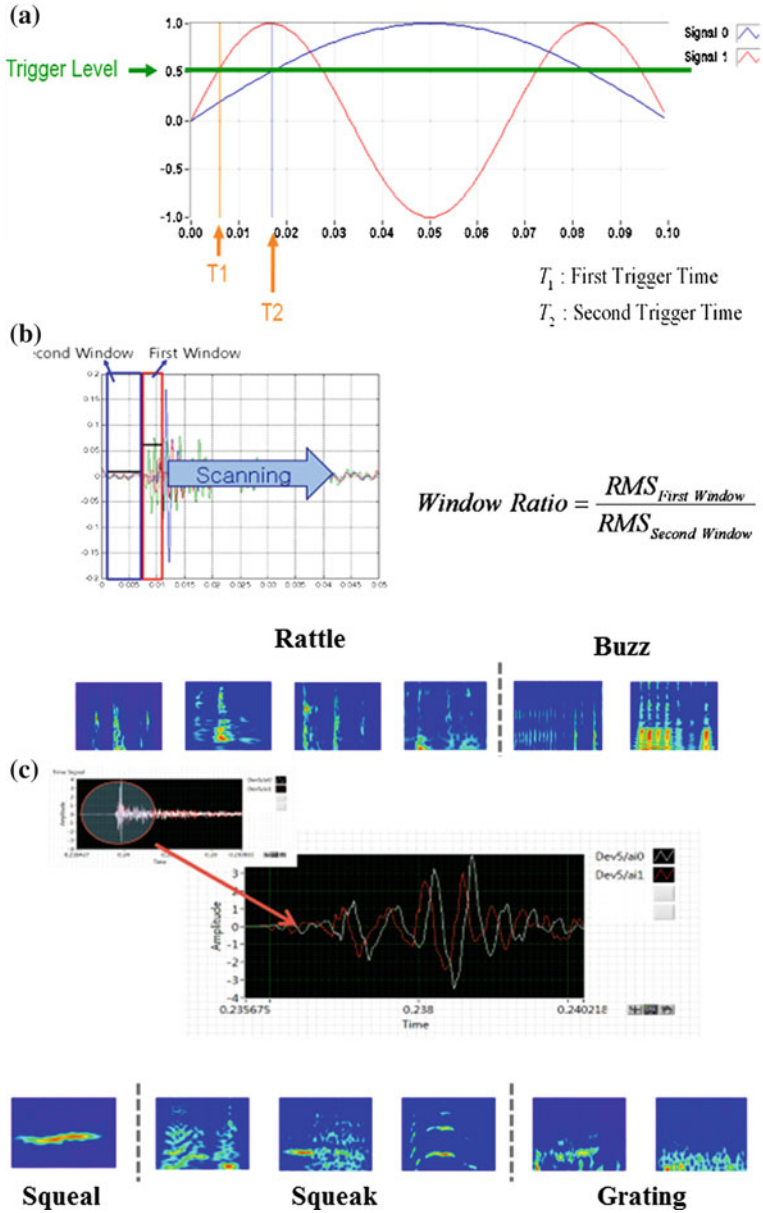


Fig. 6 Methods. a Simple trigger method. b Picking window method. c Cross correlation method

3.3 Picking Window Method

BSR is complicate and simple trigger method is not acceptable, it is one way to use picking window method. This method introduces a ratio between two windows which contain each time signal block as shown in Fig. 6b.

3.4 Cross Correlation Method

If the medium of adjacent part is almost same and the effect of vibration control device of vehicle is enough to negligible, the measured signals tend to almost same. If we use this method for estimating the position of BSR e.g., Squeal, squeak, and grating noise, this method is applicable as shown in Fig. 6c.

4 Conclusion

It is hard to estimate the position of BSR if non-experience engineer does. To resolve this, we proposed a method for patterning and categorizing BSR. Our database which has measured last ten years over 3,000 time signals and spectrograms was applied to introduce proposed method. BSR can be categorized by using a circle which radius represents frequency, clockwise rotation represents the continuity of BSR. Furthermore, another circle can be introduced as same as proposed method for categorizing the parts of BSR. It is helpful to estimate BSR without enough experience.

Three methods for estimating each BSR were proposed. Simple trigger method, picking window method, and cross correlation method were used in appropriate BSR pattern and situation.

References

1. Hall P (1996) Acoustic noise source identification in the automotive industry, The Korean society for noise and vibration engineering, 91–97
2. Mohamed El-Essawi et al. (2004) Analytical predictions and correlation with physical tests for potential buzz, squeak and rattle in a cockpit assembly, SAE Technical Paper No. 2004-01-0393
3. Gosavi SS (2005) Automotive buzz, squeak, rattle (BSR) detection and prevention, SAE Paper No 2005-26-056
4. Sohmshetty R, Kappagantu R et al. (2004) Automotive body structure enhancement buzz, squeak, rattle (BSR), SAE Paper No. 2004-01-0388
5. Choi Y (2004) Impulsive Source Localization in Noise[K]. Korean Soc Noise Vib Eng 14(9):877–883

Contribution of Pass-by Noise Sources with Acoustic Holograph and Dynamic Transfer Path Model

Sifa Zheng, Jiabi Dan, Peng Hao and Xiaomin Lian

Abstract A dynamic transfer path model was used to describe the relation between the sources on the vehicle and the test point on the ground for pass-by test. The noise signals both from the vehicle and the pass-by test were simultaneously recorded with a wireless device. The Tikhonov regularization method was described. The contribution of the pass-by noise was further analyzed and visualized with acoustic holograph. Finally, the contribution of a commercial vehicle is checked with the proposed method.

Keywords Pass-by noise · Acoustic holograph · Dynamic transfer path

1 Introduction

Identifying the noise sources and their contribution is an important to reduce the pass-by noise, which is influenced by many vehicle noise sources. Many methods are applied in the identification. Transfer Path Analysis (TPA) figure out the contribution of the main sources, and Acoustics Holograph (AH) method [1, 2] can be used to identify the sound field distribution on the exterior surface of the moving vehicles [3, 4]. However, because of the shielding effect of the body, AH

F2012-J08-009

S. Zheng (✉) · J. Dan · P. Hao · X. Lian
State Key Laboratory of Automotive Safety and Energy,
Tsinghua University, Beijing, China

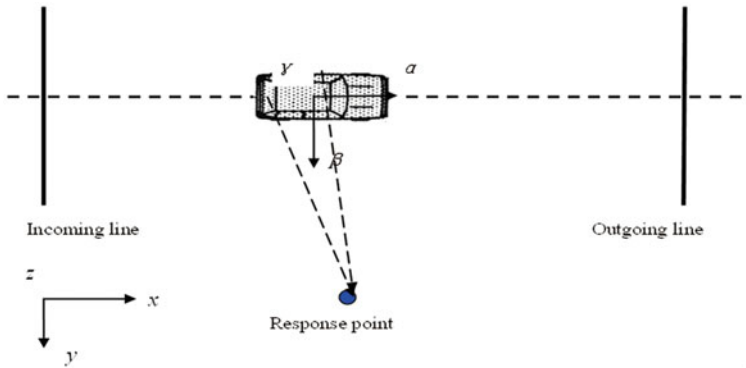


Fig. 1 The space–time relation of the measuring time and vehicle position

method could not separate the contribution from different noise sources that are behind the body surface.

A dynamic transfer path model was proposed to solve this problem [5] in the formal study. The excitation signals of the noise and vibration sources in a moving vehicle, and the pass-by noise signals, are measured simultaneously. In this study, the parameters in the dynamic model were estimated, and the results with singular value decomposition and Tikhonov regularization were compared using simulation and experiment. The contribution of the sources was decomposed with the dynamic transfer model and acoustic holograph at any test location.

2 Dynamic Transfer Path Model for Pass-by Noise

2.1 The Dynamic Transfer Path Model of Moving Vehicles

In the vehicle pass-by noise test, the position of response point is fixed, and the position of vehicle is changed continuously. The test process is showed in Fig. 1. The vehicle starts from the start line, and runs to the outgoing line along the dashed centerline with full-throttle acceleration state.

When the vehicle is at location S_v the transfer function $h_i(S_v, f)$ from the source i to the response point p is

$$h_i(s_v, f) = \frac{p_i(s_v, f)}{a_i(s_v, f)} = \frac{fft[p_i(t + \Delta t)]}{fft[a_i(t)]} \tag{1}$$

Here $a_i(S_v, f)$ is the excitation signal of source i and $p_i(S_v, f)$ is the response signal of response point p generated by source i when the vehicle is at location S_v .

If there are n excitation sources in the vehicle, when the vehicle is located at S_v , the transfer function matrix $\mathbf{H}_n(S_v, f)$ from all sources to the response point \mathbf{p} can be defined by

$$\mathbf{H}_n(S_v, f) = \{h_1(s_v, f), h_2(s_v, f), \dots, h_n(s_v, f)\}^T \tag{2}$$

And for the whole acceleration process of the vehicle, the transfer function matrix $\mathbf{H}_n(f)$ is

$$\mathbf{H}_n(f) = \{\mathbf{H}_n(s_v, f)\} \tag{3}$$

After removing the Doppler Effect, these signals were transformed into the frequency-domain and the response signals were fitted by

$$p_m(f) = A_{m \times n}(f) \mathbf{H}_n(f). \tag{4}$$

2.2 The Calculation of the Transfer Matrix

According to Eq. (4), transfer function matrix $\mathbf{H}_n(f)$ could be directly obtained by matrix inversion:

$$\mathbf{H}_n(f) = A_{m \times n}(f)^{-1} p_m(f) \tag{5}$$

However, the accuracy of the calculation of the transfer function matrix declines significantly when noise is contained in the measured signal matrix, or when there is a high correlation between the reference signals. Tikhonov regularization method is usually used in resolving ill-conditioned problems. In that way, the transfer function matrix $\mathbf{H}_{n \times m}(f)$ can be calculated by Eq. (6):

$$\mathbf{H}_{n \times m}(f) = (A^T A + \lambda^2 I)^{-1} A^T P_{k \times m}(f) \tag{6}$$

λ^2 is the regularization parameter, which could be obtained by L-curve method or generalized cross validation (GCV) method. The matrix A can be decomposed as $A = Z_s D^{1/2} U^T$, with Z_s and U unitary matrices and $D^{1/2}$ a diagonal matrix of singular value σ_i . This gives

$$\mathbf{H}_{n \times m}(f) = U \left(D^{1/2T} D^{1/2} + \lambda^2 I \right)^{-1} D^{1/2T} Z_s^T P_{k \times m}(f) \tag{7}$$

The term $(D^{1/2T} D^{1/2} + \lambda^2 I)^{-1} D^{1/2T}$ that is a diagonal matrix with elements $\sigma_i / (\sigma_i^2 + \lambda^2)$ replaces the $D^{1/2T}$, the terms of which are σ_i^{-1} .

Table 1 Comparison of the calculation method with statistic analysis

Method	$E[\delta]/\%$	Std $[\delta]/\%$
Tikhonov regularization	3.41	2.81
Pseudo Inversion	6.80	4.77

2.3 Compare the Tikhonov Regularization with the Pseudo Inversion

The calculation method of transfer matrix is compared using the stability and accuracy. For a test, 23 microphones and accelerators are mounted to record the main noise sources of the vehicle, and one microphone is used to record the response sound pressure. In this test, these signals are recorded under various working conditions, the total times of test is 97. 40 tests are selected randomly to calculate the transfer function matrix. The excitation matrix is $A_{40 \times 23}$, and the response matrix is $P_{40 \times 1}$. Other tests are used to verify the result.

Using Eqs. (5) and (7), two 23×1 matrixes H_{pi} and H_{tr} are obtained, and the computing time is also recorded. According Eq. (4), the fitting noise of any verification test is given:

$$p_{Fit}(f) = A_{1 \times 23}(f)H_{23 \times 1}(f) \tag{8}$$

The error between the fitting value and the real value is δ :

$$\delta = \left| \frac{p_m - p_{Fit}}{p_m} \right| \times 100\% \tag{9}$$

The $E[\delta]$ and Std $[\delta]$ of some method can express its accuracy and stability, it is given:

$$E[\delta] = \frac{1}{N} \sum_{i=1}^N \delta_i \tag{10}$$

$$Std[\delta] = \left(\frac{1}{N} \sum_{i=1}^N (\delta_i - \bar{\delta})^2 \right)^{\frac{1}{2}}$$

Using 120 random combinations of the 97 tests, the statistical result of δ is illustrated in Table 1.

According the above result, it is clear that Tikhonov Regularization is better than the Pseudo Inversion method in the accuracy and stability. But the Tikhonov Regularization spends an extraordinary amount of time.

3 Combined Acoustic Holograph with TPA

The sound field can be described by Eq. (11) [4].

$$U(\xi, \eta) = \frac{\beta k}{4\pi i} \iint_H \left\{ b(x, y) \left[1 + \left(1 + \frac{1}{ikr} \right) \cos \theta \right] \right\} \left(\frac{e^{-ikr}}{r} \right) dx dy \quad (11)$$

Make the signal $p_R(x, y, f)$ of one microphone in the array for the reference signal e_R , and other signal $p_M(x, y, f)$ for the measuring signal e_M . Using transfer model, the reference signal and measuring signal of the source i is

$$\begin{aligned} p_{i,R}(x, y, f) &= a_i(\xi, \eta, f) h_{i,R}(x, y, f) \\ p_{i,M}(x, y, f) &= a_i(\xi, \eta, f) h_{i,M}(x, y, f) \end{aligned} \quad (12)$$

Where $h_{i,R}(x, y, f)$ is the transfer function from the source i to the reference microphone; $h_{i,M}(x, y, f)$ is the transfer function from the source i to the measuring microphone.

According to the Eq. (12), the sound field distribution $U_i(\xi, \eta)$ in the reconstitution plane of the source i can be explained as

$$U_i(\xi, \eta) = \frac{\beta k}{4\pi i} \iint_H |a_i(\xi, \eta, f)|^2 H_{i,RM}(x, y, f) dx dy \quad (13)$$

And,

$$H_{i,RM}(x, y, f) = \left\{ h_{i,R}(x, y, f) h_{i,M}(x, y, f)^* \left[1 + \left(1 + \frac{1}{ikr} \right) \cos \theta \right] \right\} \left(\frac{e^{-ikr}}{r} \right) \quad (14)$$

4 Contribution of Pass-by Noise Sources

The dynamic transfer path combined with acoustic holograph method is used to identify the contribution and noise radiation of a commercial vehicle [6]. The microphones and accelerators are mounted on the position of main noise sources of the commercial vehicle, and one cross array is placed on the ground for recording the exterior signals. The signals collected from vehicle and ground are synchronize by a wireless device (Fig. 2).

The source signals recorded on the truck include cylinder head, engine gearbox, oil sump, muffler, turbocharger, and the truck pass through the array.

First, the sound field distribution of the moving vehicle noise sources is reconstructed with the acoustic holograph method. From Fig. 3, the noise energy of the truck external surface focused on the back of the cabin without being separated clearly.

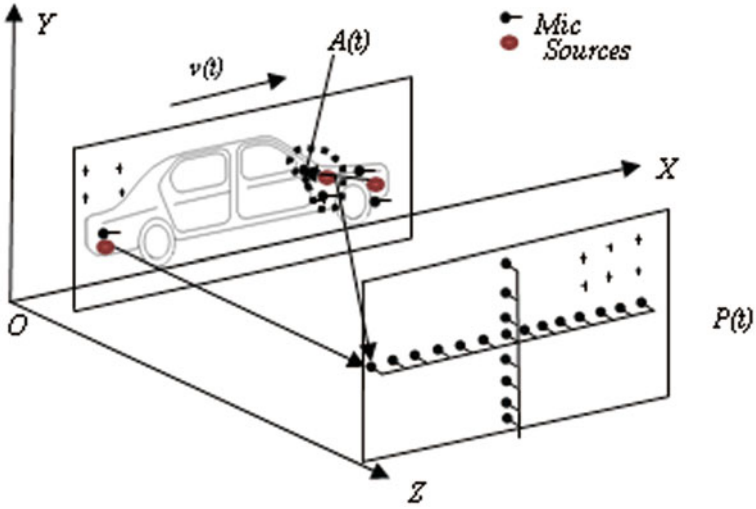


Fig. 2 The contribution of main sources test

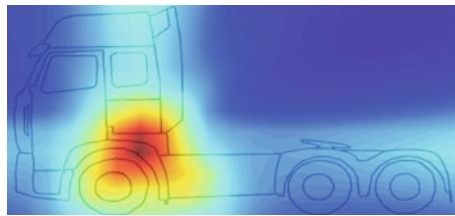


Fig. 3 The sound field distribution of the moving vehicle external surface

Table 2 The sound field of main noise sources

Turbocharger	Cylinder head	Engine gearbox
Exhaust manifold	Oil sump	Muffler

Next, the transfer function matrix between the noise source and array is calculated, and then the acoustic holograph method is used to reconstruct the sound field distribution on the vehicle external surface of each source. The radiation sound field of each main noise source is shown in Table 2.

5 Conclusions

The contribution of the pass-by noise sources was analyzed and visualized with transfer path model and the acoustic holograph. Tikhonov Regularization was used to calculate the dynamic transfer path function and contribution. It found that: the pass-by noise sources could be decomposed and visualized with the combined dynamic transfer model and acoustic holograph method; To calculate the dynamic transfer function, the accuracy and stability of Tikhonov Regularization is better than pseudo inversion method.

References

1. Park S-H, Kim Y-H (2001) Visualization of pass-by noise by means of moving frame acoustic holography. *J Acoust Soc Am* 110(5):2326–2339
2. Scott Brandes T, Benson RH (2007) Sound source imaging of low-flying airborne targets with an acoustic camera array. *Appl Acoust* 68:752–765
3. Dirk Döbler, Gunnar Heilmann (2008) Time-domain beam forming with zero-Padding. In: 2nd Berlin beam forming conference, Berlin, Germany
4. Hald J (2005) An integrated NAH/beam forming solution for efficient broad-band noise source location. In: SAE 2005 noise and vibration conference and exhibition, Grand Traverse, MI
5. Zheng S, Hao P, Lian X, Li K (2011) Time-domain transfer path analysis of multiple moving noise sources. *Noise Control Eng J* 59(5):541–548
6. Zheng S, Xu F, Lian X, Luo Y (2008) Generation method for a two-dimensional random array for locating noise sources on moving vehicles. *Noise Control Eng J* 56(2):130–140

Research of Acoustic Parts in Vehicle Sound Transmission Loss Test Method

Xiufeng Wang and Jie Shi

Abstract The sound transmission loss (STL) of the acoustic parts in the vehicle was proposed to be computed using the Sound Pressure Level measured at the several locations inside the vehicle and the transmitted Sound Intensity Level on the vehicle's exterior panel, which the acoustic treated vehicle passenger compartment is assumed as a small reverberation room. The necessary parts retrofits and acoustic treatments for Sound transmission loss tests of the acoustic parts in the vehicle were listed. The values of the appropriate number and positions of the loud speakers, microphones and sound intensity probes for Sound transmission loss of the acoustic parts in the vehicle were recommended. The in vehicle sound transmission loss tests of the acoustic parts such as the doors, carpets, wheel house etc. were achieved in the semi-anechoic room. Based on the door system, the correlation work has been done among the methods of the proposed in vehicle STL test, the reverberation—semi-anechoic chamber buck STL test and SEA analysis.

Keywords Acoustic parts · Sound transmission loss test · In vehicle · Door · Semi-anechoic chamber · Reverberation chamber

F2012-J08-012

X. Wang (✉) · J. Shi
Proving Ground and Test and Validation Department of Pan Asia Automotive Technical Centre, Shanghai, China
e-mail: xiufeng_wang@patac.com.cn

1 Introduction

Customer's awareness regarding NVH comfort and new stringent legislative requirements are posing new challenges for vehicle manufactures. With increased engine power to weight ratio, there is pressure to reduce overall vehicle weight and cost. This impose constraints to NVH engineer in designing the body structure and sound package to reduce the effect of powertrain noise, road noise and wind noise on passenger compartment.

The sound transmission loss (STL) is a key specification to measure the acoustic performance of the body structure and sound package. According to the different incident sound types, the sound transmission loss test can be divided into the normal incidence method and random incidence method [1, 2]. The normal incidence sound transmission loss test method can be measured using four microphone tube as per standard ASTM E2611 [3], which is a rapid method and require only a small size sample of the material and more suitable for the material acoustic test.

The random incidence sound transmission loss test method [1] normally includes three ways: the standard reference sample test method per SAE J1400 [4], the reverberation -reverberation chamber test method per the ASTM E 90-09 [5] and the reverberation -anechoic chamber using sound intensity test method per the ASTM E 2249-02 [6].

For the accurate, simple and convenient in implementation, the reverberation chamber—anechoic chamber using sound intensity test method is the most commonly used sound transmission loss test method in the automotive industry. While the reverberation -anechoic chamber using sound intensity test method requires body structure destructive cut and the special buck fixtures that will take a lot of time (usually a few weeks) and cost for the test preparation and system setup.

In this paper, the sound transmission loss of the acoustic parts in the vehicle was proposed to be computed using the Sound Pressure Level measured at the several locations inside the vehicle and the transmitted Sound Intensity Level on the vehicle's exterior panel, which the acoustic treated vehicle passenger compartment is assumed as a small reverberation room. The necessary parts retrofits and acoustic treatments for Sound transmission loss tests of the acoustic parts in the vehicle were listed. The values of the appropriate number and positions of the loud speakers, microphones and sound intensity probes for Sound transmission loss of the acoustic parts in the vehicle were recommended. The in vehicle sound transmission loss tests of the acoustic parts such as the doors, carpets, wheel house etc. were achieved in the semi-anechoic room. Based on the door system, the correlation work has been done among the methods of the proposed in vehicle STL test, the reverberation - semi-anechoic chamber buck STL test and SEA analysis.

2 Acoustic Parts in Vehicle Sound Transmission Loss Test Method

The sound transmission loss is defined as the ratio of the incident sound power W_{in} and the transmitted sound power W_{out} ,

$$STL = 10\lg \frac{W_{in}}{W_{out}} \quad (1)$$

The incident sound power W_{in} of the acoustic parts in vehicle sound transmission loss test method is calculated from the sound pressure level measured at the several locations in the passenger compartment, that the retrofired and acoustic treated vehicle passenger compartment is assumed as a small reverberation room(as shown in Fig. 1), i.e.

$$W_{in} = \frac{P_{in}^2}{4\rho c} S \quad (2)$$

Where P_{in}^2 is the passenger compartment multi-point sound pressure mean square value; S is the test sample area, m^2 ; ρc is the characteristic impedance of air and is 400 N s/m^3 under the normal temperature and atmosphere pressure.

The semi-anechoic chamber, where the test vehicle is parked, is used to receive the transmitted sound, and the transmitted sound power W_{out} can be calculated from the vehicle's exterior panel Sound Intensity, i.e.

$$W_{out} = I_{out} S \quad (3)$$

Where I_{out} is the semi-anechoic chamber side panel surface average sound intensity;

Put Eqs. (2 and 3) into Eq. (1), then derive Eq. (4) for the in vehicle sound transmission loss test,

$$STL = SPL_{in} - SIL_{out} - 6 \quad (4)$$

Where $SPL_{in} = 20\lg(P_{in}/P_0)$ is the average sound pressure level of the passenger compartment, P_0 is the reference sound pressure and $2 \times 10^{-5} \text{ Pa}$ in the air; $SIL_{out} = 10\lg(I_{out}/I_0)$ is the sample surface average sound intensity level of the semi-anechoic chamber side, I_0 is the reference sound intensity and is $1 \times 10^{-10} \text{ W/m}^2$ in the air.

Fig. 1 Vehicle test setup
(setup for the *right* front door
window)



3 Acoustic Parts Sound Transmission Loss in Vehicle Test

3.1 *Acoustic Parts Sound Transmission Loss in Vehicle Test Preparation*

In order to achieve the in vehicle sound transmission loss tests of the acoustic parts, it is necessary and very important for retrofits and acoustic treatments to the related parts of the vehicle, especially the passenger compartment. First, remove the powertrain, front and rear suspension s (including tire assemblies) from the vehicle; Secondly, make the passager compartment a more reverberant space. All of the windows, sunroof, and sunshade must be closed. Remove all free standing seats from the vehicle. For built in seats, such as the rear bench seat of a sedan, cover with sound barrier to achieve a more reflective surface. In order to create a more reverberant space, turn the floor mats upside down and cover any absorptive surfaces with acoustically reflective material, i.e. rubber, sound barrier, plywood, etc. Finally, treat all vehicle panels, other than the test panel, with sound barrier assembly material to eliminate any flanking paths, this includes hanging sound barrier assembly material from the vehicle's rockers to the floor of the car test room. Figure 1 shows a vehicle schematic of the retrofit and acoustic treatment.

3.2 *Acoustic Parts in Vehicle Sound Transmission Loss Test*

The acoustic parts in vehicle sound transmission loss test were implemented in the semi-anechoic chamber. Place the speakers in the 4 corners of the vehicle angled to face the center of the passenger compartment. For each vehicle panel tested the speakers may need to be moved to insure that sound is evenly distributed in the vehicle and to each of the microphones. Ensure that the speakers are at least 1.0 m from any potential microphone location. At no time should the speakers be pointed directly into any microphone, and avoid having a speaker in the near field of the

Fig. 2 Right front door glass sound transmission loss test results

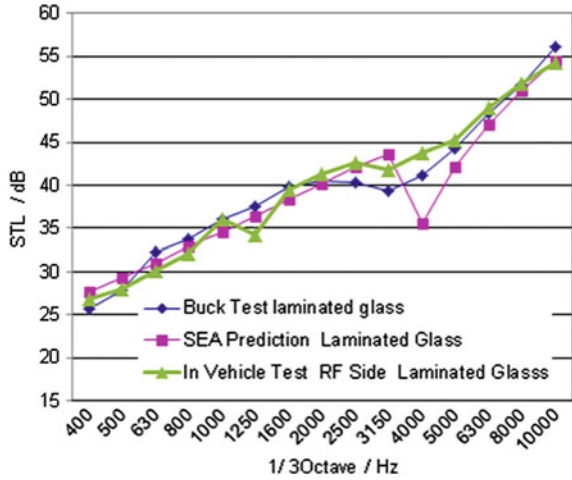
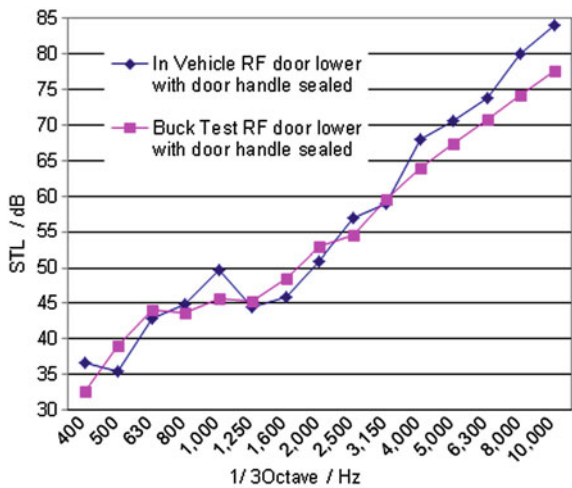


Fig. 3 Right front door lower sound transmission loss test results



vehicle panel being measured. Four or six microphones are used for this test. They should be randomly distributed inside the vehicle over the area of the vehicle panel being tested, approximately 15 ~ 20 cm off the surface of the panel. Acquire the transmitted intensity level SIL_{out} in the semi-anechoic chamber with a scanning method, that scanning speed is 0.1 ~ 0.3 m/s, sound intensity probe is 0.1 ~ 0.3 m away from the test surface, the scan mode is grid-style intertwined. Finally, with the SPL_{in} and SIL_{out} obtained, according to the Eq. (4), the sound transmission loss STL. can be calculated.

Fig. 4 *Right front door lower door handle influence*

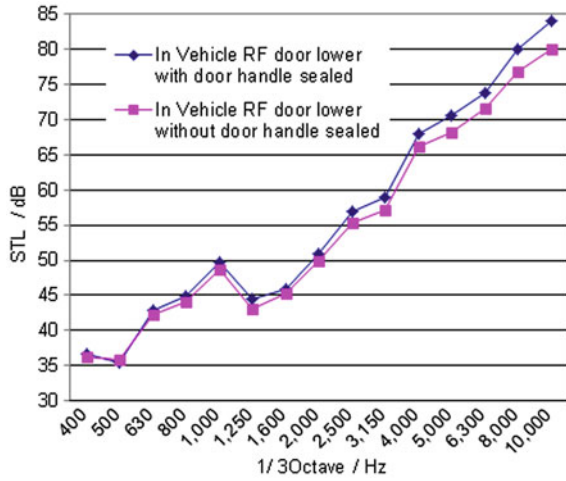
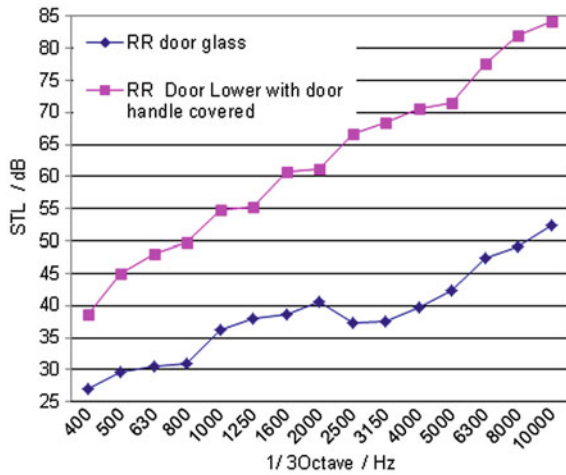


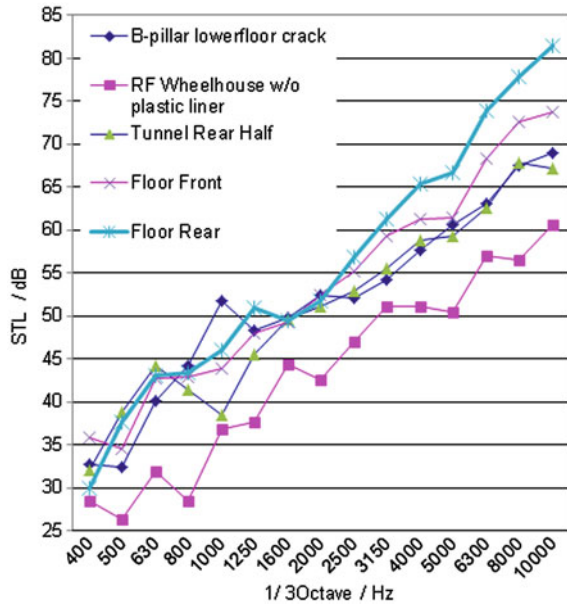
Fig. 5 *Right rear door lower sound transmission loss test results*



3.3 Acoustic Parts in Vehicle Sound Transmission Loss Test Results

In this section, acoustic parts in vehicle sound transmission loss test method was applied to vehicle as shown in Fig. 1. Figure 2 shows comparison experimental and simulated results for the left front door 5 mm acoustic laminated glass. The in vehicle sound transmission loss test results, and that of the reverberation chamber—anechoic chamber method and the analysis STL results using statistical energy analysis have a good consistency except at 4,000 Hz where the testing test results is significantly higher than the analysis results. It is because the seal treatment on the window glass run channel with tape and damping that improves

Fig. 6 Floor area sound transmission loss test results



the damping characteristics of the glass and improves the STL performance correspondingly. The in vehicle and reverberation—anechoic chamber method sound transmission loss test results of the left front door body region are depicted in Fig. 3, that also shows a good correlation. Figure 4 shows the in vehicle sound transmission loss test results of the door lower region of the left front door with and without the door handles seal, that shows the in vehicle STL test method can effectively identify STL improvement of the acoustic parts. Figures 5 and 6 list the in vehicle sound transmission loss results of the left rear door, floor region and wheel house region, that can be used to evaluate sound transmission loss performance of the above-mentioned regions in the real vehicle status and support statistical energy analysis vehicle modeling and correlation with effective data.

4 Conclusion

The body structure and the related acoustic parts are main sound insulation package of the vehicle, which can effectively block the road noise and powertrain noise and wind noise to enter the passenger compartment. A fast, accurate and relatively low cost acoustic parts sound transmission loss test method has important practical significance and engineering value. In comparison with the traditional reverberation- anechoic chamber method, acoustic parts in vehicle sound transmission loss test is a more simple, fast and convenient and vehicle based non-destructive test method that can significantly save the cost and time

(buck test takes several weeks, while in vehicle only 1–2 days), and can achieve the vehicle level acoustic parts sound insulation performance assessment and identification and effectively support the vehicle statistical energy analysis modeling and correlation. It is particularly suitable for the benchmark test and analysis for competitor vehicles.

References

1. Pang J (2006) Automotive noise and vibration—principle and application. Beijing Institute of Technology Press, Beijing
2. Zhang Z (2008) Fundamentals of automotive interior design. China Communications press, Beijing
3. ASTM (2009) E2611—09 Standard test method for measurement of normal incidence sound transmission of acoustical materials based on the transfer matrix method
4. SAE (2010) J1400-laboratory measurement of the airborne sound barrier performance of flat materials and assemblies. SAE standards
5. ASTM E (2009) 90—09 Standard test method for laboratory measurement of airborne sound transmission loss of building partitions and elements ASTM
6. ASTM E (2003) 2249-02 Standard test method for laboratory measurement of airborne transmission loss of building partitions and elements using sound intensity

Author Biographies

Wang Xiufeng Male, Born in April 1975, Zibo, Shandong Province, Ph.D., Senior Engineer, Staff Engineer of Noise and Vibration Laboratory of Pan Asia Technical Automotive Center Co., Ltd.. Address: 3999 Long Dong Avenue, Proving Ground and Test and Validation Department, Pan Asia Technical Automotive Center Co., Ltd., Shanghai, China Zip Code: 201201 Tel :86 021-50161825 E-mail: xiufeng_wang@patac.com.cn

Shi Jie Male, Born in June 1966, Shanghai, Ph.D, Senior Engineer, Executive Director of the Proving Ground and Test and Validation Department, Pan Asia Technical Automotive Center Co., Ltd.. Address: 3999 Long Dong Avenue, Proving Ground and Test and Validation Department, Pan Asia Technical Automotive Center Co., Ltd., Shanghai, China Zip Code: 201201 Tel :86 021—50161571 E-mail: jie_shi@patac.com.cn

Research of the Powertrain in Vehicle Sound Power Test Method

Xiufeng Wang and Jie Shi

Abstract In this paper, an experimental study on the powertrain in vehicle sound power test was presented. The necessary parts retrofits and acoustic treatments for the powertrain sound power test in the vehicle were listed. The criteria and correction method of the appropriate background noise level for the powertrain sound power level test in the vehicle were discussed. The powertrain sound power tests in the vehicle were achieved in the low noise chassis Dynamometer in the semi-anechoic chamber. Based on the test results, the acoustic component contributions for the powertrain sound power levels were given.

Keywords Powertrain · In vehicle sound power test · Low noise chassis dynamometer · Semi-anechoic chamber · Sound pressure based method

1 Introduction

Customer's awareness regarding NVH comfort and new stringent legislative requirements are posing new challenges for vehicle manufactures. With increased engine power to weight ratio, the challenges for NVH engineers has increased multifold. Passenger compartment comfort levels are getting affected largely due to lighter and powerful engines. Same time, there is pressure to reduce overall

F2012-J08-013

X. Wang (✉) · J. Shi
Proving Ground and Test and Validation Department of Pan Asia Automotive Technical
Centre, Shanghai, China
e-mail: xiufeng_wang@patac.com.cn

vehicle weight and cost. This impose constraints to NVH engineer in designing the body structure and sound package to reduce the effect of powertrain forces and airborne noise on passenger compartment.

The sound power is a key indicator to measure the level of powertrain noise [1–5]. According to the different test acoustic environments, the sound power test can be divided into the engineering method [6, 7], the reverberation chamber method and (semi-) anechoic chamber method [8]; According to the different test transducers, the sound power test can be divided into the surface vibration based method [7, 9, 10], the sound pressure based method [11, 12] and sound intensity based method [7, 10]. For the accurate, simple and convenient in implementation, semi-anechoic chamber sound pressure based method is the most commonly used powertrain sound power method in the automotive industry. Powertrain sound power test is normally implemented in the powertrain dynamometer [13]. While Powertrain in dynamometer sound power test requires the special tooling fixtures, wiring harness modification, engine calibration file support, and so on, that will take a long time (usually a few weeks) and cost a lot of money for test preparation and system setup. And the transverse and longitudinal powertrain systems require the different kinds of Powertrain dynamometer facilities that needs big investment. The biggest challenge to the Powertrain in dynamometer sound power method appears in benchmark test to the competitor powertrains that requires vehicle tear down and is difficult to obtain the calibration file or control signals to run up the powertrain as its road conditions. And the effectiveness and practicality of the powertrain sound power test results are often questioned. In this paper, an experimental study on the powertrain in vehicle sound power test was presented. The necessary parts retrofits and acoustic treatments for the powertrain sound power test in the vehicle were listed. The criteria and correction method of the appropriate background noise level for the powertrain sound power level test in the vehicle were discussed. The powertrain sound power tests in the vehicle were achieved in the low noise chassis Dynamometer in the semi-anechoic chamber. Based on the test results, the acoustic component contributions for the powertrain sound power levels were given.

2 Powertrain in Vehicle Sound Power Test Method

In order to determine the measuring surface and test points positions of the powertrain, define the Powertrain to be Engine, Transmission and engine-mounted Accessories, excluding cooling fan. Imagine a box with rounded edges and corners which represents the major radiating surfaces of the Powertrain as shown in Fig. 1. The l , w , and e are the the powertrain dimensions. r is the radius of the rounded edges and corners, $r \approx w/3$. The In vehicle powertrain sound power test measuring surface is a hypothetical rectangular hexahedron enveloped the powertrain box, with 1 m away from the corresponding box surface and with a $(1 + r)$ radius of the arc transition on the each adjacent surfaces as shown in Fig. 2.

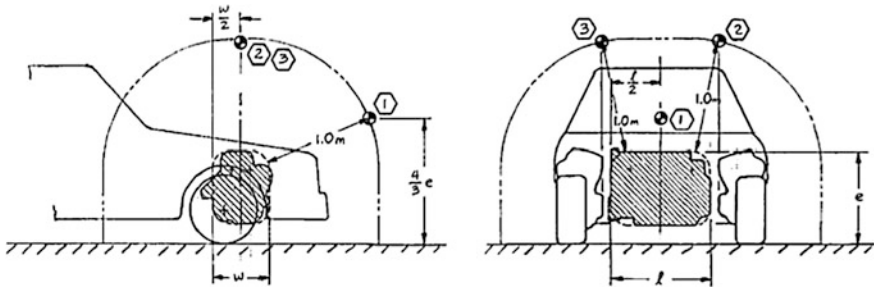
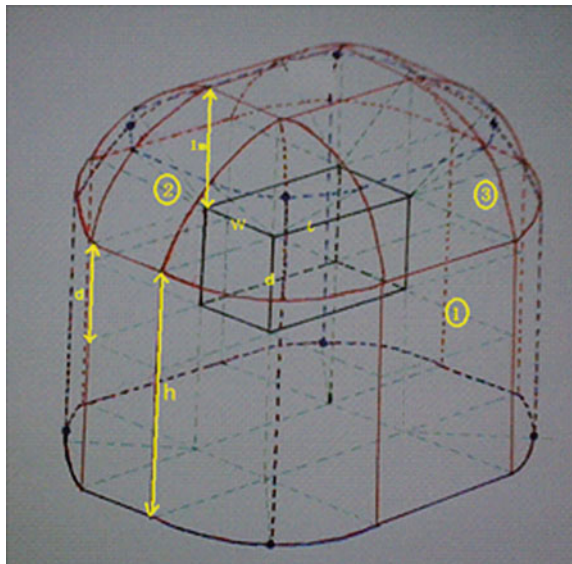


Fig. 1 A vehicle powertrain sound power testing microphone layout

Fig. 2 In vehicle powertrain sound power test measuring surface diagram



Taking into account the effectiveness and convenience of the actual test, the layout of measurement points is shown in Fig. 1, the measuring point 1 is located in front of the vehicle, the measuring points 2 and 3 are located in powertrain lateral surface, respectively, near the engine side and transmission side. The sound power equation is,

$$L_w = 10 \log_{10} \left[\left(0.9638 / P_0^2 \right) (A_1 P_1^2 + A_2 P_2^2 + A_3 P_3^2) \right] \quad (1)$$

Where L_w is the sound power level, dB; P_1, P_2, P_3 , are the sound pressure of the points 1, 2 and 3 respectively, Pa; P_0 is the reference sound pressure, 2×10^{-5} Pa in the air; A_1, A_2, A_3 is the area of measurement surface where the points 1, 2 and 3 are located, and are given in equations from (2 to 4); A is the total area of the measurement surface, m^2 .

$$A = 2(1+r)^2 + (1+r)(2e+w+1-6r) + 2(e-r)(w+1-4r) + (w-2r)(1-2r) \quad (2)$$

$$A_1 = 0.25(2^{0.5})(1+r)^2 + 0.25\pi(1+r)(1+2e-4r) + (1-2r)(e-r) \quad (3)$$

$$A_2 = A_3 = 0.5(A - A_1) \quad (4)$$

3 Powertrain in Vehicle Sound Power Test

3.1 Powertrain in Vehicle Sound Power Test Preparation

In order to achieve the in vehicle powertrain sound power test, it is necessary and very important for retrofits to the vehicle, especially to the engine compartment area and to do appropriate acoustic shielding or acoustic correction to the other main sound source components which may influence on the powertrain sound power test results. The transformation contents of the components includes the following: Firstly, remove engine compartment hood and any splash shields that are present underneath the engine and transmission. Second, as much as possible, remove batteries, fluid reservoir bottles, and other similar objects that are located within a line of sight between any of the microphones and the powertrain. Finally, as for the other main sound source components and its possible impact on the sound power test results and the corresponding acoustic shielding or acoustic correction strategy are listed in Table 1 in detail.

3.2 Powertrain in Vehicle Sound Power Test

Powertrain in vehicle sound power test was implemented on the low noise four-wheel drive chassis dynamometer in the semi-anechoic chamber of the Pan Asia Technical Automotive Centre. Firstly, attach the vehicle on the chassis dynamometer, and complete the vehicle road load simulated on the chassis dynamometer to determine the appropriate engine and vehicle speeds, road loads, and tractive efforts for the chassis dynamometer tests. (Table 3); Secondly, complete the transformation of the related parts and the acoustic shielding to the other major sound source parts listed in the paragraph 2.1. No special acoustic treatments on the tire noise and exhaust orifice noise for there are no significantly affect or only affect the individual test conditions of the powertrain sound power. Use method 2 in Table 1 to treat the cooling fan radiation noise influence. Thirdly, measure the size of the powertrain, and the positions of microphones as shown in Fig. 1; Install the thermocouple at the coolant outlet from engine location. Finally, after the test vehicle warms up, complete all the powertrain sound power test conditions listed

Table 1 The other main sound source components

No.	Other main sound source components	Influence and priority	Countermeasures or strategy
1	Cooling fan	Close to the powertrain, high priority	Disable all engine cooling fans. method 1: install a remote engine cooling system such that engine coolant temperature can be controlled in an effectively silent manner. method 2: a chilled air supplies to the vehicle radiator. If such systems are not effectively silent, subtract the noise produced by the system from the radiated noise of the powertrain
2	Snorkel noise and the intake system radiation noise	Close to the powertrain, high priority	Install an auxiliary muffler to the engine air inlet and place the muffler at least two meters from any measurement microphones. Treat the vehicle induction components by acoustic barriers/ wrapping
3	Tire noise	Close to the powertrain, big influence at high vehicle speed, middle priority	Recommend the use of same size blank-tread tires for the drive wheels of the test vehicle,
4	Exhaust tail pipe noise and exhaust radiation noise	A little far away from powertrain, low priority	Install additional exhaust muffler (optional); add acoustic barrier under the car to block the radiation noise of the exhaust system

Table 2 Background noise lists

Background noise no.	State chassis dynamometer	The external cooling system	Exhaust gas collection device, indoor air-conditioning equipment
Background noise no. 1	On, 0 km/h	On	On
Background noise no. 2	On, 0 km/h	Off	On
Background noise no. 3	Off	Off	On
Background Noise No.4	Off	Off	Off

in Table 2. Multiple measurements of the same test condition should have a good repeatability, that the differences should be within 1 dB for the steady-state conditions and within 2 dB for the engine speed scanning conditions.

The temperature monitoring at the engine coolant outlet pipe is important to ensure that the engine is running stably and effectively prevent the powertrain overheating, and the recommended value is within ± 3 °C deviation to the engine

nominal temperature. Background noise in the semi-anechoic chamber environment should be in strict inspection and control and Table 2 lists the major background noise conditions to be checked. Ideally, the powertrain SPL test results should be 20 dB higher than the corresponding background noise in each 1/3 octave frequency band and 10 dB is acceptable, within 5 dB is not recommended; If it is 5 ~ 10 dB, sound power correction should be done referred to the method 2 of the cooling fan case in Table 2.

3.3 Results Analysis and Discussion

In this section the powertrain in vehicle sound power test method was applied to vehicle equipped with a 2.4L inline four-cylinder engine, 6 forward gears automatic transmission and the powertrain dimensions $l \times w \times e$ are $0.86 \times 0.62 \times 0.86$ m and correspondingly $r = w/3 = 0.207$ m,. Table 3 lists the test conditions for the sound power, including the engine speeds, loads, gear position and air-conditioning compressor, headlights work status etc. Table 4 and Fig. 3 shows the in vehicle powertrain sound power test results and gives the engine acoustic beauty cover's acoustic contributions to the overall powertrain sound power. The beauty cover covers approximately 70 % of the engine top area and provide the acoustic improvements of 0.3–2 dB in all conditions. Figure 4 shows the in vehicle powertrain sound power test results equipped with the engine acoustic cover and the beauty cover's acoustic contribution in the engine sweep operating conditions. And the 3rd gear coast down (3 Gear Coastdown) condition means the engine throttle almost fully closed and the engine is in a very small workload, which represents the engine mechanical noise. While the 3rd gear wide open throttle(3 Gear WOT) condition means the engine throttle almost fully opened and the engine is in a full working load status and the gap with the 3 Gear Coastdown can be used to characterize the engine combustion noise contribution. In addition, the sound power curve of the 6th gear part open throttle (6 Gear POT) condition looks higher than that of the 3 Gear WOT trend extension to low-speed region, that results from the high-speed tire noise contribution for 1 380–2 880 r/min engine speed in 6th gear will correspond to 70 ~ 140 km/h vehicle speed. However, the beauty cover's acoustic contributions of 6 Gear POT seem reasonable and similar to those of other sweep conditions for the tire noise influence has just been eliminated during the beauty cover's sound power contribution calculations.

4 Conclusion

Powertrain noise and vibration is one of the most important part of traditional automotive NVH performance. A fast, accurate and relatively low cost powertrain sound power test method has important practical significance and engineering

Table 3 Test conditions

No.	Test conditions	Gear	Accessory status	Test conditions abbreviation
1	Idle 780 r/min	Drive	Off	D gear accessory off
2	Idle 850 r/min	Drive	On	D gear accessory on
3	Part open throttle 1 940 r/min	1	Off	1 gear 940 r/min
4	Part open throttle 2 500 r/min	1	Off	1 gear 2,500 r/min
5	Wide open throttle 4 000 r/min	3	Off	3 gear 4,000 r/min
6	Wide open throttle 6,500 r/min	3	Off	3 gear 6,500 r/min
7	Wide open throttle 2860 ~ 6,000 r/min	3	Off	3 gear WOT
8	Coastdown 6000 ~ 900 r/min	3	Off	3 gear coastdown
9	Part open throttle 380 ~ 2880 rpm	6	Off	6 Gear POT

Table 4 Sound power test results of the steady-state conditions

Test conditions	With beauty cover dB(A)	Without beauty Cover dB(A)	Beauty cover contribution dB
D gear accessory off	73.6	73.9	0.3
D gear accessory on	76.9	77.5	0.6
1 gear 940 r/min	84.9	86.5	1.6
1 gear 2 500 r/min	89.4	90.1	0.6
3 gear 4 000 r/min	102.2	103.0	0.9
3 gear 6 500 r/min	110.9	111.9	1.0

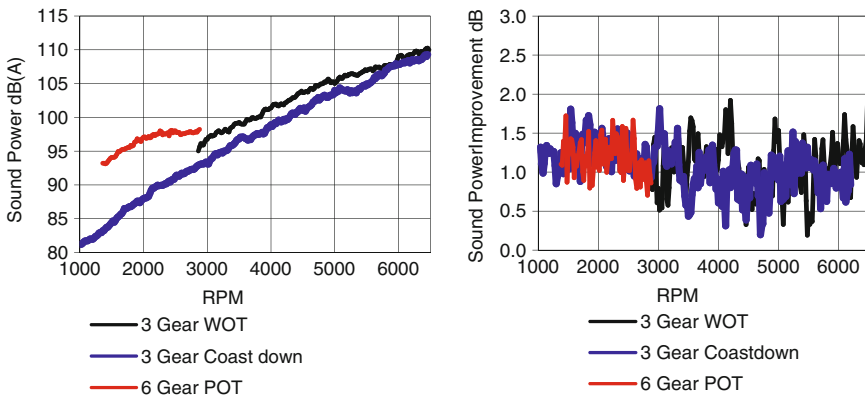


Fig. 3 Engine speed sweep conditions sound power test results

value. In comparison with the traditional powertrain sound power bench test, powertrain in vehicle sound power test is a more simple, fast and convenient and vehicle based non-destructive test method that can save a lot of cost and time (In dynamometer takes several weeks, while in vehicle only 1–2 days), and can effectively avoid the technical barriers between the different manufacturers,

accurately quantify the powertrain noise what the customers perceived. It is particularly suitable for the benchmark test and analysis for competitor vehicles.

References

1. Pang J, Chen G, He H (2006) *Automotive noise and vibration—theory and applications*. Beijing Institute of Technology Press, Beijing
2. Zhu X (2000) *China powertrain engineers' manual*. Shanghai Science and Technology Press, Shanghai
3. Yang Q (1985) *Powertrain noise control*. Shanxi People's Publishing House, Taiyuan
4. Lu X, Huang Z (2004) Diesel engine sound intensity noise source identification method. *Agric Mach* 35(5):51–54
5. Duan M, Shi J, Lu Xiaoli (2003) Engine noise source identification test method. *Liaoning Institute of Technology* 23(2):36–38
6. GB/T 1859–2000 (2000) *Reciprocating internal combustion engines—measurement of emitted airborne noise—engineering method and survey method*. National internal combustion engine standardization technical committee, Beijing
7. Hao Z, Liu Y, Bi F et al (2004) Passenger car diesel engine noise source identification methods study. *Engine Technol* 22(2):150–154
8. GB/T6882-2008 (2008) *Noise source sound power level determination of semi-anechoic chamber anechoic chamber and precise method*. National acoustics technical committee of standardization, Beijing
9. GB/T 16539-1996 (1996) *Determination of acoustic velocity noise source sound power level measurement for closed machines*. National acoustics technical committee of standardization, Beijing
10. Yue D, Hao Z, Liu Y et al (2004) Surface noise source identification diesel study. *Mech Eng* 40(6):192–195
11. Wei K, Bi F (2007) The engine combustion noise and mechanical noise, the noise contribution of the whole experimental study. *Small Intern Combust Engines Motorcycles* 36(4):82–85
12. Yu W, Shan B, Wang X et al (2011) Diesel engine combustion noise and mechanical noise identification and noise contribution of the whole experimental study. *Small Intern Combust Engines Motorcycles* 40(1):90–96
13. GB/T 1105-1987 (1987) *Powertrain performance test bench method*. National internal combustion engine standardization technical committee, Beijing

Author Biographies

Wang Xiufeng Male, Born in April 1975, Zibo, Shandong Province, Ph.D., Senior Engineer, Staff Engineer of Noise and Vibration Laboratory of Pan Asia Technical Automotive Center Co., Ltd.. Address: 3999 Long Dong Avenue, Proving Ground and Test and Validation Department, Pan Asia Technical Automotive Center Co., Ltd., Shanghai, China Zip Code: 201201 Tel :86 021-50161825 E-mail: xiufeng_wang@patac.com.cn

Shi Jie Male, Born in June 1966, Shanghai, Ph.D, Senior Engineer, Executive Director of the Proving Ground and Test and Validation Department, Pan Asia Technical Automotive Center Co., Ltd.. Address: 3999 Long Dong Avenue, Proving Ground and Test and Validation Department, Pan Asia Technical Automotive Center Co., Ltd., Shanghai, China Zip Code: 201201 Tel :86 021—50161571 E-mail: jie_shi@patac.com.cn

Part IX
Other

Research on Whine Noise of Automotive Radiator Fan During Decelerating

Wei Li, Xiaoping Gong and Haifeng Xu

Abstract This research introduces an experimental method and a theoretical analysis for the solution of automotive radiator cooling fan whine noise, and provides the optimization direction for resolving fan whine problems. The analysis of the whine root cause is put forward and validated by the modal tests with non-contact laser scanning vibrometry, in which the white noise signal is used to the fan motor as the excitation source. The results of the analysis and tests show the whine noise is mainly caused by the multiple resonances coincidentally between the excitations of the fan motor's electromagnetic force and the vibration modes of the fan assembly simultaneously. So that to eliminate or reduce the harmonic excitation (magnetic field) from the rotor grooves will reduce the fan whine noise level significantly.

Keywords Radiator fan · Whine noise · Laser vibrometry · Modal test · Electromagnetic noise

1 Introduction

The radiator cooling fan noise is one of the major noise contributions to the interior of vehicles. A driver is able to perceive the noise from the cooling fan intuitively, and his perception will directly affect on the judgment of sound quality

F2012-J09-002

W. Li (✉) · X. Gong · H. Xu
Changan Auto Global R&D Center, China
e-mail: sunqiemail@163.com

W. Li · H. Xu
State Key Laboratory of Vehicle NVH and Safety Technology, China

in vehicles, so, it is important to reduce the radiator fan noise for improving vehicle NVH performance.

A number of papers have been published in discussing radiator cooling fan noise problems. The common concerns of the mechanism of fan noise are aerodynamic noise. A methodology of CFD analysis and sound wave transmission theory was introduced in [1], it was used to predict fan Blade-Passing-Frequency (BPF) noise, and its accuracy was certificated by experimental results.

Actually, besides aerodynamic noise, some other unpleasant noises also exist in the process of fan running. An issue was described in [2]—a 50 Hz Solid-State-Relay was used to provide a pulse-width-modulated power to control engine cooling fans, which caused the cooling fans to vibrate at the switching frequency matching fan harmonics, and to degraded the vehicle's NVH performance. In that paper, the root-cause was discussed, and the solution was also proposed simultaneously. However, this paper here will present the different concerns that the fan whine noise was caused by more complicated reasons, and also introduce a new method used to detect and analyze the fan whine noise. The content of this article includes the non-contact laser scanning vibrometry applied for the fan mode shape analysis, as well as the principles of the excitation in electromagnetic field. It may provide one of the right directions for resolving fan noise issues in optimization.

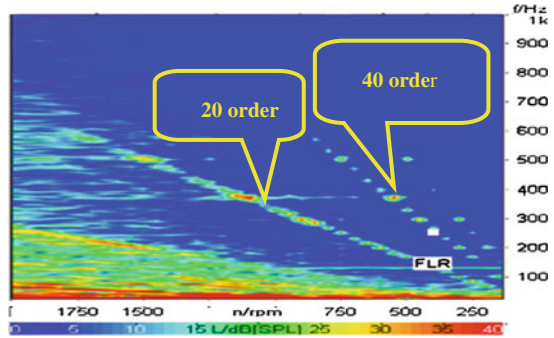
2 The Analysis of Automotive Radiator Fans Noise During Fan Deceleration

In general, radiator cooling fan noise mainly lies in four aspects: (1) The airflow pulsatile noise, so-called blade passing noise, which is caused by fan blade pushing air forward in running; (2) The electromagnetic noise, which is generated by fan's driving motor movement in magnetic field; (3) The motor whine noise, which is produced by intermittent impacted contacts between the brush and the commutator; (4) The vibration of fan blades and/or fan shroud. Briefly, the whine noise is maturely associated with the fan rotating speed. According to the possibility of 4 reasons mentioned above, to identify the root causes for a particular fan whine noise will be discussed the followings.

2.1 Acoustic Measurements and Analysis Whine During Fan Deceleration

It was an obvious whine noise from a particular radiator cooling fan perceived in subjective evaluation during the fan deceleration after the power supply to the fan is shut off. Therefore, the acoustic measurements were performed in Semi-Anechoic chamber objectively using an external DC power supply to control the

Fig. 1 Whine noise color plot at slowdown



fan running (the voltage is kept in consistent with the fan operation condition in vehicle). Meanwhile, the fan speed signal was requested with the connection to data acquisition front end and two microphones were respectively located at driver’s right ear (called FLR) inside vehicle and at a fixed position from the centre of the fan hub in front of vehicle.

Figure 1 is the plot of the acoustic measurements in FFT vs. rpm taken during the fan deceleration after the power supply was shut off. The plot shows the information of the fan whine noise occurred at several cross points of near 280, 360, 500 Hz along the lines of the 20th and the 40th order, specifically at 1,500 and 1,100 rpm. According to these characteristics of the hot spots in the plot, two additional acoustic measurements were taken at steady speed of 1,100 and 1,500 rpm, respectively, for the further analysis, as shown as in FFT of Fig. 2.

As the observation at FLR (driver’s right ear) in Fig. 1, it was found the whine noise was gradually changed along the changes of the 20 and 40th order lines with the fan rotating speed. Meanwhile, there were a few of fan structural vibration resonant bands existing near 280,360 and 500 Hz. The whine noise hot spots obviously appeared at the cross points when the noise order lines managed to meet with the fan vibration resonant band at 360 Hz with the speed 1,100 rpm and at 500 Hz with 1,500 rpm, respectively. Figure 2 shows the peaks at steady speed 1,100 and 1500 rpm are the same points as those in Fig. 1 in the characteristics of the frequencies, orders and amplitudes. Figure 3 shows the noise in order cut analysis during the fan deceleration. The whine noise at 1,500 and 1100 rpm was mainly contributed from the resonant coincidentally with the 20th order, and the whine noise at 750 and 560 rpm with the 40th order.

2.2 The Analysis of Fan Structure

In order to avoid the whine noise due to the resonant coincidence, it is necessary to understand the radiator fan assembly structure. In general, the fan assembly consists of three parts, i.e. fan, motor and shroud. The tested fan has eight blades

Fig. 2 Fan noise FFT at 1,100 and 1,500 rpm

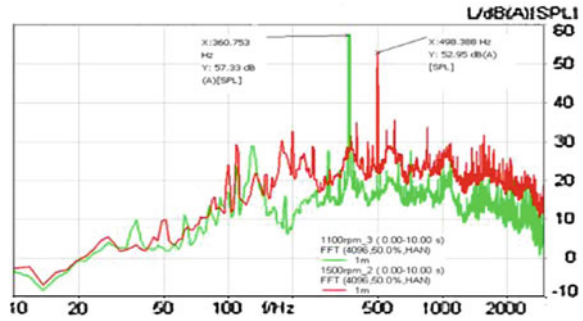
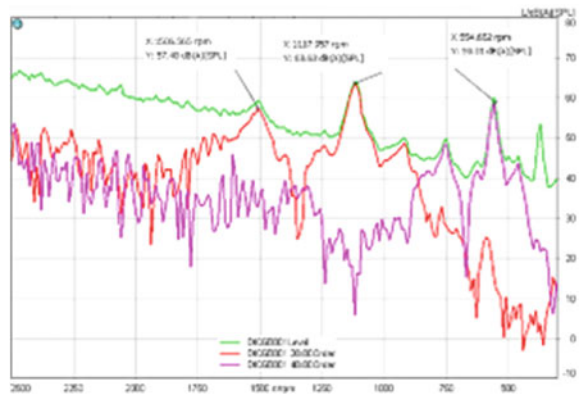


Fig. 3 Order cut analysis



with its hub in asymmetry. This tested assembly had a terrible feeling of intermittent tied obstacle when the fan was rotated with a hand; the number of the obstacle is 20 per cycle. It is observed in the Fig. 4 that there are 20 deep trenches along the circumference of the motor rotor for the wire windings and 20 slots on the commutator for the brush contacts. The characteristic of fan structure is coincides with the feature of the whine noise at the 20th order, and its harmonic noise at the 40th order, and so on.

According to the fan motor’s structure characteristic and its noise spectrum shown in Figs. 1 and 2 in Sect. 2.1, it is the preliminary inference that radiator fan noise during decelerating is caused by the resonance of structural modes and the excitation sources coincidentally. In other words, this coupling occurs when the frequency of the excitation source is the same as that of a fan structure mode, which consequently generates the whine noise. It is necessary to affirm the mode shapes of the fan assembly based on the hypothesis above.

Fig. 4 Fan motor rotor configurati



3 Theoretical Analysis

3.1 The Fundamental Theory of Modal Analysis

Modal analysis can be performed in either theoretical analysis or in experimental method for the study of structure dynamic characteristic. As a continuous system, the theoretical analysis can be approximately expressed with many number of degrees of freedom in discrete system. Its motion equation can be written as:

$$[M]\{\ddot{x}\} + [C]\{\dot{x}\} + [K]\{x\} = \{F\} \quad (1)$$

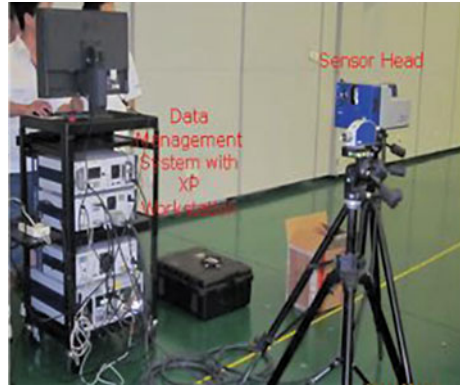
where,

- [M] mass matrix;
- [C] resistance matrix;
- [K] stiffness matrix;
- [F] force vector;

In the applications of modal theoretical analysis, the sets of modal matrixes in motion equations will become the decoupled matrixes in the equations through by the modal coordinate transfer. The process includes that decoupling the matrix of stiffness and matrix of mass in the modal matrix sets, then, breaking down the decoupled motion equations into invidious equation for the solving, finally, getting the solved solutions by a certain linear combination.

The inherent characteristics of the structure of system can be quantitatively described with a set of modal parameters, which are natural frequencies and mode shapes [3]. The precision of the results in theoretical analysis largely depends on the size of the number of degrees of freedom selected for the related discrete system, which is affected by the mass, stiffness, damping, applied forces in restrictions, mass distribution in the shapes at all. In contrast with theoretical analysis, the experimental method in modal analysis is more easy and intuitive if the testing equipments available, especially in manufacture industry. This presentation will introduce how to utilize the experimental modal analysis to obtain the fan natural frequencies and mode shapes in the next section.

Fig. 5 Overview of non-contact laser scanning vibrometry system



4 Mode Shapes of the Fan Assembly Measured with Non-Contact Laser Scanning Vibrometry

The whole testing system includes two parts, as shown in Figs. 5 and 6: one part is non-contact laser scanning vibrometry, and the other is the excitation system of radiator cooling fan.

4.1 *The Selection of the Excitation Source in White Noise*

The frequency response transfer function is used to identify modal parameters. The traditional method for modal identification use the contacted accelerometers and external forced excitation to get the frequency response transfer function, which is required to collect the excitation and response signal (multiple response) in time domain simultaneously, then the frequency response transfer function and the corresponding coherence or the impulse response transfer function are converted into frequency domain by Fast Fourier Transfer. As the example of the cooling fan assembly in this test, the material of the fan is plastic, and its size is a small, thin and light. If the traditional method is applied, the surface of fan should be needed to be attached by a large number of accelerometers. It will physically result in the changes of the fan properties in negative impact. And the disadvantages of traditional method are time-consuming and data-distorting. In contrast, this article will introduce a new testing method for the modal analysis. Using white noise random wave as excitation source with the non-contact laser scanning vibrometry system, the frequency response function is used for the modal analysis instead of the frequency response transfer function.

In this test, standard white noise is transmitted by signal generator. White noise signal amplified by a amplifier is connected into the motor for excitation signal, as shown in Fig. 6.

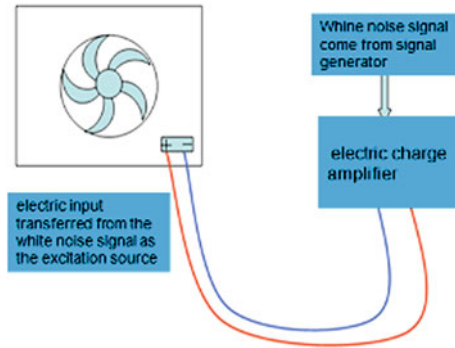


Fig. 6 The diagram of white noise excitation



Fig. 7 Overview of fan modal test instrument

4.2 Test Performing

The radiator fan is hung with bungee cords from special fixture frame; the specimen is closed to free-free status. Non-contact laser scanning vibration measurement system (including computer, laser head, signal generator and signal collecting box) and the excitation are placed and connected per the procedure, shown in Figs. 7 and 6.

4.3 Analysis of Modal Test Results

The fan modal frequencies obtained by testing are listed in Table 1.

Table 1 lists the first four modal frequencies of the fan. The data shows that the 1st mode shape of fan hub is around 365 Hz, whose amplitude is the highest

Table 1 Fan modal frequencies distribution

Serial number	Frequencies	Vibration shape description
1	70	Fan blade 1st mode vibration frequency
2	285	Fan blade 2nd mode vibration frequency
3	365	Fan hub 1st mode vibration frequency
4	500	Fan 1st twist mode

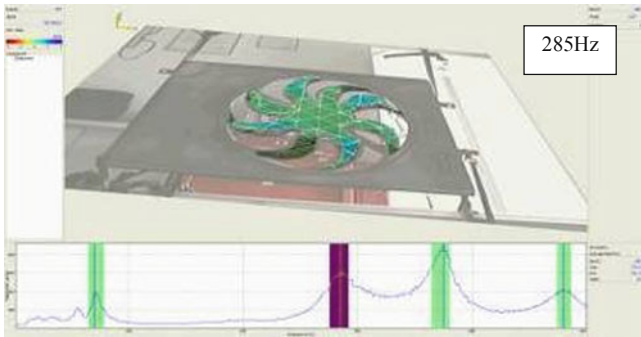


Fig. 8 Fan blade 2nd mode vibration frequency

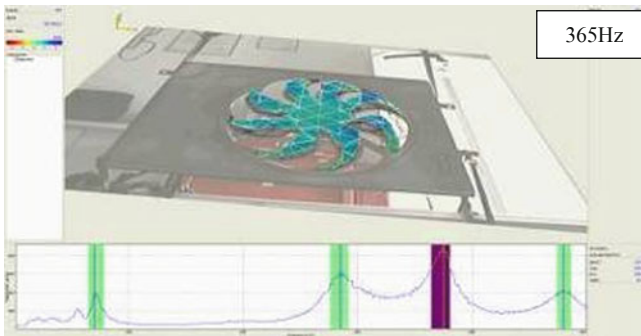


Fig. 9 Fan hub 1st mode vibration frequency

among of three. According to the noise measurements mentioned in Sect. 2.1, the noisy whine did happen just near 280,365 Hz natural frequencies. The tested results indicate that the fan whine noise relates with the fan structural resonance. The Figs. 8, 9 and 10 show the fan vibration mode shapes.

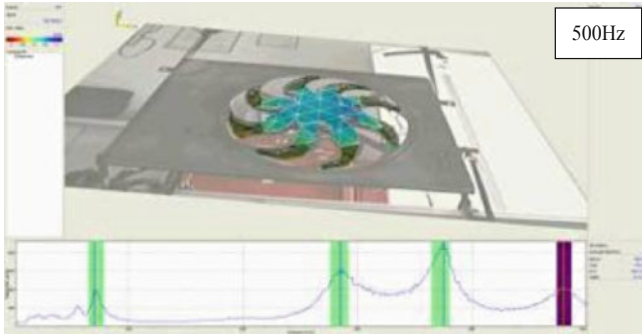


Fig. 10 Fan 1st twist mode vibration frequency

4.4 The Theoretical Analysis in Electromagnetic Noise and Brushing Noise

The whine noise will be created due to the resonance when the cooling fan is under the excitation resource in the frequency as same as its natural frequency. As the fan running, it is mainly disturbed by the aerodynamic force of blade passing in airflow and the excitations of motor running, because the fan whine noise mentioned in Sect. 2.1 has the characteristics in the 20 and 40th orders (in Figs. 1 and 2), the influence of aerodynamic force on the whine noise is not needed to be considered, but the excitation from motor.

The excitation from the motor includes two parts; the first part is the excitation from the brushing. The slots of the commutator segments would make brushes jumping radially and swing tangentially with the brushes against the commutator when the motor is rotating. The second part is from the electromagnetic force, which is generated by the alternating electro-magnet actions between rotor and stator.

Regarding the brushing noise, the fundamental frequency of brushing noise for single brush, (named commutator segment elementary frequency f_k) is K times of the frequency of motor rotation (The overall brushing multi-frequency depends on the number of the pair of brush of motor, it can be expressed as mf_k

$$f_k = kn/60 \tag{2}$$

where:

- k commutator segment
- n rotor speed, revolution per minute
- m the number of the pair of brush of motor, it is a positive integer; m = 2 as one pair of brush; m = 4 as two pairs of brush

Using the example mentioned above, the motor has one pair of brush, the number of the commutator segment is 10, and the motor is steady running at 1,100

and 1500 rpm. The frequencies of brushing noise are 367 and 500 Hz calculated in the formula $f_{k1} = 20 \times 1100/60 \approx 367$ Hz, $f_{k2} = 500$ Hz respectively. As compared to the tested results in the Sect. 2.1 (see Fig. 2), the measured frequencies of whine noise are 361 and 498 Hz which are very closed to the theoretical results.

Regarding the electromagnetic noise, it is mainly caused by the fluctuation of radial force or torque due to the uneven magnetic flux density when motor is running; mostly the frequency of electromagnetic noise has the relationship to the number of slots of wire windings. The value of frequency is expressed in the harmonic formula.

According to the theory of Maxwell and Lorentz force law, electromagnetic force or torques produced by a conductor moving in magnetic field to cut the magnetic field lines. The forces mainly include radial forces, tangential forces and bending torques, and all of these are affected by the magnetic flux density. It is important for the motor to take the analysis of the density of the magnetic field, the numbers of pole pairs and its magnet field intensity. For the simplicity, tangential torque [4] is not involved in this analysis.

Radial force wave generated by Air-gap magnetic field (unit: N/m²), its equation is:

$$\begin{aligned}
 p_n &= \frac{b^2(\theta, t)}{2\mu_0} = \frac{1}{2\mu_0} \left\{ \sum B_v \bar{\Lambda}_0 \cos v\theta + \sum_v \sum \frac{B_v \bar{\Lambda}_k}{2} \cos[(kZ_2 \pm v)\theta - kZ_2\omega_r t] \right\}^2 \\
 &\approx \frac{1}{2\mu_0} \sum_{v1} \sum_{v2} \sum_h \frac{B_{v1} B_{v2} \bar{\Lambda}_0 \bar{\Lambda}_k}{2} \cos\{[kZ_2 \pm (v_2 \pm v_1)]\theta - kZ_2\omega_r t\}
 \end{aligned}
 \tag{3}$$

where:

- $b(\theta, t)$ Air-gap magnetic density;
- $\mu_0 = 4\pi \times 10^{-7}$ H/m;
- B_v The magnitude of magnetic flux density in stator magnetomotive harmonic wave;
- $\bar{\Lambda}_k$ the Kth harmonic permeability;
- $\bar{\Lambda}_0$ average permeability;
- Z_2 The number of rotor slot;

It is found that the frequency of the vibration caused by the radial force wave is equal to the frequency of rotor teeth.

$$f = \frac{1}{2\pi} kZ_2\omega_r = k \frac{Z_2 n}{60}
 \tag{4}$$

$k = 1, 2, 3 \dots$ Where,

n rotating speed (r/min);

Z_2 the number of rotor slot;

In this study for the validation, the number of rotor slot of the fan motor is 20. Radial force wave frequencies generated by air-gap magnetic field are 367 and 500 Hz when the rotor is running at 1,100 and 1,500 r/min.

5 The Analysis and Verification of Solution

5.1 The Analysis of Solution

The optimization for the fan whine noise should be considered in two aspects, according to the results of experiments and theoretical calculation in Sects. 2.1, 4.3 and 4.4. One proposal is that we can try to change the natural frequency of the fan assembly in order to avoid the frequency of excitation source. It will need to change the mass, stiffness and distribution of fan blades, as well as the changes of the mold. Also it concerns the additional cost and timing too. The other proposal is to reduce or eliminate the excitation source through by optimizing the electromagnetic noise and brushing noise of fan motor. It is fundamental and significant for the solution of whine noise to reduce the amplitude of electromagnetic harmonic excitation force or decrease the friction vibration of brush. The second proposal is feasible in both theory and practice, therefore, the second proposal is recommended.

As the second proposal mentioned above, primary factors affecting brush noise are given in the followings.

- (a) The radial pulsation of commutator surface and the slot width to improve magnetic conductance uniformity of stator and rotor core.
- (b) The accuracy of the coaxiality of stator and rotor to reduce the fluctuation of the force
- (c) The accuracy of dynamic balancing in rotor to reduce dynamic unbalance of rotor;
- (d) The clearance fit between brush and its holder, especially in radial direction;
- (e) Pressing force of brush;
- (f) The roughness and hardness of commutator surface;

These factors influencing brush noise can be controlled and improved during machining process, manufacturing and checkout.

5.2 Verification of Optimization Effect of Radiator Cooling Fan

Several optimizations obtained in Sect. 5.1 are implemented in the fan motor. The acoustic measurements of the optimized fan were performed and analyzed in the same vehicle with the same test procedure taken in Sect. 2.1. In contrast with

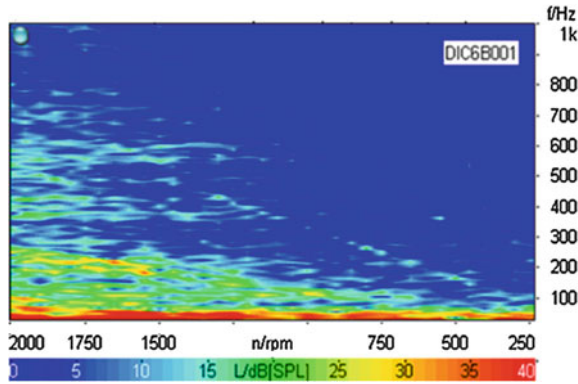


Fig. 11 Fan speed reducing color plot after optimizing

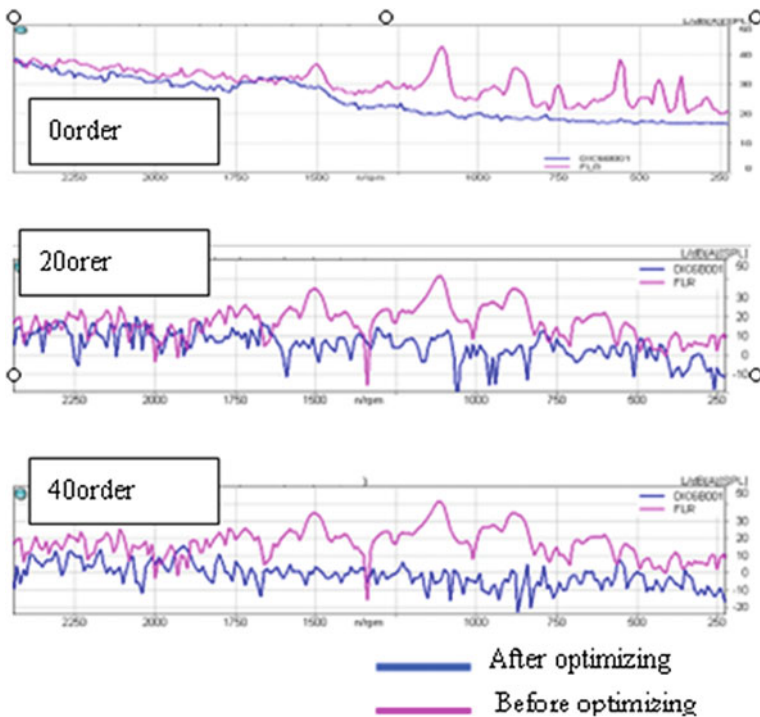


Fig. 12 Order cut compare before optimizing with after

Fig. 1, the results from the proposal in Fig. 11 shows that the 20th order noise was going to be more weak; the 40 and 60th order noise disappeared totally; and the resonance band mostly would not be observed within the range of 360–380 Hz. Meanwhile, no whine noise was heard by subjective evaluation in the car. It is observed that the harmonic wave noise from fan motor slot almost disappeared in

Fig. 11. Figure 12 shows the noise contributions for the 40 and 60th order were dropped dramatically as compared to the original fan assembly.

6 Conclusions

This article has discussed the optimization of the fan whine noise during decelerating, and validated the results subjectively and objectively in the theoretical analysis and experimental method. There are three in the conclusion:

1. The cooling fan whine noise is created by the structural resonance with the excitation sources;
2. The majority of the excitation sources are the fluctuation of the electromagnetic force from motor and the impacts periodically from brushes against the commutator. It is very significant for the reduction of the whine noise to design the trenches of windings and the structures of brushes in optimization;
3. It is a good practice for the modal analysis to use the white noise as excitation source into the non-contact laser scanning vibrometry system. This practice can be applied not only for the cooling fan whine noise and auto HVAC module assembly, but also for the similar interesting issues, like vehicle interior trim.

Acknowledgments The authors would like to thank Wu Guoming and Dr. Pang Jian for their support and guide.

References

1. Suzuki A, Soya A (2005) Study on the fan noise reduction for automotive radiator cooling fans. SAE Technical Paper 2005-01-0601. doi:[10.4271/2005-01-0601](https://doi.org/10.4271/2005-01-0601)
2. Wei W, Ghoreishi S (2003) Engine cooling fan noise and vibration problem caused by a switching power supply. SAE Technical Paper 2003-01-1672. doi:[10.4271/2003-01-1672](https://doi.org/10.4271/2003-01-1672)
3. Zhongfu L, Hanwen S, Hongxing H, Zhiyan C, Zhifang F (2002) A method of modal parameter identification under white noise excitation. J Vibr Eng
4. Chen Y, Zhu Z, Ying S (1987) The analysis and control of motor noise. Zhejiang University Press

Electromagnetic Noise Study of Permanent Magnet Synchronous Motor for Electric Vehicle

Xiumin Shen, Yong Wang, Bin Li and Yuanjian Yue

Abstract The application of PMSM for electric vehicle driving is more and more widely, but the electromagnetic noise is the main problem which restricts the development of PMSM. The electromagnetic force which acts on motor stator and the structure dynamic characteristics of motor stator are the two key factors which decide the electromagnetic noise of PMSM. In this paper, take PMSM as study object, researches are working hard on the two factors to analyze the electromagnetic noise of PMSM for electric vehicle driving. The author researched generation mechanism of PMSM electromagnetic force, deducted analytical method for electromagnetic force under both no-load and load condition, and then calculated wave orders and frequency of electromagnetic force affecting on stator surface of PMSM. The electromagnetic simulating model of PMSM is built based on electromagnetic simulation software Ansoft, and calculated air-gap flux density using time stepping finite element method under both no-load and load condition, then obtained air-gap flux density spectrum by FFT analysis with simulation results. The author calculated harmonic orders, frequency and amplitude of electromagnetic force by combining calculation results and simulation results. As for structure dynamic characteristics of PMSM, the author built three types of finite element simulation models with stator core, stator core with windings and the whole stator structure. Modal frequency and shape is obtained by finite element modal simulation with three type models. From the results we found that the first six orders modal frequency of the whole stator structure is lower, and the stator structural resonance is easily inspired by the electromagnetic force under both no-load and load condition during speed regulation.

F2012-J09-004

X. Shen (✉) · Y. Wang · B. Li · Y. Yue
State Key Laboratory of Vehicle NVH and Safety Technology, Chongqing, China
e-mail: xiuminshen@126.com

Keywords Eclectic vehicle • Permanent magnet synchronous motor • Electromagnetic noise • Electromagnetic force • Modal analysis

1 Preface

In order to solve the problems of energy shortage and environmental pollution, technology of electric vehicle has become a research hotspot both in domestic and foreign automobile companies. For improving market competitive ability and enhancing overload capacity of electric vehicle, the current density and magnetic density value of the driving motor are both designed higher, which causes higher saturation while motor working with heavy load, and increases electromagnetic force. Structure parameters of electric vehicle driving motor such as yoke thickness are smaller than general industrial driving motor, which causes reduction of structure stiffness and incassation of electromagnetic vibration. The frequency band of electromagnetic noise usually distributes from 700 to 5,000 Hz, noise in this frequency band can causes strong noise feeling and harsh whistler which makes people can not intolerant.

Electromagnetic noise of motor mainly comes from electromagnetic vibration, which is excited by electromagnetic force, which is generated while air-gap magnetic filed effecting on stator and rotor. If fundamental and harmonic wave's frequency of electromagnetic force approaches well with structure natural frequency of motor stator, resonance will occurred while working, which will trigger electromagnetic noise. So electromagnetism noise and vibration of motor is affected both by electromagnetic force which acts on motor stator and structure modal of motor stator. At present, the study of electromagnetic noise and vibration is mostly for induction motor, synchronous motor and DC motor. PMSM as an efficient special type motor, presently there is little study of electromagnetic noise and vibration for it. In this paper, the author will focus on PMSM which is the driving motor for electric vehicle to study electromagnetic noise and vibration.

2 Analysis Principle of Electromagnetic Force with PMSM

PMSM in this paper generates torque relying on minimum reluctance principle. With the effect of reluctance force, rotor rotates synchronously following the rotating magnetic field. As for motor, the main magnetic flux generally radiates into the air-gap and generates electromagnetic force, which affects on stator and rotor causing electromagnetic noise and vibration [1, 2]. The numerical and distribution of electromagnetic force generated by motor air-gap magnetic field,

which affects on unit area surface of motor stator, can be obtained according to the Maxwell law [3], as formula (1).

$$p_n(\theta, t) = \frac{b^2(\theta, t)}{2\mu_0} \text{ (N/m}^2\text{)} \tag{1}$$

where, $\mu_0 = 4\pi \times 10^{-7}$; $b(\theta, t)$ is air-gap flux density.

Air-gap flux density $b(\theta, t)$ can be obtained through air-gap magnetic potential $f(\theta, t)$ multiplying by magnetic conductance $\lambda(\theta, t)$, as formula (2).

$$b(\theta, t) = f(\theta, t)\lambda(\theta, t) \tag{2}$$

It can be seen that exciting force of motor electromagnetic noise and vibration depends on magnetic potential generated by windings and magnetic conductance generated by air-gap magnetic field, also can be say depends on magnetic field of motor stator and rotor. So the study of electromagnetic noise and vibration with PMSM for electric vehicle driving can be converted to the study of magnetic field of motor stator and rotor.

As for PMSM, the stator designed with slots and the rotor designed with smooth surface, the air-gap flux density can be approximated as formula (3).

$$\lambda(\theta, t) \approx \Lambda_0 + \sum_m^\infty \Lambda_m \cos mZ_1\theta \tag{3}$$

where, Λ_0 is average amplitude of air-gap magnetic conductance; Z_1 is the number of stator slots; Λ_m is harmonic magnetic conductance amplitude caused by stator slots design.

3 Electromagnetic Force Analysis ofPMSM

3.1 No-Load Condition

While PMSM working under no-load condition, there is no current through windings, air-gap magnetic potential only generated by rotor magnetic potential, as formula (4).

$$f(\theta, t) = \sum_\mu F_\mu \cos(\omega_\mu t - \mu\theta) = \sum_\mu F_\mu \cos(\mu \frac{\omega_1}{p} t - \mu\theta) \tag{4}$$

Where, p is the number of poles ($2p$ is the number of permanent magnets); μ is harmonic order generated by poles in rotor, $\mu = (2r + 1)p \quad r = 0, 1, 2, \dots$; ω_1 is rotating speed of rotor.

According to formula(2) (4), air-gap magnetic flux density while PMSM working under no-load condition can by obtained by formula (5).

$$b_{\mu}(\theta, t) = \sum_{\mu} F_{\mu} \Lambda_0 \cos\left(\mu \frac{\omega_1}{p} t - \mu\theta\right) + \sum_{\mu} \sum_k F_{\mu} \Lambda_k \cos\left(\mu \frac{\omega_1}{p} - v_z \theta\right) \quad (5)$$

In which, v_z is harmonic order generated by slots in stator, $v_z = p \pm kZ_1$, $k = 1, 2, 3, 4, \dots$

According to formula (5), it can be seen that air-gap magnetic field under no-load condition mainly includes magnetic field generated by poles in rotor and magnetic field generated by slots in stator. Electromagnetic force generated by the interaction between these two magnetic fields will cause electromagnetic vibration and noise. So magnetic fields generated by poles and slots are both the main noise sources of PMSM under no-load condition.

3.2 Load Condition

Under load condition, air-gap magnetic field of PMSM has changed. Air-gap magnetic field also includes magnetic field generated by windings besides magnetic field under no-load condition. According to the principle of motor, while three-phase symmetrical sinusoidal current through windings, magnetic field generated by windings can be expressed as formula (6).

$$b_v(\theta, t) = \sum_v F_v \Lambda_0 \cos\left(\frac{\omega_1}{p} t - v\theta\right) \quad (6)$$

In which, v is harmonic order generated by windings, $v = (6n + 1)p$, $n = 0, \pm 1, \pm 2, \dots$

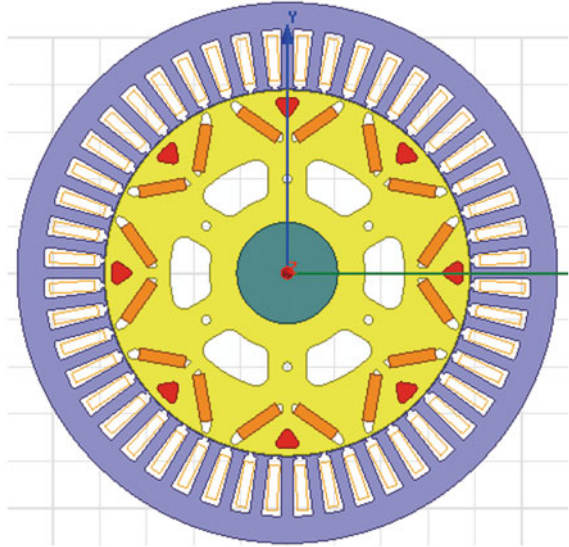
Under load condition, Air-gap magnetic field of PMSM can be calculated by overlapping harmonics of magnetic field, with formulas (5) and (6) can be obtained as formula (7).

$$\begin{aligned} b(\theta, t) &= \sum_{\mu} F_{\mu} \Lambda_0 \cos\left(\mu \frac{\omega_1}{p} t - \mu\theta\right) \\ &+ \sum_{\mu} \sum_v \sum_k (F_{\mu} + F_v) \Lambda_k \cos\left(\mu \frac{\omega_1}{p} - v_z \theta\right) \\ &+ \sum_v F_v \Lambda_0 \cos\left(\frac{\omega_1}{p} t - v\theta\right) \end{aligned} \quad (7)$$

According to formula (8), it can be seen that air-gap magnetic field under load condition mainly includes magnetic field generated by poles, magnetic field generated by windings and magnetic field generated by tooth. Electromagnetic force generated by the interaction among these three magnetic fields will cause electromagnetic vibration and noise. So magnetic fields generated by poles, windings and slots are all the main noise sources of PMSM under load condition.

While analyzing electromagnetic force, we usually consider the effect of harmonics, and mainly consider the following three parts:

Fig. 1 Electromagnetic simulation model of motor



1. Electromagnetic force generated by fundamental wave of magnetic field affected by permanent magnets;
2. Electromagnetic force generated by harmonics of magnetic field affected by poles and slots.
3. Electromagnetic force generated by harmonics of magnetic field affected by poles and windings.

4 Electromagnetic Field Analysisi of Pmsm

Take PMSM which is for electric vehicle driving for example. Specifically instruct the decomposition method and principle of electromagnetic field. This PMSM with inner rotor, 8 poles and 48 slots, rated speed is 2,800 rpm, maximum speed is 8,000 rpm, and vector control is $I_d = 0$.

The author established finite element electromagnetic simulation model of the PMSM using electromagnetic simulation software Ansoft, which is shown as Fig. 1. Analyzing electromagnetic characteristics of the PMSM under both no-load and load condition using time stepping finite element method.

4.1 No-Load Condition

Air-gap flux density of the PMSM under no-load condition is obtained by simulation using time stepping finite element method, which is shown as Fig. 2.

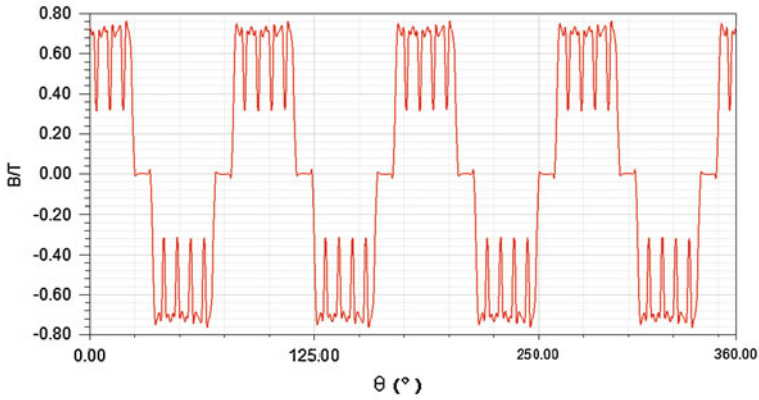


Fig. 2 Air-gap flux density of the PMSM under no-load condition

According to the derivation and analysis in Sect. 3.1, the author did harmonic analysis with air-gap magnetic field for the PMSM under no-load condition, as well as FFT analysis with air-gap flux density simulation data, derived harmonic orders and amplitude, which is shown as Tables 1 and 2.

Generally, only the harmonics, whose order is less than 4, will have greater effect on electromagnetic noise. So according to harmonics generated by poles and slots, the author focused on analyzing electromagnetic force harmonics with lower orders under no-load condition.

It can be determined that electromagnetic force of the PMSM under no-load condition is mainly caused by the interaction of the first order harmonic affected by slots and the harmonics generated by poles, as well as fundamental wave of magnetic field affected by poles, the results collected is shown as Table 3.

4.2 Load Condition

Air-gap flux density of the PMSM under load condition is obtained by simulation using time stepping finite element method, which is shown as Fig. 3.

According to the derivation and analysis in Sect. 3.2, the author did harmonic analysis with air-gap magnetic field for the PMSM under load condition, as well as FFT analysis with air-gap flux density simulation data, derived harmonic orders and amplitude, which is shown as Tables 4 and 5.

Generally, only the harmonics, whose order is less than 4, will have greater effect on electromagnetic noise. So according to harmonics generated by poles, slots and windings, the author focused on analyzing electromagnetic force harmonics with lower orders under load condition.

It can be determined that electromagnetic force of the PMSM under load condition is mainly caused by the interaction of the first order harmonic affected

Table 1 Harmonics generated by poles of the PMSM under no-load condition

r	0	1	2	3	4	5	6	7	8
μ/p	1	3	5	7	9	11	13	15	17
幅值 T	0.7656	0.1069	0.0625	0.1057	0.0803	0.0266	0.0199	0.0411	0.0345
频率 f	f	$3f$	$5f$	$7f$	$9f$	$11f$	$13f$	$15f$	$17f$

Table 2 Harmonics generated by slots of the PMSM under no-load condition

k	1	
v_z/p	-11	13
幅值 T	0.081	0.0814
频率 f	f	f

Table 3 Electromagnetic force analysis of the PMSM under no-load condition

次数	9(-11)	11(-11)	13(-11)	1 + 1
幅值/(Nm ⁻²)	2559	857.3	641.4	233219
频率 f	$10f$	$12f$	$14f$	$2f$

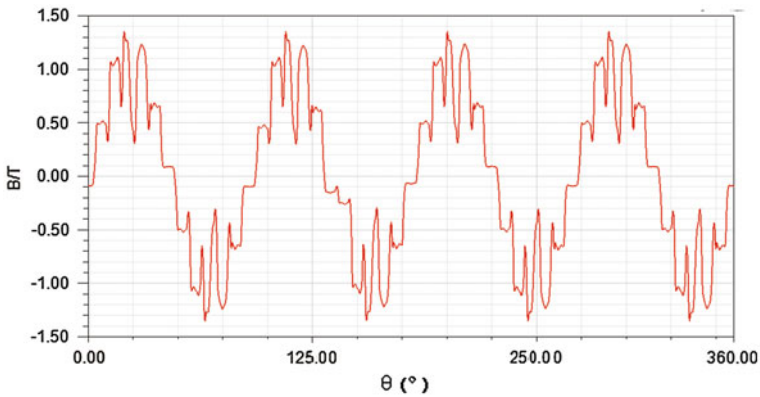


Fig. 3 Air-gap flux density of PMSM under load condition

Table 4 Harmonics generated by slots of the PMSM under load condition

k	1	
v_z/p	-11	13
幅值 T	0.2327	0.084
频率 f	f	f

by slots and the harmonics generated by poles, as well as fundamental wave of magnetic field affected by poles and windings, the results collected is shown as Table 6.

Table 5 Harmonics generated by windings of the PMSM under load condition

k	0	-1	1	-2	2
v/p	1	-5	7	-11	13
幅值/ T	1.0178	0.1274	0.0666	0.1887	0.121
频率 f	f	f	f	f	f

Table 6 Electromagnetic force analysis of the PMSM under load condition

次数	9(-11)	11(-11)	13(-11)	1 + 1
幅值/(Nm ⁻²)	7435	2463	1842.5	412178
频率 f	10 f	12 f	14 f	2 f

Where, f is the frequency of fundamental wave, $f = p \frac{n}{60}$ (Hz), n is the rotating speed of motor (rpm).

According to Tables 3 and 6, it is clearly that harmonic’s order of PMSM electromagnetic force is 0 and 2, under both un-load and load condition.

If the rotating speed of motor is determined, it can accurately calculate harmonic’s order, frequency and amplitude of electromagnetic force which acts on motor stator surface. According to the analysis of electromagnetic force of PMSM under both no-load and load condition, we know that the frequency of electromagnetic force is varying while motor speed regulating under both no-load and load condition. While the frequency of electromagnetic force goes well with motor natural frequency, resonance phenomenon of motor will be caused, as well as electromagnetic vibration and noise

5 Structural Dynamic Characteristics of PMSM

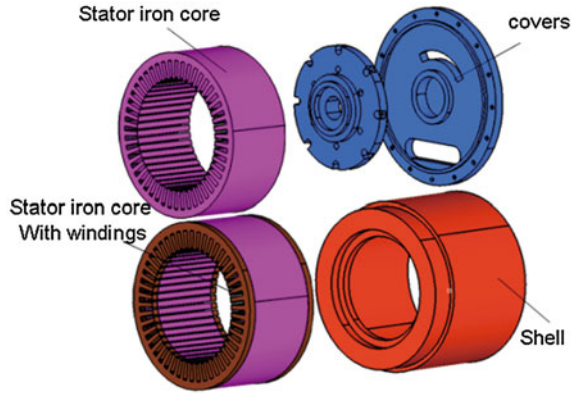
Structure vibration of motor stator is generated by electromagnetic force. The strength of vibration is related to frequency and amplitude of electromagnetic force, as well as natural frequency of motor structure and some other factors [4, 5]. Hypothesis, motor stator is simplified to cylindrical shell, the vibration displacement generated by electromagnetic force [6] is shown as formula (8).

$$A_r = \frac{\frac{F_r}{M}}{\sqrt{(\omega_r^2 - \omega_n^2)^2 + 4\zeta_r^2 \omega_n^2 \omega_r^2}} \tag{8}$$

where, M is quality of cylindrical shell (kg), ω_r is natural angular frequency(rad/s), ω_n is electromagnetic force angle frequency (rad/s), ζ_r is modal damping ratio, F_r is electromagnetic force (N), $F_r = \pi D_{im} L_i P_m$, D_{im} is inner diameter of stator (m), L_i is length of stator (m), P_m is amplitude of electromagnetic force (N/m²).

Modal damping ratio generally is calculated by the following experience formula (9).

Fig. 4 Geometric models of the PMSM components



$$\zeta_r = \frac{1}{2\pi} (2.76 \times 10^{-5} f_r + 0.062) \tag{9}$$

In which, f_r is structure natural frequency of motor (Hz).

According to formula (8), it can be seen that while fundamental wave and harmonic’s frequency of electromagnetic force approaches well with the structure natural frequency of motor, the vibration amplitude of motor will reach maximum, which will cause large electromagnetic noise.

5.1 Structure *Finite Element Model*

In order to make sure whether there exists resonance phenomenon of the PMSM. The author built three-dimensional finite element simulation models respectively using stator iron core, stator iron core with windings and the whole motor stator. Through modal simulating with three models, natural frequency under freedom constraint is obtained. Finally, the author analyzed different component’s effect on the whole stator structure natural frequency.

It is difficult to produce better finite element mesh because of the complex shape of windings. So it is necessary to do some reasonable simplification while building finite element simulation models. In this paper, windings are simplified as hollow cylinder with equivalent volume. Three-dimensional geometric models of the PMSM components are shown as Fig. 4.

In this paper, the author meshed geometric models with hex8 element using Hypermesh finite element pre-processing software, three finite element simulation models are shown as Fig. 5. Material mechanical parameters are shown as Table 7. Then the author did modal analysis with three geometric models based on Nastran solver.

Fig. 5 Finite element simulation models of the PMSM

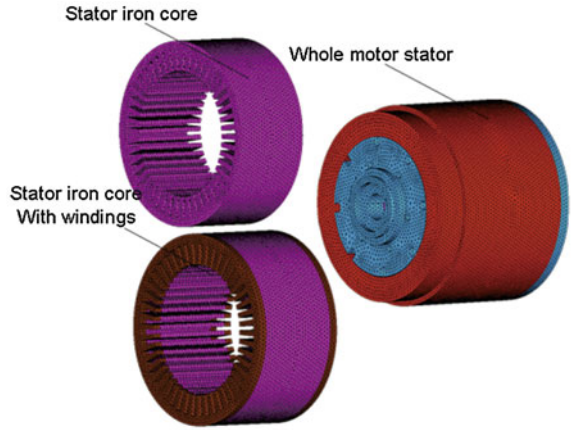


Table 7 Material mechanical parameters of PMSM

	Materials	Density(kg/m ³)	Young's modulus(GPa)	Poisson's ratio ν
Stator iron core	Steel	7.5e10 ³	210	0.3
Casing	Al	2.5e10 ³	71	0.34
Winding	Copper	8.6e10 ³	10	0.34

Table 8 Modal frequencies of PMSM

Orders	Frequency/Hz		
	Stator iron core	Stator iron core with winding	Whole motor stator
1	484.3	491	1842
2	484.5	493	1845
3	1085	1123	3101
4	1085	1125	3103
5	1300	1316	3753
6	1300	1320	3780
7	2344	2368	4071
8	2344	2371	4078
9	2418	2443	4355
10	2418	2447	4359

5.2 Structure Finite Element Analysis

Modal frequencies of three models are shown as Table 8. It can be seen that modal frequencies of the first six orders are lower, structure resonance will be easily inspired by electromagnetic force, which is generated during speed regulating under both no-load and load condition.

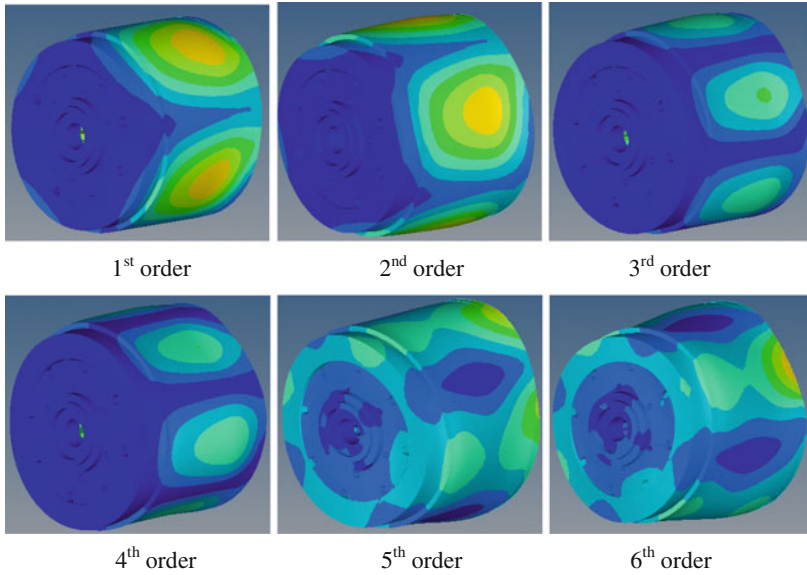


Fig. 6 Modal shapes of whole motor stator

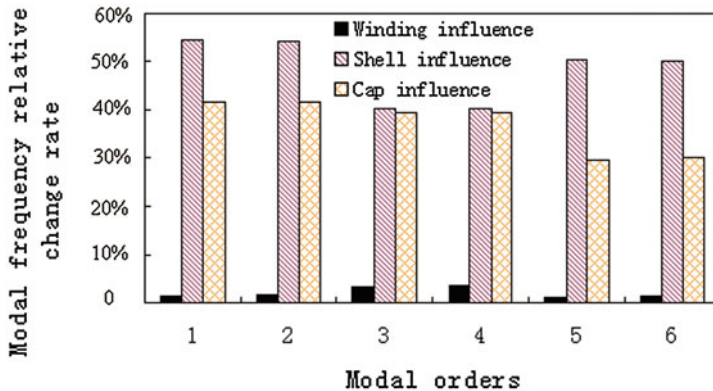


Fig. 7 Different component's effect rate for modal frequency

The first six orders of modal shapes of the whole motor stator shown as Fig. 6, from which we can see that because of symmetrical structure, there are some modal shapes of the whole motor stator with the same frequency but different phases.

Effect rate for modal frequency of the whole motor stator affected by windings, casing and cover is shown as Fig. 7. From which we can see that each component has some effect on modal frequencies of the whole motor stator, especially casing and cover.

6 Conclusion

The electromagnetic force which acts on motor stator and the structure dynamic characteristics of motor stator are the two key factors which decide the electromagnetic noise of PMSM. In this paper, take PMSM as study object, researches are working hard on the two factors to analyze the electromagnetic noise of PMSM for electric vehicle driving.

With the study in this paper, it is easily to accurately calculate the harmonic's order, frequency and amplitude of electromagnetic force. Combined with modal frequency of the motor, it can effectively judge whether resonance phenomenon exists. The research provides guidance for noise and vibration reduction of PMSM for EV, but the study in this paper is not verified by the experiment which is not only the defection of the paper but also our following job.

References

1. Yongxiao C, Zhu Z, Shancheng Ying (1987) Analysis and control of motor noise. Zhejiang University Press, Hangzhou
2. Shikun C (1982) Motor design. Machinery Industry Press
3. Gieras JF, Wang C, Lai JC (2006) Noise of polyphase electric motors. CRC Press. 21–185
4. WANG T, WANG F (2007) Vibration and modal analysis of stator of large induction motors. Proc CSEE 27(12):41–45
5. Qing-nian W, LI H, Fengjuan S (2009) Motor noise source identification based on spectrum analysis. Technical Acoustics. 28(4): 527–530
6. WANG T, WANG F (2007) Vibration and modal analysis of stator of large induction motors. Proceedings of the CSEE 27(12):41–45

Evaluation and Improvement of Door Slamming Sound Quality

Fangwu Ma and Dongmei Guo

Abstract *Research Objective* The sound quality of automobiles has drawn much attention, and sound quality of door slamming will impact psychological tendency of customers during vehicle purchase. Therefore, this chapter provides test and evaluation method for sound quality of door slamming and its improvement measures. *Methodology* For test method, the proper position of door slamming force acting location, velocity range of door slamming, consistency of slamming force each time and layout of microphone are the factors which are taken into account. For evaluation method, factors such as pulse convergence time, sharpness, loudness, duration of low-frequency residual noise and high-frequency noise are considered. Thirdly, for optimization for door slamming, subjective evaluation, objective analysis and exclusion method are applied. *Results* Through optimization of vehicle sealing, design of door latches, layout of weather strips, return spring of door handle, and contact location between handle and base, the door slamming sound quality can be improved. *Limitations of this study* CAE simulation analysis should be carried out at all stage. What does the chapter offer that is new in the field including in comparison to other work by the authors: A series of measures to improve the door slamming sound quality are introduced in detail. *Conclusion* Evaluation method for the sound quality is presented, and practical improvement measures are proposed.

Keywords Sound quality · Pulse · Loudness · Sharpness

F2012-J09-005

F. Ma (✉) · D. Guo
Geely Automobile Research Institute, Hangzhou, China
e-mail: dongmeiguo2008@126.com

The classic automotive noise strategy emphasizes the noise level, believing that the lower level noise the better vehicle performance. With the growing requirements for automotive quality and better understanding of acoustics, sound quality has become an important part of NVH strategy. Subjective feelings can be reflected by sound quality. Vehicles with similar sound pressure level can exhibit different sound feelings. Annoying sound can even be yielded by a vehicle with low sound pressure level, therefore noise reduction shall take subjective feeling into consideration, and classic noise strategy and sound quality maintains a complementary relationship.

When purchasing a car, customers intend to listen to the sound quality of door slamming, since it is believed that vehicle quality can be reflected from the door slamming sound. Hence it can cause psychological effect upon customers to choose cars. Great efforts have been devoted to improve the door slamming sound quality by car manufacturers. And the testing and evaluation methods are under improvement.

1 Introduction of Sound Quality

The sound quality is the subjective feeling of the product sound [1, 2], which reflects listeners' acceptance to the product: the higher acceptance, the better the sound quality.

BTL model is applied to describe the unpleasant sound, i.e. Psychoacoustics. It can be seen from the Fig. 1 that BTL index falls while dB value does not change significantly (Fig. 2).

The *sound* in the definition of sound quality does not refer to the physical event such as the sound wave, but the auditory perception while *quality* refers to the process for the human ears to perceive the sound events and make subjective judgments [3, 4]. *Sound quality* includes indicators of loudness, timbre, tone, sharpness, tonality, modulation, clarity and masking effects.

The masking effect, loudness and sharpness are selected to introduce in this chapter.

Masking effect of the human ear occurs when auditory perception of a weak sound (masked tone) is affected by another strong sound (masking tone). It takes some time for the human brain to process sound, so the sound masking caused by time is called temporal masking. Physiological characteristics of the human ear determine that, in the frequency domain when a strong pure tone and a weak one exist at the same time, the human ear can hear the strong one. This feature is called the frequency domain masking. Traditionally, masking effect is seldom considered in noise control. When noises are found in the objective evaluation, it is better to take account of masking effect before investing significant resources to handle it. Probably, human beings are insensitive to such sound.

Loudness is the psychoacoustic parameter that reflects the extent to which human ear subjectively experiences the sound level. It takes into account the

Fig. 1 BTL model and dB

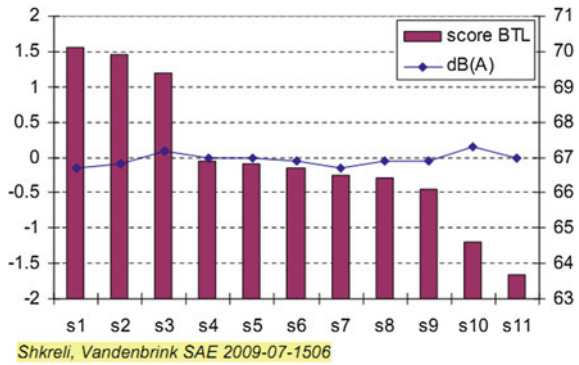
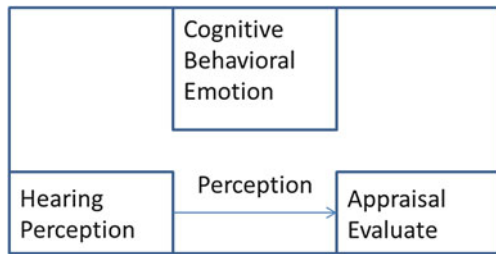


Fig. 2 Noise response schematic



human ear masking of the sound spectrum and can reflect the loudness of the sound signal more accurate than the A-weighted sound level. The unit is sone. 1 kHz, 40 dB pure tone loudness is defined as 1sone.

There are two ways to calculate loudness: Stevens and the Zwicker methods, and have been standardized internationally. This study adopts the Zwicker's, which is more applicable. Specific calculation method refers to the international standard ISO532-B.

Characteristics of loudness:

$$N' = 0.08 \left(\frac{E_{TQ}}{E_0} \right)^{0.23} \left[\left(0.5 + 0.5 \frac{E}{E_{TQ}} \right)^{0.23} - 1 \right] \tag{1}$$

$$\text{The total loudness: } N = \int_0^{24 \text{ bark}} N'(z) dz \tag{2}$$

Sharpness is the ratio of high frequencies to low frequencies. The more high frequency portion takes, the higher the sound sharpness is, and the more annoying the sound will be.

The sharpness is calculating the integral of loudness characteristics to weighted total loudness. In this chapter, the Zwicker model is adopted with the following formula:

$$S = k_2 \frac{\int_1^{24 \text{ Bark}} Nf(z) \cdot z \cdot g(z) dz}{N} \quad (3)$$

2 Testing Method of Door Slamming Sound Quality

In the test of sound quality, the main factors are the force, testing position, force-location and speed. Also, the latch structure and door sealing affect the sound quality.

Door slamming force: the force to open the door is determined by the mechanical design of latches. The force needed to open the door keeps the same. However, the force to slam doors affects the sound quality dramatically. It was found by several testing validations that door slamming force is proportional to the sound pressure level and loudness and hardly affects the sharpness. This feature can be applied to compare door slamming sound quality of different four-door passenger cars. The challenge is to ensure testing uniformity of each test if operated manually. If operated by machine, the noise generated by the machine setup will lead to inaccuracy of the testing results. Therefore, a rubber band is used to ensure the consistency of slamming force. Every time the door is pulled to the same distance and then release, then the instrument will record door slamming sound.

Force-locations: when slamming the door, the force-location of the door is usually the door rim; to fix a rubber band on the rim of the door is not easy, therefore, it can be fixed to a certain position within the acceptable tolerance.

Testing position: the acoustic head can be used for the measurement of sound quality. This chapter describes a testing method of using microphone. Outside of the vehicle, the microphone shall be laid 300 mm away from the door latches, 400 mm away from the door rim with a height of 1.6 m calculated based on normal Chinese human height. Inside of the passenger car, 4 positions shall be measured for the acoustic head, i.e. external ears of the driver, front passenger, rear left and rear right passengers. Figure 3 is the diagram of an acoustic head layout. Figure 4 shows the sound quality testing spot of a four-door passenger car.

Door slamming speed: use photoelectric sensors to test slamming speed, ensuring the speed between 1.0 and 1.7 m/s for each test.

Fig. 3 Acoustic head setup



Fig. 4 Sound quality testing spot



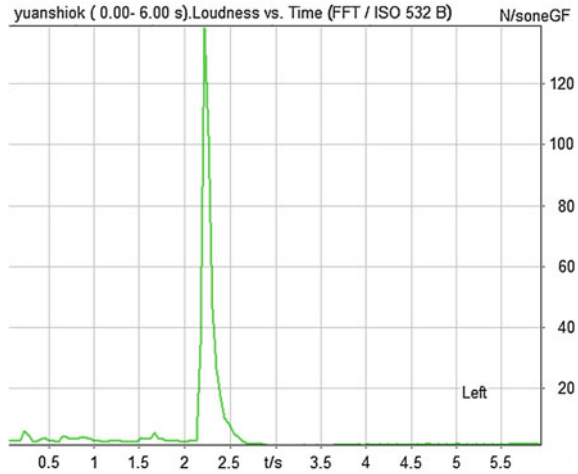
3 Evaluation Method of Door Slamming Sound Quality

Evaluation of the door slamming sound quality is classified as subjective and objective evaluations. Subjective evaluation is to record the sound through the acoustic head at first, and playback with a hi-fi headphone for experts to diagnose based on the experience. Another way is a score system in which door slamming sound is decomposed into sharpness, loudness, annoyance etc. Each item will be scored with mathematical treatment such as the radar chart or fuzzy mathematics method to get a final score.

Objective evaluation methods of door opening quality:

1. Loudness: a psychoacoustic parameter, reflecting subjective feelings of the human ear to sound intensity, which shows the degree of loudness.

Fig. 5 Loudness testing curve



2. Sharpness: a parameter that describes the proportion of the high frequency portion in the sound spectrum. The higher the sharpness is, the harsher the sound feels.
3. Colormap: reflecting the sound frequency distribution features. If low frequency is dominant, the sound is low and comfortable.
4. Duration of door slamming pulse (Figs. 5, 6, 7).

There should be not so much energy distributed in the high frequency portion; low-frequency is the energy distribution of low frequencies below 100 Hz. The longer the duration of the sound lasts, the more comfortable it feels.

4 Diagnostic Analysis and Optimization of Door Slamming Sound Quality

Several factors affecting door slamming sound quality (see Fig. 8): door latches, sealing, door tightness and panel stiffness.

Method of exclusion is often applied to diagnose sound quality of door slamming. For example, compare the case with weather strips only and the case with door latches only to determine which plays a bigger role in affecting the sound quality. When the target is set up, it shall be rectified accordingly. Usually the measures to improve sound quality are as follows (Fig. 9):

(a) Improving the Door Tightness

The door tightness not only affects the vehicle NVH, but also the quality of door slamming. The flow pattern of air flow will affect the door slamming sound. Vehicle with better door tightness emits a *bang* sound, while vehicle with poor

Fig. 6 Sharpness testing curve

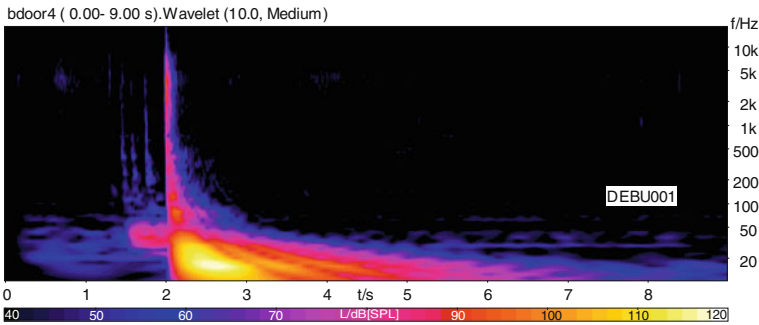
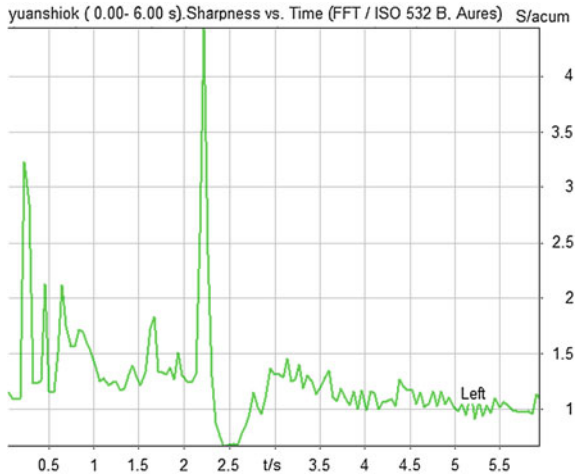


Fig. 7 Colour image of the door slamming pulse

door tightness will sound a crash of latches since the airflow blows out from the gaps.

The door tightness can be checked by the smoke generator. If smoke is found to leak from the lower parts of door, it indicates that the tightness of lower part needs to be optimized (Fig. 10).

(b) Improving the Latch Design

When slamming the door, metal collision sounds are produced. Usually, this is caused by door latches and door interlocking. Nowadays, many automakers adopt plastic or rubber to wrap the knocker to improve the sound quality of door slamming. For instance, as shown in Fig. 11, rubber coating is used for the snapping at interlocking part of the door, but it will influence the life of door latches.

(c) Weather Strip Optimization

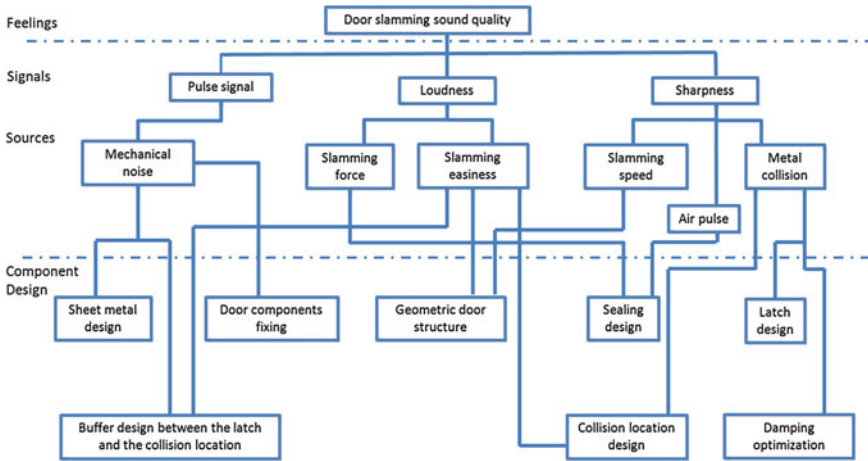


Fig. 8 Breakdown of door slamming sound quality targets



Fig. 9 Diagnostic methods of door slamming sound quality

The weather strip can not only ensure the door tightness, but also has an influence on the door slamming sound quality. Its main role is to rapidly reduce high frequency energy from the door latches or other parts to reduce the sharpness. Composite weather strip is stuck with hard rubber gripping on the door frame while the cross section acts as buffering. To prevent the excessive slamming force, punch in every certain distance. Such weather strip exhibits thick, safe and luxurious feel when slamming the door (Table 1).

(d) Door Sheet Metal Stiffness and Optimization of Damping Plate

Insufficient stiffness of door sheet metal will cause the resonance when slamming the door. The low-frequency drone it generated will lead to the prolonging of

Fig. 10 Tightness check



Fig. 11 Locking ring with a rubber coating



convergence time. Therefore, ensuring stiffness of door sheet metal and optimizing the layout of damping pads can effectively improve the sound quality of door slamming.

Figure 12 is the comparison of before and after optimization of door metal sheet of a four-door passenger car. When vibration convergence time decreased, the amplitude was significantly reduced.

(e) Door Frame Stiffness Optimization

If the stiffness of window frame is weak, modal under multiple frequencies will have a greater impact on the sound quality of door slamming. Figure 13 shows CAE analysis results of a door modal. The upper right corner of the door frame is weak in stiffness. The red section shows concentrated energy. It can be seen from

Table 1 Control measures for door slamming sound quality

Main contents	Control measures
Rebound analysis	Control amount of compression and rebound per unit length to ensure smooth door slamming
Salt spray test, environmental tests	Control durability of the weather strips to ensure long-term performance
Air vent check	Control air vent location to ensure natural exhaust
Bubble position, the amount and uniformity of compression check	Control the bubble position, compression ratio according to the door and body clearance
Variable cross-section analysis	Design different sections in accordance with door and body clearance to meet the requirements for sealing and rebound
Tightness check	Control weather strip performance of the vehicle

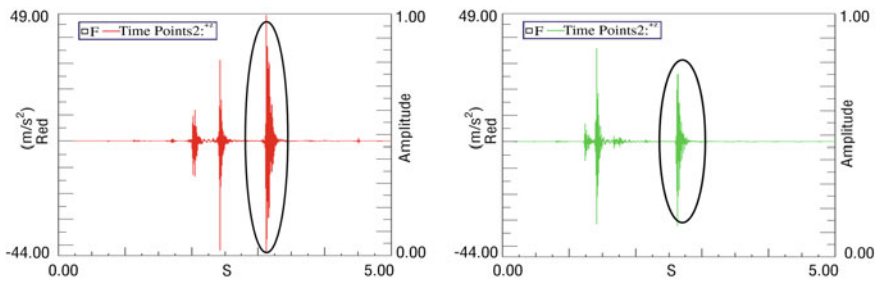


Fig. 12 Switch gate vibration pulse convergence map

Fig. 13 CAE modal analysis results for the door

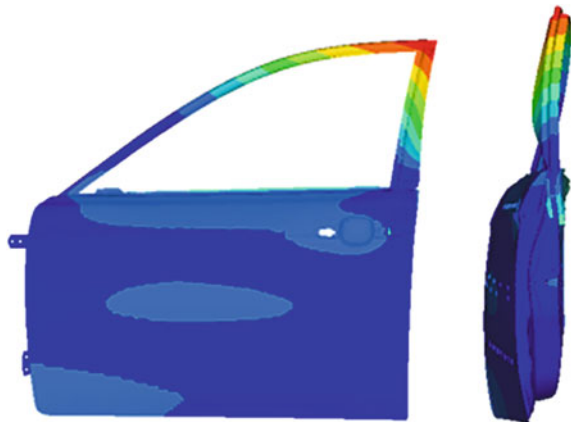


Fig. 14 Frequent and successive

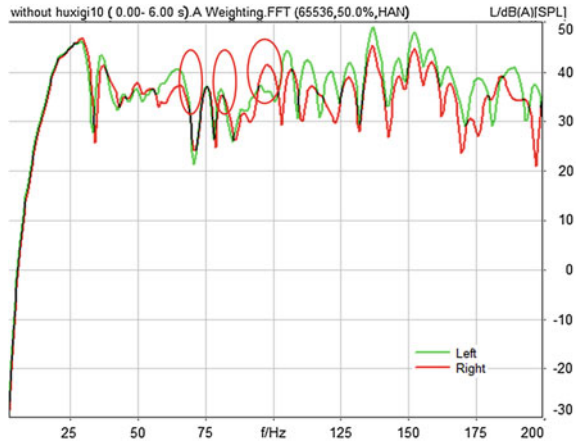


Fig. 15 Window frame model

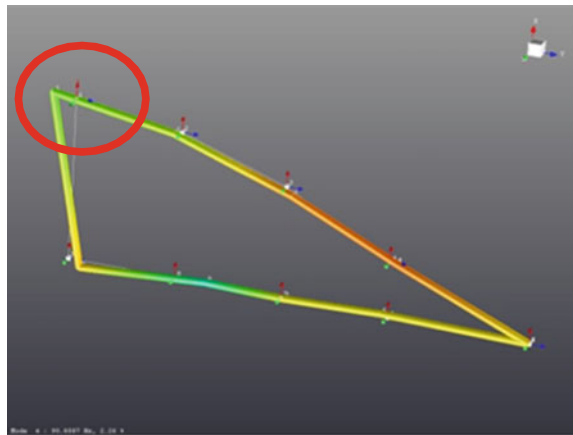


Fig. 13 that the concentrated energy is at the upper corner of door frame where the stiffness is insufficient.

As shown in the frequency spectrum of door slamming, obviously, peak values occur at 68, 75, 80 and 90 Hz, which infers that sound quality of door slamming is closely related to the door frame modal. And as illustrated in the vibration model, upper corner of door frame marked with circles vibrates severely. Such characteristics are displayed by many vibration models (Figs. 14, 15).

The stiffness of upper door frame shall be paid attention during the design phase. The CAE simulation analysis can be used to avoid the lack of stiffness in the later manufacture phase. Quality control and assembly uniformity in manufacturing process shall be emphasized.

5 Conclusions

The testing methods, evaluation methods and improvement measures for door slamming sound quality were introduced. Requirements of layout of microphone, door slamming force and speed were respectively described in the testing methods. Evaluation of door slamming sound quality were made in terms of pulse convergence time, sharpness, loudness, high-frequency noise convergence time, low-frequency duration and door uniformity. In addition, sound pressure level and sharpness are applied to evaluate the door opening sound quality. Accordingly, Improvements measures were taken with regard to door tightness, latch design, weather strips and contact location between the base and handle.

References

1. Xu X (2004) Based on the subjective feeling of the sound quality objective evaluation methods and applications. Hefei University of Technology
2. Shu G-Q, Liu N (2002) Vehicle and engine noise sound quality research and development automotive engineering (5)
3. Mao D, Yu W, Wang Z (2005) Statistical validation and criterion for paired comparison data in sound quality evaluation [J]. *Acta Acustica*
4. Hamilton D (1990) Sound quality of impulsive noise an applied study of automotive door closing sounds. SAE Paper 1999-01-1684